Cancer Cell

Volume 25
Number 4

April 14, 2014

www.cellpress.com

A Distal GATA2 Enhancer Drives Abnormal EVI1 Expression in AML

CellPress

Genomic Dark Matter Sheds Light on EVI1-Driven Leukemia

Richard P. Koche[1] and Scott A. Armstrong[1,*]
[1]Human Oncology and Pathogenesis Program and Department of Pediatrics, Memorial Sloan Kettering Cancer Center, New York, NY 10065, USA
*Correspondence: armstros@mskcc.org
http://dx.doi.org/10.1016/j.ccr.2014.03.031

The orchestration of transcriptional programs depends on proper gene-enhancer pairing. While much remains to be learned about this process in normal development, two recent studies in *Cell* (Gröschel and colleagues) and this issue of *Cancer Cell* (Yamazaki and colleagues) highlight how the genomic rearrangement of an enhancer plays a causal role in the onset of a leukemogenic program.

Genetic lesions are well-chronicled drivers of various malignancies, with evidence accumulating from early cytogenetic studies as well as modern molecular techniques. The majority of such techniques have placed an emphasis on the amplification, deletion, or rearrangement of coding sequences and have successfully identified hundreds of important drivers in cancer (Garraway and Lander, 2013). However, the vast expanse of noncoding sequence in mammalian genomes is known to contain regulatory elements that contribute to the control of gene expression and could therefore influence gene expression via mutation, rearrangement, deletion, or amplification. Precedence for the involvement of such elements in oncogenesis has been set by the demonstration that expression of MYC and other oncogenes can be deregulated in lymphoid cells via juxtaposition of the immunoglobulin heavy chain regulatory regions, which drive aberrant expression (ar-Rushdi et al., 1983). A more recent demonstration of the importance of mutations in regulatory regions was the identification of mutations in telomerase promoter regions in melanoma (Huang et al., 2013). However, it remains unclear how and to what extent deregulation of oncogene expression as a result of mutations in gene regulatory regions drives cancer pathogenesis.

Enhancer elements are regions of DNA that function as distal, nonpromoter, *cis*-acting regulators of gene expression that often operate in a tissue-specific manner. As an area that has not been queried by traditional technologies, such regulatory elements remain at the frontier in the study of both normal and aberrant gene expression, with the latter containing implications for the regulation of putative oncogenic drivers. Key challenges in the study of enhancers involve difficulties in their initial identification and the identification of the genes upon which they act. Advances in genome-wide measurements of transcription factor binding and chromatin state have begun to address the former, because enhancers can now be identified based on the presence of particular chromatin modifiers and histone modifications. With hundreds of thousands of putative enhancers identified in the human genome, it is now imperative that they be linked to their respective genes in the context of both normal development and pathogenesis. Enhancer function can be affected by factors that bind to the enhancer, chromatin modifications associated with enhancers, lineage-specific signaling pathways, and mutations altering the enhancer sequence itself; the importance of these elements in cancer is only beginning to be explored (Herz et al., 2014).

EVI1 is a proto-oncogenic transcription factor involved in the regulation of hematopoietic stem cells, and its overexpression has been linked to acute myeloid leukemia (AML) and myelodysplastic syndrome (MDS) and carries a poor prognosis (Glass et al., 2014). EVI1 deregulation is often accompanied by a nearby inversion inv(3) or translocation t(3;3) of largely nongenic sequence, but mechanistic links between these rearrangements and EVI1 expression changes have remained poorly understood. Two new studies utilize orthogonal approaches to dissect the regulatory potential of these sequences and subsequently discover how the genomic rearrangement of a single enhancer element disrupts the regulation of two genes involved in the onset of AML (Figure 1).

In a recent study published in *Cell*, Gröschel et al. (2014) utilized functional genomics and genome editing to characterize chromosome 3q-rearrangements in primary AML samples and human cell lines. Using an effective combination of chromosome conformation capture with ChIP-seq and RNA-seq, the authors isolated a 9 kb element within commonly translocated sequences, which physically contacted the EVI1 promoter and stimulated its expression. Analysis of p300 binding further allowed the elucidation of a putative enhancer element, the excision of which was shown to reduce EVI1 expression and limit proliferation, with a marked skewing toward myelomonocytic differentiation. These changes were largely phenocopied by EVI1 knockdown. Further classification of the region surrounding the enhancer indicated that it may function as part of a so-called super enhancer, with a characteristic H3K27ac pattern and BRD4 binding (Whyte et al., 2013). As such, cell lines containing the 3q-rearrangements were more responsive to the BET bromodomain inhibitor JQ1 and exhibited proliferation defects and reduced EVI1 expression.

In a complementary study in this issue of *Cancer Cell*, Yamazaki et al. (2014) took advantage of a bacterial artificial chromosome (BAC) system to recapitulate a human 3q-rearranged leukemia in a mouse model. To this end, they utilized a linked BAC strategy to precisely generate the inv(3)(q21;q26) inversion found in the human MOLM-1 leukemia

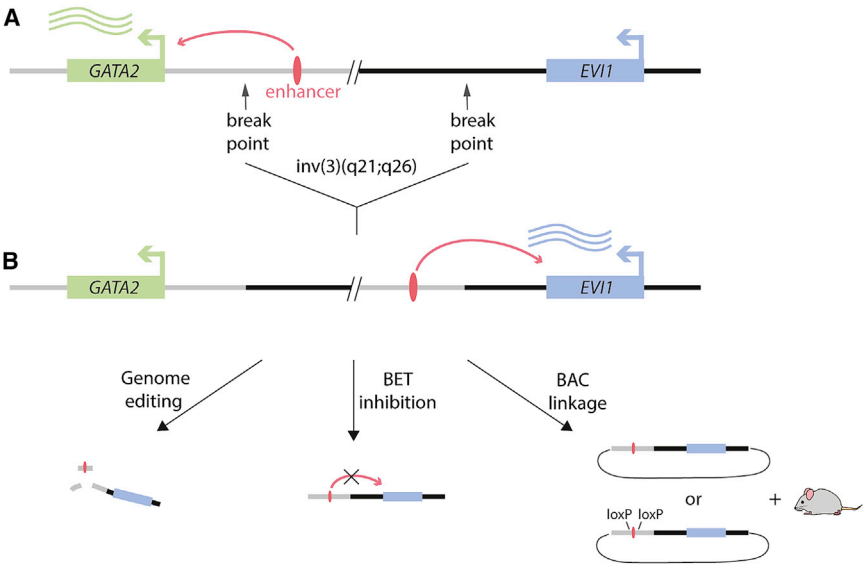

Figure 1. A Single Enhancer Rearrangement Deregulates Two Oncogenic Drivers

(A) The distal enhancer normally drives GATA2 expression in a myeloid-specific manner. Inversion or translocation of the locus simultaneously results in functional haploinsufficiency of *GATA2* and upregulation of EVI1.

(B) The enhancer can be deactivated through genome editing or pharmacologic BET inhibition. A novel BAC-linking strategy allowed a faithful recapitulation of the rearrangement and disease in a mouse model.

cell line with and without the putative enhancer element. They also generated a control BAC containing the truncated *EVI1* gene alone. The resulting transgenic mice underwent molecular and phenotypic profiling. The human *EVI1* gene was elevated in expression relative to the endogenous mouse copy in hematopoietic stem and progenitor cells and related compartments. The contribution of the enhancer was best demonstrated by the onset of hematologic pathologies. Mice harboring BACs with the full inversion developed splenomegaly and transplantable leukemias, whereas those with enhancer-deleted BACs resembled control mice. The leukemias showed both myeloid and lymphoid properties, and, although it is unknown how this arises, it is in agreement with a recent finding that EVI1 is expressed in a subset of pediatric acute lymphoblastic leukemias (Konantz et al., 2013).

Both studies establish that the regulatory element in question is a distal enhancer of *GATA2* in the context of the wild-type allele. In Gröschel et al. (2014), the enhancer-*EVI1* reporter assays established a pattern of cell type-specific activity, indicating enhancer dependence on the repertoire of available trans factors in the myeloid lineage, which was their first hint that the enhancer does not belong to the ubiquitous housekeeping gene *RPN1* as previously hypothesized. Indeed, further allele-specific analysis confirmed that the enhancer normally acts on *GATA2* and that the 3q rearrangement results in the functional haploinsufficiency of *GATA2*. Similarly, Yamazaki et al. (2014) began their study by demonstrating that a conserved homologous sequence in mouse is acting as a hematopoietic-specific distal enhancer of *GATA2*. Since GATA2 depletion has been linked to AML, MDS, and Emberger/MonoMAC syndromes (Bresnick et al., 2012), this highlights the possibility of a single enhancer rearrangement resulting in the simultaneous upregulation of a proto-oncogene and downregulation of a tumor suppressor gene in a spatiotemporal specific manner.

Taken together, these two studies emphasize the importance of noncoding regulatory sequence rearrangements as a driving mechanism for leukemogenesis. While one paper takes advantage of genomic tools to characterize human samples and at least one potential therapeutic outlet, the other study establishes a technique for the precise recapitulation of genomic rearrangements for full in vivo characterization in mouse models. However, it should be noted that there may be important ways in which the mouse models differ from the human leukemias. For example, when using human BACs to express the translocated enhancer, the mice do not have the haploinsufficiency of *GATA2* as seen in the human cells. Such a difference may lend insight into the contribution of decreased GATA2 expression in leukemogenesis and requires further study. Regardless, these findings illuminate a path to better characterize the mechanistic and therapeutic implications of non-genic rearrangements and further highlight the fact that a next frontier for cancer genomics will focus on the importance of mutations residing outside the coding exome.

ACKNOWLEDGMENTS

R.P.K. and S.A.A. are supported by grants from the National Cancer Institute and The Leukemia and Lymphoma Society.

REFERENCES

ar-Rushdi, A., Nishikura, K., Erikson, J., Watt, R., Rovera, G., and Croce, C.M. (1983). Science *222*, 390–393.

Bresnick, E.H., Katsumura, K.R., Lee, H.Y., Johnson, K.D., and Perkins, A.S. (2012). Nucleic Acids Res. *40*, 5819–5831.

Garraway, L.A., and Lander, E.S. (2013). Cell *153*, 17–37.

Glass, C., Wilson, M., Gonzalez, R., Zhang, Y., and Perkins, A.S. (2014). Blood Cells Mol. Dis. Published online February 1, 2014. http://dx.doi.org/10.1016/j.bcmd.2014.01.002.

Gröschel, S., Sanders, M.A., Hoogenboezem, R., de Wit, E., Bouwman, B.A.M., Erpelinck, C., van der Velden, V.H.J., Havermans, M., Avellino, R., van Lom, K., et al. (2014). Cell *157*, 369–381.

Herz, H.M., Hu, D., and Shilatifard, A. (2014). Mol. Cell *53*, 859–866.

Huang, F.W., Hodis, E., Xu, M.J., Kryukov, G.V., Chin, L., and Garraway, L.A. (2013). Science *339*, 957–959.

Konantz, M., André, M.C., Ebinger, M., Grauer, M., Wang, H., Grzywna, S., Rothfuss, O.C., Lehle, S., Kustikova, O.S., Salih, H.R., et al. (2013). Leukemia *27*, 56–65.

Whyte, W.A., Orlando, D.A., Hnisz, D., Abraham, B.J., Lin, C.Y., Kagey, M.H., Rahl, P.B., Lee, T.I., and Young, R.A. (2013). Cell *153*, 307–319.

Yamazaki, H., Suzuki, M., Otsuki, A., Shimizu, R., Bresnick, E.H., Engel, J.D., and Yamamoto, M.A. (2014). Cancer Cell *25*, this issue, 415–427.

CellPress

Next-Generation Genomic Profiling of Hepatocellular Adenomas: A New Era of Individualized Patient Care

Jens U. Marquardt[1,2,*] and Snorri S. Thorgeirsson[1,*]
[1]Laboratory of Experimental Carcinogenesis (LEC), Center for Cancer Research, National Cancer Institute, NIH, 37 Convent Drive, Room 4146, Bethesda, MD 20892, USA
[2]Department of Medicine I, Johannes Gutenberg University, 55131 Mainz, Germany
*Correspondence: marquarj@uni-mainz.de (J.U.M.), snorri_thorgeirsson@nih.gov (S.S.T.)
http://dx.doi.org/10.1016/j.ccr.2014.03.032

Hepatocellular adenomas (HCAs) are clinically relevant benign liver lesions that commonly occur in women on hormonal contraceptives. In this issue of *Cancer Cell*, Pilati and colleagues present an integrative multi-"omics"-based analysis of HCA and identify recurrent genetic alterations associated with adenoma-carcinoma transition and new drugable targets.

Hepatocellular adenomas (HCAs) are hormone-sensitive monoclonal benign liver lesions that are associated with the use of estrogen rich contraceptives or androgen-containing steroid anabolics. Most frequently, HCAs develop in noncirrhotic livers, displaying a clear gender disparity with a female/male ratio of 9:1 (Bioulac-Sage et al., 2011). Also, HCAs are rarely associated with hereditary metabolic disorders (i.e., glycogen storage defects). Although only a small fraction of HCAs cause clinical symptoms or undergo malignant transformation, accurate evaluation of this probability is essential for appropriate treatment.

Significant progress has been achieved on the basis of mutational analyses as well as distinct histological and radiological features, pioneered by strong French consortia, resulting in the classification of HCAs into four subtypes (Nault et al., 2013a):

(1) Hepatocyte nuclear factor 1 (HNF1α)-mutated HCAs (HHCAs) constitute 30% to 40% of all adenomas mainly characterized by disrupted glucose and lipid metabolism, leading to steatosis and downregulation of LFABP. Genomic analyses identified recurrent losses of heterozygosity at chromosome 12q, with subsequent analyses that revealed biallelic somatic mutations in the *HNF1A* gene. HHCAs are associated with maturity-onset diabetes type 3, a monogenic non-insulin-dependent diabetes (Bluteau et al., 2002).

(2) Telangiectatic/inflammatory adenomas (IHCAs) harbor activating in-frame somatic mutations in gp130-encoding *IL6ST* or, less frequently, in *GNAS* or *STAT3*. IHCAs show polymorphic inflammatory infiltrates, dystrophic vessels, and sinusoidal dilatations and constitute around 40% to 50% of all adenomas (Rebouissou et al., 2009). The cardinal feature of IHCAs is the activation of the JAK/STAT pathway (Pilati et al., 2011); however, concomitant mutations in β-catenin are observed in up to 50% of IHCAs (i.e., bIHCA).

(3) β-catenin-mutated adenomas (bHCAs) constitute approximately 10% to 15% of all HCAs, displaying cytological abnormalities including acinar pattern and cholestatic changes. Activating mutations of β-catenin are mainly localized in exon 3. Interestingly, mutations in the pathway, while overlapping with other subtypes (e.g., bIHCA), are mutually exclusive with *HNF1A* mutations. bHCAs have the highest potential of malignant transformation into hepatocellular carcinoma (HCC), ranging from 0%–18% and representing two thirds of all transformed HCAs (Farges et al., 2011). Interestingly, prevalence of malignancy in bHCA is ten times higher in men than women and is associated with metabolic changes. Identification of this subtype has the most important clinical implications for patient management (e.g., withdrawal of androgens or resection).

(4) Around 10% of HCAs show no specific morphological or immunophenotypical patterns and are, therefore, termed unclassified HCA (UHCA).

In this issue of *Cancer Cell*, Pilati et al. (2014) report further refinement of the molecular understanding of HCAs by using integrative genomic analyses combining multiple molecular layers. Due to a large collection of representative HCA samples and the use of next-generation sequencing in combination with other genomic technologies, the results provide several exciting clinical as well as mechanistic inferences (Figure 1).

The study included 250 tumors from 195 patients and is the largest to date. The cohort was well balanced regarding gender (male:female, 1:6), etiology (84% oral contraceptives), and subtypes (HHCA, 29%; bHCA, 14%; bIHCA, 16%; IHCA, 31%; UHCA, 10%). The study also included 18 HCAs with malignant transformation into HCC. The authors initially screened 35 tumors by a whole-exome sequencing approach. The analyses yielded the identification and subsequent validation of 264/508 somatic mutations as potentially protein altering. Interestingly, compared to other malignant solid tumors such as colon, lung, and pancreatic cancers with an average of 33 to 66 protein damaging mutations (Vogelstein et al., 2013) and, in particular, HCC with around 41 mutations, the genomes of HCAs appear relatively stable with an average rate of damaging mutations of 7.5. Among the mutations, only *CTNNB1*, *IL6ST*, *HNF1A*, and FRK were recurrently mutated in at least three HCAs. Of note, paired analyses of different tumors in the same patients suggested an independent development of the lesions, potentially indicating that multiple biopsies might be warranted in patients with multifocal disease.

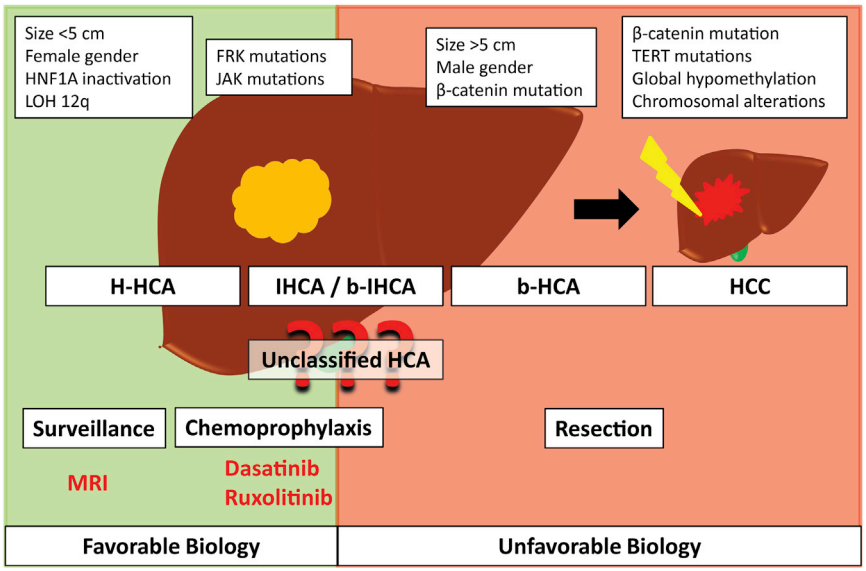

Figure 1. Several Risk Factors Predicting the Biological Traits of HCAs and Associated Complications, i.e., Hemorrhage and Malignant Transformation, Have Been Identified
Overall, HHCAs possess a relatively low risk of malignant transformation. Therefore, surveillance by imaging (e.g., MRI) seems justified. β-catenin mutations, regardless of the subtype, increased adenoma-carcinoma transition. The study by Pilati et al. (2014) further identifies a fraction of IHCA with drugable mutations in FRK and JAK1 that could benefit from chemoprophylaxis with the SRC inhibitor dasatinib or the JAK inhibitor ruxolitinib, respectively. Resection should be evaluated in all large HCAs (>5 cm) or HCAs that develop in male patients regardless of the molecular subtype. In small HCAs (<5 cm), the decision for surgery should be based on the presence of β-catenin mutation. Furthermore, TERT mutations confer a higher risk of malignant transformation in β-catenin mutated HCAs. Given the clinical implication from the present work and the importance of histological and detailed molecular evaluation for the rational and individualized management of HCAs, the need for obtaining a liver biopsy is imperative.

Subsequent validation of selected genes in the whole cohort not only nicely recapitulated the known driver mutations of the corresponding subtype, but also confirmed the presence of previously unrecognized somatic mutations in FRK, a member of the SRC kinase family, as well as JAK1. A total of 12 IHCA/bIHCA showed activating FRK mutations in two hot spots of the tyrosine kinase catalytic domain, thereby constituting the second most frequent alterations in IHCA. Gain-of-function analyses of mutant FRK induced a strong inflammatory response in a STAT3-dependent manner, but independent of interleukin-6 exposure. Consistently, administration of the SRC inhibitor dasatinib significantly reduced the oncogenic activity of FRK mutants, suggesting that the proliferative characteristics of these IHCAs are mainly driven by FRK-dependent oncogene addiction and are likely to benefit from SRC inhibition. Furthermore, the JAK1 mutation in one IHCA also induced STAT3 activation. Interestingly, protein-altering JAK1 mutations in S703I and S729C have been previously recognized in around 9% of HCCs (Kan et al., 2013). In this study JAK1-mutated hepatoma cells significantly responded to in vitro exposure to the JAK1/2 inhibitor ruxolitinib. These results suggest that the JAK1 inhibition might also be an effective therapeutic approach in the affected IHCAs.

The authors also performed integrative analyses of copy-number alterations and methylome profiling and accurately recapitulated the different molecular subclasses. While the overall frequency of copy-number alterations was relatively low, several recurrent chromosomal changes specific for HHCA were identified. Methylome analyses showed that DNA methylation particularly affect gene expression in this subtype. Furthermore, a progressive increase in chromosomal instability as well as somatic mutations in addition to global hypomethylation was observed during transition from HCA into HCC. However, more detailed investigations are needed to determine if epigenetic changes predispose specific genetic alterations or vice versa (Jones and Baylin, 2007). Nevertheless, mutational analyses confirmed that mutations in *CTNNB1* are a prerequisite for the transition into HCC. However, while results from one patient suggested that *CTNNB1* mutations occur relatively early, additional genetic alterations are necessary to promote tumor progression, indicating a two-hit model of malignant transformation in HCA. Interestingly, acquisition of activating somatic TERT promoter mutations appears to be a major genetic driver promoting the adenoma-carcinoma sequence in β-catenin-activated HCA. These investigations are in agreement with recent findings indicating that TERT promoter activation are among the earliest and most frequent alterations in HCC (Nault et al., 2013b). Therefore, bHCA and bIHCA should be closely monitored for both alterations to effectively guide treatment decisions.

In summary, the present work does not only generate prognostic information for patients at risk for malignant transformation, but also identifies molecular targets for novel therapeutic approaches in HCA and predicts a corresponding subclass of patients that are likely to benefit from a specific chemoprophylaxis. This is achieved by effective integration of genetic and genomic characteristics of the neoplastic lesions, and the current study is a splendid example of how the bench-to-bedside/translational use of next-generation technologies can directly impact and guide clinical decision making.

ACKNOWLEDGMENTS

J.U.M. is supported by a grant from the German Research Foundation (MA 4443/2-1).

REFERENCES

Bioulac-Sage, P., Cubel, G., Balabaud, C., and Zucman-Rossi, J. (2011). Semin. Liver Dis. *31*, 91–103.

Bluteau, O., Jeannot, E., Bioulac-Sage, P., Marqués, J.M., Blanc, J.F., Bui, H., Beaudoin, J.C., Franco, D., Balabaud, C., Laurent-Puig, P., and Zucman-Rossi, J. (2002). Nat. Genet. *32*, 312–315.

Farges, O., Ferreira, N., Dokmak, S., Belghiti, J., Bedossa, P., and Paradis, V. (2011). Gut *60*, 85–89.

Jones, P.A., and Baylin, S.B. (2007). Cell *128*, 683–692.

Kan, Z., Zheng, H., Liu, X., Li, S., Barber, T.D., Gong, Z., Gao, H., Hao, K., Willard, M.D., Xu, J., et al. (2013). Genome Res. *23*, 1422–1433.

Nault, J.C., Bioulac-Sage, P., and Zucman-Rossi, J. (2013a). Gastroenterology *144*, 888–902.

Nault, J.C., Mallet, M., Pilati, C., Calderaro, J., Bioulac-Sage, P., Laurent, C., Laurent, A., Cherqui, D., Balabaud, C., and Zucman-Rossi, J. (2013b). Nat. Commun. *4*, 2218.

Pilati, C., Amessou, M., Bihl, M.P., Balabaud, C., Nhieu, J.T., Paradis, V., Nault, J.C., Izard, T., Bioulac-Sage, P., Couchy, G., et al. (2011). J. Exp. Med. *208*, 1359–1366.

Pilati, C., Letouzé, E., Nault, J.-C., Imbeaud, S., Boulai, A., Calderaro, J., Poussin, K., Franconi, A., Couchy, G., Morcrette, G., et al. (2014). Cancer Cell *25*, this issue, 428–441.

Rebouissou, S., Amessou, M., Couchy, G., Poussin, K., Imbeaud, S., Pilati, C., Izard, T., Balabaud, C., Bioulac-Sage, P., and Zucman-Rossi, J. (2009). Nature *457*, 200–204.

Vogelstein, B., Papadopoulos, N., Velculescu, V.E., Zhou, S., Diaz, L.A., Jr., and Kinzler, K.W. (2013). Science *339*, 1546–1558.

Harnessing the Hidden Antitumor Power of the MLL-AF4 Oncogene to Fight Leukemia

Smita Matkar,[1] Bryson W. Katona,[1] and Xianxin Hua[1,*]
[1]Abramson Family Cancer Research Institute, Department of Cancer Biology, University of Pennsylvania Perelman School of Medicine, 421 Curie Boulevard, Philadelphia, PA 19104, USA
*Correspondence: huax@mail.med.upenn.edu
http://dx.doi.org/10.1016/j.ccr.2014.03.028

It is unclear whether the antiproliferative/proapoptotic activity of oncogenes can be pharmacologically reactivated in cancer cells. In this issue of *Cancer Cell*, Liu and colleagues report that a proteasome inhibitor reactivates an MLL-AF4 controlled antitumor program to kill leukemia cells in an oncogene dose- and cell type-dependent manner.

Oncogenes, such as constitutively activated Ras, can drive tumorigenesis; therefore, it was initially unexpected that oncogenes also possess contextual antitumor activities like causing apoptosis and cell senescence (Lowe et al., 2004; Serrano et al., 1997). It was later found that while activated oncogenes initially trigger antitumor processes in cells, they eventually lose their antitumor activity and drive tumorigenesis in a temporal and contextual manner (Lowe et al., 2004). However, it remains unclear whether the often hidden antitumor action of a particular oncogene can be reactivated pharmacologically and utilized to specifically target cancer cells. A definitive answer to this question would unravel the mechanisms choreographing the "Jekyll and Hyde" actions of oncogenes, i.e., antitumor versus oncogenic activity, and shed light on how to improve cancer therapy. In this regard, Liu et al. (2014) report in this issue of *Cancer Cell* that when pro-B *m*ixed *l*ineage *l*eukemia (MLL) cells are treated with a proteasome inhibitor, the MLL-AF4 protein level increases and subsequently triggers an antitumor program in concert with the pro-B cell-specific transcription factor PAX5. This antitumor program induces both the antiproliferative p27kip, encoded by *CDKN1B* and proapoptotic caspase-8, and ultimately leads to specific suppression of pro-B MLL-AF4 leukemia.

MLL is classified as a group of acute leukemias, often refractory to chemotherapy and with poor overall prognosis, that expresses one of a number of different leukemogenic fusion genes consisting of the 5′ part of *MLL* fused to one of many genes from other chromosomes (Krivtsov and Armstrong, 2007). MLL fusion proteins (MLL-FPs), in concert with the wild-type MLL protein (Thiel et al., 2010), drive leukemogenesis mainly through inducing the expression of HOX genes (Ayton and Cleary, 2003; Milne et al., 2002). Expression of MLL-AF4 tends to cause B cell lymphoblastic leukemia (Krivtsov et al., 2008).

The authors previously reported that MLL-FPs are regulated in leukemia cells via proteolysis by the proteasome (Liu et al., 2007), a molecular machine specialized in degrading proteins. Unlike many oncogenes that are highly expressed in cancer cells, MLL-AF4 tends to be expressed at low levels in leukemia cells. To address this distinct feature of MLL-AF4, Liu and colleagues investigated whether increased levels of MLL-AF4 leads to suppression of leukemia cells. They treated various human leukemia cell lines with the proteasome inhibitor bortezomib, which is approved for the treatment of multiple myeloma, to inhibit MLL-AF4 degradation. Many key proteins controlling cell survival and proliferation are regulated by proteasome-mediated proteolysis, and their levels are often increased by treatment with bortezomib (Frankland-Searby and Bhaumik, 2012). Bortezomib increased levels of wild-type MLL as well as MLL fusion proteins in all tested leukemia cell lines. Interestingly, pro-B MLL leukemia cell lines were more sensitive to bortezomib-induced G2/M cell cycle arrest and apoptosis when compared to non-MLL pro-B leukemia cell lines, whereas all of the cell lines showed similar sensitivity to other chemotherapeutic agents. Based on these findings, the authors suspected that MLL-AF4 participates in bortezomib-induced cytotoxicity in the pro-B MLL leukemia cells.

To explore this possibility, they demonstrated that selective knockdown of

MLL-AF4 led to a reduction in bortezomib-induced apoptosis in the pro-B MLL leukemia cells. Consistently, ectopic expression of MLL-AF4 cDNA in non-MLL pro-B leukemia cells enhanced their sensitivity to bortezomib-induced cytotoxicity, while ectopic expression of N-terminal MLL alone without a fusion partner failed to enhance the sensitivity to bortezomib. Collectively, these findings uncover a crucial role for MLL-AF4 in mediating bortezomib-induced cytotoxicity in pro-B MLL leukemia cells, but not in MLL-FP acute myeloid leukemia (AML) cells.

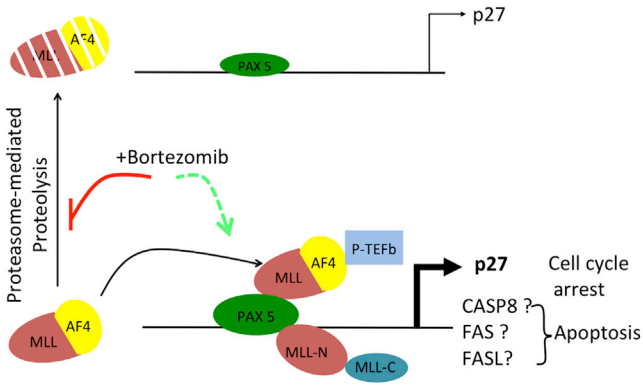

Figure 1. A Model for Proteasome Inhibitor-Induced Increase of the MLL-AF4 Level and Induction of PAX5-Dependent Transcription of p27 in Pro-B MLL-AF4 Leukemia Cells.

The proteins are not drawn to scale, nor is the protein complex precisely stoichiometric as shown.

Liu et al. (2014) further explored how bortezomib induces apoptosis in pro-B MLL-AF4 leukemia cells. They found that bortezomib induced expression of FAS, FAS ligand, and caspase-8, all important components of an apoptotic cascade, but did not affect the classic targets of MLL-FPs such as HOXA9 and MEIS1. This suggests that the increased level of MLL-AF4 induced by bortezomib is important for inducing expression of these apoptotic genes, whereas other classic MLL-FP targets such as HOXA9 and MEIS1 might already be expressed at a maximal level, thus preventing their expression from being further augmented by additional MLL-AF4. However, whether MLL-AF4 is directly involved in upregulating transcription of these proapoptotic genes remains unclear.

Next, the authors investigated the mechanism of bortezomib-induced cell cycle arrest in the pro-B MLL leukemia cells. They demonstrated that bortezomib treatment substantially upregulated p27 at both the mRNA and protein levels, while levels of other cell cycle proteins remained unchanged. Upregulation of p27 was dependent on the MLL-AF4 level as MLL-AF4 knockdown attenuated bortezomib-induced p27 expression. Wild-type MLL may play a role in the upregulation of p27, because concurrent knockdown of both MLL-AF4 and MLL impaired the induction of p27 to a greater degree than knocking down MLL-AF4 alone. Using a chromatin immunoprecipitation (ChIP) assay, Liu et al. (2014) found that bortezomib increased recruitment of MLL and MLL-AF4 at the *CDKN1B* promoter along with P-TEFb, resulting in enhanced p27 expression (Figure 1).

However, these results still beg the question of why MLL-AF4 is only critical for bortezomib-induced cytotoxicity in pro-B MLL leukemia cells, but not in MLL-FP AML cells. To address this issue, the authors explored the possibility that pro-B cell-specific transcription factors PAX5 and EBF1 may crosstalk with MLL-AF4 to enhance transcription of target genes and found that indeed PAX5 interacted with MLL-AF4. Moreover, PAX5 was essential for bortezomib-mediated induction of p27 as PAX5 knockdown blocked the increase in p27 levels. Furthermore, ChIP assay, coupled with PAX5 knockdown, showed that PAX5 is required for recruiting MLL/MLL-AF4 to the *CDKN1B* promoter. However, PAX5 overexpression alone was not sufficient to sensitize MLL-AF9 containing THP1 cells (AML cells) to bortezomib, indicating additional factors may also be critical in pro-B cells. Collectively, these data strongly suggest that bortezomib induces expression of p27 by PAX5-mediated recruitment of MLL-AF4 and P-TEFb (Figure 1).

Next, the authors determined whether bortezomib selectively suppresses human pro-B MLL-AF4 leukemia in vivo. They transplanted MLL-AF4 pro-B or non-MLL pro-B leukemia cells into immunodeficient NOD-*scid Il2rg*$^{-/-}$ mice, followed by treatment with or without bortezomib. Consistently, they found that bortezomib reduced the leukemia burden in mice with pro-B MLL-AF4 leukemia, but not those with non-MLL pro-B leukemia. Furthermore, they also showed the effectiveness of bortezomib for certain pro-B MLL leukemia patients in a small number of patients. Given these results, it is also interesting to speculate whether other FDA-approved chromatin modifying drugs, such as deacetylase inhibitors or DNA methyltransferase inhibitors, can also synergize with bortezomib to raise MLL-AF4 levels and increase MLL-AF4 antitumor target genes to suppress pro-B MLL-AF4 leukemia.

In summary, Liu et al. (2014) have shown that a clinically effective proteasome inhibitor switches on the hidden molecular tumor-suppressing networks mediated by the leukemogenic MLL-AF4 in an oncogene dose- and cell type-specific manner. These findings demonstrate that the hidden antitumor function of an oncogene can be reactivated pharmacologically through the use of an FDA-approved proteasome inhibitor. Practically, these studies highlight the intriguing possibility that stratification of leukemias based on both their underlying oncogenic driver mutations, such as MLL-AF4, and their cell type may ultimately guide the precise choice of therapeutic agents, which may soon include proteasome inhibitors.

ACKNOWLEDGMENTS

We thank Drs. Alan Diehl and Warren Pear for stimulating discussions. This work was supported in part by grants from the NIH (R01-DK085121), Caring for Carcinoid Foundation-AACR Grant Care for Carcinoid Foundation (11-60-33), a TRP grant from the Leukemia and Lymphoma Society, and a pilot grant from ITMAT of the University of Pennsylvania.

REFERENCES

Ayton, P.M., and Cleary, M.L. (2003). Genes Dev. *17*, 2298–2307.

Frankland-Searby, S., and Bhaumik, S.R. (2012). Biochim. Biophys. Acta *1825*, 64–76.

Krivtsov, A.V., and Armstrong, S.A. (2007). Nat. Rev. Cancer *7*, 823–833.

Krivtsov, A.V., Feng, Z., Lemieux, M.E., Faber, J., Vempati, S., Sinha, A.U., Xia, X., Jesneck, J.,

Bracken, A.P., Silverman, L.B., et al. (2008). Cancer Cell *14*, 355–368.

Liu, H., Cheng, E.H., and Hsieh, J.J. (2007). Genes Dev. *21*, 2385–2398.

Liu, H., Westergard, T.D., Cashen, A., Piwnica-Worms, D.R., Kumkle, L., Vij, R., Pham, C.G., Dipersio, J., Cheng, E.H., and Hsieh, J.J. (2014). Cancer Cell *25*, this issue, 530–542.

Lowe, S.W., Cepero, E., and Evan, G. (2004). Nature *432*, 307–315.

Milne, T.A., Briggs, S.D., Brock, H.W., Martin, M.E., Gibbs, D., Allis, C.D., and Hess, J.L. (2002). Mol. Cell *10*, 1107–1117.

Serrano, M., Lin, A.W., McCurrach, M.E., Beach, D., and Lowe, S.W. (1997). Cell *88*, 593–602.

Thiel, A.T., Blessington, P., Zou, T., Feather, D., Wu, X., Yan, J., Zhang, H., Liu, Z., Ernst, P., Koretzky, G.A., and Hua, X. (2010). Cancer Cell *17*, 148–159.

Cancer Cell
Article

A Remote *GATA2* Hematopoietic Enhancer Drives Leukemogenesis in inv(3)(q21;q26) by Activating *EVI1* Expression

Hiromi Yamazaki,[1,7] Mikiko Suzuki,[2,3,7] Akihito Otsuki,[1] Ritsuko Shimizu,[3] Emery H. Bresnick,[5] James Douglas Engel,[6] and Masayuki Yamamoto[1,4,*]
[1]Department of Medical Biochemistry
[2]Center for Radioisotope Sciences
[3]Department of Molecular Hematology
Tohoku University Graduate School of Medicine, Sendai 980-8575, Japan
[4]Tohoku Medical Megabank, Tohoku University, Sendai 980-8573, Japan
[5]UW-Madison Blood Research Program, Carbone Cancer Center, Department of Cell and Regenerative Biology, University of Wisconsin School of Medicine and Public Health, Madison, WI 53705, USA
[6]Department of Cell and Developmental Biology, University of Michigan Medical School, Ann Arbor, MI 48109, USA
[7]These authors contributed equally to this work
*Correspondence: masiyamamoto@med.tohoku.ac.jp
http://dx.doi.org/10.1016/j.ccr.2014.02.008

SUMMARY

Chromosomal inversion between 3q21 and 3q26 results in high-risk acute myeloid leukemia (AML). In this study, we identified a mechanism whereby a *GATA2* distal hematopoietic enhancer (G2DHE or −77-kb enhancer) is brought into close proximity to the *EVI1* gene in inv(3)(q21;q26) inversions, leading to leukemogenesis. We examined the contribution of G2DHE to leukemogenesis by creating a bacterial artificial chromosome (BAC) transgenic model that recapitulates the inv(3)(q21;q26) allele. Transgenic mice harboring a linked BAC developed leukemia accompanied by *EVI1* overexpression—neoplasia that was not detected in mice bearing the same transgene but that was missing the *GATA2* enhancer. These results establish the mechanistic basis underlying the pathogenesis of a severe form of leukemia through aberrant expression of the *EVI1* proto-oncogene.

INTRODUCTION

Leukemias are often induced by the rearrangement of chromosomes through translocations or inversions (Mitelman et al., 2007; Rowley, 2001). These chromosomal rearrangements can result in two types of abnormalities. The majority result in coding sequence fusions whereby a new protein is created. For example, in chronic myeloid leukemia, the t(9;22)(q34;q11) translocation creates a BCR-ABL fusion protein that functions as a constitutively active form of ABL tyrosine kinase (Rowley, 1973). A minor form of proto-oncogene activation is induced by linking the coding sequences of one gene to the regulatory sequences of a second gene, but approaches for exploring the underlying mechanisms by which regulatory sequence changes cause leukemias have proven to be technically challenging. One example of the latter mechanism occurs when *MYC* (located on 8q24) is placed under the regulatory control of the immunoglobulin heavy chain (*IGH*) locus on 14q32, thus creating the t(8;14)(q24;q32) translocation allele (ar-Rushdi et al., 1983).

In this regard, *EVI1* is known to be a proto-oncogene that can be activated by chromosomal translocation and inversion (Morishita et al., 1992), although the underlying mechanisms that lead

Significance

Chromosomal rearrangements commonly create fusion oncoproteins but can also induce leukemia by linking foreign enhancer elements to proto-oncogenes, resulting in their misexpression. Misexpression of the human *EVI1* gene caused by translocation or inversion between 3q21 and 3q26 induces an acute myelogenous leukemia that has a poor prognosis. In this study, we determined that a distant *GATA2* hematopoietic enhancer on 3q21 misdirects *EVI1* expression on 3q26 when inverted and that this enhancer is critical for AML neoplasia. This finding suggests potential strategies for therapies that target regulatory regions that misdirect the activity of proto-oncogenes. Additionally, this model establishes a mechanism for studying leukemias using transgenic BACs as a powerful way to create and analyze various human cancers that result from chromosomal rearrangements.

to leukemia are obscure. EVI1 is a transcription factor that is required for maintenance of hematopoietic stem cells (Goyama et al., 2008), and overexpression of EVI1 has been observed in high-risk myelodysplastic syndrome (MDS) and acute myeloid leukemia (AML) (Lugthart et al., 2008). Indeed, EVI1 harbors several hallmark functions that are normally associated with leukemogenesis, with the following four possibly being the most intriguing. First, EVI1 regulates the transcription of the transcription factor genes *GATA2* and *PBX1*, both of which play critical roles in the maintenance of hematopoietic stem cells, as well as the tumor suppressor gene *PTEN* (Sato et al., 2008; Shimabe et al., 2009; Yoshimi et al., 2011; Yuasa et al., 2005). Second, EVI1 binds to the transcription factors RUNX1, PU.1, and GATA1, thereby inhibiting their activity and blocking the differentiation of hematopoietic progenitors (Laricchia-Robbio et al., 2006, 2009; Senyuk et al., 2007). Third, EVI1 interacts with multiple epigenetic modification enzymes, each of which can alter specific target gene expression profiles (Chi et al., 2003; Goyama et al., 2010; Izutsu et al., 2001; Lugthart et al., 2011; Shimahara et al., 2010; Spensberger et al., 2008; Yoshimi et al., 2011). Fourth, forced EVI1 overexpression disrupts normal centrosome duplication, creating increased genomic instability (Stein et al., 2010).

It has been reported that both t(3;3)(q21;q26) and inv(3)(q21;q26) chromosomal translocation and inversion between 3q21 and 3q26, respectively, cause inappropriate *EVI1* gene expression (Morishita et al., 1992; Suzukawa et al., 1994). In both the translocated and inverted alleles, 3q21 has been shown to always include sequences both 5′ and 3′ to the *EVI1* gene on 3q26. Because *EVI1* is overexpressed in both kinds of mutant alleles, we speculated that the 3q21 region that is brought into close proximity to *EVI1* as a result of the translocation or inversion might harbor an enhancer that then ectopically activates *EVI1* gene expression. In this regard, because all breakpoints on 3q21 are located downstream of the ribophorin I (*RPN1*) gene, which encodes a transmembrane glycoprotein that is localized in the rough endoplasmic reticulum (Kreibich et al., 1978), we hypothesized that one attractive possibility is that *RPN1* enhancers might provide the ectopic activation required for malignant *EVI1* transcription.

The *GATA2* gene is located ~160 kb 3′ to the *RPN1* gene on 3q21. *GATA2* function is required in hematopoietic stem cells, but its expression diminishes during hematopoietic differentiation (Akashi et al., 2000; Lim et al., 2012; Minegishi et al., 2003; Suzuki et al., 2006; Tsai and Orkin, 1997; Yamamoto et al., 1990). In hematopoietic stem and progenitor cells (HSPCs), GATA2 positively regulates the expression of *GATA2*. Multiple phylogenetically conserved regions containing GATA factor binding sites reside in the mouse *Gata2* locus (at −3.9, −2.8, −1.8, and +9.5 kb from the *Gata2* hematopoietic and neuron-specific promoter I-specific [IS]), all of which bear some degree of *Gata2* enhancer activity (Grass et al., 2003, 2006; Johnson et al., 2012; Kobayashi-Osaki et al., 2005; Lim et al., 2012; Snow et al., 2011). In addition to these promoter and internal regulatory regions, another putative regulatory element identified by Bresnick and colleagues is located 77 kb 5′ to the *Gata2* gene (Grass et al., 2006). This element binds to GATA2 in the endogenous locus and acts as an enhancer in transfection assays (Grass et al., 2006). This element is located between *RPN1* and the breakpoints that occur in both the 3q21 and 3q26 translocations and inversions, thus localizing this −77-kb 5′ *GATA2* site in close proximity to the rearranged *EVI1* gene in the resulting recombinant alleles. We therefore hypothesized that the −77-kb GATA2 binding sites might be in an enhancer that misdirects *EVI1* transcription in the translocated or inverted alleles between 3q21 and 3q26 and that this ectopic expression underlies the mechanisms leading to leukemogenesis.

In this study, we asked whether the GATA2-bound sequences located −77 kb from the *Gata2* transcription start site indeed function as enhancers in mouse HSPCs in vivo. We also linked two bacterial artificial chromosomes (BACs) to generate a single recombinant human BAC clone that recapitulates the juxtaposition of the sequences just as they are found in the inverted human allele, then generated transgenic (Tg) mice harboring this recombinant BAC to create a mouse model for leukemias that are associated with chromosomal rearrangement.

RESULTS

Identification of a *Gata2* Gene Distal Hematopoietic Enhancer

The breakpoints in 3q21 AMLs all clustered within an approximately 25 kb region (Figure 1A, arrowheads in yellow region) (Suzukawa et al., 1994, 1997). We found that a region orthologous to the mouse *Gata2* gene −77-kb GATA sites is located upstream (i.e., closer to *RPN1*) of the breakpoint cluster (Figure 1A, blue circle). We first tested whether this region would exhibit enhancer activity for *Gata2* in HSPCs in vivo. To monitor *Gata2* gene expression in hematopoietic cells, we generated GFP reporter Tg mouse lines using a BAC clone bearing 186 kb of 5′ sequence flanking the *Gata2* gene (G2BAC-GFP) (Figure 1B). *LoxP* sites were then inserted on both sides of the −77-kb GATA sites to test their contribution to GFP expression as a surrogate for *Gata2*. We injected the floxed BAC (G2BAC-GFP-flox) DNA into fertilized ova and generated G2BAC-GFP-flox Tg mice (Figure 1B). The G2BAC-GFP-flox Tg mice were then crossed to *Ayu1-Cre* mice that express Cre recombinase in their germline (Niwa et al., 1993) to generate lines bearing the GATA binding-site-deleted BACs (G2BAC-GFP-delta). Deletion of the element was confirmed by PCR (Figures S1A and S1B available online).

In G2BAC-GFP-flox Tg mice, GFP fluorescence was intense in a subset of $Lin^{-}Sca\text{-}1^{+}c\text{-}kit^{+}$ (LSK) and $Lin^{-}Sca\text{-}1^{-}c\text{-}kit^{+}$ (LK) progenitor cells, whereas little fluorescence was detected in differentiated erythroid ($TER\text{-}119^{+}$), B ($B220^{+}$), or myeloid lineage ($Mac\text{-}1^{+}$) cells (Figure 1C, red lines). Thus, the BAC transgene accurately recapitulates endogenous *Gata2* gene expression in hematopoietic cells (Akashi et al., 2000; Suzuki et al., 2003, 2006). Of note, in the G2BAC-GFP-delta Tg mice, the percentages of GFP^{+} cells in both LSK and LK fractions were significantly reduced compared to those in cells recovered from the G2BAC-GFP-flox Tg mice (i.e., prior to deletion of the GATA sequences) (Figure 1C, blue lines).

We further examined GFP fluorescence in long-term hematopoietic stem cells (LT-HSCs) ($CD34^{-}Flt3^{-}$), short-term hematopoietic stem cells (ST-HSC) ($CD34^{+}Flt3^{-}$), and

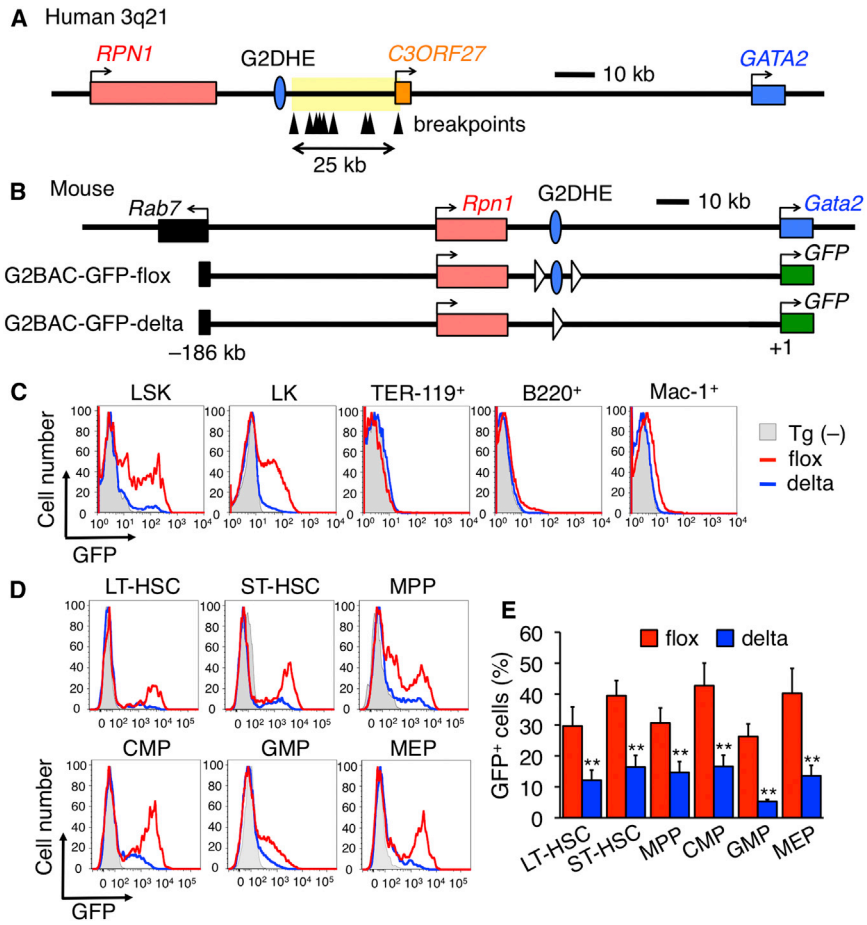

Figure 1. Identification of the *Gata2* Gene Distal Hematopoietic Enhancer

(A) Schematic structure of human 3q21 region. Arrowheads indicate documented breakpoints of translocation and inversion between 3q21 and 3q26. The breakpoints clustered in an approximately 25-kb region (yellow region). A blue circle indicates *Gata2* distal hematopoietic enhancer (G2DHE).

(B) Schematic structure of the G2BAC-GFP transgenes. The mouse *Gata2* locus is depicted at the top. G2BAC-GFP transgenes (G2BAC-GFP-flox or -delta) are shown beneath the endogenous *Gata2* locus. White triangles represent *loxP* sequences.

(C) Representative GFP histogram of bone marrow LSK, LK, TER-119$^+$, B220$^+$, and Mac-1$^+$ cells from G2BAC-GFP-flox (red lines) and G2BAC-GFP-delta (blue lines) mice. The gray-shaded histograms represent GFP fluorescence in wild-type mice without a transgene [Tg (−)].

(D) Representative GFP histogram in LT-HSCs, ST-HSCs, MPPs, CMPs, GMPs, and MEPs from G2BAC-GFP-flox (red lines) and G2BAC-GFP-delta (blue lines) mice. The gray-shaded histograms represent GFP fluorescence in Tg (−) mice.

(E) Percentages of GFP-positive cells in the indicated fractions of G2BAC-GFP-flox (red bars) and G2BAC-GFP-delta (blue bars) mice (n = 4). Data are represented as mean ± SD. **p < 0.01 compared with G2BAC-GFP-flox mice.

See also Figure S1.

multipotent progenitors (MPPs) (CD34$^+$Flt3$^+$) in the LSK fraction (Yang et al., 2005), as well as in common myeloid progenitors (CMPs) (CD34$^+$FcγRII/III3^{low}), granulocyte/macrophage progenitors (GMPs) (CD34$^+$FcγRII/III3^{high}), and megakaryocyte/erythrocyte progenitors (MEP) (CD34$^-$FcγRII/III3^{low}) in the LK fraction (Akashi et al., 2000). The fraction of GFP-positive cells was significantly reduced at all stages in hematopoietic progenitors in the G2BAC-GFP-delta Tg mice (Figures 1D and 1E). Therefore, we refer to this sequence as the *Gata2* distal hematopoietic enhancer (G2DHE).

Gata2 is also expressed in nonhematopoietic cells, such as neuronal, endothelial, and urogenital cells. As the G2BAC-GFP Tg contains a neuronal enhancer, but not endothelial or urogenital enhancers (Khandekar et al., 2004, 2007), the G2BAC-GFP Tg recapitulates *Gata2* expression only in neural tissues, especially in the midbrain (Nozawa et al., 2009). Therefore, we examined the contribution of G2DHE to *Gata2* expression in the midbrain and found that GFP fluorescence and mRNA levels in the midbrains of the G2BAC-GFP-delta Tg mice were comparable to those in the G2BAC-GFP-flox Tg mice (Figures S1C–S1E). These results indicate that G2DHE is dispensable for *Gata2* gene expression in the midbrain.

Generation of 3q21q26 Tg Mice by Linking Two BACs

To determine whether G2DHE activates *EVI1* transcription in the rearranged allele, we generated a Tg model mouse line that would precisely recapitulate the breakpoints in inv(3)(q21;q26). To do so, we duplicated the specific inversion breakpoint in the MOLM-1 cell line, which was originally established from a patient with megakaryoblastic leukemia bearing the inv(3)(q21;q26) inversion (Matsuo et al., 1991; Suzukawa et al., 1997). In MOLM-1 cells, inversion occurred between the 3rd exon of the *C3ORF27* gene in 3q21 and the 15th intron of *EVI1* in 3q26 (Suzukawa et al., 1997). As the position of the precise breakpoint has not been reported, we determined the sequence of the MOLM-1 inversion breakpoint (Figure 2A).

We next generated a BAC clone harboring recombinant human DNA that precisely recapitulated the inv(3)(q21;q26) genomic region in MOLM-1 cells by linking two BAC clones (RP11-662G11 and RP11-94J18) containing the 3q21 and 3q26 sequences, respectively (Figure 2B) (Brandt et al., 2008). During the process of BAC modification, we found both a full-length (indicated by an asterisk) and a partially deleted RP11-662G11 clone (Figure 2C, arrowhead; hereafter RP11-662G11d). Closer analysis revealed that the recombinant insert of the deleted clone lacked approximately 50 kb of flanking sequences 5′ to the *RPN1* gene (data not shown). We therefore chose to use this deleted clone in subsequent studies, thus allowing us to exclude any possible contribution of *RPN1* expression to *EVI1* transcription. We targeted *loxP514* sequences into the breakpoint positions of the RP11-662G11d

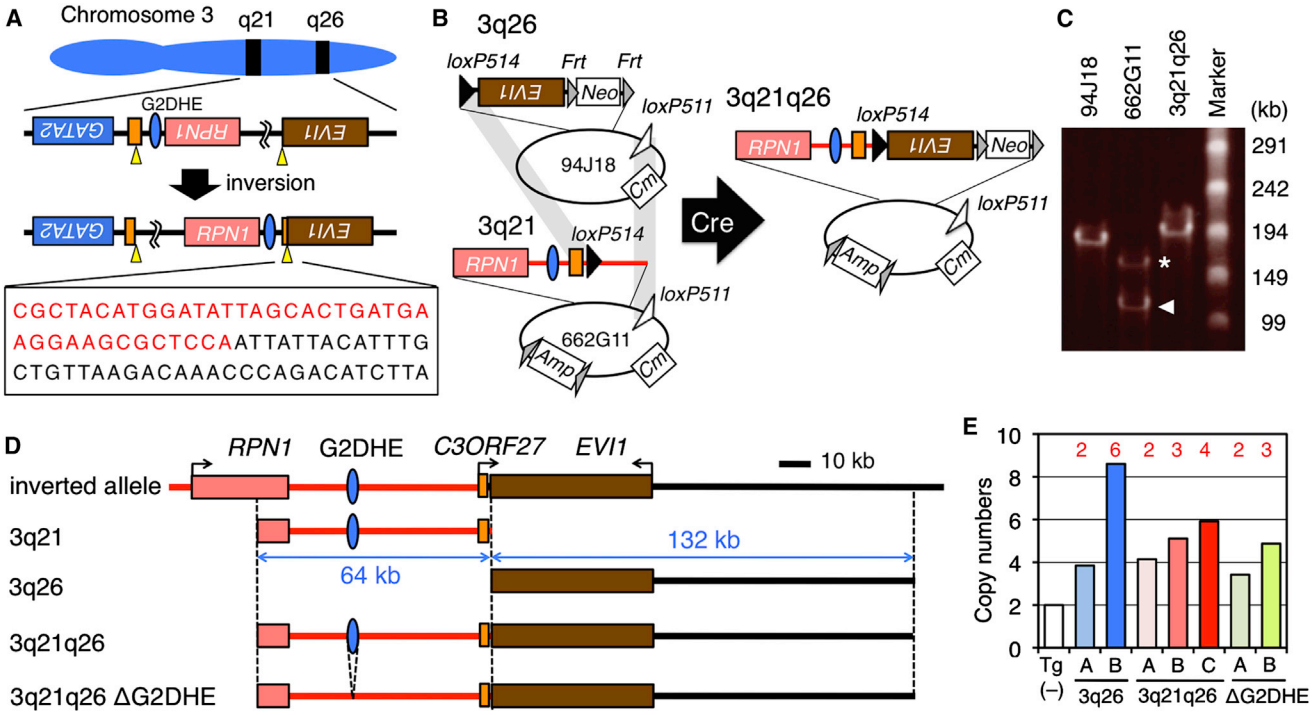

Figure 2. Generation of 3q21q26 Mice by Linking Two BACs

(A) Chromosomal inversion of the region between breakpoints (yellow arrowheads) in *EVI1* (brown box) and *C3ORF27* (orange box) genes in MOLM-1 cells. The boxed sequence shows the breakpoint between 3q21 (red) and 3q26 (black).

(B) Strategy for linking two BAC clones. Human BACs RP11-94J18 (94J18) and RP11-662G11 (662G11) contain 3q26 and 3q21, respectively. We used site-specific Cre-mediated recombination to link the two BAC clones by simultaneous intermolecular homologous recombination between the *loxP514* (black triangles) and *loxP511* (white triangles) sites. *Neo*, *Cm*, and *Amp* indicate the neomycin-, chloramphenicol-, and ampicillin-resistant genes, respectively.

(C) Pulse-field gel electrophoresis of BAC clones. We found two types of 662G11 clones: full-length (asterisk) and partially deleted (arrowhead).

(D) Schematic representations of the inverted allele, 3q21, 3q26, 3q21q26, and 3q21q26ΔG2DHE BAC transgenes. Red and black lines represent contributions from 3q21 and 3q26, respectively.

(E) Copy numbers of integrated transgenes. Copy numbers were determined by qPCR using Tg (–), 3q26 (lines A and B), 3q21q26 (lines A, B, and C), and 3q21q26ΔG2DHE (lines A and B) mice (n = 3–6). Red numbers depicted above the bar graphs represent copy numbers of transgenes.

See also Figure S2, Table S1, and Supplemental Information.

and RP11-94J18 BACs (Figure 2B; Figures S2A and S2B) and subsequently linked these two BAC clones by simultaneous Cre-mediated recombination between the *loxP514* sites inserted at the breakpoints and between the *loxP511* sites in the BAC vector backbones. The linked BAC clone was named 3q21q26. We verified that the 3q21q26 clone contained the 64-kb region of 3q21 and the expected 132-kb region of 3q26 by pulse-field gel electrophoresis, Southern blotting, and fingerprinting (Figure 2C; Figures S2C–S2G).

Utilizing the 3q21q26 clone, we generated three lines of Tg mice (3q21q26 mice) (Figure 2D). For one negative control, we also generated two lines of Tg mice harboring the unlinked 3q26 BAC clone (3q26 mice). To directly test whether the G2DHE could activate *EVI1* in the inverted allele, we also deleted the G2DHE from 3q21q26 (referred to as 3q21q26ΔG2DHE) and generated two additional lines of Tg mice (Figure 2D; Figures S2H–S2J). All of the 3q21q26, 3q26, and 3q21q26ΔG2DHE Tg mice were born in the expected Mendelian ratios, grew normally, and were fertile (Table S1). The copy numbers for the integrated transgenes was determined by quantitative PCR (qPCR), which revealed that the mice retained from two to six copies of the transgenes (Figure 2E).

Expression of the Human *EVI1* Transgene in HSPCs of 3q21q26 Mice

Whereas only hematopoietic lineage cells harbor the rearranged allele in human patients, every cell type should share the rearranged allele in the 3q21q26 mice. Therefore, it was important to determine the expression profile of the human *EVI1* transgene in the 3q21q26 mice. We quantified *EVI1* expression levels using three primer pairs that detected exclusively either the human transgene *EVI1* or the endogenous murine *Evi1* gene or detected both simultaneously. Interestingly, the human *EVI1* transgene was specifically expressed in hematopoietic tissues (spleen and thymus) in the 3q21q26 mice (Figure 3A), whereas the endogenous *Evi1* gene was also highly expressed in the lung and kidney (Figure 3B). In these mice, the abundance of human *EVI1* mRNA in hematopoietic tissues is comparable to that of the mouse *Evi1* mRNA in the lung and kidney (Figure 3C). These results are consistent with the notion that the human 3q21q26 transgene bears enhancer activity that can activate *EVI1* in hematopoietic tissues.

To more precisely examine the expression profiles of the *EVI1* transgene in hematopoietic lineages, bone marrow cells were fractionated into stem cells, progenitors, or various

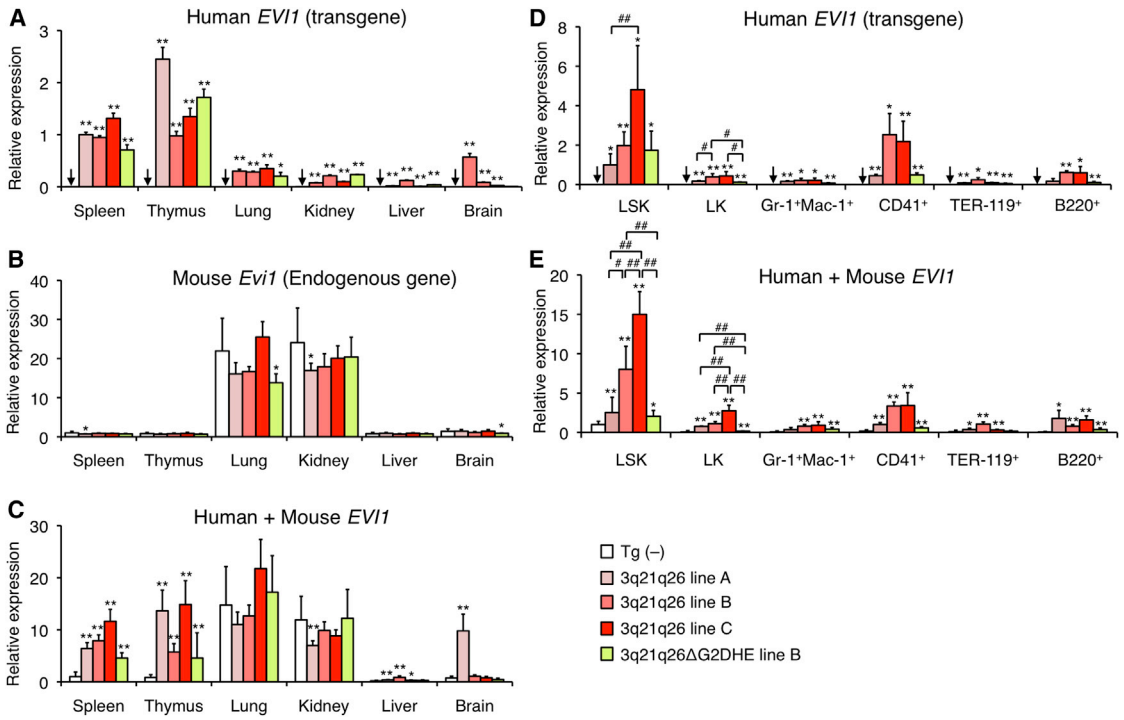

Figure 3. Expression Profiles of the Human *EVI1* Transgene in 3q21q26 Mice

(A–C) Expression levels of *EVI1* gene in hematopoietic and nonhematopoietic tissues. Expression levels of human *EVI1* mRNA (A), mouse endogenous *Evi1* mRNA (B), and total (human + mouse) *EVI1* mRNA (C) in hematopoietic tissues (spleen and thymus) and nonhematopoietic tissues (lung, kidney, liver, and brain) of Tg (–) controls (n = 10), 3q21q26 mouse lines (line A, n = 3; line B, n = 3; line C, n = 3), and 3q21q26ΔG2DHE line B (n = 4) were determined. The level of each mRNA was normalized to *rRNA* abundance. In panels (B) and (C), average values for Tg (–) spleen cells were set to 1, and in panel (A) spleen cells of 3q21q26 line A were set to 1.

(D and E) Abundance of *EVI1* gene expression in hematopoietic cells. Expression levels of human *EVI1* mRNA (D) and total *EVI1* mRNA (E) in hematopoietic stem and progenitor cells and differentiated cells in Tg (–) (n = 19), 3q21q26 (line A, n = 3–6; line B, n = 3–7; line C, n = 4), and 3q21q26ΔG2DHE line B (n = 4) bone marrow were determined. The abundance of each mRNA was normalized to the *rRNA* abundance. Average values for 3q21q26 line A LSK cells (D) and Tg (–) LSK cells (E) were set to 1.

Bar graph data are represented as mean ± SD. Arrows indicate undetectable expression levels. *$p < 0.05$; **$p < 0.01$ compared with Tg (–) controls. #$p < 0.05$; ##$p < 0.01$ compared between two indicated groups.

lineage-committed cells. The *EVI1* transgene was highly expressed in the LSK fraction, which contains HSPCs, but its expression diminished upon differentiation (Figures 3D and 3E). This expression pattern of the rearranged *EVI1* transgene recapitulates that of the endogenous *Gata2* gene (Minegishi et al., 2003; Suzuki et al., 2006; Tsai and Orkin, 1997) and is similar to that of the endogenous (murine) *Evi1* gene in hematopoietic cells (Kataoka et al., 2011). The abundance of *EVI1* mRNA was dependent on the copy number of the integrated transgenes in LSK and LK fractions of the 3q21q26 mice (Figure 3E).

In the 3q21q26ΔG2DHE mice, expression of *EVI1* transgene was also detected in hematopoietic tissues (Figures 3A–3C). Of note, we found that, when mice harbor the same copy number of transgenes, the total *EVI1* mRNA level is clearly diminished in LSK and LK fractions of the 3q21q26ΔG2DHE mice compared to those of the 3q21q26 mice (Figure 3E). These results indicate that G2DHE contributes to elevated *EVI1* gene expression in hematopoietic cells.

3q21q26 Mice Develop G2DHE-Dependent Leukemia

To determine whether the 3q21q26 mice develop leukemia, we examined a cohort of these animals, and determined by Kaplan-Meier analyses that the 3q21q26 mice survived far shorter than control [(Tg (–)] or 3q26 mice (Figure 4A). All three lines (lines A, B, and C) of 3q21q26 mice exhibited similar survival durations and began to die ~200 days after birth (Figure 4A, inset graph). Hematological indices of the 3q21q26 mice revealed that white blood cell numbers in the peripheral blood increased markedly after 24 weeks (Figure 4B) with constitutive mild anemia (Figure 4C). 3q21q26 mice that had increased (>5 × 10^4/μl) white blood cell counts were analyzed (Figures 4D and 4E) and found to display marked splenomegaly (Figures 4F and 4G). Leukocytes had infiltrated into the liver, lung, heart, and kidney in the 3q21q26 mice (Figure 4H), suggesting that the 3q21q26 mice developed leukemia.

When we carried out cohort studies of the 3q21q26ΔG2DHE mice to determine whether G2DHE contributed to leukemogenesis, we determined that 3q21q26ΔG2DHE mice survived similarly to control [Tg (–)] mice and did not develop leukemia over the 400-day time course of the experiment (Figure 4A). These results firmly support the contention that G2DHE is essential for *EVI1*-dependent leukemogenesis in the 3q21q26 mice.

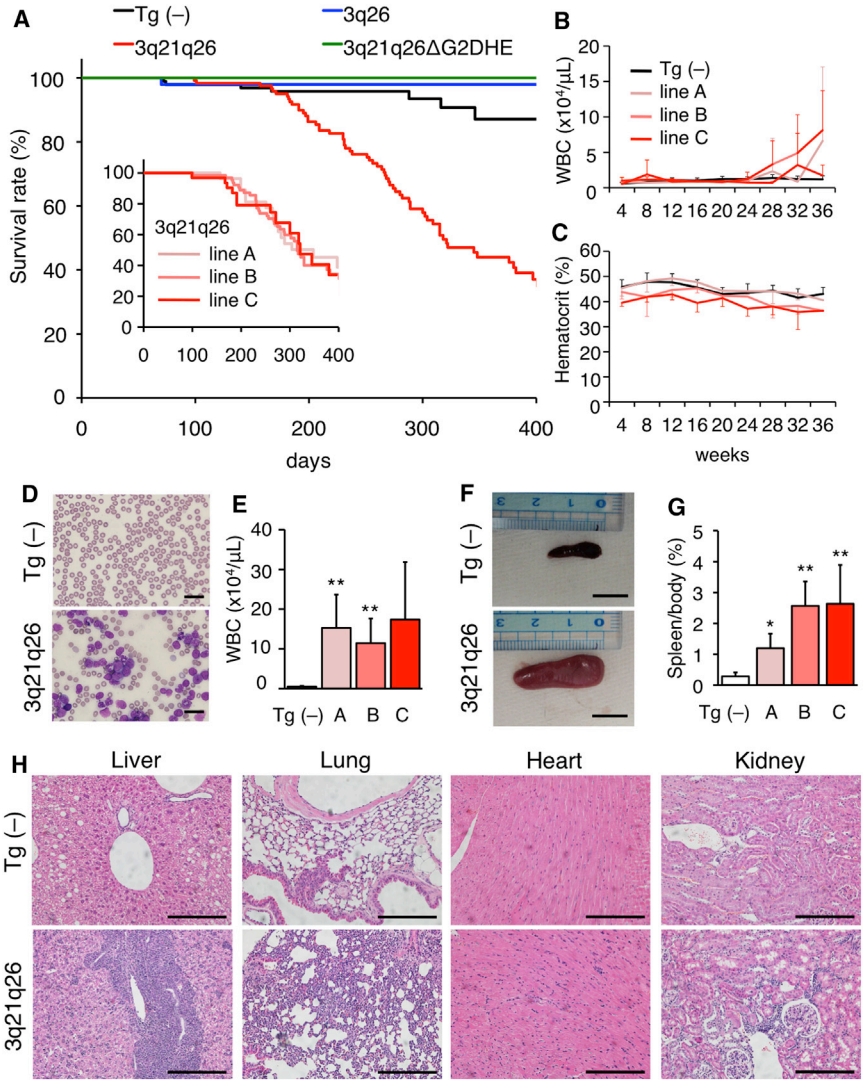

Figure 4. 3q21q26 Mice Develop G2DHE-Dependent Leukemia

(A) Kaplan-Meier survival curve of Tg (–) (n = 96), 3q26 (n = 55), 3q21q26 (n = 121), and 3q21q26ΔG2DHE (n = 26) mice. Survival rates were calculated by compiling data from multiple Tg mouse lines. The inset graph shows the overall survival of each line of 3q21q26 mice (lines A, B, and C).

(B and C) White blood cell counts (B) and hematocrit levels (C) in the peripheral blood of Tg (–) (n = 11–46) and 3q21q26 line A (n = 6–19), line B (n = 5–15), and line C (n = 3–9) mice.

(D) Representative smears of peripheral blood taken from Tg (–) and leukemic 3q21q26 mice. Scale bar, 20 μm.

(E) The numbers of white blood cells in leukemic 3q21q26 line A (n = 6), line B (n = 7), and line C (n = 3) mice and their Tg (–) (n = 5) littermates.

(F) Representative spleens from Tg (–) and leukemic 3q21q26 mice. Scale bar, 1 cm.

(G) Average spleen weights from Tg (–) (n = 5) and leukemic 3q21q26 line A (n = 6), line B (n = 7), and line C (n = 3) mice.

(H) Hematoxylin-eosin staining of tissues of Tg (–) (top panels) and leukemic 3q21q26 line B (bottom panels) mice. Scale bar, 100 μm.

Bar graph data are represented as mean ± SD. *p < 0.05; **p < 0.01 compared to Tg (–) controls.

3q21q26 Mice Develop Different Types of Leukemia

In human chromosomal rearrangements between 3q21 and 3q26, *EVI1* ectopic expression results primarily in myeloid rather than lymphoid leukemia (Lugthart et al., 2008). To determine whether leukemia in the 3q21q26 mice recapitulates the human leukemia most often associated with *EVI1* misexpression, we analyzed the peripheral blood and bone marrow of the 3q21q26 mice. In all three lines of the 3q21q26 mice, $CD34^+$ and c-kit^+ blast cells were observed in the peripheral blood (Figure 5A), whereas blast cells were only rarely observed in Tg (–) mice. $CD34^+$ and c-kit^+ cells were also more frequent in the bone marrow of 3q21q26 mice (Figure S3A). Additionally, $B220^+$ antigen was detected in the 3q21q26 line A mice, whereas Gr-1^+ and Mac-1^+ antigens were detected in the 3q21q26 lines B and C mice (Figure 5A; Figure S3A).

When different combinations of surface markers were analyzed, three distinct types of leukemia could be discerned in the 3q21q26 mice. The first is a B-cell type in which $B220^+$ cells had preferentially expanded (Figure 5B, left panel). The second is a GM type in which Gr-1^+Mac-1^+ cells had abundantly expanded (Figure 5B, right panel). Interestingly, the third type is one in which both $B220^+$ and Gr-1^+Mac-1^+ had increased (Figure 5B, center panel). Morphological analyses of the peripheral blood showed that lymphoid cells, neutrophils, or both were expanded in the B, GM, and B+GM types of leukemia, respectively (Figure 5C). In the B- and B+GM-type leukemias, $B220^+$ cells expressed c-kit and Flt3, but not CD19 (Figures S3B and S3C), indicating that these cells correspond to pre-pro-B cells (Nutt and Kee, 2007).

We note that the incidence of each type of leukemia correlated with increased copy numbers of the integrated transgenes. 3q21q26 line A mice bear two copies of the transgene and developed B-cell leukemia, whereas GM-type leukemias were observed in 3q21q26 mouse lines B and C, which bore three or four copies of the transgene, respectively (Figure 5D). These results, taken together, suggest that the 3q21q26 mice, especially mice of lines B and C that express more abundant human *EVI1*, most accurately recapitulate the phenotype and pathophysiology of human leukemia that is accompanied by *EVI1* ectopic expression.

3q21q26 Leukemic Cells Expand Autonomously

To determine whether the leukemic cells developed in the 3q21q26 mice progress autonomously if supported by wild-type cells in the leukemic niche, we isolated bone marrow cells from the 3q21q26 mice and transplanted them into nude mice. All recipient nude mice died with latencies of approximately

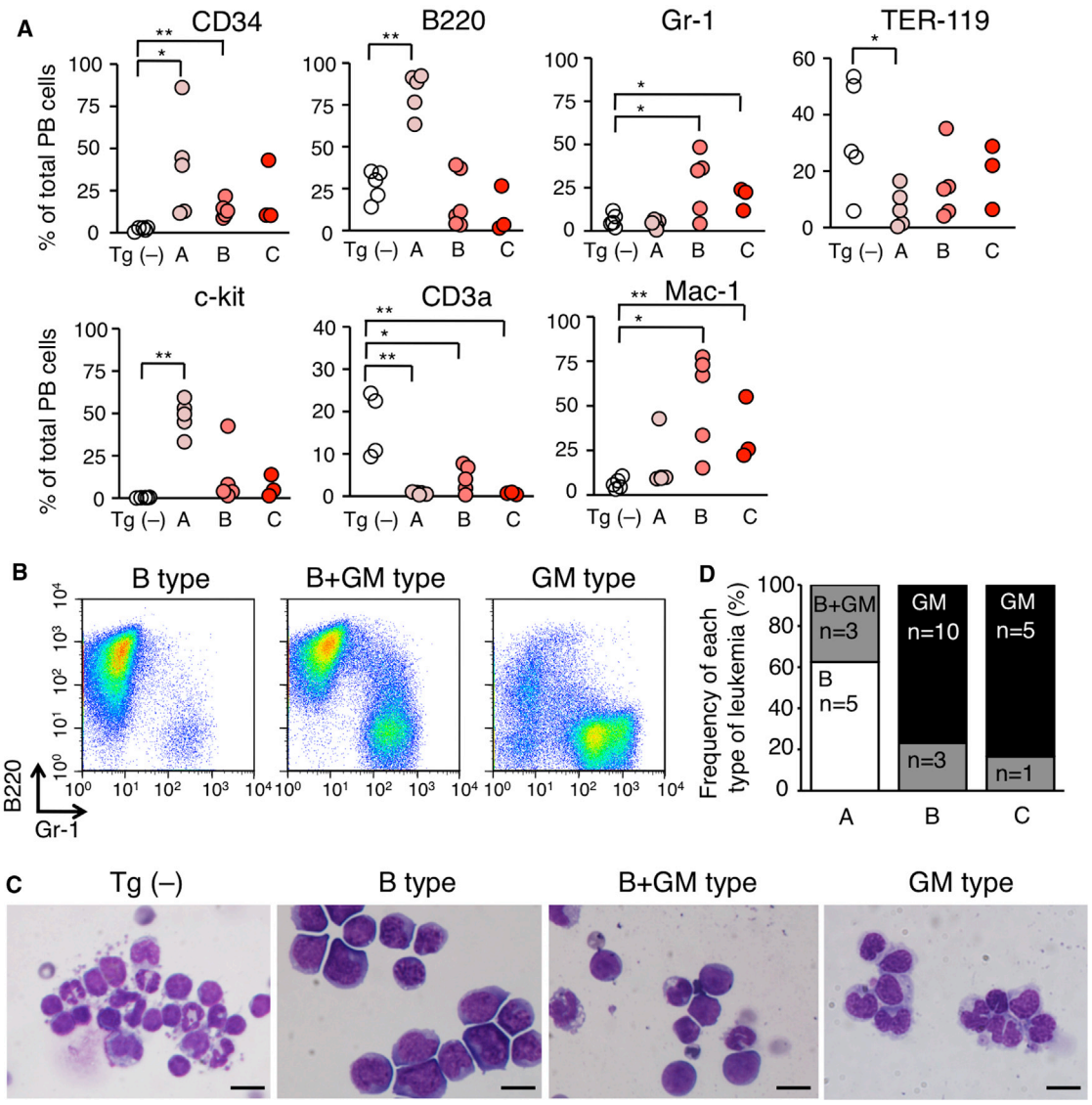

Figure 5. 3q21q26 Mice with Three Types of Leukemia

(A) Expression profiles of CD34, c-kit, B220, CD3a, Gr-1, Mac-1, and TER-119 in peripheral blood (PB) leukemic cells of 3q21q26 line A (n = 5), line B (n = 5–6), and line C (n = 3) mice, as well as mononuclear cells of Tg (–) mice (n = 4–5). *$p < 0.05$; **$p < 0.01$.

(B) Flow cytometric analysis of leukemic cells in 3q21q26 mice. Representative flow cytometric patterns of B-type (left panel), B+GM-type (middle panel), and GM-type (right panel) leukemias are shown.

(C) Wright-Giemsa staining of leukemic cells in the peripheral blood of 3q21q26 mice. Scale bar, 10 μm. As a control, mononuclear cells from Tg (–) mice are shown.

(D) Frequencies of B-type (white), B+GM-type (gray), and GM-type (black) leukemia developed in the three 3q21q26 mouse lines.

See also Figure S3.

30–40 days following transplant (Figure 6A). As in the donor mice, the recipient nude mice exhibited marked splenomegaly (Figure 6B). In the peripheral blood of the recipients, the number of white blood cells dramatically increased over time, whereas red blood cells and platelets both diminished, indicating that the recipient mice developed transplant-dependent leukemia (Figures 6C–6E).

We next carried out flow cytometry and morphological analysis of leukocytes in the peripheral blood and examined whether the phenotypes of the leukemia that developed in the recipient nude mice recapitulated that of the donors. All recipient nude mice developed leukemias (Figures 6F and 6G). In perfect agreement with analyses of the various donor animals, leukemic cells in the recipient mice developed B-, GM-, or B+GM-type leukemias in lines A, B, and C and exhibited identical morphologies in lymphoid and/or neutrophil populations (Figure 6H). These data demonstrate that leukemic cells from the 3q21q26 mice progress autonomously in the transplanted nude mice, indicating that the leukemic cells in primary mice do not require a mutant microenvironment for their propagation.

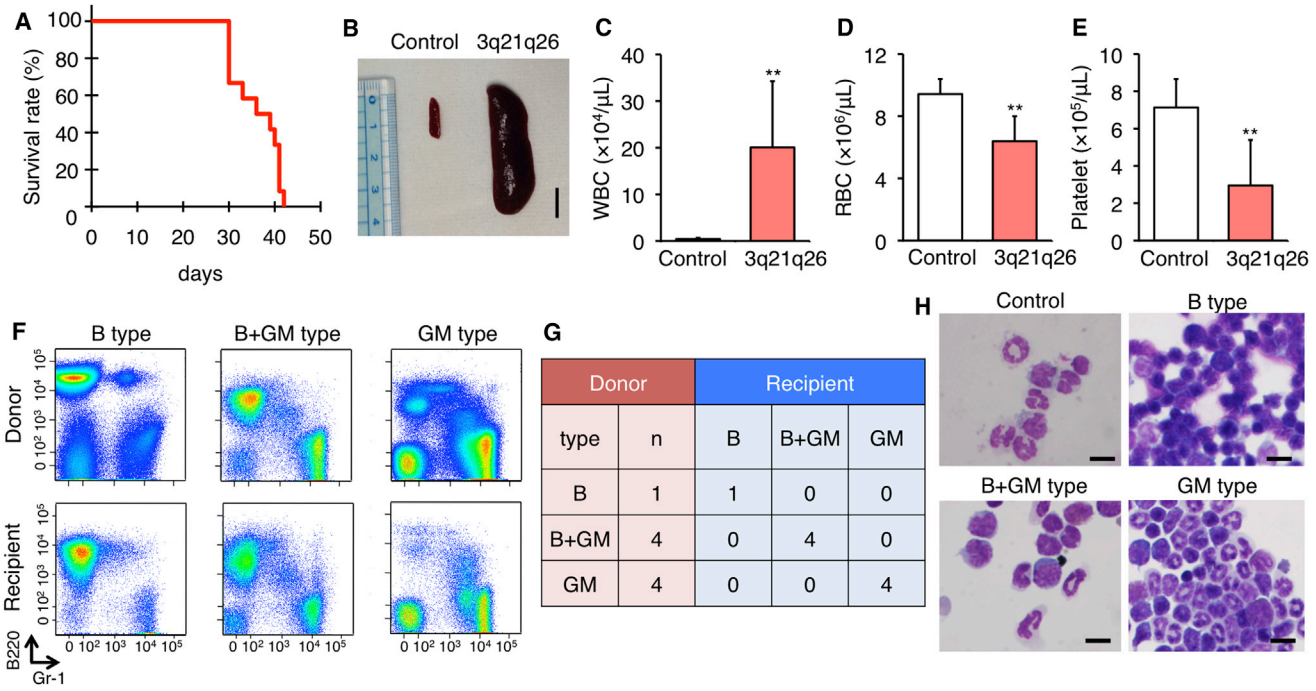

Donor		Recipient		
type	n	B	B+GM	GM
B	1	1	0	0
B+GM	4	0	4	0
GM	4	0	0	4

Figure 6. Leukemic Cells of 3q21q26 Mice Expand Autonomously

(A) Kaplan-Meier survival curve of recipient nude mice (n = 12) transplanted with 10^7 mononuclear bone marrow cells from leukemic 3q21q26 mice.

(B) Representative spleens from control or recipient nude mice 40 days after transplant. Scale bar, 1 cm.

(C–E) Numbers of white blood cells (C), red blood cells (D), and platelets (E) in peripheral blood in control (n = 3) and transplanted (n = 11) nude mice. **$p < 0.01$ compared with control nude mice.

(F) Representative flow cytometric analyses of peripheral blood cells from donor mice with B-, B+GM-, and GM-type leukemia and comparison to their respective recipient nude mice.

(G) Leukemia types of donor and recipient mice. Numbers in the table represent the number of mice with each type of leukemia.

(H) Wright-Giemsa staining of leukemic cells in the peripheral blood of transplant recipient nude mice with B-, B+GM-, and GM-type leukemia. Scale bar, 10 μm.

Bar graphs are represented as mean ± SD.

Expansion of LSK Cells and Emergence of an Abnormal Cell Population in 3q21q26 Mice

As the human *EVI1* transgene was highly expressed in LSK cells of the 3q21q26 mice, we hypothesized that misexpression of *EVI1* in Tg HSPCs might have contributed to the leukemogenesis. To address this hypothesis, we quantified the absolute number of HSPCs in the bone marrow of 12-week-old 3q21q26, 3q26, and 3q21q26ΔG2DHE mice prior to the onset of frank leukemia. Bone marrow cellularity in the 3q21q26 mice was comparable to that in the 3q26 mice, whereas the number of LSK cells increased in the 3q21q26 mice (Figures 7A and 7B). Of specific note, the number of LSK cells in 3q21q26ΔG2DHE mice was much lower than that in 3q21q26 mice.

We fractionated the LSK fraction of the 3q21q26 mice into LT-HSC, ST-HSC, and MPP as usual and discovered an abnormal $CD34^{high}Flt3^{-}$ cell fraction. The $CD34^{high}Flt3^{-}$ cells accumulated abundantly in LSK cells of the 3q21q26 mice, but not in 3q26 animals or in the LSK faction of control Tg (–) mice (Figures 7C and 7D). The $CD34^{high}Flt3^{-}$ cells were still observed in 3q21q26 mice with myeloid leukemia, suggesting that these cells are associated with myeloid leukemia (Figures S4A and S4B). We next examined the LK fractions containing CMP, MEP, and GMP cells and found that the number of CMP cells was fewer in 3q21q26 mice than in 3q26 or control [Tg (–)] mice, indicating that differentiation of the CMP cells was deficient in the 3q21q26 mice (Figures 7E and 7F). The phenotypic accumulation of $CD34^{high}Flt3^{-}$ cells was partially reversed in the LSK cells of 3q21q26ΔG2DHE mice, indicating that the differentiation defects observed in the 3q21q26 progenitor cells were rescued, at least in part, by deletion of the *GATA2* enhancer from the linked BAC (Figures 7C and 7D).

G2DHE Drives *EVI1* Overexpression in HSPCs

To elucidate whether the 3q21 region, and specifically G2DHE, is able to direct ectopic *EVI1* gene expression in HSPCs, we examined *EVI1* transcription. The abundance of human *EVI1* mRNA was significantly elevated in LT-HSCs, ST-HSCs, and MPPs from the 3q21q26 mice in comparison to 3q26 mice (Figure 7G). In contrast, human EVI1 abundance in the $CD34^{high}Flt3^{-}$ fraction was much lower than in the LT-HSCs, ST-HSCs, and MPPs fractions. Overexpression of the human *EVI1* transgene was significantly diminished in the enhancer-deleted 3q21q26ΔG2DHE mice, demonstrating that G2DHE could be directly responsible for activating the human *EVI1* transgene in LT-HSCs, ST-HSCs, and MPPs. Unexpectedly, we found that the levels of endogenous mouse *Evi1* mRNA diminished to undetectable levels in the 3q21q26 and the 3q21q26ΔG2DHE mice (Figure 7H). The total *EVI1* level (human *EVI1* + mouse *Evi1*

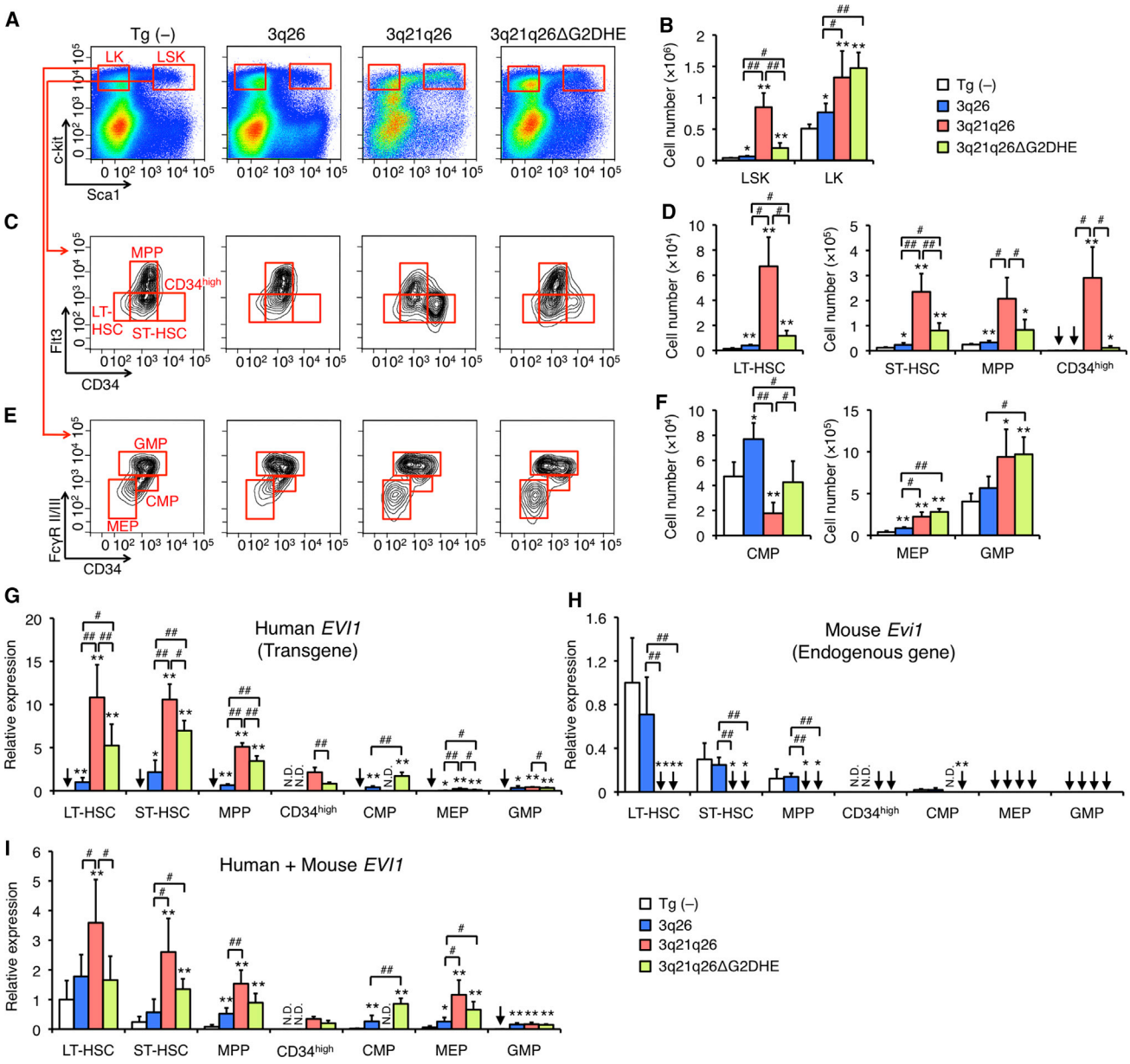

Figure 7. G2DHE Drives *EVI1* Overexpression in HSPCs

(A–F) Representative flow cytometric profiles of Lin$^-$ cells (A), LSK cells (C), and LK cells (E) in 12-week-old Tg (–), 3q26 line B, 3q21q26 line B, and 3q21q26ΔG2DHE line B mice. Analysis of cells in red boxes is shown in panels (B), (D), and (F). Absolute cell numbers of LSK and LK cells (B), LT-HSCs, ST-HSCs, MPPs, and CD34^{high}Flt3$^-$ (CD34^{high}) cells (D), and CMPs, MEPs and GMPs (F) in the Lin$^-$ cell population in 12-week-old Tg (–) (white, n = 4), 3q26 line B (blue, n = 4), 3q21q26 line B (pink, n = 4), and 3q21q26ΔG2DHE line B (green, n = 4) mice are depicted.

(G–I) Expression levels of human *EVI1* mRNA (G), mouse endogenous *Evi1* mRNA (H), and total *EVI1* mRNA (I) in LT-HSC, ST-HSC, MPP, CD34^{high}, CMP, MEP, and GMP fractions in 12-week-old Tg (–) (white, n = 4–8), 3q26 line B (blue, n = 4–8), 3q21q26 line B (pink, n = 4–8), and 3q21q26ΔG2DHE line B (green, n = 4–8) mice. The expression level of each mRNA was normalized to *rRNA* abundance. Average values for 3q26 LT-HSC cells (G) and Tg (–) LT-HSC cells (H and I) were set to 1.

Bar graph data are represented as mean ± SD. Arrows indicate undetectable levels. N.D., not determined. *$p < 0.05$; **$p < 0.01$ compared with Tg (–) controls. #$p < 0.05$; ##$p < 0.01$ compared between two indicated groups.

See also Figure S4.

mRNAs) in the 3q21q26 mice was higher than in the 3q26 mice, but the level in the 3q21q26ΔG2DHE mice was comparable to that in the 3q26 mice (Figure 7I). These results indicate that the G2DHE located in the 3q21 region activates *EVI1* transcription in the inverted 3q26 allele, leading to the observed leukemogenesis.

In LT-HSCs of 3q21q26 mice, the levels of known EVI1 target genes *Gata2* and *Pbx1* mRNAs (Shimabe et al., 2009; Yuasa

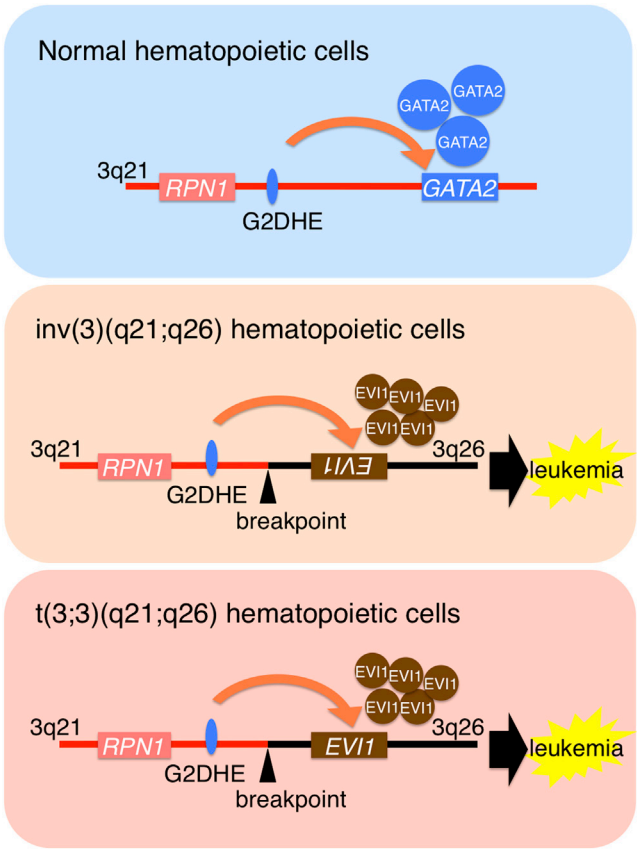

Figure 8. A Model for the Involvement of G2DHE in Normal and 3q21q26 Inverted/Translocated Hematopoietic Cells

In normal hematopoietic progenitors, G2DHE enhances *GATA2* transcription (top panel). In AML, G2DHE becomes localized downstream or upstream of the *EVI1* gene in inv(3)(q21;q26) (middle panel) or t(3;3)(q21;q26) (bottom panel) alleles, respectively. In both cases, the chromosomal rearrangement-dependent juxtaposition of G2DHE induces *EVI1* gene transcription instead of *GATA2* transcription, which subsequently leads to leukemia.

et al., 2005), but not *Myb*, *Foxo3a*, and *Meis1*, were increased compared with Tg (−) mice (Figure S4C). These results indicate that EVI1 upregulates a subset of target genes, which are important for the maintenance of HSCs, in LT-HSCs of the 3q21q26 mice. Additionally, the abundance of *Pten* tumor suppressor (Yoshimi et al., 2011) and the cyclin-dependent kinase inhibitor *p57* (Matsumoto et al., 2011) was lower in 3q21q26 LT-HSCs. We envisage that EVI1 may provoke the progression of the cell cycle by regulating *Pten* and *p57* expression. In the $CD34^{high}Flt3^{-}$ cells from the 3q21q26 mice, the abundance of *Meis1*, *Gata2*, *Pbx1*, and *p57* gene transcripts, which are all highly expressed in LT-HSCs, had largely decreased; in contrast, we detected high levels of PU.1. These results collectively suggest that the $CD34^{high}Flt3^{-}$ cells retain gene expression profiles similar to myeloid progenitor cells rather than stem cells.

DISCUSSION

Translocation or inversion between 3q21 and 3q26 induces aberrant *EVI1* gene expression, giving rise to human AML, which carries a poor prognosis. In this paper, we describe the contribution of a far upstream hematopoietic enhancer of the *GATA2* gene (G2DHE) to *EVI1* gene expression in a typically rearranged human inversion. We generated 3q21q26 mice by linking two separate BAC clones containing the 3q21 and 3q26 regions in the same physical orientation as they are found in a common AML cell line and found that the Tg mice developed leukemias only when *EVI1* was ectopically activated by G2DHE when the two genetic elements were brought into close proximity as a consequence of the inversion. We propose a model for *EVI1*-misexpressed leukemia that is associated with chromosomal rearrangements (Figure 8). In normal hematopoietic cells, the G2DHE is at least partially responsible for activating *GATA2* gene expression (Figure 8, top panel). In leukemia cells bearing inversions or translocations between 3q21 and 3q26, G2DHE becomes localized either 3′ or 5′ to the *EVI1* gene, respectively (Figure 8, middle and bottom panels). G2DHE activates the *EVI1* gene instead of *GATA2* in HSPCs, thereby leading to leukemogenesis. This model is further supported by the conclusions from a study employing a completely different approach examining leukemic cells from human patients bearing the rearranged allele (Gröschel et al., 2014).

G2DHE was originally identified as a phylogenetically conserved region containing binding sites for transcription factors GATA1 and GATA2 in the mouse *Gata2* locus (Grass et al., 2006). It has been shown that the *Gata2* gene regulation is highly dependent on these GATA factors. The *Gata2* gene is activated by GATA2 itself in HSPCs, but becomes repressed by GATA1 as progenitors differentiate into erythroid cells (Grass et al., 2003, 2006; Kobayashi-Osaki et al., 2005; Snow et al., 2010). GATA2 and GATA1 bind to several sites in the *Gata2* locus, including three sites in G2DHE. We assume that GATA2 and GATA1 differentially bind to these motifs in a differentiation-dependent manner as erythroid progenitors switch from proliferation to terminal differentiation (Bresnick et al., 2010; Kaneko et al., 2010; Suzuki et al., 2011, 2013). Similarly, we surmise that *EVI1* gene activation by G2DHE occurs in a manner that is dependent on these GATA factors. Additionally, a number of transcription factors, such as GFI1, SCL, MEIS1, RUNX1, ERG, LMO2, and FLI1 bind to G2DHE in human hematopoietic cell lines (Moignard et al., 2013). Therefore, identification of the mechanisms that regulate *EVI1* gene expression though G2DHE is a critical future objective for identifying potential therapeutic targets for EVI1 expression-based leukemia.

Several mouse models for EVI1-expressing leukemia have been reported (Buonamici et al., 2004; Louz et al., 2000; Yoshimi et al., 2011). In particular, Yoshimi et al. established a mouse model by transplanting bone marrow cells in which EVI1 was introduced using a retrovirus (Yoshimi et al., 2011). Of these experimental leukemia models, the present approach is different, because in the 3q21q26 mice, (1) the expression level of EVI1 is evenly controlled by being borne in a BAC, (2) the expression profile of EVI1 is defined by human 3q21 locus and is highly reproducible, and (3) the timing of EVI1 expression recapitulates that of the human leukemia cases bearing chromosome rearrangements. However, the leukemias that develop in the 3q21q26 mouse model appear to be similar to those utilizing retroviral infection of EVI1 in mice, in which the *EVI1* gene is expressed in hematopoietic cells. Both models develop leukemia

with long latency (more than 6 months), and both models develop both myeloid and B-cell leukemia. Nonetheless, these observations further support the contention that the leukemogenesis in the 3q21q26 mice is caused by dysregulated *EVI1* expression in hematopoietic cells; however, we need further experiments to exclude decisively the possibility that a mutant microenvironment is necessary for de novo development of the leukemia in the 3q21q26 mice.

It is still unknown how the *EVI1* misexpression induces B-cell leukemia in addition to myeloid leukemia. In this regard, it should be noted that the 3q21q26 cellular analysis clearly revealed that both types of leukemia correlate with EVI1 expression levels. EVI1 overexpression has also been observed in pediatric acute lymphoblastic leukemia (ALL) (Konantz et al., 2013). In very good agreement with these observations in the 3q21q26 mouse model, the EVI1 level in pediatric ALL patients is lower than that in AML, and EVI1 levels in ALL patients has been shown to correlate with disease prognosis (Konantz et al., 2013).

Whereas the *EVI1* gene expression level diminishes significantly in the *GATA2* enhancer-deleted BAC Tg mice and the mice no longer develop leukemia, the *EVI1* gene is still expressed to a certain extent in the enhancer-deleted mouse bone marrow cells. We do not have a salient explanation for this observation at present, but the following points may be relevant. One plausible explanation is that *EVI1* may be activated in only a minor subset of cells in the LSK fraction of 3q21q26 mice, and it is these cells that play a critical role in the leukemogenesis. As EVI1 is an essential transcription factor for normal hematopoietic stem cell maintenance (Goyama et al., 2008), it may play equally important roles in the maintenance of leukemic stem cells. Monitoring *EVI1* expression at the single-cell level using novel Tg mice in which a reporter is expressed under the control of the 3q21q26 BAC would be valuable to investigate this possibility.

An alternative explanation is that there may be a strict threshold requirement for EVI1-dependent leukemogenesis and that impaired activation of *EVI1* in the 3q21q26ΔG2DHE mice may be insufficient to surmount that threshold. The threshold model has already been proposed for the onset of leukemia that depends on the gene dosage of transcription factor PU.1 (Rosenbauer et al., 2004; Steidl et al., 2006). Deletion of the upstream regulatory element of the *Sfpi1* gene encoding PU.1 gives rise to an 80% reduction in the levels of PU.1 compared with its normal abundance, which specifically induced leukemia. Meanwhile, complete or even a 50% reduction in PU.1 did not induce leukemia, indicating that sensitive fine-tuning of transcription factor levels by specific enhancers may be critical for the suppression of leukemogenesis.

We believe that this Tg mouse model approach, exploiting the BAC-linking technique, is equally applicable to the analysis of other leukemias or diseases that are associated with chromosomal rearrangements. Especially by applying BAC clones from human genomic libraries to Tg mouse studies, we can generate very precise mouse models of human rearranged alleles. The BAC-linking method enables us to generate rearranged alleles with any combination of alleles or breakpoints, and the technique of Tg mouse generation combined with the BAC-linking method is relatively straightforward to manipulate. Therefore, this approach using linked BACs in Tg mice should prove to be useful in providing vivid insights into the mechanistic basis for the pathogenesis of various leukemias that are caused by chromosomal rearrangements.

EXPERIMENTAL PROCEDURES

Mice

Generation of Tg mice using BAC recombination is described in the Supplemental Information. All mice were handled according to the regulations of the Standards for Human Care and Use of Laboratory Animals of Tohoku University and the Guidelines for Proper Conduct of Animal Experiments of the Ministry of Education, Culture, Sports, Science, and Technology of Japan.

Hematological Analysis

Peripheral blood (30–50 μl) was collected from individual mice. Hematopoietic indices were determined using a hemocytometer (Nihon Kohden). Hemogram profiles were examined by Wright-Giemsa staining. Flow cytometric analysis is described in the Supplemental Information.

Histological Analysis

Each organ was fixed with 10% formalin (Mildform 10N; Wako) and embedded in paraffin using standard procedures. Sections (5 μm) were stained with hematoxylin-eosin.

Quantitative RT-PCR

Gene expression levels were determined by qRT-PCR as described in the Supplemental Information.

Statistical Analysis

The statistical significance of differences between parameters was assessed using a two-tailed, unpaired Student's t test.

SUPPLEMENTAL INFORMATION

Supplemental Information includes Supplemental Experimental Procedures, four figures, and one table and can be found with this article online at http://dx.doi.org/10.1016/j.ccr.2014.02.008.

ACKNOWLEDGMENTS

We thank Drs. Takashi Moriguchi, Maki Kobayashi-Osaki, and Naoko Minegishi for critical advice. We also thank Aya Goto, Koichiro Kato, Eriko Naganuma, Yohei Sato, and Hiromi Suda for technical assistance, laboratory staff members for useful discussions, and the Biomedical Research Core of Tohoku University Graduate School of Medicine for technical support. This work was supported in part by grants from the National Institutes of Health (R01AI094642 and R21HL114368 to J.D.E. and R37DK50107 and R01DK68634 to E.H.B.), the Japan Society for the Promotion of Science (JSPS) (KAKENHI 22118001 and 24249015 to M.Y. and 22790269 and 24790957 to M.S.), funds from the Midwest Athletes Against Childhood Cancer (to E.H.B.), Core Research for Evolutionary Science and Technology research program of the Japan Science and Technology Agency (to M.Y.), and the Naito Foundation, Mitsubishi Foundation, and Takeda Science Foundation (to M.Y.). H.Y. was a JSPS Research Fellow.

Received: October 13, 2013
Revised: December 20, 2013
Accepted: February 18, 2014
Published: April 3, 2014

REFERENCES

Akashi, K., Traver, D., Miyamoto, T., and Weissman, I.L. (2000). A clonogenic common myeloid progenitor that gives rise to all myeloid lineages. Nature *404*, 193–197.

ar-Rushdi, A., Nishikura, K., Erikson, J., Watt, R., Rovera, G., and Croce, C.M. (1983). Differential expression of the translocated and the untranslocated c-myc oncogene in Burkitt lymphoma. Science *222*, 390–393.

Brandt, W., Khandekar, M., Suzuki, N., Yamamoto, M., Lim, K.C., and Engel, J.D. (2008). Defining the functional boundaries of the Gata2 locus by rescue with a linked bacterial artificial chromosome transgene. J. Biol. Chem. *283*, 8976–8983.

Bresnick, E.H., Lee, H.Y., Fujiwara, T., Johnson, K.D., and Keles, S. (2010). GATA switches as developmental drivers. J. Biol. Chem. *285*, 31087–31093.

Buonamici, S., Li, D., Chi, Y., Zhao, R., Wang, X., Brace, L., Ni, H., Saunthararajah, Y., and Nucifora, G. (2004). EVI1 induces myelodysplastic syndrome in mice. J. Clin. Invest. *114*, 713–719.

Chi, Y., Senyuk, V., Chakraborty, S., and Nucifora, G. (2003). EVI1 promotes cell proliferation by interacting with BRG1 and blocking the repression of BRG1 on E2F1 activity. J. Biol. Chem. *278*, 49806–49811.

Goyama, S., Yamamoto, G., Shimabe, M., Sato, T., Ichikawa, M., Ogawa, S., Chiba, S., and Kurokawa, M. (2008). Evi-1 is a critical regulator for hematopoietic stem cells and transformed leukemic cells. Cell Stem Cell *3*, 207–220.

Goyama, S., Nitta, E., Yoshino, T., Kako, S., Watanabe-Okochi, N., Shimabe, M., Imai, Y., Takahashi, K., and Kurokawa, M. (2010). EVI-1 interacts with histone methyltransferases SUV39H1 and G9a for transcriptional repression and bone marrow immortalization. Leukemia *24*, 81–88.

Grass, J.A., Boyer, M.E., Pal, S., Wu, J., Weiss, M.J., and Bresnick, E.H. (2003). GATA-1-dependent transcriptional repression of GATA-2 via disruption of positive autoregulation and domain-wide chromatin remodeling. Proc. Natl. Acad. Sci. USA *100*, 8811–8816.

Grass, J.A., Jing, H., Kim, S.I., Martowicz, M.L., Pal, S., Blobel, G.A., and Bresnick, E.H. (2006). Distinct functions of dispersed GATA factor complexes at an endogenous gene locus. Mol. Cell. Biol. *26*, 7056–7067.

Gröschel, S., Sanders, M.A., Hoogenboezem, R., de Wit, E., Bouwman, B.A.M., Erpelinck, C., van der Velden, V.H.J., Havermans, M., Avellino, R., van Lom, K., et al. (2014). A single oncogenic enhancer-rearrangement causes concomitant deregulation of EVI1 and GATA2 in leukemia. Cell *157*, 369–381.

Izutsu, K., Kurokawa, M., Imai, Y., Maki, K., Mitani, K., and Hirai, H. (2001). The corepressor CtBP interacts with Evi-1 to repress transforming growth factor β signaling. Blood *97*, 2815–2822.

Johnson, K.D., Hsu, A.P., Ryu, M.J., Wang, J., Gao, X., Boyer, M.E., Liu, Y., Lee, Y., Calvo, K.R., Keles, S., et al. (2012). *Cis*-element mutated in *GATA2*-dependent immunodeficiency governs hematopoiesis and vascular integrity. J. Clin. Invest. *122*, 3692–3704.

Kaneko, H., Shimizu, R., and Yamamoto, M. (2010). GATA factor switching during erythroid differentiation. Curr. Opin. Hematol. *17*, 163–168.

Kataoka, K., Sato, T., Yoshimi, A., Goyama, S., Tsuruta, T., Kobayashi, H., Shimabe, M., Arai, S., Nakagawa, M., Imai, Y., et al. (2011). Evi1 is essential for hematopoietic stem cell self-renewal, and its expression marks hematopoietic cells with long-term multilineage repopulating activity. J. Exp. Med. *208*, 2403–2416.

Khandekar, M., Suzuki, N., Lewton, J., Yamamoto, M., and Engel, J.D. (2004). Multiple, distant Gata2 enhancers specify temporally and tissue-specific patterning in the developing urogenital system. Mol. Cell. Biol. *24*, 10263–10276.

Khandekar, M., Brandt, W., Zhou, Y., Dagenais, S., Glover, T.W., Suzuki, N., Shimizu, R., Yamamoto, M., Lim, K.C., and Engel, J.D. (2007). A Gata2 intronic enhancer confers its pan-endothelia-specific regulation. Development *134*, 1703–1712.

Kobayashi-Osaki, M., Ohneda, O., Suzuki, N., Minegishi, N., Yokomizo, T., Takahashi, S., Lim, K.C., Engel, J.D., and Yamamoto, M. (2005). GATA motifs regulate early hematopoietic lineage-specific expression of the *Gata2* gene. Mol. Cell. Biol. *25*, 7005–7020.

Konantz, M., André, M.C., Ebinger, M., Grauer, M., Wang, H., Grzywna, S., Rothfuss, O.C., Lehle, S., Kustikova, O.S., Salih, H.R., et al. (2013). EVI-1 modulates leukemogenic potential and apoptosis sensitivity in human acute lymphoblastic leukemia. Leukemia *27*, 56–65.

Kreibich, G., Czakó-Graham, M., Grebenau, R., Mok, W., Rodriguez-Boulan, E., and Sabatini, D.D. (1978). Characterization of the ribosomal binding site in rat liver rough microsomes: ribophorins I and II, two integral membrane proteins related to ribosome binding. J. Supramol. Struct. *8*, 279–302.

Laricchia-Robbio, L., Fazzina, R., Li, D., Rinaldi, C.R., Sinha, K.K., Chakraborty, S., and Nucifora, G. (2006). Point mutations in two EVI1 Zn fingers abolish EVI1-GATA1 interaction and allow erythroid differentiation of murine bone marrow cells. Mol. Cell. Biol. *26*, 7658–7666.

Laricchia-Robbio, L., Premanand, K., Rinaldi, C.R., and Nucifora, G. (2009). EVI1 impairs myelopoiesis by deregulation of PU.1 function. Cancer Res. *69*, 1633–1642.

Lim, K.C., Hosoya, T., Brandt, W., Ku, C.J., Hosoya-Ohmura, S., Camper, S.A., Yamamoto, M., and Engel, J.D. (2012). Conditional Gata2 inactivation results in HSC loss and lymphatic mispatterning. J. Clin. Invest. *122*, 3705–3717.

Louz, D., van den Broek, M., Verbakel, S., Vankan, Y., van Lom, K., Joosten, M., Meijer, D., Löwenberg, B., and Delwel, R. (2000). Erythroid defects and increased retrovirally-induced tumor formation in Evi1 transgenic mice. Leukemia *14*, 1876–1884.

Lugthart, S., van Drunen, E., van Norden, Y., van Hoven, A., Erpelinck, C.A., Valk, P.J., Beverloo, H.B., Löwenberg, B., and Delwel, R. (2008). High EVI1 levels predict adverse outcome in acute myeloid leukemia: prevalence of EVI1 overexpression and chromosome 3q26 abnormalities underestimated. Blood *111*, 4329–4337.

Lugthart, S., Figueroa, M.E., Bindels, E., Skrabanek, L., Valk, P.J., Li, Y., Meyer, S., Erpelinck-Verschueren, C., Greally, J., Löwenberg, B., et al. (2011). Aberrant DNA hypermethylation signature in acute myeloid leukemia directed by EVI1. Blood *117*, 234–241.

Matsumoto, A., Takeishi, S., Kanie, T., Susaki, E., Onoyama, I., Tateishi, Y., Nakayama, K., and Nakayama, K.I. (2011). p57 is required for quiescence and maintenance of adult hematopoietic stem cells. Cell Stem Cell *9*, 262–271.

Matsuo, Y., Adachi, T., Tsubota, T., Imanishi, J., and Minowada, J. (1991). Establishment and characterization of a novel megakaryoblastic cell line, MOLM-1, from a patient with chronic myelogenous leukemia. Hum. Cell *4*, 261–264.

Minegishi, N., Suzuki, N., Yokomizo, T., Pan, X., Fujimoto, T., Takahashi, S., Hara, T., Miyajima, A., Nishikawa, S., and Yamamoto, M. (2003). Expression and domain-specific function of GATA-2 during differentiation of the hematopoietic precursor cells in midgestation mouse embryos. Blood *102*, 896–905.

Mitelman, F., Johansson, B., and Mertens, F. (2007). The impact of translocations and gene fusions on cancer causation. Nat. Rev. Cancer *7*, 233–245.

Moignard, V., Macaulay, I.C., Swiers, G., Buettner, F., Schütte, J., Calero-Nieto, F.J., Kinston, S., Joshi, A., Hannah, R., Theis, F.J., et al. (2013). Characterization of transcriptional networks in blood stem and progenitor cells using high-throughput single-cell gene expression analysis. Nat. Cell Biol. *15*, 363–372.

Morishita, K., Parganas, E., William, C.L., Whittaker, M.H., Drabkin, H., Oval, J., Taetle, R., Valentine, M.B., and Ihle, J.N. (1992). Activation of EVI1 gene expression in human acute myelogenous leukemias by translocations spanning 300-400 kilobases on chromosome band 3q26. Proc. Natl. Acad. Sci. USA *89*, 3937–3941.

Niwa, H., Araki, K., Kimura, S., Taniguchi, S., Wakasugi, S., and Yamamura, K. (1993). An efficient gene-trap method using poly A trap vectors and characterization of gene-trap events. J. Biochem. *113*, 343–349.

Nozawa, D., Suzuki, N., Kobayashi-Osaki, M., Pan, X., Engel, J.D., and Yamamoto, M. (2009). GATA2-dependent and region-specific regulation of Gata2 transcription in the mouse midbrain. Genes Cells *14*, 569–582.

Nutt, S.L., and Kee, B.L. (2007). The transcriptional regulation of B cell lineage commitment. Immunity *26*, 715–725.

Rosenbauer, F., Wagner, K., Kutok, J.L., Iwasaki, H., Le Beau, M.M., Okuno, Y., Akashi, K., Fiering, S., and Tenen, D.G. (2004). Acute myeloid leukemia induced by graded reduction of a lineage-specific transcription factor, PU.1. Nat. Genet. *36*, 624–630.

Rowley, J.D. (1973). Letter: A new consistent chromosomal abnormality in chronic myelogenous leukaemia identified by quinacrine fluorescence and Giemsa staining. Nature *243*, 290–293.

Rowley, J.D. (2001). Chromosome translocations: dangerous liaisons revisited. Nat. Rev. Cancer *1*, 245–250.

Sato, T., Goyama, S., Nitta, E., Takeshita, M., Yoshimi, M., Nakagawa, M., Kawazu, M., Ichikawa, M., and Kurokawa, M. (2008). Evi-1 promotes para-aortic splanchnopleural hematopoiesis through up-regulation of GATA-2 and repression of TGF-β signaling. Cancer Sci. *99*, 1407–1413.

Senyuk, V., Sinha, K.K., Li, D., Rinaldi, C.R., Yanamandra, S., and Nucifora, G. (2007). Repression of RUNX1 activity by EVI1: a new role of EVI1 in leukemogenesis. Cancer Res. *67*, 5658–5666.

Shimabe, M., Goyama, S., Watanabe-Okochi, N., Yoshimi, A., Ichikawa, M., Imai, Y., and Kurokawa, M. (2009). Pbx1 is a downstream target of Evi-1 in hematopoietic stem/progenitors and leukemic cells. Oncogene *28*, 4364–4374.

Shimahara, A., Yamakawa, N., Nishikata, I., and Morishita, K. (2010). Acetylation of lysine 564 adjacent to the C-terminal binding protein-binding motif in EVI1 is crucial for transcriptional activation of GATA2. J. Biol. Chem. *285*, 16967–16977.

Snow, J.W., Trowbridge, J.J., Fujiwara, T., Emambokus, N.E., Grass, J.A., Orkin, S.H., and Bresnick, E.H. (2010). A single *cis* element maintains repression of the key developmental regulator Gata2. PLoS Genet. *6*, e1001103.

Snow, J.W., Trowbridge, J.J., Johnson, K.D., Fujiwara, T., Emambokus, N.E., Grass, J.A., Orkin, S.H., and Bresnick, E.H. (2011). Context-dependent function of "GATA switch" sites in vivo. Blood *117*, 4769–4772.

Spensberger, D., Vermeulen, M., Le Guezennec, X., Beekman, R., van Hoven, A., Bindels, E., Stunnenberg, H., and Delwel, R. (2008). Myeloid transforming protein Evi1 interacts with methyl-CpG binding domain protein 3 and inhibits in vitro histone deacetylation by Mbd3/Mi-2/NuRD. Biochemistry *47*, 6418–6426.

Steidl, U., Rosenbauer, F., Verhaak, R.G., Gu, X., Ebralidze, A., Otu, H.H., Klippel, S., Steidl, C., Bruns, I., Costa, D.B., et al. (2006). Essential role of Jun family transcription factors in PU.1 knockdown-induced leukemic stem cells. Nat. Genet. *38*, 1269–1277.

Stein, S., Ott, M.G., Schultze-Strasser, S., Jauch, A., Burwinkel, B., Kinner, A., Schmidt, M., Krämer, A., Schwäble, J., Glimm, H., et al. (2010). Genomic instability and myelodysplasia with monosomy 7 consequent to EVI1 activation after gene therapy for chronic granulomatous disease. Nat. Med. *16*, 198–204.

Suzukawa, K., Parganas, E., Gajjar, A., Abe, T., Takahashi, S., Tani, K., Asano, S., Asou, H., Kamada, N., Yokota, J., et al. (1994). Identification of a breakpoint cluster region 3′ of the ribophorin I gene at 3q21 associated with the transcriptional activation of the EVI1 gene in acute myelogenous leukemias with inv(3)(q21q26). Blood *84*, 2681–2688.

Suzukawa, K., Taki, T., Abe, T., Asoh, H., Kamada, N., Yokota, J., and Morishita, K. (1997). Identification of translocational breakpoints within the intron region before the last coding exon (exon 12) of the EVI1 gene in two cases of CML-BC with inv(3)(q21q26). Genomics *42*, 356–360.

Suzuki, N., Suwabe, N., Ohneda, O., Obara, N., Imagawa, S., Pan, X., Motohashi, H., and Yamamoto, M. (2003). Identification and characterization of 2 types of erythroid progenitors that express GATA-1 at distinct levels. Blood *102*, 3575–3583.

Suzuki, N., Ohneda, O., Minegishi, N., Nishikawa, M., Ohta, T., Takahashi, S., Engel, J.D., and Yamamoto, M. (2006). Combinatorial Gata2 and Sca1 expression defines hematopoietic stem cells in the bone marrow niche. Proc. Natl. Acad. Sci. USA *103*, 2202–2207.

Suzuki, M., Shimizu, R., and Yamamoto, M. (2011). Transcriptional regulation by GATA1 and GATA2 during erythropoiesis. Int. J. Hematol. *93*, 150–155.

Suzuki, M., Kobayashi-Osaki, M., Tsutsumi, S., Pan, X., Ohmori, S., Takai, J., Moriguchi, T., Ohneda, O., Ohneda, K., Shimizu, R., et al. (2013). GATA factor switching from GATA2 to GATA1 contributes to erythroid differentiation. Genes Cells *18*, 921–933.

Tsai, F.Y., and Orkin, S.H. (1997). Transcription factor GATA-2 is required for proliferation/survival of early hematopoietic cells and mast cell formation, but not for erythroid and myeloid terminal differentiation. Blood *89*, 3636–3643.

Yamamoto, M., Ko, L.J., Leonard, M.W., Beug, H., Orkin, S.H., and Engel, J.D. (1990). Activity and tissue-specific expression of the transcription factor NF-E1 multigene family. Genes Dev. *4*, 1650–1662.

Yang, L., Bryder, D., Adolfsson, J., Nygren, J., Månsson, R., Sigvardsson, M., and Jacobsen, S.E. (2005). Identification of Lin(-)Sca1(+)kit(+)CD34(+)Flt3-short-term hematopoietic stem cells capable of rapidly reconstituting and rescuing myeloablated transplant recipients. Blood *105*, 2717–2723.

Yoshimi, A., Goyama, S., Watanabe-Okochi, N., Yoshiki, Y., Nannya, Y., Nitta, E., Arai, S., Sato, T., Shimabe, M., Nakagawa, M., et al. (2011). Evi1 represses PTEN expression and activates PI3K/AKT/mTOR via interactions with polycomb proteins. Blood *117*, 3617–3628.

Yuasa, H., Oike, Y., Iwama, A., Nishikata, I., Sugiyama, D., Perkins, A., Mucenski, M.L., Suda, T., and Morishita, K. (2005). Oncogenic transcription factor Evi1 regulates hematopoietic stem cell proliferation through GATA-2 expression. EMBO J. *24*, 1976–1987.

CellPress

Cancer Cell
Article

Genomic Profiling of Hepatocellular Adenomas Reveals Recurrent FRK-Activating Mutations and the Mechanisms of Malignant Transformation

Camilla Pilati,[1,2] Eric Letouzé,[3] Jean-Charles Nault,[1,2] Sandrine Imbeaud,[1,2] Anaïs Boulai,[1,2] Julien Calderaro,[1,2,4] Karine Poussin,[1,2] Andrea Franconi,[1,2] Gabrielle Couchy,[1,2] Guillaume Morcrette,[1,2] Maxime Mallet,[1,2] Saïd Taouji,[5] Charles Balabaud,[5] Benoit Terris,[6] Frédéric Canal,[7] Valérie Paradis,[8] Jean-Yves Scoazec,[9] Anne de Muret,[10] Catherine Guettier,[11,12] Paulette Bioulac-Sage,[5,13] Eric Chevet,[5] Fabien Calvo,[14] and Jessica Zucman-Rossi[1,2,15,*]

[1]INSERM, UMR-1162, Génomique fonctionnelle des tumeurs solides, IUH, 75010 Paris, France
[2]Labex Immuno-oncology, Université Paris Descartes, Sorbonne Paris Cité, Faculté de Médecine, 75006 Paris, France
[3]Programme Cartes d'Identité des Tumeurs, Ligue Nationale Contre le Cancer, 75013 Paris, France
[4]Department of Pathology, Assistance Publique-Hôpitaux de Paris, CHU Henri Mondor, 94000 Créteil, France
[5]INSERM, UMR-1053, Université de Bordeaux, 33076 Bordeaux, France
[6]Department of Pathology, Assistance Publique-Hôpitaux de Paris, Cochin Hospital, 75014 Paris, France
[7]Institut Cochin, INSERM U1016, Université Paris Descartes, CNRS UMR8104, 75014 Paris, France
[8]Department of Pathology, Assistance Publique-Hôpitaux de Paris, Beaujon Hospital, Université Paris Diderot, 92210 Clichy, France
[9]Department of Pathology, Edouard Herriot Hospital, 69437 Lyon, France
[10]Department of Hepatogastroenterology, Centre Hospitalier de Tours, Trousseau Hospital, 37044 Tours, France
[11]Department of Pathology, Assistance Publique-Hôpitaux de Paris, CHU Bicêtre, 94275 Le Kremlin-Bicêtre, France
[12]Department of Pathology, Assistance Publique-Hôpitaux de Paris, CHU Paul Brousse, 94800 Villejuif, France
[13]Department of Pathology, CHU de Bordeaux, Pellegrin Hospital, 33076, Bordeaux, France
[14]Institut National du Cancer, INCa, 92513 Boulogne, France
[15]Assistance Publique-Hôpitaux de Paris, Hôpital Européen Georges-Pompidou, 75015 Paris, France
*Correspondence: jessica.zucman-rossi@inserm.fr
http://dx.doi.org/10.1016/j.ccr.2014.03.005

SUMMARY

Hepatocellular adenomas (HCA) are benign liver tumors predominantly developed in women using oral contraceptives. Here, exome sequencing identified recurrent somatic FRK mutations that induce constitutive kinase activity, STAT3 activation, and cell proliferation sensitive to Src inhibitors. We also found uncommon recurrent mutations activating JAK1, gp130, or β-catenin. Chromosome copy number and methylation profiling revealed patterns that correlated with specific gene mutations and tumor phenotypes. Finally, integrative analysis of HCAs transformed to hepatocellular carcinoma revealed β-catenin mutation as an early alteration and *TERT* promoter mutations as associated with the last step of the adenoma-carcinoma transition. In conclusion, we identified the genomic diversity in benign hepatocyte proliferation, several therapeutic targets, and the key genomic determinants of the adenoma-carcinoma transformation sequence.

INTRODUCTION

Hepatocellular adenomas (HCA) are rare benign tumors mainly developed in women after 2 years of oral contraceptive use (Rooks et al., 1979). HCA are also related to other risk factors (obesity, vascular diseases, and androgen and alcohol intake) or to different genetic diseases (McCune-Albright syndrome, glycogen storage disease type 1a, and maturity-onset diabetes

Significance

Malignant transformation of benign adenoma into malignant carcinoma is frequently observed in several epithelial tumor types. Adenoma-carcinoma transition is crucial for the patient prognosis; however, little is known on the molecular mechanisms involved. Here, we performed an integrated genomic analysis of hepatocellular adenomas (HCA). Among several gene mutations, we identified recurrent somatic mutation activating FRK, a Src-like kinase. FRK-activating mutations induce STAT3 activation and cell proliferation targetable by Src inhibitors. Focusing on malignant transformation of HCA in hepatocellular carcinoma, we identified *CTNNB1* and *TERT* promoter mutations as early and late genomic events, respectively, involved in adenoma-carcinoma transition. In conclusion, we propose to introduce targeted therapies and an identification of adenomas with the highest risk of malignant transformation in clinical practice.

of the young type 3 diabetes caused by HNF1A germline mutation) (Calderaro et al., 2013; Nault et al., 2013a). Bleeding and malignant transformation to hepatocellular carcinoma (HCC) can occur as severe complications observed, respectively, in 30%–50% and 5% of the cases. In the past 10 years, we identified four major molecular subgroups of HCA defined by (1) mutations inactivating HNF1A (H-HCA, 35% of the HCA) (Bacq et al., 2003; Bluteau et al., 2002; Jeannot et al., 2010), (2) activation of β-catenin by mutations in exon 3 (bHCA, 15%) (Chen et al., 2002), (3) inflammatory phenotype with STAT3 activation (IHCA, 50%) (Bioulac-Sage et al., 2009; Zucman-Rossi et al., 2006), and (4) the remaining unclassified tumors (UHCA, 10%) (Bioulac-Sage et al., 2009) (See Experimental Procedures for details on molecular group assessment.). Among bHCA, half displayed both inflammatory and β-catenin-activated phenotypes (bIHCA). Inflammatory adenomas (IHCA) are caused by *IL6ST* somatic mutation activating gp130 in 60% of the cases (Poussin et al., 2013; Rebouissou et al., 2009), whereas other IHCA are mutated for *STAT3* itself (Pilati et al., 2011) or *GNAS* (Nault et al., 2012), but in the remaining 30% of the cases no mutations were identified yet. This molecular classification is currently accepted in clinical practice using either immunohistochemical markers (Bioulac-Sage et al., 2007, 2009) or in radiology at magnetic resonance imaging (Laumonier et al., 2008), and it has dramatically improved the diagnosis and prognostic assessment of HCA.

The aim of this work was to better characterize genomic alterations causing benign proliferation of hepatocytes and their malignant transformation to improve the molecular classification and identify oncogenic events useful to propose a more personalized care of HCA patients in the future.

RESULTS

Spectrum of Mutations Identified by Exome Sequencing

We analyzed a series of 250 tumors from 195 patients including 223 classical HCAs without any suspicion of malignancy, 18 borderline lesions between HCA and HCC (HCA/HCC), and nine cases of HCCs derived from HCA malignant transformation (HCC on HCA); clinical, histological, and molecular features are described in Tables S1 and S2 (available online). Among them, whole-exome sequencing was performed using a SureSelect Enrichment System (Agilent Technologies) and a HiSeq instrument (Illumina) (see Supplemental Experimental Procedures). Tumor and corresponding nontumor DNA was sequenced in 35 classical HCAs developed in 25 patients, including nine H-HCAs, 11 IHCAs, four bHCAs, and four bIHCAs mutated in exon 3 of *CTNNB1*, and seven UHCAs (Table S3). One IHCA and one UHCA displayed a mutation of *CTNNB1* located in exon 7 and were reclassified as bIHCA and bHCA, respectively (see below). The average coverage of each base in the targeted regions was 70-fold (Figure S1). Somatic mutations were systematically verified using integrative genomics viewer inspection and/or Sanger sequencing (see Supplemental Experimental Procedures and Table S4). This strategy led to the validation of 508 somatic mutations in the 35 tumors; among them, 264 (52%) were predicted to have damaging consequences at the protein level, whereas 124 (24%) were silent and 120 (24%) were predicted to be benign functionally using PPH2 (Polyphen-2) software (Figure 1A). The mean number of predicted damaging mutations was 7.5 events per HCA tumor; it was not significantly variable in the different HCA molecular subgroups (Figure S1) but lower than that observed in hepatocellular carcinoma (41 events per HCC [Guichard et al., 2012], $p < 0.0001$). Analysis of the spectrum of nucleotide mutations identified a high frequency of transversions with a predominance of G>T changes that accumulated on nontranscribed strand in all subgroups (Figure 1B). This spectrum of nucleotide change was similar to that observed in the exome sequence of classical HCC (Guichard et al., 2012), suggesting that both benign and malignant hepatocyte proliferation could be promoted by exposure to genotoxic agents that still remain to be identified in dedicated epidemiological studies.

Exome sequencing of the 35 classical HCAs identified recurrent mutations in nine different genes (Figure 1C). *CTNNB1*, *IL6ST*, *HNF1A*, and *FRK* were mutated in at least three HCA tumors, and they were validated in the whole series of 250 tumors (Figure 1D; Table S5; Figure S1). *SLCO1B3*, *KPNA4*, *ALK*, *DDX11*, and *KIAA1109* were mutated in only two tumors representing seven different HCAs. Because these gene mutations were not associated with specific phenotype, they were not further screened in the entire series of tumors. Overall, a mutation occurring in a gene recurrently mutated was identified in 205/250 (82%) of the HCA cases (Figure 1D). *HNF1A* and *CTNNB1* mutations were identified in all H-HCA and 33/35 bHCAs, respectively. Twenty-eight of 41 bIHCAs harbored mutations in *CTNNB1* and *IL6ST*. Inflammatory adenomas displayed mutations in the known drivers *IL6ST*, *STAT3*, and *GNAS*, but also novel mutations in *FRK* and *JAK1*.

Among our whole series, the presence of two or more nodules synchronously developed in the same patient was observed in 49% of the cases (Table S1). Exome sequencing of 10 pairs of HCAs developed in 10 patients revealed in nine of these ten cases that the two tumors belonged to the same molecular subgroup: in four cases both adenomas were mutated for *HNF1A*, in three cases both tumors were IHCA (*IL6ST* mutated and *FRK* in one pair each, *IL6ST* and *JAK1* in the last pair), in one case both tumors were *CTNNB1* mutated, and in the last patient both tumors remained unclassified (Table S6). In the remaining patient one HCA was inflammatory, whereas the second HCA was unclassified. However, in nine of the ten cases, no common nucleotide mutations were identified among the paired adenomas, suggesting an independent development of the tumors. In the only pair with common mutations, the two H-HCA tumors shared one *HNF1A* mutation (Q211P) and a somatic substitution in *HDAC4* (T1055R). Interestingly, the two nodules were joined and they accumulated different private alterations, including inactivation of the second allele of *HNF1A* (Table S6), suggesting that HNF1A monoallelic inactivation added to an HDAC4 mutation could be an early event in the history of this case.

FRK-Activating Mutations in IHCA

Among the 35 HCAs analyzed by exome sequencing, three different IHCAs exhibited a somatic mutation of the fyn-related kinase (FRK, also known as RAK). FRK is a non-receptor-tyrosine kinase related to the Src kinase family, first proposed as a tumor suppressor in breast cancer cells (Yim et al., 2009). In the whole series of 250 tumors, we identified a heterozygous somatic *FRK* mutation in eight additional IHCAs and one bIHCA

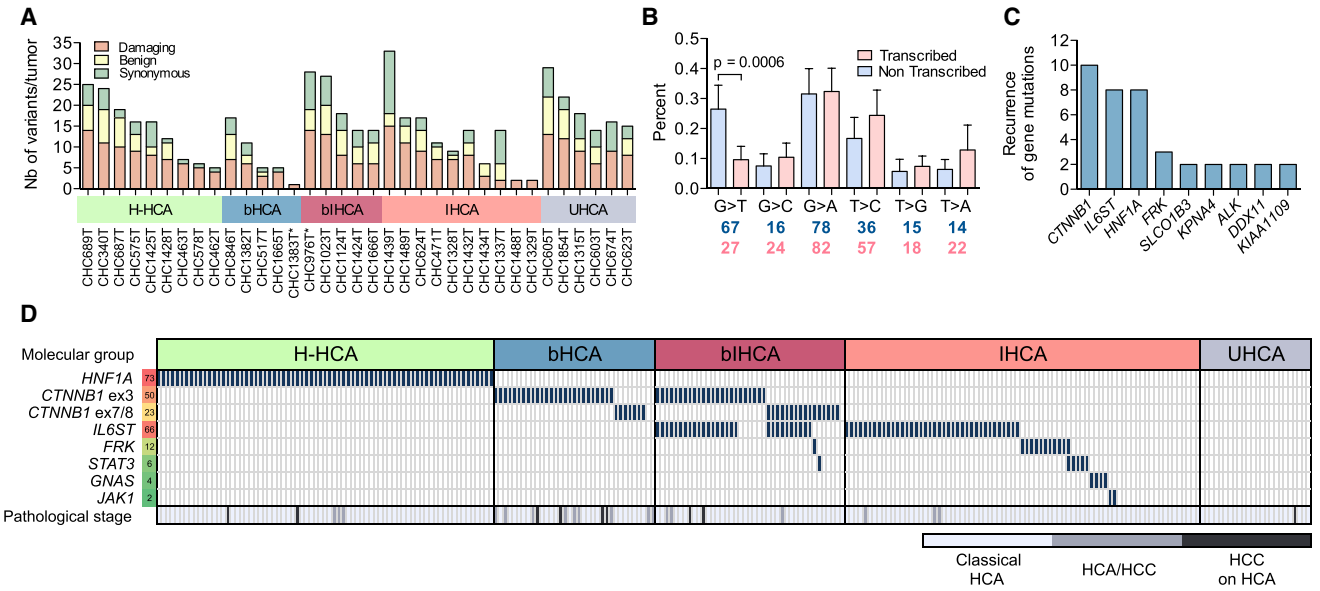

Figure 1. Profiles of Mutations in HCA Identified by Exome Sequencing

(A) Distribution of the 508 somatic mutations in the 35 HCA tumors according to their functional consequences (damaging, benign, and synonymous) predicted by PPH2 (Polyphen-2). Asterisk (*) indicates HCA with *CTNNB1* exon 7 mutations.

(B) Type of mutations on the transcribed (pink) and the nontranscribed (blue) strands for the 455 nucleotide substitutions identified in exome sequencing of 35 HCAs (means with 95% CI; two-tailed Mann-Whitney test).

(C) Genes recurrently mutated in classical HCA with damaging consequences.

(D) Somatic mutations (blue boxes) identified in 250 tumors (columns) among seven classical HCA-altered genes (rows). The number of events per gene is indicated on the left.

See also Figure S1 and Tables S1, S2, S3, S4, S5, and S6.

(Figure 1D). All FRK mutations were located in the tyrosine kinase catalytic domain, and two hot spots were identified: an amino acid substitution located at codon 346 in four cases and eight small in-frame deletions/insertions at codons V378 and/or F379 in eight cases (Figure 2A; Table S5). In one case (1130), we identified two nucleotide mutations that led to amino acid substitutions at codons 346 and 350 carried by the same allele. Overall, *FRK* was the second most frequently mutated gene in our series of IHCA (12/118, 10%).

No recurrent FRK mutations are currently described in tumors. In HCA, the mutation pattern including two hot spots and in-frame deletion/insertion suggested that FRK mutations could have gain of function. To test this hypothesis, we reproduced six different mutants identified in IHCA by site-directed mutagenesis in a *FRK* full-length cDNA. All the tested FRK mutants induced a strong acute inflammatory response in hepatocellular cell lines with overexpression of two inflammatory target genes, *SOCS3* and *CRP*, independently of interleukin-6 (IL-6) exposure (Figure 2B; Figures S2A–S2C). This inflammatory response was proportional to the amount of transfected mutants (Spearman's $r = 0.89$, $p = 0.01$; Figure S2B). FRK mutants induced the activation of STAT3 as assessed by its phosphorylation at Y705 and its nuclear translocation, whereas wild-type FRK had no effect on STAT3 phosphorylation and localization (Figures 2C and 2D). We further showed that VF and FK FRK mutant exhibited an increased kinase activity compared with the wild-type FRK, affecting both V_{max} and K_M (Figure 2E; Figure S2D). Next, we showed that four different Src inhibitors, namely, PP2, dasatinib, Src inhibitor 1, and Src inhibitor 5, were able to abrogate the constitutive kinase activity of FRK mutants (Figure 2F). Then, we selected dasatinib, an inhibitor currently used to cure leukemia patients (Talpaz et al., 2006). Treatment of Hep3B cells with dasatinib decreased the constitutive activity of FRK mutant in a dose-dependent manner, whereas it had no effect on IL-6-induced inflammation (Figure 2G).

Then, we stably transfected Ba/F3 cells, an interleukin-3 (IL-3)-dependent murine pro-B cell line, with wild-type or mutant FRK. In the presence of IL-3, cell proliferation was similar in all conditions (Figure S2E); in contrast, only Ba/F3 cells expressing the FRK mutants were able to grow upon IL-3 withdrawal (Figure 3A). We confirmed the proliferation advantage conferred by *FRK* overexpression in mice immortalized fibroblasts, NIH 3T3, cultured with a limiting amount of growth factors (Figure S2F). Also, in NIH 3T3, FRK mutants promoted cell foci formation without increasing cell migration or invasion (Figure 3B; Figures S2G and S2H). Interestingly, in Ba/F3 cells, IL-3-independent growth induced by FRK mutant was abrogated by dasatinib treatment (Figure 3C). Subcutaneous injection of Ba/F3 cells with stable expression of the VK FRK mutant in nude mice resulted in tumor growth. In contrast, Ba/F3 cells expressing wild-type *FRK* failed to promote tumor growth (Figure 3D). Allografted tumors showed nuclear and Y705-phosphorylated STAT3 (Figure 3E). Furthermore daily intraperitoneal injections of dasatinib (10 mg/kg/day) after subcutaneous tumor development and during 14 days led to a complete regression of the tumors (n = 9; Figures 3F and 3G; Figure S2I). Interestingly,

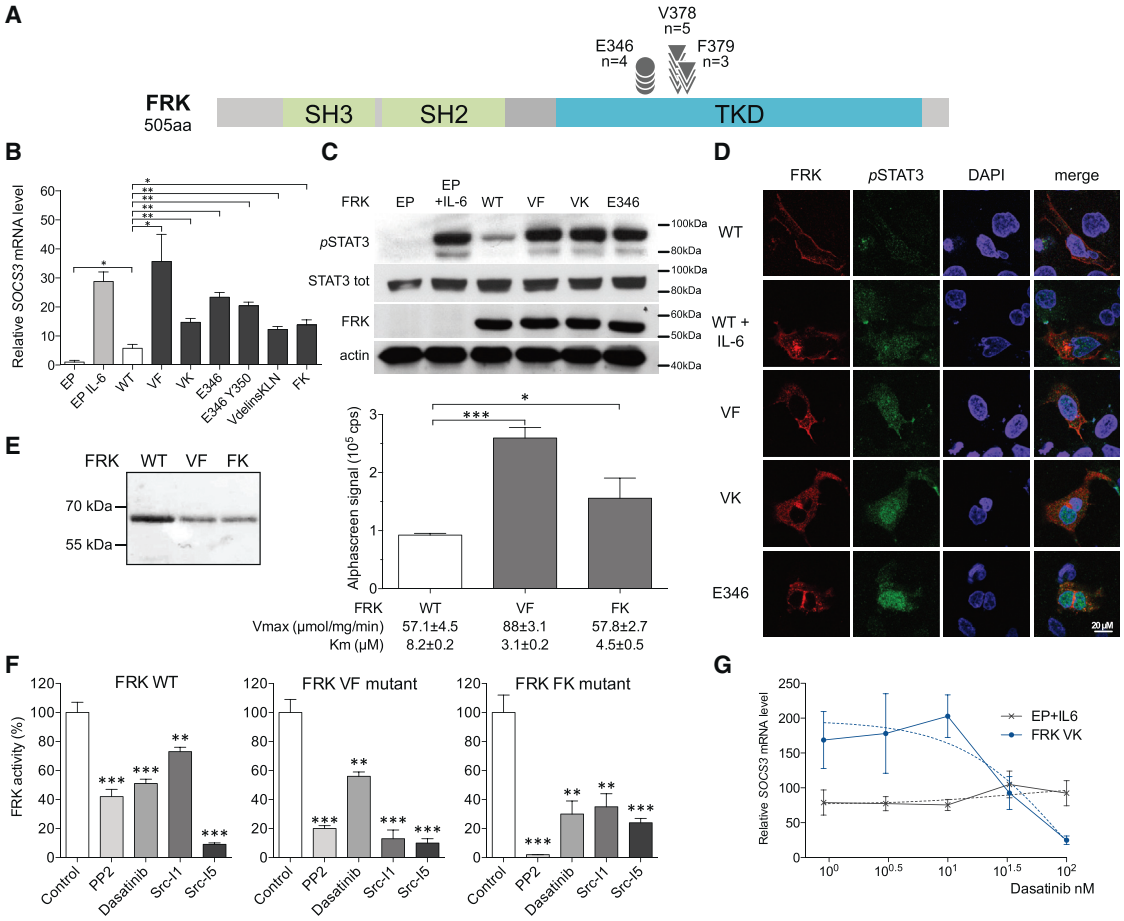

Figure 2. FRK Mutants Induce STAT3 Activation

(A) Spectrum of FRK mutations identified in 250 HCAs. Circles indicate amino acid (aa) substitutions and triangles are in-frame deletions. SH, Src homology domain; TKD, tyrosin kinase domain.

(B) Endogenous *SOCS3* mRNA expression of FRK mutants V378–F379 del (VF), V378–K380 delinsE (VK), E346G (E346), E346G Y350C (E346 Y350), V378 delinsKLN (VdelinsKLN), F379-K380 delinsL (FK), or control wild-type (WT) FRK (WT) and empty plasmid (EP) transfected in Hep3B. *$p < 0.05$; **$p < 0.01$; ***$p < 0.001$, two-tailed Student's t test.

(C) Expression of FRK, total STAT3, and Y705-phosphorylated STAT3 (pSTAT3) proteins in transfected Hep3B cells assessed by western blot.

(D) Subcellular localization of FRK and tyrosine phosphorylation of STAT3 at Y705 (pSTAT3) FRK and STAT3 proteins were analyzed by immunofluorescence, and images were obtained with a confocal microscope. Results are representative of three independent experiments.

(E) FRK proteins WT and mutants (VF and FK) were produced in *Escherichia coli*. The AlphaScreen method showed an increased kinase activity for FRK mutants with modified K_M and V_{max}. cps, counts per second.

(F) FRK kinase residual activity was measured in vitro by AlphaScreen method after treatment with four different Src inhibitors: PP2 (10 µM), dasatinib (10 µM), Src-I1 (10 µM), and Src-I5 (10 µM). *$p < 0.05$, **$p < 0.01$, ***$p < 0.001$, two-tailed Student's t test.

(G) Endogenous *SOCS3* mRNA expression of FRK VK mutant (blue) or empty vector treated with 100 ng/ml IL-6 (black) transfected in Hep3B exposed for 6 hr to increasing concentrations of dasatinib. Quantitative data are presented as mean ± SD.

See also Figure S2.

14 days after dasatinib withdrawal, tumors reappeared, confirming the oncogenic addiction of Ba/F3 cells to the FRK mutant tested (Figure 3G).

Mutations Activating JAK-STAT3 Pathway in IHCA

Exome sequencing of an inflammatory adenoma revealed a somatic missense mutation leading to S703I substitution in the JAK kinase *JAK1* previously identified in an acute lymphoblastic T cell leukemia (Zhang et al., 2012). Screening the entire sequence of *JAK1* in the whole series of 250 tumors revealed one additional IHCA with a heterozygous somatic JAK1 substitution A723D never described in tumors (Figure 1D; Figure 4A; Table S5). S703I and A723D mutants were different from the two classical V658 and R724 JAK1 substitutions known to activate the JAK-STAT pathway (Flex et al., 2008; Staerk et al., 2005). In Hep3B cells, we showed that expression of S703I or A723D was able to induce an inflammatory response and phosphorylation of STAT3 at Y705 (Figure 4B; Figures S3A and S3B). Moreover, the two JAK1 mutant proteins were phosphorylated at Y1022/1023, two regulatory tyrosines known to activate JAK1 when phosphorylated (Figure S3B). We also identified in an inflammatory HCA an unusual heterozygous somatic mutation in

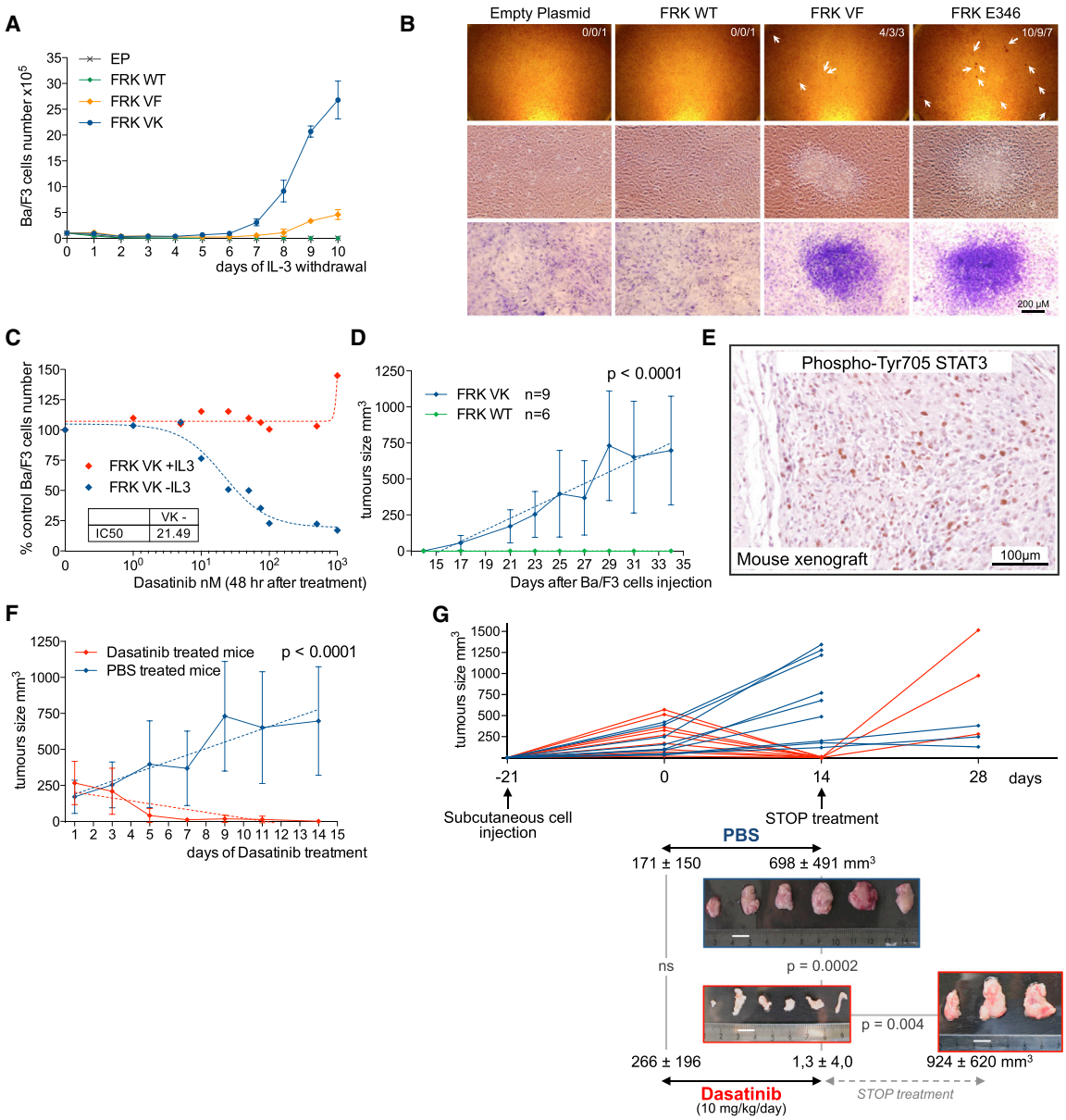

Figure 3. FRK Is a Targetable Activated Gene in HCA

(A) Growth of Ba/F3 cells stably transfected with FRK mutants (VF and VK) compared with FRK WT or EP after IL-3 withdrawal in triplicate experiments. Data shown indicate mean ± SD.

(B) Cell foci formation was observed in NIH 3T3 cells stably expressing FRK mutants VF (p = 0.003, t test) or E346 (p = 0.0009, t test) and not in cells transfected with WT FRK or EP. In white, the number of foci representative of three independent experiments.

(C) Ba/F3 cells transfected with FRK VK mutant treated (red) or untreated (blue) with 10 ng/ml IL-3 and exposed for 48 hr to increasing concentrations of dasatinib. The graph plots the proportion of treated cells relative to the transfected not-treated cells.

(D) Subcutaneous injection of 10^7 Ba/F3 cells with stable expression of VK FRK mutant (blue, n = 9) induced tumor growth in a BALB/c-nu/nu mouse model, whereas WT FRK (green, n = 6) failed (mean tumor volume, 95% CI, regression analysis).

(E) Representative staining of Y705 phosphorylation of STAT3 using immunohistochemistry in allograft tumors from VK FRK Ba/F3 cells 34 days after injection.

(F) Effect of dasatinib treatment on tumor size of mice allografted with Ba/F3 cells transfected with VK FRK mutant and treated daily with dasatinib (red, n = 9; 10 mg/kg/day) or with PBS as a control (blue, n = 9) (mean tumor volume, 95% CI, regression analysis).

(G) Effect of dasatinib withdrawal on allograft tumors from VK FRK Ba/F3 cells. Shown are the tumors of BALB/c-nu/nu mice treated daily with PBS (10 ml/kg, 14 days) as a control or with dasatinib (10 mg/kg/day, 14 days), and tumors treated with dasatinib during 14 days and left without treatment for 14 days (n = 3). Scale (white) bars, 10 mm.

the *IL6ST* gene, located at exon 10 and leading to the in-frame deletion of four amino acids (A418–F421) outside the mutation hot spot that we previously identified at the IL-6 binding site (Poussin et al., 2013; Rebouissou et al., 2009). Sequencing the entire coding sequence of *IL6ST* in the validation set of 250 tumors led to the identification of a similar A418–F421 deletion

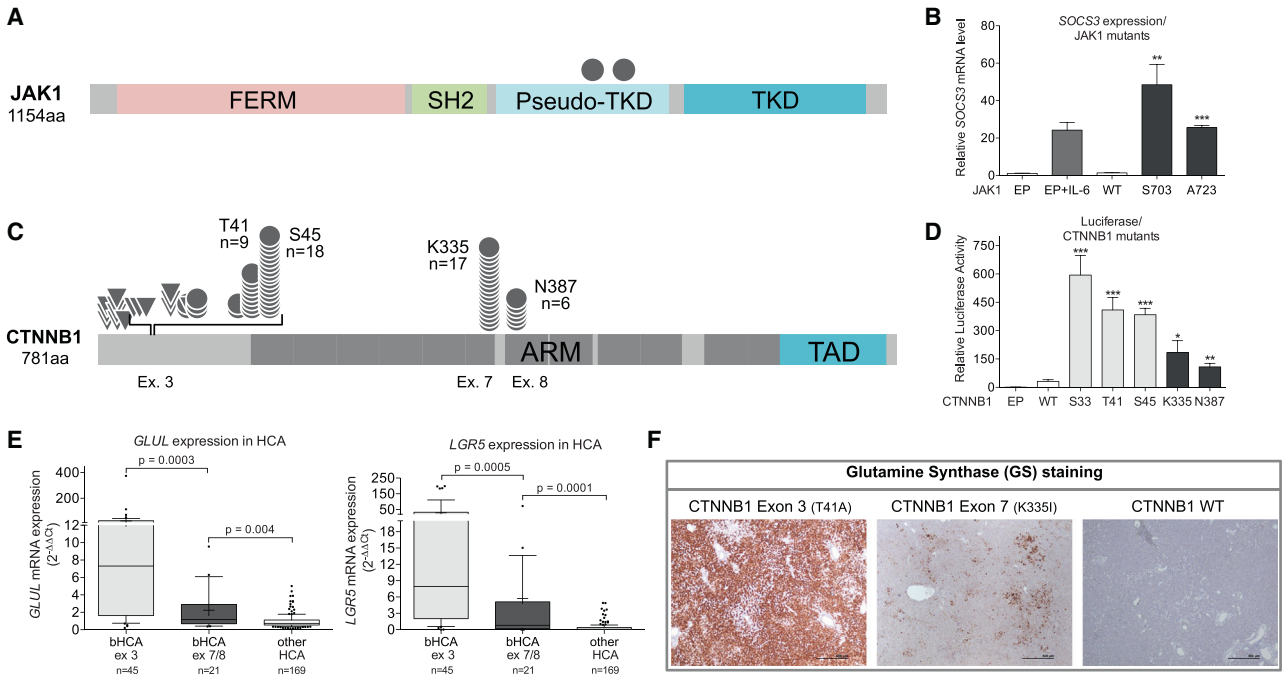

Figure 4. Identification of Uncommon Recurrent Gene Mutations in HCA and Functional Analysis

(A) Spectrum of *JAK1* mutations identified in 250 HCAs. Circles indicate aa substitutions.

(B) JAK1 mutants S703I (S703) and A723D (A723) or control WT JAK1 (WT) and EP were transfected in the Hep3B cell line. Graphs are quantitative (q)RT-PCR results showing the induction of endogenous *SOCS3* mRNA transcription measured after 6 hr of serum starvation and, when indicated, treated for 3 hr with 100 ng/ml IL-6 relative to unstimulated EP-transfected Hep3B cells. Data shown indicate mean ± SD. $^{**}p < 0.01$, $^{***}p < 0.001$, two-tailed Student's t test versus WT JAK1.

(C) Spectrum of *CTNNB1* mutations identified in 250 HCA. Circles indicate aa substitutions, and triangles are in-frame deletions. ARM, Armadillo repeat; TAD, transactivation domain.

(D) *CTNNB1* mutants S33Y (S33), T41A (T41), S45P (S45), K335I (K335), and N387K (N387) or control WT *CTNNB1* (WT) and empty plasmid (EP) were transfected in Huh7 cells expressing a *CTNNB1*-driven luciferase (TOP-FLASH) reporter construct. Shown is the luciferase activity determined from triplicate cotransfections relative to empty plasmid (EP). Data shown indicate mean ± SD. $^{*}p < 0.05$; $^{**}p < 0.01$; $^{***}p < 0.001$, two-tailed Student's t test versus WT *CTNNB1* with TOP-FLASH.

(E) Expression profiles of CTNNB1-exon 3 mutated HCA (n = 45), *CTNNB1*-exon 7- and -exon 8-mutated HCAs (n = 21) and *CTNNB1* WT HCA (n = 169). The graph shows the expression of *GLUL* (glutamine synthase) and *LGR5* by qRT-PCR relative to nontumor livers. Results are expressed as Tukey's boxplots; two-tailed Mann-Whitney test.

(F) Representative staining of glutamine synthase (GS) by immunohistochemistry in wild-type *CTNNB1* HCA, exon 7-mutated and exon 3-mutated bHCA. $^{*}p < 0.05$; $^{**}p < 0.01$; $^{***}p < 0.001$.

See also Figure S3.

in an additional IHCA (Figure S1). These mutations in exon 10 of *IL6ST* were exclusive from the classical mutation previously identified in exon 6. We further showed that this *IL6ST* mutant was able to constitutively activate gp130 in a cell culture model (Figure S3C). Finally, in the entire validation set of HCA, all the genes mutated in IHCA (*IL6ST, FRK, JAK1, STAT3*, and *GNAS*) were almost mutually exclusive; only one tumor showed mutations in both *FRK* and *STAT3* genes (Figure 1D).

Hot Spots of Mutations in *CTNNB1*

Exome sequencing in two HCAs revealed a mutation of *CTNNB1* located in exon 7 (K335I), outside *CTNNB1* exon 3 where the classical mutations activating β-catenin are usually located (Chen et al., 2002). Among the validation set of 250 tumors, we further identified two hot spots of substitutions at β-catenin codon 335 (K335I in 13 cases, K335T in four cases) and codon 387 located in exon 8 (N387K in six cases; Figure 4C). All HCAs with *CTNNB1* exon 7 and exon 8 mutations were previously considered as unclassified HCA (seven cases) or inflammatory adenoma (16 cases), and they were further classified for all analyses in the bHCA or bIHCA molecular subgroup. *CTNNB1* exon 7 and exon 8 mutations were mutually exclusive but also from mutations located at exon 3 and *HNF1A* mutations. We further showed that K335I and N387K mutants were able to activate β-catenin in a hepatocellular cell line, with a lower activity than the S33Y, T41A, and S45P mutants located within exon 3 (Figure 4D). Accordingly, most of the HCA tumors with exon 7 or exon 8 mutation exhibited a slight overexpression of glutamine synthase and *LGR5*, two classical genes activated by *CTNNB1* (Figure 4E). Immunohistochemical analyses of these cases revealed a faint patchy glutamine synthase expression without nuclear staining of β-catenin (Figure 4F). All these results showed that *CTNNB1* mutants at codons 335 and 387 weakly activate β-catenin in vivo in HCA.

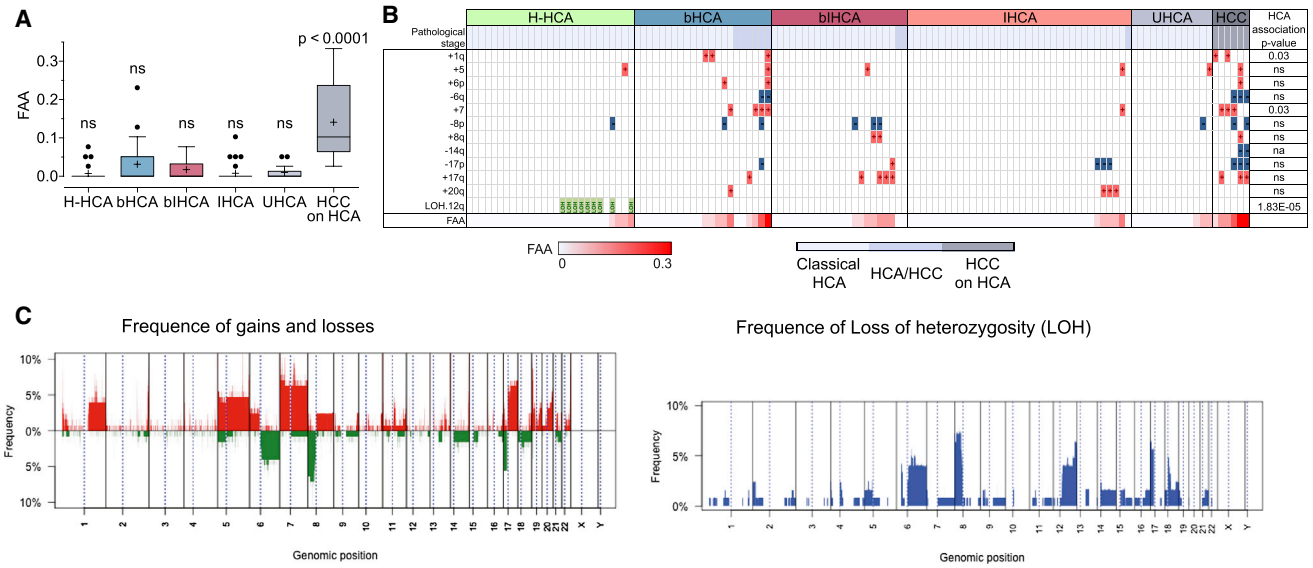

Figure 5. SNP Array Profiling of HCA Reveals Distinct Copy-Number Profiles Associated with Molecular Groups

(A) Distribution of genomic instability, defined as the FAA, in different molecular groups. Results are expressed as Tukey's boxplots; two-tailed Mann-Whitney test. ns, not significant

(B) Distribution of chromosome aberrations according to HCA molecular classification groups. LOH of chromosome 12q significantly associates with H-HCAs, whereas gains of 1q and of chromosome 7 associate with bHCA.

(C) Frequency of gains, deletions, and LOHs along the genome in a series of 111 classical HCAs, nine borderline lesions HCA/HCC, and six HCCs resulting from HCA malignant transformation.

See also Table S7.

Copy Number and Methylome Profiling

We profiled chromosome aberrations in 111 classical HCAs, nine borderline lesions HCA/HCC, and six HCC resulting from HCA malignant transformation. Although chromosomal instability, measured by the fraction of aberrant arms (FAA) score, was low and similar in the different molecular subgroups of classical adenomas (Figure 5A), we identified three recurrent events associated with specific molecular groups: bHCA showed more frequent gains of 1q ($p = 0.03$) and chromosome 7 ($p = 0.03$), whereas H-HCA presented frequent copy-neutral losses of heterozygosity (LOHs) at chromosome 12q, leading to a loss of the wild-type *HNF1A* gene and a duplication of the mutated allele ($p = 3.4 \times 10^{-6}$; Figures 5B and 5C; Table S7).

We then determined DNA methylation profiles in 50 hepatocellular adenomas and four normal liver samples using HumanMethylation450 arrays (Illumina). Consensus clustering identified two major clusters closely associated with the inflammatory phenotype (M1 and M2) or noninflammatory phenotypes (M3–M5). The partition in the five stable DNA methylation clusters (Figure 6A, M1–M5) was highly associated with specific molecular groups ($p = 3.4 \times 10^{-19}$, chi-square test; Figure 6B) and gene mutations. The M1 cluster included IHCA and mixed bIHCAs exclusively mutated in exon 7 or exon 8 of *CTNNB1*, whereas the M2 cluster included bIHCAs mutated in exon 3. Noninflammatory tumors were subdivided in clusters M3 including all H-HCA, M4 including most bHCA, and M5 including UHCA. Most DNA methylation changes occurred at CpG sites located outside CpG islands that displayed global hypomethylation in all tumor clusters compared with normal controls (Figure S4A). As described in HCC (Stefanska et al., 2011), hypomethylated regions formed genomic clusters, preferentially located at gene family loci (Figure S4B). Although the pattern of hypomethylation was similar in the five tumor clusters, the intensity of hypomethylation was significantly associated with methylation clusters ($p = 2.1 \times 10^{-4}$, ANOVA). Hypomethylation was weaker in clusters M1 and M2 (inflammatory HCA) and stronger in cluster M4 (bHCA), particularly in tumors that transformed into HCC (Figure 6C). There were few hypermethylated CpG sites, but we identified 640 genes specifically hypermethylated in cluster M3. Among them, 109 genes were hypermethylated and downregulated in H-HCA (significant overlap, $p = 2.4 \times 10^{-36}$, Fisher's exact test) (Table S8); they were significantly enriched in liver-specific genes ($p = 9.7 \times 10^{-6}$, hypergeometric test) (Figure 6D) and in genes known to be downregulated in liver cancer (Acevedo et al., 2008) ($p = 1.7 \times 10^{-14}$, hypergeometric test) (Table S9).

Alterations Involved in Malignant Transformation

Next, we aimed to investigate the genetic and epigenetic alterations involved in malignant transformation of HCA to HCC. We observed a progressively increased chromosomal instability in borderline HCA/HCC lesions and in HCC derived from malignant transformation compared with classical HCA ($p = 0.05$; Figure 7A; Table S10). Specific loss of chromosome 6q and gain of chromosome 7 were more frequent in borderline and transformed HCA (Figure 5B). Interestingly, in methylome analysis, the intensity of the beta-value in hypomethylated genomic regions increased during malignant transformation ($p = 0.002$, ANOVA) (Figure 7B). Exome sequencing and SNP array analysis (Letouzé et al., 2010) were carried out in five cases of

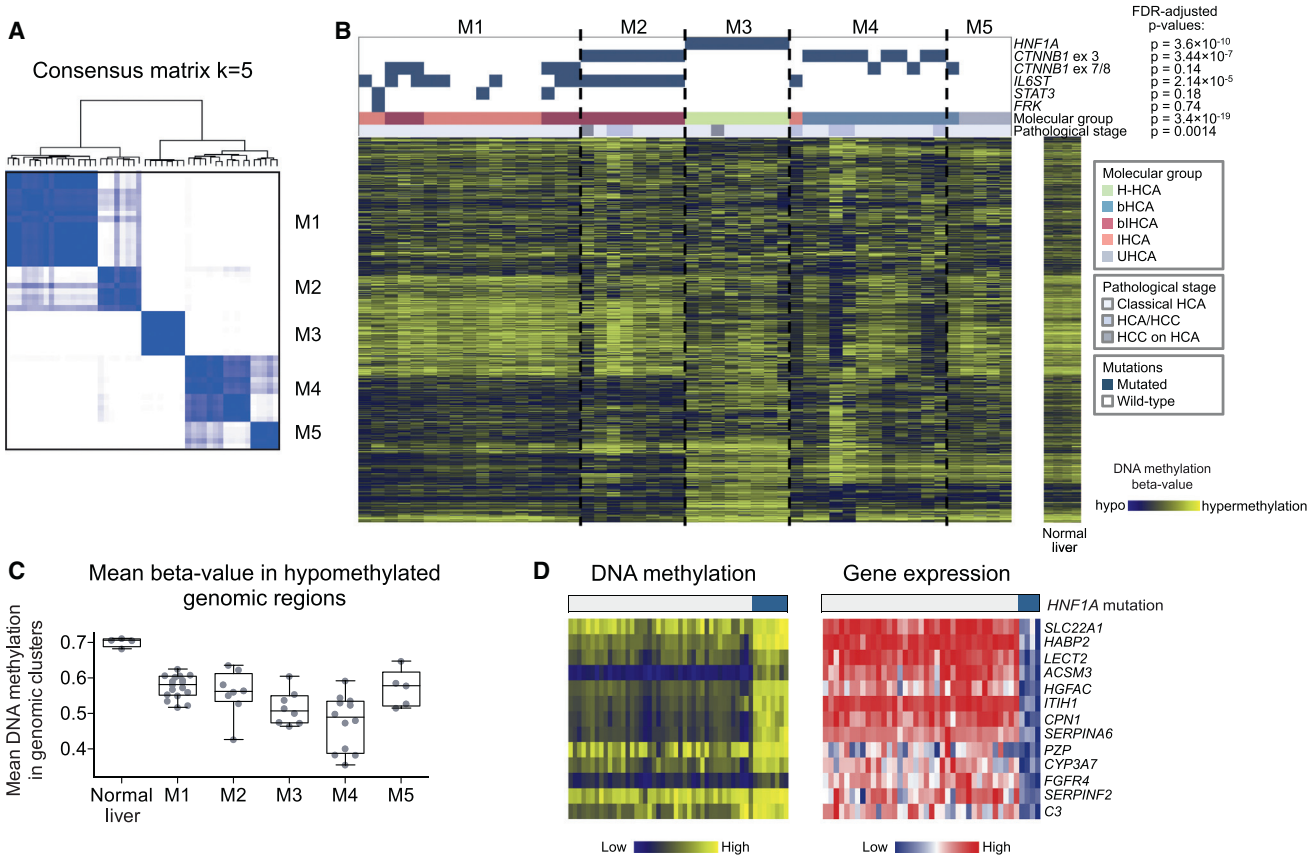

Figure 6. DNA Methylation Analysis of HCA Reveals Strong Correlation with Molecular Groups

(A) Consensus clustering analysis of 50 HCAs identifies five DNA methylation clusters.

(B) Heatmap representation of DNA methylation profiles. FDR, false discovery rate.

(C) Boxplots represent the mean DNA methylation beta-values in hypomethylated clusters in tumors of different methylation subgroups.

(D) DNA methylation and gene expression are represented for 13 liver-specific genes that are significantly hypermethylated and downregulated specifically in H-HCA.

See also Figure S4 and Tables S8 and S9.

synchronous malignant transformation for which both benign (HCA) and malignant (HCC) parts of the tumors were available. In comparison with classical HCA, the number of functional somatic mutations progressively increased in transformed HCA (mean of 24.4 events per transformed HCA, $p < 0.0001$; Figure 7C) and in malignant HCC part of the tumors (mean of 39 events per HCC counterpart) at a level similar to that observed previously in a series of classical HCC (Guichard et al., 2012) (Figures 7C and 7D). In four cases, mutations in the genes classically mutated in HCA (*CTNNB1*, *IL6ST*, and *HNF1A*) were similar in the HCA and HCC counterparts, demonstrating a common origin of the benign and transformed parts of the tumors (Figure 7G; Figure S5A). In the fifth case, the HCA and HCC parts showed different *CTNNB1* mutations, whereas 43 other mutations were found in common.

Among the other genes recurrently mutated in transformed HCA, we identified in two cases *ASH1L* (recurrently mutated in lung cancers and cell lines (Govindan et al., 2012; Liu et al., 2012) and *PEG3*, which is mutated in cholangiocarcinoma (Ong et al., 2012) (Figure S5B). A large number of private mutations were also accumulated in almost all HCA and HCC tumors, illustrating separated genetic evolution. Interestingly, in case 361, we also analyzed an HCC relapsed 3 years after the first surgical resection of a transformed HCA. Only one mutation activating β-catenin (*CTNNB1* in-frame deletion T3_A126) was common between the HCA tumor, the synchronous HCC, and the relapsed HCC. Moreover, in this patient, we identified in three different samples of nontumor liver tissues a similar T3_A126 *CTNNB1* deletion in 1/10,000 tested cells (Figure S5C). These results pointed *CTNNB1* mutation as a very early tumorigenic event in a precursor cell niche that generated three different tumors. In this case we also identified in each tumor a different mutation in the gene coding for the monoamine oxidase MAOB, suggesting that the inhibition of this gene was selected to promote the tumor development.

In the mutation screening, we added the telomerase reverse transcriptase (*TERT*) promoter, not covered in exome sequencing, because hot spot mutations were recently identified in various tumors, including HCC (Horn et al., 2013; Huang et al., 2013; Killela et al., 2013; Nault et al., 2013b). *TERT* promoter mutations were identified in five samples and in most of

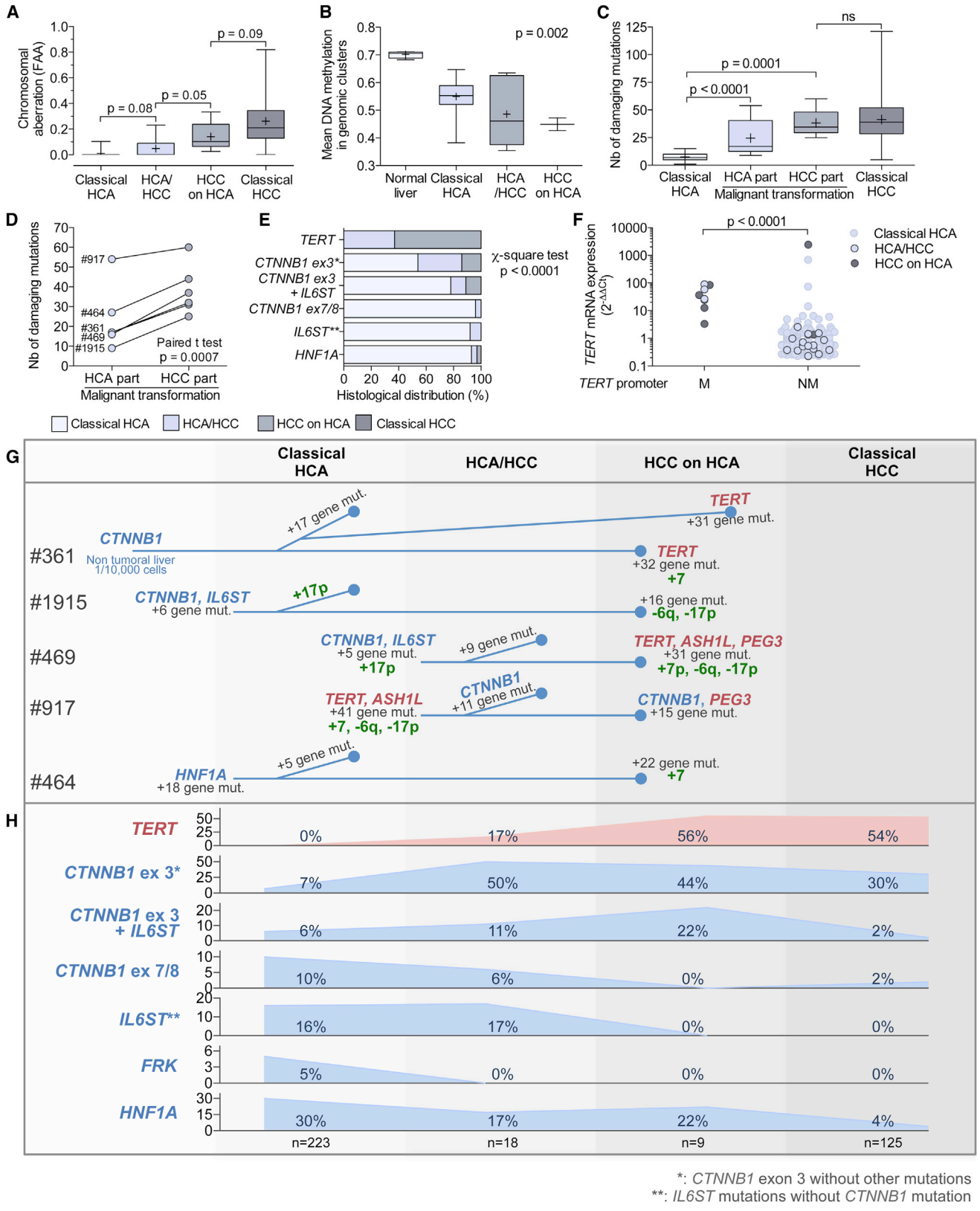

Figure 7. Time Frame of Genomic Alterations in HCA Malignant Transformation

(A) Distribution of chromosomal instability, defined as the FAA, in different pathological groups (maximum-minimum [max.-min.] boxplot, two-tailed Mann-Whitney test).

(legend continued on next page)

the cases (four of five) only in the malignant parts, suggesting that *TERT* promoter mutations could be a later oncogenic event after *CTNNB1* mutations. Then, we screened *TERT* promoter in a large series of 375 hepatocellular tumors, including 223 classical adenomas, 18 borderline lesions HCA/HCC, nine HCC derived from adenomas, and 125 classical HCC (Guichard et al., 2012). *TERT* promoter mutations were not found in classical adenomas, but they were found later in the malignant progression in borderline lesions (17%) and in transformed HCA to HCC (56%) with a frequency similar to that identified in classical HCC (54%). In HCC, *TERT* promoter mutations were significantly associated with *CTNNB1* mutations ($p < 0.0001$). Previous studies have shown that *TERT* promoter mutations create de novo consensus binding sequence for ETS/TCF transcription factors and could increase telomerase transcription (Horn et al., 2013). Here, in HCA, borderline lesion, and transformed HCA, *TERT* promoter mutations were significantly associated with an increased transcription of *TERT* ($p < 0.0001$; Figure 7F). Then, we compared the distribution of all recurrent gene mutations in the overall set of 375 tumors (Figures 7E and 7H). The proportion of *CTNNB1* exon 3 and *CTNNB1* exon 3 associated with *IL6ST* mutations progressively increased from the adenoma (13%) to the HCC-transformed lesions (66%), thus showing the significant role of these mutations in malignant progression. In contrast, the proportion of *IL6ST* alone, *CTNNB1* exon 7 and exon 8, *HNF1A*, and *FRK* mutations decreased in HCA transformed in HCC and was also lower in classical HCC, suggesting that these genes are not significantly involved in malignant transformation process.

By integrating all the omic results with the clinical and pathological features and with the identification of *FRK*, rare *JAK1*, and exon 10 *IL6ST*-activating mutations, we have enriched the mutational spectrum of inflammatory HCA, finally composed of mutations in *IL6ST* (26% of HCA), *FRK* (5%), *STAT3* (2%), *GNAS* (2%), and *JAK1* in 1% (Figure 8A). Three pathways recurrently altered in HCA (HNF1A inactivation, STAT3 or β-catenin activation alone) are associated with the benign phenotype of the tumors and specific histological features (Figure 8B). In contrast, the malignant transformation is strongly associated with characteristic gene mutations (*CTNNB1* exon 3 and *TERT* promoter mutations), chromosome alterations, and hypomethylation accumulated in time frame together with previously described specific clinical features (male sex and androgen therapy, Nault et al., 2013a; Figure 8C).

DISCUSSION

Whole-exome sequencing of hepatocellular adenomas revealed the high genetic diversity of these tumors, and the genes recurrently mutated in hepatocyte benign tumorigenesis and in the subsequent malignant transformation. In this study we identified recurrent somatic mutations of *FRK* leading to an activation of the FRK kinase activity and to constitutive STAT3 activation associated with the inflammatory phenotype of HCA. Whereas the activation of STAT3 by Src has been previously described in vitro (Bromberg et al., 1998; Turkson et al., 1998), we showed that FRK mutants induce STAT3 activation in vitro, in vivo, and in human tumors. Also, whereas FRK has been proposed as a tumor suppressor in breast cancer (Yim et al., 2009), here we demonstrated the proproliferative function of mutant FRK during benign tumorigenesis. In the liver, FRK mutants were identified only in benign tumors, whereas mouse models of gastrointestinal cancer have also demonstrated opposite functions of STAT3 at early step of tumorigenesis and during malignant transformation (Grivennikov and Karin, 2010; Lee et al., 2012; Musteanu et al., 2010). However, *FRK* was also reported as involved in a chromosome rearrangement with ETV6 in a leukemia (Hosoya et al., 2005), suggesting that this gene could be as well activated in malignant neoplasms. Also, the oncogenic properties of STAT3 constitutive activation could differ according to the cell of origin related to a malignant cell proliferation in lymphocytes (Fasan et al., 2013; Koskela et al., 2012) versus benign proliferation in hepatocytes mutated for *IL6ST* or *STAT3* (Pilati et al., 2011; Rebouissou et al., 2009). In addition, the dramatic response to the Src inhibitor dasatinib in vitro and in vivo supports FRK-activating mutations as a paradigm of a mutated gene addiction. Overall, the gene mutations identified in IHCA activate the STAT3 pathway to cause a common inflammatory phenotype within the tumors. Nowadays, inflammatory driver gene mutations remain to be identified in 18% of inflammatory HCA. Moreover, 10% of the adenomas remain unclassified and in these cases additional specific genetic or epigenetic defect remained to be identified.

Interestingly, our methylome analysis distinguished perfectly the five molecular groups of HCA, and identified genomic clusters of hypomethylation at gene family loci showing a close relationship between epigenetic changes, gene mutations, and phenotypes of the tumors. We also identified a set of liver-specific genes, hypermethylated and downregulated specifically in H-HCA. A previous report suggested that activation of HNF1A

(B) Boxplots represent the mean DNA methylation beta-values in hypomethylated clusters in tumors of different pathological stages (two-tailed Kruskal-Wallis test).
(C) Number of damaging mutations in classical HCA, in HCA transformed in HCC (HCA part) and in HCC resulting from a transformation of an adenoma (HCC part) and in 24 classical HCC(Guichard et al., 2012) (max.-min. boxplot, two-tailed Mann-Whitney test).
(D) Paired comparison of HCA and HCC counterparts of five malignant transformations (two-tailed paired t test).
(E) Distribution of the pathological groups of tumors mutated in *TERT* promoter, exon 3 of *CTNNB1* without *IL6ST* mutation, both exon 3 of *CTNNB1* and *IL6ST*, *IL6ST* without *CTNNB1* mutation, exon 7 and exon 8 of *CTNNB1*, and *HNF1A* (chi-square test).
(F) *TERT* expression in mutated and nonmutated *TERT* promoter tumors according to the different pathological stages (two-tailed Mann-Whitney test).
(G) Accumulation of genomic alterations in five malignant transformations was defined according to whole-exome sequencing and SNP array analysis. Red indicates genes recurrently mutated in transformed HCA, blue indicates genes recurrently mutated in classical HCA, and in green indicates recurrent chromosomal alterations.
(H) Frequency of mutations in *TERT* promoter, exon 3 of *CTNNB1* without *IL6ST* mutations, both exon 3 of *CTNNB1* and *IL6ST*, *IL6ST* without *CTNNB1* mutations, exon 7 and exon 8 of *CTNNB1*, and *HNF1A* according to the pathological groups.
See also Figure S5 and Table S10.

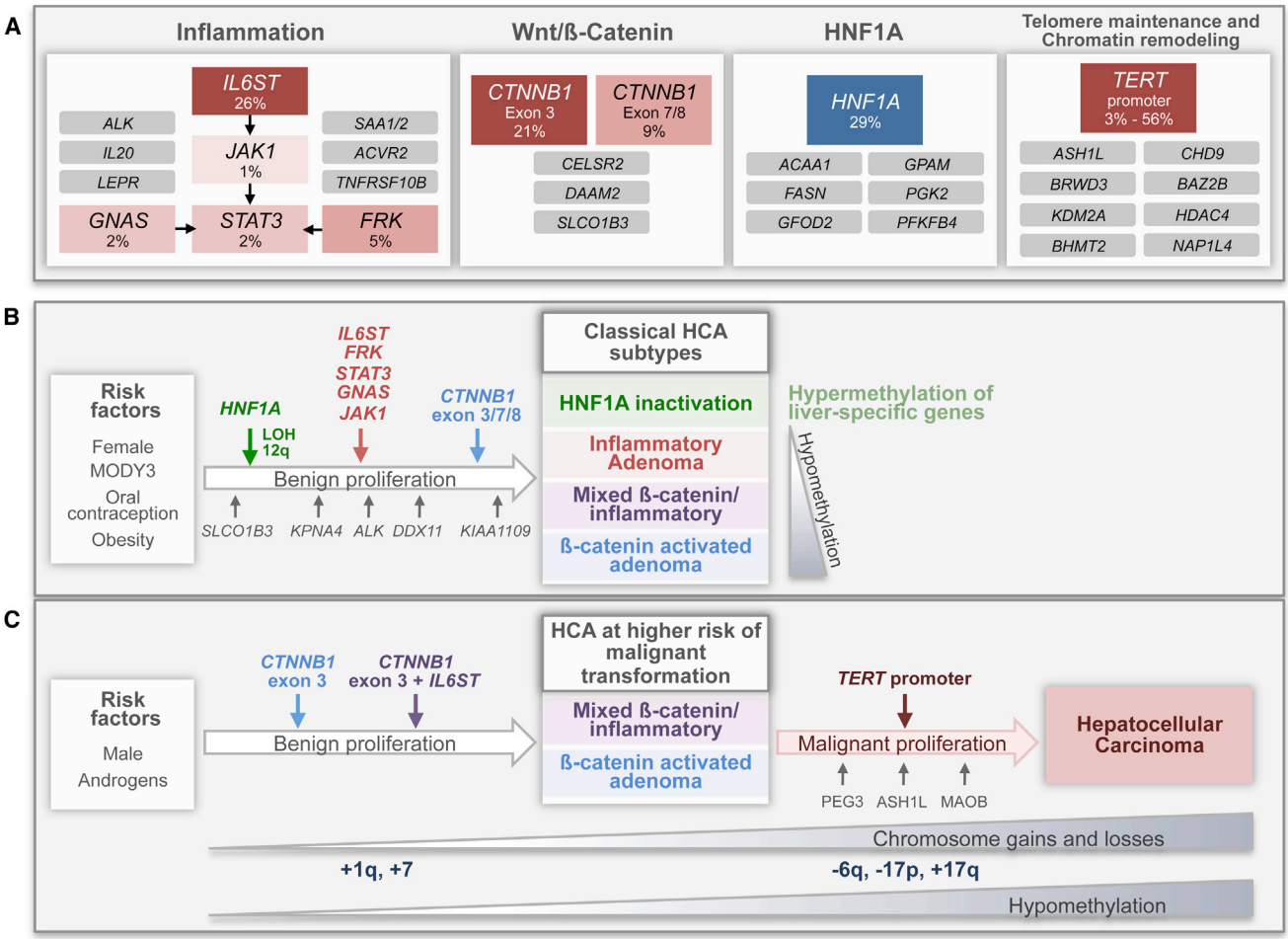

Figure 8. Genes and Pathways Implicated in HCA Initiation and Malignant Transformation

Major pathways (A) commonly altered by somatic mutations in classical HCA. Alteration frequencies are expressed as a percentage of mutation in the validation series of 250 tumors (red or blue when activated or inactivated, respectively) or 35 exome-sequenced (gray) HCAs; for unique gene mutation, no frequency is indicated. Arrows are positive interactions between two genes. Integration of the major genomic alterations occurring in classical HCA (B) and in malignant transformation of HCA in HCC (C).

target genes might involve chromatin remodeling and DNA demethylation (Pontoglio et al., 1997). Alternatively, active transcription could protect CpG islands from methylation, so hypermethylation may be a consequence of prior gene silencing (Clark and Melki, 2002). Further experiments are needed to determine whether DNA hypermethylation precedes or follows the silencing of liver-specific genes in H-HCA, but these epigenetic changes are likely to play an active role in this molecular group of HCA, and they suggest that driver genetic alterations could induce widespread epigenetic modification in hepatocellular benign tumors.

Analysis of the progression from HCA to HCC suggested that the occurrence of *CTNNB1*-activating mutation in a single cell could initiate benign liver tumorigenesis as a very early event in patient 361. However, because almost all the adenomas activated for β-catenin accumulate additional mutation in recurrent (*IL6ST*) or nonrecurrent genes, it is highly suggestive of the requirement of additional events to *CTNNB1* activating mutation to promote a benign clonal proliferation. These results are in accordance with the transgenic mouse model of hepatic *CTNNB1* mutant expression in which the constitutive Wnt pathway activation is not sufficient for hepatocarcinogenesis (Cadoret et al., 2001; Harada et al., 2002). As in other tumor types (Vogelstein et al., 1988), accumulation of chromosome aberrations is also a typical feature of malignant transformation of HCA. Here, in hepatocellular tumors, we identified somatic-activating *TERT* promoter mutations as a major event involved in the malignant transformation of hepatocellular adenomas in association with β-catenin activation. These results suggest a step-by-step model where *CTNNB1* mutations are early mutational events in benign liver tumorigenesis, although not sufficient to induce HCC in normal liver alone; telomerase reactivation through *TERT* promoter mutations is consequently required to promote full malignant transformation. Identification of *CTNNB1* and *TERT* promoter mutation as key genetic determinants of malignant transformation in HCA will be useful to propose tailored treatment in these subtypes of patients.

In conclusion, we reported a comprehensive genomic analysis of hepatocellular adenoma resulting from the benign proliferation of hepatocytes and their malignant transformation in hepatocellular carcinoma. Integrated analyses revealed the high robustness of the HCA molecular classification: all subclasses of tumors defined by the different omics are closely related together and with HCA tumor phenotypes. In addition, this classification will have clinical impact through identification of therapeutic targets and the selection of patients with high risk of malignant transformation that could require more aggressive treatment.

EXPERIMENTAL PROCEDURES

Liver Samples and Clinical Data

All tumors and corresponding nontumor liver tissues were frozen after surgical resection. These tumors were clinically and genetically characterized; they were previously included in genetic and phenotypic studies (Tables S1 and S2). The study was approved by the local Ethics Committee (Paris Saint-Louis), INSERM institutional review board in 2010, and informed consent was obtained from all subjects in accordance with French legislation. HCA were classified in (1) H-HCA according to the presence of HNF1A inactivation (73/250, 29%); (2) bHCA defined by a somatic β-catenin-activating mutation involving exon 3 and/or an overexpression of glutamine synthase and LGR5, two β-catenin target genes (53/250, 21%); and (3) IHCA defined by the presence of inflammatory infiltrates and a serum amyloid A2 and C-reactive protein overexpression (118/250, 47%); in 25 cases (10%), HCAs were both inflammatory and *CTNNB1* mutated (bIHCA). The remaining 31 cases (12%) were unclassified HCA (UHCA) when we began this study.

Genomic Analysis

Whole-exome sequencing was performed as described previously (Guichard et al., 2012). The false-positive rate of somatic mutations in WES was estimated to 2.5% after 3,000 verifications in Sanger sequencing performed in previous analyses. Comparative genomic hybridization-SNP was performed on 126 tumors with HumanCNV370-Duo v1.0 (47 tumors) or HumanOmniExpressBeadchips (79 tumors) (both from Illumina). When several samples were available from a same patient, tumor progression trees were reconstructed using the TuMult algorithm (Letouzé et al., 2010). DNA methylation profiles of 50 hepatocellular adenomas and four normal liver samples were determined using HumanMethylation450 arrays (Illumina). The ConsensusClusterPlus package (Bioconductor) was used for consensus clustering analysis. Transcriptional profiling experiments were performed using oligonucleotide GeneChips HG-U133A (Affymetrix).

Functional Analysis

FRK, *JAK1*, *IL6ST*, and *CTNNB1* mutants were obtained using the QuickChange XL site-directed mutagenesis kit (Stratagene) using primers described in Supplemental Experimental Procedures, and then used to transiently transfect Hep3B, Huh7, NIH 3T3, and Ba/F3 cells. Ba/F3- and NIH 3T3-transfected cells were selected by a treatment with Geneticin (800 and 700 μg/ml, respectively; Life Technologies). Kinase assay was performed by AlphaScreen-based assays (PerkinElmer). BALB/c-nu/nu mice used for xenograft experiments were housed in the pathogen-free animal facility at the Institut Universitaire d'Hématologie, Paris. All experimental procedures were done in compliance with the French Ministry of Agriculture regulations for animal experimentation.

A complete description of the materials and methods is provided in Supplemental Experimental Procedures.

ACCESSION NUMBERS

Sequencing data are accessible at European Genome-phenome Archive (http://www.ebi.ac.uk/ega/) under accession number EGAS00001000679. All variants and tumor features are deposited in the International Cancer Genome Consortium (ICGC) portal (ftp://data.dcc.icgc.org/version_9/). SNP array and DNA methylation data are available from Gene Expression Omnibus as accession number GSE43273.

SUPPLEMENTAL INFORMATION

Supplemental Information includes Supplemental Experimental Procedures, five figures, and ten tables and can be found with this article online at http://dx.doi.org/10.1016/j.ccr.2014.03.005.

AUTHOR CONTRIBUTIONS

C.P., S.I., E.L., J.-C.N., and A.B. designed, analyzed, and verified the genomic data; C.P., K.P., A.F., S.T., and F. Canal designed and performed the functional analyses; S.I. and E.L. performed statistical analyses; C.P., A.B., G.M., J.-C.N., M.M., and G.C. performed the sequencing validation; J.C., C.B., V.P., B.T., J.-Y.S., A.d.M., C.G., and P.B.-S. provided samples, pathological reviewing, and clinical information; J.C., K.P., and P.B.-S. performed immunohistochemical analyses; E.C. and F. Calvo participated to the achievement of the study; J.Z.-R. designed and coordinated the overall study; and all the authors contributed to writing the manuscript.

ACKNOWLEDGMENTS

We warmly thank Isabelle Desitter, Cécile Guichard, and Ichrafe Ben Maad for helpful participation in this work. We also thank Jean Saric, Christophe Laurent, Brigitte Le Bail, Anne Rullier, Laurence Chiche (CHU Bordeaux) and Jeanne Tran Van Nhieu, Daniel Cherqui, Daniel Azoulay (CHU Henri Mondor, Créteil), and the tumor bank of CHU Bordeaux and CHU Henri Mondor for contributing to the tissue collection. We thank Randall Moon (Howard Hughes Medical Institute, University of Washington) and Eric Fearon (Regents of the University of Michigan) who provided the plasmids. This work was supported by the INCa within the ICGC project and 2010-1-PL BIO-02-1, the Ligue Nationale Contre le Cancer ("Carte d'identité des tumeurs" program), the Association pour la recherche contre le Cancer, ARC (grant 3194), and the Réseau national CRB Foie and BioIntelligence (OSEO). C.P. was supported by a fellowship from MENRT and ARC and J.-C.N. was supported by a fellowship from Inca.

Received: July 10, 2013
Revised: November 14, 2013
Accepted: March 4, 2014
Published: April 14, 2014

REFERENCES

Acevedo, L.G., Bieda, M., Green, R., and Farnham, P.J. (2008). Analysis of the mechanisms mediating tumor-specific changes in gene expression in human liver tumors. Cancer Res. *68*, 2641–2651.

Bacq, Y., Jacquemin, E., Balabaud, C., Jeannot, E., Scotto, B., Branchereau, S., Laurent, C., Bourlier, P., Pariente, D., de Muret, A., et al. (2003). Familial liver adenomatosis associated with hepatocyte nuclear factor 1alpha inactivation. Gastroenterology *125*, 1470–1475.

Bioulac-Sage, P., Rebouissou, S., Thomas, C., Blanc, J.F., Saric, J., Sa Cunha, A., Rullier, A., Cubel, G., Couchy, G., Imbeaud, S., et al. (2007). Hepatocellular adenoma subtype classification using molecular markers and immunohistochemistry. Hepatology *46*, 740–748.

Bioulac-Sage, P., Laumonier, H., Couchy, G., Le Bail, B., Sa Cunha, A., Rullier, A., Laurent, C., Blanc, J.F., Cubel, G., Trillaud, H., et al. (2009). Hepatocellular adenoma management and phenotypic classification: the Bordeaux experience. Hepatology *50*, 481–489.

Bluteau, O., Jeannot, E., Bioulac-Sage, P., Marqués, J.M., Blanc, J.F., Bui, H., Beaudoin, J.C., Franco, D., Balabaud, C., Laurent-Puig, P., and Zucman-Rossi, J. (2002). Bi-allelic inactivation of TCF1 in hepatic adenomas. Nat. Genet. *32*, 312–315.

Bromberg, J.F., Horvath, C.M., Besser, D., Lathem, W.W., and Darnell, J.E., Jr. (1998). Stat3 activation is required for cellular transformation by v-src. Mol. Cell. Biol. *18*, 2553–2558.

Cadoret, A., Ovejero, C., Saadi-Kheddouci, S., Souil, E., Fabre, M., Romagnolo, B., Kahn, A., and Perret, C. (2001). Hepatomegaly in transgenic mice expressing an oncogenic form of beta-catenin. Cancer Res. *61*, 3245–3249.

Calderaro, J., Labrune, P., Morcrette, G., Rebouissou, S., Franco, D., Prévot, S., Quaglia, A., Bedossa, P., Libbrecht, L., Terracciano, L., et al. (2013). Molecular characterization of hepatocellular adenomas developed in patients with glycogen storage disease type I. J. Hepatol. *58*, 350–357.

Chen, Y.J., Chen, P.J., Lee, M.C., Yeh, S.H., Hsu, M.T., and Lin, C.H. (2002). Chromosomal analysis of hepatic adenoma and focal nodular hyperplasia by comparative genomic hybridization. Genes Chromosomes Cancer *35*, 138–143.

Clark, S.J., and Melki, J. (2002). DNA methylation and gene silencing in cancer: which is the guilty party? Oncogene *21*, 5380–5387.

Fasan, A., Kern, W., Grossmann, V., Haferlach, C., Haferlach, T., and Schnittger, S. (2013). STAT3 mutations are highly specific for large granular lymphocytic leukemia. Leukemia *27*, 1598–1600.

Flex, E., Petrangeli, V., Stella, L., Chiaretti, S., Hornakova, T., Knoops, L., Ariola, C., Fodale, V., Clappier, E., Paoloni, F., et al. (2008). Somatically acquired JAK1 mutations in adult acute lymphoblastic leukemia. J. Exp. Med. *205*, 751–758.

Govindan, R., Ding, L., Griffith, M., Subramanian, J., Dees, N.D., Kanchi, K.L., Maher, C.A., Fulton, R., Fulton, L., Wallis, J., et al. (2012). Genomic landscape of non-small cell lung cancer in smokers and never-smokers. Cell *150*, 1121–1134.

Grivennikov, S.I., and Karin, M. (2010). Inflammation and oncogenesis: a vicious connection. Curr. Opin. Genet. Dev. *20*, 65–71.

Guichard, C., Amaddeo, G., Imbeaud, S., Ladeiro, Y., Pelletier, L., Maad, I.B., Calderaro, J., Bioulac-Sage, P., Letexier, M., Degos, F., et al. (2012). Integrated analysis of somatic mutations and focal copy-number changes identifies key genes and pathways in hepatocellular carcinoma. Nat. Genet. *44*, 694–698.

Harada, N., Miyoshi, H., Murai, N., Oshima, H., Tamai, Y., Oshima, M., and Taketo, M.M. (2002). Lack of tumorigenesis in the mouse liver after adenovirus-mediated expression of a dominant stable mutant of beta-catenin. Cancer Res. *62*, 1971–1977.

Horn, S., Figl, A., Rachakonda, P.S., Fischer, C., Sucker, A., Gast, A., Kadel, S., Moll, I., Nagore, E., Hemminki, K., et al. (2013). TERT promoter mutations in familial and sporadic melanoma. Science *339*, 959–961.

Hosoya, N., Qiao, Y., Hangaishi, A., Wang, L., Nannya, Y., Sanada, M., Kurokawa, M., Chiba, S., Hirai, H., and Ogawa, S. (2005). Identification of a SRC-like tyrosine kinase gene, FRK, fused with ETV6 in a patient with acute myelogenous leukemia carrying a t(6;12)(q21;p13) translocation. Genes Chromosomes Cancer *42*, 269–279.

Huang, F.W., Hodis, E., Xu, M.J., Kryukov, G.V., Chin, L., and Garraway, L.A. (2013). Highly recurrent TERT promoter mutations in human melanoma. Science *339*, 957–959.

Jeannot, E., Mellottee, L., Bioulac-Sage, P., Balabaud, C., Scoazec, J.Y., Tran Van Nhieu, J., Bacq, Y., Michalak, S., Buob, D., Laurent-Puig, P., et al.; Groupe d'étude Génétique des Tumeurs Hépatiques (INSERM Network) (2010). Spectrum of HNF1A somatic mutations in hepatocellular adenoma differs from that in patients with MODY3 and suggests genotoxic damage. Diabetes *59*, 1836–1844.

Killela, P.J., Reitman, Z.J., Jiao, Y., Bettegowda, C., Agrawal, N., Diaz, L.A., Jr., Friedman, A.H., Friedman, H., Gallia, G.L., Giovanella, B.C., et al. (2013). TERT promoter mutations occur frequently in gliomas and a subset of tumors derived from cells with low rates of self-renewal. Proc. Natl. Acad. Sci. USA *110*, 6021–6026.

Koskela, H.L., Eldfors, S., Ellonen, P., van Adrichem, A.J., Kuusanmäki, H., Andersson, E.I., Lagström, S., Clemente, M.J., Olson, T., Jalkanen, S.E., et al. (2012). Somatic STAT3 mutations in large granular lymphocytic leukemia. N. Engl. J. Med. *366*, 1905–1913.

Laumonier, H., Bioulac-Sage, P., Laurent, C., Zucman-Rossi, J., Balabaud, C., and Trillaud, H. (2008). Hepatocellular adenomas: magnetic resonance imaging features as a function of molecular pathological classification. Hepatology *48*, 808–818.

Lee, J., Kim, J.C., Lee, S.E., Quinley, C., Kim, H., Herdman, S., Corr, M., and Raz, E. (2012). Signal transducer and activator of transcription 3 (STAT3) protein suppresses adenoma-to-carcinoma transition in Apcmin/+ mice via regulation of Snail-1 (SNAI) protein stability. J. Biol. Chem. *287*, 18182–18189.

Letouzé, E., Allory, Y., Bollet, M.A., Radvanyi, F., and Guyon, F. (2010). Analysis of the copy number profiles of several tumor samples from the same patient reveals the successive steps in tumorigenesis. Genome Biol. *11*, R76.

Liu, J., Lee, W., Jiang, Z., Chen, Z., Jhunjhunwala, S., Haverty, P.M., Gnad, F., Guan, Y., Gilbert, H.N., Stinson, J., et al. (2012). Genome and transcriptome sequencing of lung cancers reveal diverse mutational and splicing events. Genome Res. *22*, 2315–2327.

Musteanu, M., Blaas, L., Mair, M., Schlederer, M., Bilban, M., Tauber, S., Esterbauer, H., Mueller, M., Casanova, E., Kenner, L., et al. (2010). Stat3 is a negative regulator of intestinal tumor progression in Apc(Min) mice. Gastroenterology *138*, 1003–1011.

Nault, J.C., Fabre, M., Couchy, G., Pilati, C., Jeannot, E., Tran Van Nhieu, J., Saint-Paul, M.C., De Muret, A., Redon, M.J., Buffet, C., et al. (2012). GNAS-activating mutations define a rare subgroup of inflammatory liver tumors characterized by STAT3 activation. J. Hepatol. *56*, 184–191.

Nault, J.C., Bioulac-Sage, P., and Zucman-Rossi, J. (2013a). Hepatocellular benign tumors-from molecular classification to personalized clinical care. Gastroenterology *144*, 888–902.

Nault, J.C., Mallet, M., Pilati, C., Calderaro, J., Bioulac-Sage, P., Laurent, C., Laurent, A., Cherqui, D., Balabaud, C., and Zucman-Rossi, J. (2013b). High frequency of telomerase reverse-transcriptase promoter somatic mutations in hepatocellular carcinoma and preneoplastic lesions. Nat. Commun. *4*, 2218.

Ong, C.K., Subimerb, C., Pairojkul, C., Wongkham, S., Cutcutache, I., Yu, W., McPherson, J.R., Allen, G.E., Ng, C.C., Wong, B.H., et al. (2012). Exome sequencing of liver fluke-associated cholangiocarcinoma. Nat. Genet. *44*, 690–693.

Pilati, C., Amessou, M., Bihl, M.P., Balabaud, C., Nhieu, J.T., Paradis, V., Nault, J.C., Izard, T., Bioulac-Sage, P., Couchy, G., et al. (2011). Somatic mutations activating STAT3 in human inflammatory hepatocellular adenomas. J. Exp. Med. *208*, 1359–1366.

Pontoglio, M., Faust, D.M., Doyen, A., Yaniv, M., and Weiss, M.C. (1997). Hepatocyte nuclear factor 1alpha gene inactivation impairs chromatin remodeling and demethylation of the phenylalanine hydroxylase gene. Mol. Cell. Biol. *17*, 4948–4956.

Poussin, K., Pilati, C., Couchy, G., Calderaro, J., Bioulac-Sage, P., Bacq, Y., Paradis, V., Leteurtre, E., Sturm, N., Ramos, J., et al. (2013). Biochemical and functional analyses of gp130 mutants unveil JAK1 as a novel therapeutic target in human inflammatory hepatocellular adenoma. Oncoimmunology *2*, e27090.

Rebouissou, S., Amessou, M., Couchy, G., Poussin, K., Imbeaud, S., Pilati, C., Izard, T., Balabaud, C., Bioulac-Sage, P., and Zucman-Rossi, J. (2009). Frequent in-frame somatic deletions activate gp130 in inflammatory hepatocellular tumours. Nature *457*, 200–204.

Rooks, J.B., Ory, H.W., Ishak, K.G., Strauss, L.T., Greenspan, J.R., Hill, A.P., and Tyler, C.W., Jr. (1979). Epidemiology of hepatocellular adenoma. The role of oral contraceptive use. J. Am. Med. Assoc. *242*, 644–648.

Staerk, J., Kallin, A., Demoulin, J.B., Vainchenker, W., and Constantinescu, S.N. (2005). JAK1 and Tyk2 activation by the homologous polycythemia vera JAK2 V617F mutation: cross-talk with IGF1 receptor. J. Biol. Chem. *280*, 41893–41899.

Stefanska, B., Huang, J., Bhattacharyya, B., Suderman, M., Hallett, M., Han, Z.G., and Szyf, M. (2011). Definition of the landscape of promoter DNA hypomethylation in liver cancer. Cancer Res. *71*, 5891–5903.

Talpaz, M., Shah, N.P., Kantarjian, H., Donato, N., Nicoll, J., Paquette, R., Cortes, J., O'Brien, S., Nicaise, C., Bleickardt, E., et al. (2006). Dasatinib in imatinib-resistant Philadelphia chromosome-positive leukemias. N. Engl. J. Med. *354*, 2531–2541.

Turkson, J., Bowman, T., Garcia, R., Caldenhoven, E., De Groot, R.P., and Jove, R. (1998). Stat3 activation by Src induces specific gene regulation and is required for cell transformation. Mol. Cell. Biol. *18*, 2545–2552.

Vogelstein, B., Fearon, E.R., Hamilton, S.R., Kern, S.E., Preisinger, A.C., Leppert, M., Nakamura, Y., White, R., Smits, A.M., and Bos, J.L. (1988). Genetic alterations during colorectal-tumor development. N. Engl. J. Med. *319*, 525–532.

Yim, E.K., Peng, G., Dai, H., Hu, R., Li, K., Lu, Y., Mills, G.B., Meric-Bernstam, F., Hennessy, B.T., Craven, R.J., and Lin, S.Y. (2009). Rak functions as a tumor suppressor by regulating PTEN protein stability and function. Cancer Cell *15*, 304–314.

Zhang, J., Ding, L., Holmfeldt, L., Wu, G., Heatley, S.L., Payne-Turner, D., Easton, J., Chen, X., Wang, J., Rusch, M., et al. (2012). The genetic basis of early T-cell precursor acute lymphoblastic leukaemia. Nature *481*, 157–163.

Zucman-Rossi, J., Jeannot, E., Nhieu, J.T., Scoazec, J.Y., Guettier, C., Rebouissou, S., Bacq, Y., Leteurtre, E., Paradis, V., Michalak, S., et al. (2006). Genotype-phenotype correlation in hepatocellular adenoma: new classification and relationship with HCC. Hepatology *43*, 515–524.

CellPress

Cancer Cell
Article

The R882H DNMT3A Mutation Associated with AML Dominantly Inhibits Wild-Type DNMT3A by Blocking Its Ability to Form Active Tetramers

David A. Russler-Germain,[1] David H. Spencer,[2] Margaret A. Young,[1] Tamara L. Lamprecht,[1] Christopher A. Miller,[3] Robert Fulton,[3] Matthew R. Meyer,[4] Petra Erdmann-Gilmore,[4,6] R. Reid Townsend,[4,6] Richard K. Wilson,[3,5,6] and Timothy J. Ley[1,3,5,6,*]

[1]Section of Stem Cell Biology, Division of Oncology, Department of Medicine
[2]Department of Pathology and Immunology
[3]The Genome Institute
[4]Division of Metabolism, Department of Medicine
[5]Department of Genetics
[6]Siteman Cancer Center
Washington University, St. Louis, MO 63110, USA
*Correspondence: timley@wustl.edu
http://dx.doi.org/10.1016/j.ccr.2014.02.010

SUMMARY

Somatic mutations in *DNMT3A*, which encodes a de novo DNA methyltransferase, are found in ~30% of normal karyotype acute myeloid leukemia (AML) cases. Most mutations are heterozygous and alter R882 within the catalytic domain (most commonly R882H), suggesting the possibility of dominant-negative consequences. The methyltransferase activity of R882H DNMT3A is reduced by ~80% compared with the WT enzyme. In vitro mixing of WT and R882H DNMT3A does not affect the WT activity, but coexpression of the two proteins in cells profoundly inhibits the WT enzyme by disrupting its ability to homotetramerize. AML cells with the R882H mutation have severely reduced de novo methyltransferase activity and focal hypomethylation at specific CpGs throughout AML cell genomes.

INTRODUCTION

Acute myeloid leukemia (AML) is a malignancy of hematopoietic stem/progenitor cells (HSPCs) with considerable clonal and genetic heterogeneity (Welch et al., 2012; Ding et al., 2012; Ley et al., 2013). Some AML patients have recurrent translocations that cause gene fusions (i.e., *PML-RARA*, *RUNX1-RUNX1T1*, *CBFB-MYH11*, *MLL* fusions, etc.), which are associated with canonical alterations in gene expression and DNA methylation patterns (Figueroa et al., 2010; Ley et al., 2013). Recent studies have revealed that patients with normal karyotype (NK) AML exhibit a high frequency of mutations in genes involved with DNA methylation, including *DNMT3A* (~30%–35%), *IDH1* or *IDH2* (~15%–20%), and *TET2* (~25%–30%), suggesting that alterations in DNA methylation may play an important role in early disease pathogenesis for this group of AML patients (Delhommeau et al., 2009; Mardis et al., 2009; Ley et al., 2010, 2013; Marcucci et al., 2012).

DNMT3A mutations are generally present in the founding clones of AML samples, suggesting that they may initiate leukemia (Ding et al., 2012; Ley et al., 2013; Miller et al., 2013). However, the mechanisms by which they contribute to leukemogenesis are not yet clear. Previous studies of *Dnmt3a* function using mouse models have shown that haploinsufficiency for *Dnmt3a* results in no obvious alterations in hematopoiesis, whereas HSPCs completely lacking DNMT3A protein exhibit

Significance

Mutations in epigenetic modifier genes have been identified in several cancers, including *DNMT3A*, *IDH1*, *IDH2*, *TET2*, *EZH2*, *KDM6A*, *ASXL1*, *MLL*, and others in AML. The mechanisms by which mutations in *DNMT3A* contribute to AML pathogenesis are not entirely clear. Here we demonstrate that the common R882H mutation creates an altered protein with dominant-negative activity against WT DNMT3A, disrupting the ability of the WT enzyme to form active homotetramers. As a consequence, AML samples with *DNMT3A* mutations at R882 are associated with focal hypomethylation throughout their genomes. This suggests that two classes of *DNMT3A* mutations exist: R882 mutations cause a striking reduction of de novo DNA methyltransferase activity, whereas non-R882 mutations may contribute to AML pathogenesis via different mechanisms.

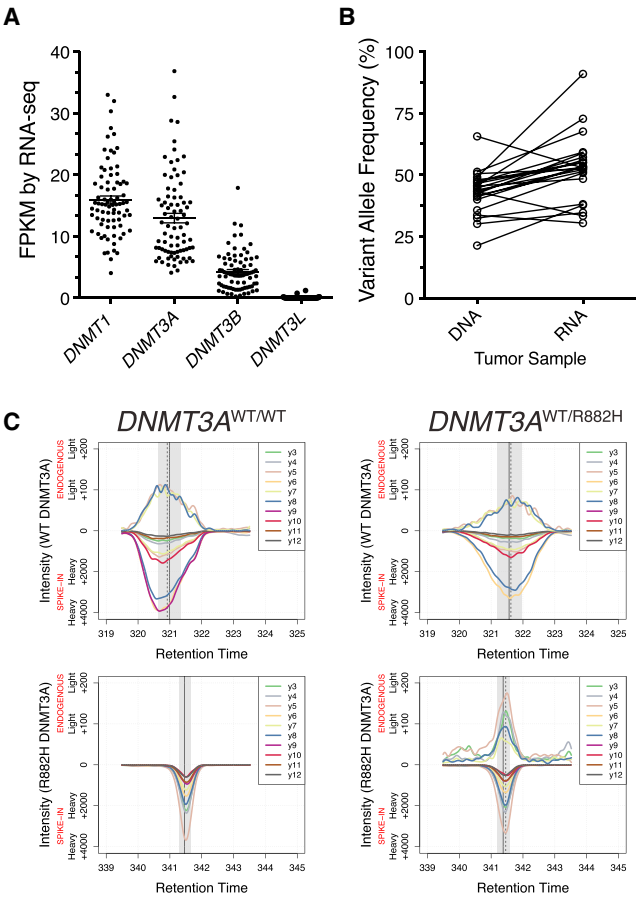

Figure 1. Expression of DNA Methyltransferase Genes in NK-AML Samples

(A) FPKM expression of DNA methyltransferase family genes in NK-AML by RNA-seq (n = 80).

(B) Variant allele frequency (%) of R882 mutant *DNMT3A* in NK-AML tumor DNA and RNA. Each set of connected points corresponds to a single patient (n = 23).

(C) TripleTOF mass spectrometry identification of WT and R882H DNMT3A in primary NK-AML cell lysates. The x axis reflects peptide retention time (min), which distinguishes between the two peptides that define WT versus R882H DNMT3A proteins. The y axis reflects signal intensity for heavy peptides ($[^{13}C_6][^{15}N_4]$-labeled internal standard synthetic peptides corresponding to WT or R882H DNMT3A; negative on axis) or light peptides (endogenous, native WT and R882H DNMT3A; positive on axis), based on specific y series ion transitions (curves y3-y12). All endogenous DNMT3A signals exhibiting mean retention times (dashed vertical lines) within the 95% confidence interval of the heavy internal standard mean retention time (vertical gray shading and solid vertical lines) are shown.

See also Figure S1.

increased self-renewal and decreased differentiation upon serial transplantation (Tadokoro et al., 2007; Challen et al., 2012). However, more than half of *DNMT3A* mutations in AML samples are heterozygous missense alterations within the catalytic domain of the enzyme at residue R882, most commonly resulting in an arginine-to-histidine change (Ley et al., 2010; Shen et al., 2011; Thol et al., 2011; Yan et al., 2011; Marcucci et al., 2012; Renneville et al., 2012; Ribeiro et al., 2012). The high frequency of mutations at this specific site raises the possibility that this amino acid change creates a gain-of-function activity and/or produces a protein with a dominant-negative effect on the residual wild-type (WT) protein.

Previous studies of R882 mutations in recombinant DNMT3A produced in several systems have demonstrated that these mutations confer reduced de novo methyltransferase activity in vitro. Prior to the discovery of this mutation in AML, the homologous R878 residue in murine DNMT3A was mutated in a screen of the C-terminal catalytic methyltransferase domain of DNMT3A purified from *E. coli* (Gowher et al., 2006); this mutation reduced its methyltransferase activity and also its DNA and *S*-adenosylmethionine (SAM, or AdoMet) binding capacity. Full-length human DNMT3A with the R882H mutation purified from Sf9 insect cells confirmed that this mutation has reduced activity in an in vitro methylation assay (Yamashita et al., 2010). Additional studies of recombinant DNMT3A have examined its interactions with DNMT3L, a related (but catalytically inactive) protein that contributes to the regulation of DNMT3A oligomerization and enhances its methyltransferase activity (Jia et al., 2007; Holz-Schietinger and Reich, 2010). Complexes of full-length DNMT3A and DNMT3L copurified from *E. coli* demonstrated the hypomorphic activity of R882H DNMT3A relative to WT DNMT3A (Yan et al., 2011). More detailed analysis of the properties of the catalytic domain of DNMT3A (also purified from *E. coli*) revealed that the R882H mutation disrupted its ability to form tetramers (Holz-Schietinger et al., 2012). This mutation reduced the processive methylation of consecutive CpG dinucleotides in vitro, but this effect was significantly rescued by the addition of DNMT3L. Importantly, the dominant-negative potential of the R882 mutations was highlighted by a recent study where murine DNMT3A R878H (equivalent to R882H in human DNMT3A) was shown to inhibit de novo DNA methylation by WT DNMT3A in murine ES cells (Kim et al., 2013).

In this study, we explored potential mechanisms that could explain how a heterozygous, hypomorphic R882H allele could affect de novo methylation beyond causing simple haploinsufficiency.

RESULTS

Characterizing the DNA Methylation Potential of NK-AML Cells

To explore the functional consequences of the R882H *DNMT3A* mutation in AML, we first characterized patterns of expression of the DNA methyltransferases in a set of 80 primary NK-AML samples from the TCGA AML cohort (Ley et al., 2013). RNA sequencing (RNA-seq) data confirmed that *DNMT1*, the maintenance DNA methyltransferase, was the most highly expressed DNMT gene (mean fragments per kilobase of transcript per million mapped reads [FPKM] = 15.91, SD = 5.82; comparison of *DNMT1* relative to *DNMT3A*, p = 0.004; Figure 1A). *DNMT3A* is known to be dynamically regulated during normal and malignant hematopoiesis (Mizuno et al., 2001; Challen et al., 2012); we observed substantial *DNMT3A* expression in all NK-AML samples (mean FPKM = 12.97, SD = 6.95, Figure 1A). Further, *DNMT3A* was expressed on average 2.3-fold higher than *DNMT3B* (mean FPKM = 4.27, SD = 3.10). Importantly, 95% (76/80) of NK-AML patients predominantly expressed inactive splice variants of *DNMT3B*, irrespective of FAB or *DNMT3A*

mutation status (median ratio of inactive to active *DNMT3B* transcripts was 3:1; Figure S1 available online). *DNMT3L* expression was not detected in the vast majority of NK-AML cases, although very minimal expression was present in 13 cases (mean FPKM = 0.04, SD = 0.16, Figure 1A).

The variant allele frequency (VAF) of somatic mutations at R882 in *DNMT3A* was approximately 50% in most samples, indicating that R882 mutations are almost always heterozygous and are present in nearly all cells in most AML samples (i.e., they are nearly always in founding clones); based on the similar VAFs of the R882 mutations in RNA-seq data, we conclude that these mutations do not alter the expression or stability of *DNMT3A* mRNA (Figure 1B).

The existence of R882H DNMT3A protein in AML cells has not yet been reported, and it is possible that the R882H mutation produces an unstable protein that causes functional haploinsufficiency for DNMT3A at the protein level. We therefore developed a selected reaction monitoring mass spectrometric assay to specifically quantify the relative abundance of WT and R882H DNMT3A proteins in NK-AML whole-cell lysates (one was WT/WT for *DNMT3A* [TCGA#3008], and the other had a heterozygous R882H *DNMT3A* mutation [TCGA#2896] with a VAF of 43.1%). We exploited the alteration of a tryptic digest site caused by the R882H mutation (WT peptide = VFGFPVHYTDVSNMSR; R882H peptide = VFGFPVHYTDVSNMSHLAR) and used heavy ([$^{13}C_6$][$^{15}N_4$]-labeled) synthetic peptides containing these sequences as internal standards to identify and quantify endogenous WT and R882H DNMT3A (Figure 1C). We demonstrated that the WT- and R882H-specific peptides from the endogenous proteins coeluted with isotopically labeled synthetic peptides of the same amino acid sequence; we detected only the WT DNMT3A peptide in the *DNMT3A*$^{WT/WT}$ lysate and found both the WT and R882H DNMT3A peptides in the mutant lysate. Positive identification was achieved by matching the ion chromatograms from the respective peptide fragmentation spectra (isotopically labeled internal standard and peptides from endogenous proteins). We compared the relative signal intensities of the endogenous WT and R882H peptides with the respective heavy internal standards and found approximately equal amounts of WT and R882H DNMT3A in the *DNMT3A*$^{WT/R882H}$ sample (WT:R882 = 5.14:6.77 fmol). Together, these data suggest that the de novo DNA methylation potential of NK-AML cells is almost exclusively provided by DNMT3A (because functional DNMT3B and DNMT3L are generally not present in these cells). Further, it suggests that the R882H mutation could produce a maximal 50% reduction in the net de novo DNA methylation potential in these cells—unless the mutant protein has a dominant-negative activity.

Hypomethylation in NK-AML Genomes with DNMT3A Mutations at R882

Although recent work in murine ES cells has shown that the mouse equivalent of the R882H *DNMT3A* mutation can lead to DNA hypomethylation in a dominant manner, it is important to note that ES cells and AML cells possess substantially different DNA methylation environments (Ziller et al., 2013)—notably, *Dnmt3l* and active *Dnmt3b* are expressed in murine ES cells (Chen et al., 2003), but not in NK-AML cells (Figure 1A). To define the consequences of *DNMT3A* mutations on DNA methylation in primary human AML cells, we analyzed Illumina Infinium HumanMethylation450 BeadChip ("450K array") data from 85 cases of NK-AML in the TCGA AML cohort (Ley et al., 2013). Although previous studies of global DNA methylation using liquid chromatography-tandem mass spectrometry showed that *DNMT3A* mutations had no measureable effects on the total (i.e., "bulk") 5-methylcytosine content in AML samples (Ley et al., 2010), the 450K array platform allowed us to conduct a high resolution analysis of DNA methylation in *DNMT3A* mutant ("R882" or "non-R882") and WT NK-AML samples at 464,198 CpGs found throughout the genome (see Supplemental Experimental Procedures). We first compared the mean methylation value across all array CpGs and found a small but statistically significant difference between *DNMT3A* WT (n = 50) and R882 mutant samples (n = 20), with R882 mutant samples having a lower mean methylation value (WT = 0.547 versus R882 = 0.511, $p = 4.5 \times 10^{-6}$; Figure 2A). In contrast, samples with non-R882 mutations (n = 15) did not demonstrate a significant difference in mean methylation relative to WT samples. However, R882 and non-R882 mutant samples showed a statistically significant difference in mean methylation that was similar to the difference between R882 mutant and WT samples (non-R882 = 0.539 versus R882 = 0.511, p = 0.029). Levels of DNA methylation in NK-AML were not influenced by *DNMT3B* expression or active/inactive *DNMT3B* splice variant ratio (Figure S2A), highlighting the influence of *DNMT3A* on shaping the methylome of NK-AML cells.

We next asked whether CpGs associated with particular genomic features accounted for the hypomethylation phenotype of samples with R882 mutations. To assess this, we compared mean methylation levels of subsets of CpGs based on their relationships to gene loci (promoter, gene body, 3′ UTR, or intergenic) as well as CpG islands or "CGIs" (islands, shores, shelves, or open sea) between WT, R882, and non-R882 mutant NK-AMLs. All eight subsets demonstrated consistent hypomethylation in NK-AMLs with R882 mutations (Figure S2B), and, similarly, hypomethylation was observed when examining each chromosome independently (Figure S2C), demonstrating the genome-wide nature of this phenotype.

To determine whether R882 mutations might have a more striking effect on the methylation of a smaller subset of CpGs, we identified the 5,000 most variably methylated CpGs according to their methylation value SDs across all 85 NK-AML samples. This set was comprised of genic (n = 3,466) versus nongenic (n = 1,534), as well as CGI (n = 1,775) versus non-CGI (n = 3,225) CpGs (Table S1). Hypomethylation was observed in R882 mutant samples relative to those with WT *DNMT3A* in 73.8% (3,690/5,000) of the CpGs (mean methylation value difference between genotypes > 0.15). Additionally, samples with R882 mutations exhibited lower mean methylation values across these 5,000 CpGs than WT samples (WT = 0.539 versus R882 = 0.306, $p = 2.2 \times 10^{-16}$; Figures 2B and S2D), a much greater difference than that detected across all CpGs on the 450K array. This effect was also observed when these 5,000 CpGs were organized by gene and CGI relationships (Figure S2E). Hierarchical clustering of all 85 NK-AML samples (as well as 15 normal human control samples derived from purified cells from human bone marrow samples: three CD34-enriched, three promyelocyte-enriched, three monocyte-enriched, and

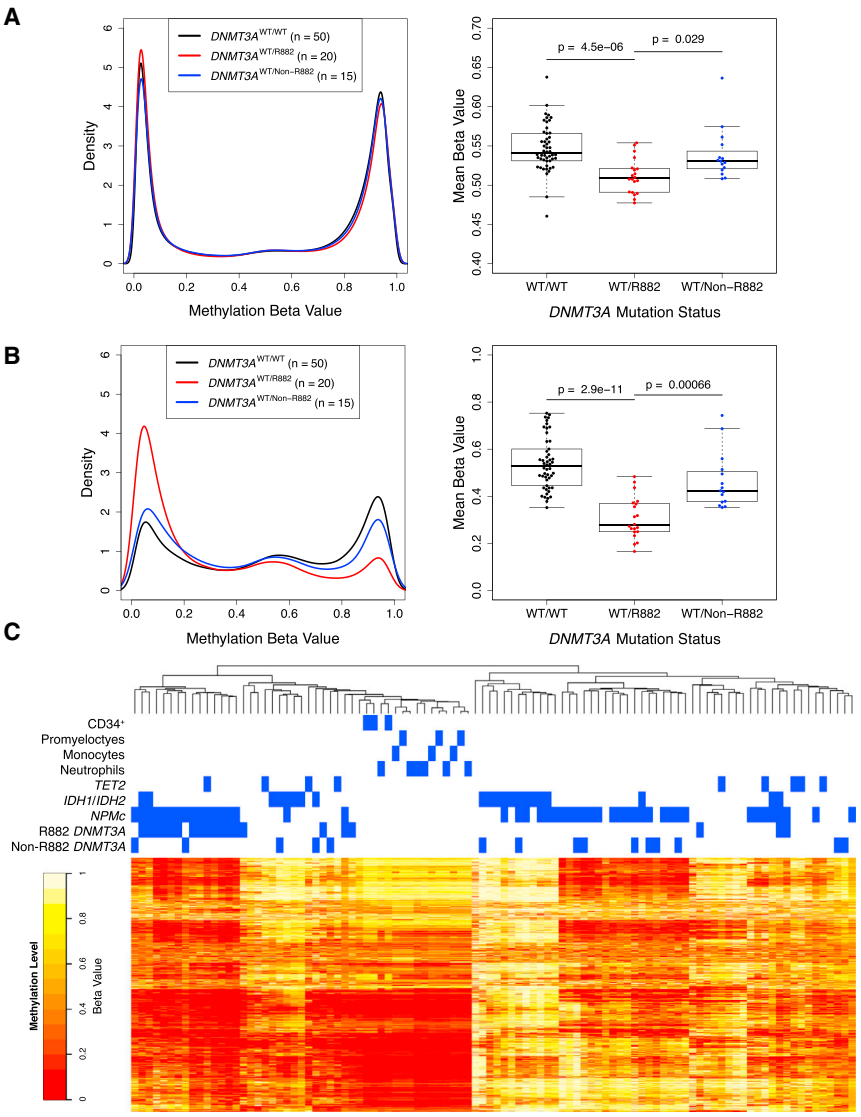

Figure 2. DNA Methylation Profiling of NK-AML Samples Identifies a Focal Hypomethylation Phenotype Associated with *DNMT3A* R882 Mutations

(A) Aggregate density distribution of methylation beta values for all CpGs for all patients based on *DNMT3A* mutation status (black, $DNMT3A^{WT/WT}$ [n = 50]; red, heterozygous *DNMT3A* mutation at R882 [n = 20]; blue, non-R882 mutation in *DNMT3A* [n = 15]). Mean methylation beta values are shown for all CpGs for each patient based on the *DNMT3A* mutation status. p values were calculated by t tests corrected for multiple testing.

(B) Aggregate density distribution of methylation beta values for the 5,000 most variably methylated CpGs for all samples (categorized by *DNMT3A* mutation status: black, $DNMT3A^{WT/WT}$ [n = 50]; red, heterozygous *DNMT3A* mutation at R882 [n = 20]; blue, non-R882 mutation in *DNMT3A* [n = 15]). Mean methylation beta values are shown for each patient (categorized by *DNMT3A* mutation status) for the 5,000 most variably methylated CpGs. p values were calculated by t tests corrected for multiple testing.

(C) Heatmap representation of unsupervised hierarchical clustering of 85 NK-AML cases and 15 normal human bone marrow-derived samples (enriched $CD34^+$ cells, promyelocytes, neutrophils, or monocytes), based on methylation beta values for the 5,000 most variably methylated CpGs in the sample set. The methylation beta value for each CpG is represented by a color scale (red, less methylated; yellow/white, more methylated). CpG probes were ordered by similarity, as assessed by hierarchical clustering analysis. The mutation status of relevant, recurrently mutated genes in these NK-AML samples is indicated above the heatmap. See also Figure S2 and Table S1.

six neutrophil-enriched samples) using these 5,000 CpGs resulted in a distinct cluster of 14 cases with R882 mutations (and 2 cases with non-R882 mutations) exhibiting very low levels of DNA methylation at these 5,000 CpGs (Figure 2C). As expected, a separate cluster of cases with *IDH1* or *IDH2* mutations was detected, which was associated with higher levels of DNA methylation at specific locations.

The most hypomethylated cluster of NK-AML cases was also highly enriched for *NPM1* mutations ($p = 3.6 \times 10^{-4}$). We therefore calculated mean methylation values across these 5,000 CpGs for all 85 NK-AML cases and compared the values for *DNMT3A* WT and R882 mutant samples without *NPM1* mutations. All comparisons (the entire 5,000 CpG set, as well as the genic/nongenic/CGI/non-CGI subsets of these 5,000 CpGs) revealed significant hypomethylation in R882 mutant samples relative to WT samples (Figure S2F), demonstrating that the hypomethylation observed in the cases with R882 mutations is independent of *NPM1* mutations (although it is exaggerated with *NPM1* mutations).

To determine whether the hypomethylation associated with R882 mutations in *DNMT3A* occurs consistently at specific CpGs, we performed a supervised differential methylation analysis to compare NK-AML genomes based on *DNMT3A* mutation status (WT versus R882). Of the 464,198 CpGs included in our analysis, 29,660 (6.4% of assessed loci) exhibited significant differential methylation between WT and R882 mutant samples (false discovery rate [FDR]-adjusted p value < 0.01 and mean methylation value difference between genotypes > 0.15; Table S2), of which 29,658 (99.9%) were hypomethylated in R882 samples (Figure 3A). We performed targeted bisulfite sequencing and validated a specific, differentially methylated CpG detected by the 450K array platform just upstream from the *p15/CDKN2B* gene (Figure S3A). Importantly, no CpGs were differentially methylated between WT and non-R882 mutant samples (Figure 3B). Genome-wide DNA methylation studies have recently shown that most tissue-specific differential DNA methylation occurs outside CGIs in the neighboring 2 kb shores (Irizarry et al., 2009). Accordingly, we found that the 29,658 hypomethylated CpGs specific to R882 mutant samples were significantly enriched for CpG island shore loci ($p = 3.14 \times 10^{-223}$ by chi-square test; Figure S3B). Further, in

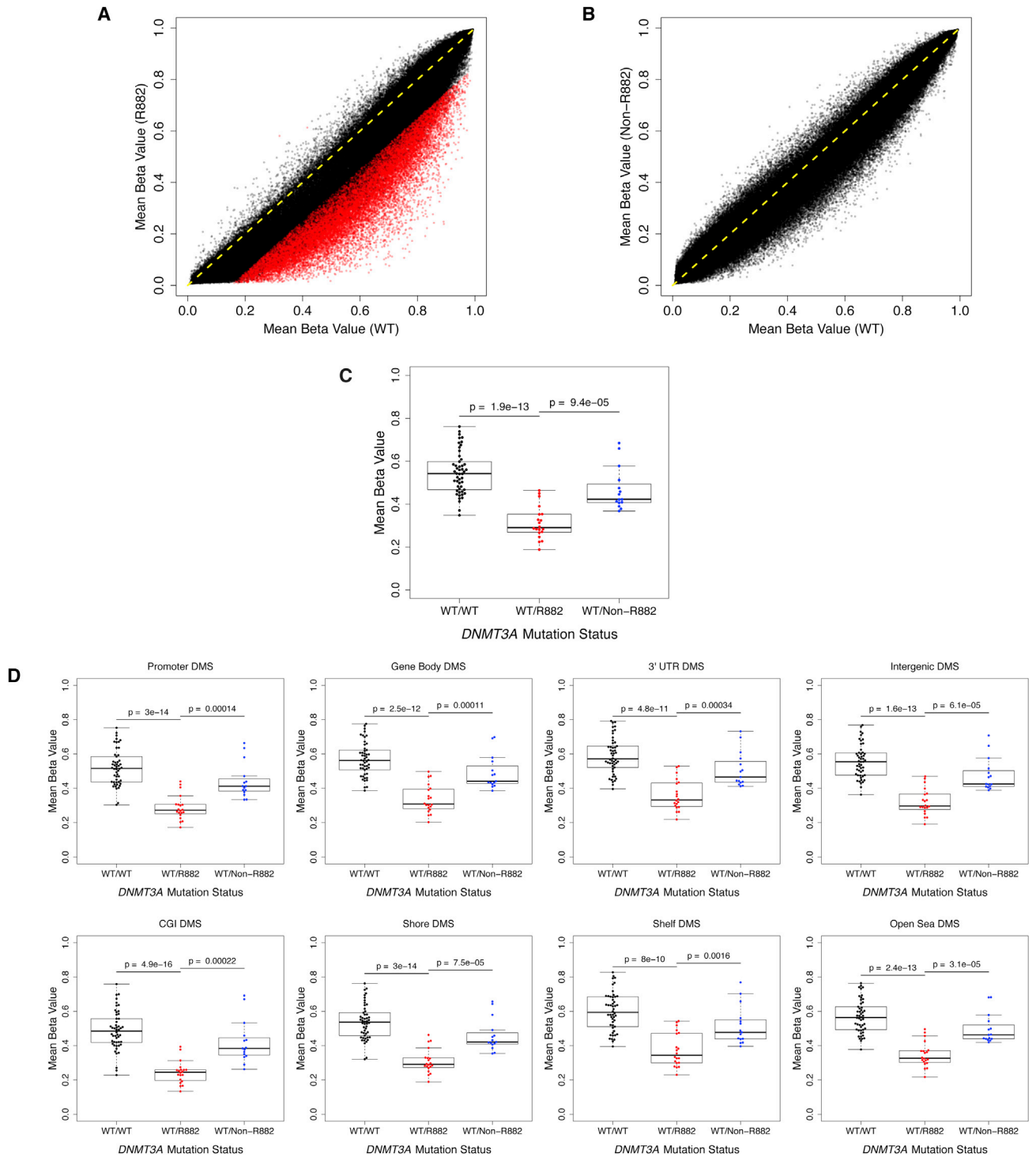

Figure 3. Differential Methylation in NK-AML Samples with R882 Mutant *DNMT3A*

(A) Scatter plot comparing mean methylation beta values at individual CpGs across all NK-AML cases categorized by *DNMT3A* mutation status (WT versus R882 mutant). Individual points represent single CpGs (x axis, mean methylation beta value for all WT samples; y axis, mean methylation beta value for all R882 mutant samples). CpGs with equal mean methylation beta values between WT and R882 samples appear along the line y = x, indicated in yellow. CpGs hypomethylated in R882 samples appear below the line y = x. CpGs that were differentially methylated between the two sample sets (FDR < 0.01 and absolute value of mean methylation difference > 0.15) are indicated in red.

(B) Scatter plot comparing mean methylation beta values at individual CpGs across all NK-AML cases categorized by *DNMT3A* mutation status (WT versus non-R882 mutant). Individual points represent single CpGs (x axis, mean methylation beta value for all WT samples; y axis, mean methylation beta value for all non-R882 mutant samples). CpGs with equal mean methylation beta values between WT and non-R882 samples appear along the line y = x, indicated in yellow. CpGs

(legend continued on next page)

this NK-AML cohort, the R882 mutant alleles consisted of both R882H (15/20) and R882C (5/20). We confirmed that the hypomethylation phenotype was nearly identical for the R882H and R882C mutant samples (no CpGs were found to be significantly differentially methylated between R882H and R882C samples by supervised analysis, and no significant differences between R882H and R882C samples were found when comparing mean methylation values across the entire genome or within subsets of CpGs based on their relation to gene loci or CGIs; Figures S3C and S3D). This suggests that the dominant-negative activity of the R882H mutation in DNMT3A can likely be extrapolated to other R882 mutations. Together, these findings demonstrate that NK-AML genomes with *DNMT3A* mutations specifically at R882 exhibit focal hypomethylation at specific CpG residues, which are found throughout the genome (Figure S3E). Discrete, large-scale regional changes in methylation (Berman et al., 2012) are not observed in these samples, however (Figures S3F and S3G).

We also assessed the relationship between gene expression and DNA methylation in the 74 NK-AML cases with both RNA-seq and 450K methylation array data. All samples exhibited canonical relationships between levels of DNA methylation and gene expression—increased promoter, CGI, and CpG island shore methylation was associated with significantly decreased gene expression, whereas increased gene body methylation was associated with increased gene expression (Figures S4A and S4B). However, hypomethylated CpGs in R882 mutant samples identified by the supervised differential methylation analysis were associated with variable expression changes (Figures 4A and S4C). Genes associated with significantly hypomethylated promoter or shore CpGs in R882 samples were statistically over-represented among upregulated genes (>2-fold mean change) relative to the overall gene expression changes between WT and R882 mutant samples ($p < 0.001$ for both promoter and shore CpGs, by chi-square test with Yates correction). In contrast, genes associated with hypomethylated gene bodies or CGI CpGs showed no enrichment in either upregulated or downregulated genes (Figure S4C).

We next conducted a supervised differential gene expression analysis (Anders and Huber, 2010), which identified only 228 differentially expressed genes between WT and R882 mutant NK-AMLs (52 upregulated and 176 downregulated in the R882 samples; Benjamini-Holm adjusted p value < 0.05 and absolute $\log_2$ fold change > 1; Tables S3 and S4; Figure S4D). Hierarchical clustering of all NK-AML samples using only these 228 differentially expressed genes revealed a high degree of intragenotype variance (Figures S4D), reiterated by the failure of the first two principal components based on gene expression to significantly distinguish R882 mutant from WT NK-AML samples (Figure S4E). This is in contrast to the extent to which the first two principal components based on global DNA methylation successfully distinguish the majority of WT and R882 mutant samples (Figure S4F), emphasizing the greater similarity of R882 mutant NK-AML samples by DNA methylation than by gene expression patterns. The 52 genes that were significantly upregulated in R882 mutant samples exhibited the predicted canonical hypomethylation of their promoters, CGIs, and CpG island shores (Figure 4B). However, the 176 genes that were significantly downregulated in R882 mutant samples were also hypomethylated compared with WT samples (Figure 4B)—these genes may be regulated by mechanisms other than DNA methylation. Overall, these findings highlight the uniformity of the hypomethylation signature found in R882 mutant samples but illustrate the lack of a universal correlation between changes in the methylation state of individual CpGs and corresponding changes in the expression of linked genes. Clearly, further studies will be needed to better understand these findings.

Structural and Functional Consequences of the R882H Mutation in DNMT3A

Several previous studies have demonstrated that the R882H mutation reduces (but does not eliminate) the de novo DNA methyltransferase activity of DNMT3A in vitro (Yamashita et al., 2010; Yan et al., 2011; Holz-Schietinger et al., 2012). However, it is not yet clear why mutations at R882 are over-represented among the spectrum of *DNMT3A* mutations if their major effect is a simple reduction in methyltransferase activity. We therefore explored the possibility that R882 mutations may also possess novel gain-of-function activities, such as altered cellular localization and/or modified CpG substrate specificity.

To determine whether R882 mutations cause improper subcellular targeting of DNMT3A, we expressed FLAG-tagged WT and R882H DNMT3A (as well as GFP for a transfection and cytoplasmic-distribution control) in HEK293T cells and used immunofluorescence to assess subcellular localization. This revealed appropriate nuclear localization of both WT and R882H DNMT3A (Figure 5A). To verify this finding in primary NK-AML cells, we performed nuclear-cytoplasmic separations after hypotonic lysis of the leukemic cells, followed by Western blotting for DNMT3A (because the abundance of this protein is too low to be detected by immunofluorescence). Because WT and R882H DNMT3A protein is present in equal abundance in primary AML cells (Figure 1C), cytoplasmic mislocalization of mutant DNMT3A protein should be easily detected by this method. All measurable DNMT3A protein was in the nuclear fraction regardless of the R882 mutation status (Figure 5B).

To further evaluate the consequences of the R882H mutation on DNMT3A functions, we purified full-length, human WT and R882H DNMT3A using a mammalian tissue culture system (Figures S5A–S5C). We first used the recombinant proteins to confirm that the R882H mutation reduces the de novo

hypomethylated in non-R882 samples appear below the line y = x. CpGs that were differentially methylated between the two sample sets (FDR < 0.01 and absolute value of mean methylation difference > 0.15) are indicated in red.

(C) Mean methylation beta values are shown for each patient (categorized by *DNMT3A* mutation status) for the 29,660 differentially methylated CpGs (by supervised analysis between WT and R882 mutant samples). p values were calculated by t tests corrected for multiple testing.

(D) Mean methylation beta values are shown for each patient (categorized by *DNMT3A* mutation status) for subsets (based on CpG relationship to gene loci or CGIs) of the 29,660 differentially methylated CpGs (by supervised analysis between WT and R882 mutant samples). p values were calculated by t tests corrected for multiple testing.

See also Figure S3 and Table S2.

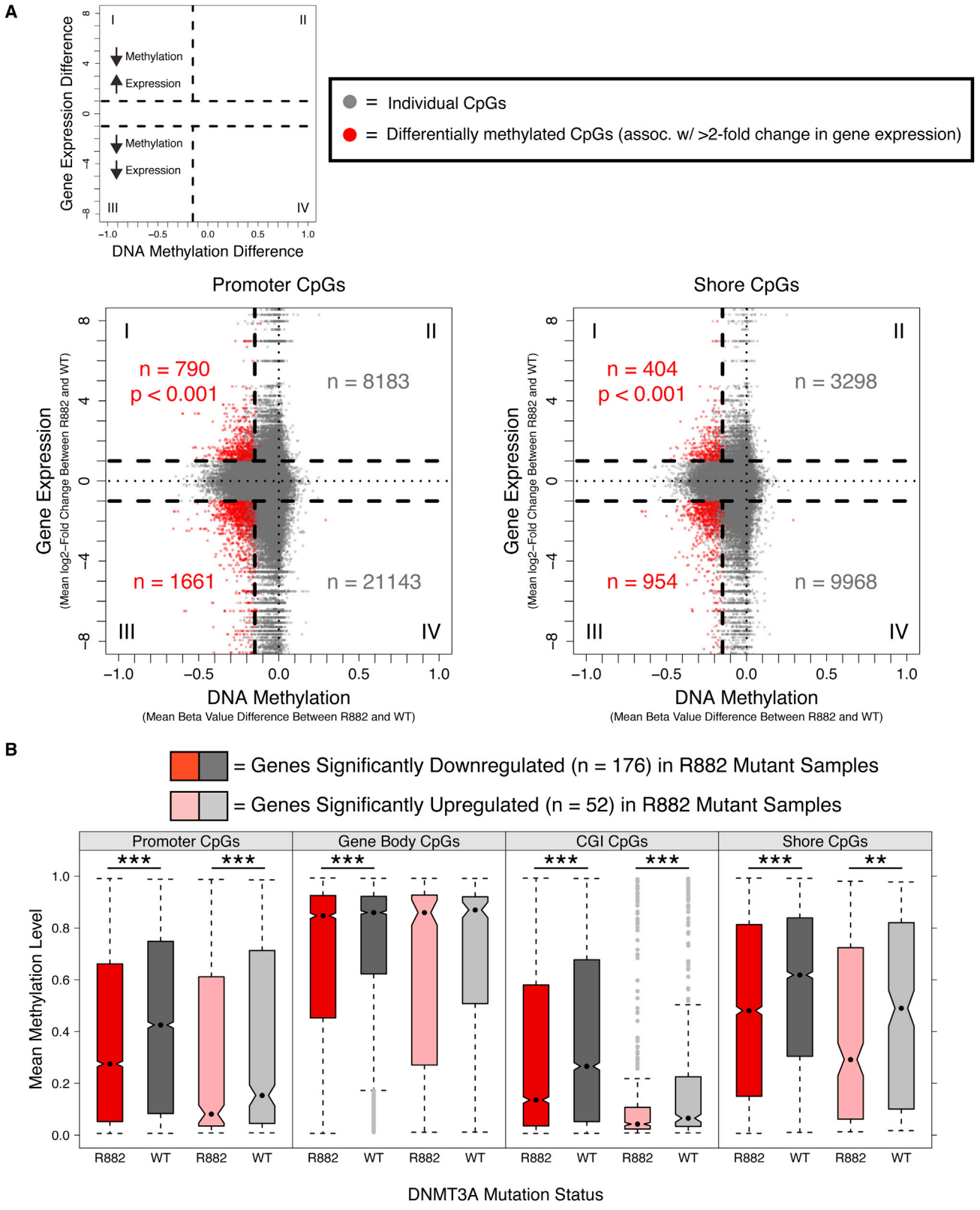

Figure 4. Effects of *DNMT3A* Mutations on the Relationship between DNA Methylation and Gene Expression in NK-AML

(A) Variable expression changes are observed in genes associated with differentially methylated promoter or shore CpGs in R882 mutant *DNMT3A* NK-AML samples. Each data point in the starburst plots represents the mean DNA methylation (x axis) and mean gene expression (y axis, $\log_2$ fold change) difference at an

(legend continued on next page)

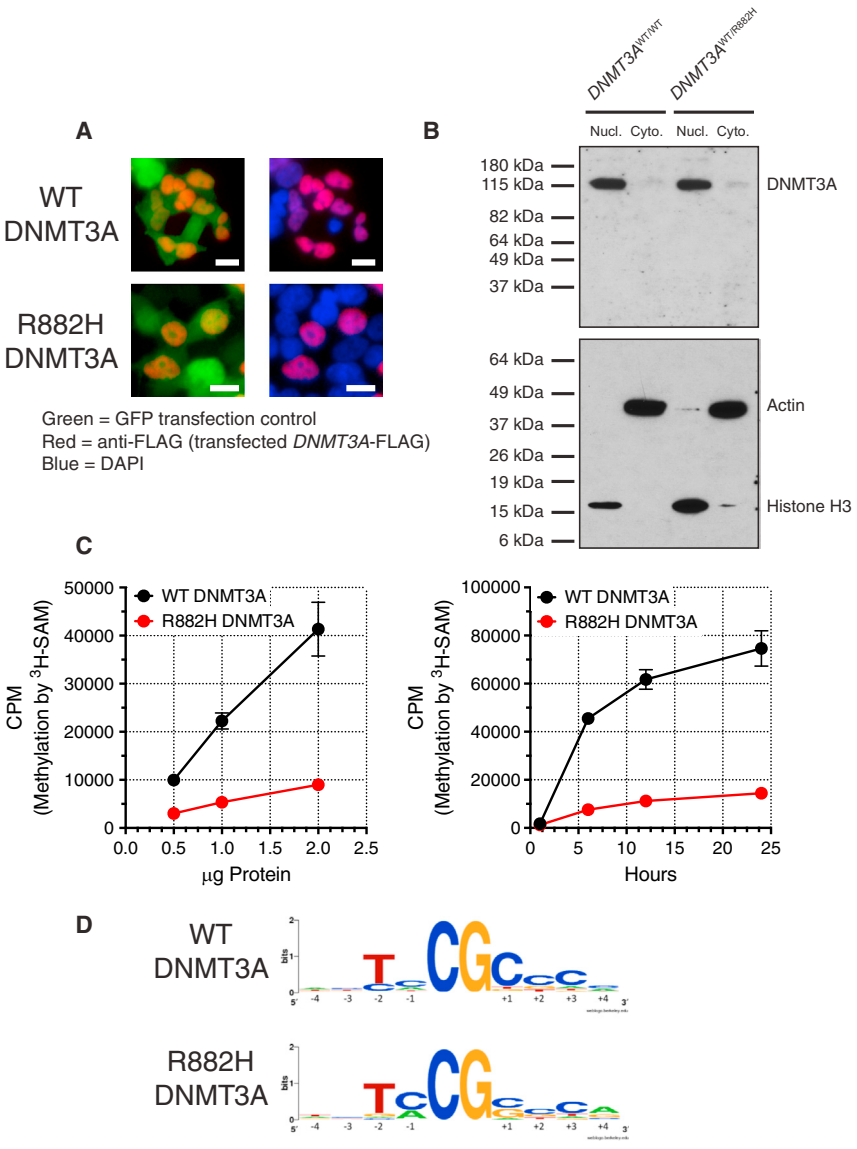

Figure 5. Cellular Localization and Function of R882H DNMT3A Protein

(A) Immunofluorescence imaging of FLAG-tagged WT and R882H DNMT3A. Note that WT and R882H DNMT3A proteins have the same nuclear distribution. Left panels show GFP transfection control (green) and anti-FLAG (red). Right panels show DAPI (blue) and anti-FLAG (red). The scale bar indicates 10 μm.

(B) Nuclear/cytoplasmic fractionation of primary NK-AML cells (WT/WT and WT/R882H for *DNMT3A*) to assess DNMT3A nuclear localization. The top panel shows Western blot with anti-DNMT3A antibody. The bottom panel shows Western blot with anti-histone-H3 (nuclear, Nucl.) and anti-actin (cytoplasmic, Cyto.) antibodies. Lanes were loaded with identical cell equivalents of lysate volumes.

(C) In vitro methylation of a linearized plasmid DNA substrate (pcDNA3.1) by recombinant full-length human WT DNMT3A or R882H DNMT3A: dose-response assay with 6 hr incubation, and time-course assay using 1 μg of total protein per reaction (250 nM). Data are means ± SEM of three independent experiments, each performed in triplicate.

(D) Logos of motifs demonstrating preferentially methylated CpG sequences of WT and R882H DNMT3A based on bisulfite sequencing of in vitro methylated DNA templates.

See also Figure S5.

methylation activity of DNMT3A. We measured the transfer of tritiated methyl groups from [^{3}H]SAM to substrate DNA (linearized DNA from the pcDNA3.1 plasmid, which contains 334 CpG residues) and found that R882H DNMT3A had only 21.7% (± SD of 4.4%) of the methyltransferase activity of WT DNMT3A (Figure 5C).

Previous work demonstrated that DNMT3A has a preference for specific DNA sequences flanking target CpGs (Wienholz et al., 2010). To assess whether the R882H mutation alters the CpG-flanking sequence preference, we performed in vitro methylation on linearized pcDNA3.1 plasmid DNA with recombinant WT or R882H DNMT3A. We then performed bisulfite sequencing of the methylated plasmid DNA from these reactions, with 13 amplicons covering 114 CpGs. Lists of −10 to +10 sequence contexts of all target CpGs were generated from the bisulfite sequencing results of these in vitro methylation reactions. Sequences were then assigned weights corresponding to their measured methylation beta values, and these weighted sequence motifs were used to quantify preferential enrichment of bases upstream or downstream of target CpGs using WebLogo (Crooks et al., 2004). These data revealed identical CpG-flanking sequence preferences for WT and R882H DNMT3A (Figure 5D; Spearman correlation of rank ordered CpGs by methylation beta value between WT DNMT3A and R882H DNMT3A = 0.99), consistent

individual CpG comparing WT and R882 mutant *DNMT3A* samples. Data points in red are CpGs exhibiting significant differential methylation (by supervised analysis between WT and R882 mutant samples) and also >2-fold changes in expression of their associated genes. Genes associated with significantly hypomethylated promoter or shore CpGs were statistically enriched for upregulated genes relative to the overall gene expression changes between WT and R882 mutant samples ($p < 0.001$ for both promoter and shore CpGs by chi-square test with Yates correction; contingency table, quadrants I/III versus II/IV). Gene body and CGI CpGs are shown in Figure S4C.

(B) Differentially expressed genes in R882 mutant NK-AML consistently exhibit hypomethylation. Box-and-whisker plots compare R882 mutant and WT samples by mean methylation levels of individual promoter, gene body, CGI, or shore CpGs associated with either significantly downregulated (n = 176) or upregulated genes (n = 52) in R882 mutant NK-AML. *$p < 0.05$; **$p < 0.005$; *** $p < 0.0005$ by Wilcoxon signed-rank test corrected for multiple testing. Note that both upregulated and downregulated differentially expressed genes are hypomethylated in R882 mutant samples.

See also Figure S4 and Tables S3 and S4.

with the expected TNCGCY motif previously described (Wienholz et al., 2010). Interestingly, the differentially methylated CpGs found in our primary AML cohort (Figure 3A; Table S2) were not enriched for the intrinsic DNMT3A −2 to +2 flanking sequence preference.

R882H DNMT3A Exhibits Dominant-Negative Inhibition of WT DNMT3A Activity

To determine whether recombinant R882H DNMT3A can inhibit the activity of the WT enzyme, we measured the methylation activity of increasing amounts of R882H DNMT3A mixed with a fixed amount of WT DNMT3A protein. Surprisingly, we observed a linear increase in the net enzymatic activity, reflecting the summed activity of the two forms of DNMT3A in these 4 hr in vitro reactions (Figure 6A). Therefore, using this assay, no dominant-negative activity of the R882H mutant protein was detected.

However, we suspected that in vitro mixing of WT and R882H DNMT3A proteins might not recapitulate their interactions in primary AML cells, where both proteins would be produced and folded in the same compartment at the same time. We therefore cotransfected HEK293T cells with equal amounts of 6×His-WT and 6×His-R882H DNMT3A expression vectors and then copurified both proteins (Figure 6B). In contrast to the in vitro mixing experiment, the coexpressed, copurified, in vivo mixed WT and R882H DNMT3A proteins displayed a >80% reduction in methyltransferase activity relative to WT DNMT3A (Figure 6C). To further test whether this represented a dominant-negative activity of the R882H protein, we measured the relative abundance of both WT and R882H proteins in each of our in vivo mixed samples generated by coexpression/copurification. We used a triple stage quadrupole (TSQ) mass spectrometric approach that exploited the altered tryptic cleavage site in DNMT3A produced by the R882H mutation, as described above. This revealed similar amounts of each protein in the copurified enzyme preparations, with WT:R882H ratios ranging from 0.79 to 1.60 in four separate purifications (mean = 1.05; Figure 6D). The R882H mutant protein therefore must act in a dominant fashion to inhibit the methyltransferase function of the WT protein, but only when the two proteins are coproduced in the same cell.

Given the location of the R882H mutation in one of the self-interacting domains of DNMT3A (specifically the 'RD interface'; Jurkowska et al., 2011) and the knowledge that the catalytic domain of WT DNMT3A preferentially forms tetramers, we postulated that the dominant-negative effect of R882H may be due to an altered and/or disrupted oligomerization potential of DNMT3A when WT and R882H proteins form complexes. Using a Superose 6 size-exclusion column, we identified two populations of full-length WT DNMT3A oligomers: a macro-oligomer peak with a mean molecular weight of ~800 kDa (i.e., eight or more DNMT3A molecules) and a tetramer peak of DNMT3A molecules with a mean molecular weight of ~450 kDa (Figure 7A). A significant deficit in the tetramer complex was observed for R882H DNMT3A, and a second, minor peak at a later elution time (consistent with dimers) was also detected. In vivo mixed (copurified) WT and R882H DNMT3A complexes exhibited a pattern of oligomerization identical to R882H DNMT3A alone. In contrast, in vitro mixed WT and R882H DNMT3A exhibited a distribution of oligomers corresponding to the expected average of the WT and R882H curves (Figure 7A). All species (WT, R882H, as well as in vivo and in vitro mixed WT and R882H DNMT3A) were able to form macro-oligomers. Previous studies, however, have suggested that tetramers of the catalytic domain represent the most active form of the methyltransferase (Kareta et al., 2006; Jia et al., 2007; Holz-Schietinger et al., 2011).

To assess the relative methyltransferase activity of the different oligomeric complexes, we used Superose 6 fractions of WT DNMT3A in in vitro methylation assays that were assessed by pyrosequencing (Figure 7B). Of the eight fractions with detectable levels of methyltransferase activity, the three most active fractions were found in the tetramer elution peak. In contrast, the three DNMT3A fractions associated with the macro-oligomer peak contained only 53% of the total methyltransferase activity of the three tetramer-associated DNMT3A fractions. We additionally verified the absence of catalytic activity from the corresponding tetramer fraction for R882H DNMT3A (Figure 7B). Together, these findings provide further evidence that the homotetramer is the most active multimeric species of WT DNMT3A and suggest that the R882H protein must interact with the WT protein intracellularly to form stable heterodimers that are virtually inactive and that inhibit the formation of the active WT homotetramers.

DISCUSSION

In this study, we explored the consequences of the R882H mutation on DNMT3A function and identified the mechanism of its dominant-negative effect on WT DNMT3A in mammalian cells. Further, we identified a focal hypomethylation phenotype in NK-AML cases possessing heterozygous *DNMT3A* mutations at R882, which demonstrates the profound loss of de novo methyltransferase activity resulting from the dominant-negative consequences of these heterozygous alterations.

We and others have shown that recombinant DNMT3A with the R882H mutation has a reduced de novo DNA methyltransferase activity (~20% of WT levels), which therefore would predict only a ~40% reduction of the total de novo DNA methyltransferase activity of an AML cell with a heterozygous mutation—unless the mutant protein acts as a dominant negative against the WT protein. Surprisingly, mixing of purified recombinant WT and R882H DNMT3A demonstrated additive methylation capacity in an in vitro methylation assay, reflecting the summed activities of the two enzymes. This suggests that WT and R882H DNMT3A do not functionally interact with each other when purified separately and mixed in solution.

DNMT3A possesses two protein-protein interacting faces within the C-terminal catalytic domain. One is a hydrophobic "FF interface," which mediates both homo-oligomerization and the DNMT3A-DNMT3L interaction via stacking of four phenylalanine residues (two from each subunit). The other is a polar RD interface for DNMT3A-DNMT3A self-interaction, which occurs through a hydrogen-bonding network between arginine and aspartate residues (Jurkowska et al., 2011). This RD interface, in which the R882H mutation is found, forms the DNA binding site, whereas both interfaces are essential for cofactor SAM binding and overall catalytic activity of the enzyme (Holz-Schietinger et al., 2011). In vitro, DNMT3A-DNMT3A self-interactions are

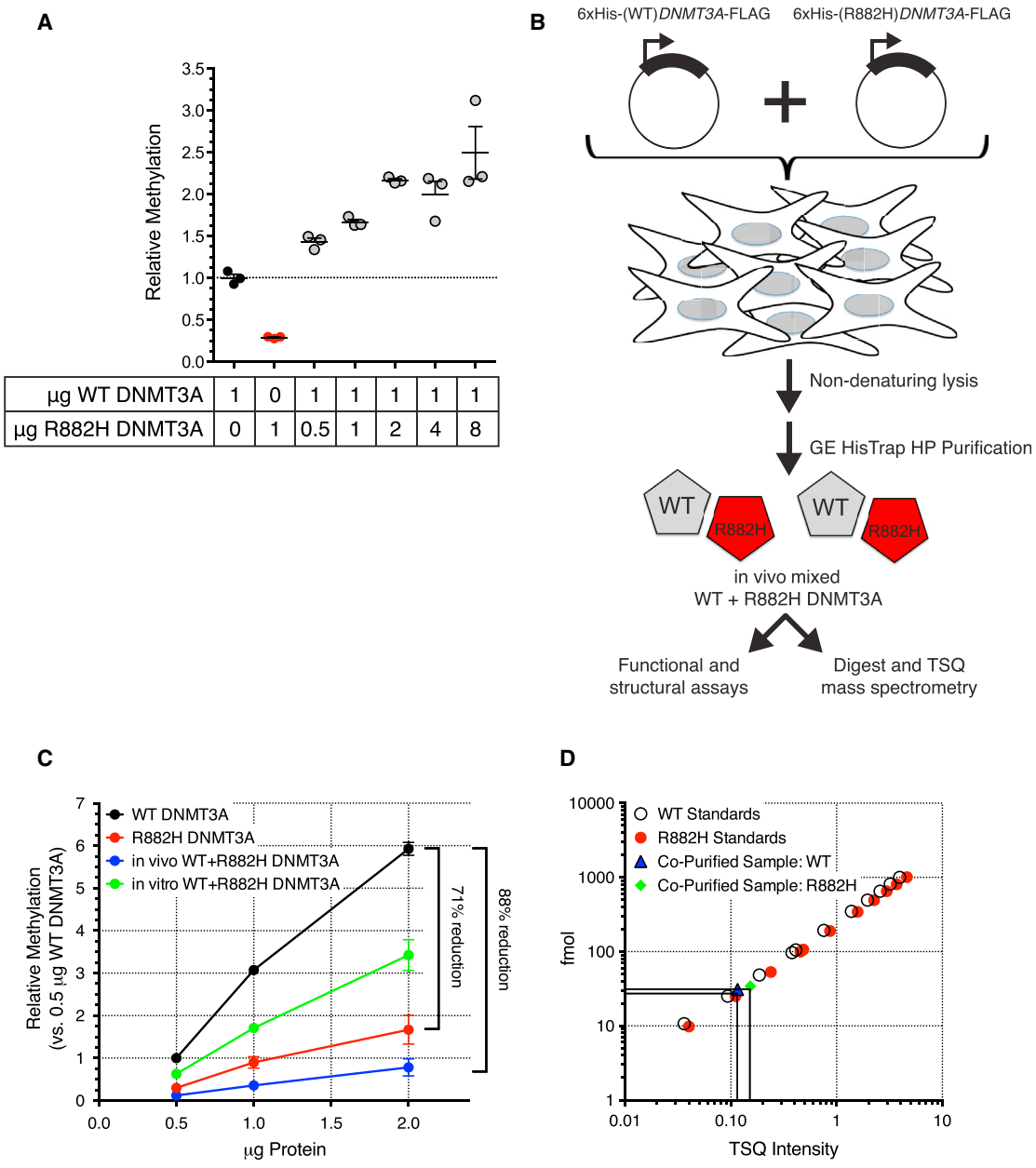

Figure 6. Dominant-Negative Effects of Recombinant R882H DNMT3A Protein Are Found Only after In Vivo Mixing

(A) In vitro methylation assay of linearized pcDNA3.1 using recombinant full-length human WT, R882H, or in vitro mixed WT and R882H DNMT3A.

(B) Schematic of cotransfection/copurification of WT and R882H DNMT3A for structure/function analysis and TSQ mass spectrometry quantification of DNMT3A proteins.

(C) In vitro methylation assay of linearized pcDNA3.1 using WT, R882H, in vitro mixed WT, and R882H DNMT3A versus cotransfected/copurified in vivo mixed WT and R882H DNMT3A. Data are means ± SEM of four independent experiments, each performed in triplicate.

(D) Example of WT:R882H DNMT3A ratio quantification by TSQ mass spectrometry in in vivo mixed samples. Open circles, WT DNMT3A standards; red closed circles, R882H DNMT3A standards; blue triangle, WT DNMT3A peptide from copurified WT+R882H sample; green diamond, R882H DNMT3A peptide from copurified WT+R882H sample.

stable even in the presence of 2 M NaCl and 0.1% Triton X-100 (Purdy et al., 2010), suggesting that these complexes may have a very slow dissociation rate.

We suspected that in vitro mixing of WT and R882H DNMT3A might not recapitulate the DNMT3A complexes that would form within a NK-AML cell that express both WT and R882H DNMT3A. In vitro mixing may simply combine two pools of highly stable DNMT3A multimers (one exclusively WT, the other exclusively R882H) that do not form mixed multimers of WT and R882H enzymes during incubations lasting several hours. We therefore performed an in vivo mixing experiment by cotransfecting and then copurifying WT and R882H DNMT3A from the same

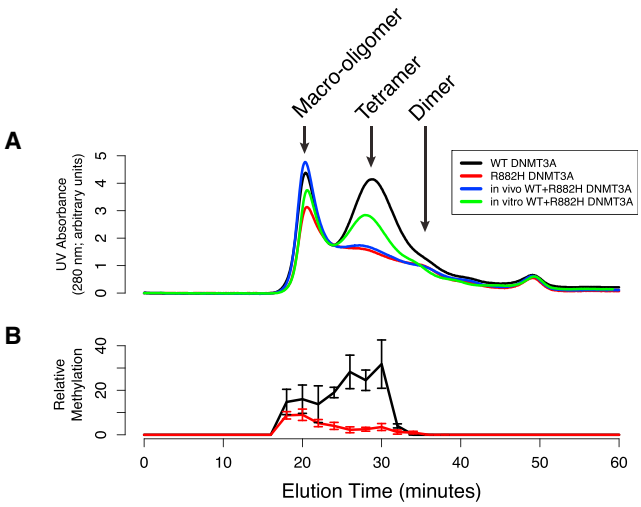

Figure 7. R882H DNMT3A Fails to Form Homotetramers and Blocks WT Homotetramer Formation in a Dominant-Negative Fashion

(A) Size-exclusion chromatography tracings of DNMT3A complexes (black, WT; red, R882H; blue, cotransfected/copurified in vivo mixed WT and R882H; green, in vitro WT and R882H DNMT3A). The x axis reflects the Superose 6 column elution time (run at 0.5 ml/min; 20 min = ~800 kDa estimated molecular weight, 30 min = ~450 kDa estimated molecular weight). The y axis reflects arbitrary units of $UV_{280\ nm}$ absorption of column eluates.

(B) Methyltransferase activity of WT DNMT3A or R882H DNMT3A complexes (purified with size-exclusion chromatography) assessed by bisulfite pyrosequencing of column fractions after in vitro methylation reactions. The x axis reflects Superose 6 column elution time (run at 0.5 ml/min; 20 min = ~800 kDa estimated molecular weight, 30 min = ~450 kDa estimated molecular weight). The y axis reflects relative methyltransferase activity, calculated as the sum of methylation beta values across all 14 CpGs within the pyrosequencing amplicon. The data are means ± SEM of three independent experiments.

mammalian cells. Copurified enzymes (which were shown to possess WT and R882H DNMT3A in equal abundance by mass spectrometry) indeed demonstrated that the R882H mutant form of DNMT3A possesses a potent dominant-negative activity, essentially eliminating the methyltransferase activity of the WT enzyme. Size-exclusion chromatography analysis demonstrated that the mutant enzyme inhibits the ability of the WT enzyme to form functional tetramers. Earlier work suggests that tetrameric WT DNMT3A catalytic domains formed the most active methyltransferase (Kareta et al., 2006; Purdy et al., 2010; Jurkowska et al., 2011); we have shown here that tetramers of full-length WT DNMT3A protein are required for maximal de novo methyltransferase activity. Together, these findings define the mechanism through which R882H DNMT3A is able to function as a dominant-negative inhibitor of de novo DNA methylation.

We also examined the 85 NK-AML cases from the TCGA AML cohort (Ley et al., 2013), identifying a small (but statistically significant) overall reduction in CpG methylation in the genomes of AML cases with *DNMT3A* mutations at R882, which was not found in cases with non-R882 mutations. Many common cancer-associated DNA methylation phenotypes involve changes at specific functional or structural elements of the genome, such as the CpG-island methylator phenotype in glioblastoma (Noushmehr et al., 2010) and the long-range hypomethylation of nuclear lamina-associated domains in colon cancer (Berman et al., 2012). In contrast, the focal hypomethylation associated with R882 mutations occurred at specific CpGs throughout the genome, instead of in specific blocks.

The hypomethylated loci in R882 mutant NK-AML samples were enriched for CpG island shores, which others have shown to be regions of enrichment for tissue-specific differential methylation (Irizarry et al., 2009). Nonetheless, the profound R882 mutant hypomethylation phenotype entailed significant reductions in methylation in all subsets of CpGs based on their relationships to annotated genetic loci (promoter, gene body, 3′ UTR, or intergenic) or CGIs (CpG island, shore, shelf, or open sea). Both WT and R882 mutant cases exhibited canonical relationships between global levels of DNA methylation and gene expression; however, significantly hypomethylated CpGs in R882 mutant samples were associated with variable changes in the expression of linked genes. Although many of the affected genes have been shown to play important roles in AML, additional studies will be required to fully understand how these changes in gene expression may contribute to leukemogenesis.

In sum, we have elucidated the protein-intrinsic mechanism that explains the dominant-negative potential of the R882H alteration in DNMT3A and have demonstrated that mutations at this residue contribute to a focal hypomethylation phenotype in NK-AML samples. These genetic and molecular data suggest that there are two distinct classes of *DNMT3A* mutations that contribute to leukemogenesis in different ways. The first entails the dominant-negative R882 mutations, which are expected to cause a near complete loss of de novo methyltransferase activity in an affected AML cell, which may directly cause the focal hypomethylation phenotype. The second class includes the other ~40% of *DNMT3A* mutations, which are equally distributed between frameshift/nonsense/splice-site mutations and other missense alleles (the most common of which, S714C, has only been reported in 11 samples to date, compared with >1000 R882 mutations; Forbes et al., 2011). Many cases with non-R882 mutations are predicted to cause haploinsufficiency for *DNMT3A* (e.g., deletions, frameshifts, splice-site, and nonsense mutations); these cases do not exhibit significant changes in DNA methylation. Additional missense mutations in *DNMT3A* that are not at position R882 may contribute to AML pathogenesis by alternative mechanisms that do not directly involve altered de novo methyltransferase activity or DNA methylation patterns. Because DNMT3A interacts with many other proteins, one or more alternative mechanisms may be relevant for AML associated with the wide variety of mutations that are non-R882. Regardless, these data suggest that R882 and non-R882 *DNMT3A* mutations in AML patients may in fact be different entities that will ultimately require different therapeutic approaches.

EXPERIMENTAL PROCEDURES

Mass Spectrometry, Immunofluorescence, Western Blot, Cell Culture, Bisulfite Pyrosequencing, Bisulfite Sequencing, and Oligonucleotide Sequences

These procedures are described in Supplemental Experimental Procedures.

Primary AML Samples

All cryopreserved primary AML samples were collected as part of a study approved by the Human Research Protection Office at Washington University

School of Medicine after patients provided informed consent in accordance with the Declaration of Helsinki.

DNA Methylation and RNA-seq Analysis

Illumina Infinium HumanMethylation450 BeadChip and RNA-seq data from NK-AML patients (and normal human control samples derived from purified cells from bone marrow) were obtained from the TCGA-AML data set (Ley et al., 2013). All DNA methylation and RNA-seq analyses were performed using the "R" software environment. The methylation data were normalized for background correction using the BioConductor MethyLumi package. Probes were removed from the data set that were nonunique, within 10 bases of a single-nucleotide polymorphism found in dbSNP, and/or on the X or Y chromosomes (yielding 464,198 probes for downstream analysis). Supervised differential methylation analysis was performed using CpGassoc with logit-transformed methylation beta values. Gene and CGI annotations were based on annotation provided by Illumina. For the purposes of this study, CpGs from the four categories TSS1500, TSS200, 5′ UTR, and first exon were grouped into one "promoter" annotation. Hierarchical clustering analysis was performed with the heatmap.2 function (gplots package) using the 5,000 CpGs with the greatest SD across all NK-AML samples. Supervised differential expression analysis was performed using DESeq2.

Statistical Analysis

Statistical analyses were performed using chi-square tests for categorical variables and t tests for continuous variables. All reported significance metrics are corrected for multiple testing by Benjamini-Holm (FDR) or Bonferonni methods (p values) unless otherwise noted.

Protein Purification

N-terminal 6×His tags and C-terminal FLAG tags were cloned into a full-length DNMT3A (NM_175629.1) expression vector using the pCMV6 (Origene) backbone. Five million HEK293T cells were plated per 15 cm plate and transfected after 24 hr by standard calcium-phosphate transfection protocols with 25 μg of WT, 25 μg of R882H, or 12.5:12.5 μg of WT:R882H 6×His-DNMT3A-FLAG expression vectors. Twenty-four hours after transfection, the media on the cells were replaced, and at 48 hr, the cells were harvested in PBS by trituration. The cells were then centrifuged and resuspended at five million cells/ml in 20 mM sodium phosphate, 250 mM NaCl, 30 mM imidazole (pH 7.4) plus a protease inhibitor cocktail (Sigma P8465). Cells were lysed by repeated (more than three times) snap-freezing, and thawing, and then the lysates were clarified by centrifugation at 10,000 × *g* for 20 min. The supernatants were filtered through a Whatman 25 mm GD/X PES 0.45 μm pore filter and then loaded onto a 2 ml GE HisTrap HP column and washed with 20 ml of 20 mM sodium phosphate, 500 mM NaCl, 30 mM imidazole (pH 7.4). The protein was eluted in 20 mM sodium phosphate, 250 mM NaCl, 400 mM imidazole (pH 7.4) and then dialyzed into 25 mM Tris-HCl, 150 mM NaCl, 0.5 mM dithiothreitol (DTT), 0.5 mM EDTA (pH 7.2; with 5% v/v glycerol for making −80°C frozen stocks). Protein concentrations were determined by Pierce BCA Kit (ThermoScientific), and then purity was confirmed using the Pierce Silver Stain Kit (ThermoScientific).

In Vitro Methylation

In vitro methylation reactions were performed on linearized pcDNA3.1 (Invitrogen) or linearized pcDNA3.1 containing a 144 bp fragment of the *GSTP1* promoter (see Supplemental Experimental Procedures) cloned into the EcoRI restriction digest site. Reactions were carried out at 37°C in a buffer of 20 mM HEPES, 30 mM NaCl, 0.5 mM DTT, 1 mM EDTA (pH 7.2), plus 0.2 mg/ml BSA and 5 μM ^{3}H-labeled SAM (PerkinElmer). Reactions were quenched by 100-fold dilution in ice-cold 10% trichloroacetic acid (TCA) with 35 μg of tRNA carrier (Sigma). Samples were spotted onto Whatman GF/C 25 mm filters and washed with 5 ml of ice-cold 10% TCA twice and then 5 ml of 95% ethanol once, dried, and measured by a scintillation counter.

Size-Exclusion Chromatography

Purified DNMT3A proteins (100 μl of 0.5 mg/ml protein) were loaded onto a Superose 6 HR 10/30 column controlled by an AKTApurifier with UNICORN software (GE v5.11). The flow rate was kept constant at 0.5 ml/min using a running buffer of 25 mM Tris-HCl, 150 mM NaCl, 0.5 mM DTT, 0.5 mM EDTA (pH 7.2). To generate a standard molecular weight curve, 100 μg of each of five proteins were used (urease, BSA, chicken egg albumin, carbonic anhydrase, and α-lactalbumin; Sigma MWND500). The molecular weights of DNMT3A complexes were calculated by nonlinear regression based on K_{av} values determined from elution values, the column void volume, and the total column volume (GraphPad Prism 6.0).

SUPPLEMENTAL INFORMATION

Supplemental information includes Supplemental Experimental Procedures, five figures, and four tables and can be found with this article online at http://dx.doi.org/10.1016/j.ccr.2014.02.010.

ACKNOWLEDGMENTS

The authors thank Daniel George and Anne Kettler for technical assistance. This work was funded by the National Institutes of Health (grants T32-HL007088 to D.A.R.-G. and CA162086 and CA101937 to T.J.L.) and the Barnes Jewish Hospital Foundation (to T.J.L.). The Washington University Proteomics Core is supported by grants from the National Institute of General Medical Sciences (8 P41 GM103422-35), the National Cancer Institute (P30 CA091842), and the National Center for Advancing Translational Sciences (UL1 TR000448).

Received: October 18, 2013
Revised: January 8, 2014
Accepted: February 19, 2014
Published: March 20, 2014

REFERENCES

Anders, S., and Huber, W. (2010). Differential expression analysis for sequence count data. Genome Biol. *11*, R106.

Berman, B.P., Weisenberger, D.J., Aman, J.F., Hinoue, T., Ramjan, Z., Liu, Y., Noushmehr, H., Lange, C.P.E., van Dijk, C.M., Tollenaar, R.A.E.M., et al. (2012). Regions of focal DNA hypermethylation and long-range hypomethylation in colorectal cancer coincide with nuclear lamina-associated domains. Nat. Genet. *44*, 40–46.

Challen, G.A., Sun, D., Jeong, M., Luo, M., Jelinek, J., Berg, J.S., Bock, C., Vasanthakumar, A., Gu, H., Xi, Y., et al. (2012). Dnmt3a is essential for hematopoietic stem cell differentiation. Nat. Genet. *44*, 23–31.

Chen, T., Ueda, Y., Dodge, J.E., Wang, Z., and Li, E. (2003). Establishment and maintenance of genomic methylation patterns in mouse embryonic stem cells by Dnmt3a and Dnmt3b. Mol. Cell. Biol. *23*, 5594–5605.

Crooks, G.E., Hon, G., Chandonia, J.-M., and Brenner, S.E. (2004). WebLogo: a sequence logo generator. Genome Res. *14*, 1188–1190.

Delhommeau, F., Dupont, S., Della Valle, V., James, C., Trannoy, S., Massé, A., Kosmider, O., Le Couedic, J.P., Robert, F., Alberdi, A., et al. (2009). Mutation in TET2 in myeloid cancers. N. Engl. J. Med. *360*, 2289–2301.

Ding, L., Ley, T.J., Larson, D.E., Miller, C.A., Koboldt, D.C., Welch, J.S., Ritchey, J.K., Young, M.A., Lamprecht, T., McLellan, M.D., et al. (2012). Clonal evolution in relapsed acute myeloid leukaemia revealed by whole-genome sequencing. Nature *481*, 506–510.

Figueroa, M.E., Lugthart, S., Li, Y., Erpelinck-Verschueren, C., Deng, X., Christos, P.J., Schifano, E., Booth, J., van Putten, W., Skrabanek, L., et al. (2010). DNA methylation signatures identify biologically distinct subtypes in acute myeloid leukemia. Cancer Cell *17*, 13–27.

Forbes, S.A., Bindal, N., Bamford, S., Cole, C., Kok, C.Y., Beare, D., Jia, M., Shepherd, R., Leung, K., Menzies, A., et al. (2011). COSMIC: mining complete cancer genomes in the Catalogue of Somatic Mutations in Cancer. Nucleic Acids Res. *39* (Database issue), D945–D950.

Gowher, H., Loutchanwoot, P., Vorobjeva, O., Handa, V., Jurkowska, R.Z., Jurkowski, T.P., and Jeltsch, A. (2006). Mutational analysis of the catalytic domain of the murine Dnmt3a DNA-(cytosine C5)-methyltransferase. J. Mol. Biol. *357*, 928–941.

Holz-Schietinger, C., and Reich, N.O. (2010). The inherent processivity of the human de novo methyltransferase 3A (DNMT3A) is enhanced by DNMT3L. J. Biol. Chem. *285*, 29091–29100.

Holz-Schietinger, C., Matje, D.M., Harrison, M.F., and Reich, N.O. (2011). Oligomerization of DNMT3A controls the mechanism of de novo DNA methylation. J. Biol. Chem. *286*, 41479–41488.

Holz-Schietinger, C., Matje, D.M., and Reich, N.O. (2012). Mutations in DNA methyltransferase (DNMT3A) observed in acute myeloid leukemia patients disrupt processive methylation. J. Biol. Chem. *287*, 30941–30951.

Irizarry, R.A., Ladd-Acosta, C., Wen, B., Wu, Z., Montano, C., Onyango, P., Cui, H., Gabo, K., Rongione, M., Webster, M., et al. (2009). The human colon cancer methylome shows similar hypo- and hypermethylation at conserved tissue-specific CpG island shores. Nat. Genet. *41*, 178–186.

Jia, D., Jurkowska, R.Z., Zhang, X., Jeltsch, A., and Cheng, X. (2007). Structure of Dnmt3a bound to Dnmt3L suggests a model for de novo DNA methylation. Nature *449*, 248–251.

Jurkowska, R.Z., Rajavelu, A., Anspach, N., Urbanke, C., Jankevicius, G., Ragozin, S., Nellen, W., and Jeltsch, A. (2011). Oligomerization and binding of the Dnmt3a DNA methyltransferase to parallel DNA molecules: heterochromatic localization and role of Dnmt3L. J. Biol. Chem. *286*, 24200–24207.

Kareta, M.S., Botello, Z.M., Ennis, J.J., Chou, C., and Chédin, F. (2006). Reconstitution and mechanism of the stimulation of de novo methylation by human DNMT3L. J. Biol. Chem. *281*, 25893–25902.

Kim, S.J., Zhao, H., Hardikar, S., Singh, A.K., Goodell, M.A., and Chen, T. (2013). A DNMT3A mutation common in AML exhibits dominant-negative effects in murine ES cells. Blood *122*, 4086–4089.

Ley, T.J., Ding, L., Walter, M.J., McLellan, M.D., Lamprecht, T., Larson, D.E., Kandoth, C., Payton, J.E., Baty, J., Welch, J., et al. (2010). DNMT3A mutations in acute myeloid leukemia. N. Engl. J. Med. *363*, 2424–2433.

Ley, T.J., Miller, C., Ding, L., Raphael, B.J., Mungall, A.J., Robertson, A.G., Hoadley, K., Triche, T.J., Jr., Laird, P.W., Baty, J.D., et al.; Cancer Genome Atlas Research Network (2013). Genomic and epigenomic landscapes of adult de novo acute myeloid leukemia. N. Engl. J. Med. *368*, 2059–2074.

Marcucci, G., Metzeler, K.H., Schwind, S., Becker, H., Maharry, K., Mrózek, K., Radmacher, M.D., Kohlschmidt, J., Nicolet, D., Whitman, S.P., et al. (2012). Age-related prognostic impact of different types of DNMT3A mutations in adults with primary cytogenetically normal acute myeloid leukemia. J. Clin. Oncol. *30*, 742–750.

Mardis, E.R., Ding, L., Dooling, D.J., Larson, D.E., McLellan, M.D., Chen, K., Koboldt, D.C., Fulton, R.S., Delehaunty, K.D., McGrath, S.D., et al. (2009). Recurring mutations found by sequencing an acute myeloid leukemia genome. N. Engl. J. Med. *361*, 1058–1066.

Miller, C.A., Wilson, R.K., and Ley, T.J. (2013). Genomic landscapes and clonality of de novo AML. N. Engl. J. Med. *369*, 1472–1473.

Mizuno, S.I., Chijiwa, T., Okamura, T., Akashi, K., Fukumaki, Y., Niho, Y., and Sasaki, H. (2001). Expression of DNA methyltransferases DNMT1, 3A, and 3B in normal hematopoiesis and in acute and chronic myelogenous leukemia. Blood *97*, 1172–1179.

Noushmehr, H., Weisenberger, D.J., Diefes, K., Phillips, H.S., Pujara, K., Berman, B.P., Pan, F., Pelloski, C.E., Sulman, E.P., Bhat, K.P., et al.; Cancer Genome Atlas Research Network (2010). Identification of a CpG island methylator phenotype that defines a distinct subgroup of glioma. Cancer Cell *17*, 510–522.

Purdy, M.M., Holz-Schietinger, C., and Reich, N.O. (2010). Identification of a second DNA binding site in human DNA methyltransferase 3A by substrate inhibition and domain deletion. Arch. Biochem. Biophys. *498*, 13–22.

Renneville, A., Boissel, N., Nibourel, O., Berthon, C., Helevaut, N., Gardin, C., Cayuela, J.-M., Hayette, S., Reman, O., Contentin, N., et al. (2012). Prognostic significance of DNA methyltransferase 3A mutations in cytogenetically normal acute myeloid leukemia: a study by the Acute Leukemia French Association. Leukemia *26*, 1247–1254.

Ribeiro, A.F.T., Pratcorona, M., Erpelinck-Verschueren, C., Rockova, V., Sanders, M., Abbas, S., Figueroa, M.E., Zeilemaker, A., Melnick, A., Löwenberg, B., et al. (2012). Mutant DNMT3A: a marker of poor prognosis in acute myeloid leukemia. Blood *119*, 5824–5831.

Shen, Y., Zhu, Y.M., Fan, X., Shi, J.Y., Wang, Q.R., Yan, X.J., Gu, Z.H., Wang, Y.Y., Chen, B., Jiang, C.L., et al. (2011). Gene mutation patterns and their prognostic impact in a cohort of 1,185 patients with acute myeloid leukemia. Blood *118*, 5593–5603.

Tadokoro, Y., Ema, H., Okano, M., Li, E., and Nakauchi, H. (2007). De novo DNA methyltransferase is essential for self-renewal, but not for differentiation, in hematopoietic stem cells. J. Exp. Med. *204*, 715–722.

Thol, F., Damm, F., Lüdeking, A., Winschel, C., Wagner, K., Morgan, M., Yun, H., Göhring, G., Schlegelberger, B., Hoelzer, D., et al. (2011). Incidence and prognostic influence of DNMT3A mutations in acute myeloid leukemia. J. Clin. Oncol. *29*, 2889–2896.

Welch, J.S., Ley, T.J., Link, D.C., Miller, C.A., Larson, D.E., Koboldt, D.C., Wartman, L.D., Lamprecht, T.L., Liu, F., Xia, J., et al. (2012). The origin and evolution of mutations in acute myeloid leukemia. Cell *150*, 264–278.

Wienholz, B.L., Kareta, M.S., Moarefi, A.H., Gordon, C.A., Ginno, P.A., and Chédin, F. (2010). DNMT3L modulates significant and distinct flanking sequence preference for DNA methylation by DNMT3A and DNMT3B in vivo. PLoS Genet. *6*, e1001106.

Yamashita, Y., Yuan, J., Suetake, I., Suzuki, H., Ishikawa, Y., Choi, Y.L., Ueno, T., Soda, M., Hamada, T., Haruta, H., et al. (2010). Array-based genomic resequencing of human leukemia. Oncogene *29*, 3723–3731.

Yan, X.J., Xu, J., Gu, Z.H., Pan, C.M., Lu, G., Shen, Y., Shi, J.Y., Zhu, Y.M., Tang, L., Zhang, X.W., et al. (2011). Exome sequencing identifies somatic mutations of DNA methyltransferase gene DNMT3A in acute monocytic leukemia. Nat. Genet. *43*, 309–315.

Ziller, M.J., Gu, H., Müller, F., Donaghey, J., Tsai, L.T.-Y., Kohlbacher, O., De Jager, P.L., Rosen, E.D., Bennett, D.A., Bernstein, B.E., et al. (2013). Charting a dynamic DNA methylation landscape of the human genome. Nature *500*, 477–481.

Cancer Cell
Article

SPOP Promotes Tumorigenesis by Acting as a Key Regulatory Hub in Kidney Cancer

Guoqiang Li,[1,3,16] Weimin Ci,[2,16] Subhradip Karmakar,[4,5,16] Ke Chen,[1] Ruby Dhar,[4,5] Zhixiang Fan,[9] Zhongqiang Guo,[1,10] Jing Zhang,[1] Yuwen Ke,[1] Lu Wang,[1,3] Min Zhuang,[12] Shengdi Hu,[13] Xuesong Li,[10] Liqun Zhou,[10] Xianghong Li,[11] Matthew F. Calabrese,[14] Edmond R. Watson,[14] Sandip M. Prasad,[7] Carrie Rinker-Schaeffer,[7] Scott E. Eggener,[7] Thomas Stricker,[4,8] Yong Tian,[13] Brenda A. Schulman,[14,15] Jiang Liu,[1,*] and Kevin P. White[4,5,6,*]
[1]Key Laboratory of Genome Sciences and Information
[2]Laboratory of Disease Genomics and Individualized Medicine
Beijing Institute of Genomics, Chinese Academy of Sciences, Beijing 100101, China
[3]University of Chinese Academy of Sciences, Beijing 100049, China
[4]Institute for Genomics and Systems Biology, University of Chicago and Argonne National Laboratory, Chicago, IL 60637, USA
[5]Department of Human Genetics
[6]Section on Genetic Medicine, Department of Medicine
[7]Section of Urology, Department of Surgery
[8]Department of Pathology
University of Chicago, Chicago, IL 60637, USA
[9]Kunming Medical University, Kunming, Yunnan 650500, China
[10]Department of Urology, First Hospital of Peking University, Beijing 100034, China
[11]Department of Pathology, Peking University Cancer Hospital, Beijing 100142, China
[12]Department of Pharmaceutical Chemistry, University of California, San Francisco, San Francisco, CA 94158, USA
[13]Laboratory of Animal Research Center, Institute of Biophysics, Chinese Academy of Sciences, Beijing 100101, China
[14]Department of Structural Biology
[15]Howard Hughes Medical Institute
St. Jude Children's Research Hospital, Memphis, TN 38105, USA
[16]These authors contributed equally to this work
*Correspondence: liuj@big.ac.cn (J.L.), kpwhite@uchicago.edu (K.P.W.)
http://dx.doi.org/10.1016/j.ccr.2014.02.007

SUMMARY

Hypoxic stress and hypoxia-inducible factors (HIFs) play important roles in a wide range of tumors. We demonstrate that *SPOP*, which encodes an E3 ubiquitin ligase component, is a direct transcriptional target of HIFs in clear cell renal cell carcinoma (ccRCC). Furthermore, hypoxia results in cytoplasmic accumulation of SPOP, which is sufficient to induce tumorigenesis. This tumorigenic activity occurs through the ubiquitination and degradation of multiple regulators of cellular proliferation and apoptosis, including the tumor suppressor PTEN, ERK phosphatases, the proapoptotic molecule Daxx, and the Hedgehog pathway transcription factor Gli2. Knockdown of SPOP specifically kills ccRCC cells, indicating that it may be a promising therapeutic target. Collectively, our results indicate that SPOP serves as a regulatory hub to promote ccRCC tumorigenesis.

Significance

Tumor cells can adapt to hypoxic microenvironments in several different ways to promote tumor growth, including stimulating angiogenesis. Herein, we demonstrate that hypoxia can drive the cytoplasmic accumulation of SPOP and that cytoplasmic accumulation of SPOP is sufficient to convey tumorigenic properties on to otherwise nontumorigenic cells by targeting PTEN and several other tumor suppressor molecules for E3 ligase-mediated degradation. This tumor-promoting function of SPOP stands in contrast to its proapoptotic role in the cell nucleus. These results have elucidated a major mechanism that contributes to tumorigenesis in ccRCC, connecting hypoxia response and ubiquitin-mediated degradation of tumor suppressors. The oncogenic role of cytoplasmic SPOP makes it a promising candidate for therapeutic intervention.

INTRODUCTION

Renal cell carcinoma (RCC) is the eighth leading malignancy in the United States, accounting for 4% of all cancers. More than 209,000 new cases and 102,000 deaths are estimated to occur worldwide each year (Rini et al., 2009). Approximately 30% of RCC patients present with metastatic disease at the time of diagnosis and nearly half of the remainder will subsequently develop metastasis (McDermott et al., 2005; Negrier et al., 1998). As RCC is highly resistant to chemotherapy, first-line treatment of metastatic disease in the 1990s and 2000s relied on immunotherapies such as interleukin-2 and interferon alpha, despite low response rates (5% to 20%) (Fyfe et al., 1996; McDermott et al., 2005; Wardle, 1991). However, hypoxic response mediated though hypoxia-inducible factors (HIFs) is a key feature of most solid tumors but is particularly important in kidney cancers (Chi et al., 2006). Accordingly, recent targeted therapies that inhibit HIF-regulated pathways, including angiogenesis inhibitors directed against vascular endothelial growth factor (VEGF) and platelet-derived growth factor (PDGF) signaling pathways, have been developed. Although these therapies represent improvements in patient care, the majority of patients with advanced disease remain refractory to treatment, suggesting that certain critical HIF targets remain unknown (Escudier et al., 2007; Motzer et al., 2007, 2013).

It has been shown that, under normoxic conditions, the oxygen-sensitive HIFα subunit is degraded by ubiquitination via the von Hippel-Lindau (*VHL*) tumor suppressor gene (Kaelin, 2002). However, under hypoxic conditions, HIFα degradation is suppressed, leading to enhanced nuclear localization of HIFα and transcription of various target genes, including the angiogenic gene *VEGF* (Kaelin, 2008). Inactivating mutations or silencing of the *VHL* tumor suppressor gene can also suppress the degradation of HIFα, and *VHL* mutation or silencing is found in at least 80% of all clear cell RCCs (ccRCCs) (Kim and Kaelin, 2004; Motzer and Molina, 2009; Nickerson et al., 2008). ccRCCs are the most common form of kidney cancer, accounting for 75% of all cases (Lopez-Beltran et al., 2006). Results from ccRCC xenograft experiments indicate that HIF accumulation is critical for VHL tumor suppressor function during ccRCC oncogenesis (Kaelin, 2008). It has also been found that RCCs have evolved an alternative hypoxia signaling pathway compared with normal renal cells (Jiang et al., 2003) and that the ccRCCs are in a high hypoxia response state compared to the normal kidney samples and other subtypes of kidney cancer (Chi et al., 2006).

Although hypoxia response plays a critical role in kidney cancer, other cell regulatory pathways are also important for tumor development and progression (Brugarolas, 2007). For example, another promising target for RCC therapies is the mammalian Target of Rapamycin (mTOR) pathway, which is abnormally activated during the development of kidney cancer (Robb et al., 2007). mTOR is negatively regulated by the tumor suppressor phosphatase and tensin homolog (PTEN) (Hollander et al., 2011), which is mutated or downregulated in many cancers, including ccRCC (Vivanco and Sawyers, 2002). The mTOR pathway positively regulates cell growth and proliferation through enhanced mRNA translation by phosphorylated S6 kinase 1 and 4E binding protein-1 (Sarbassov et al., 2005). In spite of its promise, the mTOR inhibitor temsirolimus produces only low objective responses in patients with advanced RCC, although it contributes to a modest improvement in overall survival (Hudes et al., 2007; Kapoor and Figlin, 2009). Further investigation of the mechanisms of PTEN downregulation in ccRCC is critical for an understanding of RCC pathogenesis.

Our previous studies demonstrated that the SPOP protein is overexpressed in 85% of kidney cancers and that nearly 100% of primary and metastatic ccRCCs exhibit SPOP accumulation (Liu et al., 2009). SPOP is a BTB/POZ domain protein, and *MEL-26*, the *C. elegans SPOP* ortholog, was first identified as an adaptor for the E3 ligase Cullin3 (Cul3). In *C. elegans*, MEL-26 promotes the meiotic/mitotic transition through the degradation of MEI-1/katanin (Mains et al., 1990; Pintard et al., 2003; Xu et al., 2003). In *Drosophila*, D-SPOP (also known as Roadkill) can promote the ubiquitination and degradation of the Gli transcription factor ortholog Cubitus interruptus and the JNK phosphatase Puckered to regulate the Hedgehog (Hh) and tumor necrosis factor (TNF) pathways, respectively (Kent et al., 2006; Zhang et al., 2006; Liu et al., 2009). In humans, the roles for SPOP in regulating the Hh and TNF pathways have been conserved (Zhang et al., 2006; Liu et al., 2009), and several other SPOP substrates have been identified as well, including the death domain-associated protein (Daxx) (Kwon et al., 2006), the polycomb group protein BMI-1, and the Histone variant MacroH2A (Hernández-Muñoz et al., 2005). Together, these previous results indicate that SPOP plays important roles during cell apoptosis, proliferation, and animal development, and they suggest that overexpression of SPOP in ccRCCs may lead to dysregulation of pathways involved in tumorigenesis. However, it is unclear how SPOP becomes overexpressed or whether it may function directly in kidney tumorigenesis. Adding to this puzzle, recent deep sequencing studies of breast, prostate, and endometrial cancers found that *SPOP* is frequently mutated, and the *SPOP* locus is observed to undergo loss of heterozygosity (LOH), indicating that SPOP may act as a tumor suppressor (Berger et al., 2011; Li et al., 2011). However, no *SPOP* mutations have been detected in kidney cancers thus far (Liu et al., 2009; Cancer Genome Atlas Research Network, 2013). In this study, we aim to determine whether SPOP promotes tumorigenesis in the kidney.

RESULTS

HIF Regulates SPOP Expression

Immunohistochemistry results have suggested that SPOP is overexpressed in virtually all ccRCCs (Liu et al., 2009). We confirmed this finding by immunoblot assays in multiple pairs of ccRCC primary tumor tissue and matched normal adjacent tissue (Figure 1A). However, the mechanism underlying this SPOP overexpression is unknown. Considering the frequent accumulation of HIF in ccRCC patients, we were interested in whether HIF can drive SPOP overexpression. We identified a HIF-1α binding peak in the first intron of *SPOP* by chromatin immunoprecitation sequencing (ChIP-seq) (Figure 1B) and further validated it by ChIP-quantitative PCR (qPCR) (Figure S1A available online). To determine whether this intronic DNA sequence region functions as a HIF-responsive regulatory element, we performed a luciferase reporter assay by inserting

the wild-type HIF binding sequence into a pGL3-promoter reporter vector. In human embryonic kidney HEK293 cells, the wild-type sequence exhibits increased luciferase activity under hypoxic exposure (1% O_2/5% CO_2/94% N_2) compared to normoxia, while HIF-1α knockdown impairs the luciferase activity (Figure 1C). Additionally, we constructed several mutations or deletions of the predicted hypoxia response elements (HREs; 5′-RCGTG-3′ and 5′-[A/C]ACAG-3′) (Miyazaki et al., 2002). Although mutants of CACAG showed marginal decrease in luciferase activity (Figure S1B), both point mutations and deletion of the CGTG site showed significant decrease in luciferase activity (Figure 1C), demonstrating that the HIF binding site is functional in this hypoxia-responsive *cis*-regulatory element.

To further elucidate whether HIF can regulate SPOP, the *VHL* wild-type ccRCC cell line Caki-2 was cultured under hypoxic conditions. Hypoxic culture resulted in the accumulation of HIF-1α and HIF-2α proteins. Both SPOP mRNA (Figure 1D) and protein (Figure 1E) levels increased in ccRCC cells under hypoxic conditions. Additionally, ectopic overexpression of either HIF-1α or HIF-2α led to SPOP accumulation in HEK293 cells (Figure 1F), indicating that both HIF-1α and HIF-2α can regulate *SPOP* expression. Although knockdown of HIF-1α alone in Caki-2 cells, which express both HIF-1α and HIF-2α (Kucejova et al., 2011), can reduce SPOP protein abundance (Figure 1G), double knockdown of HIF-1α and HIF-2α is more effective than either alone (Figure S1C). Consistent with these results, knocking down HIF-2α by siRNA in the ccRCC cell line A498 that predominantly expresses HIF-2α (Shinojima et al., 2007) resulted in a reduction in the mRNA (Figure 1H) and protein (Figure 1I) abundance of SPOP, as well as the known HIF target VEGF. Because *VHL* mutation is one of the most common causes of kidney cancer and affects abundance of HIFs, we examined SPOP abundance after restoring VHL in the *VHL* null cell lines 786-O and A498. Accordingly, restoration of VHL led to decreased protein abundance of SPOP (Figure 1J), and conversely, VHL knockdown in HEK293 cells resulted in an increase in SPOP (Figure S1D). Taken together, these results demonstrate that HIF can directly regulate *SPOP* expression.

SPOP Accumulation in the Cytoplasm of ccRCC Cells

SPOP was first identified as a nuclear protein (Nagai et al., 1997), and several studies have confirmed its nuclear location in HEK293 and HeLa cells (Bunce et al., 2008; Hernández-Muñoz et al., 2005; Kwon et al., 2006). To investigate SPOP localization in kidney cancer, we used a monoclonal anti-SPOP antibody (Liu et al., 2009) to stain kidney tissue biopsies. We found that SPOP was predominately localized in the nucleus of normal kidney tissue. However, we observed SPOP accumulation in the cytoplasm of neoplastic ccRCC cells, with residual SPOP remaining in the nucleus (Figure 2A). Immunocytochemistry staining also revealed that SPOP predominately accumulated in the cytoplasm of Caki-2 cells but was primarily localized within the nucleus of HeLa (Figure 2B) and HEK293 cells (Figure S2A). Ectopically expressed GFP-tagged SPOP in ccRCC cell lines (Caki-2 and A498) and in non-ccRCC cell lines (HEK293 and HeLa cells) yielded similar results as those for endogenous SPOP (Figure S2B). Furthermore, cell fractionation assays confirmed the cytoplasmic localization of SPOP in ccRCC cell lines and predominantly nuclear localization in HEK293 cells (Figure S2C).

Hypoxia Drives SPOP Accumulation in the Cytoplasm

Previous studies have shown that some proteins accumulate in the cytoplasm under stress conditions such as hypoxia (Arimoto et al., 2008). Given that ccRCC tumorigenesis is associated with hypoxia signaling, we tested whether hypoxic conditions could stimulate SPOP accumulation in the cytoplasm. Immunofluorescence staining showed that endogenous SPOP localizes in the nucleus of HeLa cells under normoxia, while hypoxic treatment (1% O_2/5% CO_2/94% N_2) led to SPOP accumulation in the cytoplasm (Figure 2B). Additionally, HIF overexpression further enhanced the cytoplasmic accumulation of SPOP (Figure 2B). SPOP accumulation in the cytoplasm under hypoxic treatment was further confirmed by cell fractionation assays (Figures 2C and 2D). Although previous data showed that ectopically expressed GFP-SPOP localized in the nucleus of HeLa and HEK293 cells under normoxia (Figure S2B), we found that it also accumulated in the cytoplasm under hypoxia in these cells (Figure S2D). Thus, hypoxia appears to be a sufficient condition to stimulate the cytoplasmic accumulation of SPOP.

Cytoplasmic SPOP Promotes Tumorigenesis

Next, we wanted to test whether cytoplasmic SPOP is associated with tumorigenic phenotypes. Sequence analysis indicated that SPOP contains a nuclear localization signal (NLS) at its C terminus, amino acids 367–373 (PRKRLKQ). Crystallographic analysis indicates that the deletion of the NLS peptide from the SPOP C terminus is unlikely to affect the binding of SPOP with the E3 ligase Cullin3 or SPOP substrates (Zhuang et al., 2009). Additionally, the in vitro ubiquitination of SPOP substrates is unaffected by deletion of the NLS from SPOP (Zhuang et al., 2009). Therefore, we deleted the NLS peptide from SPOP to test whether SPOP lacking the NLS would accumulate in the cytoplasm when ectopically expressed in non-ccRCC cells. As expected, ectopic expression of GFP-SPOP lacking the NLS accumulates in the cytoplasm of HEK293 cells (Figure S2E). We refer to SPOP lacking the NLS as SPOP-cyto.

We overexpressed SPOP-cyto and wild-type SPOP in non-ccRCC cell lines to determine whether there are differences in phenotypic effects. A bromodeoxyuridine (BrdU) incorporation assay showed that wild-type SPOP inhibited cell proliferation (Figure 3A), which is consistent with previous results that SPOP can induce apoptosis in HEK293 (Liu et al., 2009) and HeLa cells (Kwon et al., 2006) (Figure S3A). It is striking that SPOP-cyto enhanced proliferation rather than inducing apoptosis (Figure 3A). As a marker for apoptotic state of the cells, we used the proapoptotic protein Bax, which has been shown to be inactivated by phosphorylation at Ser184 (Gardai et al., 2004). Overexpression of SPOP-cyto increased the level of Ser184-phosphorylated Bax (p-Bax), indicating that SPOP-cyto can inhibit Bax-mediated apoptosis (Figure 3B). Overexpression of SPOP-cyto also increased the protein abundance of the cellular proliferation markers ser10-phosphorylated histone H3 (p-Histone H3) (Bhatia et al., 2011) and proliferating cell nuclear antigen (PCNA), consistent with the observation that SPOP-cyto promotes cell proliferation (Figure 3B). Thus, the accumulation of cytoplasmic SPOP appears to alter the function of the protein in comparison to its nuclear form, changing SPOP function from proapoptotic to antiapoptotic and proproliferative. Furthermore, siRNA knockdown of SPOP

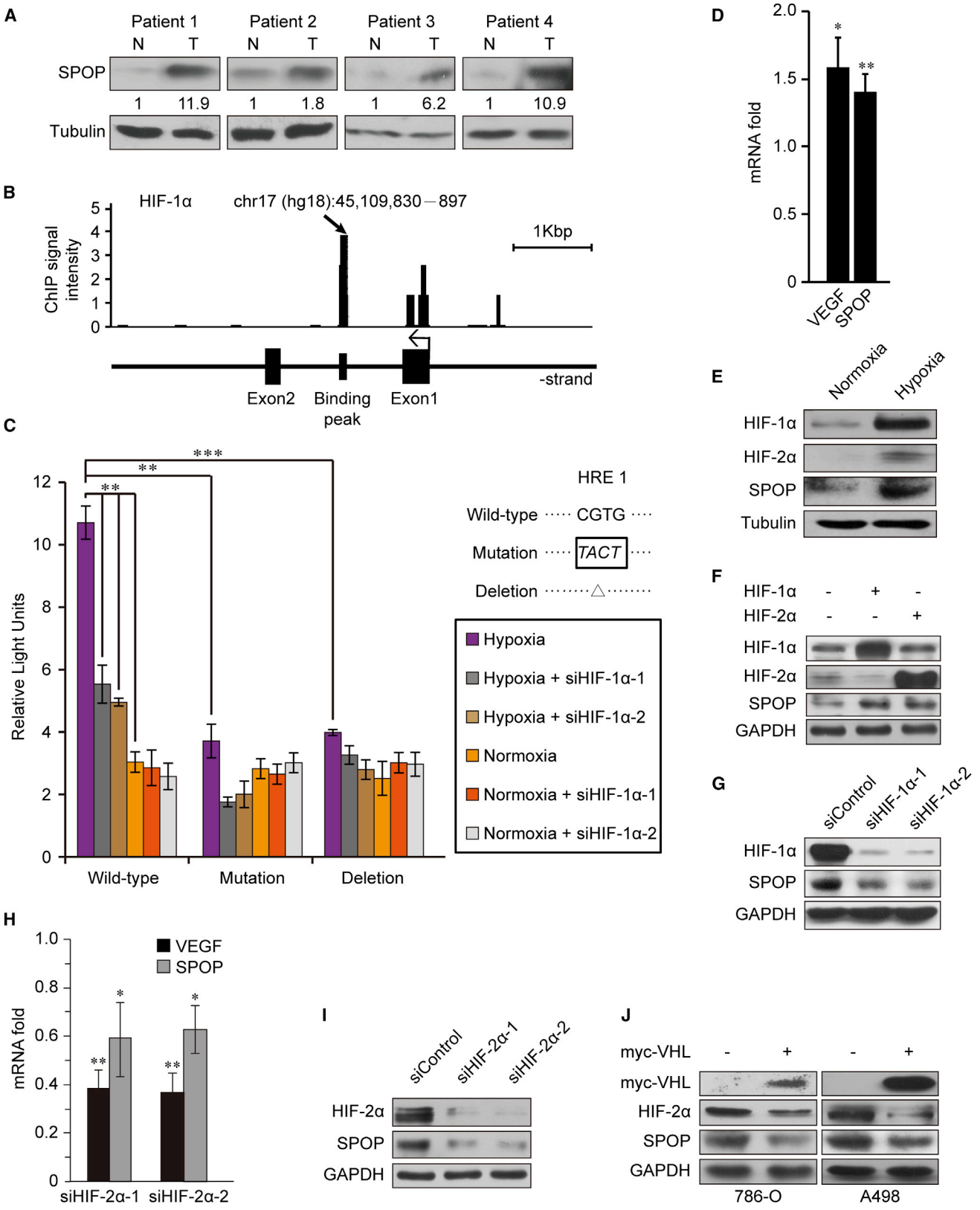

(legend on next page)

(Figure S3B) induced apoptosis in ccRCC cells where SPOP is in the cytoplasm, but not in HeLa or HEK293 cells (Figures 3C, S3C, and S3D). Knockdown of SPOP in ccRCC cells also resulted in decreased levels of p-Bax (Ser184), PCNA, and p-Histone H3 levels (Figure S3E). However, we wondered whether hypoxia-induced cytoplasmic localization of SPOP in non-ccRCC cells would also lead to an SPOP "addicted" state in which knockdown of SPOP would lead to cell death. Indeed, RNAi knockdown of SPOP in HeLa cells under hypoxia exposure led to significantly increased apoptosis compared to cells treated with only hypoxia stress (Figure S3F), similar to the results of SPOP knockdown in ccRCC cell lines. Together, these results indicate that inhibition of SPOP can specifically induce apoptosis and inhibit proliferation in ccRCC cells but not in non-ccRCC cells, suggesting that SPOP could serve as a therapeutic target specific to cancer cells.

We further investigated whether cytoplasmic SPOP could promote tumorigenesis in a nude mouse xenograft model. HEK293 cells have previously been used to demonstrate the tumorigenic potential of oncogenes (Hamid et al., 2005). We generated stable polyclonal HEK293 cell lines transfected with *SPOP-cyto*, *SPOP*, or empty vector (*pcDNA3*) (Figure S3G), and the levels of exogenous SPOP-cyto and SPOP are comparable to the endogenous protein in primary ccRCC samples (Figure 1A). Subcutaneous injection of the stably transfected HEK293-SPOP-cyto cells into nude mice induced tumor formation in approximately 80% of mice (15/19) within 6 weeks, whereas wild-type SPOP and control empty vector produced no visible tumor growth (0/19 and 0/19, respectively) (Figure 3D). Furthermore, histopathologic analyses of the xenograft tumors reveal typical cancerous lesions (Figure S3H). Thus, cytoplasmic SPOP, but not nuclear SPOP, promotes tumorigenesis.

SPOP Mediates the Ubiquitination and Degradation of Tumor Suppressor PTEN

We next wanted to investigate the mechanism by which cytoplasmic SPOP promotes tumorigenesis. SPOP was previously identified as a regulatory "hub" molecule in *Drosophila* (Liu et al., 2009) and can degrade substrates in multiple signaling pathways via Cul3-mediated ubiquitination (Bunce et al., 2008; Hernández-Muñoz et al., 2005; Kwon et al., 2006; Xu et al., 2003; Zhuang et al., 2009). SPOP crystal structure studies demonstrated that all known SPOP substrates share a conserved SPOP-binding consensus (SBC) motif (Φ-π-S-S/T-S/T; Φ is nonpolar, π is polar) (Zhuang et al., 2009). Thus, we hypothesized that cytoplasmic SPOP might promote cancer phenotypes by mediating the degradation of cytoplasmic proteins that contain SBC motifs.

Previously, we found that SPOP can mediate the ubiquitination and degradation of Puc, a dual-specificity phosphatase (DUSP) class molecule in *Drosophila* that regulates JNK signaling (Liu et al., 2009). DUSPs have been implicated as major modulators of critical signaling pathways that are dysregulated in various diseases (Patterson et al., 2009). Therefore, we computationally searched the human proteome for DUSP domain proteins that contain the SBC motif. We found seven DUSP domain containing proteins with at least one SBC motif (Table S1), including the cytoplasmic tumor suppressor protein PTEN with substrate specificity to phosphatidylinositol phosphates (Myers et al., 1998) and that contains the SBC motif ASSST (residues 359–363).

Genetic alterations targeting the PTEN tumor suppressor are among the most frequently noted somatic mutations in human cancers (Sansal and Sellers, 2004). PTEN functions to antagonize phosphoinositide 3-kinase (PI3K)/Akt signaling through its lipid phosphatase activity, thereby controlling cell growth, survival, and metabolic processes (Wu et al., 1998). Based on previous crystal structures, the SBC motif in PTEN is in a flexible region that is not folded into any three-dimensional domains and is thus potentially accessible for SPOP binding (Lee et al., 1999). To understand the molecular basis for potential SPOP MATH domain interactions with the PTEN SBC, we determined the crystal structure of the SPOP MATH complex with a peptide corresponding to PTEN residues 354–368, which constitutes the PTEN SBC motif. The SPOP MATH domain forms an antiparallel β sandwich, and the PTEN SBC motif adopts an extended conformation to bind within the MATH central shallow groove

Figure 1. HIF Activates SPOP Expression

(A) Immunoblots of endogenous SPOP in four paired ccRCC tumor and adjacent nontumor tissue samples. Numbers indicate the relative density of the tumor tissue (T) versus normal tissue (N) as evaluated using ImageJ software. SPOP was detected by immunoblotting with an anti-SPOP antibody (clone 6C). Tubulin was used as a loading control.

(B) HIF-1α ChIP-seq peak within the first intron of the *SPOP* gene (arrow). ChIP signal intensity represents differential binding between input/mock IP control and HIF-1α antibody ChIP.

(C) Luciferase reporter assays indicate that the HIF binding peak in the first intron of *SPOP* (hg18, chr17:45,109,830–45,109,897) is functional. The wild-type and HRE (CGTG) mutated or deleted HIF binding sequence were cloned into a pGL3-promoter vector. Luciferase activities were normalized to Renella luciferase, and the results are represented as values relative to the empty vector. Hypoxia was induced using a hypoxia chamber (1% O_2/5% CO_2/94% N_2). RNAi knockdown was performed with two independent siRNAs to *HIF-1α*.

(D) *SPOP* mRNA expression is activated under hypoxic conditions in the Caki-2 ccRCC cell line. *VEGF* was used as a positive control.

(E) SPOP protein abundance increases after hypoxia treatment in Caki-2 cells. Tubulin was used as a loading control.

(F) In either *HIF-1α*- or *HIF-2α*-transfected HEK293 cells, SPOP protein expression was induced. GAPDH was used as a loading control.

(G) Knockdown HIF-1α downregulated the expression of SPOP in Caki-2 cells. RNAi knockdown was performed as in (C).

(H) *SPOP* mRNA expression is suppressed after two independent siRNAs' knockdown of HIF-2α in 786-O ccRCC cells. mRNA expression was normalized to control cells exposed to negative control siRNAs. *VEGF* was used as a positive control.

(I) SPOP protein abundance decreases after knockdown of HIF-2α in A498 cells. Tubulin was used as a loading control.

(J) SPOP protein abundance decreases when restoring of VHL in 786-O and A498 cells. Cells were harvested 72 hr after transfection. GAPDH was used as a loading control.

Data in (C), (D), and (H) are presented as means ± SD of at least three independent experiments. *$p < 0.05$, **$p < 0.01$, and ***$p < 0.001$, based on Student's t test. See also Figure S1.

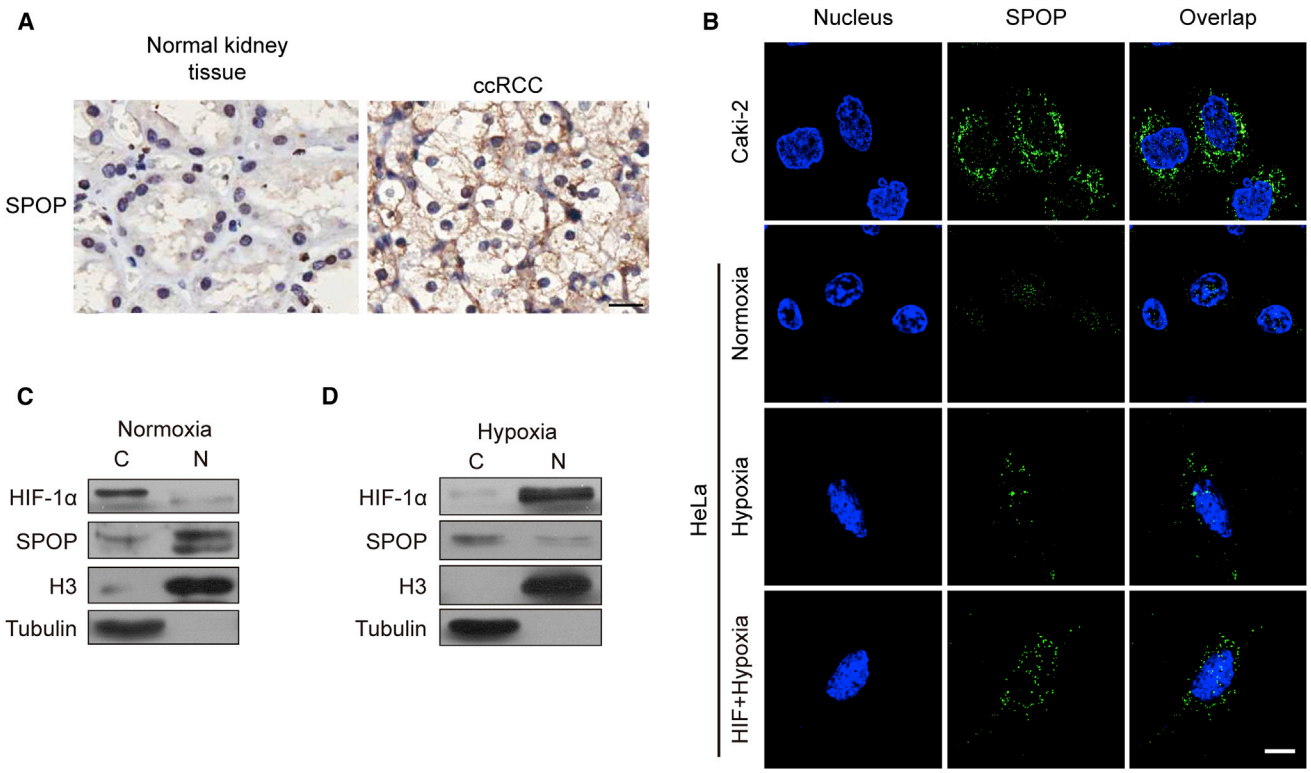

Figure 2. Hypoxia Drives SPOP Accumulation in the Cytoplasm of ccRCC Cells

(A) Immunohistochemistry reveals that SPOP accumulates in the cytoplasm of ccRCC tumor cells but in the nuclei of adjacent nontumor cells. An SPOP-specific monoclonal antibody (SPOP-5G) was used for staining (diaminobenzidine, brown staining). Scale bar, 20 μm.

(B) SPOP localizes in the nucleus in HeLa cells under normoxic conditions but accumulates in the cytoplasm under hypoxic conditions (1% O_2), comparable to that in Caki-2 cells; additional HIF expression enhances SPOP accumulation in the cytoplasm. Cells were stained with SPOP-5G antibody (green), and the nuclei were counterstained with DAPI (4′,6-diamidino-2-phenylindole; blue). Scale bar, 10 μm.

(C) Separation of the nuclear (N) and cytoplasmic (C) fractions confirms SPOP accumulation in the cytoplasm of HeLa cells under mormoxic conditions. Histone H3 and tubulin served as nuclear and cytoplasmic markers, respectively.

(D) Separation of the nuclear (N) and cytoplasmic (C) fractions confirms SPOP accumulation in the cytoplasm of HeLa cells under hypoxic conditions (1% O_2). Histone H3 and tubulin served as nuclear and cytoplasmic markers, respectively.

See also Figure S2.

(Figures S4A and S4B). SPOP MATH-SBC interactions are anchored by both hydrophobic and polar interactions with the PTEN SBC residues ASSST (Figure 4A).

We further validated whether PTEN acts as a SPOP substrate in cells. Coimmunoprecipitation (Co-IP) data showed that both SPOP and SPOP-cyto can bind PTEN, whereas the deletion of the PTEN SBC motif eliminated binding (Figure 4B). Overexpressed SPOP-cyto also bound endogenous PTEN in HeLa cells (Figure 4C). Furthermore, exogenous PTEN abundance was reduced when PTEN was coexpressed with SPOP-cyto in HeLa cells, whereas a PTEN SBC mutant was resistant to SPOP-cyto-mediated degradation (Figure 4D). A cycloheximide (CHX) chase assay also indicated that PTEN is rapidly degraded by SPOP-cyto after cotransfection (Figure 4E). Notably, SPOP can mediate the ubiquitination of PTEN, but the SBC-mutated PTEN was not affected by SPOP, as demonstrated by in vivo (Figure 4F) and in vitro ubiquitination assays (Figure 4G; Figure S4C). Taken together, these results indicate that SPOP promotes the degradation of tumor suppressor PTEN.

SPOP Mediates the Degradation of ERK Phosphatase DUSP7

Our computational scan for SBC motifs also indicated that DUSP6 and DUSP7, ERK-specific cytoplasmic MAPK phosphatases, are candidate SPOP targets (Table S1). DUSP6 contains the motif CSSSS (residues 155–159), and DUSP7 contains the motif VDSSS (residues 191–195). The classical ERK pathway has long been associated with the ability of cancer cells to grow independently, and this pathway is dysregulated in approximately 30% of human tumors (Dhillon et al., 2007; Keyse, 2008). Reports from several groups have indicated that the level of ERK phosphorylation is significantly elevated in ccRCCs (Campbell et al., 2009; Lee et al., 2009). We found that the levels of ERK phosphorylation increased after dual knockdown of DUSP6 and DUSP7 in Caki-2 cells (Figure S5A), indicating that DUSP6 and DUSP7 regulate the ERK pathway in ccRCC cells.

Based on their SBC domains, DUSP6 and DUSP7 have similar predicted SPOP interaction properties; therefore, we focused our biochemical analysis on DUSP7. Co-IP assays showed that both SPOP and SPOP-cyto bind DUSP7, whereas a mutant

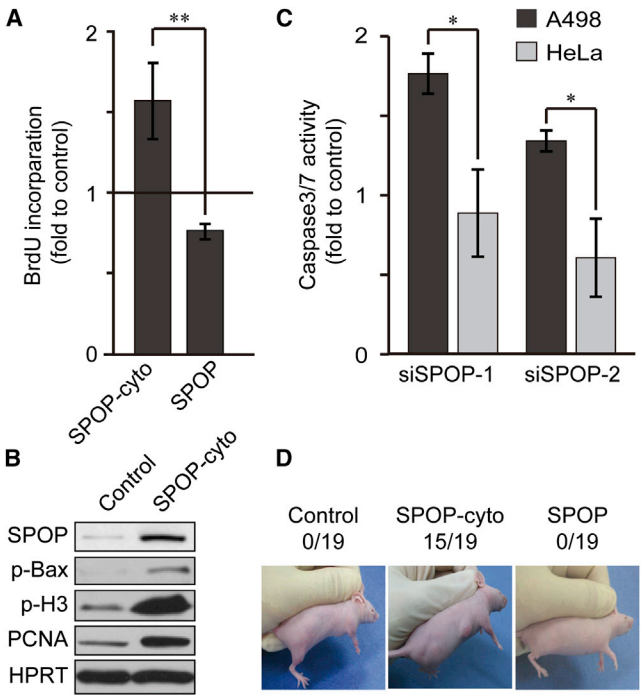

Figure 3. Cytoplasmic SPOP Promotes Tumorigenesis

(A) SPOP-cyto promotes cell proliferation. HEK293 cells were transfected with the indicated vectors for 48 hr, and cell proliferation was measured by BrdU incorporation. Values are normalized to empty vector-transfected control cells.

(B) SPOP-cyto overexpression upregulates the indicated antiapoptotic marker p-Bax and proliferation markers, p-Histone H3 and PCNA. SPOP-5G antibody was used to blot SPOP. HPRT served as a loading control.

(C) RNAi knockdown of SPOP induces apoptosis in A498 but not HeLa cells. Apoptosis was evaluated by caspase 3/7 activity 48 hr after siRNA transfection.

(D) SPOP-cyto promotes tumorigenesis in a xenograft model. HEK293-pcDNA3, HEK293-SPOP, or HEK293-SPOP-cyto polyclonal stable cell lines were injected subcutaneously into the nude mice. Six weeks later, the number of mice that formed tumors in each group was counted.

Data in (A) and (C) are presented as the means ± SD of three independent experiments. *$p < 0.05$ and **$p < 0.01$, based on Student's t test.

See also Figure S3.

DUSP7 SBC motif eliminated binding with SPOP (Figure 5A). Furthermore, overexpressed SPOP-cyto bound to endogenous DUSP7 in HeLa cells (Figure 5B). DUSP7 is also downregulated in SPOP- and SPOP-cyto-overexpressing cells (Figure 5C), while neither SPOP nor SPOP-cyto can degrade the DUSP7-SBC mutant (Figure 5D). A CHX chase assay indicated that DUSP7 is rapidly degraded by SPOP-cyto (Figure S5B). Notably, SPOP mediated the ubiquitination of DUSP7 but not its SBC mutant in both in vivo (Figure 5E) and in vitro (Figure 5F; Figure S5C) ubiquitination assays.

Cytoplasmic SPOP Acts as a Regulatory Hub by Modulating Multiple Pathways during Kidney Tumorigenesis

PI3K/Akt and ERK pathways are hyperactivated in different types of tumors, including ccRCC (Campbell et al., 2009; Lee et al., 2009). While it has been shown that these pathways are sometimes genetically altered in ccRCC, such mutations contribute to a limited percentage of ccRCC patients (Cancer Genome Atlas Research Network, 2013; Sato et al., 2013). Considering that SPOP is overexpressed in nearly 100% of ccRCCs, we wondered whether cytoplasmic SPOP might deregulate these pathways through mediating degradation of PTEN, DUSP6, and DUSP7 in ccRCC. Thus, we examined the effects of RNAi knockdown of SPOP on these signaling pathways in A498 ccRCC cells. As shown in Figure 6A, SPOP knockdown resulted in increased levels of PTEN and DUSP7 and a decrease in phosphorylated Akt levels and ERK, respectively (Figure 6A). These results indicate that SPOP can deregulate these pathways by degrading PTEN and DUSP7 in ccRCC.

SPOP has been found to also degrade many other substrates, some of which are candidates for promoting tumorigenesis if posttranslationally degraded, including Daxx (Kwon et al., 2006) and Gli2 (Wang et al., 2010). Daxx protein is expressed in both the nucleus and cytoplasm. In the cytoplasm, Daxx has been reported to interact with ASK1 and other apical kinases to induce cell death (Salomoni and Khelifi, 2006). Degradation of Daxx would impair the ability of the cells to respond to apoptotic cues. Gli2 acts as a mediator of Hh signaling and has both transcriptional repression and activation domains (Sasaki et al., 1999). Gli2 is primarily localized in cytoplasm and can transfer to nucleus under Hh stimulation (Kim et al., 2009). Both Daxx and Gli2 are upregulated when SPOP is knocked down in Caki-2 ccRCC cells (Figure 6B). Additionally, knockdown of Gli2 in ccRCC cells showed a further increase in the proliferation marker p-Histone H3 (Figure S6A). To further explore the possibility that cytoplasmic SPOP degrades these key substrates in ccRCC, we examined their protein abundance under hypoxic exposure in non-ccRCC cells. As expected, the abundance of PTEN, DUSP7, and Daxx proteins were all reduced in HeLa cells when SPOP was increased and accumulated in the cytoplasm under hypoxia (Figure 6C).

To further validate the role of SPOP on these targets, we examined the abundance of these SPOP targets in primary ccRCC tissue samples. We found an inverse relationship between PTEN levels and SPOP levels in 100% (14/14) of examined primary ccRCC tumor samples. These ccRCC tumor tissues exhibited high levels of SPOP and low levels of PTEN, consistent with previous reports that PTEN levels are reduced in ccRCCs (Brenner et al., 2002). By contrast, normal adjacent kidney tissues exhibit the opposite relationship (Figure 6D). Similarly, we observed inverse relationships for all other examined substrates, DUSP7 (10/10), Daxx (14/14), and Gli2 (14/14).

Finally, to determine whether the decrease of SPOP targets promotes ccRCC tumor cell survival, we restored PTEN and DUSP7 by ectopic expression in A498 ccRCC cells and found that cellular apoptosis was strongly induced (Figure 6E). Consistent with this finding, knockdown of DUSP6 and DUSP7 together led to an increase of cell proliferation in ccRCC cells (Figures S6B and S6C).

DISCUSSION

Our results indicate that HIF can drive SPOP overexpression in ccRCC and that overexpressed SPOP accumulates in the cytoplasm of ccRCC. In turn, accumulation of cytoplasmic

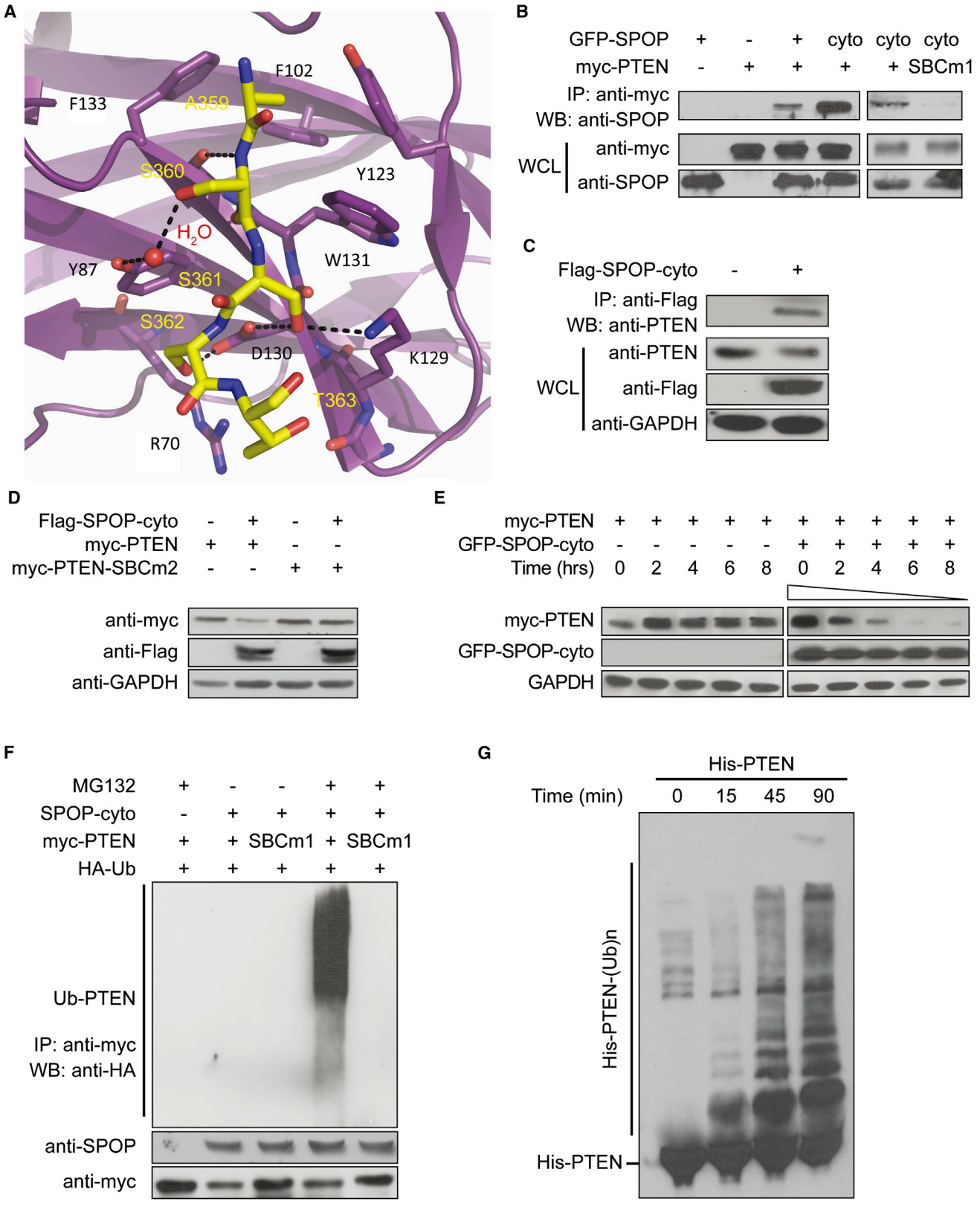

(legend on next page)

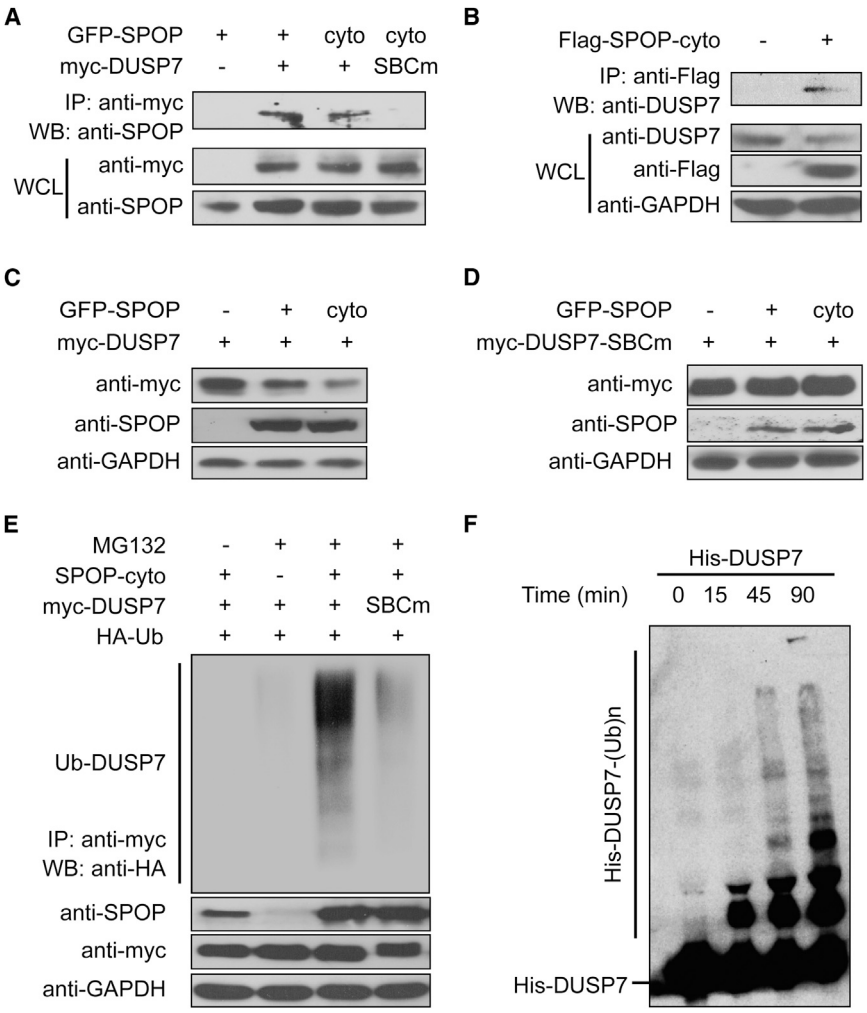

Figure 5. SPOP Mediates the Ubiquitination and Degradation of DUSP7

(A) Ectopically expressed SPOP or SPOP-cyto can interact with DUSP7 in an in vivo Co-IP assay, whereas DUSP7-SBCm (replace SBC motif VDSSS with VDGGG) eliminates the interaction. HeLa cells were transfected with the indicated constructs and incubated with 10 μM MG132 for 4 hr before harvesting.

(B) Co-IP and immunoblots indicate that overexpressed SPOP-cyto can interact and degrade endogenous DUSP7 in HeLa cells. GAPDH served as a loading control.

(C) SPOP promotes DUSP7 degradation. HEK293 cells were transfected with the indicated constructs. GFP-SPOP and GFP-SPOP-cyto were detected with monoclonal antibody SPOP-6C. GAPDH was used as loading control.

(D) Immunoblots demonstrate that neither SPOP nor SPOP-cyto can degrade DUSP7-SBCm.

(E) In vivo ubiquitination assay reveals that SPOP promotes DUSP7 ubiquitination through the DUSP7 SBC domain. Cell lysates were prepared under a denaturing condition. Myc-DUSP7 was immunoprecipitated, and HA-Ub was detected by immunoblotting.

(F) In vitro ubiquitination assay demonstrates that DUSP7 is a substrate of SPOP.

See also Figure S5.

SPOP in ccRCC cells appears to directly result in the degradation of PTEN, DUSP6, DUSP7, Daxx, and Gli2. We suggest that the concerted loss of function of these proteins in ccRCCs leads to tumorigenic phenotypes. Therefore, cytoplasmic SPOP appears to drive tumorigenesis by acting as a key regulatory hub protein that orchestrates cancer phenotypes through the modulation of several critical cellular pathways (Figure 6F).

The HIF signaling pathway and the PTEN/mTOR pathway are currently the major therapeutic targets in ccRCC treatment. We suggest here that, as a regulatory hub driving tumorigenesis in ccRCC, SPOP has the potential to be an efficient drug target. Knocking down SPOP leads to apoptosis in ccRCC cell lines but not in HEK293 and HeLa cells, where SPOP is in the nucleus. In addition to considering SPOP itself as a target, we also suggest that combinatorial modulation of the signaling pathways regulated by SPOP may have the potential to be more effective than the current targeted therapies alone.

Several issues about SPOP function in ccRCC remain to be explored. For example, given the promiscuity of SPOP in

Figure 4. SPOP Mediates the Ubiquitination and Degradation of PTEN

(A) Crystal structure of the SPOP MATH domain complex with a peptide corresponding to the PTEN SBC motif.

(B) Co-IP reveals that SPOP and SPOP-cyto bind PTEN, whereas a PTEN mutant lacking a functional SBC motif (SBC1, deletion of the SBC peptide residues 359–363) is unable to bind SPOP. HeLa cells were transfected with the indicated plasmids and incubated with 10 μM MG132 for 4 hr before harvesting. GFP-SPOP and GFP-SPOP-cyto were detected with monoclonal antibody SPOP-6C. WB, western blot; WCL, whole cell lysates.

(C) Co-IP and immunoblots indicate that overexpressed SPOP-cyto can interact with and degrade endogenous PTEN in HeLa cells. GAPDH served as a loading control. WCL, whole cell lysates.

(D) SPOP promotes the degradation of PTEN but not a PTEN SBC mutant (SBC2: the SBC motif ASSST was replaced with GGSGG). GAPDH was used as a loading control.

(E) Measurement of PTEN protein abundance by CHX chase assay. HEK293 cells were transfected with the indicated plasmids. Thirty-six hours after transfection, the cells were treated with CHX (100 μg/ml) for 2–8 hr, and western blotting was performed. GFP-SPOP-cyto was detected with monoclonal antibody SPOP-6C. GAPDH was used as a loading control.

(F) In vivo ubiquitination assay reveals that SPOP promotes PTEN ubiquitination through the PTEN SBC domain. Cell lysates were prepared under denaturing conditions. myc-PTEN was immunoprecipitated, and hemagglutinin-ubiquitin (HA-Ub) was detected by immunoblot.

(G) In vitro ubiquitination assay demonstrates that PTEN is a substrate of SPOP.

See also Figure S4 and Table S1.

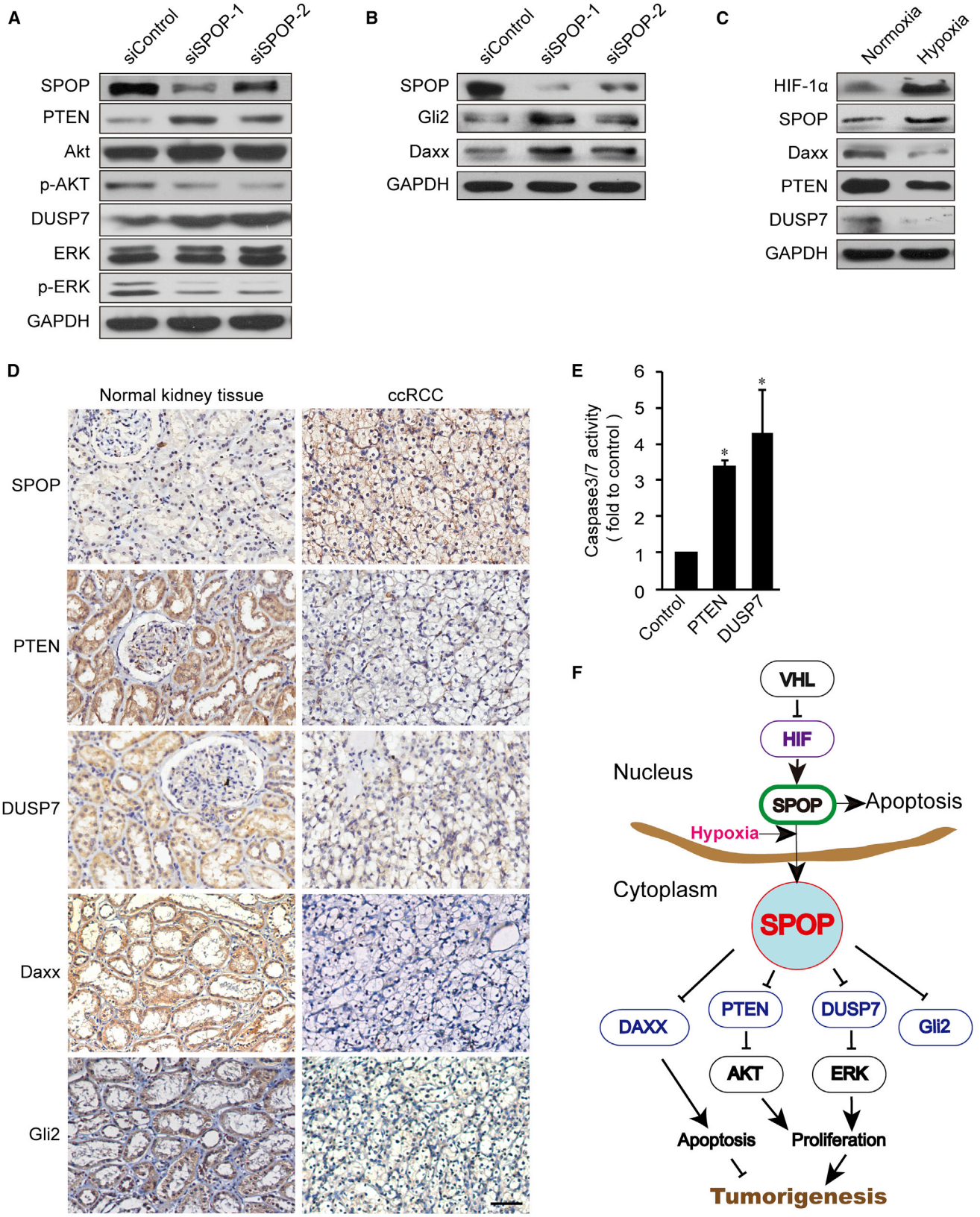

(legend on next page)

targeting critical proliferative and apoptotic pathway components, it is unlikely that the proteins studied here are the only critical cellular targets. While we focused our identification of targets on proteins with DUSP domains, genomewide, there are dozens of potential SPOP substrates. However, the modulation of PTEN, ERK, and Hh (through Gli2) signaling clearly has major effects on proliferation, and these results clearly demonstrate that SPOP is acting as a critical hub in a network involving multiple cancer-related pathways. In doing so, SPOP appears to be both necessary and sufficient for tumorigenic phenotypes.

Another open question is what molecular mechanism accounts for SPOP mislocalization to the cytoplasm. Although we demonstrate that hypoxia can drive accumulation of SPOP in cytoplasm, a number of possibilities exist for how it transfers from the nucleus to the cytoplasm or vice versa. Since no *SPOP* mutation has been detected in kidney cancers thus far (Liu et al., 2009; Cancer Genome Atlas Research Network, 2013), posttranscriptional modifications on SPOP, such as phosphorylation and ubiquitination on its nuclear localization signal, may regulate its location. It has been extensively reviewed elsewhere that posttranscriptional modifications can regulate nuclear import (Hung and Link, 2011; Nardozzi et al., 2010). Alternatively, this translocation may also be regulated by interaction with transfer proteins regulated by hypoxia, since protein-protein interactions also serve as an important regulatory mechanism of protein translocation (Hung and Link, 2011). Localized and targeted degradation of SPOP is also an intriguing mechanism, although attempts in our hands to determine whether it could be a target of obvious candidates such as VHL have been negative (S.K. and K.P.W., unpublished data). Exploring the molecular mechanisms of cytoplasmic SPOP accumulation is an important direction to pursue in the future.

Finally, our previous screening also observed that SPOP was overexpressed in several other tumors, including some cases of endometrial and germ cell tumors (Liu et al., 2009). The role of SPOP in these tumor types is unexplored, as is the role of mutant *SPOP* or its LOH in prostate and breast cancers (Berger et al., 2011; Li et al., 2011). The identification of loss-of-function SPOP in these other tissues warrants caution in development of any therapeutic interventions that systemically inhibit SPOP function. Indeed, SPOP may be acting as a tumor suppressor in breast and/or prostate cancers, but our results indicate that it acts as an oncoprotein in ccRCCs. Considering that hypoxia stress plays important roles in many different tumors, future efforts to develop tools that selectively modulate SPOP may be beneficial for treating a wide range of tumors.

EXPERIMENTAL PROCEDURES

ChIP

ChIP was performed as described elsewhere (Polo et al., 2008). Briefly, ChIPs for HIF-1α were performed with 10 to 20 × 10^6 Caki-2 cells under normoxic and hypoxic conditions using 5 μg HIF-1α antibody (Novus, NB100-134). An immunoglobulin G antibody (Upstate Biotechnology) was used as a negative control. Enriched DNA fragments were detected by qPCR and are presented as enrichment relative to input.

Luciferase Reporter Assay

DNA fragments spanning the potential HIF binding peak in *SPOP* (chromosome 17 [chr17]: 45,109,830–45,109,897 and a series of mutations in the potential hypoxia-response elements (HRE) were cloned into PGL4.23 [luc2/minP] vector (Promega, E841A). Plasmids were then cotransfected in K293 cells with a transfection-controlling plasmid pGL4.23 [hRluc/TK] (Promega, E692A). After 24 hr, cells were transfected with two independent siRNA oligos to HIF-1α (Dharmacon, J-004018-07 and J-004018-10) and further cultured under normoxic and hypoxic (1% O_2/5% CO_2/94% N_2) conditions for another 20 hr. Luciferase activity was measured using the Dual-glo Luciferase Assay kit (Promega, E2920).

Immunohistochemistry

Primary human kidney cancer samples were obtained from the Department of Urology, First Hospital of Peking University with patients' consent and approval of the institutional review board of Peking University. Immunohistochemistry was performed according to the method previously used (Cen et al., 2007) with appropriate antibodies (Supplemental Experimental Procedures).

Immunofluorescence Microscopy

Immunofluorescence was carried out as described elsewhere (Gottfried et al., 2004). Mouse anti-SPOP mAb (clone 5G) was used as the primary antibody. The slides were examined using a Leica Tcs Sp5 confocal laser scanning microscope (Supplemental Experimental Procedures).

Proliferation Assay

HEK293 cells were transfected with *SPOP*, *SPOP-cyto*, or control empty vector. Cell proliferation was measured by BrdU incorporation (Roche, Cell Proliferation ELISA kit) according to the manufacturer's instructions.

Apoptosis Assay

Caspase 3/7 activities were measured using the Apo-ONE Homogenous Caspase Assay kit (Promega) according to the manufacturer's instructions. After incubation for 2 hr at room temperature, fluorescence was detected by a Fluoroskan Ascent FL microplate reader (Thermo Scientific).

Tumor Xenograft Experiments

Stable HEK293 cell lines expressing *SPOP*, *SPOP-cyto*, or the control empty vector were established as described elsewhere (Kass et al., 2007). Briefly, a total of 5 × 10^6 tumor cells were injected subcutaneously into BALB/c nude mice. Animals were sacrificed at 6 weeks after cell injection to investigate the tumor formation. A total of 19 mice were used for each construct, with

Figure 6. SPOP Regulates Multiple Targets in Kidney Cancer

(A) Immunoblots indicate that knockdown of SPOP induces PTEN and DUSP7 protein accumulation and decreased phosphor-Akt (Thr308) and phospho-ERK (Thr202/Tyr204) levels in A498 cells. GAPDH served as a loading control.

(B) Immunoblots demonstrate that knockdown of SPOP in Caki-2 cells induced Daxx and Gli2 protein accumulation. GAPDH was used as loading control.

(C) Daxx, PTEN, and DUSP7 protein abundance decrease under hypoxia treatment in HeLa cells.

(D) Immunohistochemistry staining indicates a reduction in multiple SPOP targets: PTEN, DUSP7, Daxx, and Gli2 are reduced in ccRCC patient samples compared with their adjacent normal tissues (diaminobenzidine, brown staining). One pair of representative samples is shown. Scale bar, 50 μm.

(E) Restoring of PTEN and DUSP7 induces apoptosis in A498. Caspase 3/7 activity was analyzed to evaluate cell apoptosis. Values were normalized to control and expressed as means ± SD of three independent experiments. *$p < 0.05$ based on Student's t test.

(F) Schematic overview of SPOP action as a regulatory hub in promoting tumorigenesis in ccRCC. Although SPOP is localized to the nucleus in normal cells, in cancer cells it accumulates in the cytoplasm and promotes tumorigenesis by targeting tumor suppressor (PTEN, DUSP7, Gli2) and proapototic protein (Daxx) for ubiquitin-mediated degradation.

See also Figure S6.

experiments replicated under similar conditions at the Chinese Academy of Sciences (CAS) and The University of Chicago. All of the animal experiments were approved by the Committee on the Use of Live Animals in Teaching and Research at the Institute of Biophysics, CAS, as well as the Institutional Care and Use Committee at the University of Chicago in accordance with the National Institutes of Health (NIH) Guide for the Care and Use of Laboratory Animals.

Immunoprecipitation

Cells were transiently transfected with the indicated plasmids. Twenty-four hours after transfection, cells were harvested with radio immunoprecipitation assay (RIPA) buffer and briefly sonicated at 4°C. Lysates were immunoprecipitated with anti-myc- or anti-flag-conjugated agarose beads (Sigma). Precipitates were analyzed on SDS-polyacrylamide gels.

In Vivo Ubiquitination Assay

In vivo ubiquitination assays were based on the protocol described elsewhere (Liu et al., 2009). Briefly, HeLa cells were transfected with the indicated plasmids. Twenty-four hours after transfection, cells were treated with 10 μM MG132 (Calbiochem) for 4 hr before harvesting. Cells were then lysed in denaturing buffer (1% SDS/50 mM Tris [pH 7.5], 0.5 mM EDTA/1 mM dithiothreitol). After incubation for 5 min at 100°C, the lysate was sonicated and diluted 10 times with RIPA lysis buffer and subjected to Co-IP with anti-c-*myc*-conjugated agarose beads (Sigma, rabbit antibody) followed by immunoblotting analysis with anti-hemagglutinin antibody (Sigma, H9658).

In Vitro Ubiquitination Assay

In vitro ubiquitination was performed as reported elsewhere (Zhuang et al., 2009) (Supplemental Experimental Procedures).

ACCESSION NUMBERS

The Gene Expression Omnibus accession number for the ChIP-seq data is GSE54327. The coordinates and structural data of the PTEN SBC motif binding with SPOP have been deposited to RCSB with the accession number 4O1V.

SUPPLEMENTAL INFORMATION

Supplemental Information includes Supplemental Experimental Procedures, six figures, and one table and can be found with this article online at http://dx.doi.org/10.1016/j.ccr.2014.02.007.

ACKNOWLEDGMENTS

We thank Erin E. Mowers for critical reading and editing of the manuscript. W.C. was supported by grant 2011CB510101 from the Ministry of Science and Technology (MOST) 973 Program. K.Y. was supported by the National 863 High-Tech Foundation (grant 2014AA020608). K.C. was supported by National Science Foundation of China (NSFC) grant 81101940. W.C. was supported by NSFC grants 91231112 and 31171244. M.C. was supported by a Howard Hughes Medical Institute (HHMI) postdoctoral fellowship from the Damon Runyon Cancer Research Foundation (DRG 2021-9). T.S. was supported by a National Research Service Award from the NIH. B.S. was supported by ALSAC, the HHMI, NIH grant 5R01GM069530, and NIH grant 5P30CA021765. Y.T. was supported by CAS grant 09CF011001. J.L. was supported by the MOST 973 Program (2011CB510101), NSFC grant 81171902, and Beijing Science Foundation grant 5102031. K.P.W. was supported by the W.M. Keck Foundation, the United States National Institute of General Medical Sciences grant P50GM081892 and by the Searle Funds at The Chicago Community Trust from the Chicago Biomedical Consortium.

Received: March 25, 2013
Revised: October 26, 2013
Accepted: February 14, 2014
Published: March 20, 2014

REFERENCES

Arimoto, K., Fukuda, H., Imajoh-Ohmi, S., Saito, H., and Takekawa, M. (2008). Formation of stress granules inhibits apoptosis by suppressing stress-responsive MAPK pathways. Nat. Cell Biol. *10*, 1324–1332.

Berger, M.F., Lawrence, M.S., Demichelis, F., Drier, Y., Cibulskis, K., Sivachenko, A.Y., Sboner, A., Esgueva, R., Pflueger, D., Sougnez, C., et al. (2011). The genomic complexity of primary human prostate cancer. Nature *470*, 214–220.

Bhatia, B., Hsieh, M., Kenney, A.M., and Nahlé, Z. (2011). Mitogenic Sonic hedgehog signaling drives E2F1-dependent lipogenesis in progenitor cells and medulloblastoma. Oncogene *30*, 410–422.

Brenner, W., Färber, G., Herget, T., Lehr, H.A., Hengstler, J.G., and Thüroff, J.W. (2002). Loss of tumor suppressor protein PTEN during renal carcinogenesis. Int. J. Cancer *99*, 53–57.

Brugarolas, J. (2007). Renal-cell carcinoma—molecular pathways and therapies. N. Engl. J. Med. *356*, 185–187.

Bunce, M.W., Boronenkov, I.V., and Anderson, R.A. (2008). Coordinated activation of the nuclear ubiquitin ligase Cul3-SPOP by the generation of phosphatidylinositol 5-phosphate. J. Biol. Chem. *283*, 8678–8686.

Campbell, L., Nuttall, R., Griffiths, D., and Gumbleton, M. (2009). Activated extracellular signal-regulated kinase is an independent prognostic factor in clinically confined renal cell carcinoma. Cancer *115*, 3457–3467.

Cancer Genome Atlas Research Network (2013). Comprehensive molecular characterization of clear cell renal cell carcinoma. Nature *499*, 43–49.

Cen, L., Arnoczky, K.J., Hsieh, F.-C., Lin, H.-J., Qualman, S.J., Yu, S., Xiang, H., and Lin, J. (2007). Phosphorylation profiles of protein kinases in alveolar and embryonal rhabdomyosarcoma. Mod. Pathol. *20*, 936–946.

Chi, J.-T., Wang, Z., Nuyten, D.S.A., Rodriguez, E.H., Schaner, M.E., Salim, A., Wang, Y., Kristensen, G.B., Helland, Å., Børresen-Dale, A.-L., et al. (2006). Gene expression programs in response to hypoxia: cell type specificity and prognostic significance in human cancers. PLoS Med. *3*, e47.

Dhillon, A.S., Hagan, S., Rath, O., and Kolch, W. (2007). MAP kinase signalling pathways in cancer. Oncogene *26*, 3279–3290.

Escudier, B., Eisen, T., Stadler, W.M., Szczylik, C., Oudard, S., Siebels, M., Negrier, S., Chevreau, C., Solska, E., Desai, A.A., et al.; TARGET Study Group (2007). Sorafenib in advanced clear-cell renal-cell carcinoma. N. Engl. J. Med. *356*, 125–134.

Fyfe, G.A., Fisher, R.I., Rosenberg, S.A., Sznol, M., Parkinson, D.R., and Louie, A.C. (1996). Long-term response data for 255 patients with metastatic renal cell carcinoma treated with high-dose recombinant interleukin-2 therapy. J. Clin. Oncol. *14*, 2410–2411.

Gardai, S.J., Whitlock, B.B., Xiao, Y.Q., Bratton, D.B., and Henson, P.M. (2004). Oxidants inhibit ERK/MAPK and prevent its ability to delay neutrophil apoptosis downstream of mitochondrial changes and at the level of XIAP. J. Biol. Chem. *279*, 44695–44703.

Gottfried, Y., Rotem, A., Lotan, R., Steller, H., and Larisch, S. (2004). The mitochondrial ARTS protein promotes apoptosis through targeting XIAP. EMBO J. *23*, 1627–1635.

Hamid, T., Malik, M.T., and Kakar, S.S. (2005). Ectopic expression of PTTG1/securin promotes tumorigenesis in human embryonic kidney cells. Mol. Cancer *4*, 3.

Hernández-Muñoz, I., Lund, A.H., van der Stoop, P., Boutsma, E., Muijrers, I., Verhoeven, E., Nusinow, D.A., Panning, B., Marahrens, Y., and van Lohuizen, M. (2005). Stable X chromosome inactivation involves the PRC1 Polycomb complex and requires histone MACROH2A1 and the CULLIN3/SPOP ubiquitin E3 ligase. Proc. Natl. Acad. Sci. USA *102*, 7635–7640.

Hollander, M.C., Blumenthal, G.M., and Dennis, P.A. (2011). PTEN loss in the continuum of common cancers, rare syndromes and mouse models. Nat. Rev. Cancer *11*, 289–301.

Hudes, G., Carducci, M., Tomczak, P., Dutcher, J., Figlin, R., Kapoor, A., Staroslawska, E., Sosman, J., McDermott, D., Bodrogi, I., et al.; Global

ARCC Trial (2007). Temsirolimus, interferon alfa, or both for advanced renal-cell carcinoma. N. Engl. J. Med. *356*, 2271–2281.

Hung, M.-C., and Link, W. (2011). Protein localization in disease and therapy. J. Cell Sci. *124*, 3381–3392.

Jiang, Y., Zhang, W., Kondo, K., Klco, J.M., St Martin, T.B., Dufault, M.R., Madden, S.L., Kaelin, W.G., Jr., and Nacht, M. (2003). Gene expression profiling in a renal cell carcinoma cell line: dissecting VHL and hypoxia-dependent pathways. Mol. Cancer Res. *1*, 453–462.

Kaelin, W.G., Jr. (2002). Molecular basis of the VHL hereditary cancer syndrome. Nat. Rev. Cancer *2*, 673–682.

Kaelin, W.G., Jr. (2008). The von Hippel-Lindau tumour suppressor protein: O2 sensing and cancer. Nat. Rev. Cancer *8*, 865–873.

Kapoor, A., and Figlin, R.A. (2009). Targeted inhibition of mammalian target of rapamycin for the treatment of advanced renal cell carcinoma. Cancer *115*, 3618–3630.

Kass, E.M., Ahn, J., Tanaka, T., Freed-Pastor, W.A., Keezer, S., and Prives, C. (2007). Stability of checkpoint kinase 2 is regulated via phosphorylation at serine 456. J. Biol. Chem. *282*, 30311–30321.

Kent, D., Bush, E.W., and Hooper, J.E. (2006). Roadkill attenuates Hedgehog responses through degradation of Cubitus interruptus. Development *133*, 2001–2010.

Keyse, S.M. (2008). Dual-specificity MAP kinase phosphatases (MKPs) and cancer. Cancer Metastasis Rev. *27*, 253–261.

Kim, W.Y., and Kaelin, W.G. (2004). Role of VHL gene mutation in human cancer. J. Clin. Oncol. *22*, 4991–5004.

Kim, J., Kato, M., and Beachy, P.A. (2009). Gli2 trafficking links Hedgehog-dependent activation of Smoothened in the primary cilium to transcriptional activation in the nucleus. Proc. Natl. Acad. Sci. USA *106*, 21666–21671.

Kucejova, B., Peña-Llopis, S., Yamasaki, T., Sivanand, S., Tran, T.A.T., Alexander, S., Wolff, N.C., Lotan, Y., Xie, X.-J., Kabbani, W., et al. (2011). Interplay between pVHL and mTORC1 pathways in clear-cell renal cell carcinoma. Mol. Cancer Res. *9*, 1255–1265.

Kwon, J.E., La, M., Oh, K.H., Oh, Y.M., Kim, G.R., Seol, J.H., Baek, S.H., Chiba, T., Tanaka, K., Bang, O.S., et al. (2006). BTB domain-containing speckle-type POZ protein (SPOP) serves as an adaptor of Daxx for ubiquitination by Cul3-based ubiquitin ligase. J. Biol. Chem. *281*, 12664–12672.

Lee, J.O., Yang, H., Georgescu, M.M., Di Cristofano, A., Maehama, T., Shi, Y., Dixon, J.E., Pandolfi, P., and Pavletich, N.P. (1999). Crystal structure of the PTEN tumor suppressor: implications for its phosphoinositide phosphatase activity and membrane association. Cell *99*, 323–334.

Lee, H.J., Kim, D.I., Kang, G.H., Kwak, C., Ku, J.H., and Moon, K.C. (2009). Phosphorylation of ERK1/2 and prognosis of clear cell renal cell carcinoma. Urology *73*, 394–399.

Li, C., Ao, J., Fu, J., Lee, D.F., Xu, J., Lonard, D., and O'Malley, B.W. (2011). Tumor-suppressor role for the SPOP ubiquitin ligase in signal-dependent proteolysis of the oncogenic co-activator SRC-3/AIB1. Oncogene *30*, 4350–4364.

Liu, J., Ghanim, M., Xue, L., Brown, C.D., Iossifov, I., Angeletti, C., Hua, S., Nègre, N., Ludwig, M., Stricker, T., et al. (2009). Analysis of Drosophila segmentation network identifies a JNK pathway factor overexpressed in kidney cancer. Science *323*, 1218–1222.

Lopez-Beltran, A., Scarpelli, M., Montironi, R., and Kirkali, Z. (2006). 2004 WHO classification of the renal tumors of the adults. Eur. Urol. *49*, 798–805.

Mains, P., Kemphues, K., Sprunger, S., Sulston, I., and Wood, W. (1990). Mutations affecting the meiotic and mitotic divisions of the early Caenorhabditis elegans embryo. Genetics *126*, 593–605.

McDermott, D.F., Regan, M.M., Clark, J.I., Flaherty, L.E., Weiss, G.R., Logan, T.F., Kirkwood, J.M., Gordon, M.S., Sosman, J.A., Ernstoff, M.S., et al. (2005). Randomized phase III trial of high-dose interleukin-2 versus subcutaneous interleukin-2 and interferon in patients with metastatic renal cell carcinoma. J. Clin. Oncol. *23*, 133–141.

Miyazaki, K., Kawamoto, T., Tanimoto, K., Nishiyama, M., Honda, H., and Kato, Y. (2002). Identification of functional hypoxia response elements in the promoter region of the DEC1 and DEC2 genes. J. Biol. Chem. *277*, 47014–47021.

Motzer, R.J., and Molina, A.M. (2009). Targeting renal cell carcinoma. J. Clin. Oncol. *27*, 3274–3276.

Motzer, R.J., Hutson, T.E., Tomczak, P., Michaelson, M.D., Bukowski, R.M., Rixe, O., Oudard, S., Negrier, S., Szczylik, C., Kim, S.T., et al. (2007). Sunitinib versus interferon alfa in metastatic renal-cell carcinoma. N. Engl. J. Med. *356*, 115–124.

Motzer, R.J., Escudier, B., Tomczak, P., Hutson, T.E., Michaelson, M.D., Negrier, S., Oudard, S., Gore, M.E., Tarazi, J., Hariharan, S., et al. (2013). Axitinib versus sorafenib as second-line treatment for advanced renal cell carcinoma: overall survival analysis and updated results from a randomised phase 3 trial. Lancet Oncol. *14*, 552–562.

Myers, M.P., Pass, I., Batty, I.H., Van der Kaay, J., Stolarov, J.P., Hemmings, B.A., Wigler, M.H., Downes, C.P., and Tonks, N.K. (1998). The lipid phosphatase activity of PTEN is critical for its tumor supressor function. Proc. Natl. Acad. Sci. USA *95*, 13513–13518.

Nagai, Y., Kojima, T., Muro, Y., Hachiya, T., Nishizawa, Y., Wakabayashi, T., and Hagiwara, M. (1997). Identification of a novel nuclear speckle-type protein, SPOP. FEBS Lett. *418*, 23–26.

Nardozzi, J.D., Lott, K., and Cingolani, G. (2010). Phosphorylation meets nuclear import: a review. Cell Commun. Signal. *8*, 32.

Negrier, S., Escudier, B., Lasset, C., Douillard, J.Y., Savary, J., Chevreau, C., Ravaud, A., Mercatello, A., Peny, J., Mousseau, M., et al. (1998). Recombinant human interleukin-2, recombinant human interferon alfa-2a, or both in metastatic renal-cell carcinoma. Groupe Français d'Immunothérapie. N. Engl. J. Med. *338*, 1272–1278.

Nickerson, M.L., Jaeger, E., Shi, Y., Durocher, J.A., Mahurkar, S., Zaridze, D., Matveev, V., Janout, V., Kollarova, H., Bencko, V., et al. (2008). Improved identification of von Hippel-Lindau gene alterations in clear cell renal tumors. Clin. Cancer Res. *14*, 4726–4734.

Patterson, K.I., Brummer, T., O'Brien, P.M., and Daly, R.J. (2009). Dual-specificity phosphatases: critical regulators with diverse cellular targets. Biochem. J. *418*, 475–489.

Pintard, L., Willis, J.H., Willems, A., Johnson, J.-L.F., Srayko, M., Kurz, T., Glaser, S., Mains, P.E., Tyers, M., Bowerman, B., et al. (2003). The BTB protein MEL-26 is a substrate-specific adaptor of the CUL-3 ubiquitin-ligase. Nature *425*, 311–316.

Polo, J.M., Ci, W., Licht, J.D., and Melnick, A. (2008). Reversible disruption of BCL6 repression complexes by CD40 signaling in normal and malignant B cells. Blood *112*, 644–651.

Rini, B.I., Campbell, S.C., and Escudier, B. (2009). Renal cell carcinoma. Lancet *373*, 1119–1132.

Robb, V.A., Karbowniczek, M., Klein-Szanto, A.J., and Henske, E.P. (2007). Activation of the mTOR signaling pathway in renal clear cell carcinoma. J. Urol. *177*, 346–352.

Salomoni, P., and Khelifi, A.F. (2006). Daxx: death or survival protein? Trends Cell Biol. *16*, 97–104.

Sansal, I., and Sellers, W.R. (2004). The biology and clinical relevance of the PTEN tumor suppressor pathway. J. Clin. Oncol. *22*, 2954–2963.

Sarbassov, D.D., Ali, S.M., and Sabatini, D.M. (2005). Growing roles for the mTOR pathway. Curr. Opin. Cell Biol. *17*, 596–603.

Sasaki, H., Nishizaki, Y., Hui, C., Nakafuku, M., and Kondoh, H. (1999). Regulation of Gli2 and Gli3 activities by an amino-terminal repression domain: implication of Gli2 and Gli3 as primary mediators of Shh signaling. Development *126*, 3915–3924.

Sato, Y., Yoshizato, T., Shiraishi, Y., Maekawa, S., Okuno, Y., Kamura, T., Shimamura, T., Sato-Otsubo, A., Nagae, G., Suzuki, H., et al. (2013). Integrated molecular analysis of clear-cell renal cell carcinoma. Nat. Genet. *45*, 860–867.

Shinojima, T., Oya, M., Takayanagi, A., Mizuno, R., Shimizu, N., and Murai, M. (2007). Renal cancer cells lacking hypoxia inducible factor (HIF)-1alpha expression maintain vascular endothelial growth factor expression through HIF-2alpha. Carcinogenesis *28*, 529–536.

Vivanco, I., and Sawyers, C.L. (2002). The phosphatidylinositol 3-Kinase AKT pathway in human cancer. Nat. Rev. Cancer *2*, 489–501.

Wang, C., Pan, Y., and Wang, B. (2010). Suppressor of fused and Spop regulate the stability, processing and function of Gli2 and Gli3 full-length activators but not their repressors. Development *137*, 2001–2009.

Wardle, E.N. (1991). Cyclophosphamide pulse therapy in relapsing nephrotic syndrome. Nephron *58*, 377.

Wu, X., Senechal, K., Neshat, M.S., Whang, Y.E., and Sawyers, C.L. (1998). The PTEN/MMAC1 tumor suppressor phosphatase functions as a negative regulator of the phosphoinositide 3-kinase/Akt pathway. Proc. Natl. Acad. Sci. USA *95*, 15587–15591.

Xu, L., Wei, Y., Reboul, J., Vaglio, P., Shin, T.H., Vidal, M., Elledge, S.J., and Harper, J.W. (2003). BTB proteins are substrate-specific adaptors in an SCF-like modular ubiquitin ligase containing CUL-3. Nature *425*, 316–321.

Zhang, Q., Zhang, L., Wang, B., Ou, C.Y., Chien, C.T., and Jiang, J. (2006). A hedgehog-induced BTB protein modulates hedgehog signaling by degrading Ci/Gli transcription factor. Dev. Cell *10*, 719–729.

Zhuang, M., Calabrese, M.F., Liu, J., Waddell, M.B., Nourse, A., Hammel, M., Miller, D.J., Walden, H., Duda, D.M., Seyedin, S.N., et al. (2009). Structures of SPOP-substrate complexes: insights into molecular architectures of BTB-Cul3 ubiquitin ligases. Mol. Cell *36*, 39–50.

Cancer Cell
Article

MicroRNA-135b Promotes Cancer Progression by Acting as a Downstream Effector of Oncogenic Pathways in Colon Cancer

Nicola Valeri,[1,11,*] Chiara Braconi,[1,11] Pierluigi Gasparini,[2] Claudio Murgia,[3] Andrea Lampis,[1,11] Viola Paulus-Hock,[1] Jonathan R. Hart,[4] Lynn Ueno,[4] Sergei I. Grivennikov,[5] Francesca Lovat,[2] Alessio Paone,[2] Luciano Cascione,[2,12] Khlea M. Sumani,[2] Angelo Veronese,[6] Muller Fabbri,[2,13,14] Stefania Carasi,[2] Hansjuerg Alder,[2] Giovanni Lanza,[7] Roberta Gafa',[7] Mary P. Moyer,[8] Rachel A. Ridgway,[3] Julia Cordero,[3] Gerard J. Nuovo,[2] Wendy L. Frankel,[9] Massimo Rugge,[10] Matteo Fassan,[10] Joanna Groden,[2] Peter K. Vogt,[4] Michael Karin,[5] Owen J. Sansom,[3] and Carlo M. Croce[2,*]

[1]Institute of Cancer Sciences, University of Glasgow, Glasgow G61 1BD, UK
[2]Human Cancer Genetics Program, Ohio State University Comprehensive Cancer Center, Columbus, OH 43212, USA
[3]Cancer Research UK Beatson Institute, Glasgow G61 1BD, UK
[4]Department of Molecular & Experimental Medicine, The Scripps Research Institute, La Jolla, CA 92037, USA
[5]Department of Pharmacology, School of Medicine, University of California, San Diego, San Diego, CA 92093, USA
[6]Aging Research Center, G.d'Annunzio University Foundation, Chieti 66100, Italy
[7]Department of Pathology, University of Ferrara, Ferrara 44121, Italy
[8]INCELL Corporation, San Antonio, TX 78249, USA
[9]Department of Pathology, Ohio State University Comprehensive Cancer Center, Columbus, OH 43212, USA
[10]Department of Pathology, University of Padova, Padova 35121, Italy
[11]Present address: The Institute of Cancer Research and The Royal Marsden NHS Trust, Sutton, Surrey SM2 5NG, UK
[12]Present address: Bioinformatics Unit, Lymphoma and Genomics Research Program, Institute of Oncology Research, 6500 Bellinzona, Switzerland
[13]Present address: Department of Pediatrics and Department of Molecular Microbiology & Immunology, Norris Comprehensive Cancer Center, Keck School of Medicine, University of Southern California, Los Angeles, CA 90027, USA
[14]Children's Center for Cancer and Blood Diseases and The Saban Research Institute, Children's Hospital Los Angeles, Los Angeles, CA 90027, USA
*Correspondence: nicola.valeri@icr.ac.uk (N.V.), carlo.croce@osumc.edu (C.M.C.)
http://dx.doi.org/10.1016/j.ccr.2014.03.006

SUMMARY

MicroRNA deregulation is frequent in human colorectal cancers (CRCs), but little is known as to whether it represents a bystander event or actually drives tumor progression in vivo. We show that miR-135b overexpression is triggered in mice and humans by APC loss, PTEN/PI3K pathway deregulation, and SRC overexpression and promotes tumor transformation and progression. We show that miR-135b upregulation is common in sporadic and inflammatory bowel disease-associated human CRCs and correlates with tumor stage and poor clinical outcome. Inhibition of miR-135b in CRC mouse models reduces tumor growth by controlling genes involved in proliferation, invasion, and apoptosis. We identify miR-135b as a key downsteam effector of oncogenic pathways and a potential target for CRC treatment.

INTRODUCTION

Colorectal cancer (CRC) arises through the progressive accumulation of mutations in oncogenes and tumor-suppressor genes (Sjöblom et al., 2006). Targeting driver pathways represents the best option to tailor cancer treatment and improve survival in patients with metastatic cancer (De Roock et al., 2011; Catenacci et al., 2011). Although there has been recent breakthroughs in

Significance

Precision medicine relies on the ability to track cancer-related pathways and target their downstream effectors to minimize drug resistance and increase therapeutic potential. We show that mutations frequently occurring in the colorectal adenoma-carcinoma sequence converge and synergize in promoting the progressive accumulation of miR-135b by conserved mechanisms in mice and humans. In turn, miR-135b acts as one of the driving forces promoting cancer phenotype. We prove that use of anti-miR-135b in CRC mouse models has a significant therapeutic potential. Our results define miR-135b as a key molecule downstream of oncogenic pathways involved in CRC progression, providing the rationale for its use as a robust biomarker and a promising target for therapy.

targeted therapy (e.g., BRAF inhibition), this approach has two main disadvantages: (1) resistance frequently occurs as the result of the activation of collateral pathways circumventing therapeutic blockage (Prahallad et al., 2012), and (2) re-expression of lost tumor-suppressor genes such as *Adenomatous Polyposis Coli* (*APC*) is challenging to translate into drug development.

MicroRNAs (miRs) are a class of small noncoding RNAs involved in cell homeostasis and carcinogenesis (Croce 2009). Several miRs are aberrantly expressed in CRC, and their deregulation is linked to cancer progression and clinical outcome (Valeri et al., 2009). Different oncogenic pathways can converge to affect the same miR and in turn a single miR can control an entire posttranscriptional program affecting dozens of target genes. Because miRs often act as downstream effectors of protein kinases or driver genes mutated in cancer (Croce 2009), targeting miRs may represent a strategy to increase specificity and overcome drug resistance. Preliminary data on the efficacy of miR inhibition are available and prompt the use of anti-miR technology in CRC treatment in vivo (Kasinski and Slack, 2011).

RESULTS

Identification of miRs Dysregulated in CRC Mouse Models

To define miRs deregulated in relation to CRC-specific pathways, we performed a genomewide miR profiling on matched tumor and normal tissues from six mice from two different CRC mouse models: the CDX2P-NLS Cre;$Apc^{+/loxP}$ (CPC;Apc) model harbors a truncating mutation affecting one *APC* allele (Hinoi et al., 2007). In the azoxymethane (AOM)/dextran sulfate sodium (DSS) model (Grivennikov et al., 2009), mice develop CRC as the result of the mutations in several genes including *phosphoinositide 3-kinase* (*Pi3K*), *V-Ki-ras2 Kirsten rat sarcoma viral oncogene homolog* (*K-ras*), *Catenin* (*Cadherine Associated-protein*) *Beta 1* (*Ctnnb1*) and *Proto-oncogene tyrosine-protein kinase Src* (*Src*) pathways (Chen and Huang 2009)

Thirty-five miRs were aberrantly expressed in polyps from the CPC;Apc model with $p < 0.001$, with seven miRs increased and 14 decreased by greater than 2-fold. In the AOM/DSS model; 57 miRs were aberrantly expressed in tumor compared to normal tissues with $p < 0.001$; among these, 13 miRs increased and nine decreased by greater than 2-fold (Figure 1A; Tables S1 and S2 available online). We focused on overexpressed miRs because these may be easier to harness as prognostic biomarkers (Croce 2009) or as therapeutic targets compared to downregulated ones (Kasinski and Slack, 2011). MiR-135b was the most overexpressed miR in both models (Figure 1A). RT-PCR and in situ hybridization (ISH) confirmed miR-135b overexpression in tumor tissues (Figures 1B and 1C).

MiR-135b Is Overexpressed in Human CRC

We analyzed 454 sporadic and 31 inflammatory bowel disease (IBD)-associated CRCs to confirm miR-135b upregulation previously reported in smaller CRC cohorts (Necela et al., 2011; Nagel et al., 2008; Gaedcke et al., 2012). A first set including 62 sporadic CRCs was analyzed for miR-135b expression by RT-PCR. MiR-135b expression showed an average 4-fold change in cancer compared to paired normal tissue and correlated with tumor progression as it was increased in the sequence from stage I to stage IV CRC (Figure 1D, upper). Re-analysis of 392 tumor samples for which tumor stage and miR-135b expression were available from the miR-seq data set of the CRC Cancer Genome Atlas (The Cancer Genome Atlas Network, 2012; Figure 1D) confirmed that miR-135b upregulation follows tumor progression. Paired analysis of matched normal and cancer tissues from the same cohort also showed that miR-135b reads are virtually absent in normal tissues (Table S3), suggesting that miR-135b is a CRC specific deregulated miR; thus, a valuable biomarker and target for therapy.

For IBD-associated CRCs, three different cohorts were analyzed: miR-135b was upregulated by > 7.0-fold in cancer compared to normal tissues in all the different sets. Interestingly, 135b overexpression was found in dysplasia compared to normal tissues, suggesting it might be an early event in colon carcinogenesis (Figure 1D, lower). ISH showed that miR-135b is strongly expressed in the cytoplasm of dysplastic and cancer cells whereas, in line with the TCGA data, little signal is observed in normal mucosa (Figure 1E).

Tumor stage and nodal status were confirmed as prognostic markers in our cohort of sporadic CRC (Figure S1). To test if miR-135b is associated with clinical outcome in CRC, patients were stratified according to the logarithmic ratio between miR-135b expression in cancer and normal tissues: high if log2 miR-135b expression was >2 (above the average miR-135b overexpression observed in Figure 1D), and low if log2 miR-135b expression was ≤ 2. High miR-135b expression was associated with poor overall survival and relapse-free survival (Figure 1F). A subgroup analysis in patients with stage II CRC identified a trend toward a worse prognosis for patients with high miR-135b. However, the difference was not statistically significant ($p = 0.055$), likely due to the small sample size (Figure 1F).

MiR-135b Overexpression Is Associated with Mutations in Specific CRC Pathways

Loss of Apc is the initiating mutation in the CPC;Apc model (Hinoi et al., 2007). To confirm that miR-135b overexpression is due to APC loss, we re-induced APC by transfecting a plasmid encoding the *APC* full coding sequence (CDS) in the SW480 human CRC cells, which only contains a mutated *APC* allele leading to a truncated protein (Qian et al., 2008) . Re-expression of wild-type (WT) *APC* caused a 65% reduction in miR-135b expression ($p = 0.03$), whereas inhibition of *APC* by siRNA resulted in a 5-fold increase ($p = 0.01$) in miR-135b expression in normal colon epithelial cell lines (Moyer et al., 1996; Figures 2A, 2B, and S2A–S2C) Inactivating mutations in *APC* cause stabilization and nuclear translocation of β-catenin with induction of a complex transcriptional program. To test whether APC loss results in miR-135b overexpression through β-catenin stabilization, we increased β-catenin expression either by transfecting NCM 460 cells with a plasmid encoding the β-catenin transcript or by stabilizing β-catenin with lithium chloride (LiCl) treatment. Both experiments resulted in increased miR-135b expression (3-fold [$p = 0.003$] and 4.6-fold [$p = 0.007$], respectively; Figures 2C and S2D). An siRNA screen against the major transcription factors involved in the APC/β-catenin axis was run on two cell lines with high basal β-catenin activity, HCT-116 (β-catenin mutant; Ilyas et al., 1997) and SW480 (*APC* null cells; Qian et al., 2008), revealing that TCF4 and LEF1 silencing causes miR-135b

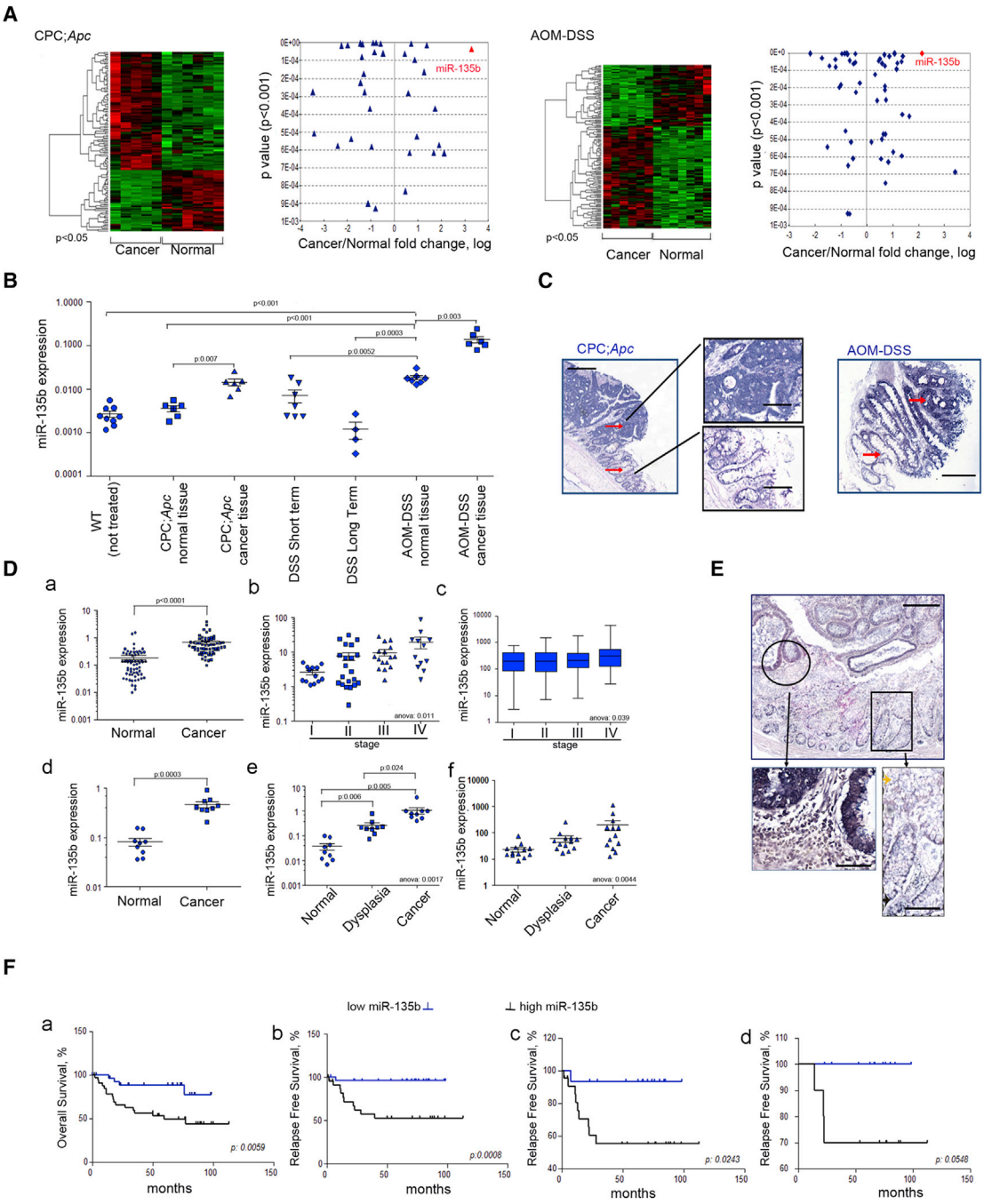

Figure 1. MiR-135b Upregulation in Mouse and Human CRC

(A) Genome-wide miR expression analysis in tumor and normal adjacent colon tissues from CPC;Apc and AOM/DSS treated mice. Selected deregulated miRNAs in cancer relative to normal tissues are plotted against the p value.

(B and C) MiR-135b expression by RT-PCR (B) and ISH (C) in both CRC mouse models. Scale bars, 200 um (100 um in the magnification).

(D) MiR-135b expression was assessed in human tissues. Paired analysis (a) and miR expression according to stage (b) in sporadic CRC (n = 62) are shown. Reads for miR-135b from the TCGA miR-seq data set (n = 392) are shown (c). miR-135b upregulation in three different cohorts of IBD-associated CRC (n = 31): OSU (n = 9; d), University of Ferrara (n = 9; e), and University of Padua (n = 13; f).

(E) ISH for miR-135b in human cancer and normal epithelial cells. Scale bars, 200 um (50 um in the magnification).

(F) Prognosis of sporadic CRC patients according to miR-135b expression: (a) overall survival (OS) in the entire cohort, (b) relapse-free survival (RFS) in stage I-II-III CRC, (c) RFS in stage II-III only CRC and (d) in stage II only CRC. High or low miR-135b expression was defined as low if Log_2-miR-135b-ratio (cancer/normal) ≤ 2 or high if Log_2-miR-135b-ratio > 2.

See also Tables S1–S3 and Figure S1.

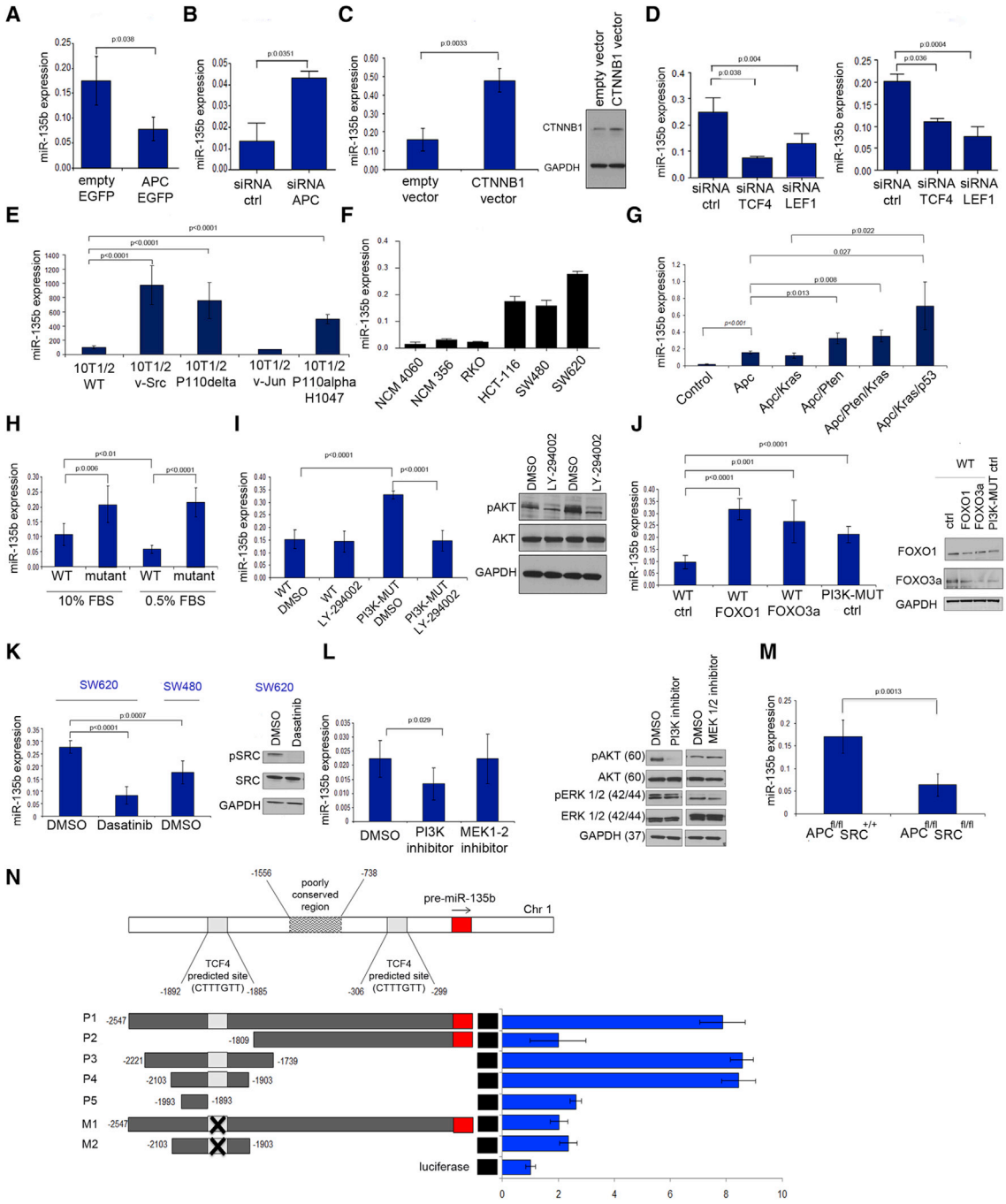

Figure 2. MiR-135b Overexpression Is Associated with Mutations in Specific CRC Pathways

(A) miR-135b expression following transfection with a plasmid encoding the APC CDS in *APC* mutant SW480 cells.

(B) miR-135b expression following APC silencing in normal colon (NCM 460) epithelial cells.

(C) miR-135b expression (left) following overexpression of CTNNB1 (right) in NCM 460 normal epithelial cells.

(D) miR-135b expression following silencing of TCF4 and LEF1 transcription in *APC* mutant SW480 cells (left) or *CTNNB1* mutant HCT-116 cells (right).

(E–G) miR-135b expression in MEFs (E), human normal and CRC cell lines (F), and tumor-derived organoids from GEMMs (G) harboring different rounds of mutations in genes commonly mutated in human CRC.

(H–J) miR-135b expression in *PI3KCA* WT and mutant HCT-116 cells after serum starvation (H), treatment with LY-294002 (I), and transfection with specific siRNAs to FoxO1 and FoxO3A (J).

(K) miR-135b expression in parental SW480 and SW620 CRC cell lines after treatment with dasatinib.

(L) miR-135b expression in Src-MEFs after treatment with PI3K or MEK1/2 inhibitors.

(M) miR-135b expression in tumor derived from *AhCre* $Apc^{fl/fl}Src^{+/+}$ and *AhCre* $Apc^{fl/fl}Src^{fl/fl}$ mice.

(legend continued on next page)

inhibition (Figures 2D and S2E) . Taken together, these data suggest that miR-135b can be activated by the APC/β-catenin/TCF4-LEF1 pathway.

To study other pathways involved in miR-135b overexpression that may account for the higher expression of miR-135b in AOM/DSS compared to CPC;Apc tumors, we screened miR-135b expression in a series of mouse embryonic fibroblasts (MEFs) engineered to harbor mutations in specific oncogenes and in human CRC cell lines (Figures 2E and 2F). The analysis revealed increased levels of miR-135b (5-fold change; $p < 0.001$) in cells expressing the H1047R mutant of *PIK3CA*, which encodes the α isoform of the catalytic subunit of PI3K. Expression of the δ isoform of Pi3k and of Src also led to increased levels of miR-135b (7.5 and 9.7, respectively; $p < 0.001$), whereas viral Jun did not affect the expression of miR-135b (Figure 2E). The effect of PI3K and Src on miR-135b was correlated with their oncogenic potency in 10T1/2 mouse fibroblasts. The cells overexpressing these proteins are morphologically transformed and capable of anchorage-independent growth (Hart et al., 2011). In contrast, the cells expressing v-Jun show fibroblastic morphology, with only a minority of cells producing colonies in agar suspension.

In human CRC cells, miR-135b expression follows the accumulation of mutation in *APC*, *PI3KCA*, and *SRC* (Figure 2F). RKO cells lack mutations in APC/β-catenin, show low basal SRC activity, and harbor an H1047R mutation in *PIK3CA* and are characterized by low miR-135b basal expression. HCT-116 cells are characterized by β-catenin activating mutations, *PI3KCA* mutations, and moderate SRC activity and display increased miR-135b expression. Parental SW480 cells and their metastatic derivative SW620 have the same mutations in *APC*, and no mutations in *PI3KCA*, but have different SRC activity and show high miR-135b expression (da Costa et al., 1999; Samuels et al., 2005; Dehm et al., 2001).

To study the effect of collateral pathways frequently mutated in CRC, we tested miR-135b expression in tumor-derived organoids from CRC genetically engineered mouse models (GEMMs) that underwent different rounds of knock-in or knock-out mutations in *Apc*, *Kras*, *the Phosphatase and Tensin homolog deleted on chromosome TEN* (*Pten*), and *p53* (Figure 2G). In keeping with our initial findings, Apc loss was associated with miR-135b upregulation in comparison to normal controls. Pten is a negative regulator of the PI3K pathway and these genes are mutually lost in breast and CRC cancer (Frattini et al., 2005), thus we decided to use $Pten^{fl/fl}$ mice as a model to study PI3K activation in CRC (Marsh et al., 2008). Consistent with our in vitro data, simultaneous loss of Apc and Pten caused further upregulation in miR-135b compared to $Apc^{fl/fl}$ organoids. In contrast, $Kras^{G12}$-activating mutations did not affect miR-135b expression. $Apc^{fl/fl}$ /$Pten^{fl/fl}$ /$Kras^{G12}$ triple mutant organoids showed miR-135b deregulation similar to that of the $Apc^{fl/fl}$ /$Pten^{fl/fl}$ organoids supporting the hypothesis that the PI3K/PTEN pathway exerts a critical role in controlling miR-135b expression. Finally, loss of p53 caused a 10-fold change in miR-135b compared to $Apc^{fl/fl}$ organoids.

To study the role of PI3K in the modulation of miR-135b, we used human CRC cell lines (HCT-116, *H1047R* and DLD-1, and *E545K*) in which either the *PI3KCA* mutant or WT allele was disrupted (Samuels et al., 2005). *PIK3CA* mutations have little effect on cancer phenotype under basal conditions, but they cause reduced cellular dependence on growth factors affecting cell growth and apoptosis in serum starvation. MiR-135b expression is increased in *PI3KCA* mutant compared to WT cells (less than 2-fold change) in basal conditions. Serum starvation forced the *PI3KCA* mutation phenotype, increasing the difference in miR-135b expression (3.7 and 4.3 fold change; $p < 0.001$ in HCT116 and DLD-1, respectively; Figures 2H and S2F). These experiments suggest that miR-135b is dependent upon PI3K activation. We treated HCT-116 cells with the PI3KCA inhibitor LY294002 after starvation and observed marginal effects on WT cells, but reduction (65%; $p < 0.001$) of miR-135b in mutant cells (Figure 2I). The transcription factors FoxO1 and FoxO3A promote the PI3K cancer-associated phenotype in these cell lines (Samuels et al., 2005). To investigate whether miR-135b is under the control of the FoxO transcription factors family, we silenced *FoxO1* and *FoxO3A* with siRNA in HCT-116 *PI3KCA* WT cells and observed an increase in miR-135b expression. Silencing FoxO1 and 3A in WT cells increased miR-135b to levels similar to those observed in PI3K mutant cells (Figure 2J). In conclusion, *PI3KCA* mutations may induce miR-135b by phosphorylating and inactivating FoxO1 and FoxO3A or altering FoxO1/3A targets.

SRC is nonmembrane receptor tyrosine kinase (Yeatman 2004) and induces activation of several pathways. MiR-135b was overexpressed in v-Src expressing MEFs compared to WT cells (Figure 2E). Dasatinb, a SRC inhibitor (Serrels et al., 2006), reduced the expression of miR-135b in SW620 CRC cells to levels observed in their parental nonmetastatic counterpart (SW480; Figure 2K). Because SRC can activate a plethora of downstream effectors, we focused only on those previously analyzed in our MEF screening: PI3K and MAPK. Our data suggested that the MAPK pathway is not responsible for miR-135b overexpression because overexpression of v-Jun (Shaulian 2010) showed no effect on miR-135b expression. LY294002 reduced the expression of miR-135b by 40% ($p = 0.03$) in v-Src expressing MEFs, whereas a MEK1-2 (Yoon et al., 2011) inhibitor did not affect miR-135b expression (Figure 2L). Loss of Src attenuates the intestinal phenotype caused by Apc loss both in flies and mice (J.C. and O.J.S., unpublished data). Interestingly, in our system, loss of Src in AhCRE $Apc^{fl/fl}$ mice was associated with a reduction in miR-135b expression (Figure 2M). These observations suggested that, at least in part, SRC induces miR-135b overexpression through the PI3K/AKT/FoxO pathway. However, we cannot rule out the possibility that other SRC effectors contribute to miR-135b overexpression. This hypothesis is supported by the observation that PI3K inhibition only partially

(N) Luciferase reporter assay was performed after LiCl treatment using different vectors containing predicted TCF4 binding sites upstream of the pre–miR-135b; −1 position corresponds to the 5′ terminus of the miR-135b hairpin. Putative TCF4 responsive sequences (CTTTGTT)) are indicated in the gray boxes, and the miR-135b sequence is in red. Deletion of the TCF4 binding site is represented by a X.
Human or mouse miR-135b expression was assessed by RT-PCR and normalized to that of RNU48 or SNU234, respectively. Bars represent the mean and SD of three experiments; p values are reported within the figures. See also Figure S2.

reduces miR-135b expression and by the recent observation that STAT3 can induce miR-135b overexpression in large cell lymphomas (Matsuyama et al., 2011).

MiR-135b is located on the negative strand of 1q32.1 and overlaps with exon 1 of the LEM domain-containing 1 (*LEMD1*) gene (Figure S2G). LEMD1 is overexpressed in prostate cancer (Ghafouri-Fard et al., 2010) and anaplastic cell lymphoma (Matsuyama et al., 2011). Gene expression analysis suggests that only a (657 nt) *LEMD1* isoform is expressed in CRC (Yuki et al., 2004).

To test whether miR-135b transcription is depended upon LEMD1 activation, we analyzed the expression of *LEMD1* and miR-135b following inhibition of transcription factors involved in miR-135b expression (Figure S2H). RT-PCR using *LEMD1* primers covering all the different spliced LEMD1 isoforms revealed no change in *LEMD1* expression in relation to TCF4/LEF1 silencing suggesting that miR-135b activation is independent from *LEMD1* in CRC. Because the loss of APC and the activation of the β-catenin/TCF4 pathway seem to be the initiating event in miR-135b deregulation, we subcloned the ~2.5 kb area up-stream of the 5′ terminus of miR-135b hairpin into the pGL3 reporter vector (PGL3-miR-135b-P1 for the full-length, WT plasmid) and we tested luciferase activity following LiCl stimulation (Figure 2N). Two putative TCF4 binding sites (distal and proximal to the 135b hairpin) were identified in this area (http://genome-euro.ucsc.edu; Figure 2N). Subcloning of the two predicted binding sites and mutagenesis experiments allowed to define the distal binding site as the one involved in miR-135b activation (PGL3-miR-135b-P2/P5 M1-M2; Figure 2N).

We previously showed that FoxO transcription factors exert a negative control on miR-135b activation (Figure 2J). To test whether FoxO binds to miR-135b promoter, we looked for potential FoxO consensus sequences and we identified a conserved area located 300 bp (−289 to 280) upstream of the hairpin precursor. When NCM460 cells were cotransfected with siRNA to FoxO3a or FoxO1 and the PGL3-miR-135b-P1 plasmid, no effect was seen on promoter activation (data not shown), suggesting that FoxOs do not have a direct interaction with miR-135b promoter. Because FoxOs can bind β-catenin preventing the activation of TCF4 (Hoogeboom et al., 2008), we tested whether modulation of Foxo3a would cause any change to promoter activation induced by β-catenin stabilization. Interestingly, silencing of Foxo3a increased miR-135b promoter activation (1.9-fold change; $p = 0.004$), whereas FoxO overexpression reduced (63% reduction; $p = 0.003$) the luciferase activity (Figure S2I, blue bars). A TOPFLASH plasmid containing multiple copies of an optimal TCF-binding site and a FOPFLASH plasmid containing multiple copies of a mutant form of a TCF-binding site were used in parallel to confirm TCF4 inhibition by FoxO (Figure S2I, red bars). These data underpin the synergic activity of the PI3K and APC pathways in controlling miR-135b activation, proving that different oncogenic pathways merge on miR-135b activation directly and indirectly.

MiR-135b Affects Apoptosis and Cell Growth

APC/Wnt/β-catenin signaling is pivotal for cell division and is linked to reduced apoptosis (Morin et al., 1996; Groden et al., 1995). To test the contribution of miR-135b on APC/β-catenin-mediated apoptosis, we cotransfected SW480 cells with a plasmid encoding the full *APC* CDS (*APC*-EGFP) or an empty vector (empty EGFP) in combinations with LNA-anti-miR-135b, pre-miR-135b or controls. In line with previous evidence (Morin et al., 1996; Groden et al., 1995), APC re-expression caused apoptosis (Figure 3A). Similarly, the inhibition of miR-135b alone induced apoptosis. The cotransfection of miR-135b and *APC*-EGFP rescued the effect on apoptosis due to the re-induction of APC (Figure 3A). *APC* is a target of miR-135b (Nagel et al., 2008); however, in our experiments the *APC*-EGFP vector contains only the *APC* CDS and not the 3′UTR. These data suggest that re-expression of APC causes apoptosis, at least in part, by downregulating miR-135b.

To test the effects of miR-135b on cell growth, we used HCT-116 *PI3KCA* WT and mutant cells (Samuels et al., 2005). *PI3K* WT cells overexpressing miR-135b showed increased proliferation after 48 hr, and the difference was still statistically significant after 5 days. Similarly, *PI3KCA* mutant cells transfected with anti-miR-135b showed reduced proliferation compared to the LNA-control cells (Figures 3B, S3A, and S3B; Tables S4 and S5). The presence of *PI3KCA* mutations also affected growth in soft agar. Silencing of miR-135b reduced the number of colonies in the *PI3KCA* mutant cells, whereas miR-135b overexpression resulted in increased colony formation (Figures 3C and S3C). Moreover, inhibition of miR-135b in SRC-MEFs inhibited their ability to form colonies in soft agar. Anti-miR-135b or scramble lenti-viral vectors were used to infect SRC-MEFs (Figure 3D). MiR-135b repression caused a 95% reduction ($p < 0.001$) in the number of colonies in SRC-transformed MEFs (Figures 3E and 3F), supporting the hypothesis that miR-135b is a major driver of SRC-induced transformation.

Targeting miR-135b Affects Tumor Growth In Vivo

Apc loss causes alterations in the crypt-villus architecture promoting classical features of neoplastic transformation such as increased proliferation and loss of differentiation. To investigate the role of miR-135b in Apc loss-mediated transformation in vivo, we designed specific oligonucleotides to target endogenous miR-135b (anti-miR-135b oligonucleotides [miR-135b-AMO] and scrambled-oligonucleotides [Scramble-AMO]). The miR-135b-AMO silencing efficacy was initially tested in vitro and in vivo (Figures S4A and S4B). A custom probe recognizing the-miR-135b-AMO oligonucleotides was used for ISH and revealed a strong signal in colon epithelium, suggesting that the miR-135b-AMO was taken up and retained in mice intestine for at least 48 hr following injection (Figure S4B). Off-target effects of miR-135b-AMO on other miRs were excluded (Figure S4C).

To study the contribution of miR-135b to the phenotype induced by APC loss, we triggered rapid *Apc* inactivation by the administration of β-napthoflavone to $AhCre^{+}Apc^{fl/fl}$ mice as previously described (Sansom et al., 2004). MiR-135b-AMO and Scrambled-AMO were given intraperitoneally at a dose of 50 mg/kg on days 2 and 4 and mice were euthanized on day 4 (Figure 4A). *Apc* inactivation was associated with β-catenin activation and nuclear localization in both treatment groups (Figure S4D). Apc loss caused a 10-fold increase in miR-135b expression in $Cre^{+}Apc^{fl/fl}$ compared to $Cre^{+}Apc^{+/+}$ controls (WT hereafter) definitively showing that mir135b is directly activated following Apc loss. MiR-135b-AMO caused a marked reduction in miR-135b expression (70%; $p < 0.001$) in the

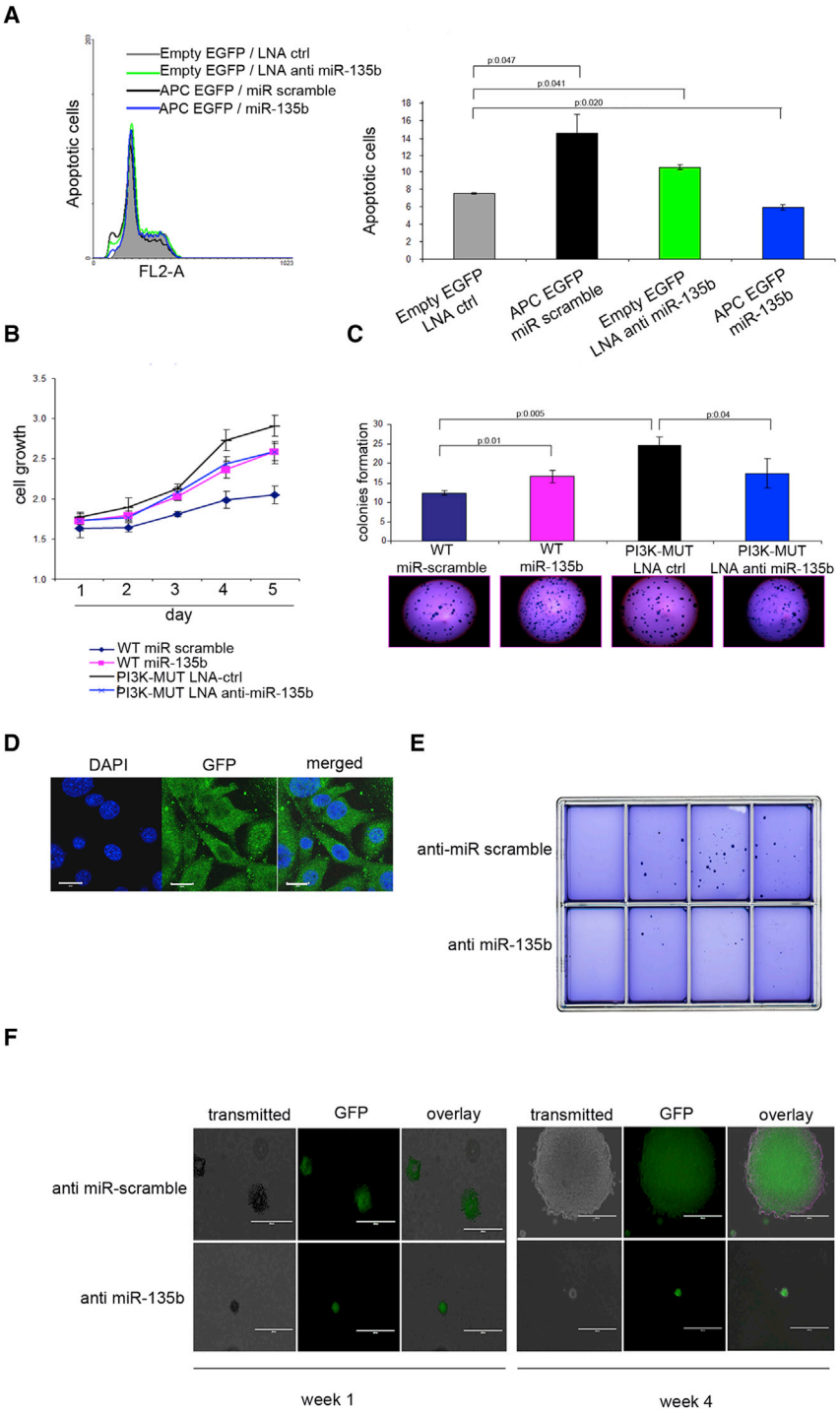

Figure 3. MiR-135b Mediates the Cancer Phenotype Induced by *APC* and *PI3KCA* Mutations

(A) *APC* mutant SW480 cells were transfected with pre-miR-135b, LNA anti-miR-135b, or controls in combination with a plasmid encoding the *APC* CDS or an empty vector. Apoptotic cells were measured by flow cytometer (left) and quantitated (right).

(B) Isogenic *PI3KCA* WT and mutant HCT-116 cells were transfected with pre-miR-135b, LNA anti-miR-135b, or relative controls. Cell viability was measured at selected time points.

(C) Isogenic *PI3KCA* mutant and WT HCT-116 cells overexpressing miR-135b or anti-miR-135b were plated in soft agar and grown in low fetal bovine serum conditions. Colonies greater than 2 mm in size were counted and quantitated. Representative images are shown.

(D–F) v-SRC transformed MEFs were infected with lentiviruses encoding an anti-miR-135b or a scramble hairpin. Cells were selected with puromycin and checked for viral integration using GFP (scale bars, 20 um; D). Cells were grown in soft agar and colonies were counted after 4 weeks. On the far left of the plate, no cells were seeded as negative control (E). GFP was used to monitor viral integration during for the entire duration of the experiment (F). Scale bars, 200 um (week 1) and 400 um (week 4). Bars represent the mean and SD of three experiments; p values are reported within the figures. See also Tables S4 and S5 and Figure S3.

miR-135b-AMO-treated mice (n = 6 [135b-AMO mice hereafter]) compared to scrambled-AMO-treated mice (n = 6 [scrambled-AMO mice hereafter]; Figure S4E). In the scrambled-AMO, loss of the crypt structures and occupation of the crypt-villus axis by atypical cells was observed; indeed, cellularity was doubled compared to that of WT mice (89.8 ± 6 cells per crypt VS 41.6 ± 2.3 cells per crypt; p = 0.0001) and the number of mitotic figures per crypt was increased (average 3.16 vs. 1.35; p = 0.03; Figures 4B and 4C). In the $Cre^{+}Apc^{fl/fl}$ 135b-AMO, a normal morphology was retained, cellularity and number of mitosis (54.8 ± 3; p 0.02 and 1.6 ± 0.7, respectively) were importantly reduced compared to scrambled-AMO mice (Figures 4B and 4C). To define changes in proliferation, mice from all the three groups (n = 3) were injected with BrdU and killed 2 hr later on day 4. Scoring of the proportion of cells in S phase revealed a 43% increase in proliferation in the scrambled-AMO mice compared to the WT mice (BrDU-positive cells 40.5 vs. 28.4; p = 0.01). 135b-AMO mice showed decreased proliferation compared to scrambled-AMO (mitotic index: 27.1; p = 0.02) and no difference compared to the WT mice (Figure 4B, right) with a clear cleavage plain between the expected mid crypt proliferation region and the upper compartment (Figure 4C).

Because the AOM/DSS better resembles the high level of genetic instability observed in human CRC (The Cancer Genome Atlas Network, 2012) compared to the CPC;Apc model, we tested this model to study the therapeutic potential of 135b-AMO in vivo. Colorectal carcinogenesis was induced using the AOM/DSS protocol and 135b-AMO or scrambled-AMO were administered simultaneously twice a week for the entire duration of the treatment (Figure 5A). After 100 days, the mice were

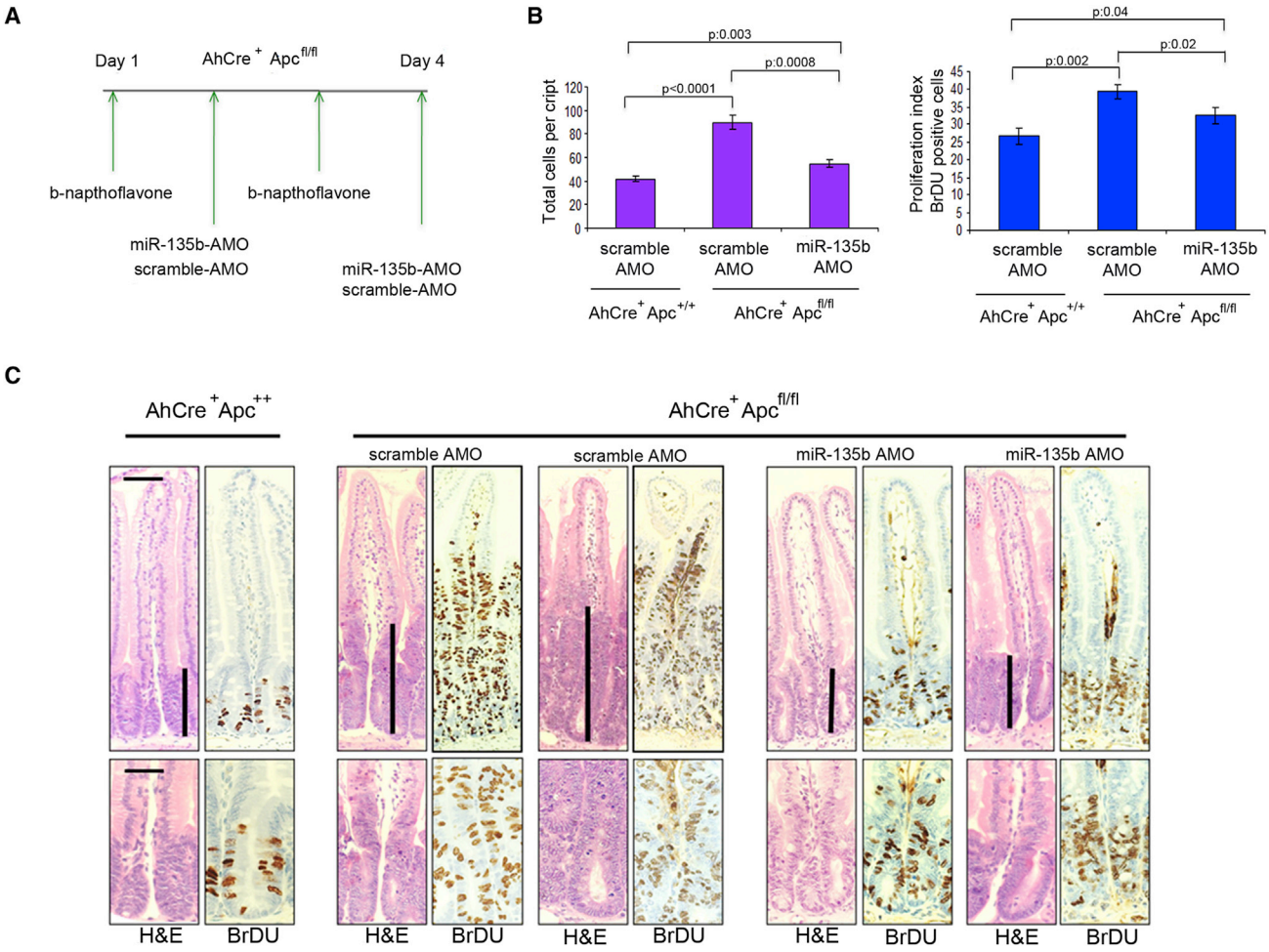

Figure 4. miR-135b Inhibition Rescues Apc-Induced Phenotype In Vivo

(A) Conditional *Apc* deletion induced by b-napthoflavone injection in *AhCre*$^{+}$*Apc*$^{+/+}$ mice on days 1 and 3. miR-135b-AMO or scrambled-AMO were injected on days 2 and 4. Mice (n = 6 for each group) were euthanized on day 4.

(B) Graphs show total cells per crypt (left) and proliferation index (ratio between BrDU-positive cells and total cells per crypt; right) in *AhCre*$^{+}$*Apc*$^{+/+}$ and *AhCre*$^{+}$*Apc*$^{fl/fl}$ mice treated with scramble-AMO or anti-135b-AMO. BrDU was injected in three mice per group 2 hr prior to euthanization. Error bars represent SD; p values are shown within the graphs. Magnification bars, 100 um (top), 50 um (bottom).

(C) Hematoxylin and eosin (H&E) and BrDU-stained sections for AhCre^{+}Apc$^{+/+}$ and AhCre^{+}Apc$^{fl/fl}$ mice treated with scramble-AMO or anti-135b-AMO. Bars show size of the crypts. Magnification bars, 100 um (top), 50 um (bottom).

See also Figure S4.

euthanized and tumors were analyzed (Figures 5B and 5C). None of the mice showed signs of toxicity related to AMO treatment or had to be euthanized before the end of the study due to toxicity.

MiR-135b-AMO reduced the median number and the size of tumors (Figures 5B–5D). No differences were observed between the scrambled-AMO and the control group. Microscopy showed that MiR-135b-AMO tumors were well differentiated with an acinar pattern, whereas tumors in the scrambled-AMO group showed poor differentiation and an adenomatous pattern (Figure 5C). Effective miR-135b downregulation in 135b-AMO treated mice was confirmed by RT-PCR and ISH (Figures S5A and S5B). Proliferation was remarkably reduced in tumors from miR135b-AMO compared to scrambled-AMO (Ki-67 positive cells 60% vs. 35% $p < 0.01$; Figure 5E). Apoptosis was analyzed by an immunofluorescence-based TUNEL assay. The percentage of apoptotic cells and the intensity of the signal were increased in the anti-miR-135b tumors in comparison to the scrambled-AMO tumors (Figure 5F). No significant differences were observed in other organs (Figure S5C).

To dissect the contribution of miR-135b overexpression to each single pathway, we infected CRC GEMM-derived organoids with lentiviruses silencing miR-135b or controls; we xenotransplanted the tumors in nude mice and monitored tumor growth (Figure 6A). Given that *Apc*$^{fl/fl}$/*Pten*$^{fl/fl}$ and *Apc*$^{fl/fl}$/*Kras*$^{G12/+}$/*P53*$^{R172H/fl}$-derived organoids were the two models that showed progressive deregulation of miR-135b compared to *Apc*$^{fl/fl}$ organoids, these were used for the experiments. Apc$^{fl/fl}$/Kras$^{G12/+}$ organoids did not show any significant difference in miR-135b expression compared with *Apc*$^{fl/fl}$ and were

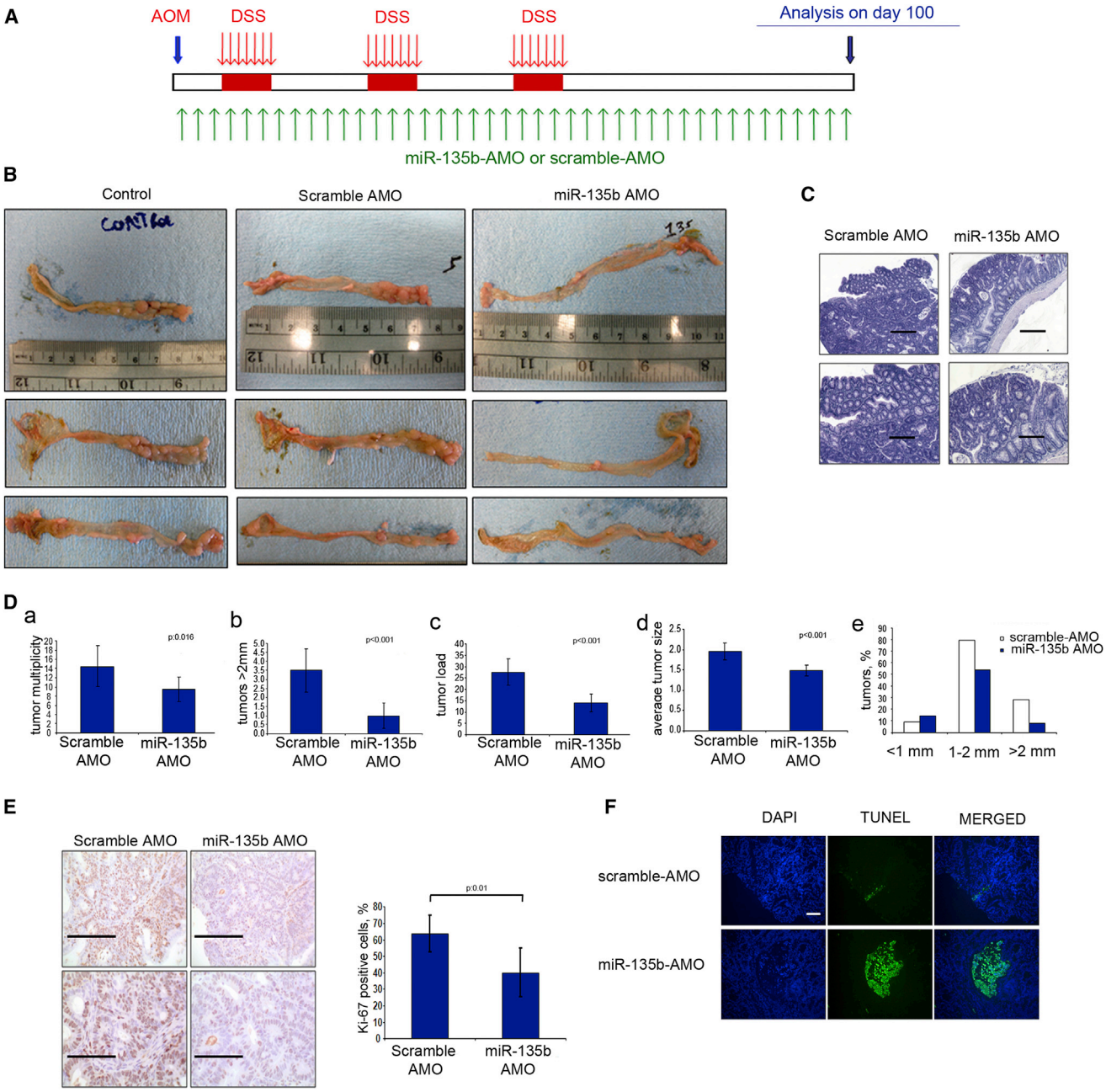

Figure 5. Anti-miR-135b Exerts an Antitumor Effect In Vivo in the AOM/DSS Model

(A–C) Overview of the study (A): AOM was given once, followed by periodic administration of DSS in water. MiR-135b-AMO or scrambled-AMO were given twice a week for 100 days. Mice were treated with miR-135b-AMO (n = 8), scrambled-AMO (n = 8), or left untreated (n = 8). Following euthanization, macroscopic (B) and microscopic (C) analysis of the tumors was performed. Scale bars, 200 um (top), 100 um (bottom).

(D) Statistical analysis of tumor number (multiplicity, a), tumor number for tumors >2 mm (b), tumor volume (load, c), average size (d), and tumor size distribution in the two groups (e).

(E and F) Cancer tissues from mice treated with miR-135b-AMO or scrambled-AMO were analyzed. (E) Ki-67 expression was assessed with immunohistochemistry (a) and quantitated (b; scale bars, 200 um [top], 100 um [bottom]). (F) Apoptosis was assessed by immunofluorescence (scale bar, 200 um).

See also Figure S5.

not included. *Apc*$^{fl/fl}$ cells grow slowly in xenografts and for this reason were not included in the study.

For each genotype, organoids were infected with lentiviral vectors inhibiting miR-135b (anti-135b) or controls (anti-miR-scramble; Figure 6B). Mir-135b downregulation was checked by RT-PCR following infection and puromycin selection (Figure 6C). Xenotransplanted tumors (50 organoids for each mouse, six mice per group) were measured twice a week for 2 months or

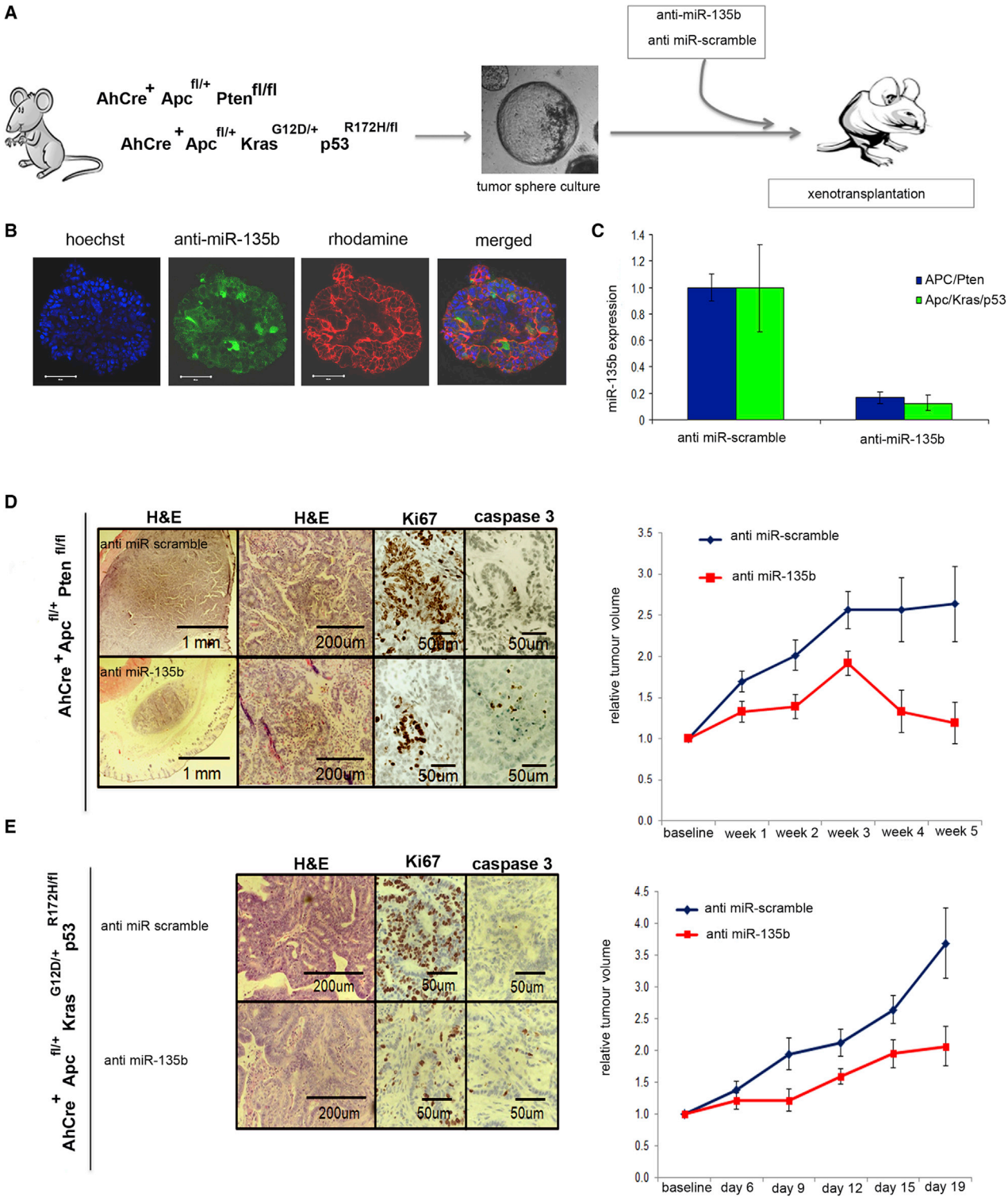

Figure 6. miR-135b Inhibition Causes Tumor Inhibition in Organoids Derived from CRC GEMMs

(A and B) Tumor-derived organoids from *Apc*$^{fl/fl}$/*Pten*$^{fl/fl}$ and *Apc*$^{fl/fl}$/*Kras*$^{G12/+}$/*P53*$^{R172H/fl}$ (A) infected with lentiviruses encoding anti-miR-135b or scramble hairpins (B) were xenotransplanted in nude mice. Tumors were measured twice a week for 8 weeks or until ulceration.

(C) miR-135b expression was assessed by RT-PCR in tumor-derived organoids after infection. Bars represent the mean and SD of three experiments; $p < 0.01$.

(D) Microscopic analysis (left) and tumor growth (right) in *Apc*$^{fl/fl}$/*Pten*$^{fl/fl}$ organoids.

(E) Microscopic analysis (left) and tumor growth (right) in *Apc*$^{fl/fl}$/*Kras*$^{G12/+}$/*P53*$^{R172H/fl}$ organoids.

Results are expressed as the mean percentage of change in tumor volume for each group of mice, ± SEM. See also Figure S6 and Tables S6 and S7.

until tumor ulceration. At the end of the study, tumors were harvested and analyzed for proliferation and apoptosis. Lentiviral integration and miR-135b downregulation were controlled by GFP staining and RT-PCR, respectively (Figure S5).

In the *Apc*$^{fl/fl}$/*Pten*$^{fl/fl}$, we observed striking differences in tumor growth (Figure 6D; Table S6). Six weeks following transplantation, three of six tumors regressed to the point that they could not be detected macroscopically and the other three showed a cessation of growth. Immunohistochemical analysis showed that proliferation was almost entirely abolished in the miR-135b group compared to controls (Figure 6D).

Apc$^{fl/fl}$/*Kras*$^{G12/+}$/*P53*$^{R172H/fl}$ xenografts infected with anti-miR-scramble grew rapidly, and four of six tumors ulcerated after 3 weeks (Figure 6E; Table S7). In contrast, anti-135b tumors only doubled in 3 weeks and no ulceration was observed until week 8. Tumor growth was inhibited in the anti-135b group and this was supported by the observation that proliferation was inhibited in the lenti-135b group compared to controls (Figure 6E).

MiR-135b Targets Tumor-Suppressor Genes

To find potential target genes affected by miR-135b overexpression, we performed a gene expression analysis in normal epithelial colon cells overexpressing miR-135b (Figure 7A). The analysis of a cancer-associated gene panel revealed that 35 genes were dysregulated by miR-135b overexpression (Table S8). A matched analysis of miR-135b downregulated genes and target prediction algorithms (Lewis et al., 2003; Rehmsmeier et al., 2004) showed that several genes were potentially controlled by miR-135b: transforming growth factor β receptor 2 (*TGFβR2*), death-associated protein kinase 1 (*DAPK1*), and *APC*. Data from the array analysis were confirmed by RT-PCR in the same cell line and in a second normal epithelial cell line (NCM 356; Figures 7B and S7A). We identified predicted binding sites for miR-135b in each of these genes (Lewis et al., 2003; Rehmsmeier et al., 2004; Figure 7C). Luciferase experiments confirmed the specificity of the miR-135b-target interaction (Figure 7D).

DAPK1 is frequently downregulated in CRC, and promoter methylation does not seem to be the main mechanism by which this occurs (Xu et al., 2004; Borinstein et al., 2010). Western blot analysis proved that miR-135b can affect DAPK1 protein expression (Figure 7E). Analysis of *DAPK1* expression in human IBD-associated CRC confirmed the downregulation of this gene in cancer and dysplasia compared to normal tissues (Figure 7F). Correlation analysis between miR-135b expression and *DAPK1* mRNA showed an inverse correlation ($r = -0.4$, $p = 0.036$).

TGFβR2 downregulation is common in CRC (Biswas et al., 2004; Guda et al., 2001) and in vitro evidence suggests that dynamic changes in TGFβR2 expression can have an effect on p21-mediated/TGF-β-induced apoptosis (Rojas et al., 2009) . Stimulation of cells with TGF-β (10 nM) induced p21 activation in scrambled transfected cells whereas miR-135b overexpression or *TGFβR2* silencing caused reduced p21 activation and reduced apoptosis (Figures 7G and 7H). These data suggest that the miR-135b effect on apoptosis is partially mediated by TGFβR2 downregulation. Analysis of TGFβR2 expression in IBD-associated CRC showed *TGFβR2* downregulation in cancer compared to normal and dysplastic tissues (Figure 7I). Correlation analysis between miR-135b expression and *TGFβR2* mRNA showed an inverse correlation ($r = -0.46$, $p = 0.015$).

Our gene expression analysis revealed that miR-135b upregulation induces interleukin 8 (*IL8*) overexpression (Table S8; Figures 7J and S7B). IL-8 is an important cytokine involved in proliferation, invasion, migration, and neo-angiogenesis (Waugh and Wilson 2008). IL-8 is frequently involved in hypoxia response; thus, we looked at whether miR-135b could have an effect on IL-8 through HIF1α transcriptional regulation. No changes in *HIF1α* mRNA were observed following miR-135b overexpression (fold change 1.01; $p = 0.77$; Table S8), suggesting that *IL8* overexpression was independent from *HIF1α* transcriptional regulation. Because our experiments were performed in condition of normoxia, we looked for a nontranscriptional regulator of HIF1α and searched for potential miR-135b binding sites in HIF1α regulators. FIH is an asparagine hydroxylase that prevents HIF1α activation in normoxia (Mahon et al., 2001). Interestingly *FIH* harbors a miR-135b binding site (Figure 7K). We proved *FIH* as a target of miR-135b (Figures 7K–7M and S7C). To support a role of miR-135b in FIH regulation in vivo, we measured *FIH* mRNA expression in human IBD-associated CRC and found the gene was downregulated in cancer compared to normal and dysplastic tissues (Figure S7D). Correlation analysis between miR-135b expression and *FIH* mRNA showed an inverse correlation ($r = -0.42$; $p = 0.02$). To confirm that miR-135b controls IL-8 production through FIH/HIF1α, we measured *IL8* and *VEGFA* expression after miR-135b manipulation (Figures 7N and S7E). MiR-135b promoted IL-8 and VEGFA overexpression and a similar effect was caused by *FIH* silencing or by hypoxia. Interestingly HIF1α siRNAs were able to rescue the effect on IL-8 and VEGFA by miR-135b. These observations suggested that miR-135b was acting on both cytokines through a FIH/HIF1α axis (Figure 7N). To test if the increase in IL-8 induced by miR-135b was relevant in promoting a functional effect on neo-angiogenesis, the supernatant from miR-135b overexpressing cells was used for a neo-angiogenesis assay. HUVEC grown with media from miR-135b transfected cells showed a 3-fold change increase in their ability to form tubes compared to those cultured with media from scrambled transfected cells (Figure 7O).

DISCUSSION

Using in vitro and in vivo models, we define the genetic events driving miR-135b deregulation in CRC. Our observations explain why miR-135b upregulation is consistently observed in human and mouse CRC (Nagel et al., 2008; Gaedcke et al., 2012), making this miR a robust and reproducible biomarker. Our findings complement those of a recent report that identifies miR-135b as one of the most upregulated miRs in Apc$^{min/+}$ mice (Necela et al., 2011), suggesting that miR-135b deregulation is independent of the specific *Apc* mutation or site of inactivation. Data from mouse tumors and human dysplastic tissues suggest that miR-135b upregulation is an early event in tumor transformation as supported by the observation that miR-135b is directly linked to rapid Apc loss in the *AhCreApc*$^{fl/fl}$ model and inhibition of miR-135b rescues the phenotype induced by Apc loss in a way that resembles *c-Myc* deletion in mice intestines (Sansom et al., 2007). According to our siRNA experiments, miR-135b regulation seemed to be independent from c-Myc activation; thus, these two factors may control collateral transcriptional programs

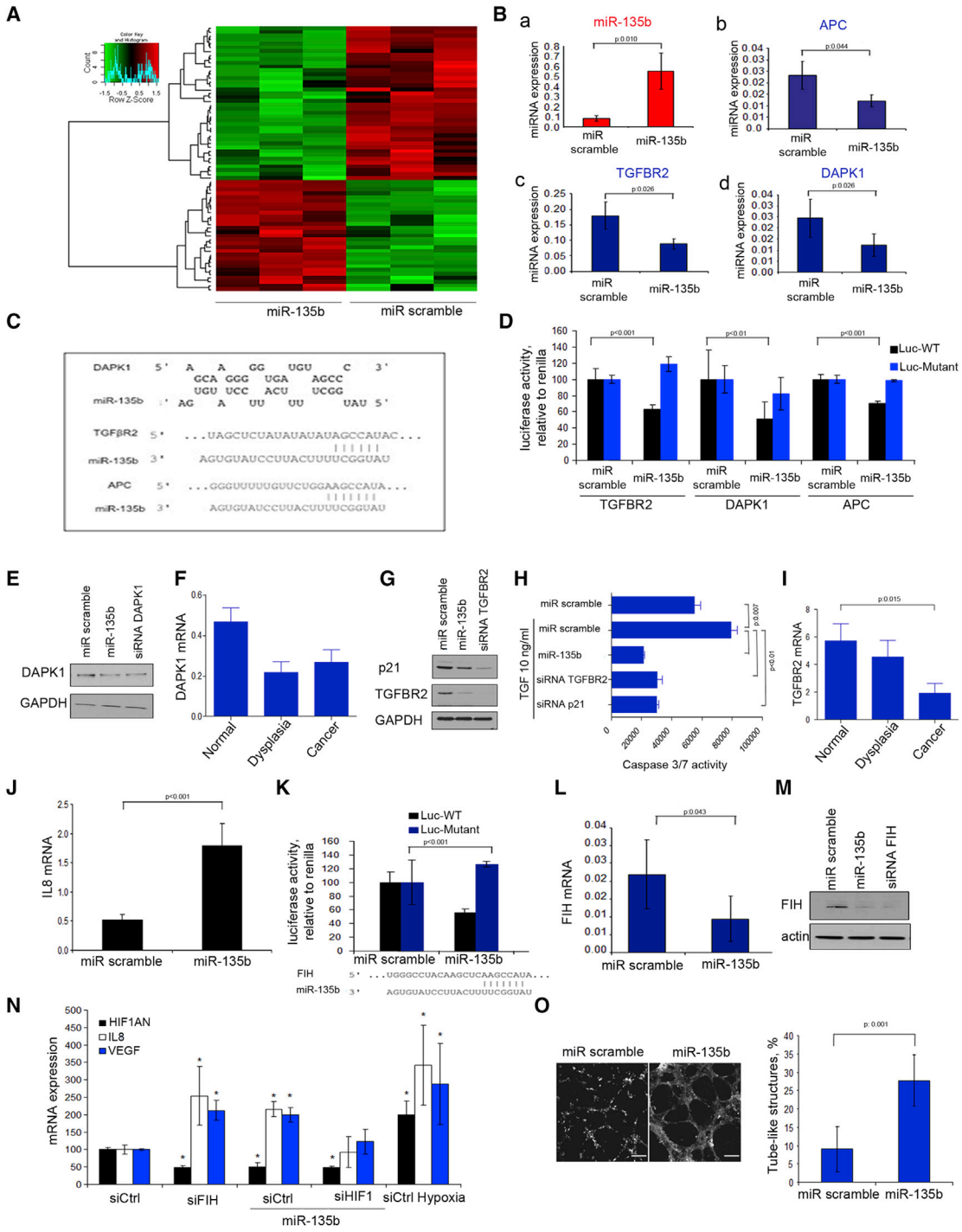

Figure 7. MiR-135b Controls Tumor-Suppressor Genes

(A) Analysis of a cancer gene-associated panel in 460NCM cell transfected with pre-miR-135b or scrambled probes.

(B) *APC (b)*, *TGFβR2* (c), and *DAPK1* (d) mRNA expression analyzed by RT-PCR following miR-135b overexpression (a).

(C) In silico target prediction for miR-135b binding sites in *APC*, *TGFβR2*, and *DAPK1* 3′UTRs.

(D) Luciferase experiments for *TGFβR2*, *DAPK1*, and *APC* in NCM460 cells transfected with target-gene-Luc-WT or target-gene-Luc mutant, pre-miR-135b, or scrambled miR.

(E) DAPK1 protein expression by WB following transfection with pre-miR-135b and specific siRNA.

(F) *DAPK1* mRNA expression in dysplasia and cancer compared to normal adjacent tissues in IBD-associated CRC.

(G and H) TGFβR2 and p21 protein expression assessed following miR-135b overexpression and TGF-β stimulation (G). Apoptosis measured by caspase 3/7 assay following TGF-β stimulation (H).

(legend continued on next page)

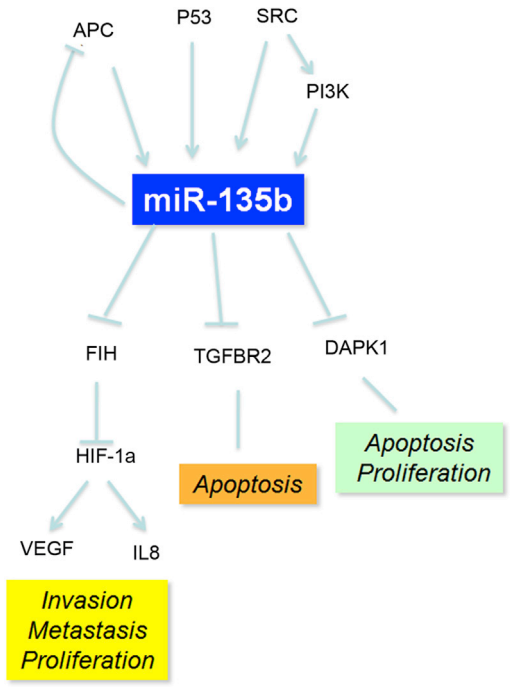

Figure 8. MiR-135b Is a Key Oncogenic Hub Mediating the Cancer Phenotype Downstream of Genes Frequently Mutated in CRC
Schematic representation of genetic aberrations promoting miR-135b overexpression and miR-135b downstream targets.

orchestrating the tumor initiation process. Indeed, even though proliferation was completely inhibited by miR-135b, some differences between the WT and the 135b-AMO mice were still observed in term of total number of cells per crypt, suggesting that other pathways independent from miR-135b regulation may still be active upon miR-135b inhibition. A second potential explanation to this observation may be technical in nature and related to the ability to silence miR-135b completely by oligonucleotides as compared to complete knockdown caused by Myc deletion in Sansom's model.

Compared to other downstream effectors of the Apc/β-catenin pathway, such as cyclin D1, that are mostly involved in tumor initiation rather than progression (Sansom et al., 2005), miR-135b seems to retain its malignant potential in more advanced carcinogenesis as suggested by the observation that tumor growth was deeply affected by miR-135b silencing in organoids harboring *Apc*, *Pten*, and *p53* mutations. Our data suggest that the progressive upregulation of miR-135b in more advanced tumors may be caused by the convergence of several pathways on miR-135b transcriptional regulation as suggested by the analysis of miR-135b promoter activation. Because miR-135b overexpression follows the kinetics of mutations in CRC, it may represent a good biomarker of tumor progression.

Crosstalk among different pathways is frequently observed in colon carcinogenesis and may affect miR-135b expression at different stages of disease and in different epithelial compartments (progenitor versus mature cells). In IBD-associated cancers, for example, PI3K feeds positively on the Wnt pathway, causing β-catenin phosphorylation and nuclear β-catenin accumulation in progenitor epithelial cells (Lee et al., 2010). Thus, PI3K mutations might have a feed-forward effect on miR-135b expression in this setting. As previously shown (Nagel et al., 2008), miR-135b in turn can control *APC* expression. The presence of this complex feedback loop (Figure 8) might explain several in vivo observations. First, several pathways converging on the same miR explain why no correlation has been previously found between *APC* mutations and miR-135b expression (Nagel et al., 2008). Second, the feedback loop might be responsible for the fine-tuning of miR-135b and the generation of a threshold effect on its target *APC*. IBD-associated CRCs are characterized by rare mutations in the Wnt pathway (Aust et al., 2002) and miR-135b overexpression. According to these observations, we would expect most IBD cancers to show low APC expression and nuclear β-catenin accumulation. On the contrary, only 30%–50% of IBD-invasive tumors show nuclear β-catenin with little or no accumulation in low- or high-grade dysplasia (Leedham et al., 2009). Several reports (Valeri et al., 2010; Mukherji et al., 2011) suggest the presence of a threshold effect in miR function. We speculate that miR-135b deregulation might be responsible for APC loss and β-catenin stabilization only in the fraction of IBD tumors for which miR-135b expression has reached a defined threshold.

MiR-based therapeutics represent a promising approach to tailor cancer therapy; however, off-target effects may represent a major issue for those microRNAs involved in physiological conditions such as miR-21 (Han et al., 2011). Contrary to other miRs, miR-135b basal expression is very low in normal epithelium and other organs as supported by the TCGA analysis. The low miR-135b expression in normal epithelium may be explained either by the observation that, as observed for other Wnt targets (i.e., Lgr5 or Ascl2), a limited number of normal epithelial cells are under Wnt control in physiological conditions or by the observation that transcription factors such as FoxOs or USF1 may act as brakes on miR-135b transcription in physiological conditions. For these reasons, silencing miR-135b in CRC may represent a promising targeted therapy characterized by high specificity and limited toxicity.

(I) *TGFβR2* mRNA expression in dysplasia and cancer compared to normal adjacent tissues in IBD-associated CRC.
(J) *IL8* mRNA expression following miR-135b overexpression in NCM460 cells.
(K) Luciferase assay in NCM460 transfected with FIH-Luc-WT or FIH-gene-Luc mutant vectors, pre-miR-135b, or scrambled miR. MiR-135b seed region in *FIH* 3′UTR is shown.
(L and M) *FIH* mRNA (L) and protein (M) expression following miR-135b overexpression in 460NCM cells.
(N) *FIH*, *IL8*, and *VEGFA* mRNA following siRNA transfection. *$p < 0.05$.
(O) Tube formation in HUVEC cells cultured with media from scrambled or miR-135b transfected cells: representative picture (left) and normalization (right) are shown.
Bars represent the mean and SD of three experiments; p values are reported within the figures. See also Table S8 and Figure S7.

EXPERIMENTAL PROCEDURES

MiR and mRNA Expression Analysis

MiR expression profiling and mRNA expression of cancer-associated genes were analyzed with nCounter from NanoString Technologies, using the nCounter Mouse miRNA Expression assay kit and the nCounter Human Cancer reference kit, respectively. The NanoString nCounter gene expression system quantitates abundances of miRNAs and mRNA.

Technical normalization is performed using the synthetic positive controls to adjust the counts for each miRNA target in that assay. Then biological normalization is performed to correct for differences in sample abundances. Each sample is normalized to the geometric mean of the top 50 most highly expressed miRs. Student's t test is used on normalized counts to calculate statistical significances of pairwise comparisons. All of the calculations are performed in R statistical computing and graphics environment (http://www.r-project.org).

Animal Experiments and Tumor Induction

RNAs from CpC/Apc (matched tumor and normal), AOM/DSS (matched cancer and normal), wild-type (untreated normal epithelium), and short-term (3–5 days) DSS-treated mice (inflamed epithelium) for the initial miR expression screening were provided by Prof. Michael Karin (University of California at San Diego). RNA from the intestinal epithelium of long-term (three cycles [1 week each] over a 78 day period) DSS-treated mice was collected at Ohio State University (OSU). All mice were C75BL/6 strain mice. For in vivo silencing experiments, C57BL/6 mice were obtained from The Jackson Laboratory. All mice were maintained in filter-topped cages on autoclaved food and water at OSU according to National Institutes of Health guidelines, and all experiments were performed in accordance with OSU and NIH guidelines and regulations. CAC was induced as previously described (Grivennikov et al., 2009). All experiments were approved by the Ethical Review Process of The University of Glasgow. Experiments were carried out in compliance with UK Home Office Animal (Scientific Procedures) Act 1986 and the EU Directive 2010.

Human Tissue Collection

Fresh-frozen and paraffin-embedded tissues from sporadic and IBD-related CRC were collected following informed consent and approval of the ethical committees at (1) Istituto Scientifico Romagnolo per lo Studio e la Cura dei Tumori; (2) Ohio State University Pathology Archive; (3) Department of Pathology, University of Ferrara; and (4) Department of Pathology, University of Padova.

ACCESSION NUMBERS

The Gene Expression Omnibus (GEO) accession numbers for miRNA and mRNA expression data are GSE54177 (mouse tissue) and GSE54163 (human cell lines).

SUPPLEMENTAL INFORMATION

Supplemental Information includes Supplemental Experimental Procedures, seven figures, and eight tables and can be found with this article online at http://dx.doi.org/10.1016/j.ccr.2014.03.006.

AUTHOR CONTRIBUTIONS

N.V., C.B., P.G., C.M., A.L., V.P.-H., J.R.H., L.U., S.I.G., F.L., A.P., K.M.S., A.V., M.F., S.C., R.A.R., and J.C. performed experiments; L.C. performed bioinformatics analysis; H.A. provided support and analyzed data for nCounter analysis; G.L., R.G., W.L.F., M.R., and M.F. provided human samples and provided support for immunohistochemistry; G.J.N. analyzed data for in situ hybridization; M.P.M. provided support with the human normal epithelial cell lines; N.V., C.B., J.G., P.K.V., M.K., O.J.S., and C.M.C. analyzed data and provided funding for the study; and N.V., C.B., and C.M.C. wrote the paper.

ACKNOWLEDGMENTS

The work was supported by the Kimmel Cancer Foundation Translational Scholar Award to N.V. and by NIH grants U01 CA152758 and RC2 CA148302 to C.M.C., 1R01 CA078230 to P.K.V., and NIH (AI043477; DK035108) and AACR (07-60-21-KARI) grants to M.K., who is an American Cancer Society Research Professor. S.I.G. was supported by Crohn's and Colitis Foundation of America (Career Development award no. 2693) and NIH/NIDDK (K99-DK088589). N.V. is the recipient of a Cancer Research UK Career Establishment award (A18052) and a Marie Curie Integration grant (TamiRCRT). C.B. is the recipient of a Scottish Senior Clinical Research Fellowship and recipient of a Chief Scientist Office grant. We acknowledge support from the National Institutes for Health Research Royal Marsden-Institute of Cancer Research Biomedical Research Centre. We thank Prof. Bert Vogelstein, Johns Hopkins University for the *PIK3CA* isogenic cell lines.

The results relative to miR-135b expression in human colorectal cancers published here are partially based upon data generated by The Cancer Genome Atlas pilot project established by the NCI and NHGRI. Information about TCGA, and the investigators and institutions that constitute the TCGA research network can be found at http://cancergenome.nih.gov.

Received: September 7, 2012
Revised: November 14, 2013
Accepted: March 6, 2014
Published: April 14, 2014

REFERENCES

Aust, D.E., Terdiman, J.P., Willenbucher, R.F., Chang, C.G., Molinaro-Clark, A., Baretton, G.B., Loehrs, U., and Waldman, F.M. (2002). The APC/beta-catenin pathway in ulcerative colitis-related colorectal carcinomas: a mutational analysis. Cancer *94*, 1421–1427.

Biswas, S., Chytil, A., Washington, K., Romero-Gallo, J., Gorska, A.E., Wirth, P.S., Gautam, S., Moses, H.L., and Grady, W.M. (2004). Transforming growth factor beta receptor type II inactivation promotes the establishment and progression of colon cancer. Cancer Res. *64*, 4687–4692.

Borinstein, S.C., Conerly, M., Dzieciatkowski, S., Biswas, S., Washington, M.K., Trobridge, P., Henikoff, S., and Grady, W.M. (2010). Aberrant DNA methylation occurs in colon neoplasms arising in the azoxymethane colon cancer model. Mol. Carcinog. *49*, 94–103.

Cancer Genome Atlas Network (2012). Comprehensive molecular characterization of human colon and rectal cancer. Nature *487*, 330–337.

Catenacci, D.V., Kozloff, M., Kindler, H.L., and Polite, B. (2011). Personalized colon cancer care in 2010. Semin. Oncol. *38*, 284–308.

Chen, J., and Huang, X.F. (2009). The signal pathways in azoxymethane-induced colon cancer and preventive implications. Cancer Biol. Ther. *8*, 1313–1317.

Croce, C.M. (2009). Causes and consequences of microRNA dysregulation in cancer. Nat. Rev. Genet. *10*, 704–714.

da Costa, L.T., He, T.C., Yu, J., Sparks, A.B., Morin, P.J., Polyak, K., Laken, S., Vogelstein, B., and Kinzler, K.W. (1999). CDX2 is mutated in a colorectal cancer with normal APC/beta-catenin signaling. Oncogene *18*, 5010–5014.

De Roock, W., De Vriendt, V., Normanno, N., Ciardiello, F., and Tejpar, S. (2011). KRAS, BRAF, PIK3CA, and PTEN mutations: implications for targeted therapies in metastatic colorectal cancer. Lancet Oncol. *12*, 594–603.

Dehm, S., Senger, M.A., and Bonham, K. (2001). SRC transcriptional activation in a subset of human colon cancer cell lines. FEBS Lett. *487*, 367–371.

Frattini, M., Signoroni, S., Pilotti, S., Bertario, L., Benvenuti, S., Zanon, C., Bardelli, A., and Pierotti, M.A. (2005). Phosphatase protein homologue to tensin expression and phosphatidylinositol-3 phosphate kinase mutations in colorectal cancer. Cancer Res. *65*, 11227.

Gaedcke, J., Grade, M., Camps, J., Søkilde, R., Kaczkowski, B., Schetter, A.J., Difilippantonio, M.J., Harris, C.C., Ghadimi, B.M., Møller, S., et al. (2012). The rectal cancer microRNAome—microRNA expression in rectal cancer and matched normal mucosa. Clin. Cancer Res. *18*, 4919–4930.

Ghafouri-Fard, S., Ousati Ashtiani, Z., Sabah Golian, B., Hasheminasab, S.M., and Modarressi, M.H. (2010). Expression of two testis-specific genes, SPATA19 and LEMD1, in prostate cancer. Arch. Med. Res. *41*, 195–200.

Grivennikov, S., Karin, E., Terzic, J., Mucida, D., Yu, G.Y., Vallabhapurapu, S., Scheller, J., Rose-John, S., Cheroutre, H., Eckmann, L., and Karin, M. (2009).

IL-6 and Stat3 are required for survival of intestinal epithelial cells and development of colitis-associated cancer. Cancer Cell *15*, 103–113.

Groden, J., Joslyn, G., Samowitz, W., Jones, D., Bhattacharyya, N., Spirio, L., Thliveris, A., Robertson, M., Egan, S., Meuth, M., et al. (1995). Response of colon cancer cell lines to the introduction of APC, a colon-specific tumor suppressor gene. Cancer Res. *55*, 1531–1539.

Guda, K., Giardina, C., Nambiar, P., Cui, H., and Rosenberg, D.W. (2001). Aberrant transforming growth factor-beta signaling in azoxymethane-induced mouse colon tumors. Mol. Carcinog. *31*, 204–213.

Han, M., Toli, J., and Abdellatif, M. (2011). MicroRNAs in the cardiovascular system. Curr. Opin. Cardiol. *26*, 181–189.

Hart, J.R., Liao, L., Ueno, L., Yates, J.R., 3rd, and Vogt, P.K. (2011). Protein expression profiles of C3H 10T1/2 murine fibroblasts and of isogenic cells transformed by the H1047R mutant of phosphoinositide 3-kinase (PI3K). Cell Cycle *10*, 971–976.

Hinoi, T., Akyol, A., Theisen, B.K., Ferguson, D.O., Greenson, J.K., Williams, B.O., Cho, K.R., and Fearon, E.R. (2007). Mouse model of colonic adenoma-carcinoma progression based on somatic Apc inactivation. Cancer Res. *67*, 9721–9730.

Hoogeboom, D., Essers, M.A., Polderman, P.E., Voets, E., Smits, L.M., and Burgering, B.M. (2008). Interaction of FOXO with beta-catenin inhibits beta-catenin/T cell factor activity. J. Biol. Chem. *283*, 9224–9230.

Ilyas, M., Tomlinson, I.P., Rowan, A., Pignatelli, M., and Bodmer, W.F. (1997). Beta-catenin mutations in cell lines established from human colorectal cancers. Proc. Natl. Acad. Sci. USA *94*, 10330–10334.

Kasinski, A.L., and Slack, F.J. (2011). Epigenetics and genetics. MicroRNAs en route to the clinic: progress in validating and targeting microRNAs for cancer therapy. Nat. Rev. Cancer *11*, 849–864.

Lee, G., Goretsky, T., Managlia, E., Dirisina, R., Singh, A.P., Brown, J.B., May, R., Yang, G.Y., Ragheb, J.W., Evers, B.M., et al. (2010). Phosphoinositide 3-kinase signaling mediates beta-catenin activation in intestinal epithelial stem and progenitor cells in colitis. Gastroenterology *139*, 869–881, e1–e9.

Leedham, S.J., Graham, T.A., Oukrif, D., McDonald, S.A., Rodriguez-Justo, M., Harrison, R.F., Shepherd, N.A., Novelli, M.R., Jankowski, J.A., and Wright, N.A. (2009). Clonality, founder mutations, and field cancerization in human ulcerative colitis-associated neoplasia. Gastroenterology *136*, 542–550, e6.

Lewis, B.P., Shih, I.H., Jones-Rhoades, M.W., Bartel, D.P., and Burge, C.B. (2003). Prediction of mammalian microRNA targets. Cell *115*, 787–798.

Mahon, P.C., Hirota, K., and Semenza, G.L. (2001). FIH-1: a novel protein that interacts with HIF-1alpha and VHL to mediate repression of HIF-1 transcriptional activity. Genes Dev. *15*, 2675–2686.

Marsh, V., Winton, D.J., Williams, G.T., Dubois, N., Trumpp, A., Sansom, O.J., and Clarke, A.R. (2008). Epithelial Pten is dispensable for intestinal homeostasis but suppresses adenoma development and progression after Apc mutation. Nat. Genet. *40*, 1436–1444.

Matsuyama, H., Suzuki, H.I., Nishimori, H., Noguchi, M., Yao, T., Komatsu, N., Mano, H., Sugimoto, K., and Miyazono, K. (2011). miR-135b mediates NPM-ALK-driven oncogenicity and renders IL-17-producing immunophenotype to anaplastic large cell lymphoma. Blood *118*, 6881–6892.

Morin, P.J., Vogelstein, B., and Kinzler, K.W. (1996). Apoptosis and APC in colorectal tumorigenesis. Proc. Natl. Acad. Sci. USA *93*, 7950–7954.

Moyer, M.P., Stauffer, J.S., Manzano, L.A., Tanzer, L.R., and Merriman, R.L. (1996). NCM460, a normal human colon mucosal epithelial cell line. In Vitro Cell Dev. Biol. Anim. *32*, 315–317.

Mukherji, S., Ebert, M.S., Zheng, G.X., Tsang, J.S., Sharp, P.A., and van Oudenaarden, A. (2011). MicroRNAs can generate thresholds in target gene expression. Nat. Genet. *43*, 854–859.

Nagel, R., le Sage, C., Diosdado, B., van der Waal, M., Oude Vrielink, J.A., Bolijn, A., Meijer, G.A., and Agami, R. (2008). Regulation of the adenomatous polyposis coli gene by the miR-135 family in colorectal cancer. Cancer Res. *68*, 5795–5802.

Necela, B.M., Carr, J.M., Asmann, Y.W., and Thompson, E.A. (2011). Differential expression of microRNAs in tumors from chronically inflamed or genetic (APC(Min/+)) models of colon cancer. PLoS ONE *6*, e18501.

Prahallad, A., Sun, C., Huang, S., Di Nicolantonio, F., Salazar, R., Zecchin, D., Beijersbergen, R.L., Bardelli, A., and Bernards, R. (2012). Unresponsiveness of colon cancer to BRAF(V600E) inhibition through feedback activation of EGFR. Nature *483*, 100–103.

Qian, J., Sarnaik, A.A., Bonney, T.M., Keirsey, J., Combs, K.A., Steigerwald, K., Acharya, S., Behbehani, G.K., Barton, M.C., Lowy, A.M., and Groden, J. (2008). The APC tumor suppressor inhibits DNA replication by directly binding to DNA via its carboxyl terminus. Gastroenterology *135*, 152–162.

Rehmsmeier, M., Steffen, P., Hochsmann, M., and Giegerich, R. (2004). Fast and effective prediction of microRNA/target duplexes. RNA *10*, 1507–1517.

Rojas, A., Padidam, M., Cress, D., and Grady, W.M. (2009). TGF-beta receptor levels regulate the specificity of signaling pathway activation and biological effects of TGF-beta. Biochim. Biophys. Acta *1793*, 1165–1173.

Samuels, Y., Diaz, L.A., Jr., Schmidt-Kittler, O., Cummins, J.M., Delong, L., Cheong, I., Rago, C., Huso, D.L., Lengauer, C., Kinzler, K.W., et al. (2005). Mutant PIK3CA promotes cell growth and invasion of human cancer cells. Cancer Cell *7*, 561–573.

Sansom, O.J., Reed, K.R., Hayes, A.J., Ireland, H., Brinkmann, H., Newton, I.P., Batlle, E., Simon-Assmann, P., Clevers, H., Nathke, I.S., et al. (2004). Loss of Apc in vivo immediately perturbs Wnt signaling, differentiation, and migration. Genes Dev. *18*, 1385–1390.

Sansom, O.J., Reed, K.R., van de Wetering, M., Muncan, V., Winton, D.J., Clevers, H., and Clarke, A.R. (2005). Cyclin D1 is not an immediate target of beta-catenin following Apc loss in the intestine. J. Biol. Chem. *280*, 28463–28467.

Sansom, O.J., Meniel, V.S., Muncan, V., Phesse, T.J., Wilkins, J.A., Reed, K.R., Vass, J.K., Athineos, D., Clevers, H., and Clarke, A.R. (2007). Myc deletion rescues Apc deficiency in the small intestine. Nature *446*, 676–679.

Serrels, A., Macpherson, I.R., Evans, T.R., Lee, F.Y., Clark, E.A., Sansom, O.J., Ashton, G.H., Frame, M.C., and Brunton, V.G. (2006). Identification of potential biomarkers for measuring inhibition of Src kinase activity in colon cancer cells following treatment with dasatinib. Mol. Cancer Ther. *5*, 3014–3022.

Shaulian, E. (2010). AP-1—The Jun proteins: Oncogenes or tumor suppressors in disguise? Cell. Signal. *22*, 894–899.

Sjöblom, T., Jones, S., Wood, L.D., Parsons, D.W., Lin, J., Barber, T.D., Mandelker, D., Leary, R.J., Ptak, J., Silliman, N., et al. (2006). The consensus coding sequences of human breast and colorectal cancers. Science *314*, 268–274.

Valeri, N., Croce, C.M., and Fabbri, M. (2009). Pathogenetic and clinical relevance of microRNAs in colorectal cancer. Cancer Genomics Proteomics *6*, 195–204.

Valeri, N., Gasparini, P., Fabbri, M., Braconi, C., Veronese, A., Lovat, F., Adair, B., Vannini, I., Fanini, F., Bottoni, A., et al. (2010). Modulation of mismatch repair and genomic stability by miR-155. Proc. Natl. Acad. Sci. USA *107*, 6982–6987.

Waugh, D.J., and Wilson, C. (2008). The interleukin-8 pathway in cancer. Clin. Cancer Res. *14*, 6735–6741.

Xu, X.L., Yu, J., Zhang, H.Y., Sun, M.H., Gu, J., Du, X., Shi, D.R., Wang, P., Yang, Z.H., and Zhu, J.D. (2004). Methylation profile of the promoter CpG islands of 31 genes that may contribute to colorectal carcinogenesis. World J. Gastroenterol. *10*, 3441–3454.

Yeatman, T.J. (2004). A renaissance for SRC. Nat. Rev. Cancer *4*, 470–480.

Yoon, J., Koo, K.H., and Choi, K.Y. (2011). MEK1/2 inhibitors AS703026 and AZD6244 may be potential therapies for KRAS mutated colorectal cancer that is resistant to EGFR monoclonal antibody therapy. Cancer Res. *71*, 445–453.

Yuki, D., Lin, Y.M., Fujii, Y., Nakamura, Y., and Furukawa, Y. (2004). Isolation of LEM domain-containing 1, a novel testis-specific gene expressed in colorectal cancers. Oncol. Rep. *12*, 275–280.

CellPress

Cancer Cell
Article

Dual Function of p38α MAPK in Colon Cancer: Suppression of Colitis-Associated Tumor Initiation but Requirement for Cancer Cell Survival

Jalaj Gupta,[1] Ivan del Barco Barrantes,[1] Ana Igea,[1] Stratigoula Sakellariou,[2] Ioannis S. Pateras,[2] Vassilis G. Gorgoulis,[2,3] and Angel R. Nebreda[1,4,*]

[1]Institute for Research in Biomedicine (IRB Barcelona), 08028 Barcelona, Spain
[2]Department of Histology and Embryology, School of Medicine, University of Athens, Athens 11527, Greece
[3]Biomedical Research Foundation of the Academy of Athens, Athens 11527, Greece
[4]Institució Catalana de Recerca i Estudis Avançats (ICREA), 08010 Barcelona, Spain
*Correspondence: angel.nebreda@irbbarcelona.org
http://dx.doi.org/10.1016/j.ccr.2014.02.019

SUMMARY

Colorectal cancer is frequently associated with chronic inflammation, with the intestinal epithelial barrier playing an important protective role against the infections and injuries that cause colitis. The p38α pathway regulates inflammatory responses but can also suppress tumor initiation in epithelial cells. We have found that p38α signaling has a dual function in colorectal tumorigenesis. On one side, p38α protects intestinal epithelial cells against colitis-associated colon cancer by regulating intestinal epithelial barrier function. Accordingly, p38α downregulation results in enhanced colitis-induced epithelial damage and inflammation, which potentiates colon tumor formation. Surprisingly, inhibition of p38α in transformed colon epithelial cells reduces tumor burden. Thus, p38α suppresses inflammation-associated epithelial damage and tumorigenesis but contributes to the proliferation and survival of tumor cells.

INTRODUCTION

Cancer is a complex disease that arises through a multistep, mutagenic process. Acquisition of cancer cell features involves changes in the wiring of signaling pathways that are normally tightly regulated to control processes such as cell proliferation, survival, and differentiation, which are critical to maintain tissue homeostasis.

Colorectal tumors are of epithelial origin and develop from sequential mutations in the Wnt signaling pathway, K-Ras, p53, and the transforming growth factor (TGF)-β pathway (Fearon and Vogelstein, 1990; Ullman and Itzkowitz, 2011). Most of these mutations are induced by environmental factors, such as chronic inflammation of the colon epithelia. It is well established that chronic inflammation may lead to increased risk of several types of cancer (Mantovani et al., 2008; Schetter et al., 2010). For example, patients with inflammatory bowel disease (IBD), such as Crohn's disease and ulcerative colitis, have higher risk of colorectal cancer development than the healthy population (Gillen et al., 1994). The intestinal epithelial barrier plays an important role protecting the gastrointestinal tract. This barrier consists of a mucus layer, which acts as a physical barrier, and the epithelial layer firmly adhered with epithelial tight junctions (Rescigno, 2011). Defects in the barrier function allow direct contact of intestinal mucosa with the luminal invading pathogens and ingested toxins promoting inflammatory responses. IBD and colon cancer have been associated with abnormal epithelial barrier function (Schmitz et al., 1999; Westbrook et al., 2010; Grivennikov et al., 2012). Moreover, mouse models with defects in epithelial barrier have increased susceptibility to colitis and colorectal tumor formation, providing evidence for the regulation of inflammation and tumorigenesis

Significance

Inflammatory bowel disease (IBD) patients have higher risk of colorectal cancer development, but the knowledge of signaling pathways involved in the pathogenesis of IBD is limited. In this study, we show that p38α signaling in epithelial cells is required to maintain epithelial barrier function and intestinal homeostasis, controlling the severity of colitis. Thus, p38α negatively regulates the formation of colitis-associated colon tumors. It is striking that transformed intestinal epithelial cells rely on p38α signaling for survival and proliferation. The reduced colon tumor burden observed on genetic downregulation or pharmacological inhibition of p38α suggests therapeutic opportunities for colorectal cancer by targeting this pathway.

by the intestinal epithelial barrier in vivo (Laukoetter et al., 2007; Van der Sluis et al., 2006).

p38α is a mitogen-activated protein kinase (MAPK) that regulates the cellular responses to stress but also has other functions, including crucial roles in inflammation and tissue homeostasis (Cuenda and Rousseau, 2007). Genetic inactivation of p38α in myeloid cells supports the importance of this pathway in cytokine production and inflammatory responses (Kang et al., 2008; Kim et al., 2008a). There is also evidence that p38α signaling controls tissue homeostasis by inducing differentiation while negatively regulating proliferation of many cell types, including epithelial cells (Cuadrado and Nebreda, 2010). It is interesting that p38α-deficient mice are more susceptible to K-Ras-induced lung tumorigenesis and to diethylnitrosamine (DEN)/phenobarbital (Pb)-induced liver cancer, indicating that p38α can function as a tumor suppressor in vivo (Hui et al., 2007; Ventura et al., 2007). However, there is little evidence for p38α inactivating mutations in tumors, which probably reflects that cancer cells take advantage of the ability of this signaling pathway to control multiple cellular processes. In line with this idea, chemical inhibitors of p38α have been shown to impair the proliferation of some human cancer cell lines (Wagner and Nebreda, 2009).

Given the role of the p38α pathway in orchestrating inflammatory responses while negatively regulating epithelial cell transformation, we investigated how these two functions are balanced in colon epithelia during colitis-associated colorectal cancer (CAC).

RESULTS

Downregulation of p38α in Intestinal Epithelial Cells Increases CAC

We generated mice expressing Villin-Cre and p38α-lox alleles to downregulate p38α in intestinal epithelial cells (IEC) (p38α-Δ^{IEC}). The efficiency of p38α downregulation was confirmed by western blotting in isolated IEC and in whole-colon lysates (Figure 1A). To investigate the role of p38α in CAC, we used a protocol that combines the carcinogen azoxymethane (AOM) with dextran sodium sulfate (DSS)-induced colitis (Figure 1B). When we applied the AOM/DSS protocol, p38α-Δ^{IEC} mice and wild-type (WT) littermates developed colon tumors mainly in the distal to middle colon (Figure 1C), which is the predominant localization of human colorectal tumors. We noticed that p38α-Δ^{IEC} mice had more macroscopic tumors (Figure 1D; Figure S1A available online), and the average tumor load was also higher but the average size was not affected (Figure 1D). Histological analyses confirmed more low-grade and high-grade tumors in p38α-Δ^{IEC} mice, but the relative proportion of low- versus high-grade tumors was similar in p38α-Δ^{IEC} and WT mice (Figure 1E). We also analyzed cell proliferation and apoptosis in these tumors and found no significant differences between WT and p38α-Δ^{IEC} mice (Figures 1F and S1B).

Inflammatory mediators are upregulated during AOM/DSS-induced colon tumorigenesis. We found that AOM/DSS-treated p38α-Δ^{IEC} mice showed higher COX-2 and interleukin (IL)-6 mRNA levels in the colon than the treated WT mice (Figure S1C). It is interesting that circulating IL-6 levels were also higher in serum from p38α-Δ^{IEC} mice at the end of the AOM/DSS protocol (Figure S1D). This is consistent with the known importance of IL-6 in colon tumor development.

Analysis of genomic DNA by quantitative PCR (qPCR) showed a substantial deletion of the floxed exon 2 of p38α in EpCAM$^+$ tumor epithelial cells, but not in CD45$^+$ leukocytes, from p38α-Δ^{IEC} mice versus WT mice (Figure 1G). Western blot analysis confirmed the downregulation of p38α protein in colon tumors from p38α-Δ^{IEC} mice (Figure S1E). The increased tumor burden observed in p38α-Δ^{IEC} mice without apparent effect on tumor size suggests that epithelial p38α signaling suppresses CAC by regulating tumor initiation.

p38α-Δ^{IEC} Mice Are More Susceptible to DSS-Induced Colitis and Epithelial Damage

AOM is a potent DNA damage-inducing agent that induces rapid p53-dependent apoptosis of IEC at the crypt base (Toft et al., 1999). However, AOM-induced DNA damage and apoptosis were similar in the colon from WT and p38α-Δ^{IEC} mice (Figures S2A and S2B), suggesting that the differences in tumorigenesis between WT and p38α-Δ^{IEC} mice were not due to a different initial response of IEC to AOM.

Next, we investigated the role of p38α in DSS-induced acute colitis, which is critical for AOM/DSS-induced tumorigenesis. After 5 days of DSS administration, p38α-Δ^{IEC} mice lost more body weight than WT mice (Figure 2A) suggesting that p38α-Δ^{IEC} mice probably had enhanced inflammation and intestinal damage, as body weight loss is one of the indicators for the severity of DSS-induced colitis. To confirm this possibility, mice were given DSS for 5 days and analyzed 1 or 3 days later. At both days 6 and 9, the WT colon showed minimal to mild inflammation, while colon from p38α-Δ^{IEC} mice showed moderate to severe inflammation, with many areas of complete crypt loss and erosions (Figure 2B). We also noticed that DSS-treated p38α-Δ^{IEC} mice had significantly more epithelial damage in the distal-middle part of the colon (Figure 2C).

Increased Inflammatory Cell Infiltration in p38α-Δ^{IEC} Mice Treated with DSS

Since p38α-Δ^{IEC} mice showed higher epithelial damage and inflammation, we characterized immune cell infiltration in the colon from DSS-treated mice. At day 6, we found a higher number of infiltrating cells in the colon of p38α-Δ^{IEC} mice than in WT mice (Figure 2D). Flow cytometry analyses showed more leukocytes (CD45$^+$ cells) in both epithelial/intraepithelial and lamina propria fractions of p38α-Δ^{IEC} mice. B cells (CD45$^+$CD19$^+$) also accumulated more in the lamina propria of p38α-Δ^{IEC} mice, whereas neutrophil (CD45$^+$CD11b$^+$Gr1$^+$) infiltration was very similar in the colons of WT and p38α-Δ^{IEC} mice (Figure S2C). We also found more macrophages in the colon of DSS-treated p38α-Δ^{IEC} mice compared to WT mice, whereas untreated mice showed no differences in macrophage infiltration (Figure S2D).

Infiltrating immune cells produce cytokines and chemokines to resolve the inflammation process. We found that IL-6 and COX-2 mRNAs were both upregulated in the colon from DSS-treated p38α-Δ^{IEC} mice compared to WT mice, whereas IL-1α and tumor necrosis factor α (TNF-α) mRNAs did not change. Basal expression levels of these mRNAs were comparable in untreated WT and p38α-Δ^{IEC} mice (Figure 2E). We also found higher IL-6

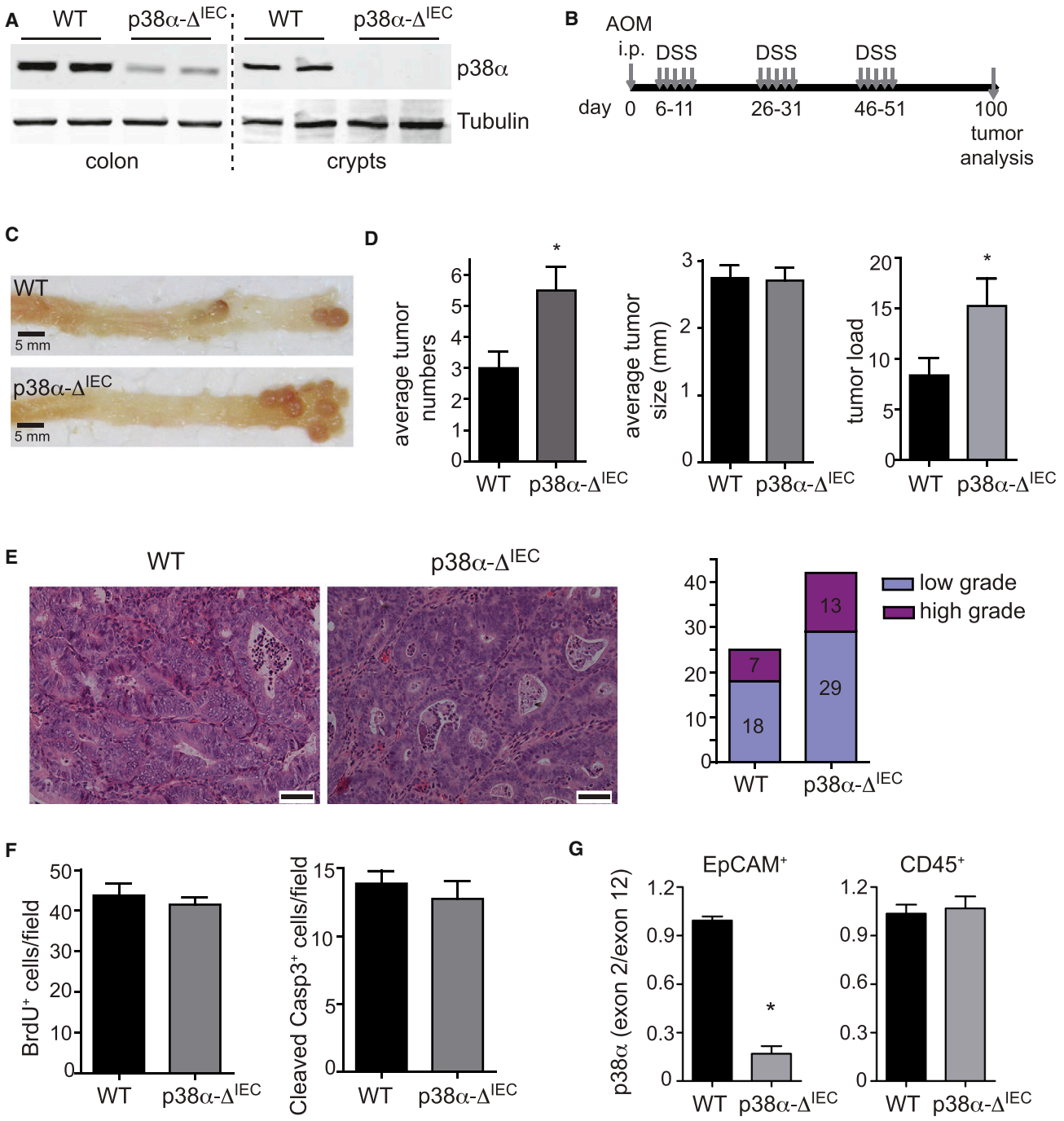

Figure 1. Downregulation of p38α in IEC Increases Susceptibility to AOM/DSS-Induced Colon Tumorigenesis

(A) Western blotting of p38α in whole-colon lysates (colon) and in isolated IEC (crypts).

(B) Schematic representation of the AOM/DSS protocol. i.p., intraperitoneal.

(C) Representative images of colon tumors.

(D) Average tumor number, size, and load. Data represent means ± SEM ($n \geq 6$). *$p < 0.05$.

(E) Representative images of H&E-stained colon tumors at the end of the AOM/DSS protocol. Scale bars, 50 μm. Tumors were microscopically analyzed and classified into low or high grade (n = 8).

(F) Colon sections were stained for bromodeoxyuridine (BrdU) or cleaved caspase 3 and quantified. Data represent means ± SEM (n = 4).

(G) Relative amount of the floxed exon 2 of p38α versus exon 12 (as a control) was determined by qPCR in EpCAM$^+$ epithelial cells and CD45$^+$ leukocytes. Data are means ± SEM ($n \geq 11$). *$p < 0.05$.

See also Figure S1.

protein levels both in colon lysates and in blood serum from DSS-treated p38α-Δ^{IEC} mice (Figure 2F). The increased IL-6 levels observed in p38α-Δ^{IEC} mice were unexpected, since the p38α pathway is known to positively regulate IL-6 expression in several cell types (Cuenda and Rousseau, 2007). Expression analysis using flow-cytometry-isolated cells showed that IL-6, IL-1α, and COX-2 mRNAs were all upregulated in IEC from DSS-treated p38α-Δ^{IEC} mice compared to WT mice, whereas TNF-α mRNA levels did not change. In contrast, the aforementioned inflammatory mediators were expressed at similar levels in the leukocytes from colon of WT or p38α-Δ^{IEC} mice (Figure S2E), which is consistent with the leukocytes being WT in both cases. Thus, the upregulation of IL-6 and COX-2 can be probably explained by both the presence of more infiltrating immune cells in colon of p38α-Δ^{IEC} mice and the enhanced expression of these cytokines in p38α-deficient IEC. Consistent with the increased IL-6 expression observed in DSS-treated p38α-Δ^{IEC} mice, we also detected phosphorylation and degradation of IκBα, suggesting activation of the NF-κB pathway, as well as enhanced phosphorylation of STAT3, a downstream target of IL-6 family receptors (Figure 2G).

Loss of p38α in IEC Induces Apoptosis and Hyperproliferation on DSS Treatment

Epithelial apoptosis is one of the mechanisms by which DSS can induce intestinal inflammation and colitis. We found that treatment with DSS induced more apoptosis in p38α-Δ^{IEC} mice than in WT mice (Figure 3A). Western blotting of IEC isolated from WT mice confirmed that DSS treatment increased the activating phosphorylation of p38α (Figure 3B). Analysis of Bcl-2 family members revealed that the proapoptotic protein Bak was significantly upregulated in DSS-treated p38α-Δ^{IEC} mice, whereas Bax and the antiapoptotic proteins Mcl-1, Bcl-2, and Bcl-XL were expressed at similar levels in DSS-treated WT and p38α-Δ^{IEC} mice (Figure 3B). In contrast, p53 expression and JNK phosphorylation levels were not changed (Figure 3B), suggesting that these pathways do not contribute to the enhanced apoptosis observed in DSS-treated p38α-Δ^{IEC} mice. Therefore, increased apoptosis, probably mediated by upregulation of Bak, could explain the increased epithelial damage and inflammation observed in the p38α-Δ^{IEC} mice on DSS treatment.

In response to the DSS-induced damage, the intestinal epithelium starts the repair and regeneration process by increasing cell proliferation. Since we detected more IL-6, an important regulator of the proliferation and survival of IEC (Bollrath et al., 2009; Grivennikov et al., 2009), we analyzed cell proliferation in the colon from DSS-treated mice. At day 6, we observed similar cell proliferation levels in intact crypts of WT and p38α-Δ^{IEC} mice; however, p38α-Δ^{IEC} mice had more proliferative cells than WT mice had in the areas of complete crypt loss, which probably represents a mixture of IEC and inflammatory cells (Figure 3C). At days 9 and 13, we found higher proliferation rates in IEC from WT and p38α-Δ^{IEC} mice compared to untreated mice. It is surprising that IEC proliferation was much higher in p38α-Δ^{IEC} than in WT mice during epithelium regeneration (Figure 3C). These data suggest that p38α downregulation results in IEC hyperproliferation after DSS-induced epithelial damage.

DSS Treatment Suffices to Induce Colon Tumors in p38α-Δ^{IEC} Mice

Unchecked compensatory proliferation and regeneration induced in response to repetitive tissue injury can promote tumorigenesis (Kuraishy et al., 2011). To test this possibility, we treated mice with three cycles of DSS but in the absence of the AOM carcinogen (Figure 4A). Macroscopic examination revealed that WT mice did not develop any tumors; however, about 60% of the p38α-Δ^{IEC} mice developed at least one colon tumor (Figure 4A). Histological examination confirmed the presence of colon tumors in p38α-Δ^{IEC} mice, which also contained more aberrant crypt foci with hyperchromatism of nuclei and hyperplastic crypts compared to WT mice (Figure 4B). The tumors formed in p38α-Δ^{IEC} mice had mutated β-catenin, corresponding to a GSK3β phosphorylation site, which leads to β-catenin activation and nuclear localization (Figures S3A and S3B). In addition, there were more macrophages in colon from p38α-Δ^{IEC} mice than from WT mice (Figure 4C). The inflammatory mediators COX-2, IL-6, TNF-α, and IL-12p40 were also expressed at higher levels in the colon from p38α-Δ^{IEC} mice than from WT mice (Figure 4D). Taking together, these data suggest that repeated DSS-induced epithelial injury in the absence of p38α results in uncontrolled hyperproliferation of IEC and a protumorigenic microenvironment that ultimately can induce colon hyperplasia and tumor formation.

p38α Regulates Homeostasis and Barrier Function in Normal Intestinal Epithelium

Alterations in epithelial barrier function have been associated with IBD and colon cancer (Grivennikov et al., 2012; Westbrook et al., 2010). We hypothesized that the increased epithelial damage and inflammation observed on p38α downregulation could be due to altered intestinal homeostasis and barrier function. In agreement with a recent report (Otsuka et al., 2010), we found that p38α downregulation in IEC had no effect on colon morphology, although p38α-Δ^{IEC} mice had more proliferative colon cells than the WT littermates. We also analyzed two main types of differentiated colon cells and found fewer chromogranin A^+ (ChgA) enteroendocrine cells and periodic acid-Schiff $^+$ (PAS) goblet cells in p38α-Δ^{IEC} mice compared to WT mice (Figure 5A; Figure S4A). Expression analysis confirmed upregulation of genes encoding proteins associated with cell proliferation (Ki67 and cyclin D1) and downregulation of differentiation-related genes (*MUC-2*, *TFF3*, and *ChgA*) in p38α-Δ^{IEC} mice (Figure S4B). These results indicate that p38α signaling can modulate both proliferation and differentiation of IEC.

Epithelial tight junctions are intercellular junctional complexes that regulate the paracellular permeability and are important for integrity of the epithelial barrier. Each tight junction contains a series of apparent fusions, called kissing points, where the intercellular space is completely obliterated (Tsukita et al., 2001). To investigate the epithelial barrier function, we first analyzed the effect of p38α downregulation on intestinal permeability. Using fluorescein isothiocyanate (FITC)-dextran, we found that in vivo intestinal permeability was notably increased in p38α-Δ^{IEC} mice (Figure 5B). Electron microscopy analysis revealed that epithelial tight junctions in colon from p38α-Δ^{IEC} mice were morphologically disrupted and had fewer kissing points compared to WT mice (Figures 5C and S4C). ZO-1 is a key

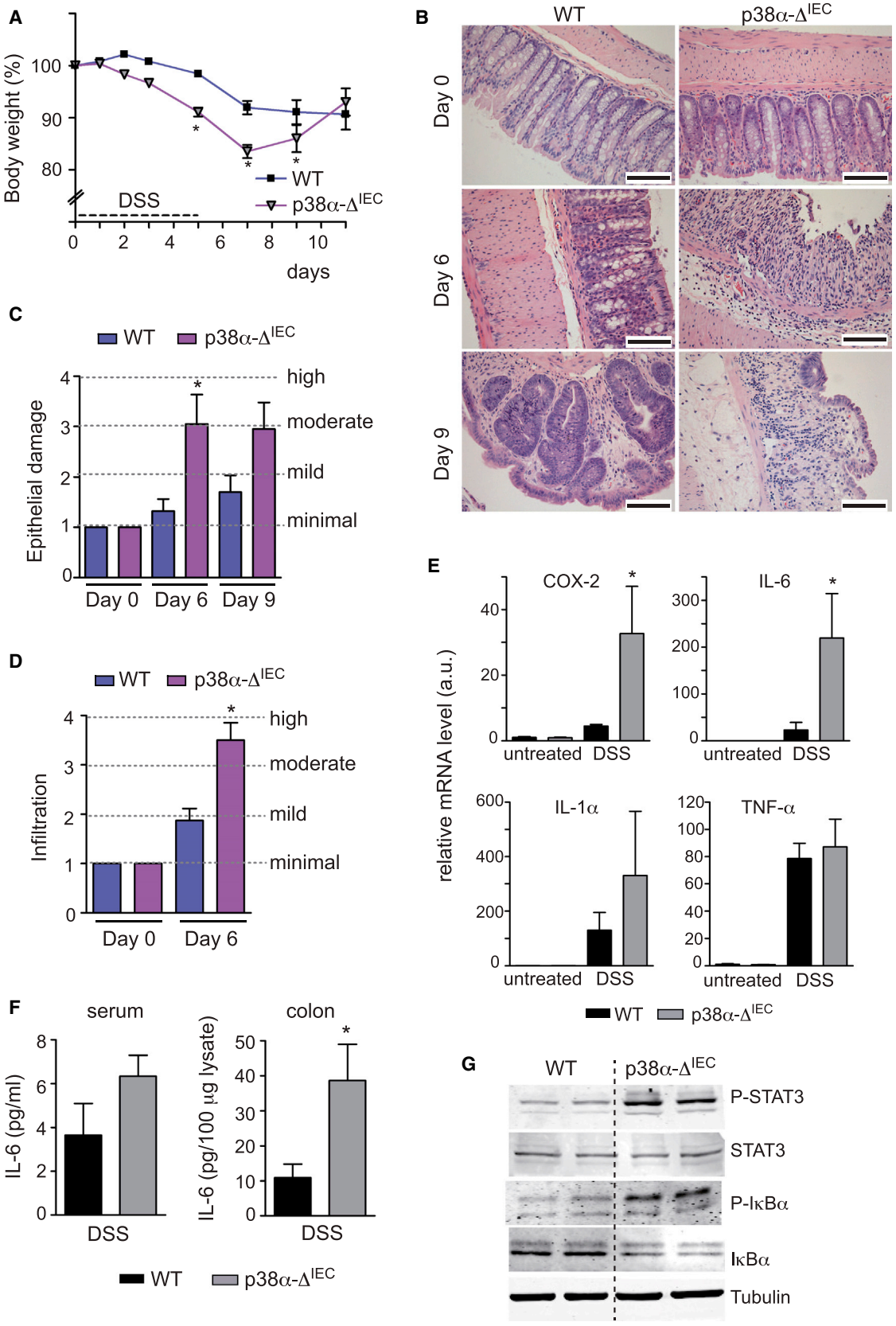

(legend on next page)

component of tight junctions, which helps other proteins such as claudins and occludin to assemble at a tight junction (McNeil et al., 2006). Expression of ZO-1 was reduced in p38α-Δ^{IEC} mice, while claudin-1 and occludin seemed to be expressed at similar levels in WT and p38α-Δ^{IEC} mice (Figures 5D and S4D). These results suggest a role for p38α in the regulation of intestinal epithelia tight junction assembly and barrier function. In agreement with a recent study (Grivennikov et al., 2012), we also found upregulation of IL-23 mRNA in colon tumors versus normal tissue, but no differences were detected between WT and p38α-Δ^{IEC} mice. Similarly, IL-17 mRNA was expressed at similar levels in WT and p38α-Δ^{IEC} mice (Figure S4E). Thus, the epithelial barrier defect observed in p38α-Δ^{IEC} mice does not seem to be associated with IL-23 and IL-17 upregulation, but it is probably a consequence of the regulation by p38α of epithelial tight junction assembly.

To investigate whether intestinal barrier defects have a causal role in the enhanced epithelial damage induced by DSS in p38α-Δ^{IEC} mice, we used the probiotic mixture VSL#3 to protect the epithelial barrier (Mennigen et al., 2009). It is interesting that VSL#3 treatment for 7 days rescued the increased intestinal permeability observed in p38α-Δ^{IEC} mice (Figure 5E). Moreover, VSL#3 also rescued the enhanced apoptosis, the body weight loss, and the epithelial damage induced by DSS in p38α-Δ^{IEC} mice (Figures 5F–5H). These results support that the impaired epithelial barrier function contributes to the DSS-induced phenotypes of p38α-Δ^{IEC} mice, and it seems therefore likely that the epithelial barrier defect also contributes to the enhanced CAC observed in p38α-Δ^{IEC} mice.

Downregulation of p38α in Tumor Epithelial Cells Reduces Tumor Burden

Chemical inhibitors of p38α have been reported to inhibit proliferation in some cancer cells, including human colon cancer cell lines (Wagner and Nebreda, 2009). However, our genetic analysis indicated that p38α suppressed colon tumor formation. To clarify the role of p38α in colon tumorigenesis, we generated a mouse line with Villin-CreERT2 and p38α-lox alleles (p38α-$\Delta^{IEC\text{-}ERT2}$). We confirmed that treatment with 4-hydroxy tamoxifen (4-OHT) induced p38α downregulation in colon but not in other tissues of p38α-$\Delta^{IEC\text{-}ERT2}$ mice (Figure S5A). Next, we verified our results using constitutive Villin-Cre by inducing p38α downregulation before DSS or AOM/DSS treatments (Figure S5B). We found that 4-OHT-treated p38α-$\Delta^{IEC\text{-}ERT2}$ mice developed more tumors than WT mice, but of similar size (Figure S5C). Moreover, after DSS treatment, p38α-$\Delta^{IEC\text{-}ERT2}$ mice lost more body weight than WT mice, as in the case of p38α-Δ^{IEC} mice (Figure S5D).

We next investigated the effect of p38α downregulation once colon tumors were formed. First, mice were subjected to the AOM/DSS protocol, and the presence of colon tumors was confirmed 65 days after the AOM injection. Then, mice with p38α-lox, and either with or without Villin-CreERT2, were injected with 4-OHT (Figure 6A). Three days after 4-OHT injection, p38α downregulation was poor, and no differences were detected in tumor number and size (Figure S5E). The downregulation of p38α improved at 10 days after 4-OHT injection when both tumor number and size started to decrease (Figure S5F). It is interesting that, 20 days after the last 4-OHT injection, tumors from p38α-$\Delta^{IEC\text{-}ERT2}$ mice were mostly p38α deficient, as determined by western blotting (Figure 6B), by immunohistochemistry (IHC) (Figure S5G), and by analyzing the deletion of the floxed exon 2 of p38α in genomic DNA (Figures S5H and S5I). At this time, we observed that the average number, size, and load of macroscopic tumors were significantly reduced in p38α-$\Delta^{IEC\text{-}ERT2}$ mice compared with WT mice (Figure 6C and 6D). Of note, tumor burden and average tumor size both increased in WT mice compared to those of the initial tumors, suggesting that tumors continue to grow after 4-OHT injection (Figure 6D). When tumor size distribution was analyzed, we found fewer big colon tumors on p38α downregulation in tumor epithelial cells (Figure 6D). However, histological analysis revealed no differences in tumors from WT or p38α-$\Delta^{IEC\text{-}ERT2}$ mice (Figure 6E). These results indicate a protumorigenic role for p38α in transformed colon epithelia cells.

Downregulation of p38α in Tumor Epithelial Cells Does Not Affect Tumor Permeability and Invasiveness

Recent studies described the importance of epithelial barrier function in colorectal tumors and invasiveness (Grivennikov et al., 2012; Schwitalla et al., 2013). We therefore investigated if the downregulation of p38α could result in more aggressive colon tumors. To test this hypothesis, p38α-$\Delta^{IEC\text{-}ERT2}$ mice were analyzed 45 days after 4-OHT injections. Initial experiments showed no differences in tumor burden or grading (Figures S6A and S6B), but western blotting revealed significant amounts of p38α in these tumors, probably corresponding to p38α-expressing escaper cells that repopulated the tumors in p38α-$\Delta^{IEC\text{-}ERT2}$ mice (Figure S6C). To circumvent this problem, we performed two rounds of 4-OHT injections (Figure S6D). In this case, we confirmed the sustained downregulation of p38α in the tumors (Figure S6E), which correlated with reduced tumor number and size in p38α-$\Delta^{IEC\text{-}ERT2}$ mice (Figure S6F). However, no differences were detected in histological tumor grading or aggressiveness between p38α-$\Delta^{IEC\text{-}ERT2}$ and WT mice (Figure S6G), suggesting that constant inhibition of p38α signaling is required

Figure 2. Downregulation of p38α in IEC Increases Susceptibility to DSS-Induced Colitis and Immune Cell Infiltration

(A) DSS was administered in drinking water for 5 days, and body weight was recorded. Data are means ± SEM ($n \geq 8$). *$p < 0.05$.

(B) Representative H&E-stained colon sections from mice either untreated or treated with DSS for 5 days and analyzed at days 6 and 9. Scale bars, 100 μm.

(C and D) Quantification of DSS-induced epithelial damage (C) and immune cell infiltration (D) in H&E-stained colon sections. Data represent means ± SEM (n = 4). *$p < 0.05$.

(E) Relative mRNA expression levels of inflammatory mediators in the distal colon of untreated and DSS-treated mice were determined by quantitative reverse transcription PCR (qRT-PCR). Expression levels in untreated WT and p38α-Δ^{IEC} mice were the same and were given the value of 1. Data are means ± SEM (n = 4). *$p < 0.05$.

(F) IL-6 protein levels in blood serum and whole-colon lysates of DSS-treated mice. Data are means ± SEM (n = 5).

(G) Colon lysates were prepared from DSS-treated mice and were analyzed by western blotting (one mouse per lane) with the indicated antibodies.

See also Figure S2.

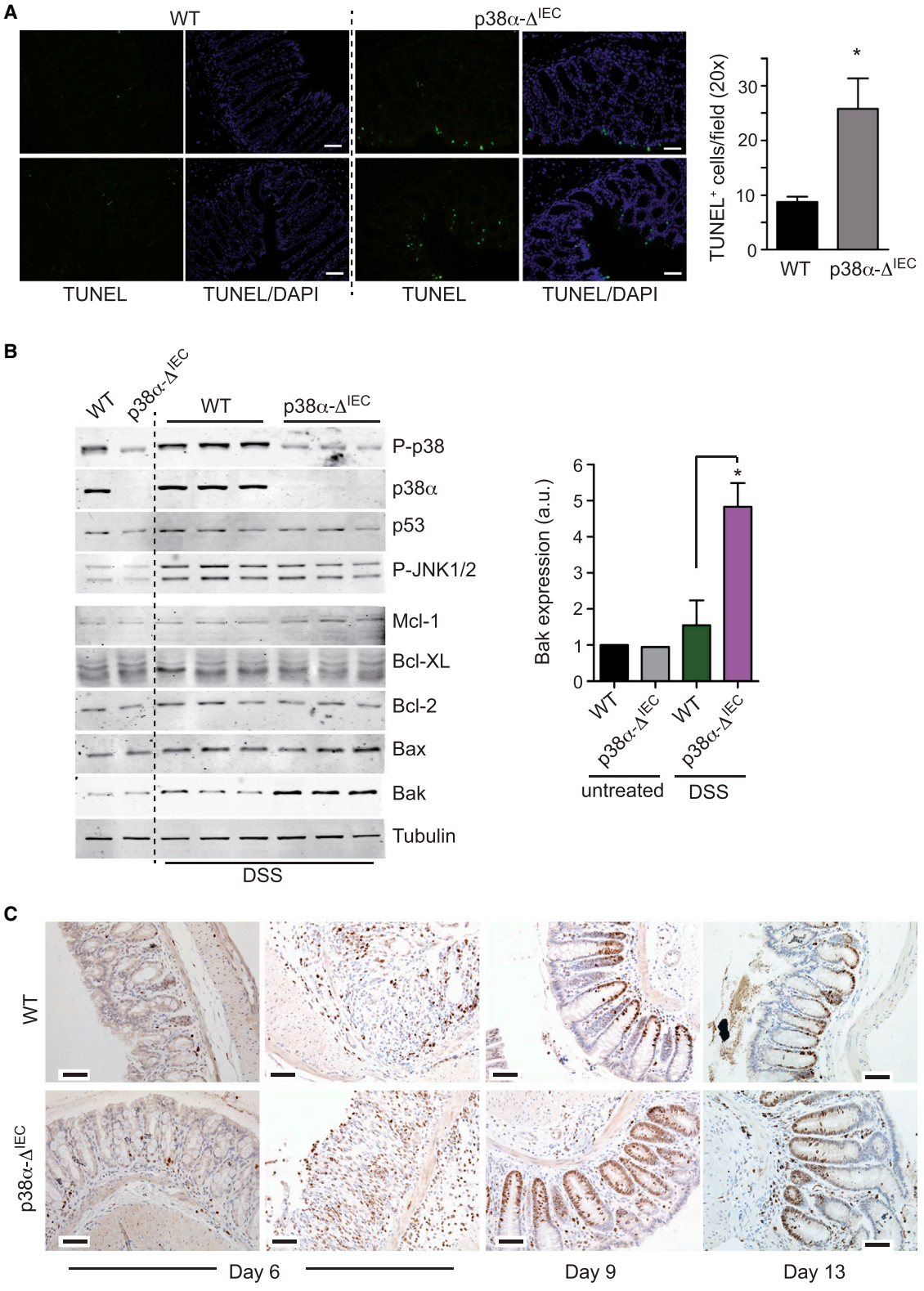

Figure 3. Downregulation of p38α in IEC Results in Enhanced DSS-Induced Apoptosis and Compensatory Proliferation

(A) Representative TUNEL staining of colon sections after 3 days of treatment with 3% DSS. Quantification is shown in the histogram. Data represent means ± SEM (n = 3). *p < 0.05.

(legend continued on next page)

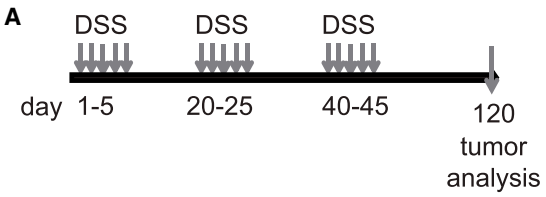

	WT	p38α-Δ^{IEC}
Number of mice	5	3 2 2
Tumors/mouse	0	0 1 2
Mice with tumors	0	57%

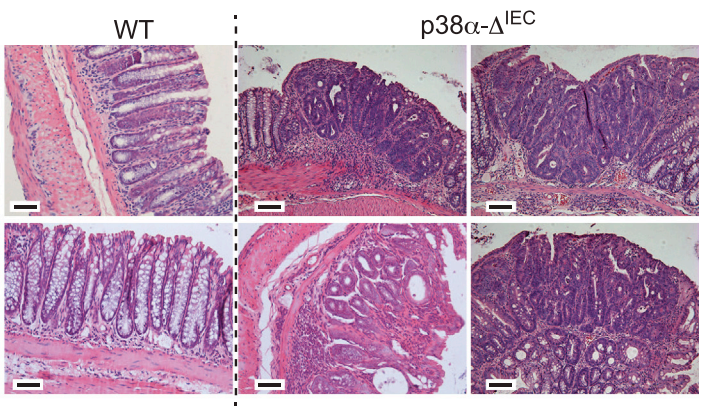

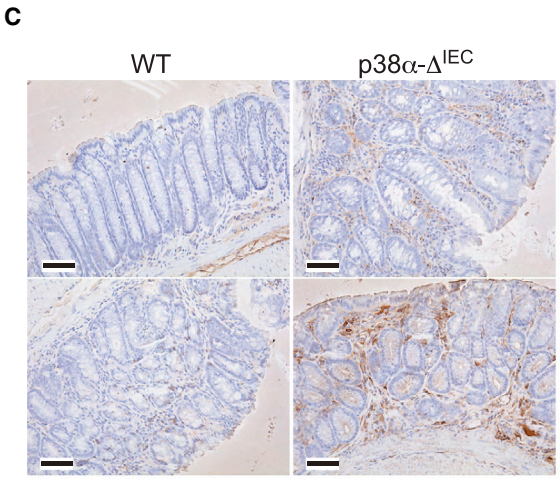

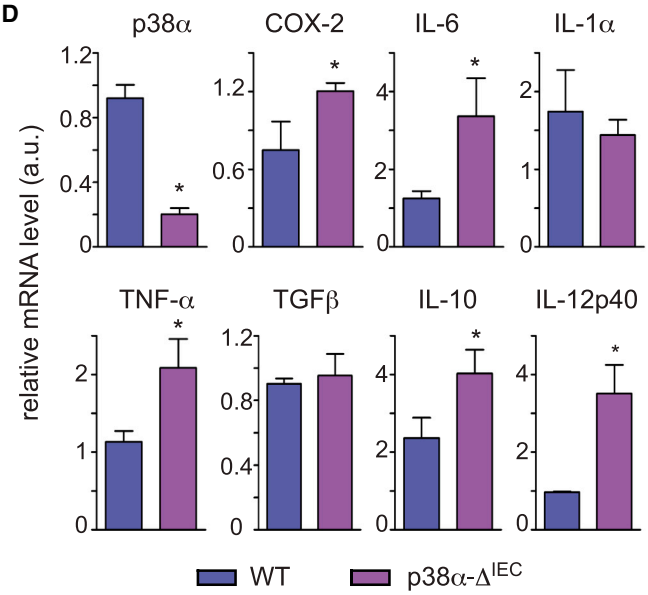

Figure 4. DSS Alone Suffices to Induce Colon Tumors in p38α-Δ^{IEC} Mice

(A) Schematic representation of the DSS protocol used to induce chronic colitis (top) and the summarized results (bottom).

(B) Representative images of H&E-stained colon sections at the end of the DSS treatment.

(C) Colon sections from mice treated with three cycles of DSS were stained for F4/80 to detect macrophages.

(D) Relative mRNA expression levels of the indicated genes in mouse colons were determined by qRT-PCR. Data are means ± SEM (n = 4). *p < 0.05.

Scale bars, 50 μm.

See also Figure S3.

to reduce colon tumor burden but that this apparently has no effect on tumor aggressiveness.

Next, we measured intestinal permeability and found that, similar to p38α-Δ^{IEC} mice, permeability was higher in untreated p38α-Δ$^{IEC\text{-}ERT2}$ mice than in WT mice, but we could detect no differences in tumor permeability between WT and p38α-Δ$^{IEC\text{-}ERT2}$ mice (Figure S6H; see also Supplemental Experimental Procedures for tumor permeability calculation). In agreement with the permeability analysis, we found that p38α downregulation in colon tumors did not affect expression of the tight junction components ZO-1, ZO-2, Claudin-1, Occludin, and JAM-C (Figures S6I and S6J). Taken together, these results indicate that the reduced tumor burden observed in p38α-Δ$^{IEC\text{-}ERT2}$ mice is unlikely to be associated with enhanced tumor

(B) Colon epithelial cells were obtained from untreated or DSS-treated mice, and samples were analyzed by western blotting (one mouse per lane) with the indicated antibodies. The histogram shows the quantification of Bak expression. Data represent means ± SEM (n = 3). *p < 0.05.

(C) Sections from the distal colon of mice treated with 2% DSS for 5 days were stained for Ki67 at days 6, 9, and 13. For day 6: the left panels show an area with intact crypts; the right panels show an area with damage and crypt loss. Panels for days 9 and 13 show regenerating epithelia.

Scale bars, 50 μm.

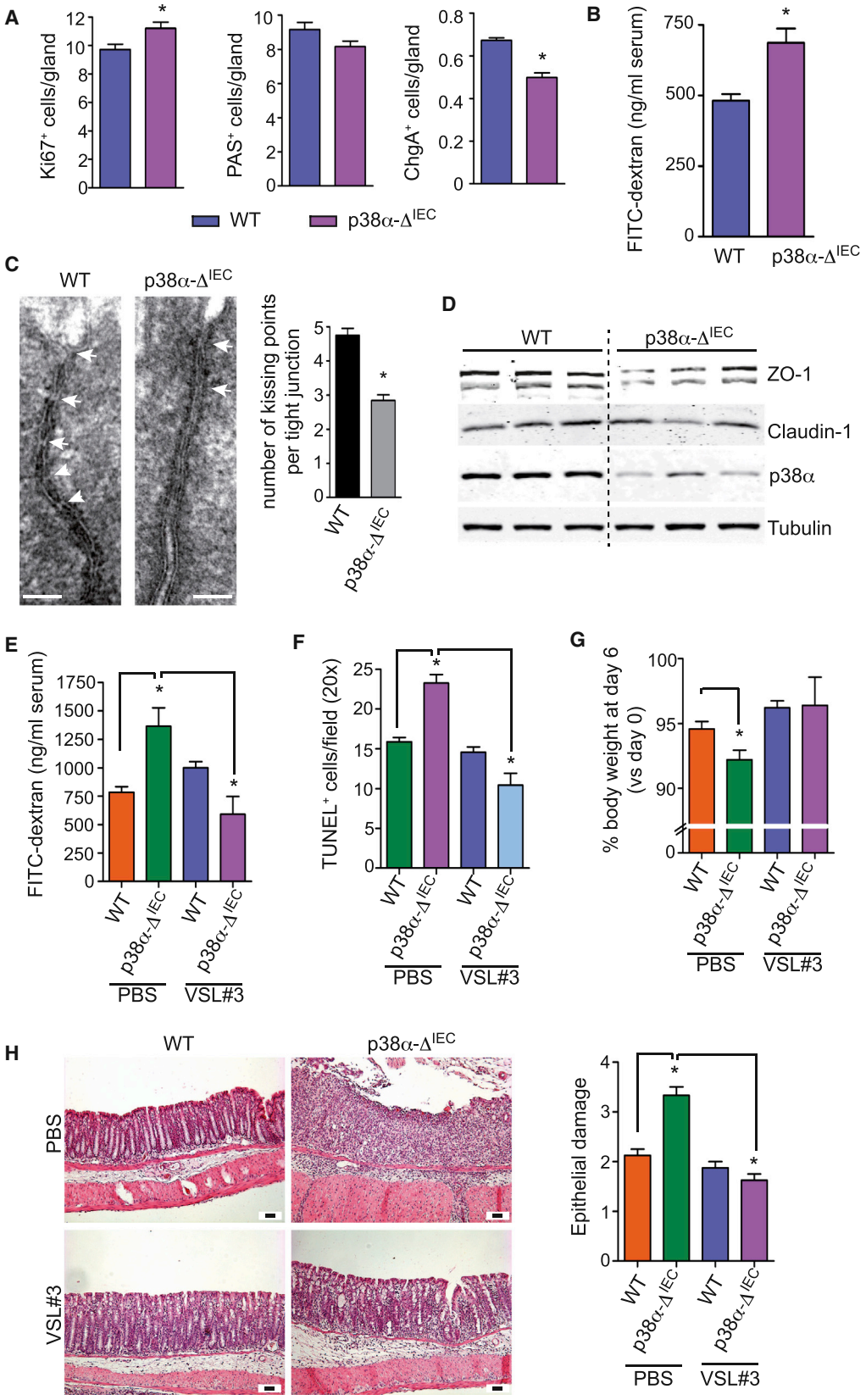

(legend on next page)

permeability and the alteration of tight junctions on p38α downregulation.

Downregulation of p38α Reduces Proliferation and Increases Apoptosis in Colon Tumor Cells

To investigate the molecular basis for the reduced tumorigenesis in p38α-$\Delta^{IEC\text{-}ERT2}$ mice, we analyzed the levels of cell proliferation and apoptosis. We found significantly reduced cell proliferation but increased apoptosis in the tumors from p38α-$\Delta^{IEC\text{-}ERT2}$ mice compared to WT mice (Figure 7A). In agreement with the known importance of the cytokines IL-6 and IL-11 and the chemokines CXCL-1 and CXCL-2 for colon tumorigenesis (Grivennikov et al., 2009; Jamieson et al., 2012; Katoh et al., 2013; Putoczki et al., 2013), we found that IL-6, IL-11, CXCL-1, and CXCL-2 were all significantly downregulated in the colon tumors from p38α-$\Delta^{IEC\text{-}ERT2}$ mice (Figure 7B). Both CXCL-1 and CXCL-2 attract cells expressing the CXCR2 receptor, mostly neutrophils and myeloid-derived suppressor cells that are positive for myeloperoxidase (MPO) staining and contribute to inflammation-driven tumorigenesis (Jamieson et al., 2012; Katoh et al., 2013). Reduced expression of CXCL-1 and CXCL-2 correlated with fewer MPO^+ cells in p38α-deficient tumors (Figure S6K). However, macrophage infiltration was not affected by downregulation of p38α in tumor cells (Figure 7C). We also found that p38α downregulation in colon tumors resulted in enhanced levels of phosphorylated JNK and reduced levels of phosphorylated STAT3, whereas the prosurvival pathways ERK1/2 and Akt were not affected (Figure 7D). Moreover, expression of the anti-apoptotic protein Mcl-1 was reduced in the p38α downregulated colon tumors, which may contribute to the enhanced apoptosis observed in p38α-$\Delta^{IEC\text{-}ERT2}$ mice (Figure 7E). These results support an important role for p38α in colon tumor maintenance by promoting proliferation and inhibiting apoptosis of the tumor cells.

Chemical Inhibition of p38α Reduces Colon Tumor Burden in Mice

The aforementioned findings were confirmed using PH797804, a chemical compound that potently inhibits p38α and is being used in clinical trials for inflammatory diseases (Goldstein et al., 2010). Colon tumors were induced using the AOM/DSS protocol, and then mice were separated in two groups that received either PH797804 or vehicle for 12 days (Figure 8A). We found that mice treated with the p38α inhibitor had a significantly reduced colon tumor load, reflecting both fewer tumors and smaller sizes compared to vehicle-treated mice (Figure 8B). IHC analysis confirmed the inhibition of colon tumorigenesis by administration of PH797804, which also reduced p38 MAPK signaling in the colon tumors and in adjacent normal epithelia (Figures 8C and 8D). These results extend our genetic analysis, indicating a protumorigenic role for p38α signaling in colon tumor cells. Moreover, incubation of Caco-2 and SW-620 human colon cancer cell lines with three different p38 MAPK chemical inhibitors resulted in enhanced apoptosis (Figure 8E), which correlated with increased levels of phosphorylated JNK (Figure 8E), as observed on p38α downregulation in mouse colon tumors.

Collectively, our results indicate that p38α signaling plays a dual role during colorectal tumorigenesis, suppressing the initial stages that lead to IEC transformation but contributing to tumor maintenance (Figure 8F).

DISCUSSION

In this study, we show that p38α suppresses colitis-associated colon tumor initiation by regulating the epithelial barrier function, which protects against epithelial damage and inflammation. However, once colon tumors are formed, p38α facilitates tumorigenesis by promoting proliferation and inhibiting apoptosis of the transformed epithelial cells.

In agreement with previous evidence for the tumor suppressor role of p38α in mouse models of lung and liver cancer (Hui et al., 2007; Ventura et al., 2007), we show that p38α downregulation in IEC enhances CAC. The AOM/DSS protocol is highly dependent on DSS, which induces epithelial apoptosis and inflammation. For example, downregulation of NEMO (NF-κB essential modulator) or STAT3 in IEC results in chronic colitis due to excessive IEC apoptosis (Bollrath et al., 2009; Nenci et al., 2007). Similarly, we show that p38α-deficient IEC undergo extensive apoptosis on DSS exposure, which correlates with the accumulation of the proapoptotic protein Bak. It has been proposed, in a different context, that negative regulation of Bak expression by p38α attenuates ionizing radiation-induced cell death (Kim et al., 2008b). The increased apoptosis observed in DSS-treated p38α-Δ^{IEC} mice extends a recent report showing more epithelial damage in p38α-deficient than in WT mice treated with DSS (Otsuka et al., 2010). In addition, we have found enhanced DSS-induced inflammatory cell infiltration in p38α-Δ^{IEC} mice. Different DSS treatment conditions might account for the discrepancies.

DSS-treated p38α-Δ^{IEC} mice produce increased levels of IL-6, a critical cytokine for colorectal tumorigenesis that regulates IEC

Figure 5. Downregulation of p38α in IEC Affects Intestinal Homeostasis and Paracellular Permeability

(A) Quantification of proliferating $Ki67^+$ cells, PAS^+ goblet cells, and $ChgA^+$ enteroendocrine cells. Data are means ± SEM (n = 4). *p < 0.05.

(B) Intestinal permeability was measured by determining the concentration of FITC-dextran in blood serum. Data are means ± SEM (n = 4). *p < 0.05.

(C) Representative electron microscope images showing tight junctions in colon epithelia. Scale bars, 50 nm. At least 25 tight junctions were analyzed. Histogram shows the quantification of the number of kissing points per tight junction. Data are means ± SEM. *p < 0.05.

(D) Colon lysates were analyzed by western blotting (one mouse per lane) with the indicated antibodies.

(E) Mice were treated with PBS or probiotic mixture VSL#3 for 1 week, and intestinal permeability was determined as in (B). Data are means ± SEM (n ≥ 3). *p < 0.05.

(F) Mice were treated as in (E) and then with 3% DSS for 3 days. $TUNEL^+$ apoptotic cells were quantified. Data are means ± SEM (n = 3). *p < 0.05.

(G) Mice were treated as in (E) and then with 2% DSS for 5 days. Body weights were recorded before starting the DSS treatment and at day 6. Data are means ± SEM (n ≥ 4). *p < 0.05.

(H) Mice were treated as in (G) and killed at day 6. Colon sections were stained with H&E and histologically analyzed. Scale bars, 50 μm. The histogram shows quantification of the epithelial damage. Data are means ± SEM (n ≥ 3). *p < 0.05.

See also Figure S4.

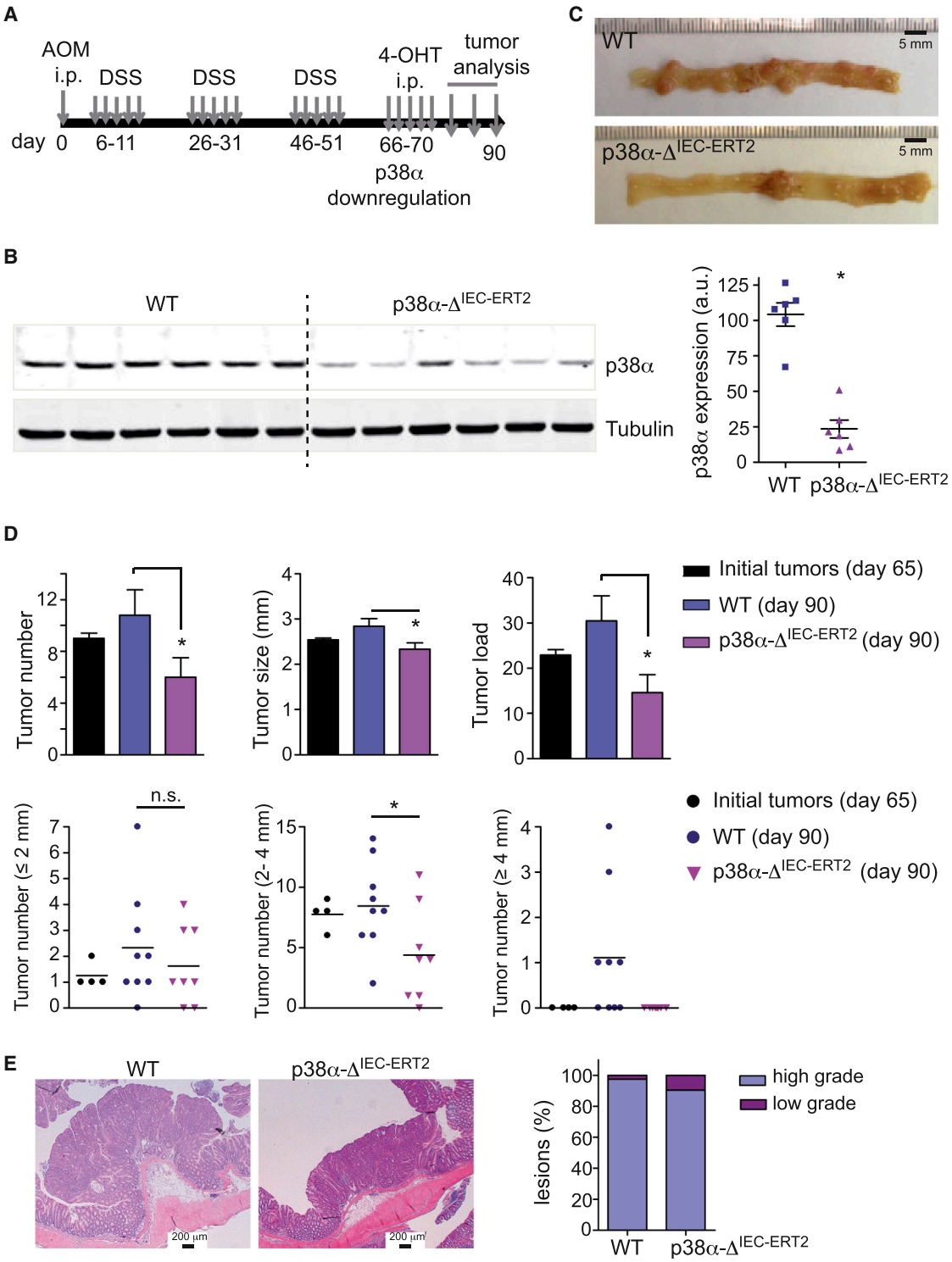

Figure 6. Downregulation of p38α in Colon Tumor Cells Reduces Tumor Burden

(A) Schematic representation of the protocol used to downregulate p38α in AOM/DSS-induced colon tumors.

(B) Colon tumors were analyzed by western blotting (one mouse per lane). Quantification is shown in the right panel. Data represent means ± SEM (n = 6). *$p < 0.05$.

(C) Representative images of colon tumors.

(D) Average tumor number, size, load, and tumor size distribution in initial tumors (day 65) and 20 days after the last 4-OHT injection (day 90). Data represent means ± SEM (n = 4 for initial tumors and n = 8 for WT and p38α-$\Delta^{IEC-ERT2}$). *$p < 0.05$.

(E) Colon tumor sections were stained with H&E and classified into low or high grade based on histological analysis (n = 8).

See also Figure S5.

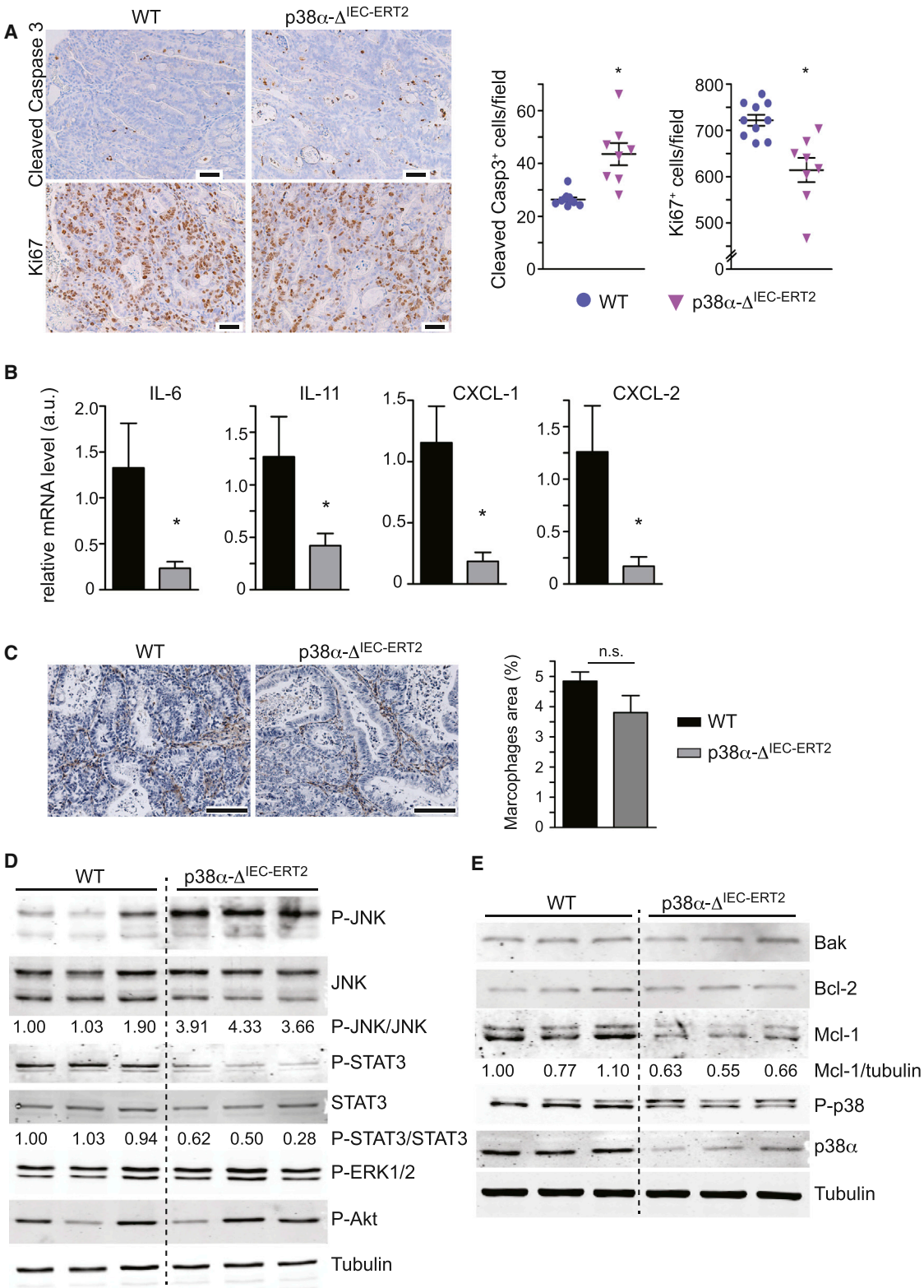

Figure 7. Downregulation of p38α Reduces Proliferation and Increases Apoptosis in Colon Tumor Cells

(A) Colon tumor sections were stained with the indicated antibodies. Scale bars, 50 μm. Quantifications are shown in the right panels. Data represent means ± SEM (n = 8). *p < 0.05.

(B) Relative mRNA expression levels for the indicated genes were determined by qRT-PCR. Data are means ± SEM (n = 4). *p < 0.05.

(legend continued on next page)

survival and proliferation and whose protumorigenic functions relay on the activation of the transcription factor STAT3 (Becker et al., 2004; Bollrath et al., 2009; Grivennikov et al., 2009). Sustained activation of the NF-κB pathway also contributes to tumor development by inducing expression of inflammatory mediators and growth factors (Greten et al., 2004). Consistent with these results, the STAT3 and NF-κB pathways are both upregulated in p38α-Δ^{IEC} mice after DSS-induced colitis. Enhanced damage and the inflammation-associated release of cytokines probably contribute to the hyperproliferation of IEC in p38α-Δ^{IEC} mice on repetitive DSS-induced epithelial injury.

Our results demonstrate the importance of p38α signaling in intestinal homeostasis and integrity of the colon epithelia. Of particular importance is the reduced number of mucus-producing goblet cells, which we and others (Otsuka et al., 2010) have observed in p38α-Δ^{IEC} mice. Mucins produced by goblet cells form a protective mucous layer, which serves as a first barrier to pathogens or chemical injury (Rescigno, 2011). Accordingly, *Muc2* knockout mice spontaneously develop colitis and intestinal tumors, but with a very low incidence (1.5 tumors per mouse at 1 year of age) (Van der Sluis et al., 2006; Velcich et al., 2002). However, *Muc2*$^{+/-}$ mice do not develop spontaneous colitis but are more sensitive to DSS-induced colitis (Van der Sluis et al., 2006). Similarly, the decreased expression of MUC2 in p38α-Δ^{IEC} mice is not sufficient to induce spontaneous colitis or tumors but is likely to facilitate DSS-induced colitis and colon tumor formation as in *Muc2*$^{+/-}$ mice.

The importance of intestinal epithelial integrity is emphasized by the altered paracellular permeability and tight junction functions observed in IBD patients (Schmitz et al., 1999; Westbrook et al., 2010). Moreover, it has been recently reported that colon tumors have defective epithelial barrier function, which has been associated with upregulation of IL-23 and IL-17 (Grivennikov et al., 2012). Mice lacking the tight junction protein JAM-A also show increased intestinal permeability and are more susceptible to DSS-induced colitis (Laukoetter et al., 2007). Downregulation of p38α in IEC affects epithelial barrier function, which does not correlate with IL-23 and IL-17 upregulation but with reduced expression of ZO-1, an important regulator of tight junction assembly. The probiotic mix VSL#3 can improve defective barrier function in a model of acute DSS-induced colitis (Mennigen et al., 2009). Experiments with VSL#3 support an important role for p38α in the regulation of intestinal barrier integrity, which protects against colitis-induced epithelial damage and the initiation of colon tumorigenesis. However, probiotics can also modify the gut microbiota, which might provide further beneficial effects by restoration of microbial communities and suppression of pathogens and immunomodulation (Preidis and Versalovic, 2009).

In contrast to the in vivo tumor suppressor function of p38α during the onset of several types of cancer, p38α might facilitate cancer cell proliferation and survival in established human cell lines and in some mouse models (reviewed by Wagner and Nebreda, 2009). These studies are mainly based on the use of SB203580 and SB202190, two chemical inhibitors that are known to have off-target effects (Fabian et al., 2005). For example, the induction of autophagy by SB202190 in colorectal cancer cells (Chiacchiera et al., 2009; Comes et al., 2007) has been ascribed to nonspecific effects rather than to the inhibition of p38α signaling (Menon et al., 2011). Here, we provide genetic and pharmacological evidence supporting the implication of p38α in colon tumor maintenance.

The defective barrier function of colon tumors results in increased permeability, which contributes to tumorigenesis by facilitating an enhanced inflammatory response and can also enable invasiveness by reducing adhesion of tumor epithelial cells (Grivennikov et al., 2012; Schwitalla et al., 2013). Given the role of p38α in normal epithelial barrier function, p38α downregulation could further enhance tumor permeability, which should promote tumorigenesis. However, our results show that p38α does not regulate tumor permeability, which is severely affected in colon tumors compared with normal intestine. Moreover, the downregulation of p38α reduces tumor burden without increasing tumor invasiveness, suggesting that p38α is unlikely to regulate the barrier function in tumors.

Previous studies showed that STAT3 is an important regulator of colon tumor cell survival and proliferation (Bollrath et al., 2009; Grivennikov et al., 2009), whose activation is strongly associated with expression of IL-6 and IL-11. Inhibition of STAT3, IL-6, or IL-11 greatly reduces tumor burden in inflammation-associated colon cancer (Grivennikov et al., 2009; Putoczki et al., 2013). The p38α pathway can control the production of proinflammatory cytokines (Cuenda and Rousseau, 2007). We have shown that expression of IL-6 and IL-11 is reduced in the tumors on p38α downregulation, which also correlates with reduced phosphorylation of STAT3. Autocrine mechanisms, such as the production of the aforementioned cytokines, could account for the observed link between p38α activity and STAT3 phosphorylation, although we cannot rule out that p38α might also regulate intracellular signaling pathways leading to STAT3 phosphorylation in tumor cells.

Inactivation of p38α in colon tumors induces significant apoptosis, which correlates with reduced expression of the antiapoptotic protein Mcl-1 and increased phosphorylation of JNK. It is interesting that p38α can negatively regulate JNK signaling by several mechanisms (Wagner and Nebreda, 2009), and sustained activation of JNK has been linked to the induction of apoptosis (Ventura et al., 2006). Moreover, JNK has been reported to mediate phosphorylation and degradation of Mcl-1 (Morel et al., 2009). Altogether, it seems likely that activation of JNK signaling together with reduced expression of Mcl-1 contribute to the increased apoptosis observed in colon tumors on p38α downregulation.

The reappearance of p38α-expressing tumors at 45 days after 4-OHT administration suggests that Villin-CreERT2 induction does not delete p38α in all transformed epithelial cells and that the WT escapers eventually repopulate the tumors (Figure 8F). Thus p38α-deficient tumor cells are at a selective disadvantage and are outcompeted by WT tumor cells, which is consistent with the increased apoptosis and reduced proliferation observed in

(C) Colon tumor sections were stained with F4/80 to detect macrophages. Scale bars, 100 μm. Quantifications are shown in the right panels. Data represent means ± SEM (n = 3).
(D and E) Colon tumor lysates were analyzed by western blotting (one mouse per lane) with the indicated antibodies.
See also Figure S6.

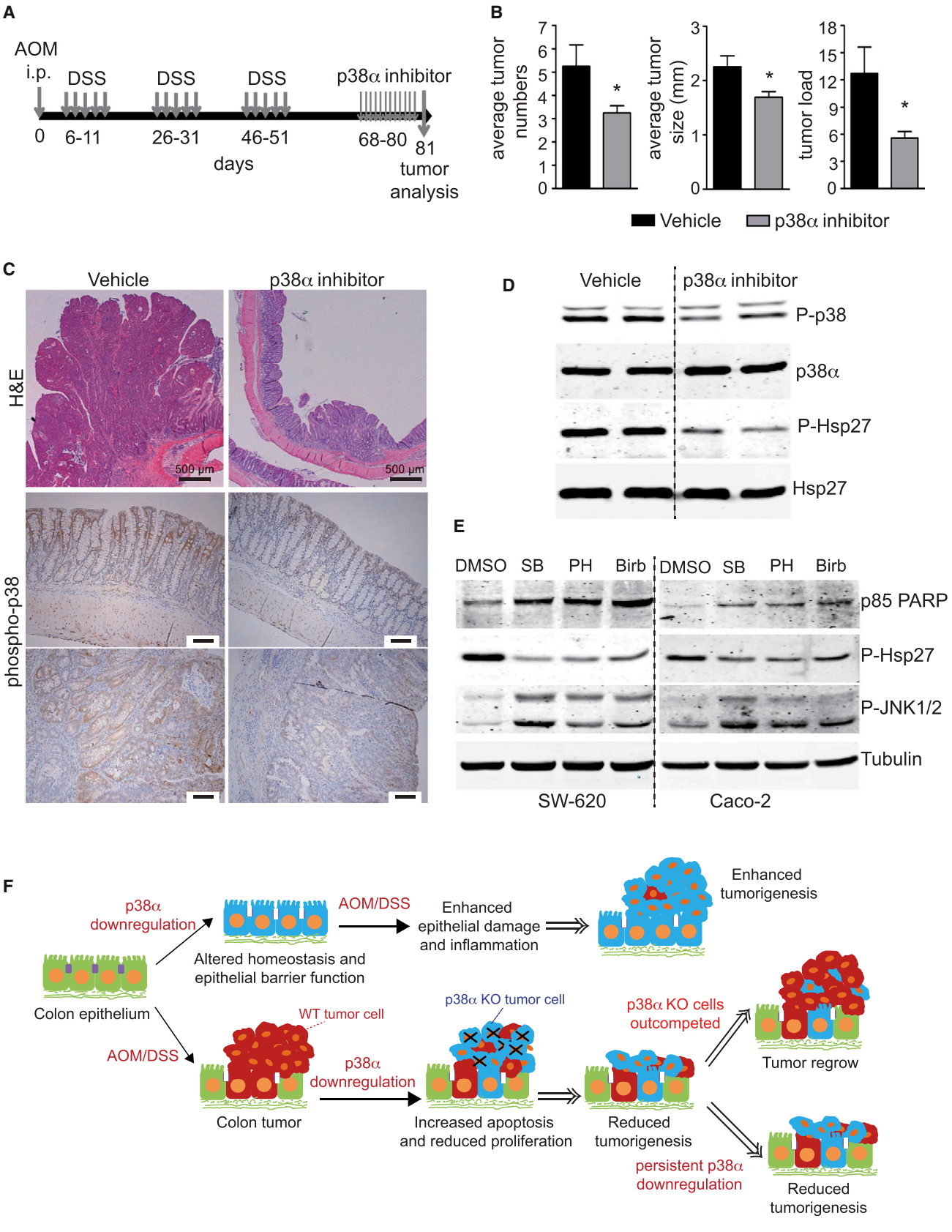

(legend on next page)

tumors on p38α downregulation. It is possible that the inducible Villin-CreERT2 might not be so effective in cancer intestinal stem cells. However, Villin-CreERT2 has been shown to be active in all IEC, including putative progenitor cells in the crypts (el Marjou et al., 2004), as well as during APC (adenomatous polyposis coli)-induced polyp formation (Sonoshita et al., 2011). Moreover, global gene expression analysis has shown that normal intestinal stem cells are very similar to the cancer stem cells (Merlos-Suárez et al., 2011). It is, therefore, likely that Villin-CreERT2 works in normal intestinal stem cells as well as in all compartments of the intestinal epithelia during cell transformation and adenoma progression. In any case, it seems that p38α promotes viability of the majority of colon tumor cells, based on the substantially impaired colon tumor growth observed on downregulation or inhibition of p38α, and the observation that colon tumors do not regrow when p38α downregulation is maintained.

Our results also provide an example of a nononcogenic addictive pathway that is important for tumor maintenance (Luo et al., 2009). The requirement of p38α for colon cancer cell survival and proliferation does not imply that the pathway should be necessarily upregulated in colon tumor cells. Nevertheless, enhanced levels of phosphorylated p38 MAPK have been detected in human colon tumor samples, both in cancer cells and in stromal cells (Hardwick et al., 2001; Paillas et al., 2011).

In summary, we describe a dual role of p38α signaling in colon tumorigenesis, suppressing inflammation-associated colon tumor initiation but contributing to tumor maintenance (Figure 8F). It has been reported that the p38α pathway can play different roles during skin tumorigenesis in epithelial or endothelial cells (Yoshizuka et al., 2012). Our in vivo experiments indicate that p38α functions as tumor suppressor or promoter in normal and transformed IEC, respectively. It remains to be determined how p38α signaling in other cell types contributes to colorectal tumorigenesis.

EXPERIMENTAL PROCEDURES

Mice

p38α-Δ^{IEC} mice and p38α-$\Delta^{IEC\text{-}ERT2}$ mice were generated by crossing p38α$^{lox/lox}$ mice (Ventura et al., 2007) with Villin-Cre and Villin-CreERT2 mice (el Marjou et al., 2004), respectively. The Villin-Cre mice were mostly in C57BL/6 background, while Villin-CreERT2 mice were of mixed C57BL/6-129v background. Littermate controls were used in all experiments. Mice were housed according to national and European Union regulations, and protocols were approved by the animal care and use committee of the Barcelona Science Park.

Induction of Colitis and CAC

To induce colorectal tumors, we used a combination of the carcinogen AOM with repeated administration of DSS in the drinking water, which causes colitis (Neufert et al., 2007). Mice (8–10 weeks old) were injected intraperitoneally with a single dose of AOM (10 mg/kg; Sigma, #A2853). After 5 days, 2% DSS (molecular weight, 36–50 kDa; MP Biomedicals, #160110) was given in the drinking water for 5 days, followed by 14 days of regular drinking water. The DSS treatment was repeated for two additional cycles, and mice were sacrificed 100 days after the AOM injection, except when indicated otherwise. For short-term colitis and inflammation studies, mice were given 2% DSS for 5 days and sacrificed at the indicated time points. Body weights were recorded during DSS treatment. Colons were removed from mice, flushed with cold PBS, opened longitudinally, fixed as "swiss-rolls" in 10% formalin solution (Sigma, #HT-501128) at room temperature overnight, and paraffin embedded. Before fixing the colons, size measurements were performed using a digital caliper in a blinded fashion.

Histopathological Analysis

Paraffin-embedded colon sections were stained with hematoxylin and eosin (H&E) and analyzed by pathologists in blinded fashion for tumor grades, epithelial damage, and inflammation using the scoring systems described in the Supplemental Information.

IHC

For IHC, colon sections were stained with the antibodies indicated in the Supplemental Information. Signals were visualized with 3,3-diaminobenzidine, using hematoxylin as a counterstain. PAS reagent was used to detect goblet cells.

TUNEL Assay

Apoptosis was detected in paraffin-embedded colon samples using the Fluorescein In Situ Cell Death Detection Kit (Roche) according to the manufacturer's instructions. Images were taken with a Nikon E800 upright microscope using appropriate fluorescence filters.

Analysis of Intestinal Permeability in Mice

To determine in vivo intestinal permeability, mice were starved overnight, and then FITC-dextran (Sigma #FD4) was administered by oral gavage (44 mg/100 g body weight). After 4 hr, mice were anesthetized, blood was collected by cardiac puncture, and mice were sacrificed. Serum was separated from whole blood using BD Microtainer SST Tubes (BD #365968), diluted with an equal volume of PBS (pH 7.4), and 100 μl of diluted serum was added to a 96-well microplate. The concentration of FITC in serum was determined by spectrophotofluorometry (BioTek), with an excitation of 485 nm and an emission wavelength of 528 nm, using serially diluted FITC-dextran as standard. Tumor permeability was calculated as described in the Supplemental Information.

Probiotic Treatment

Probiotic mixture VSL#3 (15 mg, Grifols) was dissolved in PBS (200 μl) and administered daily by oral gavage. Control mice were administered PBS.

Statistical Methods

Data are presented as means ± SEM. Statistical significance was determined by Student's t test using GraphPad Prism 4 software. p values less than 0.05 were considered statistically significant.

SUPPLEMENTAL INFORMATION

Supplemental Information includes Supplemental Experimental Procedures and six figures and can be found with this article online at http://dx.doi.org/10.1016/j.ccr.2014.02.019.

Figure 8. Chemical Inhibition of p38α Reduces Colon Tumor Burden

(A) Schematic representation of the protocol used to induce colorectal tumors in C57BL/6 mice and for administration of the p38α inhibitor PH797804.

(B) Average tumor number, size, and load at the end of the AOM/DSS protocol. Data are means ± SEM (n = 7). *p < 0.05.

(C) Representative images of colon sections stained with H&E or the phospho-p38 MAPK antibody at the end of the AOM/DSS protocol. Scale bars, 100 μm for phospho-p38.

(D) Colon lysates were analyzed by western blotting (one mouse per lane) with the indicated antibodies.

(E) Human colon cancer cell lines were treated with the p38 MAPK inhibitors SB203580 (SB, 10 μM), PH797804 (PH, 1 μM) or Birb0796 (Birb, 200 nM) for 4 days, and cell lysates were then analyzed by western blotting with the indicated antibodies.

(F) In normal colon epithelial cells, p38α maintains intestinal homeostasis and barrier function to suppress colitis-associated tumor initiation. On the other hand, p38α contributes to colon tumor development by supporting proliferation and inhibiting apoptosis of transformed epithelial cells. Tumor cells deficient in p38α appear to be at a selective disadvantage compared with WT cells.

ACKNOWLEDGMENTS

This work was initiated while J.G., I.B.B., and A.R.N. were working at Centro Nacional de Investigaciones Oncológicas (Madrid). We are grateful to Elisabeth Llonch and Lorena Ramirez for excellent technical assistance and Marianna Tedesco, Nuria Matesanz, Monica Comalada, and Raquel Batlle for their support and many helpful discussions. We thank Rafael Rosell and Miquel Taron for help with laser-captured tumor microdissection; the Fluorescence-Activated Cell Sorting and Electron Microscopy units of the University of Barcelona for expert technical assistance; Manolis Pasparakis and Jorge Caamaño for useful suggestions; and Eduard Batlle, Peter Jung, and the Batlle group members for discussions and support. This work was supported by the Fundación BBVA and by grants from the Spanish Ministry of Science and Innovation (BFU2010-17850) and the European Commission FP7 (INFLA-CARE 223151, INSPiRE 284460, and ERC 294665).

Received: December 13, 2012
Revised: November 1, 2013
Accepted: February 22, 2014
Published March 27, 2014

REFERENCES

Becker, C., Fantini, M.C., Schramm, C., Lehr, H.A., Wirtz, S., Nikolaev, A., Burg, J., Strand, S., Kiesslich, R., Huber, S., et al. (2004). TGF-beta suppresses tumor progression in colon cancer by inhibition of IL-6 trans-signaling. Immunity *21*, 491–501.

Bollrath, J., Phesse, T.J., von Burstin, V.A., Putoczki, T., Bennecke, M., Bateman, T., Nebelsiek, T., Lundgren-May, T., Canli, O., Schwitalla, S., et al. (2009). gp130-mediated Stat3 activation in enterocytes regulates cell survival and cell-cycle progression during colitis-associated tumorigenesis. Cancer Cell *15*, 91–102.

Chiacchiera, F., Matrone, A., Ferrari, E., Ingravallo, G., Lo Sasso, G., Murzilli, S., Petruzzelli, M., Salvatore, L., Moschetta, A., and Simone, C. (2009). p38alpha blockade inhibits colorectal cancer growth in vivo by inducing a switch from HIF1alpha- to FoxO-dependent transcription. Cell Death Differ. *16*, 1203–1214.

Comes, F., Matrone, A., Lastella, P., Nico, B., Susca, F.C., Bagnulo, R., Ingravallo, G., Modica, S., Lo Sasso, G., Moschetta, A., et al. (2007). A novel cell type-specific role of p38alpha in the control of autophagy and cell death in colorectal cancer cells. Cell Death Differ. *14*, 693–702.

Cuadrado, A., and Nebreda, A.R. (2010). Mechanisms and functions of p38 MAPK signalling. Biochem. J. *429*, 403–417.

Cuenda, A., and Rousseau, S. (2007). p38 MAP-kinases pathway regulation, function and role in human diseases. Biochim. Biophys. Acta *1773*, 1358–1375.

el Marjou, F., Janssen, K.P., Chang, B.H., Li, M., Hindie, V., Chan, L., Louvard, D., Chambon, P., Metzger, D., and Robine, S. (2004). Tissue-specific and inducible Cre-mediated recombination in the gut epithelium. Genesis *39*, 186–193.

Fabian, M.A., Biggs, W.H., 3rd, Treiber, D.K., Atteridge, C.E., Azimioara, M.D., Benedetti, M.G., Carter, T.A., Ciceri, P., Edeen, P.T., Floyd, M., et al. (2005). A small molecule-kinase interaction map for clinical kinase inhibitors. Nat. Biotechnol. *23*, 329–336.

Fearon, E.R., and Vogelstein, B. (1990). A genetic model for colorectal tumorigenesis. Cell *61*, 759–767.

Gillen, C.D., Walmsley, R.S., Prior, P., Andrews, H.A., and Allan, R.N. (1994). Ulcerative colitis and Crohn's disease: a comparison of the colorectal cancer risk in extensive colitis. Gut *35*, 1590–1592.

Goldstein, D.M., Kuglstatter, A., Lou, Y., and Soth, M.J. (2010). Selective p38alpha inhibitors clinically evaluated for the treatment of chronic inflammatory disorders. J. Med. Chem. *53*, 2345–2353.

Greten, F.R., Eckmann, L., Greten, T.F., Park, J.M., Li, Z.W., Egan, L.J., Kagnoff, M.F., and Karin, M. (2004). IKKbeta links inflammation and tumorigenesis in a mouse model of colitis-associated cancer. Cell *118*, 285–296.

Grivennikov, S., Karin, E., Terzic, J., Mucida, D., Yu, G.Y., Vallabhapurapu, S., Scheller, J., Rose-John, S., Cheroutre, H., Eckmann, L., and Karin, M. (2009). IL-6 and Stat3 are required for survival of intestinal epithelial cells and development of colitis-associated cancer. Cancer Cell *15*, 103–113.

Grivennikov, S.I., Wang, K., Mucida, D., Stewart, C.A., Schnabl, B., Jauch, D., Taniguchi, K., Yu, G.Y., Osterreicher, C.H., Hung, K.E., et al. (2012). Adenoma-linked barrier defects and microbial products drive IL-23/IL-17-mediated tumour growth. Nature *491*, 254–258.

Hardwick, J.C., van den Brink, G.R., Offerhaus, G.J., van Deventer, S.J., and Peppelenbosch, M.P. (2001). NF-kappaB, p38 MAPK and JNK are highly expressed and active in the stroma of human colonic adenomatous polyps. Oncogene *20*, 819–827.

Hui, L., Bakiri, L., Mairhorfer, A., Schweifer, N., Haslinger, C., Kenner, L., Komnenovic, V., Scheuch, H., Beug, H., and Wagner, E.F. (2007). p38alpha suppresses normal and cancer cell proliferation by antagonizing the JNK-c-Jun pathway. Nat. Genet. *39*, 741–749.

Jamieson, T., Clarke, M., Steele, C.W., Samuel, M.S., Neumann, J., Jung, A., Huels, D., Olson, M.F., Das, S., Nibbs, R.J., and Sansom, O.J. (2012). Inhibition of CXCR2 profoundly suppresses inflammation-driven and spontaneous tumorigenesis. J. Clin. Invest. *122*, 3127–3144.

Kang, Y.J., Chen, J., Otsuka, M., Mols, J., Ren, S., Wang, Y., and Han, J. (2008). Macrophage deletion of p38alpha partially impairs lipopolysaccharide-induced cellular activation. J. Immunol. *180*, 5075–5082.

Katoh, H., Wang, D., Daikoku, T., Sun, H., Dey, S.K., and Dubois, R.N. (2013). CXCR2-expressing myeloid-derived suppressor cells are essential to promote colitis-associated tumorigenesis. Cancer Cell *24*, 631–644.

Kim, C., Sano, Y., Todorova, K., Carlson, B.A., Arpa, L., Celada, A., Lawrence, T., Otsu, K., Brissette, J.L., Arthur, J.S., and Park, J.M. (2008a). The kinase p38 alpha serves cell type-specific inflammatory functions in skin injury and coordinates pro- and anti-inflammatory gene expression. Nat. Immunol. *9*, 1019–1027.

Kim, M.J., Choi, S.Y., Park, I.C., Hwang, S.G., Kim, C., Choi, Y.H., Kim, H., Lee, K.H., and Lee, S.J. (2008b). Opposing roles of c-Jun NH2-terminal kinase and p38 mitogen-activated protein kinase in the cellular response to ionizing radiation in human cervical cancer cells. Mol. Cancer Res. *6*, 1718–1731.

Kuraishy, A., Karin, M., and Grivennikov, S.I. (2011). Tumor promotion via injury- and death-induced inflammation. Immunity *35*, 467–477.

Laukoetter, M.G., Nava, P., Lee, W.Y., Severson, E.A., Capaldo, C.T., Babbin, B.A., Williams, I.R., Koval, M., Peatman, E., Campbell, J.A., et al. (2007). JAM-A regulates permeability and inflammation in the intestine in vivo. J. Exp. Med. *204*, 3067–3076.

Luo, J., Solimini, N.L., and Elledge, S.J. (2009). Principles of cancer therapy: oncogene and non-oncogene addiction. Cell *136*, 823–837.

Mantovani, A., Allavena, P., Sica, A., and Balkwill, F. (2008). Cancer-related inflammation. Nature *454*, 436–444.

McNeil, E., Capaldo, C.T., and Macara, I.G. (2006). Zonula occludens-1 function in the assembly of tight junctions in Madin-Darby canine kidney epithelial cells. Mol. Biol. Cell *17*, 1922–1932.

Mennigen, R., Nolte, K., Rijcken, E., Utech, M., Loeffler, B., Senninger, N., and Bruewer, M. (2009). Probiotic mixture VSL#3 protects the epithelial barrier by maintaining tight junction protein expression and preventing apoptosis in a murine model of colitis. Am. J. Physiol. Gastrointest. Liver Physiol. *296*, G1140–G1149.

Menon, M.B., Kotlyarov, A., and Gaestel, M. (2011). SB202190-induced cell type-specific vacuole formation and defective autophagy do not depend on p38 MAP kinase inhibition. PLoS ONE *6*, e23054.

Merlos-Suárez, A., Barriga, F.M., Jung, P., Iglesias, M., Céspedes, M.V., Rossell, D., Sevillano, M., Hernando-Momblona, X., da Silva-Diz, V., Muñoz, P., et al. (2011). The intestinal stem cell signature identifies colorectal cancer stem cells and predicts disease relapse. Cell Stem Cell *8*, 511–524.

Morel, C., Carlson, S.M., White, F.M., and Davis, R.J. (2009). Mcl-1 integrates the opposing actions of signaling pathways that mediate survival and apoptosis. Mol. Cell. Biol. *29*, 3845–3852.

Nenci, A., Becker, C., Wullaert, A., Gareus, R., van Loo, G., Danese, S., Huth, M., Nikolaev, A., Neufert, C., Madison, B., et al. (2007). Epithelial NEMO links innate immunity to chronic intestinal inflammation. Nature *446*, 557–561.

Neufert, C., Becker, C., and Neurath, M.F. (2007). An inducible mouse model of colon carcinogenesis for the analysis of sporadic and inflammation-driven tumor progression. Nat. Protoc. *2*, 1998–2004.

Otsuka, M., Kang, Y.J., Ren, J., Jiang, H., Wang, Y., Omata, M., and Han, J. (2010). Distinct effects of p38alpha deletion in myeloid lineage and gut epithelia in mouse models of inflammatory bowel disease. Gastroenterology *138*, 1255–1265.

Paillas, S., Boissière, F., Bibeau, F., Denouel, A., Mollevi, C., Causse, A., Denis, V., Vezzio-Vié, N., Marzi, L., Cortijo, C., et al. (2011). Targeting the p38 MAPK pathway inhibits irinotecan resistance in colon adenocarcinoma. Cancer Res. *71*, 1041–1049.

Preidis, G.A., and Versalovic, J. (2009). Targeting the human microbiome with antibiotics, probiotics, and prebiotics: gastroenterology enters the metagenomics era. Gastroenterology *136*, 2015–2031.

Putoczki, T.L., Thiem, S., Loving, A., Busuttil, R.A., Wilson, N.J., Ziegler, P.K., Nguyen, P.M., Preaudet, A., Farid, R., Edwards, K.M., et al. (2013). Interleukin-11 is the dominant IL-6 family cytokine during gastrointestinal tumorigenesis and can be targeted therapeutically. Cancer Cell *24*, 257–271.

Rescigno, M. (2011). The intestinal epithelial barrier in the control of homeostasis and immunity. Trends Immunol. *32*, 256–264.

Schetter, A.J., Heegaard, N.H., and Harris, C.C. (2010). Inflammation and cancer: interweaving microRNA, free radical, cytokine and p53 pathways. Carcinogenesis *31*, 37–49.

Schmitz, H., Barmeyer, C., Fromm, M., Runkel, N., Foss, H.D., Bentzel, C.J., Riecken, E.O., and Schulzke, J.D. (1999). Altered tight junction structure contributes to the impaired epithelial barrier function in ulcerative colitis. Gastroenterology *116*, 301–309.

Schwitalla, S., Ziegler, P.K., Horst, D., Becker, V., Kerle, I., Begus-Nahrmann, Y., Lechel, A., Rudolph, K.L., Langer, R., Slotta-Huspenina, J., et al. (2013). Loss of p53 in enterocytes generates an inflammatory microenvironment enabling invasion and lymph node metastasis of carcinogen-induced colorectal tumors. Cancer Cell *23*, 93–106.

Sonoshita, M., Aoki, M., Fuwa, H., Aoki, K., Hosogi, H., Sakai, Y., Hashida, H., Takabayashi, A., Sasaki, M., Robine, S., et al. (2011). Suppression of colon cancer metastasis by Aes through inhibition of Notch signaling. Cancer Cell *19*, 125–137.

Toft, N.J., Winton, D.J., Kelly, J., Howard, L.A., Dekker, M., te Riele, H., Arends, M.J., Wyllie, A.H., Margison, G.P., and Clarke, A.R. (1999). Msh2 status modulates both apoptosis and mutation frequency in the murine small intestine. Proc. Natl. Acad. Sci. USA *96*, 3911–3915.

Tsukita, S., Furuse, M., and Itoh, M. (2001). Multifunctional strands in tight junctions. Nat. Rev. Mol. Cell Biol. *2*, 285–293.

Ullman, T.A., and Itzkowitz, S.H. (2011). Intestinal inflammation and cancer. Gastroenterology *140*, 1807–1816.

Van der Sluis, M., De Koning, B.A., De Bruijn, A.C., Velcich, A., Meijerink, J.P., Van Goudoever, J.B., Büller, H.A., Dekker, J., Van Seuningen, I., Renes, I.B., and Einerhand, A.W. (2006). Muc2-deficient mice spontaneously develop colitis, indicating that MUC2 is critical for colonic protection. Gastroenterology *131*, 117–129.

Velcich, A., Yang, W., Heyer, J., Fragale, A., Nicholas, C., Viani, S., Kucherlapati, R., Lipkin, M., Yang, K., and Augenlicht, L. (2002). Colorectal cancer in mice genetically deficient in the mucin Muc2. Science *295*, 1726–1729.

Ventura, J.J., Hübner, A., Zhang, C., Flavell, R.A., Shokat, K.M., and Davis, R.J. (2006). Chemical genetic analysis of the time course of signal transduction by JNK. Mol. Cell *21*, 701–710.

Ventura, J.J., Tenbaum, S., Perdiguero, E., Huth, M., Guerra, C., Barbacid, M., Pasparakis, M., and Nebreda, A.R. (2007). p38alpha MAP kinase is essential in lung stem and progenitor cell proliferation and differentiation. Nat. Genet. *39*, 750–758.

Wagner, E.F., and Nebreda, A.R. (2009). Signal integration by JNK and p38 MAPK pathways in cancer development. Nat. Rev. Cancer *9*, 537–549.

Westbrook, A.M., Szakmary, A., and Schiestl, R.H. (2010). Mechanisms of intestinal inflammation and development of associated cancers: lessons learned from mouse models. Mutat. Res. *705*, 40–59.

Yoshizuka, N., Chen, R.M., Xu, Z., Liao, R., Hong, L., Hu, W.Y., Yu, G., Han, J., Chen, L., and Sun, P. (2012). A novel function of p38-regulated/activated kinase in endothelial cell migration and tumor angiogenesis. Mol. Cell. Biol. *32*, 606–618.

Cancer Cell
Article

Cancer-Secreted miR-105 Destroys Vascular Endothelial Barriers to Promote Metastasis

Weiying Zhou,[1,13] Miranda Y. Fong,[1] Yongfen Min,[16] George Somlo,[2] Liang Liu,[1,14] Melanie R. Palomares,[2,3] Yang Yu,[1,14] Amy Chow,[1] Sean Timothy Francis O'Connor,[1] Andrew R. Chin,[1,12] Yun Yen,[4,9] Yafan Wang,[9] Eric G. Marcusson,[15] Peiguo Chu,[5] Jun Wu,[6] Xiwei Wu,[10] Arthur Xuejun Li,[7] Zhuo Li,[11] Hanlin Gao,[1,10] Xiubao Ren,[14] Mark P. Boldin,[8] Pengnian Charles Lin,[16] and Shizhen Emily Wang[1,*]

[1]Department of Cancer Biology
[2]Department of Medical Oncology
[3]Department of Population Sciences
[4]Department of Molecular Pharmacology
[5]Department of Pathology
[6]Department of Comparative Medicine
[7]Department of Information Science
[8]Department of Molecular and Cellular Biology
[9]Core of Translational Research Laboratory
[10]Core of Integrative Genomics
[11]Core of Electron Microscopy
City of Hope Beckman Research Institute and Medical Center, Duarte, CA 91010, USA
[12]City of Hope Irell & Manella Graduate School of Biological Sciences, Duarte, CA 91010, USA
[13]Department of Pharmacology, College of Pharmacy, The Third Military Medical University, Chongqing, 400038, China
[14]Department of Biotherapy and Key Laboratory of Cancer Immunology, Tianjin Medical University Cancer Institute and Hospital, Tianjin, 300060, China
[15]Oncology and Basic Mechanisms, Regulus Therapeutics, San Diego, CA 92121, USA
[16]Center for Cancer Research, National Cancer Institute, Frederick, MD 21702, USA
*Correspondence: ewang@coh.org
http://dx.doi.org/10.1016/j.ccr.2014.03.007

SUMMARY

Cancer-secreted microRNAs (miRNAs) are emerging mediators of cancer-host crosstalk. Here we show that miR-105, which is characteristically expressed and secreted by metastatic breast cancer cells, is a potent regulator of migration through targeting the tight junction protein ZO-1. In endothelial monolayers, exosome-mediated transfer of cancer-secreted miR-105 efficiently destroys tight junctions and the integrity of these natural barriers against metastasis. Overexpression of miR-105 in nonmetastatic cancer cells induces metastasis and vascular permeability in distant organs, whereas inhibition of miR-105 in highly metastatic tumors alleviates these effects. miR-105 can be detected in the circulation at the premetastatic stage, and its levels in the blood and tumor are associated with ZO-1 expression and metastatic progression in early-stage breast cancer.

INTRODUCTION

Metastasis is the leading cause of mortality in cancer patients. Nearly 50% of breast cancer (BC) patients treated with chemotherapeutic and/or hormonal agents develop distant metastatic disease (Nicolini et al., 2006; Rubens, 2001); these patients face a 5-year survival rate of only ~20% (Yardley, 2010). Therefore, there is a great and urgent need to develop predictive or

Significance

In this study, we set out to identify cancer-secreted miRNAs that participate in cancer metastasis by adapting the niche cells. Our results demonstrate an important role of miR-105 in destroying the vascular endothelial barriers in the host during early premetastatic niche formation by targeting the cellular tight junctions. In breast cancer patients, increased levels of miR-105 in the circulation can be detected at the premetastatic stage and correlate with the occurrence of metastasis. Anti-miR-105 treatment suppresses metastasis and abolishes the systemic effect of tumor-derived miR-105 on niche adaptation. Therefore, these observations strongly suggest clinical applications of miR-105 as a predictive or early diagnostic blood-borne marker as well as a therapeutic target for breast cancer metastasis.

early diagnostic markers for metastasis and to elucidate the molecular mechanisms of metastasis that would allow the development of efficient treatment options. In the "seed and soil" hypothesis for metastasis (Paget, 1889), migratory tumor cells leave the primary tumor through intravasation, disseminate throughout the body via the circulation, and eventually engraft in a distant organ that provides an appropriate microenvironment. These consecutive steps require close interplay between cancer cells and their microenvironment. Among the multiple factors underlying metastasis, the adaptation of the primary tumor microenvironment and premetastatic or metastatic niches by cancer to facilitate cancer cell dissemination and distant engraftment plays an important prometastatic role that is starting to be recognized (Chambers et al., 2002; Kaplan et al., 2005; Podsypanina et al., 2008; Psaila and Lyden, 2009; Sethi and Kang, 2011). The recent discovery of microRNAs (miRNAs) and their extracellular presence suggest a potential role of these regulatory molecules in defining the metastatic potential of cancer cells and mediating the cancer-host communication.

miRNAs are small noncoding RNAs that base-pair with the 3′ untranslated regions (UTRs) of protein-encoding mRNAs, resulting in mRNA destabilization and/or translational inhibition. The biogenesis of miRNAs is tightly controlled, and dysregulation of miRNAs is linked to cancer (Calin and Croce, 2006; Iorio et al., 2005). miRNAs are also present extracellularly, either through binding to protein or lipid carriers (Arroyo et al., 2011; Turchinovich et al., 2011; Vickers and Remaley, 2012) or as a major RNA component of exosomes (Redis et al., 2012; Valadi et al., 2007). Exosomes are small (30–100 nm) membrane-encapsulated vesicles that are released into the extracellular environment by many cell types, including cancer cells (Skog et al., 2008; Valadi et al., 2007; Yuan et al., 2009). Exosomal RNAs are heterogeneous in size but enriched in small RNAs, such as miRNAs. Cancer-secreted exosomes and miRNAs can be internalized by other cell types in the primary tumor microenvironment and premetastatic or metastatic niches (Hood et al., 2011; Peinado et al., 2012; Skog et al., 2008; Yuan et al., 2009; Zhang et al., 2010; Zhuang et al., 2012). miRNAs loaded in these exosomes, which to a certain extent reflect the dysregulated miRNA profile in cancer cells, can thus be transferred to recipient niche cells to exert genome-wide regulation of gene expression. In addition, cancer-derived exosomal miRNAs may bind as ligands to Toll-like receptors in surrounding immune cells (Fabbri et al., 2012). Therefore, cancer-secreted miRNAs may play a crucial role in regulating various cellular components of the tumor microenvironment in order to facilitate metastasis.

Cancer-derived miRNAs have been detected in the blood of cancer patients, and their levels distinguish cancer patients from healthy controls (Mitchell et al., 2008; Taylor and Gercel-Taylor, 2008). Previous studies by us and by other groups have identified circulating miRNAs associated with the histopathological features of breast tumors and clinical outcomes in BC patients (Heneghan et al., 2010; Jung et al., 2012; Roth et al., 2010; Wu et al., 2012; Zhu et al., 2009). Some of these miRNAs may play a role in the metastatic process. The goal of this study was to identify cancer-secreted miRNAs that participate in cancer metastasis by adapting the niche cells.

RESULTS

Metastatic BC-Secreted Exosomal RNA Regulates the Migration of Endothelial Cells

We chose the MDA-MB-231 metastatic BC (MBC) line and the MCF-10A noncancerous mammary epithelial line as models for studying cancer-secreted exosomes and miRNAs. Exosomes purified from conditioned media by ultracentrifugation exhibited typical cup-shaped morphology by electron microscopy and a size range of 30 to 100 nm (Figure 1A). We focused on endothelial cells in this study for their critical barrier function during metastasis. When exosomes labeled with the fluorescent dye 1,1′-dioctadecyl-3,3,3′,3′-tetramethylindocarbocyanine perchlorate (DiI) were incubated with primary human microvascular endothelial cells (HMVECs), the recipient cells exhibited high uptake efficiency, as indicated by fluorescence microscopy (Figure 1B) and flow cytometry (Figure 1C), without a significant difference between MCF-10A- and MDA-MB-231-derived exosomes. After a 24 hr incubation with labeled exosomes, >90% of recipient cells were positive for DiI fluorescence (Figure 1C). Among a series of cellular analyses in exosome-treated HMVECs, we found that the transwell migration of endothelial cells was significantly stimulated by MDA-MB-231-secreted, but not MCF-10A-secreted, exosomes (Figure 1D). Transfection of total or small RNA extracted from MDA-MB-231 exosomes, but not that from the MCF-10A exosomes, recapitulated the migration-inducing effect (Figure 1E), thereby indicating that the unique small RNA content of MDA-MB-231 exosomes functions as a migratory regulator in endothelial cells.

miR-105 Is Specifically Expressed and Secreted by MBC Cells and Can Be Transferred to Endothelial Cells via Exosome Secretion

To identify the exosome-associated small RNA(s) that induce migration, we selected and profiled all small RNAs in the exosomes by Solexa (Illumina) deep sequencing. Exosomes from MDA-MB-231 and MCF-10A cells exhibited similar small RNA composition (Figure S1A available online). We focused on miRNAs that are known for their gene-regulatory function, identifying a list of miRNAs differentially secreted between the two lines (Table S1). Among these, some showed the corresponding up- or downregulation in the cells and the exosomes, whereas others exhibited opposite changes between the exosomal and cellular compartments, which may suggest cell-type-specific mechanisms for highly selective enrichment or exclusion of the miRNA in exosome-mediated secretion. We further focused on miR-105 that was predicted by multiple algorithms (TargetScan, miRDB, and PicTar) to target *TJP1* (tight junction [TJ] protein 1; also known as zonula occludens 1 [ZO-1]), a migration-related gene. The secretion of mature miR-105 was highly specific to MDA-MB-231, and its expression was significantly higher in these cells compared with MCF-10A (Figures 2A and 2B; Table S1). Although the primary (pri-) and precursor (pre-) miR-105 also exhibited higher intracellular levels in MDA-MB-231, these forms were not detectable in exosomes (Figures S1B and S1C). Among a panel of BC lines, the expression and secretion of miR-105 were specific to highly metastatic cells originally isolated from pleural effusion (Figures 2A and 2B).

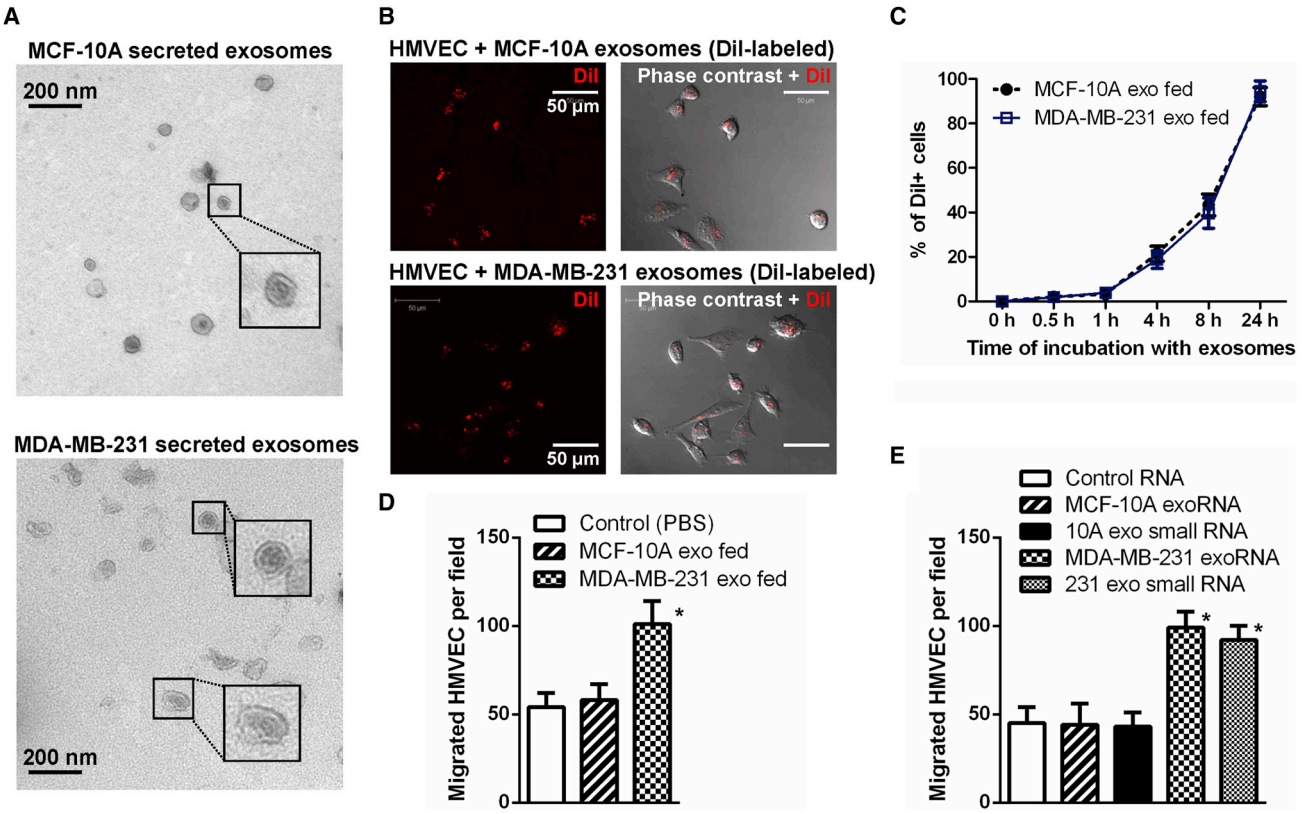

Figure 1. MBC-Secreted Exosomal RNA Regulates Migration of Endothelial Cells

(A) EM images of exosomes secreted by MCF-10A and MDA-MB-231 cells.

(B) Primary HMVECs were incubated with DiI-labeled exosomes (red) for 24 hr before fluorescent and phase contrast images were captured.

(C) HMVECs incubated with DiI-labeled exosomes for indicated time were analyzed by flow cytometry for DiI uptake.

(D) After 48 hr incubation with exosomes or PBS (as control), HMVECs were analyzed for transwell migration, and cells that had migrated within 8 hr were quantified from triplicate wells.

(E) HMVECs transfected with equal amount of total or small (<200 nt) RNA extracted from MCF-10A or MDA-MB-231 (abbreviated as MDA-231 or 231 in figures) secreted exosomes, or control RNA (cel-miR-67), were subjected to transwell migration at 48 hr after transfection.

*$p < 0.005$ compared with control group. Results are presented as mean ± SD.

To confirm that MBC-secreted miR-105 can be transferred to endothelial cells via exosomes, we measured the miR-105 levels in HMVECs treated with exosomes derived from MCF-10A or MDA-MB-231 cells. An increase of the cellular level of mature miR-105, but not pri- or pre-miR-105, was observed in recipient HMVECs following the treatment with MBC-originated exosomes with kinetics starting at 4 hr and peaking at 24 hr (Figures 2C and 2D), similar to that observed for exosome uptake (Figure 1C). We conclude that this increase of miR-105 reflects the exosome-mediated miRNA transfer but not an induction of miR-105's endogenous expression in the recipient cells, as its level in exosome-treated cells was not significantly affected by an RNA polymerase II inhibitor (Figure 2E). When we treated HMVECs with PKH67 (Sigma-Aldrich)-labeled exosomes secreted by MDA-MB-231 cells that were transfected with Cy3-labeled miR-105, the Cy3 fluorescence was observed in >90% of recipient cells, in which it largely colocalized with the PKH67 lipid dye that labeled the exosomal membranes (Figure S1D). In contrast, no internalization of naked Cy3-labeled miR-105 was observed in HMVECs (Figure S1D).

Cancer-Secreted miR-105 Downregulates Tight Junctions and Destroys the Barrier Function of Endothelial Monolayers

We next examined the miR-105 regulation of the putative target ZO-1, a central molecular component of TJs, which comprise a major group of cell-cell adhesion complexes in endothelial and epithelial cells. The four predicted miR-105 binding sites in the 3′UTR of human ZO-1 were cloned into a reporter plasmid and assessed for their responsiveness to miR-105 in HMVECs. Site I and site II, which are conserved among most species, responded to retrovirus-expressed miR-105 by directing a 50% to 65% reduction in reporter gene expression, whereas the other two sites did not. When both sites I and II were present downstream of reporter gene, a greater reduction in gene expression was observed (Figure S2A).

Consistent with the results from the reporter assay, ectopic expression of miR-105, or treatment with exosomes derived from the MDA-MB-231 (high-miR-105) but not the MCF-10A cells (low-miR-105), resulted in a significant decrease of ZO-1 expression at both the mRNA and protein levels in HMVECs (Figures 3A–3C). The effect of MDA-MB-231 exosomes could be abolished

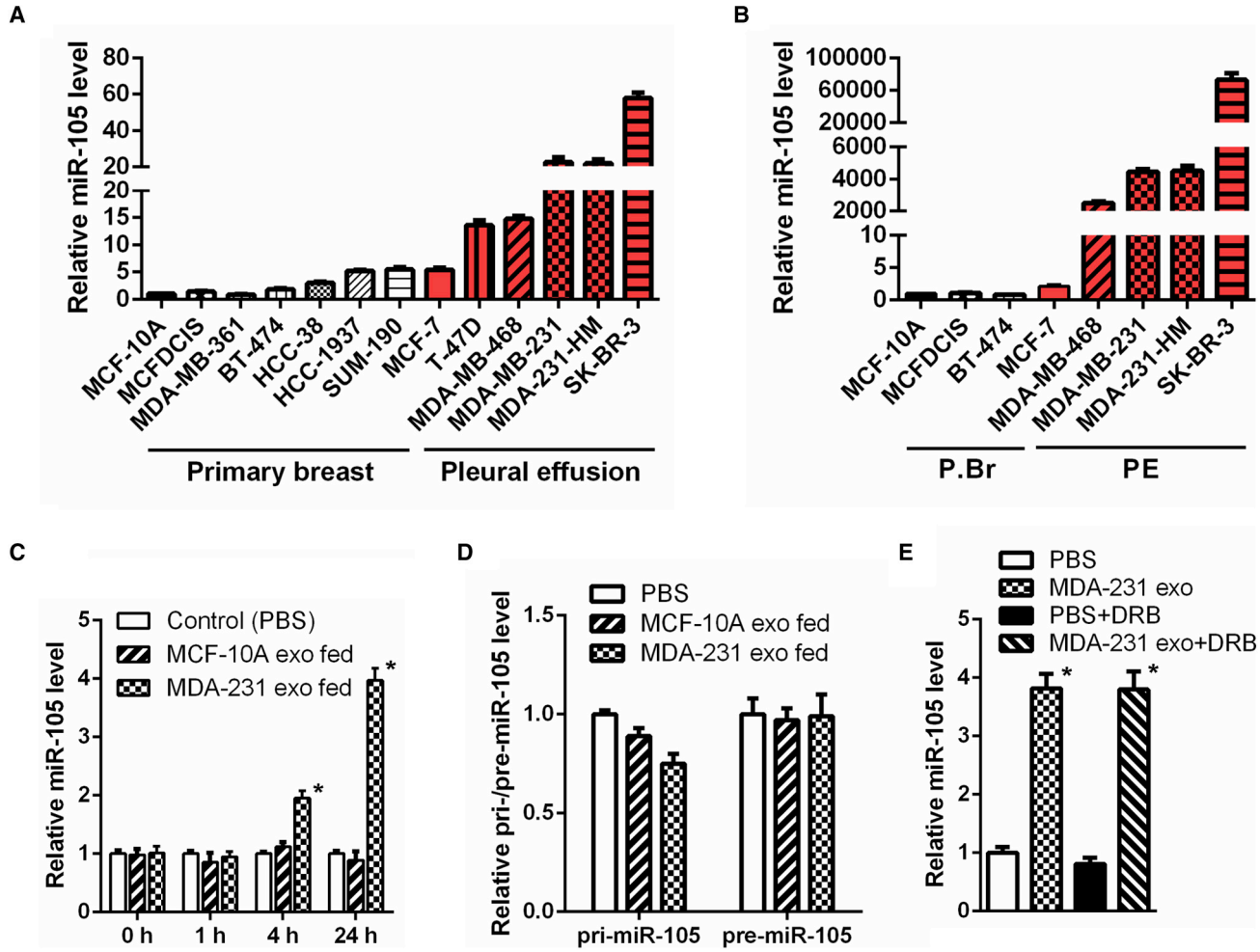

Figure 2. miR-105 Is Specifically Expressed and Secreted by MBC Cells and Can Be Transferred to Endothelial Cells via Exosome Secretion

(A and B) Cellular (A) and exosomal (B) RNA was extracted from various breast cell lines and subjected to miR-105 RT-qPCR. Data were normalized to levels of U6 (cellular; A) or miR-16 (exosomal; B) and compared with the nontumor line MCF-10A. MBC lines originally isolated from pleural effusion (PE) are indicated by red columns.

(C) RNA was extracted from HMVECs incubated with exosomes of different origins for indicated time and analyzed for miR-105 level using U6 as internal control. At each time point, data were compared with PBS-treated cells.

(D) RNA extracted from HMVECs incubated with exosomes of different origins for 24 hr (or PBS as control) was analyzed for the level of pri-miR-105 or pre-miR-105.

(E) MDA-MB-231-secreted exosomes were fed to HMVECs in the presence or absence of 5,6-dichloro-1-β-D-ribofuranosylbenzimidazole (20 μM). After 24 hr, RNA extracted from the recipient cells was analyzed for miR-105 level.

*$p < 0.005$ compared with PBS treatment. Results are presented as mean ± SD (see also Figure S1 and Table S1). P.Br, primary breast.

by transfecting the recipient cells with miR-105 inhibitor (Figures 3B and 3C). It was unlikely to require additional exosomal components that are unique to MDA-MB-231, as exosomes secreted by MCF-10A cells stably overexpressing and secreting miR-105 (Figure S2B) and by other high-miR-105 BC cells but not by low-miR-105 BC cells (Figures 2A and 2B) also downregulated ZO-1 expression in recipient HMVECs (Figure 3C; Figure S2C). When HMVEC monolayers were analyzed by immunofluorescence, those treated with high-miR-105 exosomes (secreted by MCF-10A/miR-105 and MDA-MB-231) exhibited marked reduction of ZO-1 and internalization of another TJ protein occludin from cell junctions, whereas the junctional level of vascular endothelial cadherin (VE-cadherin) was not significantly affected (Figure 3D).

We next performed an in vitro permeability assay by measuring the traversing of rhodamine-labeled dextran (relative molecular mass 70,000) probes through HMVEC monolayers growing on 0.4-μm filters. Similar to the effect induced by vascular endothelial growth factor (VEGF), treatment of the endothelial barrier with MDA-MB-231 exosomes also induced passage of the fluorescent probes from the top to the bottom wells in a manner that was dependent on functional miR-105 and downregulation of ZO-1 (Figure 3E). When the transendothelial electrical resistance was measured in HMVEC monolayers, treatment with MDA-MB-231 exosomes significantly reduced the unit area resistance compared with PBS or MCF-10A exosome treatment. Inhibition of miR-105 and restored

expression of ZO-1 in recipient HMVECs both abolished the effect of MBC-derived exosomes (Figure 3F). The effect of miR-105-containing exosomes on vascular destruction was further tested in a 3D vascular sprouting assay. In this system, endothelial cells formed vascular sprouts after 4 to 5 days in culture. At this time, purified exosomes from MCF-10A/vec (control) or MCF-10A/miR-105 cells were added into the culture media, and the effects on already established vascular structures were analyzed 5 days later. We observed a clear and significant destruction of vascular structures with the treatment of miR-105-containing exosomes (from MCF-10A/miR-105) compared with the control (Figure 3G). Consistent with these results, ectopic expression of miR-105 or treatment with MBC exosomes significantly induced migration in HMVECs through the miR-105/ZO-1-mediated mechanism (Figure 3H). Last, to directly simulate the barrier-traversing step in metastasis, transendothelial invasion of cancer cells was examined using HMVEC monolayers grown on 3-μm filters. The number of GFP-labeled MDA-231-HM cells that had invaded through HMVECs treated with MDA-MB-231 exosomes was significantly greater compared with those that had invaded through untreated or MCF-10A exosome-treated HMVECs, and both miR-105 inhibition and ZO-1 restoration in recipient cells interfered with this effect (Figure 3I).

Cancer-Secreted miR-105 Induces Vascular Permeability and Promotes Metastasis In Vivo

To further demonstrate the in vivo effect of exosomal miR-105 on endothelial barriers, we injected exosomes secreted by MCF-10A/vec (low-miR-105), MCF-10A/miR-105 (high-miR-105), or MDA-MB-231 cells (high-miR-105), or PBS as control, into the tail veins of NOD/SCID/IL2Rγ null (NSG) mice and examined the lung and brain, organs that frequently host BC metastases, after exosome treatment. The results indicated that exosomes with high-miR-105, but not those with low-miR-105, significantly increased miR-105 levels in lung and brain (Figure 4A), accompanied by reduced ZO-1 expression in endothelial cells positive for cluster of differentiation 31 (CD31) (Figure 4B) and enhanced vascular permeability (Figure 4C; Figure S3). In another experiment, mice were pretreated with exosomes secreted by MCF-10A or MDA-MB-231 cells (or PBS as control) before an intracardiac injection of luciferase-labeled MDA-MB-231 cells. Three weeks later, tissues were collected for reverse transcription quantitative PCR (RT-qPCR) of luciferase gene using mouse 18S as internal control to quantify metastases. Consistent with their effect on destroying the endothelial barriers, MDA-MB-231 but not MCF-10A exosomes significantly increased metastases in the lung and brain (Figure 4D).

miR-105 Overexpression in Poorly Metastatic BC Cells Promotes Metastasis In Vivo

To determine if the miR-105 level in primary tumors regulates endothelial barriers and metastasis, we stably overexpressed miR-105 in an MCF-10A-derived tumorigenic line, MCFDCIS, which forms lesions similar to comedo ductal carcinoma in situ that spontaneously progress to invasive tumors (Hu et al., 2008; Miller et al., 2000). Compared with vector-transduced control cells, the miR-105-overexpressing MCFDCIS cells also secreted a higher level of miR-105 (Figure S4A) and showed reduced ZO-1 protein expression and significantly enhanced migration in transwell and wound closure assays (Figures S4B–S4D). Restoration of ZO-1 using an overexpressing plasmid that lacks the 3′UTR abolished the promigratory effect of miR-105. We next established orthotopic xenografts using luciferase-labeled MCFDCIS cells with or without miR-105 overexpression. Although miR-105 did not seem to affect primary tumor growth (Figures S4E and S4F), distant metastases were significantly induced in the lung and brain in mice bearing miR-105-overexpressing tumors at week 6 (Figures 5A and 5B). Histological staining indicated that in contrast to the MCFDCIS/vec tumors, which showed moderate local invasiveness, MCFDCIS/miR-105 tumors displayed no clear margin and extensively infiltrated into the surrounding tissues (Figure 5C). In addition, the in vivo vascular permeability in the lung, liver, and brain of mice bearing miR-105-overexpressing tumors was dramatically increased compared with that in the control group (Figure 5D; Figure S4H), whereas relatively high vascular permeability was observed in the primary tumors of both groups (Figures S4G and S4H). In mice bearing miR-105-overexpressing tumors, miR-105 was detected not only in primary tumors but also in the metastasis-free areas of distant organs (Figure 5E). Reduced level of ZO-1 was observed in the $CD31^+$ vascular endothelial cells in the lung and brain of mice with high-miR-105 xenografts (Figure 5F). These results collectively suggest that tumor cells expressing and consequently secreting higher level of miR-105 acquire greater metastatic potential through the dual advantages of enhanced tumor cell invasion and weakened endothelial barriers in the host.

miR-105 Inhibition Suppresses Metastasis and Restores Vascular Integrity In Vivo

To further explore the potential therapeutic effect of miR-105 intervention, we established xenografts from high-miR-105, high-metastatic MDA-231-HM cells that were generated through explant culture of a spontaneous meningeal metastasis of MDA-MB-231. In vitro treatment of these cells with an anti-miR-105 compound increased ZO-1 expression and suppressed migration (Figures S5A and S5B), consistent with the effect of miR-105 observed in other experiments. In vivo treatment with the anti-miR-105 compound reduced the volume of primary tumors and suppressed distant metastases to the lung and brain compared with the groups receiving PBS or control compound (Figures 6A–6C). Tumors treated with anti-miR-105 had clear margins with significantly reduced tumor cell infiltration into the surrounding tissues (Figure 6D). Although Ki-67 staining did not show a significant difference among the tumor groups, anti-miR-105-treated tumors showed higher levels of ZO-1 and higher percentages of apoptotic cells, as indicated by cleaved caspase-3 (Figure 6E). The in vivo vascular permeability assay indicated a lack of rhodamine-dextran penetration into various tissues in tumor-free mice; conversely, leakage of the dye into these tissues in tumor-bearing animals occurred even at a premetastatic stage (Figure 6F; Figure S5C), which suggests an effect of tumor-secreted factors in destroying the vascular integrity of a distant organ during early premetastatic niche formation. Notably, treatment with anti-miR-105 efficiently blocked this effect, restoring the vascular integrity in tumor-bearing animals (Figure 6F; Figure S5C). Restored ZO-1 expression in $CD31^+$ vascular endothelial cells was observed in the lung and brain

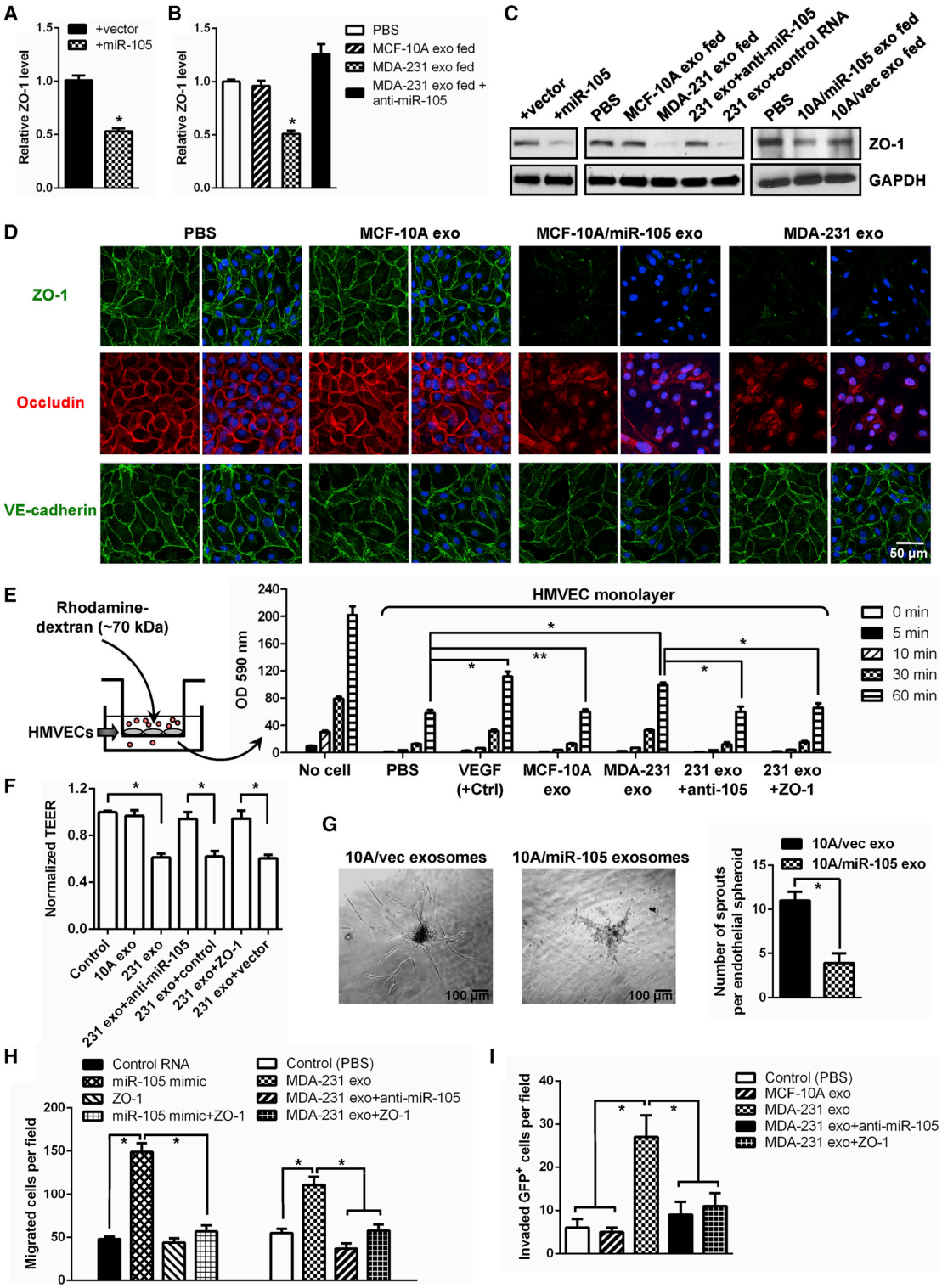

Figure 3. Cancer-Secreted miR-105 Downregulates TJs and Destroys the Barrier Function of Endothelial Monolayer

(A) HMVECs transduced with miR-105 or vector were analyzed for ZO-1 expression by RT-qPCR.

(B) HMVECs treated as indicated were analyzed for the RNA level of ZO-1.

(C) HMVECs treated as indicated were analyzed by Western blot.

(D) HMVEC monolayers were treated as indicated for 48 hr and analyzed by immunofluorescence (IF) for ZO-1 (green), occludin (red), and VE-cadherin (green). DAPI (blue): cell nuclei.

(legend continued on next page)

of tumor-bearing mice treated with anti-miR-105 compound (Figure 6G). Thus, anti-miR-105 treatment suppresses metastasis by reducing tumor invasiveness and restoring the barrier function of endothelial niche cells.

miR-105 Is Associated with ZO-1 Expression and Metastatic Progression in BC

Because miR-105 is uniquely expressed and secreted by MBC cells, it is possible that cancer-secreted miR-105 can be detected in the circulation of BC patients, such that miR-105 may serve as a prognostic marker for metastatic potential. To explore this, we first measured the serum miRNA levels in mice bearing MDA-231-HM xenograft tumors at either the premetastatic (week 3 after cancer cell implantation) or metastatic (week 6 after cancer cell implantation) stage in comparison with tumor-free animals. Circulating miR-105, but not two other miRNAs (miR-155 and miR-375), was significantly elevated in tumor-bearing animals at both premetastatic and metastatic stages (Figure 7A), suggesting that miR-105 derived from primary tumors with high miR-105 levels and high metastatic potential can be detected in the blood at an early stage before the clinical detection of metastasis. We next compared serum miRNA levels among 38 stage II and III BC patients. By comparing miRNA levels in circulating exosomes and the corresponding exosome-depleted serum fraction, we found that circulating miR-105 and miR-181a predominantly existed in exosomes, whereas two other miRNAs (miR-375 and miR-422b) were detected in both exosomes and exosome-depleted fraction at comparable levels (Figure S6). In circulating exosomes purified from sera, levels of miR-105, but not two other miRNAs (miR-181a and miR-375), were significantly higher in patients who later developed distant metastases during the 4.2 years of mean follow-up (n = 16) than those who did not (n = 22) (Figure 7B). To further determine if circulating miR-105 in BC patients is functionally active in regulating endothelial cells, we treated established 3D vascular structures with serum from a healthy donor or a BC patient with a high level of circulating miR-105. The patient serum but not normal serum resulted in a destruction of vascular structures, which was abolished by the anti-miR-105 compound (Figure 7C).

In patients with paired serum and tumor specimens, we further detected a strong positive correlation between circulating (exosomal) and tumor miR-105 levels ($r = 0.85$, $p < 0.01$). In contrast, significant inverse correlations were detected between tumor miR-105 and ZO-1 ($r = -0.48$, $p = 0.03$) and between circulating (exosomal) miR-105 and tumor-adjacent vascular ZO-1 expression ($r = -0.49$, $p = 0.04$) (Figures 7D and 7F). These observations are consistent with the role of miR-105 in downregulating ZO-1. In addition, higher levels of tumor miR-105 and lower levels of tumor and vascular ZO-1 were observed in patients who later developed distant metastases compared with those who did not and compared with normal mammary tissues (Figures 7E and 7F), thus supporting the functional association of these genes with cancer metastasis. In a BC tissue array, significantly higher miR-105 and lower ZO-1 levels were detected in the primary tumors with distant or lymph node metastases (n = 15) compared with those without (n = 60), and the inverse correlation between miR-105 and ZO-1 remained significant among all cases ($r = -0.24$, $p = 0.04$) (Figure 7G). Overall, our clinical data suggest that cancer-derived miR-105 can serve as a blood-based marker for the prediction or early diagnosis of BC metastasis and may play a role in promoting cancer progression by targeting ZO-1.

DISCUSSION

Exchange of cellular materials between cells through various paracrine and endocrine mechanisms is an important means of intercellular communication and can be mediated by exosomes. The tumor-derived adaptation of endothelial cells by miR-105 occurs during early premetastatic niche formation. Enhanced vascular permeability could then enhance cancer cell dissemination and growth at distant sites through multiple means, including (1) plasma protein leakage that results in enhanced entrapment and hence concentration of tumor cells; (2) enhanced dissemination of tumor cells to distant sites, resulting in autocrine signaling that overwhelms any inhibitory signaling at the distant site; and (3) additional exosome cargos and/or plasma proteins that leak into secondary organs and alter cellular physiology toward a prometastatic/tumor-supportive phenotype. In fact, vascular destabilization at the premetastatic lung niche has been previously described and involves a synergistic effect among angiopoietin 2, matrix metalloproteinase (MMP) 3, and MMP10 (Huang et al., 2009). Thus, therapies targeting miR-105 and these protein factors, in combination with existing conventional therapies, may serve as an effective treatment for cancer patients with high risk for metastasis (e.g., indicated by high levels of circulating miR-105). Understanding mechanisms leading to miR-105 overexpression in MBC, which is an ongoing direction in our laboratory, may reveal additional strategies for miR-105 intervention.

(E) The permeability of treated HMVEC monolayers grown on 0.4 μm filters was measured by the appearance of rhodamine-dextran, which was added to the top well at the beginning of the experiment, in the bottom well during a 1 hr time course. The absorbance at 590 nm at each time point was indicated. Treatment of the HMVEC monolayer with VEGF (50 ng/ml) for 8 hr was included as a positive control to show cytokine-induced permeability. The absorbance at the 1 hr time point was compared with the PBS (control) condition. *$p < 0.005$. **$p > 0.05$.

(F) HMVEC monolayers grown on filters and treated as indicated were analyzed for transendothelial electrical resistance. Calculated unit area resistance from triplicate wells was normalized to the control (PBS) treatment.

(G) Treatment with miR-105-containing exosomes resulted in a vascular destruction. Vascular sprouting assay was established for 5 days, at which time 1 μg of purified exosomes from MCF-10A/vec (control) or MCF-10A/miR-105 cells were added into the culture media. Vascular structures were imaged 5 days after the treatment, and representative images are shown (left). Vascular sprouts per spheroid were counted and graphed (right). At least 50 spheroids were counted in each experiment, and the experiment was repeated three times. *$p < 0.05$.

(H) HMVECs treated as indicated were subjected to transwell migration. Cells that had migrated within 8 hr were quantified from triplicate wells. *$p < 0.005$.

(I) HMVEC monolayers grown on 3 μm filters were treated as indicated before GFP-labeled MDA-231-HM cells were seeded in the transwell inserts. After 10 hr, the GFP^+ cells on the bottom side of filters were quantified under a fluorescent microscope. *$p < 0.005$.

Results are presented as mean ± SD (see also Figure S2). GAPDH, glyceraldehyde 3-phosphate dehydrogenase.

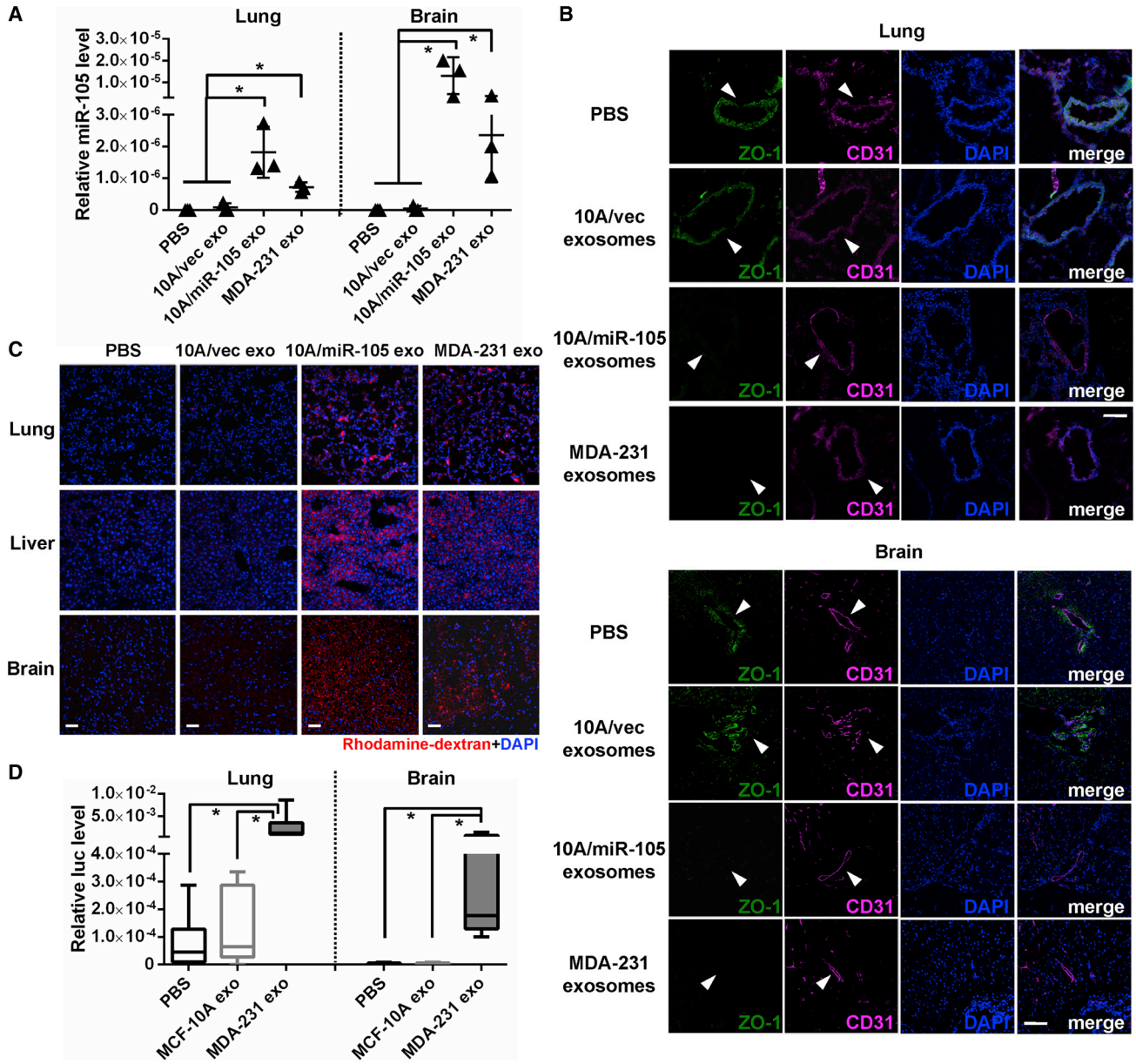

Figure 4. Cancer-Secreted miR-105 Induces Vascular Permeability and Promotes Metastasis In Vivo

(A) Exosomes secreted by MCF-10A/vec, MCF-10A/miR-105, or MDA-MB-231 cells, or PBS (as control), were intravenously injected into the tail veins of NSG mice (n = 3) twice a week. After five injections, tissues were collected for RT-qPCR of miR-105 using U6 as internal control. *$p < 0.05$.

(B) Collected lung and brain tissues were subjected to double-label IF for ZO-1 (green) and CD31 (pink). Structures positive for CD31 are indicated by arrowheads. The scale bar represents 100 μm.

(C) In vivo vascular permeability determined by the appearance of intravenously injected rhodamine-dextran (red) (n = 3). Representative images are shown. DAPI (blue): cell nuclei. The scale bar represents 100 μm.

(D) Exosomes secreted by MCF-10A or MDA-MB-231 cells, or PBS (as control), were intravenously injected into the tail veins of NSG mice (n = 6) twice a week. After five injections, all mice received intracardiac injection of luciferase-labeled MDA-MB-231 cells. Three weeks later, tissues were collected for RT-qPCR of luciferase gene using mouse 18S as internal control to quantify metastases. *$p < 0.05$.

Results are presented as mean ± SD (see also Figure S3).

Downregulation or loss of TJs, frequently as a result of reduced expression of TJ-associated proteins, contributes to cancer progression by altering cell migration, proliferation, polarity, and differentiation (Brennan et al., 2010; Georgiadis et al., 2010; Itoh and Bissell, 2003; Martin and Jiang, 2009). Reduction of TJ-associated ZO-1 in primary breast tumors due to decreased expression or cytoplasmic localization is associated with metastasis in BC patients (Martin et al., 2004; Polette et al., 2005). Our study identifies miR-105 as a key regulator of ZO-1, suggesting one mechanism of TJ disruption associated

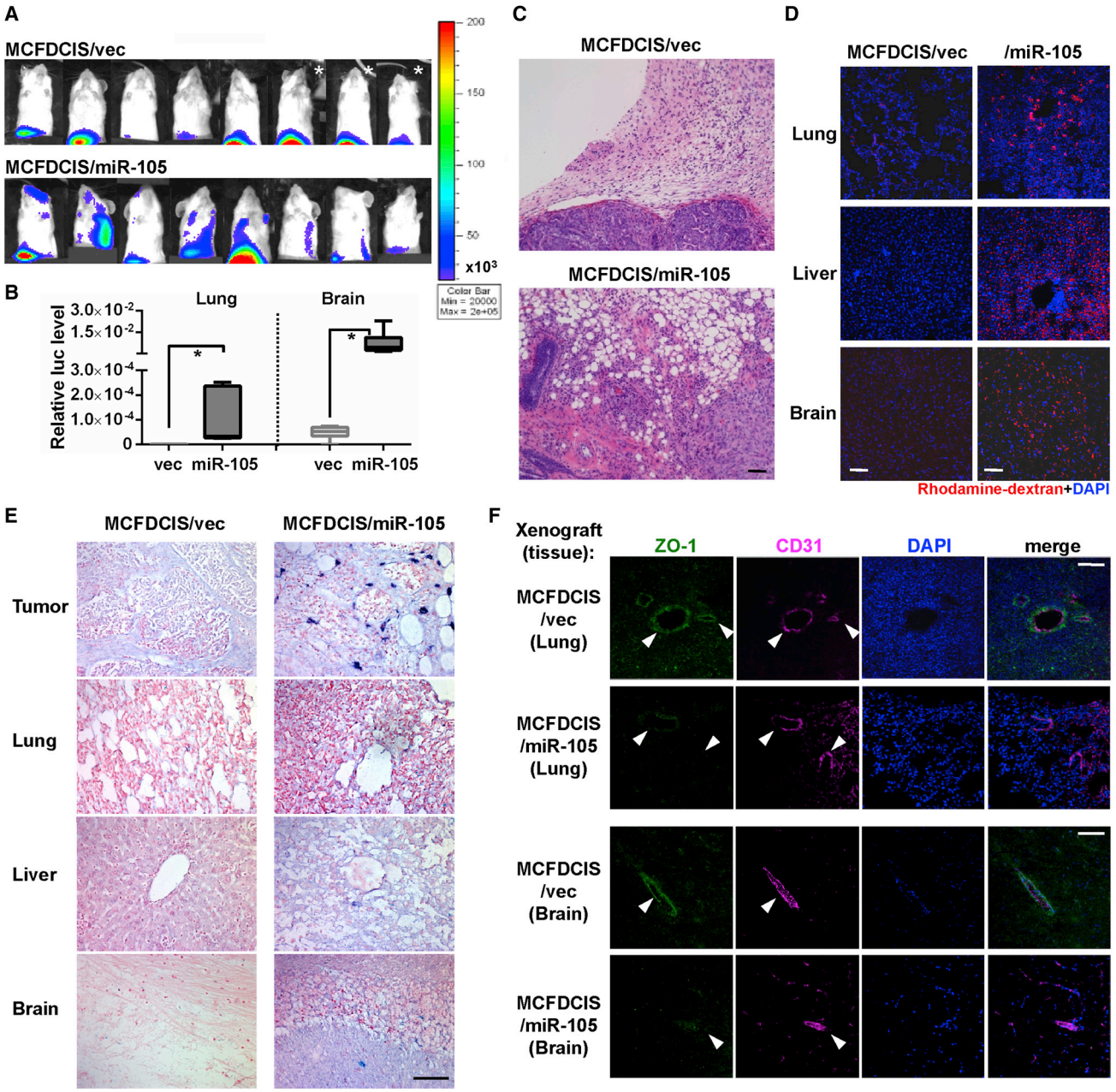

Figure 5. miR-105 Overexpression in Poorly Metastatic BC Cells Promotes Metastasis In Vivo

(A) Luciferase-labeled MCFDCIS/vec or MCFDCIS/miR-105 cells were injected into the number 4 mammary fat pads of NSG mice (n = 8). Bioluminescent imaging (BLI) at week 6 is shown. *Because of the extensive tumor burden, these three mice were sacrificed at week 5.5; their images at week 5 are shown.

(B) Quantification of metastases in the lung and brain. Mice shown in (A) were sacrificed at week 6, and tissues were subjected to RT-qPCR of luciferase gene using mouse 18S as internal control (n = 8). Results are presented as mean ± SD. *$p < 0.05$.

(C) Representative hematoxylin and eosin (H&E) stained images of the tumor edges showing local invasiveness. The scale bar represents 50 μm.

(D) In vivo vascular permeability determined by the appearance of intravenously injected rhodamine-dextran (red) in various organs. Tissues were collected from mice bearing MCFDCIS/vec or MCFDCIS/miR-105 xenografts (n = 3) that were sacrificed at week 6. Representative images are shown. DAPI (blue): cell nuclei. The scale bar represents 100 μm.

(E) Representative images of miR-105 in situ hybridization (ISH) in tissues collected from the two groups. The scale bar represents 50 μm.

(F) Collected tissues were subjected to double-label IF for ZO-1 (green) and CD31 (pink). Structures positive for CD31 are indicated by arrowheads. The scale bar represents 100 μm.

See also Figure S4.

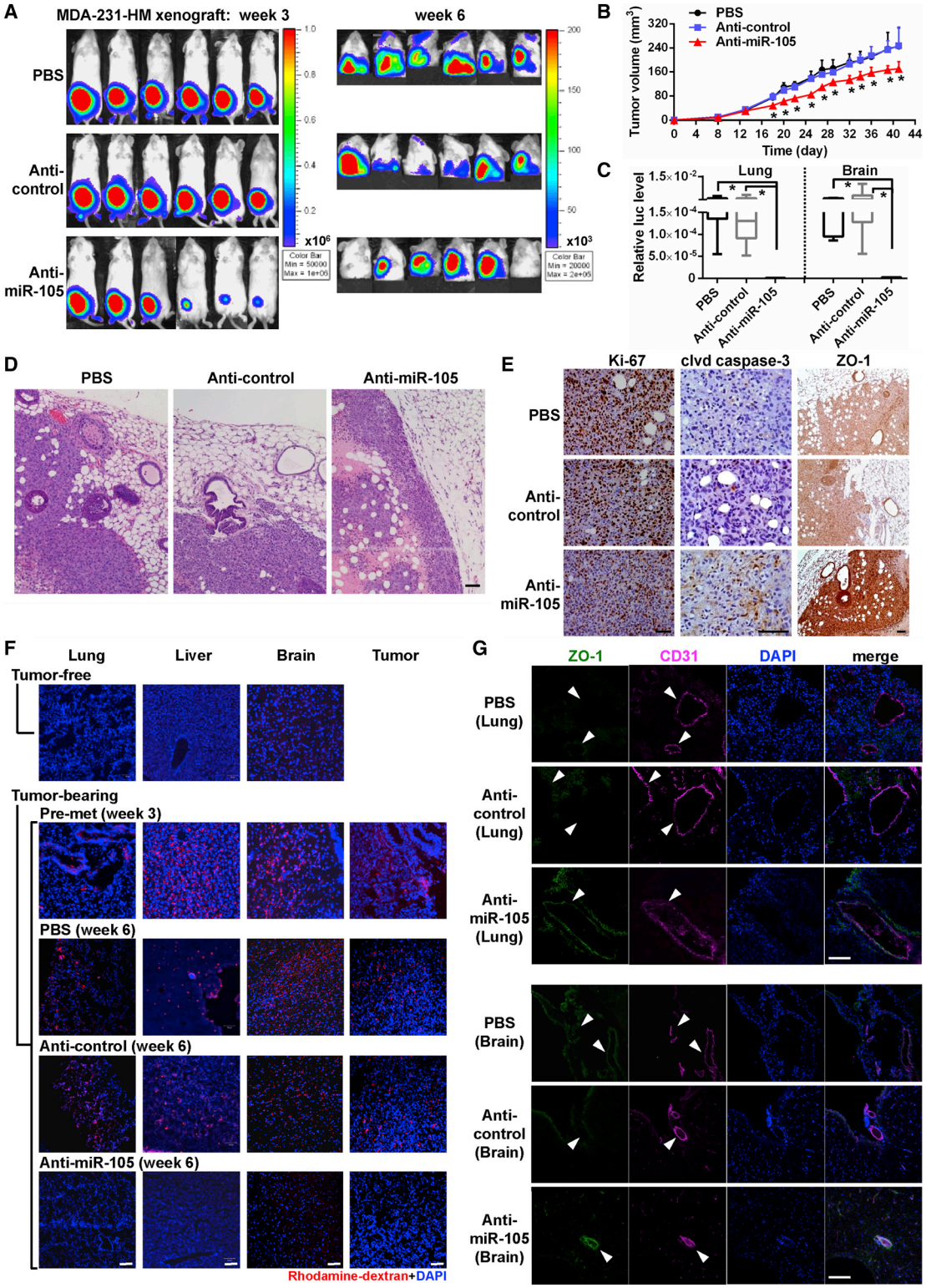

Figure 6. miR-105 Inhibition Suppresses Metastasis and Restores Vascular Integrity In Vivo

(A) Luciferase-labeled MDA-231-HM cells were injected into the number 4 mammary fat pads of NSG mice. Mice were divided into three groups (n = 6) for treatment with PBS, anti-miR-105 compound, or control compound. BLI at week 3 and week 6 is shown.

(B) Tumor volume determined in the three groups. *$p < 0.005$ compared with the other two groups.

(C) Quantification of metastases in the lung and brain. Mice shown in (A) were sacrificed at week 6 and tissues were subjected to RT-qPCR of luciferase gene using mouse 18S as internal control (n = 6). *$p < 0.01$.

(legend continued on next page)

with cancer progression and metastasis. The Rho family of small guanosine triphosphatases (GTPases) has been implicated in the regulation and function of TJs (Connolly et al., 2002; González-Mariscal et al., 2008; Jou et al., 1998; Shen et al., 2006). The Rho-associated protein kinase, a downstream effector of RhoA, regulates actomyosin contractility, TJ assembly, and endothelial capillary formation through phosphorylation of the regulatory myosin light chain (MLC2). Relevant to our study, junctional proteins including ZO-1 have been reported to regulate Rho GTPases through interacting with guanine nucleotide exchange factors and GTPase activating proteins (Citi et al., 2011). In our study, overexpression of miR-105 or treatment with exosomes carrying miR-105 did not alter the activity of RhoA, Rac1/2/3, or Cdc42, or the phosphorylation of MLC2, in recipient HMVECs (data not shown), suggesting that the small GTPases are not downstream effectors of the herein identified miR-105/ZO-1 pathway. In endothelial cells that normally express low miR-105 levels (data not shown), ectopic, cancer-derived miR-105 transferred via exosomes can effectively reduce ZO-1 expression and disrupt the barrier function of these cells both in vitro and in vivo. Although miR-105 secreted by the primary tumor may only affect a fraction of endothelial niche cells, this would be sufficient to open ''gates'' in these natural monolayer barriers for traversal of cancer cells, thereby facilitating metastasis. In addition, contact-dependent intercellular miRNA transfer between two adjacent cells through the transmembrane channel protein SIDT1 has recently been reported (Elhassan et al., 2012). Through this pathway, cancer-derived miRNAs (e.g., miR-105) that are transferred to a distant organ via circulating exosomes may further extend their regulatory effect to those interconnected niche cells without direct exosome uptake. In patients with familial hypercholesterolemia but not normal subjects, circulating miR-105 can be detected on high-density lipoprotein, which delivers the miRNA to recipient cells as an exosome-independent mechanism (Vickers et al., 2011). It would be interesting to determine the noncancer source of circulating miR-105 and its role in regulating vascular permeability through the herein demonstrated pathway in these patients.

It is likely that additional target genes and pathways regulated by miR-105 also contribute to its prometastatic effect. Although overexpression of miR-105 in MCFDCIS xenografts did not significantly affect primary tumor growth, anti-miR-105 treatment in animals bearing MDA-231-HM xenografts reduced tumor volume and induced apoptosis of tumor cells. This may suggest a cancer- or/and niche-specific effect of miR-105 that facilitates cancer cell survival and, therefore, promotes metastasis. Interestingly, miR-105 has been reported as a tumor suppressor that inhibits proliferation through downregulating cyclin-dependent kinase 6 in prostate cancer cells (Honeywell et al., 2013). This miRNA may also have an anti-inflammatory effect in gingival keratinocytes through targeting Toll-like receptor 2 (Benakanakere et al., 2009). In several cancer cell lines of non-breast origin, mature miR-105 is undetectable, possibly because of the nuclear retention of miR-105 precursors (Lee et al., 2008). These suggest important tissue-specific mechanisms controlling the biogenesis and function of miR-105. Understanding these mechanisms and their relevance to cancer progression and metastasis will provide further rationales for targeting miR-105 as a treatment for MBC.

miRNA transfer between cancer cells and the genetically normal niche cells is apparently bidirectional. In addition to the cancer-derived adaptation of niche cells, normal epithelial cells also secrete and transfer antiproliferative miRNAs (e.g., miR-143) to cancer cells, as a potential strategy to maintain tissue homeostasis at an early stage in cancer formation (Kosaka et al., 2012). In contrast, exosomes secreted by stromal fibroblasts promote BC cell protrusion and motility through Wnt-planar cell polarity signaling (Luga et al., 2012). Because exosomes are secreted by multiple types of normal cells and mediate their natural functions such as antigen presentation (Théry et al., 2002), targeting exosome secretion as a potential means of blocking this mode of cancer-host crosstalk requires the identification of cancer-specific molecules or pathways that control exosome production. The recently reported high expression of Rab27A in cancer and the effect of Rab27A interference by reducing exosome production in multiple melanoma cell lines may provide an approach to specifically inhibit cancer-derived exosomes (Peinado et al., 2012). In addition, as the exosomal secretion of miRNAs exhibits a highly selective pattern that differs between cancer and normal cells (Table S1) (Pigati et al., 2010), understanding the cellular selection mechanism for miRNA secretion, which may involve RNA-binding proteins, recognizing the primary or secondary structures of miRNA and its dysregulation in cancer may reveal unique strategies to block cancer-specific miRNA secretion. Last, characterization of cancer-secreted messengers and effectors, such as miR-105, will enable the selection of patients for the corresponding targeted therapy and eventually combination therapy simultaneously targeting multiple secretory miRNAs and/or proteins. Such patient selection may be achieved by a quantitative blood test for circulating miR-105, which correlates with metastasis in early-stage BC patients. In developing personalized diagnostics and therapeutics, a combination of miR-105 with other miRNA and/or protein markers in the blood that would better specify the disease traits at the individual level will likely enhance our ability to select BC patients with high risk for metastasis for preventive treatment that targets miR-105 and other effectors.

(D) Representative H&E images of the tumor edges showing local invasiveness. The scale bar represents 50 μm.
(E) Immunohistochemistry (IHC) was performed in xenograft tumors using antibodies of Ki-67, cleaved (clvd) caspase-3, and ZO-1. Representative images are shown. The scale bar represents 50 μm.
(F) In vivo vascular permeability indicated by the penetration of rhodamine-dextran (red) into various organs. Tissues were collected from tumor-free NSG mice as well as mice bearing MDA-231-HM tumors that were untreated when sacrificed at week 3 after tumor cell implantation (the premetastatic [pre-met] group) or treated as indicated and sacrificed at week 6 (n = 4). Representative images are shown. DAPI (blue): cell nuclei. The scale bar represents 100 μm.
(G) Tissues were subjected to double-label IF for ZO-1 (green) and CD31 (pink). Structures positive for CD31 are indicated by arrowheads. The scale bar represents 100 μm.
Results are presented as mean ± SD (see also Figure S5).

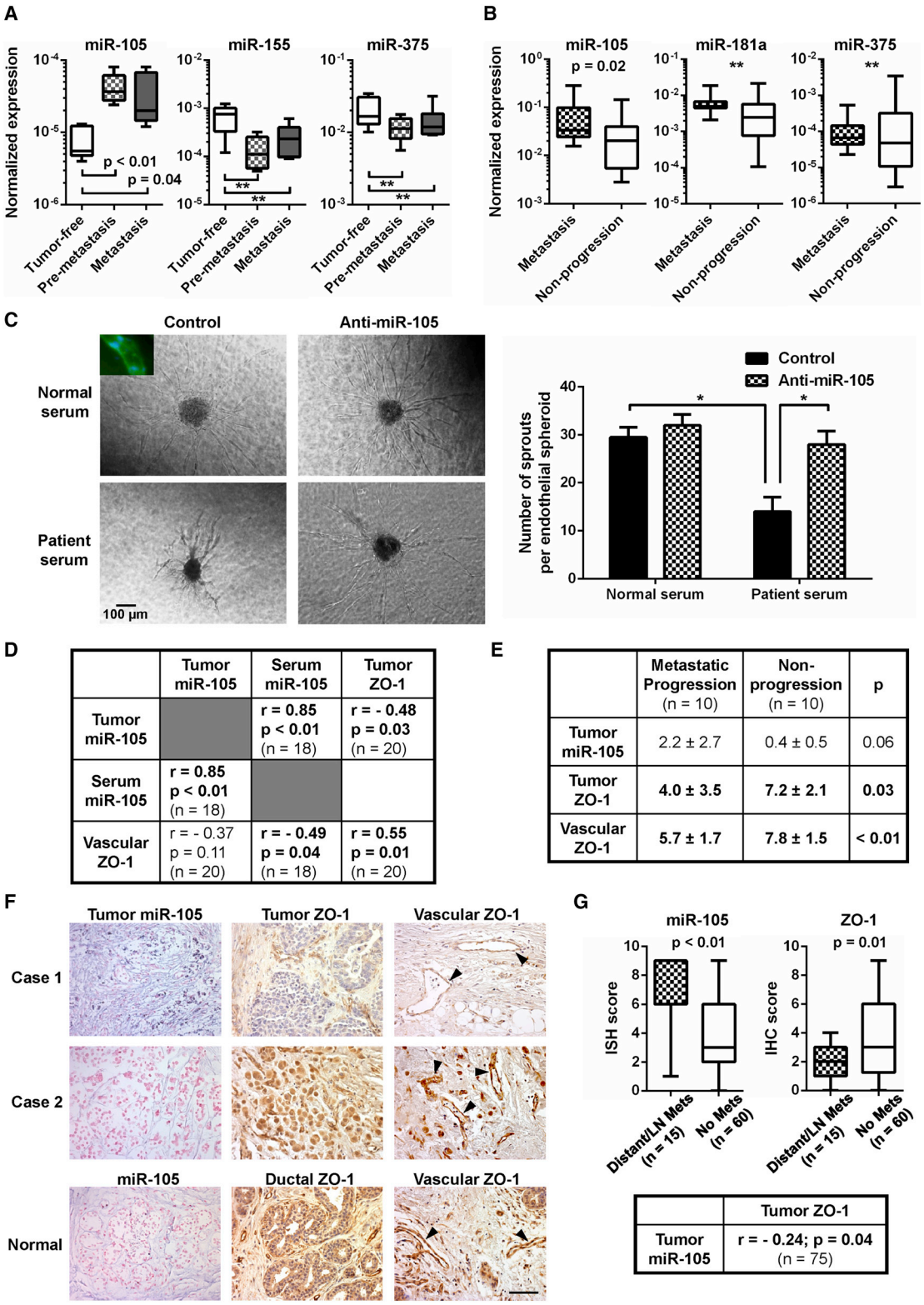

	Tumor miR-105	Serum miR-105	Tumor ZO-1
Tumor miR-105		**r = 0.85 p < 0.01** (n = 18)	**r = - 0.48 p = 0.03** (n = 20)
Serum miR-105	**r = 0.85 p < 0.01** (n = 18)		
Vascular ZO-1	r = - 0.37 p = 0.11 (n = 20)	**r = - 0.49 p = 0.04** (n = 18)	**r = 0.55 p = 0.01** (n = 20)

	Metastatic Progression (n = 10)	Non-progression (n = 10)	p
Tumor miR-105	2.2 ± 2.7	0.4 ± 0.5	0.06
Tumor ZO-1	**4.0 ± 3.5**	**7.2 ± 2.1**	**0.03**
Vascular ZO-1	**5.7 ± 1.7**	**7.8 ± 1.5**	**< 0.01**

	Tumor ZO-1
Tumor miR-105	**r = - 0.24; p = 0.04** (n = 75)

Figure 7. miR-105 Is Associated with ZO-1 Expression and Metastatic Progression in BC

(A) miRNA levels in the sera of tumor-free or MDA-231-HM tumor-bearing mice (premetastasis: serum collected at week 3; metastasis: serum collected at week 6; n = 5 or 6) were measured by RT-qPCR and normalized to miR-16. **p > 0.05.

(B) Circulating exosomes were isolated from serum samples of stage II and III BC patients. miRNAs were measured by RT-qPCR, normalized to miR-16, and compared among patients who developed distant metastases (mets) during follow-up (n = 16) and those who did not (n = 22). **p > 0.05.

(legend continued on next page)

EXPERIMENTAL PROCEDURES

Clinical Specimens

Human specimens were obtained from voluntarily consenting patients at the City of Hope Medical Center (Duarte, CA) under institutional review board-approved protocols. The clinical information is summarized in Tables S2–S5. Details can be found in Supplemental Experimental Procedures.

Cells, Plasmids, and Viruses

Please see Supplemental Experimental Procedures.

Exosome Purification and Electron Microscopy

Detailed protocols for preparing exosomes by ultracentrifugation can be found in Supplemental Experimental Procedures. For electron microscopy (EM), exosomes were fixed with 2% paraformaldehyde, loaded on 200-mesh Formvar-coated grids, and then contrasted and embedded as previously described (Thery et al., 2006). Solexa deep sequencing of exosomal and cellular RNA and genome-wide interrogation were performed as described (Wu et al., 2012); data sets were submitted to Gene Expression Omnibus (GEO) (GSE50429).

RNA Extraction, RT-qPCR, Western Blot Analysis, and Immunofluorescence

These procedures were performed as described previously (Tsuyada et al., 2012; Wang et al., 2011; Yu et al., 2010). See Supplemental Experimental Procedures for details.

Transendothelial Electrical Resistance, Endothelial Permeability, and 3D Vascular Sprouting Assays

Detailed protocols can be found in Supplemental Experimental Procedures. Vascular sprouting assay was performed as described using microcarrier beads coated with endothelial cells and embedded in 3D fibrin gel (Newman et al., 2011).

Wound Closure, Transwell Migration, and Transendothelial Invasion Assays

Wound closure and transwell migration assays were performed as previously described (Wang et al., 2006). Detailed protocols for transendothelial invasion assay can be found in Supplemental Experimental Procedures.

Animals

All animal experiments were approved by the institutional animal care and use committee at City of Hope. Detailed procedures can be found in Supplemental Experimental Procedures. The control and miR-105 targeted compounds used in the miR-105 intervention study had the same chemical modification pattern, chimeric 2′-fluoro and 2′-methoxyethyl modifications on a phosphorothioate backbone (Davis et al., 2006), and were synthesized at Regulus Therapeutics. The same compounds were also used in vitro to transfect MDA-231-HM cells (Figures S5A and S5B).

In Situ Hybridization and Immunohistochemistry

Please see Supplemental Experimental Procedures.

Statistical Analyses

All results were confirmed in at least three independent experiments, and data from one representative experiment were shown. All quantitative data are presented as mean ± SD. The statistical analysis was performed using SAS 9.2 software (SAS Institute). Student's t tests were used for comparisons of means of quantitative data between groups. The correlations between serum and tumor miR-105 and between miR-105 and ZO-1 expression were evaluated using Pearson's correlation coefficient (r). Values of $p < 0.05$ were considered significant.

ACCESSION NUMBERS

The GEO accession number for the exosomal and cellular RNA sequencing data reported in this paper is GSE50429.

SUPPLEMENTAL INFORMATION

Supplemental Information includes Supplemental Experimental Procedures, six figures, and five tables and can be found with this article online at http://dx.doi.org/10.1016/j.ccr.2014.03.007.

ACKNOWLEDGMENTS

This work was supported by the City of Hope Women's Cancer Program, National Institutes of Health (NIH)/National Cancer Institute (NCI) grants R01CA166020 (to S.E.W.) and R01CA163586 (to S.E.W.), California Breast Cancer Research Program grant 17IB-0054 (to S.E.W.), Breast Cancer Research Foundation-American Association for Cancer Research grant 12-60-26-WANG (to S.E.W.), and National Key Basic Research Development Program (973 Program) of China No. 2012CB9333004 (to X.R.). Research reported in this publication included work performed at core facilities supported by the NIH/NCI under grant P30CA33572. We thank the Center for Cancer Research, NCI, for funding support to P.C.L. We acknowledge Dr. Alan Fanning for kindly providing the ZO-1 plasmid. We also thank Drs. John Rossi, Hua Yu, John Shively, Linda Malkas, Andrew Raubitschek, Ren-Jang Lin, Michael Barish, Susan Kane, Shiuan Chen, and Joanne Mortimer for valuable comments as well as the City of Hope Core Facilities for highly professional services. G.S. had grant support from Celgene. E.G.M. was a full-time employee of a company developing miRNA therapeutics, Regulus Therapeutics.

Received: March 7, 2013
Revised: August 23, 2013
Accepted: March 7, 2014
Published: April 14, 2014

REFERENCES

Arroyo, J.D., Chevillet, J.R., Kroh, E.M., Ruf, I.K., Pritchard, C.C., Gibson, D.F., Mitchell, P.S., Bennett, C.F., Pogosova-Agadjanyan, E.L., Stirewalt, D.L., et al. (2011). Argonaute2 complexes carry a population of circulating microRNAs

(C) Circulating miR-105 in patient serum resulted in a vascular destruction. Vascular structures established from HMVECs that were transfected with anti-miR-105 compound or control compound were treated with human serum from a healthy donor or a BC patient with a high level of circulating miR-105. Representative images of the treated vascular structures are shown (left). Inset: Structures were stained with CD31 antibody (green) and DAPI (blue). Vascular sprouts per spheroid were counted and graphed (right). At least 50 spheroids were counted in each experiment, and the experiment was repeated three times. *$p < 0.05$.
(D) Correlation analyses of tumor miR-105, serum (exosomal) miR-105, and ZO-1 levels in BC patients. miR-105 levels in tumor cells and ZO-1 levels in tumor cells (tumor ZO-1) or tumor-adjacent vascular structures (vascular ZO-1) were determined by ISH and IHC, respectively, and scored as described in Experimental Procedures. Serum (exosomal) miR-105 levels were determined by PCR using miR-16 as a normalizer. Correlation analyses were carried out between two sets of quantified data as indicated. Pearson's correlation coefficient (r) and p value are shown.
(E) The scores of tumor miR-105, tumor ZO-1, and vascular ZO-1 staining were compared between stage II and III BC patients who developed distant metastases (n = 10) and those who did not (n = 10). Mean and SD of the staining scores in each group are shown.
(F) Representative images of miR-105 and ZO-1 staining in tumor and normal breast tissue sections. Vascular structures are indicated by arrowheads. The scale bar represents 100 μm.
(G) Levels of tumor miR-105 and ZO-1 determined in a BC tissue array. The ISH or IHC scores were compared between primary tumors with distant or lymph node (LN) metastases (n = 15) and those without (n = 60). The correlation between miR-105 and ZO-1 was analyzed among all cases (n = 75).
Results are presented as mean ± SD (see also Figure S6 and Tables S2–S5).

independent of vesicles in human plasma. Proc. Natl. Acad. Sci. USA *108*, 5003–5008.

Benakanakere, M.R., Li, Q., Eskan, M.A., Singh, A.V., Zhao, J., Galicia, J.C., Stathopoulou, P., Knudsen, T.B., and Kinane, D.F. (2009). Modulation of TLR2 protein expression by miR-105 in human oral keratinocytes. J. Biol. Chem. *284*, 23107–23115.

Brennan, K., Offiah, G., McSherry, E.A., and Hopkins, A.M. (2010). Tight junctions: a barrier to the initiation and progression of breast cancer? J. Biomed. Biotechnol. *2010*, 460607.

Calin, G.A., and Croce, C.M. (2006). MicroRNA signatures in human cancers. Nat. Rev. Cancer *6*, 857–866.

Chambers, A.F., Groom, A.C., and MacDonald, I.C. (2002). Dissemination and growth of cancer cells in metastatic sites. Nat. Rev. Cancer *2*, 563–572.

Citi, S., Spadaro, D., Schneider, Y., Stutz, J., and Pulimeno, P. (2011). Regulation of small GTPases at epithelial cell-cell junctions. Mol. Membr. Biol. *28*, 427–444.

Connolly, J.O., Simpson, N., Hewlett, L., and Hall, A. (2002). Rac regulates endothelial morphogenesis and capillary assembly. Mol. Biol. Cell *13*, 2474–2485.

Davis, S., Lollo, B., Freier, S., and Esau, C. (2006). Improved targeting of miRNA with antisense oligonucleotides. Nucleic Acids Res. *34*, 2294–2304.

Elhassan, M.O., Christie, J., and Duxbury, M.S. (2012). Homo sapiens systemic RNA interference-defective-1 transmembrane family member 1 (SIDT1) protein mediates contact-dependent small RNA transfer and microRNA-21-driven chemoresistance. J. Biol. Chem. *287*, 5267–5277.

Fabbri, M., Paone, A., Calore, F., Galli, R., Gaudio, E., Santhanam, R., Lovat, F., Fadda, P., Mao, C., Nuovo, G.J., et al. (2012). MicroRNAs bind to Toll-like receptors to induce prometastatic inflammatory response. Proc. Natl. Acad. Sci. USA *109*, E2110–E2116.

Georgiadis, A., Tschernutter, M., Bainbridge, J.W., Balaggan, K.S., Mowat, F., West, E.L., Munro, P.M., Thrasher, A.J., Matter, K., Balda, M.S., and Ali, R.R. (2010). The tight junction associated signalling proteins ZO-1 and ZONAB regulate retinal pigment epithelium homeostasis in mice. PLoS ONE *5*, e15730.

González-Mariscal, L., Tapia, R., and Chamorro, D. (2008). Crosstalk of tight junction components with signaling pathways. Biochim. Biophys. Acta *1778*, 729–756.

Heneghan, H.M., Miller, N., Lowery, A.J., Sweeney, K.J., Newell, J., and Kerin, M.J. (2010). Circulating microRNAs as novel minimally invasive biomarkers for breast cancer. Ann. Surg. *251*, 499–505.

Honeywell, D.R., Cabrita, M.A., Zhao, H., Dimitroulakos, J., and Addison, C.L. (2013). miR-105 inhibits prostate tumour growth by suppressing CDK6 levels. PLoS ONE *8*, e70515.

Hood, J.L., San, R.S., and Wickline, S.A. (2011). Exosomes released by melanoma cells prepare sentinel lymph nodes for tumor metastasis. Cancer Res. *71*, 3792–3801.

Hu, M., Yao, J., Carroll, D.K., Weremowicz, S., Chen, H., Carrasco, D., Richardson, A., Violette, S., Nikolskaya, T., Nikolsky, Y., et al. (2008). Regulation of in situ to invasive breast carcinoma transition. Cancer Cell *13*, 394–406.

Huang, Y., Song, N., Ding, Y., Yuan, S., Li, X., Cai, H., Shi, H., and Luo, Y. (2009). Pulmonary vascular destabilization in the premetastatic phase facilitates lung metastasis. Cancer Res. *69*, 7529–7537.

Iorio, M.V., Ferracin, M., Liu, C.G., Veronese, A., Spizzo, R., Sabbioni, S., Magri, E., Pedriali, M., Fabbri, M., Campiglio, M., et al. (2005). MicroRNA gene expression deregulation in human breast cancer. Cancer Res. *65*, 7065–7070.

Itoh, M., and Bissell, M.J. (2003). The organization of tight junctions in epithelia: implications for mammary gland biology and breast tumorigenesis. J. Mammary Gland Biol. Neoplasia *8*, 449–462.

Jou, T.S., Schneeberger, E.E., and Nelson, W.J. (1998). Structural and functional regulation of tight junctions by RhoA and Rac1 small GTPases. J. Cell Biol. *142*, 101–115.

Jung, E.J., Santarpia, L., Kim, J., Esteva, F.J., Moretti, E., Buzdar, A.U., Di Leo, A., Le, X.F., Bast, R.C., Jr., Park, S.T., et al. (2012). Plasma microRNA 210 levels correlate with sensitivity to trastuzumab and tumor presence in breast cancer patients. Cancer *118*, 2603–2614.

Kaplan, R.N., Riba, R.D., Zacharoulis, S., Bramley, A.H., Vincent, L., Costa, C., MacDonald, D.D., Jin, D.K., Shido, K., Kerns, S.A., et al. (2005). VEGFR1-positive haematopoietic bone marrow progenitors initiate the pre-metastatic niche. Nature *438*, 820–827.

Kosaka, N., Iguchi, H., Yoshioka, Y., Hagiwara, K., Takeshita, F., and Ochiya, T. (2012). Competitive interactions of cancer cells and normal cells via secretory microRNAs. J. Biol. Chem. *287*, 1397–1405.

Lee, E.J., Baek, M., Gusev, Y., Brackett, D.J., Nuovo, G.J., and Schmittgen, T.D. (2008). Systematic evaluation of microRNA processing patterns in tissues, cell lines, and tumors. RNA *14*, 35–42.

Luga, V., Zhang, L., Viloria-Petit, A.M., Ogunjimi, A.A., Inanlou, M.R., Chiu, E., Buchanan, M., Hosein, A.N., Basik, M., and Wrana, J.L. (2012). Exosomes mediate stromal mobilization of autocrine Wnt-PCP signaling in breast cancer cell migration. Cell *151*, 1542–1556.

Martin, T.A., and Jiang, W.G. (2009). Loss of tight junction barrier function and its role in cancer metastasis. Biochim. Biophys. Acta *1788*, 872–891.

Martin, T.A., Watkins, G., Mansel, R.E., and Jiang, W.G. (2004). Loss of tight junction plaque molecules in breast cancer tissues is associated with a poor prognosis in patients with breast cancer. Eur. J. Cancer *40*, 2717–2725.

Miller, F.R., Santner, S.J., Tait, L., and Dawson, P.J. (2000). MCF10DCIS.com xenograft model of human comedo ductal carcinoma in situ. J. Natl. Cancer Inst. *92*, 1185–1186.

Mitchell, P.S., Parkin, R.K., Kroh, E.M., Fritz, B.R., Wyman, S.K., Pogosova-Agadjanyan, E.L., Peterson, A., Noteboom, J., O'Briant, K.C., Allen, A., et al. (2008). Circulating microRNAs as stable blood-based markers for cancer detection. Proc. Natl. Acad. Sci. USA *105*, 10513–10518.

Newman, A.C., Nakatsu, M.N., Chou, W., Gershon, P.D., and Hughes, C.C. (2011). The requirement for fibroblasts in angiogenesis: fibroblast-derived matrix proteins are essential for endothelial cell lumen formation. Mol. Biol. Cell *22*, 3791–3800.

Nicolini, A., Giardino, R., Carpi, A., Ferrari, P., Anselmi, L., Colosimo, S., Conte, M., Fini, M., Giavaresi, G., Berti, P., and Miccoli, P. (2006). Metastatic breast cancer: an updating. Biomed. Pharmacother. *60*, 548–556.

Paget, S. (1889). The distribution of secondary growths in cancer of the breast. Lancet *133*, 571–573.

Peinado, H., Alečković, M., Lavotshkin, S., Matei, I., Costa-Silva, B., Moreno-Bueno, G., Hergueta-Redondo, M., Williams, C., García-Santos, G., Ghajar, C., et al. (2012). Melanoma exosomes educate bone marrow progenitor cells toward a pro-metastatic phenotype through MET. Nat. Med. *18*, 883–891.

Pigati, L., Yaddanapudi, S.C., Iyengar, R., Kim, D.J., Hearn, S.A., Danforth, D., Hastings, M.L., and Duelli, D.M. (2010). Selective release of microRNA species from normal and malignant mammary epithelial cells. PLoS ONE *5*, e13515.

Podsypanina, K., Du, Y.C., Jechlinger, M., Beverly, L.J., Hambardzumyan, D., and Varmus, H. (2008). Seeding and propagation of untransformed mouse mammary cells in the lung. Science *321*, 1841–1844.

Polette, M., Gilles, C., Nawrocki-Raby, B., Lohi, J., Hunziker, W., Foidart, J.M., and Birembaut, P. (2005). Membrane-type 1 matrix metalloproteinase expression is regulated by zonula occludens-1 in human breast cancer cells. Cancer Res. *65*, 7691–7698.

Psaila, B., and Lyden, D. (2009). The metastatic niche: adapting the foreign soil. Nat. Rev. Cancer *9*, 285–293.

Redis, R.S., Calin, S., Yang, Y., You, M.J., and Calin, G.A. (2012). Cell-to-cell miRNA transfer: from body homeostasis to therapy. Pharmacol. Ther. *136*, 169–174.

Roth, C., Rack, B., Müller, V., Janni, W., Pantel, K., and Schwarzenbach, H. (2010). Circulating microRNAs as blood-based markers for patients with primary and metastatic breast cancer. Breast Cancer Res. *12*, R90.

Rubens, R.D. (2001). 7. Management of advanced breast cancer. Int. J. Clin. Pract. *55*, 676–679.

Sethi, N., and Kang, Y. (2011). Unravelling the complexity of metastasis - molecular understanding and targeted therapies. Nat. Rev. Cancer *11*, 735–748.

Shen, L., Black, E.D., Witkowski, E.D., Lencer, W.I., Guerriero, V., Schneeberger, E.E., and Turner, J.R. (2006). Myosin light chain phosphorylation regulates barrier function by remodeling tight junction structure. J. Cell Sci. *119*, 2095–2106.

Skog, J., Würdinger, T., van Rijn, S., Meijer, D.H., Gainche, L., Sena-Esteves, M., Curry, W.T., Jr., Carter, B.S., Krichevsky, A.M., and Breakefield, X.O. (2008). Glioblastoma microvesicles transport RNA and proteins that promote tumour growth and provide diagnostic biomarkers. Nat. Cell Biol. *10*, 1470–1476.

Taylor, D.D., and Gercel-Taylor, C. (2008). MicroRNA signatures of tumor-derived exosomes as diagnostic biomarkers of ovarian cancer. Gynecol. Oncol. *110*, 13–21.

Théry, C., Zitvogel, L., and Amigorena, S. (2002). Exosomes: composition, biogenesis and function. Nat. Rev. Immunol. *2*, 569–579.

Thery, C., Amigorena, S., Raposo, G., and Clayton, A. (2006). Isolation and characterization of exosomes from cell culture supernatants and biological fluids. Curr. Protoc. Cell Biol., Chapter 3, Unit 3.22.

Tsuyada, A., Chow, A., Wu, J., Somlo, G., Chu, P., Loera, S., Luu, T., Li, A.X., Wu, X., Ye, W., et al. (2012). CCL2 mediates cross-talk between cancer cells and stromal fibroblasts that regulates breast cancer stem cells. Cancer Res. *72*, 2768–2779.

Turchinovich, A., Weiz, L., Langheinz, A., and Burwinkel, B. (2011). Characterization of extracellular circulating microRNA. Nucleic Acids Res. *39*, 7223–7233.

Valadi, H., Ekström, K., Bossios, A., Sjöstrand, M., Lee, J.J., and Lötvall, J.O. (2007). Exosome-mediated transfer of mRNAs and microRNAs is a novel mechanism of genetic exchange between cells. Nat. Cell Biol. *9*, 654–659.

Vickers, K.C., and Remaley, A.T. (2012). Lipid-based carriers of microRNAs and intercellular communication. Curr. Opin. Lipidol. *23*, 91–97.

Vickers, K.C., Palmisano, B.T., Shoucri, B.M., Shamburek, R.D., and Remaley, A.T. (2011). MicroRNAs are transported in plasma and delivered to recipient cells by high-density lipoproteins. Nat. Cell Biol. *13*, 423–433.

Wang, S.E., Narasanna, A., Perez-Torres, M., Xiang, B., Wu, F.Y., Yang, S., Carpenter, G., Gazdar, A.F., Muthuswamy, S.K., and Arteaga, C.L. (2006). HER2 kinase domain mutation results in constitutive phosphorylation and activation of HER2 and EGFR and resistance to EGFR tyrosine kinase inhibitors. Cancer Cell *10*, 25–38.

Wang, Y., Yu, Y., Tsuyada, A., Ren, X., Wu, X., Stubblefield, K., Rankin-Gee, E.K., and Wang, S.E. (2011). Transforming growth factor-β regulates the sphere-initiating stem cell-like feature in breast cancer through miRNA-181 and ATM. Oncogene *30*, 1470–1480.

Wu, X., Somlo, G., Yu, Y., Palomares, M.R., Li, A.X., Zhou, W., Chow, A., Yen, Y., Rossi, J.J., Gao, H., et al. (2012). De novo sequencing of circulating miRNAs identifies novel markers predicting clinical outcome of locally advanced breast cancer. J. Transl. Med. *10*, 42.

Yardley, D.A. (2010). Visceral disease in patients with metastatic breast cancer: efficacy and safety of treatment with ixabepilone and other chemotherapeutic agents. Clin. Breast Cancer *10*, 64–73.

Yu, Y., Wang, Y., Ren, X., Tsuyada, A., Li, A., Liu, L.J., and Wang, S.E. (2010). Context-dependent bidirectional regulation of the MutS homolog 2 by transforming growth factor β contributes to chemoresistance in breast cancer cells. Mol. Cancer Res. *8*, 1633–1642.

Yuan, A., Farber, E.L., Rapoport, A.L., Tejada, D., Deniskin, R., Akhmedov, N.B., and Farber, D.B. (2009). Transfer of microRNAs by embryonic stem cell microvesicles. PLoS ONE *4*, e4722.

Zhang, Y., Liu, D., Chen, X., Li, J., Li, L., Bian, Z., Sun, F., Lu, J., Yin, Y., Cai, X., et al. (2010). Secreted monocytic miR-150 enhances targeted endothelial cell migration. Mol. Cell *39*, 133–144.

Zhu, W., Qin, W., Atasoy, U., and Sauter, E.R. (2009). Circulating microRNAs in breast cancer and healthy subjects. BMC Res. Notes *2*, 89.

Zhuang, G., Wu, X., Jiang, Z., Kasman, I., Yao, J., Guan, Y., Oeh, J., Modrusan, Z., Bais, C., Sampath, D., and Ferrara, N. (2012). Tumour-secreted miR-9 promotes endothelial cell migration and angiogenesis by activating the JAK-STAT pathway. EMBO J. *31*, 3513–3523.

CellPress

Cancer Cell
Article

Pemetrexed and Gemcitabine as Combination Therapy for the Treatment of Group3 Medulloblastoma

Marie Morfouace,[1] Anang Shelat,[2] Megan Jacus,[3] Burgess B. Freeman III,[4] David Turner,[3] Sarah Robinson,[1] Frederique Zindy,[1] Yong-Dong Wang,[5] David Finkelstein,[5] Olivier Ayrault,[6] Laure Bihannic,[6] Stephanie Puget,[7] Xiao-Nan Li,[8] James M. Olson,[9] Giles W. Robinson,[10] R. Kiplin Guy,[2] Clinton F. Stewart,[3] Amar Gajjar,[10] and Martine F. Roussel[1,*]

[1]Department of Tumor Cell Biology
[2]Department of Chemical Biology and Therapeutics
[3]Department of Pharmaceutical Sciences
[4]Department of Preclinical Pharmacokinetics
[5]Department of Computational Biology
St. Jude Children's Research Hospital, Memphis, TN 38105, USA
[6]Institut Curie/CNRS UMR 3306/INSERM U1005 Building 110, Centre Universitaire, 91405 Orsay, Cedex, France
[7]AP-HP, Department of Neurosurgery, Necker-Enfants Malades Hospital, Université Rene Descartes, 75015 Paris, France
[8]Department of Pediatrics, Section of Hematology-Oncology, Baylor College of Medicine, Houston, TX 77030, USA
[9]Department of Pediatric Hematology-Oncology, Fred Hutchinson Cancer Research Center, Seattle, WA 98109, USA
[10]Department of NeuroOncology, St. Jude Children's Research Hospital, Memphis, TN 38105, USA
*Correspondence: martine.roussel@stjude.org
http://dx.doi.org/10.1016/j.ccr.2014.02.009

SUMMARY

We devised a high-throughput, cell-based assay to identify compounds to treat Group3 medulloblastoma (G3 MB). Mouse G3 MBs neurospheres were screened against a library of approximately 7,000 compounds including US Food and Drug Administration-approved drugs. We found that pemetrexed and gemcitabine preferentially inhibited G3 MB proliferation in vitro compared to control neurospheres and substantially inhibited G3 MB proliferation in vivo. When combined, these two drugs significantly increased survival of mice bearing cortical implants of mouse and human G3 MBs that overexpress MYC compared to each agent alone, while having little effect on mouse MBs of the sonic hedgehog subgroup. Our findings strongly suggest that combination therapy with pemetrexed and gemcitabine is a promising treatment for G3 MBs.

INTRODUCTION

Medulloblastoma (MB), a tumor of the posterior fossa, is primarily a pediatric disease, although it occasionally occurs in adults (Ellison et al., 2011). MB is classified into four major subgroups based on clinical and molecular profiles (Taylor et al., 2012). Two subgroups exhibit constitutive activation of the sonic hedgehog (SHH) or wingless (WNT) developmental pathways. The other two are referred to as group 3 (G3) and G4. Importantly, the molecular subgrouping of these tumors also relates to distinct patient demographics, histologic classification, somatic genetic variations, and clinical outcome. For example, patients with WNT MB tend to be older, female, and to uniformly survive with current therapy (Northcott et al., 2012). In contrast, patients with G3 MB tend to be younger, male, have anaplastic histology, exhibit a higher incidence of metastatic disease, and have a poor prognosis (Dubuc et al., 2013; Kool et al., 2012; Parsons et al., 2011; Pugh et al., 2012; Rausch et al., 2012; Robinson et al., 2012). One characteristic feature of G3 MB is their high MYC expression in >75% of cases. Indeed, one study shows that MYC expression is elevated in 20 of 26 (77%) G3 MBs (named group C), compared to 1 of 35 (3%) G4 MBs (named group D; Northcott et al., 2011). Whole genome sequencing studies on 17 G3 MBs reveals only one tumor (5.9%) with true

Significance

Despite the recent identification of four molecular groups of human MB, patients are currently treated with similar chemotherapies independent of classification. G3 MB has a high incidence of metastasis and poor prognosis. Thus, more effective therapeutic approaches for these patients are desperately needed. The development of a mouse model of G3 MB enabled production of cultured neurospheres that provided an ideal platform to identify additional chemotherapies. We found two FDA-approved drugs that significantly inhibited mouse and human G3 MB neurosphere cultures, mouse allografts, and xenografts from G3 MB primary patient samples, but not mouse SHH MBs. These findings provide a strong rationale for combination therapy with pemetrexed and gemcitabine to treat patients with G3 MB.

MYC amplification, whereas two other tumors display an aberrant copy number gain of the *MYC* gene. However, 15 of these 17 (88%) G3 MBs demonstrate high MYC expression (Robinson et al., 2012). Despite these pronounced differences, patients with MB are typically treated with uniform surgery, radiotherapy, and adjuvant chemotherapy including vincristine, cisplatin, and cyclophosphamide (Packer et al., 2013) or lomustine and carboplatin (Massimino et al., 2012). These therapies fail to cure one-third of all patients and carry widespread morbidities that impair survivor's quality of life.

Molecular subgrouping has the potential to improve risk stratification and tailor therapy to reduce toxicities to potential survivors. Paramount to this strategy is the development of accurate models that recapitulate the subgroups for preclinical therapeutic testing. We developed a mouse model of G3 MB through the orthotopic transplantation of transgenic cerebellar granule neuronal progenitors (GNPs) in the cortices of naive recipient animals. GNPs were purified by percoll density gradient from the cerebella of 5- to 7-day-old *Trp53*$^{-/-}$;*Cdkn2c*$^{-/-}$ mice and infected with retroviruses encoding MYC (Kawauchi et al., 2012). MB tumors develop within 30 days of transplantation with as few as 100 tumor cells that recapitulate the high level of trimethylation of histone H3 at lysine 27 (H3K27me3) seen in human G3 and G4 (Robinson et al., 2012). Tumors grow as neurospheres that, when transplanted into cortices of recipient mice, induce secondary MBs that mimic the primary tumors (Kawauchi et al., 2012). Because neurospheres can be passaged repeatedly while maintaining their functional and molecular properties, they provide a unique platform to conduct screens of compounds to identify those with therapeutic potential against human G3 MB. We here report the outcome of screening a library of compounds that included US Food and Drug Administration (FDA)-approved drugs and candidate compounds in development.

RESULTS

High-Throughput Screen Using Mouse G3 MB Neurospheres

Tumor cells purified from several independently derived primary mouse G3 MBs were grown as neurospheres for four to five passages providing lines with comparable cell proliferation characteristics. Two lines, derived from independent tumors and infections, were hereafter referred to as "Myc1" and "Myc2." Neurospheres from the cerebellum of 7-day-old (P7) *Trp53*$^{-/-}$;*Cdkn2c*$^{-/-}$ mice (hereafter referred to as *Trp53*-null) were used as control. To determine the number of cells necessary for exponential growth 4 days after plating, mouse *Trp53*-null and Myc1 were plated at different densities (Figure S1A available online). Other control cells included TERT^{-} human fibroblasts (BJ) to identify compounds with nonspecific toxicities and HepG2 (a human hepatocellular carcinoma cell line) to eliminate highly cytotoxic compounds.

We performed a primary screen of a "bioactive" library using a luminescence-based assay that measures cell proliferation via ATP. The library contained 7,389 compounds (6,568 unique) obtained from different sources, including 830 FDA-approved drugs (Figure S1B; see Supplemental Experimental Procedures for details). Compounds were tested at a single concentration (10 μM) in triplicate. Z-prime and other assay diagnostics were acceptable (Figure S1C) and the scatterplot of controls and compound activities showed adequate separation between signal and noise for both Myc1 and *Trp53*-null (Figure S1D, left). Receiver operator characteristic analysis indicated that the assay demonstrated acceptable discriminatory power between true-positive and true-negative results, with the area under the curve (AUC) >0.8 for both lines, and that an assay cutoff of >50% returned ~70% of all true-positive results for Myc1 (Figure S1D, right). A total of 690 of the 7,389 compounds, including all with inhibition >50% in the primary screen with Myc1, analogs of these hits, and other compounds of interest, were tested in dose-response experiments in triplicate using concentrations ranging from 4 nM to 10 μM. Of the 690 hits, we identified 65 compounds with potency <1 μM against Myc 1 (Figure 1; Table S1).

Screening Results of FDA-Approved Drugs

To accelerate the transition of potential therapeutics into the clinic, we prioritized the FDA-approved drugs with oncology indications and potencies below or near 1 μM for further study. We conducted dose-response experiments on 35 FDA-approved drugs in triplicate on Myc1, *Trp53*-null, HepG2, and BJ cell lines (Figure S2A; Table 1). Drugs were grouped into nine activity classes: folate pathway inhibitors, other inhibitors of DNA/RNA synthesis, purine antimetabolites, microtubule inhibitors, sterol biosynthesis inhibitors, topoisomerase inhibitors, epigenetic regulators, proteasome inhibitors, and RNA polymerase inhibitors. Myc1 was extremely sensitive to folate pathway inhibitors with pemetrexed, methotrexate, and raltitrexed being the most selective. The DNA/RNA synthesis inhibitor gemcitabine was highly potent in both Myc1 and *Trp53*-null, but achieved 100% efficacy in only Myc1. The purine antimetabolite cladribine showed promising activity against Myc1, but a narrower therapeutic window against the control cell lines HepG2 and BJ compared to other drugs. The proteasome inhibitor bortezomib and the RNA polymerase inhibitor dactinomycin were equipotent and equally efficacious against both Myc1 and *Trp53* null. Microtubule inhibitors, including vincristine and vinblastine, and topoisomerase inhibitors, such as doxorubicin, etoposide, and topotecan, were active in G3 MB. Because they are already used in the clinic for the treatment of MB, they were not considered further. Cerivastatin and fluvastatin, two sterol biosynthesis inhibitors targeting 3-hydroxy-3-methyl-glutaryl-coenzyme A reductase, had high efficacy but low potency relative to the other compound classes. Decitabine, a drug that causes both DNA damage and alterations in DNA methylation, was moderately potent, and had much higher efficacy for Myc1 over *Trp53*-null.

We selected decitabine, pemetrexed, and gemcitabine for further study because of their selectivity and diversity in mechanism of action. As noted earlier, mouse and human G3 MBs are marked by a high level of H3K27me3. Decitabine is an S-adenosyl methionine and cytidine analog. At low dose and prolonged exposure, decitabine targets DNA and histone methylation, whereas it induces DNA damage at high doses (Figure 2A; Palii et al., 2008). After 72 hr of treatment, the half-maximal effective concentration (EC_{50}) for decitabine was 1.3 μM against Myc1 with 100% efficacy (Figure S2A, blue curve; Table 1), whereas

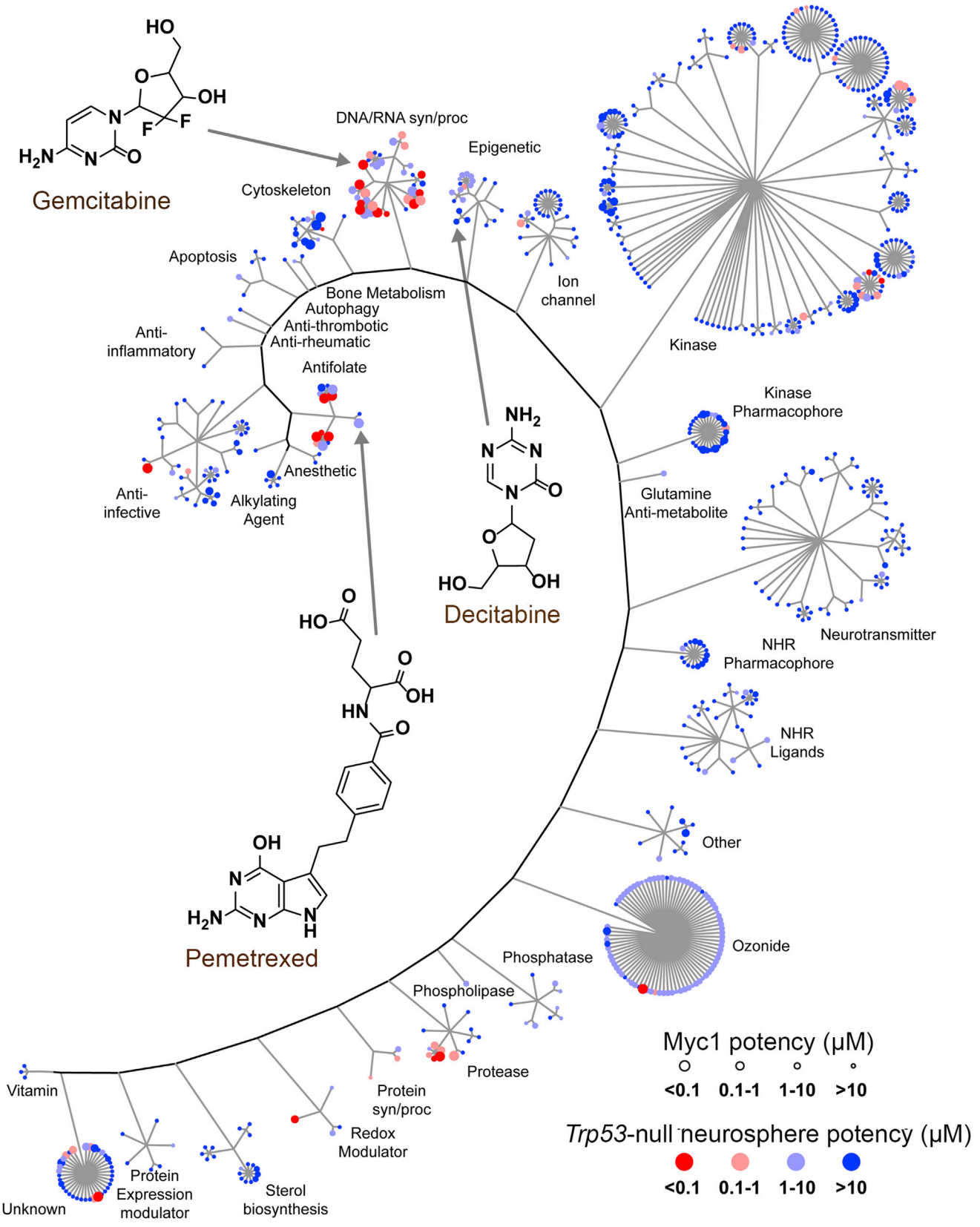

(legend on next page)

Table 1. EC_{50} Values for FDA-Approved Drugs on Myc1, *Trp53*-null, and Control Cell Lines

Compound	Myc1 (μM)	*Trp53*-null (μM)	HepG2 (μM)	BJ (μM)
Amsacrine	0.16 (0.097–0.27)	0.55 (0.18–1.7)	11 (5.6–23)	13 (7.6–21)
Ancitabine	0.031 (0.024–0.04)	0.55 (0.29–1)	ND	ND
Bortezomib	0.0063 (0.0051–0.0078)	0.0027 (0.0018–0.004)	0.026 (0.0076–0.087)	0.023 (0.0086–0.061)
Cerivastatin	0.77 (0.65–0.9)	2.5 (1.3–4.7)	0.92 (0.55–1.6)	ND
Cladrabine	0.0043 (0.0024–0.0078)	0.25 (0.026–2.4)	3.3 (2.6–4.3)	1.4 (0.13–17)
Clofarabine	0.15 (0.13–0.18)	0.34 (0.28–0.4)	ND	ND
Cycloguanil	0.11 (0.059–0.21)	0.18 (0.14–0.23)	ND	ND
Cytarabine	0.083 (0.066–0.1)	0.2 (0.092–0.42)	0.078 (0.041–0.15)[a]	ND
Dactinomycin	9e-04 (0.00016–0.005)	0.0024 (0.0012–0.005)	0.0084 (0.005–0.014)	ND
Daunorubicin	0.0075 (0.0059–0.0097)	0.036 (0.016–0.079)	1.7 (0.11–25)	0.1 (0.02–0.52)[a]
Decitabine	1.3 (0.72–2.2)	0.032 (0.014–0.073)[a]	ND	ND
Doxorubicin	0.028 (0.015–0.052)	0.11 (0.058–0.2)	0.58 (0.14–2.3)	0.14 (0.027–0.77)[a]
Etoposide	0.24 (0.17–0.36)	0.046 (0.013-0.15)	ND	ND
Floxuridine	0.0016 (0.0013–0.002)	0.0001[b]	ND	ND
Fluorouracil	0.36 (0.3–0.43)	0.22 (0.17–0.29)	ND	ND
Fluvastatin	4.5 (1.6–13)	ND	ND	ND
Gemcitabine	0.0021 (0.0018–0.0025)	0.00032 (0.00012–0.00087)	ND	ND
Lovastatin	4 (3.3–4.8)	2.1 (0.11–38)[a]	13 (4.7–38)	ND
Methotrexate	0.0052 (0.0024–0.012)	0.15 (0.05–0.46)	ND	ND
Mitoxanthrone	0.18 (0.11–0.29)	0.19 (0.12–0.31)	0.12 (0.072–0.2)[a]	ND
Nocodazole	0.11 (0.036–0.32)	0.094 (0.037–0.23)[a]	0.015 (0.0073–0.03)[a]	ND
Pemetrexed	0.035 (0.027–0.046)	15 (0.57–410)	ND	ND
Pitavastatin	3.5 (1.5–8.6)	ND	5 (2.8–8.7)	ND
Podofilox	0.0064 (0.0015–0.028)	0.0074 (0.0048–0.012)[a]	0.0039 (0.0025–0.0059)[a]	ND
Pyrimethamine	4.9 (3–8.1)	0.87 (0.2–3.9)	ND	ND
Raltiterxed	0.003 (0.0024–0.0038)	0.34 (0.18–0.63)	ND	ND
Rosuvastatin	2.6 (2.3–3)	ND	ND	ND
Simvastatin	3 (2.6–3.5)	ND	9.4 (6–15)	5.8 (4.7–7.2)
Tenoposide	0.052 (0.003–0.89)	0.11 (0.0097–1.2)	7.7 (1.5–39)	29 (3.8–230)
Thioguanine	0.44 (0.082–2.4)	0.8 (0.52–1.2)	11 (2.3–52)	ND
Topotecan	0.075 (0.05–0.11)	0.18 (0.06–0.53)	0.09 (0.026–0.31)	ND
Trifluridine	0.038 (0.034–0.043)	0.0029 (0.0022–0.0039)	ND	ND
Trimetrexate	0.035 (0.0028–0.45)	0.0047 (0.0033–0.0066)	ND	ND
Vinblastine	0.012 (0.0028–0.053)	0.015 (0.011–0.021)[a]	ND	ND
Vincristine	0.0094 (0.0044–0.02)	0.01 (0.0071–0.014)[a]	ND	ND

Concentration range in parentheses. ND, EC_{50} could not be determined in the concentration range tested.
[a]Indicates regression curve failed to reach 50% efficacy.
[b]Indicates questionable EC_{50} due to regression artifacts.

efficacy against *Trp53*-null never exceeded 35% (Figure S2A, red curve; Table 1). Treatment of Myc1 with 0.5 μM decitabine for 72 hr significantly decreased H3K27me3 levels while 40 nM of pemetrexed had no effect (Figure 2B).

A comparative study of gene expression profiles in mouse G3 and SHH MBs and GNPs suggested that mouse G3 MBs were sensitive to inhibitors of purine (Figure 2C, top), pyrimidine (Figure 2C, middle), and folate (Figure 2C, bottom) metabolism compared to SHH MBs and GNPs. In agreement with this gene expression pattern, pemetrexed and gemcitabine targeted these pathways. Pemetrexed targets three enzymes in the folate pathway; phosphoribosylglycinamide formyltransferase (GART), dihydrofolate reductase, and thymidylate synthase (Figure 2D; Chattopadhyay et al., 2007). After 72 hr of

Figure 1. Summary of the HTS on Mouse Myc1 and *Trp53*-null Neurospheres
Distribution of 690 active compounds from dose response in Myc1 and *Trp53*-null neurospheres according to their mechanism of action. Each compound is represented as a colored circle, with potency against Myc1 depicted by size and potency against *Trp53*-null shown by blue-red color. Potent compounds selective for Myc1 are represented by large, blue circles.
See also Figure S1 and Table S1.

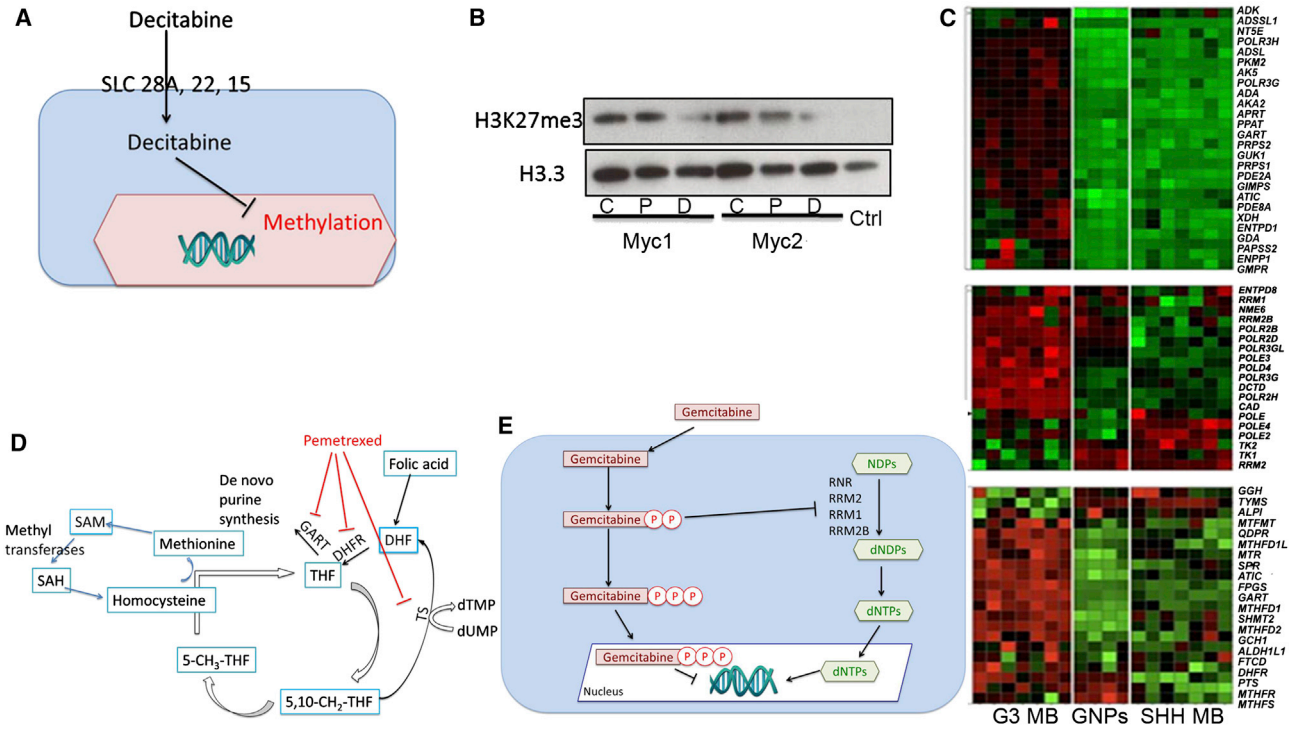

Figure 2. Pattern of Sensitivity of *Trp53*-null and G3 Neurospheres to the Different Classes of Compounds

(A) An outline of the decitabine pathway.

(B) Detection of H3K27me3 by immunoblotting from cell lysates of Myc1 and Myc 2, untreated (C), or treated with decitabine (D) or pemetrexed (P). Ctrl, recombinant human H3.

(C) mRNA levels of enzymes involved in purine (top), pyrimidine (middle) metabolism, and the folate pathway (one carbon pool and folate biosynthesis; bottom; from KEGG pathway) between mouse G3 MB, SHH MB, and *Trp53*-null GNPs.

(D) Pemetrexed effects on the folate pathway: pemetrexed inhibits phosphoribosylglycinamide formyltransferase (GART), dihydrofolate reductase (DHFR), and thymidylate synthase (TS).

(E) Gemcitabine targets: gemcitabine blocks DNA replication and deoxynucleotide triphosphate (dNTP) synthesis.

See also Figure S2.

pemetrexed treatment, the EC_{50} for Myc1 was 35 nM (Figure S2A, blue curve; Table 1), compared to 15 μM in *Trp53*-null (Figure S2A, red curve; Table 1). Gemcitabine disrupts DNA synthesis via incorporation in DNA or inhibition of the ribonucleotide reductase (Figure 2E; van Moorsel et al., 2000). When incorporated into DNA, gemcitabine causes single-strand breaks that lead to apoptosis (Ewald et al., 2007). After 72 hr treatment, the Myc1 EC_{50} for gemcitabine was 2.1 nM with 100% efficacy, whereas efficacy against *Trp53*-null never exceeded 63% (Figure S2A; Table 1).

Decitabine, pemetrexed, and gemcitabine were further tested on four additional mouse G3 MB lines derived from independently derived tumors and infections; all displayed comparable potency and efficacy compared to Myc1 (Figure S2B). In contrast, we found a SHH MB-derived line was as sensitive to pemetrexed as Myc1 but was greater than 5-fold less sensitive to gemcitabine compared to Myc1 (Figure S2C).

Pharmacological Assessment of Decitabine, Pemetrexed, and Gemcitabine on Mouse G3 MBs

To determine the concentration-time threshold required to inhibit proliferation of neurospheres in vitro, we performed ''wash-out'' experiments with each of the three compounds. The EC_{50} values for decitabine were approximately 2.4 μM, 920 nM, and 500 nM after 1, 10, and 24 hr drug exposure, respectively (Figure 3A, top). While the EC_{50} for pemetrexed was 1.2 μM after 1 hr exposure, it decreased to 500 nM after 10 hr, and to 180 nM after 24 hr (Figure 3A, middle). With gemcitabine, the EC_{50} values were 44 nM, 13 nM, and 3.8 nM after 1, 10, and 24 hr exposure, respectively (Figure 3A, bottom).

Although decitabine affected the viability of Myc1 and decreased H3K27me3 in vitro (Figure 2B), a review of the published preclinical and clinical pharmacokinetic data (Chabot et al., 1983; George et al., 2010) strongly suggested that the maximally achievable decitabine brain concentrations in humans would be well below those required to induce significant inhibition of proliferation. Therefore, decitabine was not considered for further in vivo studies.

For gemcitabine and pemetrexed, total plasma and tumor extracellular fluid (tECF) drug concentrations were assessed in separate groups of mice bearing Myc1-induced G3 MB after single intravenous (i.v.) injections of pemetrexed (200 mg/kg) and gemcitabine (60 mg/kg). A three-compartment pharmacokinetic model adequately described the plasma and tECF concentration-time data for each drug. The murine plasma pharmacokinetics for each agent differed only modestly from

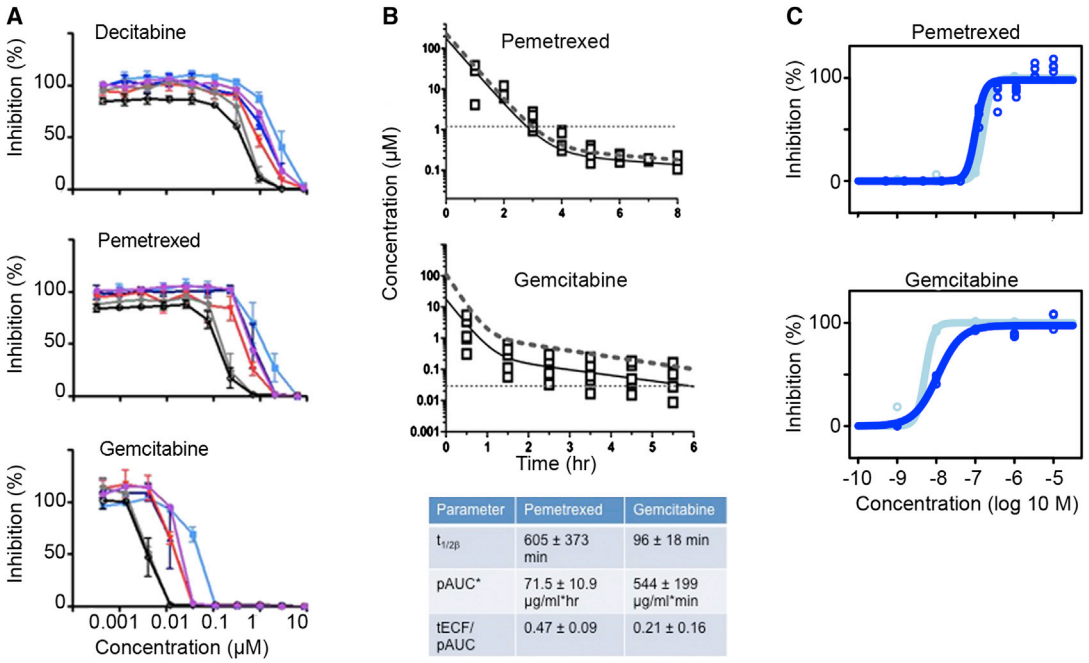

Figure 3. Effects of Pemetrexed and Gemcitabine on Mouse and Human G3 Neurospheres In Vitro and Pharmacokinetics in G3 MB-Bearing Mice

(A) In vitro "washout" of decitabine (top), pemetrexed (middle), and gemcitabine (bottom) on Myc1. Cells incubated with drugs for indicated times (1 hr, light blue line; 3 hr, red line; 6 hr, dark blue line; 10 hr, brown line; 24 hr, gray line; 72 hr, black line) after which the medium was replaced by fresh medium and plates were read 72 hr later. Error bars represent SD.

(B) Concentration-time plot for pemetrexed (top) and gemcitabine (middle). Observed tumor extracellular fluid concentrations (tECF; open squares), population simulation of tECF concentration-time data (solid black line), and population simulation of total plasma concentration-time data (dotted line) included in both plots. The horizontal dashed line represents the 1 hr EC_{50} derived from Myc1. PK parameters are described in the bottom ($t_{1/2}$, half-life; pAUC, area under the plasma concentration-time curve; and tECF/AUC, tumor extracellular fluid/AUC ratio). Values in the bottom represent averages ± SD.

(C) Neurospheres from two G3 MB PDXs, TB-12-5950 (light blue curves) and OA-2012-1 (dark blue curves), treated with concentrations from 1 nM to 10 μM of pemetrexed and gemcitabine, and read 72 hr later; top, pemetrexed EC_{50} = 160 nM (light blue line) or 100 nM (dark blue line); bottom, gemcitabine EC_{50} = 5.1 nM (light blue line) or 11 nM (dark blue line).

See also Figure S3.

previously published reports, with the clearance of gemcitabine and pemetrexed being approximately 2-fold higher in our studies (Rocchetti et al., 2007; Wang et al., 2004; Woodland et al., 1997). The plasma exposure of each drug, quantified by the area under the plasma concentration-time curve (pAUC), was similar to that achieved in humans at clinically relevant dosages (Figure 3B, upper and middle; Malempati et al., 2007; Reid et al., 2004). We found that the tECF concentrations of pemetrexed and gemcitabine exceeded the in vitro EC_{50} versus time threshold, suggesting that these compounds should have in vivo efficacy in G3 MB (Figure 3B, bottom).

To address how much drug crosses the normal blood-brain barrier, studies of pemetrexed and gemcitabine were conducted in six non-tumor-bearing mice. Pemetrexed (200 mg/kg i.v.) or gemcitabine (60 mg/kg i.v.) was administered, the brain was harvested, and the drug concentration was measured in the brain parenchyma and in the plasma. The brain-to-plasma ratio of pemetrexed and gemcitabine in these samples was 7.3% and 45%, respectively, indicating that both drugs cross a normal blood-brain barrier in a mouse model.

Pemetrexed and Gemcitabine Inhibit Human G3 MB Proliferation In Vitro

To assess whether pemetrexed and gemcitabine inhibited proliferation of human G3 MB in vitro, we generated patient-derived xenografts (PDXs) from primary G3 MBs overexpressing the MYC protein with or without *MYC* amplification and derived neurospheres for two of them. Gene expression profiling of Icb-1572 (Zhao et al., 2012) and TB-12-5950 (St. Jude Children's Research Hospital [SJCRH]) confirmed clustering with previously published human G3 MB (Robinson et al., 2012), and demonstrated that a similar profile was maintained through several passages in mice (Figure S3A). Fluorescence in situ hybridization analysis revealed that *MYC* was not amplified in Icb-1572 (Figure S3B, left; Shu et al., 2008) but was amplified in TB-12-5950 that also displayed leptomeningeal dissemination (Figure S3B, right). PDX OA-2012-1 overexpressed the MYC protein without amplification, as measured by aCGH (O.A., unpublished data), whereas PDX Med-511-FH was confirmed to have *MYC* amplification by nanostring analysis (J.M.O., unpublished data).

TB-12-5950, OA-2012-1, and human neural stem cells H9 formed neurospheres in vitro, allowing us to test the effects of

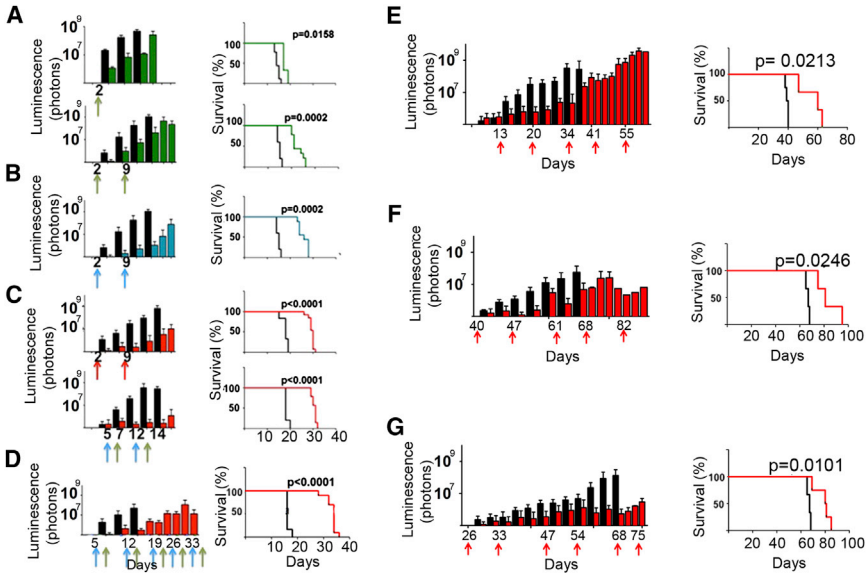

Figure 4. In Vivo Efficacy of Pemetrexed and Gemcitabine against G3 MBs

Mice injected with luciferase marked 1×10^5 Myc1 (A–D) or 1×10^6 G3 MB PDX cells (E–G). Treatment was initiated when luciferase signal reached 5.10^5 photons/sec. Luciferase measurements (left), survival (right).

(A) Top: mice treated at day 2 (green arrow) with pemetrexed (green bars and line) or saline (black bars and line). Bottom: mice treated at days 2 and 9 with pemetrexed (green arrows). n = 10 drug treatment, n = 5 saline.

(B) Mice treated at days 2 and 9 (blue arrows) with gemcitabine (treated group, blue bars and line) or saline (control group, black bars and line). n = 10 drug treatment, n = 5 saline.

(C) Top: mice treated at days 2 and 9 (red arrows) with pemetrexed and gemcitabine administered together (treated group, red bars and line) or saline (control group, black bars and line). Bottom: mice treated with gemcitabine at days 5 and 12 (blue arrows) and pemetrexed at days 7 and 14 (green arrows; treated group, red bars and line) or saline (control group, black bars and line). n = 10 treated group, n = 5 control group.

(D) Long-term treatment of Myc1-bearing mice with vehicle (black bars and line), or treated (red bars and line) with pemetrexed (green arrows) and gemcitabine (blue arrows).

(E) Mice bearing G3 MB PDX Icb-1572 (passage 8) treated at day 13 after implant and days, 20, 34, and 41 (red arrows) with pemetrexed and gemcitabine (n = 5, red bars and red line) or saline (n = 5, black bars and black line).

(F) Mice bearing G3 MB PDX TB-12-5950, treated after implant at days 40, 47, 61, and 68 (red arrows) with pemetrexed and gemcitabine (n = 5, red bars and line) or saline (n = 5, black bars and line).

(G) Mice bearing G3 MB PDX Med-511-FH treated at days 26, 33, 47, and 54 (red arrows) with pemetrexed and gemcitabine (n = 5, red bars and line) or saline (n = 5, black bars and line). Error bars represent SD.

See also Figure S4.

pemetrexed and gemcitabine in vitro. Neurospheres were treated for 72 hr at doses ranging from 1 nM to 10 μM. Cell viability was measured. For TB-12-5950 and OA-2012, EC_{50} for pemetrexed were 160 nM and 100 nM (Figure 3C, top), whereas those for gemcitabine were 5.1 nM and 11 nM, respectively (Figure 3C, bottom). These EC_{50} values were similar to those found for Myc1 (within 2- to 5-fold; Table 1). For H9 cells, the EC_{50} for pemetrexed was 0.29 μM and for gemcitabine 0.0015 μM (Figure S3C), which corresponded to the response seen in mouse control *Trp53*-null (Figure S2A, Table 1).

Pemetrexed and Gemcitabine Activity in Mouse G3 MBs In Vivo

To determine how efficacious pemetrexed and gemcitabine were in suppressing proliferation of mouse G3 MB in vivo, we stereotactically transplanted 1×10^5 purified tumor cells, retrovirally transduced with luciferase, in the cortices of CD1 mice. We previously determined that this cell number induces MBs that kill the animals within 15 days after transplant and recapitulate the primary tumors (Kawauchi et al., 2012). Bioluminescence detection of tumor progression correlated with tumor volume measured with magnetic resonance imaging (Figures S4A–S4C). Hematoxylin and eosin (H&E) staining of tumor sections performed 3 days after transplant confirmed the presence of an organized tumor mass that was vascularized and surrounded by blood vessels (Figure S4D).

The schedule and dosage of drug delivery was calculated based upon modeling and simulation of data from our pharmacokinetic studies, and related to pAUC values tolerable in pediatric clinical trials (Malempati et al., 2007; Reid et al., 2004). Mice transplanted with Myc1 were treated by tail vein injection with 200 mg/kg pemetrexed (Figure 4A), 60 mg/kg gemcitabine (Figure 4B), or a combination of both drugs (Figure 4C). When combined, pemetrexed and gemcitabine were either given together in the same injection (Figure 4C, top) or split by a 2-day interval (first gemcitabine, 2 days later pemetrexed; Figure 4C, bottom) to reduce stress on the mice.

Five mice treated with vehicle survived up to 14 to 20 days after transplant, as expected (Figures 4A–4C, black bars). One dose of pemetrexed at day 3 increased median survival by 3 days (Figure 4A, top). Mice treated with two doses of pemetrexed at days 3 and 10 had an increased 7-day median survival (Figure 4A, bottom). Two doses of gemcitabine at 60 mg/kg, at days 2 and 9 after tumor implant, had an 11-day increased median survival compared to mice treated with vehicle (Figure 4B). Treatment of mice with the two drugs given at the same time on days 2 and 9 increased their median survival by 13 days compared to vehicle-treated animals (Figure 4C, top). Similarly, mice treated with gemcitabine at days 5 and 12 and with pemetrexed at days 7 and 14 (Figure 4C, bottom) had a 12-day increase in median survival (from 18 to 30 days). Therefore, mice receiving both drugs together or separately had a similar increased median survival compared to vehicle-treated animals.

We repeated the efficacy studies with Myc2 and obtained similar results (Figure S4E). The survival of animals treated with

vehicle was 11 days, whereas treatment with pemetrexed at days 4 and 11 increased the median survival up to 28 days. Mice treated with gemcitabine at days 4 and 11 had a median survival of 26 days whereas cotreatment with pemetrexed and gemcitabine given together increased the median survival by 33 days (Figure S4E).

Because the treatment of mice with the two drugs administered singly or together was well tolerated, based on weekly observations of signs of morbidity (loss of motion, head dome, and lethargy) and white blood cell count, and because the tumors returned despite treatment, we assessed the effects of a longer treatment course on tumor growth. Ten Myc1-induced G3 MB-bearing mice were either treated with vehicle or once a week with gemcitabine from days 4 to 32 and pemetrexed from days 6 to 34 after tumor implant. Long-term treatment increased mouse median survival by 18 days (Figure 4D). Similar results were obtained when mice were transplanted with Myc2, and treated long term with the two drugs administered together (Figure S4F).

Pemetrexed and Gemcitabine Inhibit Human G3 MB Proliferation In Vivo

The PDX Icb-1572, passage 8, was marked with luciferase and implanted in the cortex of CD1 mice that were treated 13 days after tumor implant with pemetrexed and gemcitabine at days 13, 20, 34, and 41 (Figure 4E). When added together, the two drugs increased mouse median survival by 21 days. We confirmed these results in two other G3 MB PDXs, with *MYC* amplification, TB-12-5950, passaged once in NSG and three times in CD1 mice and Med-511-FH, passaged once in NSG animals (J.M.O., unpublished; Figures 4F and 4G). Because each PDX had a different proliferation rate, treatment was initiated at different times after implant when the luminescence signal reached 5×10^5 photons/sec (TB-12-5950, 40 days [Figure 4F] and Med-511-FH, 26 days [Figure 4G; Figure S4G]). In both cases, all mice treated with vehicle died of tumor burden with a median survival of 67 days after implant whereas those treated with gemcitabine and pemetrexed survived longer—up to 81 days. Thus, for each PDX, the median survival was significantly longer in the treatment group than in the control.

Effects of the Treatment of Mouse G3 and SHH MBs with Pemetrexed and Gemcitabine Combined to Cisplatin and Cyclophosphamide In Vivo

In an attempt to compare the pemetrexed and gemcitabine combination to agents already in clinical use, we treated mice bearing mouse G3 MB with cisplatin and cyclophosphamide (cycle A) followed with pemetrexed and gemcitabine (cycle B; Figure 5A; White and Sterling-Levis, 2008). Vincristine, the third drug used in the clinic, could not be used due to intolerable toxicity in mice (data not shown). Mice treated with vehicle had to be euthanized 21 days after implant (Figure 5B, black bars and lines). Mice treated for two cycles with pemetrexed and gemcitabine combined (cycle B) had an 18-day increased median survival compared to vehicle-treated mice (Figure 5B, green bars and line; $p = 0.035$). Mice treated with i.v. cisplatin, 5 mg/kg at day 1 and intraperitoneally with cyclophosphamide, 130 mg/kg for 5 consecutive days, days 2–6, had a median survival of 12 days longer than the vehicle-treated mice (Figure 5B, blue bars and line; $p = 0.035$); however, two of the five mice died from acute drug-induced toxicity. Remarkably, mice treated with cisplatin and cyclophosphamide alternating with pemetrexed and gemcitabine survived 25 days longer than the vehicle-treated animals but still succumbed to tumors (Figure 5B, red bars and line; $p = 0.0069$). Therefore, the combination of cisplatin and cyclophosphamide with pemetrexed and gemcitabine resulted in a longer median survival than either treatment alone.

We evaluated the potential toxicity of each therapeutic regimen by analyzing blood chemistries, including while blood cells, absolute neutrophil and platelet counts, once a week from cohorts of animals bearing mouse G3 MB treated with cisplatin and cyclophosphamide (Figure 5C, blue lines), pemetrexed and gemcitabine (Figure 5C, green lines), versus the combination of both cycles (Figure 5C, red lines). One cycle of cisplatin and cyclophosphamide dramatically decreased the number of white blood cells, neutrophils, and platelets, but this was reversible because the values recovered to normal once treatment was stopped (Figure 5C).

To assess whether the combination of pemetrexed, gemcitabine, and/or cisplatin and cyclophosphamide could also suppress proliferation of human G3 MB and mouse SHH MB, tumor cells purified from Icb-1572 and from a mouse SHH MB marked with luciferase were implanted in the cortex of recipient CD1 mice. Animals were treated with the same regimen as for mouse G3 MB. Mice bearing the Icb-1572 tumor died at 39 days post-implant when treated with vehicle (Figure 5D, black line). When treated with two rounds of cycle A, they died at 55 days (Figure 5D, blue line), but survive up to 60 days with two rounds of cycle B (Figure 5D, green line). Mice treated with cycle A and B died 63 days after transplant (Figure 5D, red line). Mice with mouse SHH MB treated with vehicle had to be sacrificed 28 days after transplant (Figure 5E). Mice treated for two rounds of cycle B had a 2-day increased median survival compared to vehicle-treated mice (Figure 5E, green bars and line) but when treated with two rounds of cycle A survived 14 days longer than vehicle-treated mice (Figure 5E, panels, blue bars and line). Finally, mice treated with alternating cycle A and B survived 8 days longer than the vehicle-treated animals but succumbed to tumors (Figure 5E, red bars and line). This demonstrated that treatment with pemetrexed and gemcitabine had little effect on the survival of mice bearing mouse SHH MB. However, SHH MBs responded to cisplatin and cyclophosphamide, as expected from clinical experience.

Resistance to Pemetrexed and Gemcitabine

In all cases, tumors relentlessly regrew and eventually killed the animals. To test whether tumor regrowth could potentially be due to intrinsic drug resistance, tumor cells were purified from four G3 MBs, two from untreated animals (tumors 1 and 2) and two from mice treated with pemetrexed and gemcitabine (tumors 3 and 4; Figure 4D), and grown as neurospheres in the presence or absence of drugs (Figure 6A). Regardless of whether the tumor cells came from untreated or treated animals, they had similar sensitivity to pemetrexed and gemcitabine, suggesting that tumor regrowth was not due to intrinsic resistance to either drug (Figure 6A). Moreover, gene expression analysis of tumors harvested at sacrifice from treated or control mice showed no significant difference in their global transcriptome; principal

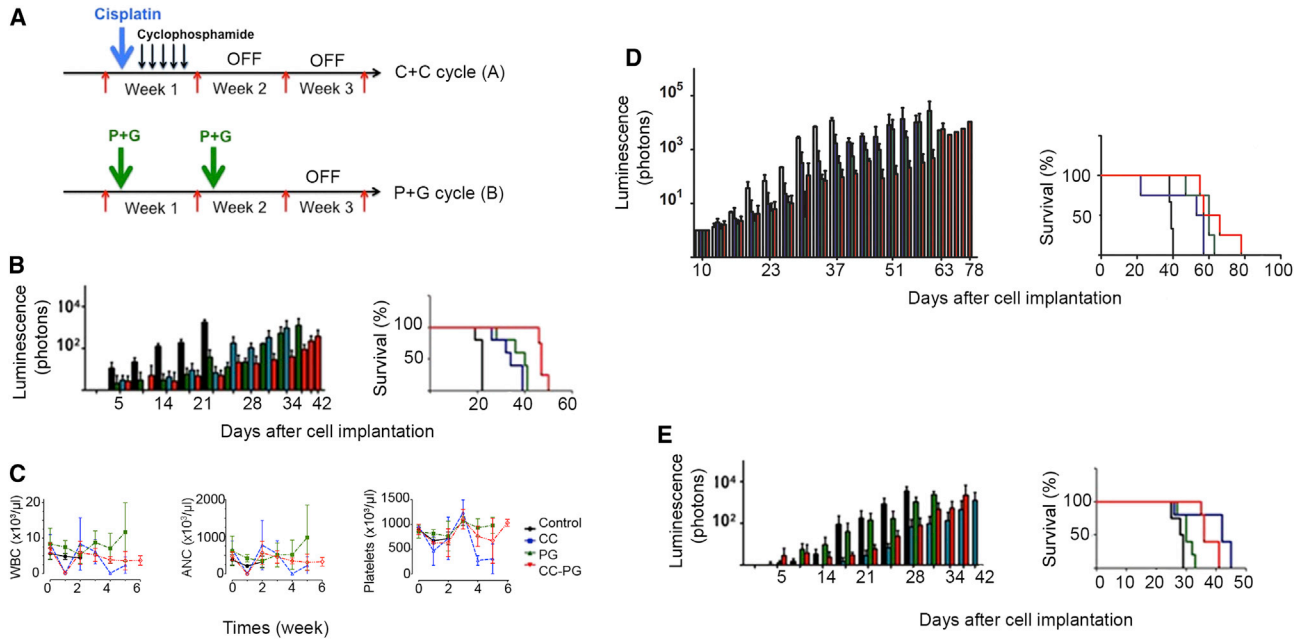

Figure 5. Treatment of Mouse G3 and SHH MBs with Pemetrexed and Gemcitabine Combined with Cyclophosphamide and Cisplatin

(A) Treatment schedule with cisplatin (C, bold blue arrow) at day 1 and cyclophosphamide (C, dark blue arrows) from days 2 to 6 every 3 weeks (C+C, cycle A, top) or pemetrexed and gemcitabine together twice every 3 weeks (P+G, cycle B, bottom).

(B) Mice bearing mouse G3 MB treated with saline (black bars and line), C+C at each course, (blue bars and line), P+G at each course (green bars and line), or with C+C for the first course and P+G for the second course (red bars and line). Error bars represent SD.

(C) White blood cells (WBC), neutrophils (ANC), and platelet counts for mice treated with saline (black curves), C+C at each course (blue curves lines), P+G at each course (green curves) or alternative cycle of C+C first followed by P+G (red curves). Error bars represent SD.

(D) Mice bearing G3 MB PDX Icb-1572 treated with saline (black bars and line; median survival 39 days), with C+C at each course (blue bars and curve; median survival 55 days, $p = 0.0724$), with P+G at each course (green bars and curve; median survival 60 days, $p = 0.0084$), or with C+C for the first course and P+G for the second course (red bars and curve; median survival 62 days, $p = 0.0044$). Error bars represent SD.

(E) Mice bearing mouse SHH tumors treated with saline (black bars and line; median survival 28 days), with C+C at each course (blue bars and curve; median survival 42 days, $p = 0.045$), with P+G at each course (green bars and curve; median survival 30 days, $p = 0.1042$), or with C+C first course and P+G second course (red bars and curve; median survival 36 days, $p = 0.040$). Error bars represent SD.

component analysis of either primary or secondary G3 MBs from untreated animals or from G3 MBs treated with pemetrexed, gemcitabine, or both, clustered together (Figure 6B).

To gage whether mouse G3 MBs harvested from animals treated long-term with pemetrexed and gemcitabine (Figure S4F) remained sensitive to the two drugs in vivo, tumor cells were purified from G3 MBs from treated mice at euthanasia and re-implanted into the cortices of naive recipients. Mice bearing MB were either left untreated (Figure 6C, black bars and line) or treated with the two drugs added together, once a week from days 6 to 34 (Figure 6C, red bars and line). Whether the tumors were from animals treated or not, mouse median survival was similar (compare Figure 6C to Figure S4F). To assess the role of pharmacokinetics in drug resistance, mice bearing G3 MB were treated with pemetrexed and gemcitabine at days 3, 10, and 24. Plasma and brain samples were collected 1, 3, and 6 hr after the last day 24 treatment. Plasma exposure of both pemetrexed and gemcitabine were equivalent to that observed after single-dose treatment, and brain concentrations remained above the respective EC_{50} concentrations for both drugs. These results suggest that neither intrinsic acquired drug resistance of tumor cells nor altered drug delivery accounted for the observed persistent tumor growth after therapy.

Others have shown that the spatial distribution of chemotherapeutics in solid tumors is highly dependent on the presence of blood vessels (Minchinton and Tannock, 2006; Saggar et al., 2013). Two independently derived mouse G3 MBs were immunostained with an antibody to caspase 3 after treatment with pemetrexed and gemcitabine. Caspase 3 staining was not detected in the vehicle-treated tumors (Figure S5A, control) but was found in tumors from treated mice. Even though tumors were well vascularized, areas of apoptosis were detected (Figure S5A). Moreover, we found that pemetrexed and gemcitabine induced cell death in tumor cells in vitro by Annexin V staining (Figure S5B) and that gemcitabine induced histone 2AX (H2AX) foci after 1 hr treatment at 5 nM (Figure S5C, bottom). Proliferation measured by bromo-deoxy-uridine (BrdU) incorporation was similar in treated and untreated MBs (Figure S5D). These data suggest that host factors and/or vascularization of the tumors may limit the efficacy of pemetrexed and gemcitabine.

Purine metabolism is directly linked to the folate pathway through the action of GART. We found that increasing the concentration of folate in the medium (up to 10 µM) significantly decreased the sensitivity of mouse G3 MB neurospheres to pemetrexed, highlighting the importance of the folate pathway in these tumors (Figure S5E). We also noticed that when G3

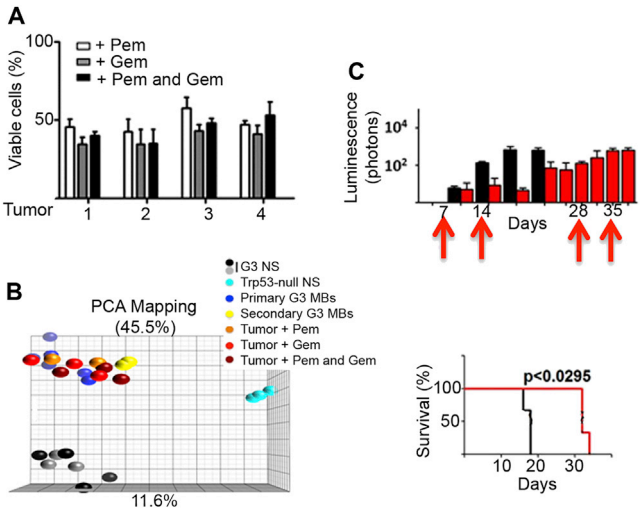

Figure 6. Resistance of Mouse G3 MBs to Gemcitabine and Pemetrexed Treatment

(A) Viability of tumor cells purified from four individual tumors (1–4) from animals treated in Figure S4F grown in vitro and treated with 40 nM pemetrexed (pem, white bars), 5 nM gemcitabine (gem, gray bars), or both drugs together (black bars). Cell viability was measured after 72 hr treatment by trypan blue normalized to cells treated with DMSO. Error bars represent SD.

(B) Principal component analysis (PCA) for G3 neurospheres (G3 NS, black and gray dots, n = 7), *Trp53*-null neurospheres (NS, clear blue dots, n = 3), primary G3 MBs (dark blue dots, n = 3), secondary G3 MBs (yellow dots, n = 3), or G3 MBs (tumors) from animal treated with pem (orange dots, n = 3), gem (red dots, n = 3) or both drugs (dark red dots, n = 3).

(C) Mice implanted with tumors harvested from mice treated in (A) were treated with vehicle (black bars, top; black line, bottom) or with pem and gem combined (red bars, top; red line, bottom) at days 7, 14, 28, and 35 (red arrows). Error bars represent SD.

See also Figure S5.

MB-bearing animals were treated with cisplatin/cyclophosphamide or pemetrexed/gemcitabine for one cycle, tumor cells harvested from these mice responded to the four drugs similarly in culture with no significant differences in EC_{50} (Figure S5F).

DISCUSSION

G3 MB, characterized by high levels of MYC expression due to gene amplification or overexpression (Northcott et al., 2011, 2012), is a particularly aggressive tumor for which current therapy is inadequate. The generation of a MYC-driven murine model of G3 MB and its propagation as robust neurospheres enabled the testing and identification of compounds from a "bioactive" library including 830 FDA-approved drugs, to select and prioritize agents for clinical development. The integration of this in vitro drug screen with in vivo pharmacokinetic and pharmacodynamic studies identified two FDA-approved drugs, pemetrexed and gemcitabine, as therapy for this deadly disease.

Overall, the screening process identified all expected drugs known to have clinical effect including vincristine, vinblastine, and etoposide (cisplatin and cyclophosphamide were not tested due to incompatibility with the high-throughput screen [HTS]) as well as agents not previously known to be active. Among the latter category, decitabine was a very interesting "hit" because its use in vitro resulted in a decrease of H3K27me3, an epigenetic mark characteristic of G3 and G4 MBs (Dubuc et al., 2013; Robinson et al., 2012). Unfortunately, it was unsuitable for further in vivo studies due to predicted inadequate central nervous system exposure in humans. Nonetheless, the in vitro efficacy of decitabine suggested that similar hypomethylating drugs with adequate brain penetration should be considered for the treatment of G3 MBs. On the other hand, pemetrexed and gemcitabine showed high antiproliferative potency against mouse and PDX G3 MBs in vitro and in vivo. When used as single agents, each inhibited proliferation of mouse and human G3 MB neurospheres. When administered in combination to mice bearing murine or PDXs G3 MB, survival time doubled compared to vehicle-treated animals. In contrast, mouse SHH MBs did not respond to the combination of pemetrexed and gemcitabine, suggesting that the combination of the two drugs should specifically target G3 MBs. It would be informative to know whether this combination chemotherapy has a similar efficacy in G4 MBs. However, if the response to the drugs is MYC driven, then average lower levels of MYC expression in G4 MB (Northcott et al., 2011) suggest that it will not be an effective therapeutic approach. Furthermore, the large number and heterogeneity of G4 MBs, without the availability of several adequate mouse models, preclude comprehensive preclinical studies similar to those that cover the spectrum of G3 MB with MYC overexpression.

Previous reports suggested that the combination of gemcitabine and pemetrexed was synergistic (Adjei, 2002; Tonkinson et al., 1999), which prompted their use in the treatment of non-small-cell lung cancer (NSCLC), pancreatic cancer, and advanced breast cancer (Monnerat and Le Chevalier, 2006). Clinical trials in adults have shown this combination of drugs to be well tolerated for multiple cycles at doses of gemcitabine ranging between 1,250 and 1,500 mg/m^2 on days 1 and 8 and of pemetrexed at 500 mg/m^2 on day 8. Response rates have been promising in the range of 10% to 44% in NSCLC. Furthermore, a number of clinical trials have tested different delivery schedules of pemetrexed and gemcitabine, alternating the administration sequence and intervals between administration (Ma et al., 2005; Monnerat and Le Chevalier, 2006).

Both pemetrexed and gemcitabine have been used to treat pediatric cancers with each agent exhibiting an acceptable toxicity profile. A phase 1 pediatric clinical trial conducted in children with refractory solid tumors evaluated a range of pemetrexed dosages from 400 to 2480 mg/m^2, and identified a maximum tolerated dose (MTD) in children of 1,910 mg/m^2 i.v. given once every 21 days with folate and B12 supplementation (Malempati et al., 2007). The results of a pediatric phase 1 study with gemcitabine as single agent showed that the MTD was 1,200 mg/m^2 when given as a 30 min infusion once weekly for 3 consecutive weeks of a 4-week cycle. The MTD for a 2-week schedule has not been established; however, the dose escalation concluded at 2,100 mg/m^2 given on days 1 and 8 without reaching a defined MTD, indicating that this regimen was well tolerated (Reid et al., 2004).

Our studies in mice bearing G3 MB clearly showed that both gemcitabine and pemetrexed exceeded their respective EC_{50} values in the tECF and studies in mice not bearing tumor showed that both drugs penetrated the brain. This finding is consistent

with published reports (Kerr et al., 2001; Stapleton et al., 2007; Kumthekar et al., 2013) in other animal models and humans that showed modest, but clinically relevant brain penetration of both gemcitabine and pemetrexed.

Our preclinical studies suggest that both pemetrexed and gemcitabine are efficacious on mouse G3 MB when given 7 days apart, and we observed no difference in efficacy when gemcitabine preceded pemetrexed or when administered together. The plasma AUC values for pemetrexed (200 mg/kg/dose) and gemcitabine (60 mg/kg/dose) in mice were similar to those reported in humans at dosages in the 400–670 mg/m^2 ranges for pemetrexed and 1,250 mg/m^2 for gemcitabine (Malempati et al., 2007; Reid et al., 2004). This suggested that the combination of pemetrexed and gemcitabine was clinically feasible at dosages well below the already established MTD in children.

The comparison of pemetrexed and gemcitabine in combination to the more clinically analogous combination of cisplatin and cyclophosphamide led to the unexpected finding that the integration of these four drugs produced a heightened tumor response. We assessed the effect of cisplatin and cyclophosphamide alone, pemetrexed and gemcitabine alone, or a combination of those drugs. Whereas treatment with pemetrexed and gemcitabine or cyclophosphamide and cisplatin increased the median survival of mice bearing murine G3 MB by 18 and 12 days, respectively, versus vehicle treated animals, when given as alternating cycles, median survival was increased by 25 days. Moreover, no additional toxicity was detected. When transplanted with the PDX Icb-1572, the combination of the two cycles led to an increased median survival of 23 days. In contrast, treatment of mice bearing mouse SHH MB with cycles of pemetrexed, gemcitabine, and cisplatin and cyclophosphamide did not improve mouse survival compared to treatment with cisplatin and cyclophosphamide alone. These results provide stronger rationale for adding pemetrexed and gemcitabine to the current therapeutic regimen for the treatment of human G3 MBs.

Folates are essential for purine and pyrimidine synthesis and consequently rapid cellular division and proliferation of cancer cells. Gene set enrichment analysis confirmed that both the folate and purine metabolic pathways were significantly enriched in mouse G3 MBs compared with GNPs and SHH MBs. Although the antifolate agents methotrexate and 5-fluorouracil have been widely used for decades in the treatment of malignant tumors, pemetrexed is a relatively new therapeutic agent currently approved as a first line treatment for mesothelioma (Dowell et al., 2012), NSCLC in association with platinum-based chemotherapy (Mubarak et al., 2012), and in newly diagnosed brain metastasis (Bailon et al., 2012). It also showed clinical activity in other adult tumors such as breast, colorectal, bladder, cervical, gastric, and pancreatic cancers (Adjei, 2004; Chattopadhyay et al., 2007; Warwick et al., 2013). Genes regulating pyrimidine metabolism were also enriched in mouse G3 MBs compared with mouse GNPs and SHH MBs, in agreement with the antiproliferation effects of gemcitabine, a pyrimidine cytidine analog.

In summary, our studies identified gemcitabine and pemetrexed, two FDA-approved drugs, as efficacious in increasing survival of mice bearing PDX G3 MBs in which MYC is overexpressed. In combination with two chemotherapeutic drugs in current clinical use, cyclophosphamide and cisplatin, we found increased prolonged survival of mice bearing either mouse or human G3 MB for as long as 40 days after tumor implant compared to untreated animals. Pemetrexed and gemcitabine have both been evaluated in single agent phase 1 studies in childhood central nervous system and solid tumors, and are recommended in phase 2 clinical trials, although there are very limited data specific to MB. Due to the specificity of this combination therapy in G3 over SHH MBs that harbor high MYC levels and have a worse prognosis, it seems prudent to evaluate this therapy in human G3 MBs. G3, *MYC* amplification or overexpression, presence of metastatic disease, and large cell/anaplastic MBs are all overlapping poor prognostic features of MB that represent a huge challenge to the clinical management of the disease because as a group these have an approximate 60% 5-year overall survival in comparison to an 80% 5-year overall survival in patients who do not harbor these characteristics. Furthermore, the majority of these patients currently get maximal "high risk" therapy, which includes high-dose craniospinal radiation and adjuvant postradiation chemotherapy. Current and future protocols are risk-stratifying patients based on the presence or absence of these and other molecular characteristics. However, without having any additional effective agents to add to high-risk therapy, there will be little change to these patients' overall survival times.

These data are exciting from a clinical perspective because they suggest that pemetrexed and gemcitabine can be added to currently used chemotherapy with an enhanced effect and little additional myelosuppressive toxicity. Therefore, these medications, which have already been used clinically in combination with other chemotherapy regimens in other cancers, could be incorporated into high-risk MB therapy for patients with G3 MBs. We do not know whether the combination of pemetrexed and gemcitabine will be effective in G3 MBs that do not overexpress or amplify *MYC*. However, because approximately 17% of G3 MB amplify the *MYC* gene (Northcott et al., 2012), and >75% of G3 MB exhibit high MYC expression (Northcott et al., 2011), this supports our recommendation to try this therapy in G3 MB. These agents must be introduced in stringently designed clinical trials that can strictly monitor for expected and unexpected toxicities of these agents as well as measure whether the suggested enhanced effect of this therapy translates to human disease.

EXPERIMENTAL PROCEDURES

Development of Mouse G3 and SHH MB and G3 MB PDXs

Mouse G3 MBs were generated by orthotopic transplantation of GNPs from cerebella of P7 *Trp53*$^{-/-}$; *Cdkn2c*$^{-/-}$ mice infected with MYC-encoding retroviruses (Kawauchi et al., 2012). Mouse SHH MBs spontaneously occur in *Ptch1*$^{+/-}$; *Trp53*$^{-/-}$ animals (Wetmore et al., 2001) and were previously described (Uziel et al., 2005). G3 MB PDXs were developed from primary tumor samples, from previously untreated patients, and implanted into the cortex or cerebella of NSG mice. The generation of PDXs is provided in detail in the Supplemental Experimental Procedures. In all cases, primary human brain tumor specimens were obtained under written informed consent approved by the Institutional Review Boards of SJCRH; the Necker Sick Children's Hospital, Paris, France; the Baylor College of Medicine in Houston, Texas; and the Seattle Children's Hospital. All animal studies were conducted according to the National Institutes of Health guidelines and regulation and de-identified

specimens were used to make patient-derived xenograft mice in accordance with the Institutional Animal Care and Use Committee-approved protocols of SJCRH, Fred Hutchinson Cancer Center, and Baylor College of Medicine. The care and use of animal studies in Orsay, France were performed by strictly applying European and National Regulation in force for the Protection of Vertebrate Animals used in experimental and other scientific purposes (directive 86/609). The protocol also complied with internationally established 3R principles, in accordance with United Kingdom Coordinating Committee on Cancer Research guidelines.

Cell Culture

Mouse and human G3 MBs, mouse SHH MBs, and *Trp53*-null GNPs were grown as neurospheres in supplemented neurobasal medium, as described previously (Kawauchi et al., 2012). HepG2 and TERT$^-$ BJ lines were purchased from ATCC (#77400, CRL-4001) and human neural stem cells (H9) from Invitrogen.

High-Throughput Screen

The SJCRH "bioactive" library consisted of 7,389 compounds (6,568 unique) that were screened on mouse G3 MB and *Trp53*-null neurospheres. The HTS was performed at one 10 μM concentration and the luminescent signal from the plates were read 72 hr after treatment using CellTiter-Glo, as described previously (Atkinson et al., 2011). Dose-response experiments identified 35 FDA-approved drugs from which three, decitabine, pemetrexed and gemcitabine, were chosen for further analysis. Additional details concerning the chemical library screened, the HTS assay protocol, the hits validation and data analysis, and "washout" experiments are reported in the Supplemental Experimental Procedures.

Pharmacological Studies

Murine plasma and tECF samples were analyzed for pemetrexed and gemcitabine using separate validated liquid chromatography-tandem mass spectroscopy assays. To assay gemcitabine samples, tetrahydrouridine was added during sample collection to prevent deamination of gemcitabine to 2′,2′-difluorodeoxyuridine by cytidine deaminase. For pemetrexed and gemcitabine plasma pharmacokinetic (PK) studies, a serial sacrifice plasma-only PK study (single sample per mouse) was performed in tumor-bearing mice to obtain initial plasma PK parameter estimates. These estimates were used to inform a D-optimal, limited sampling model for microdialysis experiments, minimizing blood withdrawal and maximizing information content. Using a previously published microdialysis technique (Zhuang et al., 2006), we assessed pemetrexed and gemcitabine tumor penetration separately in orthotopically implanted mouse G3 MBs. Prior to the in vivo microdialysis study, microdialysis probe recovery was assessed for each compound using an in vitro recovery technique. More details on pemetrexed and gemcitabine liquid chromatography-tandem mass spectroscopy bioanalytical assays, plasma PK studies, and cerebral microdialysis studies are described in the Supplemental Experimental Procedures.

Statistical Analysis

Statistical analyses were performed in the GraphPad Prism software version 5.0. The Kaplan-Meier (log rank) test was used for testing significant mouse survival.

Gene Expression Profiling

Total RNA was extracted using Trizol, as previously published (Kawauchi et al., 2012). RNA was subjected to Affymetrix Gene Chip analysis (HT430PM, Affymetrix). Data were analyzed with Spotfire (Kawauchi et al., 2012) and for gene set enrichment analysis (Broad Institute). Gene expression of xenografts TB-12-5950 and Icb-1572 were compared to gene expression profiles from 72 primary human medulloblastoma samples (Robinson et al., 2012). Total RNA was extracted from the snap-frozen human MBs and xenograft samples using STAT-60. mRNA profiles were generated using U133 Plus 2.0 microarray (Affymetrix). The data were imported into Spotfire Decision Site, and for each probe set and subject, *Z* scores were calculated by computing the mean and SD across subjects within each probe set.

Immunoblotting, In Vivo BrdU Incorporation, Caspase 3 and BrdU Immunostaining, Gamma-H2AX, and Fluorescence In Situ Hybridization Analysis

All procedures and reagents are described in detail in the Supplemental Experimental Procedures.

ACCESSION NUMBERS

The NCBI Gene Expression Omnibus accession number for the microarray results reported in this paper is GSE46406.

SUPPLEMENTAL INFORMATION

Supplemental Information includes Supplemental Experimental Procedures, five figures, and one table and can be found with this article online at http://dx.doi.org/10.1016/j.ccr.2014.02.009.

AUTHOR CONTRIBUTIONS

M.M., A.S., M.J., B.B.F., D.T., S.R., F.Z., Y-D.W., D.F., and L.B. performed the experiments; O.A., S.P., X.-N.L., and J.M.O. provided PDXs; and M.M., R.K.G., C.F.S., G.R.W., A.G., and M.F.R. wrote the paper.

ACKNOWLEDGMENTS

We thank Charles J. Sherr, Richard J. Gilbertson, and all members of the Brain Tumor Program for helpful discussions and insights and members of the Roussel and Sherr laboratories for helpful comments. We are indebted to Dana Farmer, Shelly Wilkerson, Jose Grenet, and Coralie Lefevre for excellent technical expertise; the Small Imaging Core for mouse surgery, MRI, luciferase imaging, and assistance with PK studies; the diagnostic laboratory core for blood analysis; the flow cytometry core for Annexin V and FACS analysis; Marc Valentine for fluorescence in situ hybridization analysis; John Gray for lentiviruses; Brian L. Murphy for IP; Daisuke Kawauchi for neurospheres; Cynthia Wetmore, Michael A. Dyer, and Richard Rahija for establishment of PDXs; and Charles O. Rock for the folate rescue experiment. This work was supported in part by NIH grants CA-096832 (to M.F.R.), CA-155360 and CA-114567 (to J.M.O.), Cancer Center Core grant CA-021765 (to M.F.R. and A.G.), Institut National du Cancer (AVENIR INSERM team, INCa R10067LS to O.A. and L.B.), CNRS (to O.A. and L.B.), Institut Curie (to O.A. and L.B.), a V foundation translational award (to M.F.R. and A.G.), and the American Lebanese-Syrian Associated Charities of St. Jude Children's Research Hospital.

Received: April 26, 2013
Revised: October 29, 2013
Accepted: February 18, 2014
Published: March 27, 2014

REFERENCES

Adjei, A.A. (2002). Preclinical and clinical studies with combinations of pemetrexed and gemcitabine. Semin. Oncol. *29* (6, Suppl 18), 30–34.

Adjei, A.A. (2004). Pemetrexed (ALIMTA), a novel multitargeted antineoplastic agent. Clin. Cancer Res. *10*, 4276s–4280s.

Atkinson, J.M., Shelat, A.A., Carcaboso, A.M., Kranenburg, T.A., Arnold, L.A., Boulos, N., Wright, K., Johnson, R.A., Poppleton, H., Mohankumar, K.M., et al. (2011). An integrated in vitro and in vivo high-throughput screen identifies treatment leads for ependymoma. Cancer Cell *20*, 384–399.

Bailon, O., Chouahnia, K., Augier, A., Bouillet, T., Billot, S., Coman, I., Ursu, R., Belin, C., Zelek, L., Des Guetz, G., et al. (2012). Upfront association of carboplatin plus pemetrexed in patients with brain metastases of lung adenocarcinoma. Neuro-oncol. *14*, 491–495.

Chabot, G.G., Rivard, G.E., and Momparler, R.L. (1983). Plasma and cerebrospinal fluid pharmacokinetics of 5-Aza-2′-deoxycytidine in rabbits and dogs. Cancer Res. *43*, 592–597.

Chattopadhyay, S., Moran, R.G., and Goldman, I.D. (2007). Pemetrexed: biochemical and cellular pharmacology, mechanisms, and clinical applications. Mol. Cancer Ther. *6*, 404–417.

Dowell, J.E., Dunphy, F.R., Taub, R.N., Gerber, D.E., Ngov, L., Yan, J., Xie, Y., and Kindler, H.L. (2012). A multicenter phase II study of cisplatin, pemetrexed, and bevacizumab in patients with advanced malignant mesothelioma. Lung Cancer *77*, 567–571.

Dubuc, A.M., Remke, M., Korshunov, A., Northcott, P.A., Zhan, S.H., Mendez-Lago, M., Kool, M., Jones, D.T., Unterberger, A., Morrissy, A.S., et al. (2013). Aberrant patterns of H3K4 and H3K27 histone lysine methylation occur across subgroups in medulloblastoma. Acta Neuropathol. *125*, 373–384.

Ellison, D.W., Kocak, M., Dalton, J., Megahed, H., Lusher, M.E., Ryan, S.L., Zhao, W., Nicholson, S.L., Taylor, R.E., Bailey, S., and Clifford, S.C. (2011). Definition of disease-risk stratification groups in childhood medulloblastoma using combined clinical, pathologic, and molecular variables. J. Clin. Oncol. *29*, 1400–1407.

Ewald, B., Sampath, D., and Plunkett, W. (2007). H2AX phosphorylation marks gemcitabine-induced stalled replication forks and their collapse upon S-phase checkpoint abrogation. Mol. Cancer Ther. *6*, 1239–1248.

George, R.E., Lahti, J.M., Adamson, P.C., Zhu, K., Finkelstein, D., Ingle, A.M., Reid, J.M., Krailo, M., Neuberg, D., Blaney, S.M., and Diller, L. (2010). Phase I study of decitabine with doxorubicin and cyclophosphamide in children with neuroblastoma and other solid tumors: a Children's Oncology Group study. Pediatr. Blood Cancer *55*, 629–638.

Kawauchi, D., Robinson, G., Uziel, T., Gibson, P., Rehg, J., Gao, C., Finkelstein, D., Qu, C., Pounds, S., Ellison, D.W., et al. (2012). A mouse model of the most aggressive subgroup of human medulloblastoma. Cancer Cell *21*, 168–180.

Kerr, J.Z., Berg, S.L., Dauser, R., Nuchtern, J., Egorin, M.J., McGuffey, L., Aleksic, A., and Blaney, S. (2001). Plasma and cerebrospinal fluid pharmacokinetics of gemcitabine after intravenous administration in nonhuman primates. Cancer Chemother. Pharmacol. *47*, 411–414.

Kool, M., Korshunov, A., Remke, M., Jones, D.T., Schlanstein, M., Northcott, P.A., Cho, Y.J., Koster, J., Schouten-van Meeteren, A., van Vuurden, D., et al. (2012). Molecular subgroups of medulloblastoma: an international meta-analysis of transcriptome, genetic aberrations, and clinical data of WNT, SHH, Group 3, and Group 4 medulloblastomas. Acta Neuropathol. *123*, 473–484.

Kumthekar, P., Grimm, S.A., Avram, M.J., Kaklamani, V., Helenowski, I., Rademaker, A., Cianfrocca, M., Gradishar, W., Patel, J., Mulcahy, M., et al. (2013). Pharmacokinetics and efficacy of pemetrexed in patients with brain or leptomeningeal metastases. J. Neurooncol. *112*, 247–255.

Ma, C.X., Nair, S., Thomas, S., Mandrekar, S.J., Nikcevich, D.A., Rowland, K.M., Fitch, T.R., Windschitl, H.E., Hillman, S.L., Schild, S.E., et al.; North Central Cancer Treatment Group; Mayo Clinic; Eli Lilly & Company (2005). Randomized phase II trial of three schedules of pemetrexed and gemcitabine as front-line therapy for advanced non-small-cell lung cancer. J. Clin. Oncol. *23*, 5929–5937.

Malempati, S., Nicholson, H.S., Reid, J.M., Blaney, S.M., Ingle, A.M., Krailo, M., Stork, L.C., Melemed, A.S., McGovern, R., Safgren, S., et al.; Children's Oncology Group (2007). Phase I trial and pharmacokinetic study of pemetrexed in children with refractory solid tumors: the Children's Oncology Group. J. Clin. Oncol. *25*, 1505–1511.

Massimino, M., Cefalo, G., Riva, D., Biassoni, V., Spreafico, F., Pecori, E., Poggi, G., Collini, P., Pollo, B., Valentini, L., et al. (2012). Long-term results of combined preradiation chemotherapy and age-tailored radiotherapy doses for childhood medulloblastoma. J. Neurooncol. *108*, 163–171.

Minchinton, A.I., and Tannock, I.F. (2006). Drug penetration in solid tumours. Nat. Rev. Cancer *6*, 583–592.

Monnerat, C., and Le Chevalier, T. (2006). Review of the pemetrexed and gemcitabine combination in patients with advanced-stage non-small cell lung cancer. Ann. Oncol. *17* (*Suppl 5*), v86–v90.

Mubarak, N., Gaafar, R., Shehata, S., Hashem, T., Abigeres, D., Azim, H.A., El-Husseiny, G., Al-Husaini, H., and Liu, Z. (2012). A randomized, phase 2 study comparing pemetrexed plus best supportive care versus best supportive care as maintenance therapy after first-line treatment with pemetrexed and cisplatin for advanced, non-squamous, non-small cell lung cancer. BMC Cancer *12*, 423.

Northcott, P.A., Korshunov, A., Witt, H., Hielscher, T., Eberhart, C.G., Mack, S., Bouffet, E., Clifford, S.C., Hawkins, C.E., French, P., et al. (2011). Medulloblastoma comprises four distinct molecular variants. J. Clin. Oncol. *29*, 1408–1414.

Northcott, P.A., Korshunov, A., Pfister, S.M., and Taylor, M.D. (2012). The clinical implications of medulloblastoma subgroups. Nat Rev Neurol *8*, 340–351.

Packer, R.J., Zhou, T., Holmes, E., Vezina, G., and Gajjar, A. (2013). Survival and secondary tumors in children with medulloblastoma receiving radiotherapy and adjuvant chemotherapy: results of Children's Oncology Group trial A9961. Neuro. Oncol. *15*, 97–103.

Palii, S.S., Van Emburgh, B.O., Sankpal, U.T., Brown, K.D., and Robertson, K.D. (2008). DNA methylation inhibitor 5-Aza-2′-deoxycytidine induces reversible genome-wide DNA damage that is distinctly influenced by DNA methyltransferases 1 and 3B. Mol. Cell. Biol. *28*, 752–771.

Parsons, D.W., Li, M., Zhang, X., Jones, S., Leary, R.J., Lin, J.C., Boca, S.M., Carter, H., Samayoa, J., Bettegowda, C., et al. (2011). The genetic landscape of the childhood cancer medulloblastoma. Science *331*, 435–439.

Pugh, T.J., Weeraratne, S.D., Archer, T.C., Pomeranz Krummel, D.A., Auclair, D., Bochicchio, J., Carneiro, M.O., Carter, S.L., Cibulskis, K., Erlich, R.L., et al. (2012). Medulloblastoma exome sequencing uncovers subtype-specific somatic mutations. Nature *488*, 106–110.

Rausch, T., Jones, D.T., Zapatka, M., Stütz, A.M., Zichner, T., Weischenfeldt, J., Jäger, N., Remke, M., Shih, D., Northcott, P.A., et al. (2012). Genome sequencing of pediatric medulloblastoma links catastrophic DNA rearrangements with TP53 mutations. Cell *148*, 59–71.

Reid, J.M., Qu, W., Safgren, S.L., Ames, M.M., Krailo, M.D., Seibel, N.L., Kuttesch, J., and Holcenberg, J. (2004). Phase I trial and pharmacokinetics of gemcitabine in children with advanced solid tumors. J. Clin. Oncol. *22*, 2445–2451.

Robinson, G., Parker, M., Kranenburg, T.A., Lu, C., Chen, X., Ding, L., Phoenix, T.N., Hedlund, E., Wei, L., Zhu, X., et al. (2012). Novel mutations target distinct subgroups of medulloblastoma. Nature *488*, 43–48.

Rocchetti, M., Simeoni, M., Pesenti, E., De Nicolao, G., and Poggesi, I. (2007). Predicting the active doses in humans from animal studies: a novel approach in oncology. Eur. J. Cancer *43*, 1862–1868.

Saggar, J.K., Fung, A.S., Patel, K.J., and Tannock, I.F. (2013). Use of molecular biomarkers to quantify the spatial distribution of effects of anticancer drugs in solid tumors. Mol. Cancer Ther. *12*, 542–552.

Shu, Q., Wong, K.K., Su, J.M., Adesina, A.M., Yu, L.T., Tsang, Y.T., Antalffy, B.C., Baxter, P., Perlaky, L., Yang, J., et al. (2008). Direct orthotopic transplantation of fresh surgical specimen preserves CD133+ tumor cells in clinically relevant mouse models of medulloblastoma and glioma. Stem Cells *26*, 1414–1424.

Stapleton, S.L., Reid, J.M., Thompson, P.A., Ames, M.M., McGovern, R.M., McGuffey, L., Nuchtern, J., Dauser, R., and Blaney, S.M. (2007). Plasma and cerebrospinal fluid pharmacokinetics of pemetrexed after intravenous administration in non-human primates. Cancer Chemother. Pharmacol. *59*, 461–466.

Taylor, M.D., Northcott, P.A., Korshunov, A., Remke, M., Cho, Y.J., Clifford, S.C., Eberhart, C.G., Parsons, D.W., Rutkowski, S., Gajjar, A., et al. (2012). Molecular subgroups of medulloblastoma: the current consensus. Acta Neuropathol. *123*, 465–472.

Tonkinson, J.L., Worzalla, J.F., Teng, C.H., and Mendelsohn, L.G. (1999). Cell cycle modulation by a multitargeted antifolate, LY231514, increases the cytotoxicity and antitumor activity of gemcitabine in HT29 colon carcinoma. Cancer Res. *59*, 3671–3676.

Uziel, T., Zindy, F., Xie, S., Lee, Y., Forget, A., Magdaleno, S., Rehg, J.E., Calabrese, C., Solecki, D., Eberhart, C.G., et al. (2005). The tumor suppressors Ink4c and p53 collaborate independently with Patched to suppress medulloblastoma formation. Genes Dev. *19*, 2656–2667.

van Moorsel, C.J., Bergman, A.M., Veerman, G., Voorn, D.A., Ruiz van Haperen, V.W., Kroep, J.R., Pinedo, H.M., and Peters, G.J. (2000). Differential effects of gemcitabine on ribonucleotide pools of twenty-one solid tumour and leukaemia cell lines. Biochim. Biophys. Acta *1474*, 5–12.

Wang, H., Li, M., Rinehart, J.J., and Zhang, R. (2004). Pretreatment with dexamethasone increases antitumor activity of carboplatin and gemcitabine in mice bearing human cancer xenografts: in vivo activity, pharmacokinetics, and clinical implications for cancer chemotherapy. Clin. Cancer Res. *10*, 1633–1644.

Warwick, A.B., Malempati, S., Krailo, M., Melemed, A., Gorlick, R., Ames, M.M., Safgren, S.L., Adamson, P.C., and Blaney, S.M. (2013). Phase 2 trial of pemetrexed in children and adolescents with refractory solid tumors: a Children's Oncology Group study. Pediatr. Blood Cancer *60*, 237–241.

Wetmore, C., Eberhart, D.E., and Curran, T. (2001). Loss of p53 but not ARF accelerates medulloblastoma in mice heterozygous for patched. Cancer Res. *61*, 513–516.

White, L., and Sterling-Levis, K. (2008). Multiagent chemotherapy studied in a xenograft model of medulloblastoma/primitive neuroectodermal tumour: analysis of the VETOPEC regimen. J. Clin. Neurosci. *15*, 49–54.

Woodland, J.M., Barnett, C.J., Dorman, D.E., Gruber, J.M., Shih, C., Spangle, L.A., Wilson, T.M., and Ehlhardt, W.J. (1997). Metabolism and disposition of the antifolate LY231514 in mice and dogs. Drug Metab. Dispos. *25*, 693–700.

Zhao, X., Liu, Z., Yu, L., Zhang, Y., Baxter, P., Voicu, H., Gurusiddappa, S., Luan, J., Su, J.M., Leung, H.C., and Li, X.N. (2012). Global gene expression profiling confirms the molecular fidelity of primary tumor-based orthotopic xenograft mouse models of medulloblastoma. Neuro-oncol. *14*, 574–583.

Zhuang, Y., Fraga, C.H., Hubbard, K.E., Hagedorn, N., Panetta, J.C., Waters, C.M., and Stewart, C.F. (2006). Topotecan central nervous system penetration is altered by a tyrosine kinase inhibitor. Cancer Res. *66*, 11305–11313.

CellPress

Cancer Cell
Article

Proteasome Inhibitors Evoke Latent Tumor Suppression Programs in Pro-B MLL Leukemias through MLL-AF4

Han Liu,[1,2] Todd D. Westergard,[3] Amanda Cashen,[3] David R. Piwnica-Worms,[4] Lori Kunkle,[5] Ravi Vij,[3] Can G. Pham,[1] John DiPersio,[3] Emily H. Cheng,[1,6,7,*] and James J. Hsieh[1,8,9,*]

[1]Human Oncology & Pathogenesis Program, Memorial Sloan Kettering Cancer Center, New York, NY 10065, USA
[2]State Key Laboratory of Medical Genomics, Shanghai Institute of Hematology, Ruijin Hospital, Shanghai Jiao Tong University School of Medicine, Shanghai 200025, China
[3]Department of Medicine, Washington University, St. Louis, MO 63105, USA
[4]BRIGHT Institute, Molecular Imaging Center, Mallinckrodt Institute of Radiology, Washington University, St. Louis, MO 63105, USA
[5]Pharmacyclics, Sunnyvale, CA 94085, USA
[6]Department of Pathology, Memorial Sloan Kettering Cancer Center, New York, NY 10065, USA
[7]Department of Pathology and Laboratory Medicine, Weill Cornell Medical College, New York, NY 10065, USA
[8]Department of Medicine, Memorial Sloan Kettering Cancer Center, New York, NY 10065, USA
[9]Department of Medicine, Weill Cornell Medical College, New York, NY 10065, USA
*Correspondence: chenge1@mskcc.org (E.H.C.), hsiehj@mskcc.org (J.J.H.)
http://dx.doi.org/10.1016/j.ccr.2014.03.008

SUMMARY

Chromosomal translocations disrupting *MLL* generate MLL-fusion proteins that induce aggressive leukemias. Unexpectedly, MLL-fusion proteins are rarely observed at high levels, suggesting excessive MLL-fusions may be incompatible with a malignant phenotype. Here, we used clinical proteasome inhibitors, bortezomib and carfilzomib, to reduce the turnover of endogenous MLL-fusions and discovered that accumulated MLL-fusions induce latent, context-dependent tumor suppression programs. Specifically, in MLL pro-B lymphoid, but not myeloid, leukemias, proteasome inhibition triggers apoptosis and cell cycle arrest involving activation cleavage of BID by caspase-8 and upregulation of p27, respectively. Furthermore, proteasome inhibition conferred preliminary benefit to patients with MLL-AF4 leukemia. Hence, feasible strategies to treat cancer-type and oncogene-specific cancers can be improvised through harnessing inherent tumor suppression properties of individual oncogenic fusions.

INTRODUCTION

During tumorigenesis, the accumulation of genetic and epigenetic alterations is a key mechanism that contributes to the malignant phenotype and is a hallmark of cancer (Hanahan and Weinberg, 2011). Driver mutations appear important for tumorigenesis, and tumor cells frequently develop dependence on select oncogenes during cancer evolution for tumor maintenance and malignant progression, hence, develop "oncogene addiction" (Sharma and Settleman, 2007). In several exemplary cases, oncogene addiction can be broken by molecularly targeted agents aimed at therapeutic inhibition of the oncogenic signaling pathway or the oncoprotein itself (Luo et al., 2009).

Classically known oncogenes, such as *MYC*, *RAS*, and *E2F1*, induce transformation and promote tumorigenesis in various settings, but paradoxically incur cellular tumor suppression responses, such as cellular senescence and programmed cell

Significance

The oncogene addiction hypothesis posits that cancers driven by select oncogenes are vulnerable to therapeutic inhibition of the culprit oncoprotein. Surprisingly, recent studies have demonstrated that oncogenes have cryptic intrinsic tumor suppression activity that requires downregulation for tumorigenesis. Here, we investigated whether MLL-fusions possess latent tumor suppression activity and if so, whether it could be redirected to inflict self-destruction. Indeed, we found pro-B MLL leukemia cells were sensitive to bortezomib and carfilzomib. We treated five patients with MLL leukemia that failed standard therapies with bortezomib and observed complete remission in one patient and hematological improvement in another; both had pro-B leukemia. Our study supports further exploration of latent tumor suppression properties of individual oncogenes for cancer treatment.

death. Highlighting this phenomenon, MYC-induced lymphomagenesis depends on an inhibition of apoptosis, often through upregulation of prosurvival proteins of the anti-apoptotic BCL-2 family. Like many oncogenes, MYC is not directly druggable, thereby posing challenges to cancer therapy development. Intriguingly, tumorigenesis by oncogenes may involve cell-type specificity and proper oncogene dosage (Lowe et al., 2004). Regarding oncogene dosage, for example, whereas moderate MYC expression leads to transformation, excess MYC accumulation triggers apoptosis. Thus, tumor suppressive surveillance may depend on a threshold of oncogene abundance.

The mixed-lineage leukemia gene (*MLL*) encodes a large, 500 kDa nuclear protein that contains multiple conserved domains, including a SET domain endowed with methlytransferase activity that is used to methylate histone H3 at lysine 4 (H3K4), a mark associated with euchromatin and active transcription (Dou et al., 2006; Milne et al., 2002). MLL functions as heterodimeric complexes composed of its amino (MLL^{N320}) and carboxy (MLL^{C180}) terminal segments following site-specific proteolysis of its full-length precursor polypeptide by the Taspase1 protease (Hsieh et al., 2003; Oyama et al., 2013; Takeda et al., 2006, 2013). Additional regulation of MLL function involves its biphasic accumulation and proteasome-mediated degradation coinciding with the cell cycle, coordinated by the ubiquitin-proteasome system E3 SCF^{Skp2} and APC^{Cdc20} at S and M phases, respectively (Liu et al., 2007, 2010). Interestingly, MLL is also subject to proteasome-mediated degradation by the ECS^{ASB2} E3 ligase (Wang et al., 2012).

Chromosome 11q23 translocations involving *MLL* account for ~80% of infant leukemias, ~10% of adult acute leukemias, and ~33% of therapy-related myelodysplastic syndrome/secondary acute leukemias (Liu et al., 2009). Leukemogenic *MLL* translocations fuse the common *MLL* 5′ part that encodes its N-terminal ~1,400 amino acid in frame with more than 60 translocation partner genes (TPGs) (Krivtsov and Armstrong, 2007; Liedtke and Cleary, 2009; Liu et al., 2009; Muntean and Hess, 2012; Yip and So, 2013). MLL translocations involving fusion of chromosome 11 with chromosomes 4 and 19 resulting in *MLL-AF4* and *MLL-ENL*, respectively, are prevalent in acute lymphoblastic leukemia (Bhojwani et al., 2009), whereas its translocations with chromosomes 9 and 6 producing *MLL-AF9* and *MLL-AF6*, respectively, are commonly associated with acute myeloid leukemia (AML). MLL-induced leukemias often show resistance to chemotherapies and consequently, patients with these malignancies typically undergo rapid relapse following these conventional treatments. The lack of adequate therapy for leukemias is likely due, in part, to the wide diversity of TPGs and potent oncogenic capacity of MLL-TPG fusion proteins. Hence, much remains to be learned about the activities of the MLL-fusion proteins.

Unexpectedly, expression of certain MLL-fusion products appears to compromise leukemia cell survival (Ayton and Cleary, 2001; Caslini et al., 2000; Xia et al., 2005), and clinical samples from leukemia patients rarely show high-level accumulation of these oncoproteins. Here, we investigated the hypothesis that the accumulation of high levels of endogenous MLL-fusion proteins is detrimental to leukemia cell survival and proliferation.

RESULTS

MLL-Fusion Proteins Accumulate upon Proteasome Inhibition

We previously observed that MLL-fusion proteins typically do not reach excessive levels in vivo (Liu et al., 2007, 2010), indicating that their high-levels may result in undesirable cellular consequences. To examine this further, we monitored the accumulation of MLL and MLL-fusion proteins upon proteasome inhibition in different human leukemia cell lines, including pro-B MLL leukemia cell lines RS4;11 and SEM, and pro-B non-MLL; that is, without *MLL* translocation, leukemia lines JM1 and REH (Drexler et al., 2004; Figure 1A). Before exposure to bortezomib, RS4;11 and SEM cell lines had detectable MLL-AF4 levels that were more abundant than in MLL, which is consistent with the fact that MLL-fusion proteins exhibit reduced turnover by the cell-cycle-dependent ubiquitin proteasome system (Liu et al., 2007) and that MLL-fusions can reduce the levels of MLL (Liu et al., 2010). Significantly, upon exposure to bortezomib, the levels of MLL and MLL-fusion proteins increased in all tested leukemia cell lines (Figure 1B). In pro-B MLL leukemia cells, MLL-AF4 levels increased over the duration of bortezomib treatment, and a similar increase of MLL-AF9 was observed in treated myelogenous MLL cell lines THP-1 and NOMO-1 (Figure 1B). Furthermore, stability analysis demonstrated that MLL-AF4 has a longer protein half-life than MLL (Figure S1A available online). Therefore, MLL-fusion proteins in leukemia cells are continually turned over and their levels appear restricted from reaching an overabundance.

Pro-B MLL Leukemia Cells Show Greater Sensitivity upon Proteasome Inhibition, Exhibiting Apoptosis and G2/M Cell Cycle Block

Next, we investigated what effect bortezomib treatment has on MLL leukemia cells. Importantly, the pro-B MLL leukemia cell lines RS4;11 and SEM showed a dosage-dependent reduction in cell viability (Figure 1C). The reduction in cell viability observed in these lines was greater than that in non-MLL pro-B lines JM1 and REH cells (Figure 1C). The half-maximal inhibitory concentration of bortezomib was determined to be approximately 3 nM in both RS4;11 and SEM cell lines, which was ten times lower than that for the other cell lines tested (Figure 1C). This difference in sensitivity to proteasome inhibition was confirmed with carfilzomib, another US Food and Drug Administration-approved proteasome inhibitor (Demo et al., 2007; Figure S1B). Interestingly, in AML, MLL leukemia lines MV4-11, MOLM-13, NOMO-1, and THP-1 were similarly resistant to bortezomib as non-MLL lines HL60 and U937 (Figure 1C). Notably, despite displaying significant sensitivity to bortezomib, RS4;11 and SEM cells displayed equivalent sensitivity as the other leukemia lines to common chemotherapeutic agents, including doxorubicin (DNA topoisomerase II inhibitor), etoposide (DNA topoisomerase II inhibitor), paclitaxel (microtubule stabilizing agent), cisplatin (DNA cross-linker), and dexamethasone (corticosteroid) (Figures S1C–S1G). Thus, these pro-B MLL-AF4 leukemia cells do not have an intrinsic cell survival impairment. We concluded that pro-B MLL-AF4 leukemia cells display a selective sensitivity to proteasome inhibition.

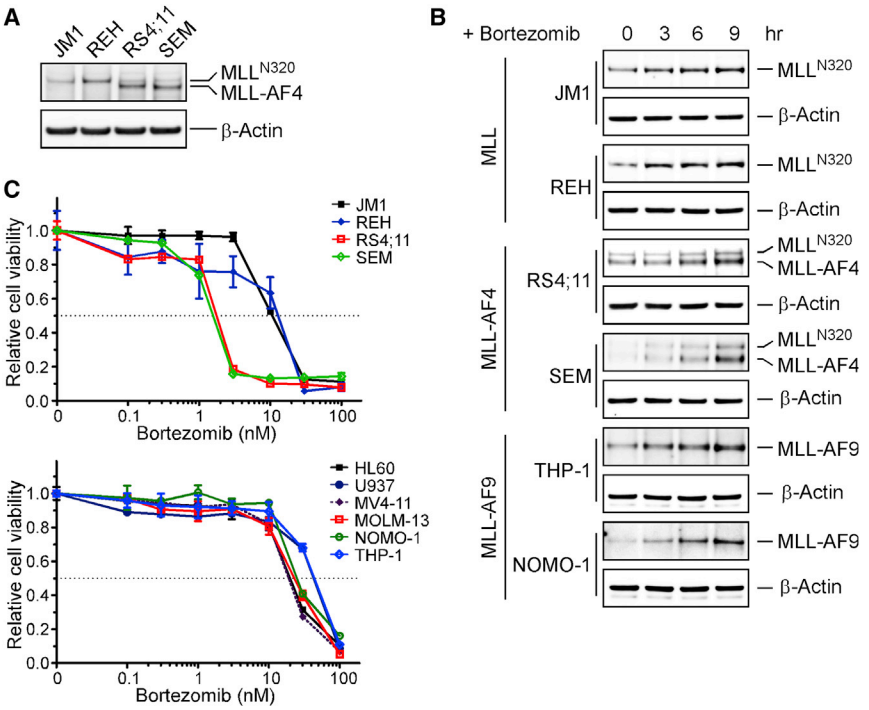

Figure 1. Pro-B MLL-AF4 Leukemia Cells Display Marked Sensitivity to Proteasome Inhibitors

(A) Immunoblots of MLL (MLL^{N320}) and the MLL-AF4 fusion protein in pro-B leukemia cell lines. Antibody against the shared amino terminus of MLL among all MLL-fusions was utilized. The β-actin blot is included to demonstrate similar loading.

(B) Immunoblots of MLL^{N320} and MLL-fusion proteins in the indicated cell lines at 0, 3, 6, and 9 hr after treatment with 5 nM bortezomib.

(C) Cell viability was measured with MTT assay 24 hr after the addition of bortezomib at the indicated concentrations. Top, viability plots of pro-B ALL cell lines; bottom, of AML cell lines. Relative cell viability was calculated by the absorbance reading for bortezomib-treated cells normalized by untreated cells. Error bars reflect ± SEM measured from three independent experiments.

See also Figure S1.

We sought to better understand the susceptibility to bortezomib in the pro-B MLL-AF4 leukemia cells. Annexin V staining of RS4;11, SEM, JM1, and REH cells following exposure to bortezomib confirmed that the pro-B MLL-AF4 leukemia cells were more prone to undergo cell death than their pro-B non-MLL leukemia counterparts (Figure 2A). Furthermore, cell cycle analysis demonstrated that compared to JM1 and REH, the RS4;11 and SEM cell lines displayed a reduction in the S phase and an accumulation in the G2/M phase (Figure 2B). These cells also displayed a greater ratio of sub-G1 ploidy (Figure 2B), indicative of increased DNA cleavage that associates with apoptosis. These results suggest that bortezomib selectively induces apoptosis and G2/M block in pro-B leukemia cells bearing the MLL-AF4 oncoprotein.

To investigate that MLL-AF4 could be involved in the bortezomib-induced cytotoxicity, we performed shRNA-mediated knockdown studies. SEM and RS4;11 cells were retrovirally transduced with an shRNA specifically targeting the junction sequence of MLL-AF4 (shMLL-AF4) or a control shRNA. Whereas the control shRNA had no effect on bortezomib-induced killing, shMLL-AF4 led to a reduction in bortezomib-triggered apoptosis (Figures 2C, S2A, and S2B). Furthermore, ectopic expression of MLL-AF4 in SEM cells appeared to render increased sensitivity to bortezomib (Figure S2C). Conversely, because non-MLL pro-B leukemia cells were less susceptible to the bortezomib-stimulated cytotoxicity (Figure 1), we determined if ectopic expression of MLL-fusions in REH cells would alter their sensitivity to proteasome inhibition. To this end, we generated REH cell lines stably transduced with MLL-AF4, MLL-AF9, or MLL-ENL (Figure 2D). Remarkably, introduction of MLL-AF4, MLL-AF9, or MLL-ENL caused REH cells to become more susceptible to bortezomib (Figure 2D). Of note, reconstitution of the common MLL amino-terminus alone in REH cells (Figures 2D and S2D) or MLL-AF4 or MLL-ENL in HL60 myelogenous leukemia cells (Figure S2E) did not confer bortezomib sensitivity. Altogether, these results demonstrate that apoptosis induced by proteasome inhibition in the pro-B MLL leukemia cells is likely dependent on the MLL-fusion proteins. They also suggest that distinct leukemia cells are intrinsically equipped with an oncogenic fusion protein that could be retooled as a self-destructive weapon.

Bortezomib Triggers Apoptosis in Pro-B MLL Leukemia through BID Activation

Multiple death stimuli culminate in activation of the pro-apoptotic BCL-2 cascade, resulting in mitochondrial outer membrane permeabilization and cytochrome c efflux into the cytosol for caspase activation (Danial and Korsmeyer, 2004; Kim et al., 2006, 2009; Ren et al., 2010). To determine whether caspase-mediated apoptosis is involved in bortezomib-induced cancer cell death, RS4;11 and SEM cells were cotreated with zVAD, a pan-caspase inhibitor, during their exposure to bortezomib. Cotreatment of zVAD efficiently reduced the number of annexin V-positive cells caused by bortezomib (Figures 3A and S3A). We next examined if anti-apoptotic BCL-2 family proteins BCL-2 or BCL-X_L could suppress this death. In RS4;11 and SEM cells, retroviral transduction of BCL-2 or BCL-X_L disrupted bortezomib-induced cell death (Figures 3B and S3B), indicating that proteasome inhibition induces cell death through the mitochondrion-dependent apoptotic pathway. Consistent with these pharmacological and genetic evidences of apoptosis, RS4;11 and SEM, but not JM1 or REH, cells displayed cleavage of caspase-3 and poly ADP-ribose polymerase (Figure 3C). Thus, in pro-B MLL leukemia cell lines, bortezomib induces mitochondrial apoptosis that can be blocked by anti-apoptotic BCL-2 and BCL-X_L.

Bortezomib has been reported to trigger apoptosis in multiple myeloma cells through both (nuclear factor kappa-light-chain-enhancer of activated B cells (NF-κB)-dependent and -independent mechanisms (Adams, 2004; Cvek and Dvorak, 2011;

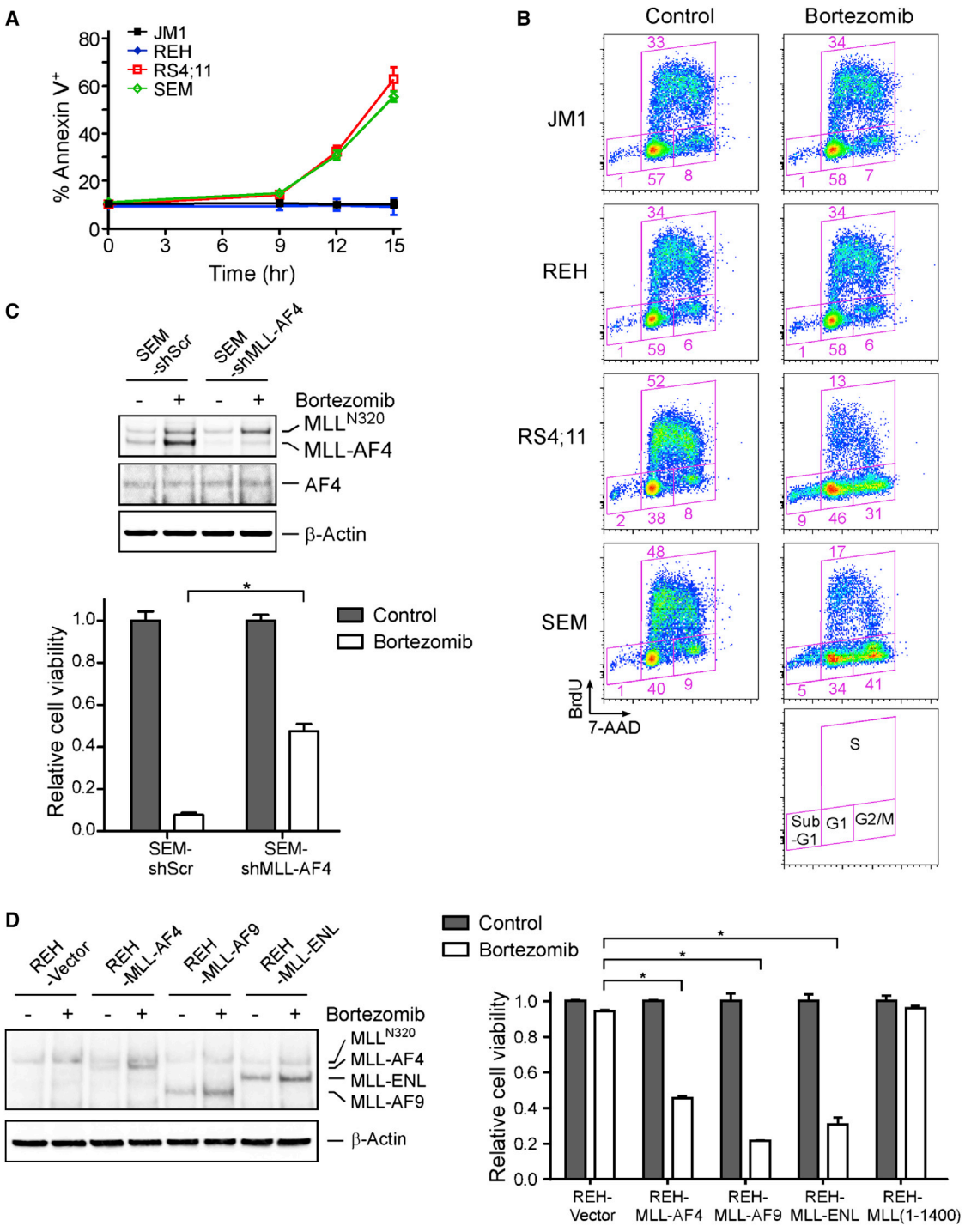

Figure 2. Proteasome Inhibition Induces Apoptosis and Cell Cycle Arrest in the Pro-B Leukemia Cells Harboring MLL-Fusion Proteins

(A) Cells were stained with annexin V after treatment with 5 nM bortezomib.

(B) Cell cycle profiles were analyzed upon a 12 hr exposure to 5 nM bortezomib. Cell cycle profiling was performed after a 30 min pulse incorporation of bromodeoxyuridine (BrdU), followed by flow cytometry analyses. Regions of the fluorescence-activated cell sorting plot delineating different cell cycle phases are specified.

(C) Top, immunoblots demonstrated shMLL-AF4-mediated specific knockdown of MLL-AF4 but not MLL (MLL^{N320}) in SEM cells. The indicated cells were treated with 12 hr of 5 nM bortezomib. Bottom, MTT assays of the indicated cells after a 24 hr exposure to 5 nM bortezomib are presented.

(D) Left, immunoblots demonstrated exogenous expression of FLAG-tagged MLL-AF4, MLL-AF9, MLL-ENL, and MLL (amino acids 1–1,400), determined by an anti-MLL amino-terminus antibody. Right, MTT assay were performed after a 24 hr treatment with 5 nM bortezomib.

Error bars reflect ± SEM calculated from three independent experiments. *Indicates statistical significance ($p < 0.05$). See also Figure S2.

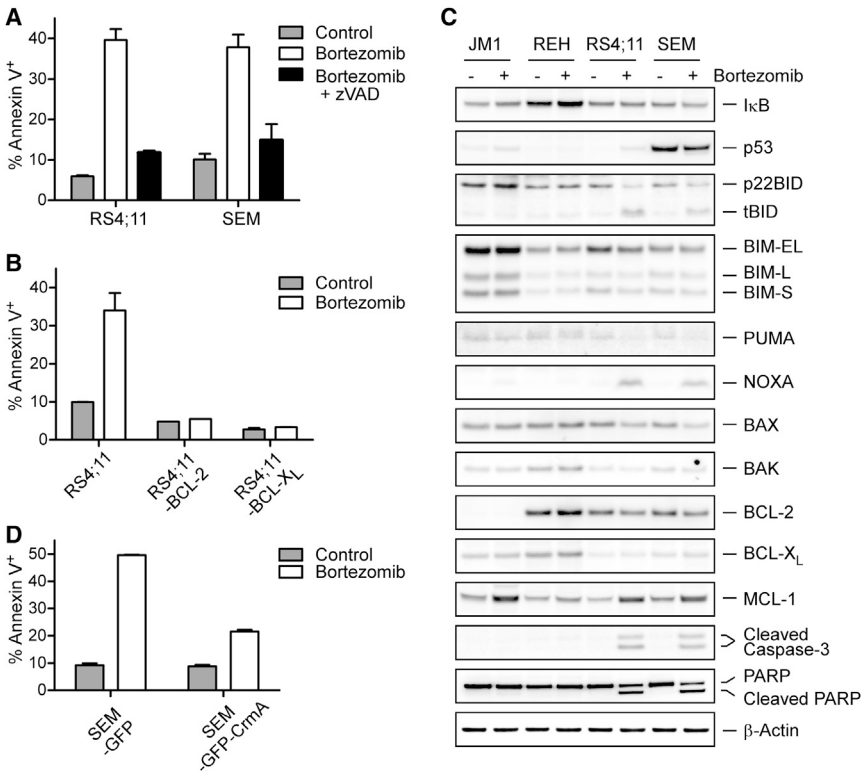

Figure 3. The Cell Death of Pro-B Leukemia Cells Induced upon Proteasome Inhibition Involves the Extrinsic Apoptotic Pathway

(A) The percentage of annexin V-positive cells was determined after a 12 hr exposure to 5 nM bortezomib with or without cotreatment of 50 μM zVAD.

(B) Annexin V staining of the indicated cells was assessed after a 12 hr treatment with 5 nM bortezomib.

(C) Immunoblots of key apoptosis regulators of the indicated pro-B leukemia cells before and after a 12 hr exposure to 5 nM bortezomib.

(D) Annexin V staining of the indicated cells was assessed after a 12 hr treatment with 5 nM bortezomib.

Error bars reflect ± SEM calculated from three independent experiments. See also Figure S3.

Hideshima et al., 2009). However, upon proteasome inhibition in RS4;11 and SEM cells, no increase was seen in the levels of I-κB, a major regulatory protein of NF-κB complexes that is controlled by stimulus-dependent proteasome-mediated degradation (Figure 3C). This suggests that NF-κB inhibition is unlikely to be the main mechanism underlying bortezomib-induced apoptosis. The observation that bortezomib-induced apoptosis can be inhibited by BCL-2 and BCL-X_L indicates the involvement of mitochondrion-dependent cell program. In response to death signals, activator BH3-only molecules, including truncated BID (tBID), BIM, and PUMA, directly interact with BAX and BAK to induce a stepwise structural reorganization and the ensuing oligomerization of BAX and BAK, leading to mitochondrial outer membrane permeabilization (Cheng et al., 2001; Kim et al., 2006, 2009; Ren et al., 2010). To interrogate further, we examined the levels of pro- and anti-apoptotic BCL-2 family proteins—key players that integrate death and survival signals at the mitochondria (Cvek and Dvorak, 2011; Fennell et al., 2008). In RS4;11 and SEM cells, but not JM1 or REH cells, conversion of BID to tBID p15 was observed upon proteasome inhibition (Figure 3C), suggesting that caspase-8 is likely activated to cleave BID. BID normally resides in the cytosol, and, once cleaved by caspase-8 (tBID), translocates to the mitochondrion where it activates BAX and BAK to induce cytochrome c release, serving as an amplification loop for caspase-3 activation. Caspase-8 can be autoactivated within the death-inducing signaling complex upon ligation of death receptors such as FAS. Indeed, quantitative RT-PCR (qRT-PCR) analysis of RS4;11 and SEM cells showed that bortezomib increased transcript levels of *FAS*, *FASLG*, and *CASP8*, likely contributing to the activation of caspase-8, but not those of *HOXA9* or *MEIS1,* two key downstream leukemogenic effectors of MLL-AF4 (Figures S3C–S3H). Furthermore, bortezomib-mediated transcriptional upregulation of *CASP8*, *FAS*, and *FASLG* was inhibited by knockdown of MLL-AF4 in SEM cells (Figures S3I–S3K). Proteasome inhibition was reported to increase the duration and amount of caspase-8 activity upon death receptor engagement (Gonzalvez et al., 2012). To further interrogate the involvement of caspase-8 activation in bortezomib-induced apoptosis in pro-B MLL leukemia, we exogenously expressed CrmA, an inhibitor of caspase-8 (Garcia-Calvo et al., 1998; Muzio et al., 1996), and found that CrmA expression significantly protected SEM cells from bortezomib-induced apoptosis (Figure 3D). As previously reported, MCL-1 protein, which is rapidly turned over by the ubiquitin-proteasome system, was stabilized by bortezomib (Figure 3C; Perciavalle and Opferman, 2013). However, the potent inactivator of MCL-1, NOXA, was also highly induced by bortezomib (Figure 3C). Consequently, NOXA would prevent MCL-1 from sequestering tBID, allowing tBID to activate BAX and BAK (Kim et al., 2006). Although both NOXA and PUMA are known transcriptional targets of p53, only NOXA was induced upon proteasome inhibition. Furthermore, the levels of p53 did not correlate with bortezomib-induced apoptosis in these cell lines that carry wild-type p53 alleles based on the cancer cell line encyclopedia (Barretina et al., 2012; Figure 3C). Hence, p53 is unlikely to play a role in proteasome inhibitor-induced apoptosis in our experimental setting. Taken together, these results are consistent with a model in which proteasome inhibition activates caspase-8 to convert BID to tBID, which in turn, initiates BAX- and BAK-dependent mitochondrial apoptosis in pro-B MLL leukemia cells.

Bortezomib Induces Cell Cycle Dysfunction in RS4;11 and SEM Cells through p27 Activation

Because bortezomib triggers both apoptosis and cell cycle arrest (Figures 2A and 2B), we examined whether these two processes are separable. First, we determined if the bortezomib-induced G2/M block is affected when apoptosis is abrogated. For this, anti-apoptotic BCL-X_L was ectopically expressed in

SEM cells to inhibit apoptosis. Despite acquiring a marked resistance to apoptosis, the BCL-X_L-expressing SEM cells still exhibited a G2/M block upon proteasome inhibition (Figure 4A). Similarly, cotreatment of zVAD in SEM cells did not affect the G2/M block caused by bortezomib (Figure S4A). To investigate further, we performed immunoblotting to detect levels of cyclins and cyclin-dependent kinase inhibitors, key regulators of cell cycle progression. In RS4;11 and SEM cells, we observed a marked upregulation of p27 that correlated with the bortezomib-induced cell cycle arrest (Figure 4B). In contrast, the levels of p15, p16, p21, and cyclins D1, E2, A, B1, were unchanged by bortezomib, and hence these were unlikely to be directly involved in the bortezomib-induced cell cycle arrest (Figure 4B).

We next examined the role of p27 in the bortezomib-induced G2/M block. In SEM-BCL-2 cells, knockdown of p27 led to an attenuation of the bortezomib-induced G2/M block (Figure 4C), indicating that p27 is important for these pro-B MLL leukemia cells to undergo cell cycle arrest in response to proteasome inhibition. Levels of p27 can be controlled by protein degradation (Chu et al., 2008) and by direct transcriptional activation through MLL and MLL-AF4 (Milne et al., 2005; Xia et al., 2005). Thus, we examined if the upregulation of p27 upon bortezomib treatment depends on MLL-AF4. qRT-PCR analysis showed that the p27 mRNA level in SEM and RS4;11, but not JM1 or REH, cells was increased by the bortezomib treatment (Figure 4D). Significantly, in SEM cells, specific knockdown of MLL-AF4 impeded p27 induction (Figure 4E). Conversely, enforced expression of MLL-AF4 or MLL-AF9 in REH cells rendered capability to upregulate p27 (Figure 4F). Taken together, these results suggest that bortezomib principally stabilizes MLL-AF4 or MLL-AF9, which in turn activates the transcription of the p27 gene (*CDKN1B*). Similarly, knockdown of MLL-AF4 in RS4;11 cells also compromised p27 induction but to a lesser degree, which could be due to a less efficient knockdown (Figure S4B). Intriguingly, concurrent knockdown of both MLL-AF4 and MLL by targeting the shared amino terminus (shMLL-N) in RS4;11 cells seemed to further impair the p27 induction upon the bortezomib treatment, implicating a possible assistance of MLL in the MLL-AF4-dependent induction of p27 (Figure S4B), reminiscent of what was shown before that MLL-AF9-induced leukemogenesis required MLL (Thiel et al., 2010).

We further evaluated the mechanisms by which MLL-fusion proteins contribute to the p27 upregulation. Interestingly, MLL-fusion partner proteins, including AF4, AF9, ENL, and ELL, are functional components of the P-TEFb complex (positive transcription elongation factor b) that functions in transcriptional elongation (Mohan et al., 2010). Moreover, MLL-AF4, but not MLL, is able to recruit P-TEFb (Yokoyama et al., 2010). Therefore, we examined whether the bortezomib-stabilized MLL-AF4 recruits P-TEFb to enhance *CDKN1B* transcription. To this end, we performed chromatin immunoprecipitation (ChIP) assays. In bortezomib-treated REH and SEM cells, anti-MLL N terminus antibody detected an increased occupancy of MLL and/or MLL-AF4 at both the *CDKN1B* promoter and exon 2 (Figure 4G). Of note, this N terminus antibody recognizes both MLL and MLL-fusions (Liu et al., 2010). Like the MLL-AF4 protein, cyclin T1, a key component of the P-TEFb complex (Mohan et al., 2010), was also observed to have an increased promoter and gene body occupancy in SEM but not REH cells (Figures 4G). Altogether, the body of evidence indicates that accumulation of MLL-AF4 in response to bortezomib leads to recruitment of the P-TEFb complex to promote transcriptional processivity along *CDKN1B*, thereby increasing the production of p27 mRNA.

MLL-Fusions Target the *CDKN1B* Locus through Binding B Cell-Specific Transcription Factor PAX5

Recruitment of the P-TEFb complex to the *CDKN1B* locus by MLL-AF4 could explain how MLL-fusion proteins might stimulate the induction of p27. However, it could not explain why these MLL-fusions did not induce p27 in AML cells despite similarly increased protein abundance. MLL and MLL-fusion proteins do not consist of any apparent sequence-specific DNA binding domain (Liu et al., 2009). Therefore, we envisioned that MLL-fusion proteins may upregulate *CDKN1B* transcription through DNA binding protein partners, such as PAX5 and EBF1 (early B cell factor) transcription factors, that are selectively expressed in pro-B cells (Busslinger, 2004). By co-immunoprecipitation assays, MLL-AF4 was found to interact with PAX5, but not EBF1 (Figures 5A and S5A). Other MLL-fusion proteins, including MLL-AF9, MLL-ENL, and MLL-ELL, also interacted with PAX5 (Figure 5B), suggesting that the PAX5-interaction domain of the MLL-fusion proteins is located within the common MLL N-terminal 1,400 amino acids. Indeed, whereas the different MLL translocation partners failed to pull down PAX5 by themselves, the amino-terminal 1,400 amino acids of MLL were sufficient to pull down PAX5 (Figure S5B). Mapping experiments using individual MLL fragments demonstrated that the minimal interaction domain of MLL encompasses the first 400 amino acids (Figure 5C).

Using JM1, REH, RS4;11, and SEM pro-B leukemia cells, we confirmed with co-immunoprecipitation assays that endogenous MLL/MLL-AF4 interacted with PAX5 (Figure 5D). Functionally, in SEM cells, knockdown of PAX5 abrogated the ability of bortezomib to induce p27 mRNA and protein (Figures 5E, 5F, and S5C). Furthermore, PAX5 knockdown did not affect MLL-AF4 stability (Figure 5F). We noted that PAX5 levels increased upon bortezomib treatment (Figure S5D), and this increase was also associated with an increased PAX5 occupancy at the *CDKN1B* promoter (Figure 5G). Moreover, the increased abundance of MLL/MLL-AF4 at the *CDKN1B* promoter was lost when PAX5 was knocked down (Figure 5G), indicating that PAX5 is required for MLL/MLL-AF4 to bind the *CDKN1B* promoter. Our collective data support a model in which the MLL-AF4 recruitment to the *CDKN1B* locus depends on PAX5, and the interaction between MLL-AF4 and PAX5 enhances transcriptional processivity of *CDKN1B*, resulting in the cell cycle arrest.

Because PAX5 appears to be the critical link for recruiting the MLL fusion protein to the promoters of cell cycle genes such as *CDKN1B*, we assessed the effect of enforced PAX5 expression in THP-1 cells an acute myelogenous MLL leukemia cell line. Interestingly, introduction of exogenous PAX5 did not restore the sensitivity of the MLL-AF9-harboring THP-1 cells to the proteasome inhibitors (Figures S5E and S5F). Furthermore, ChIP assays revealed that neither ectopically expressed PAX5 nor MLL or MLL fusion proteins could be recruited to the *CDKN1B* promoter (Figure S5G), suggesting that additional factors and/

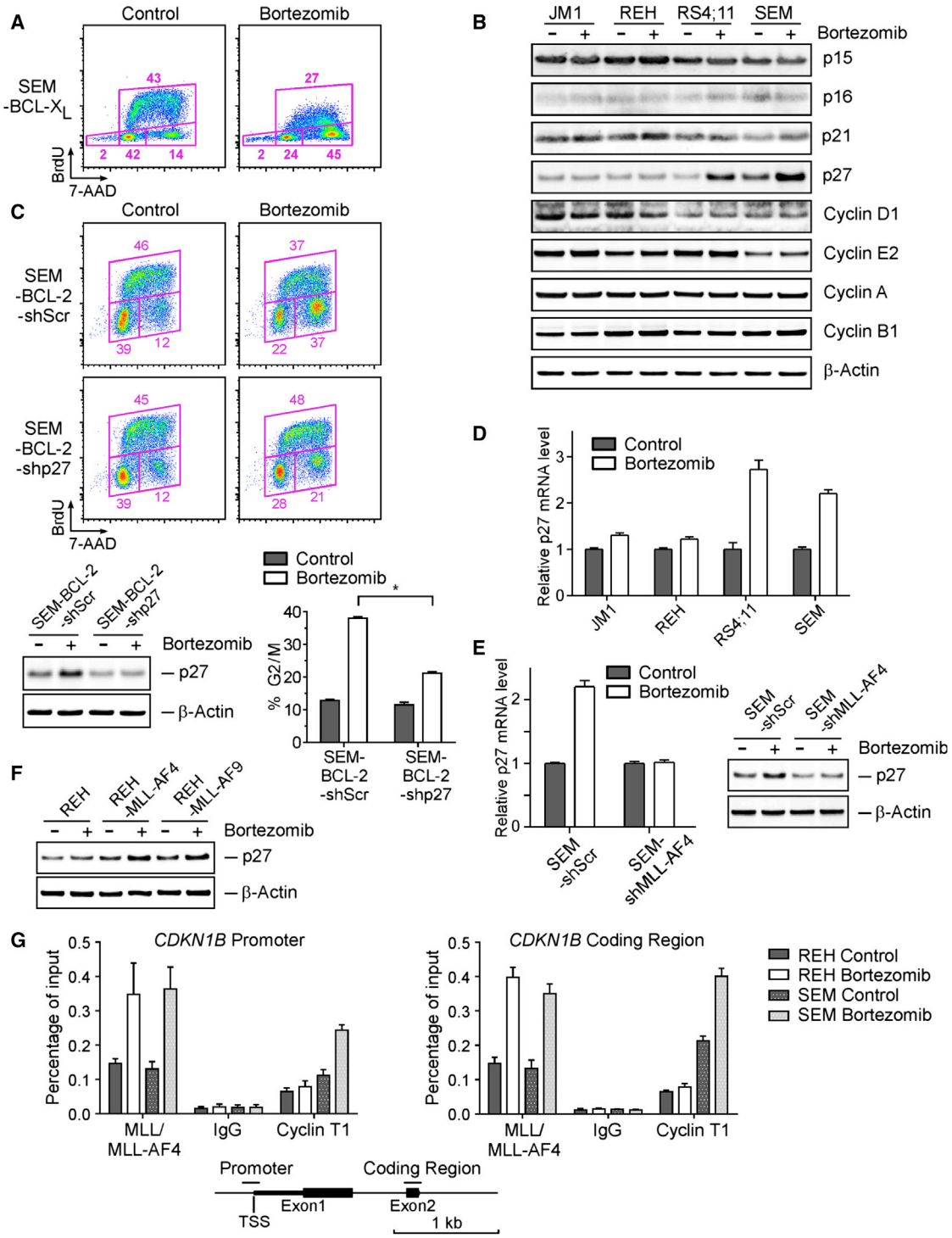

Figure 4. The p27 Upregulation Plays a Key Role in Bortezomib-Induced Cell Cycle Arrest of Pro-B Leukemia Cells Expressing MLL-Fusions

(A) Cell cycle profiles of the SEM-BCL-X_L cells exposed to 5 nM bortezomib for 12 hr were obtained after a 30 min BrdU pulse incorporation, followed by flow cytometry analyses. Percentages of gated cells are indicated.

(B) Immunoblots of the indicated pro-B leukemic cells following a 12 hr treatment with 5 nM bortezomib.

(C) Top, cell cycle profiles of BCL-2 reconstituted SEM cells expressing shRNA-scramble (shScr) or shRNA-p27 (shp27) were obtained after a 12 hr exposure to 5 nM bortezomib. Bottom left, immunoblots of p27 in knockdown cells. The percentage of the cells in G2/M phase is plotted in the bottom right.

(D) p27 mRNA levels were detected with qRT-PCR in pro-B MLL leukemia cells after a 12 hr treatment with 5 nM bortezomib. Values were normalized against *GAPDH*.

(E) The changes of p27 mRNA and protein in the indicated SEM cells upon bortezomib treatment were determined.

(legend continued on next page)

or the epigenetic status of the *CDKN1B* locus unique to pro-B leukemia cells are likely required for the recruitment of the PAX5/MLL-fusion complex to it.

Preclinical and Clinical Evidence Supports a Role of Proteasome Inhibition in Treating Pro-B MLL Leukemias

To investigate if the anticancer effects of proteasome inhibitors on pro-B MLL-leukemias extend to in vivo settings, we performed xenograft studies by transplanting luciferase-GFP-tagged REH or SEM cells into NOD-scid *Il2rg*$^{-/-}$ (NSG) recipient mice. Subsequently, engrafted mice were treated with bortezomib (Luker et al., 2003) and monitored by bioluminescent imaging over approximately 3 weeks. Mice transplanted with REH or SEM cells without bortezomib therapy developed rapid tumor progression that was apparent 10 days after transplantation and that aggressively pervaded nearly the entire animal over the ensuing 7 days (Figure 6A). Importantly, mice engrafted with SEM cells and then treated with bortezomib showed a striking resistance to leukemia accumulation and had only a minor detectable tumor burden during the same assay period, thus suggesting significant bortezomib responsiveness in vivo. In contrast, mice transplanted with REH showed little responsiveness to this form of therapy, and displayed a significant tumor burden (Figure 6A). Hence, similar to the results obtain from our in vitro studies, our xenograft studies strongly suggested that bortezomib treatment is an effective agent against pro-B MLL-AF4 leukemia cells in vivo.

Patients with leukemia bearing MLL translocations generally have a poor overall prognosis, and this aggressive disease tends to be refractory to conventional anticancer therapies (Liedtke and Cleary, 2009). Indeed, MLL leukemia patients frequently suffer relapse after high-dose chemotherapy and/or bone marrow transplantation. Regrettably, those who fail to respond to standard therapeutic regimens are often left with limited medical options. Few clinical trials exist due to the low overall prevalence of adult MLL-fusion leukemias. A group of five adult MLL leukemia patients, comprised of two pro-B, one biphenotypic, and two myeloid leukemia cases, were compassionately treated with bortezomib at standard dosing recommended for multiple myeloma (Figure 6B and Table S1). Remarkably, patient 1, a 21-year-old female with pro-B MLL-AF4 leukemia, achieved a complete cytogenetic remission after two standard cycles of bortezomib (1.3 mg/m^2 on days 1, 4, 8, and 11 of a 21 day cycle; Figure 6C). Due to neurotoxicity, she was given reduced doses of bortezomib at 1 mg/m^2 once a week as maintenance, which was discontinued after 8 weeks. This patient remained in complete remission without further treatment for longer than 1 year. Unfortunately, her leukemia eventually re-emerged and was minimally responsive to bortezomib, and she died soon thereafter. She had previously relapsed 6 months after allogeneic bone marrow transplant from a matched unrelated donor following hyper-CVAD chemotherapy. Patient 2, who also had pro-B MLL-AF4 leukemia, exhibited nondurable hematologic improvement. Patient 3, who had biphenotypic MLL leukemia, experienced nondurable reduction in bone marrow blasts. Consistent with our preclinical findings showing that bortezomib has no efficacy on myelogenous MLL leukemia cells, patients 4 and 5 derived no clinical benefit from bortezomib therapy.

DISCUSSION

Oncogenes, such as *MYC*, *RAS*, and *E2F1*, underlie various human malignancies and promote cancer formation in various experimental settings. Yet, despite acting as important drivers of tumorigenesis, these oncogenes can trigger tumor suppression in a cell-context and dose-dependent manner (Lowe et al., 2004). Indeed, whereas moderate oncogene levels induce cancer initiation and maintenance, high-level expression can inadvertently activate tumor suppression surveillance programs including programmed cell death (Murphy et al., 2008; Sarkisian et al., 2007). Most notably, excessive Myc overexpression, in a titratable Myc mouse model, triggers apoptosis through the induction of BIM and PUMA, ''activator'' BH3-only molecules (Egle et al., 2004; Hemann et al., 2004, 2005). Hence, this mechanism serves as a powerful way to curb the emergence of cancer and acts as an organismal protective mechanism (Pelengaris et al., 2002). Similarly, E2F1-induced oncogenesis is antagonized by apoptosis in RB-deficient cancer cells (Chen et al., 1999; Mendoza et al., 2003). However, whereas oncogenes can activate tumor suppression programs, it remains undetermined if such latent programs persist in tumor cells and whether they can be reactivated and thereby render clinical benefit for cancer patients. There are obvious important issues limiting this application. First, in many cancers, driver oncogenes are overexpressed. Second, during tumor progression, cancer cells usually acquire additional mutations that either abolish or bypass inherent tumor suppression functions. Third, ideal targets should be different between cancer and surrounding normal cells. Here, we demonstrate that MLL-fusion proteins can be stabilized and reactivated upon proteasome inhibition, triggering latent tumor suppression programs (Figure 7).

The transcriptional regulation of p27 by MLL, MLL-AF9, MLL-AF4, and MLL-ENL has been reported in various experimental settings and appears to be very complex (Caslini et al., 2000; Milne et al., 2005; Wang et al., 2008; Xia et al., 2005). Intriguingly, in Jurkat cells overexpression of MLL-AF4 induces p27 whereas in 293T cells it suppresses (Xia et al., 2005). Furthermore, in human MLL-AF5 leukemia cells KP-L-RY and MLL-ENL-transformed murine myeloid progenitors, pharmacological inhibition of GSK3 induces p27 and yields preclinical therapeutic benefits (Wang et al., 2008). In U937 cells, overexpression of the MLL amino terminus (amino acids 1–410) induces p27 (Caslini et al., 2000). In pancreatic neuroendocrine cells and transformed mouse embryonic fibroblasts, wild-type MLL complexes with Menin to activate p27 (Milne et al., 2005), which further refines

(F) The p27 protein level in REH cells expressing either MLL-AF4 or MLL-AF9 after a 12 hr exposure to 5 nM bortezomib.
(G) ChIP analyses at promoter and exon 2 of the *CDKN1B* locus on the indicated cells upon bortezomib treatment. Assays were performed with the indicated antibodies and immunoprecipitates were subjected to quantitative PCR analyses using primers covering the depicted genomic regions. TSS, transcription start site.
Error bars reflect ± SEM calculated from three independent experiments. *Indicates statistical significance ($p < 0.05$). See also Figure S4.

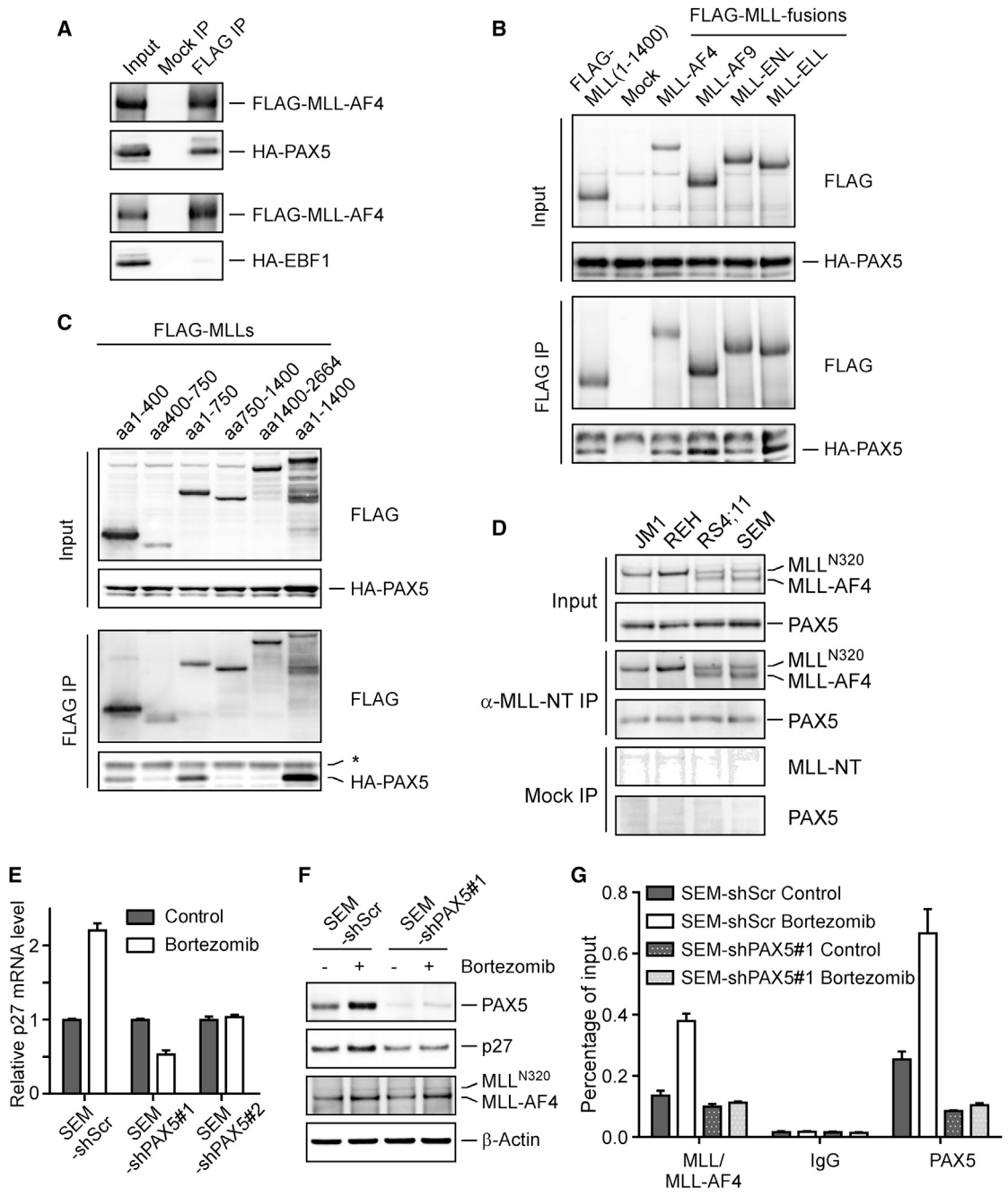

Figure 5. The Recruitment of MLL-AF4 through PAX5 to the *CDKN1B* Locus Underlies the Specific Cytotoxicity upon Proteasome Inhibition in Pro-B Leukemia Cells

(A) 293T cells were transfected with FLAG-MLL-AF4 and HA-PAX5 or HA-EBF1 expression constructs as indicated, subjected to anti-FLAG immunoprecipitation, and analyzed with the indicated antibodies.

(B) 293T cells transfected with the indicated FLAG-MLL constructs and HA-PAX5 were subjected to anti-FLAG immunoprecipitation, and analyzed with immunoblots.

(C) 293T cells transfected with the indicated FLAG-MLL constructs expressing individual MLL amino terminus fragments and HA-PAX5 were subjected to anti-FLAG immunoprecipitation and analyzed with immunoblots.

(D) An antibody that recognizes the common amino-terminal region of MLL and MLL-fusions was used for immunoprecipitation, and the precipitates were analyzed with the indicted antibodies.

(E) SEM cells with the indicated knockdown were subjected to qRT-PCR analysis after a 12 hr treatment with 5 nM bortezomib.

(F) PAX5, p27, and MLL-AF4 protein levels of the indicated SEM cells were determined after a 12 hr treatment with 5 nM bortezomib.

(G) SEM cells of the indicated knockdown were subjected to ChIP after a 12 hr treatment with 5 nM bortezomib using the indicated antibodies, and immunoprecipitates were subjected to quantitative PCR analyses.

Error bars reflect ± SEM calculated from three independent experiments. See also Figure S5.

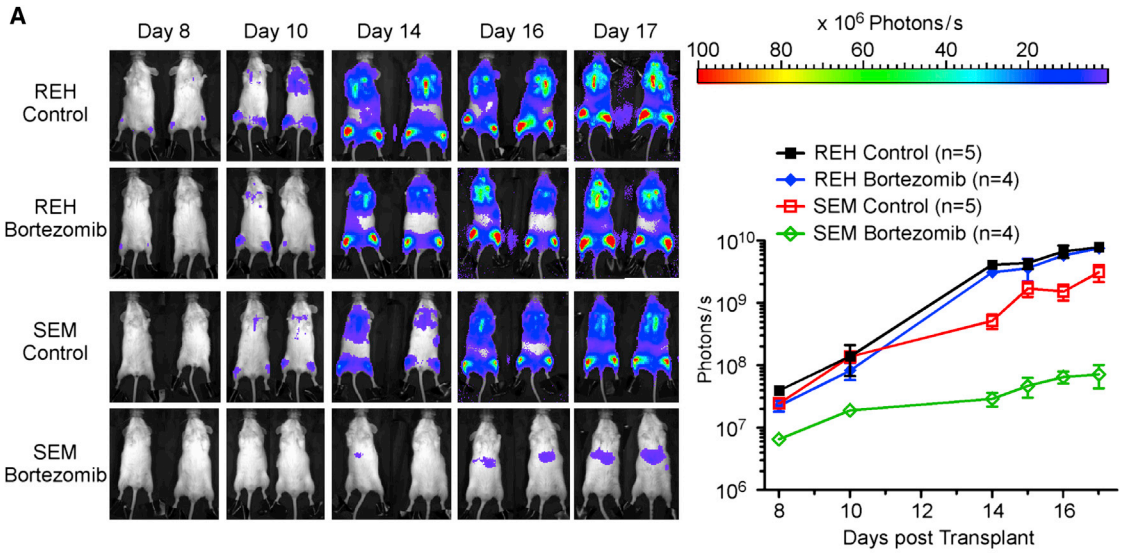

B

Patient	Diagnosis	Cytogenetics	Response to velcade
1	pre-B-cell ALL	t(4;11)	complete cytogenetic remission
2	pre-B-cell ALL	t(4;11)	hematologic improvement
3	biphenotypic leukemia	t(2;11)	improvement in bone marrow blasts
4	M5-AML	t(6;11)	no response
5	t-AML	t(9;11)	no response

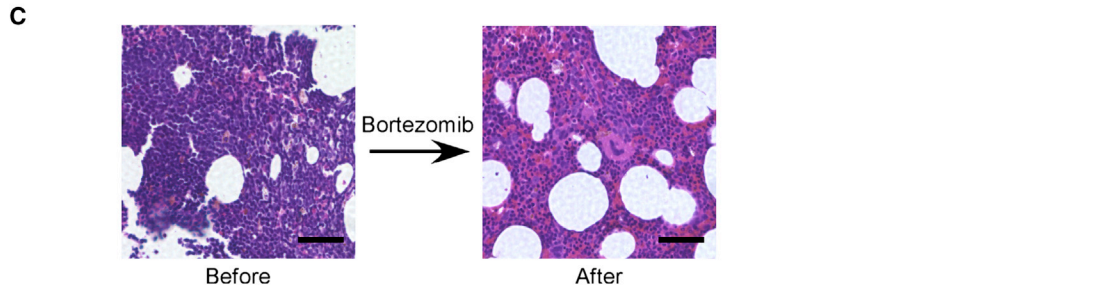

Figure 6. The In Vivo Therapeutic Benefits of Proteasome Inhibition in Pro-B MLL Leukemias

(A) NSG mice transplanted with luciferase-expressing REH or SEM cells were treated with bortezomib. On the indicated days after the xenograft, mice were imaged to assess for leukemia progression. Representative bioluminescence images are shown on the left and the quantification of bioluminescence (photonic flux) over the duration of treatment is shown on the right. Error bars reflect ± SEM.

(B) Pathological and clinical summary of five adult patients with MLL leukemia treated with bortezomib.

(C) Hematoxylin and eosin staining of bone marrow biopsies of patient 1 before (left) and after (right) bortezomib treatment. Scale bars, 100 μm. See also Table S1.

the Menin-p27 tumor suppressor axis in the pancreas (Karnik et al., 2005). Surprisingly, although the loss of Menin in MLL-ENL-transformed myeloid leukemia blasts results in reduced *Hoxa7* and *Hoxa9* expression and thus compromises the leukemia phenotype, the Menin loss under this experimental setting did not affect *Cdkn1b* (Yokoyama et al., 2005). Taken together, most data, including ours, favor a positive correlation between MLL/MLL-fusion and p27 expression. This begs several outstanding questions: Why do leukemia fusions activate p27? Is this a necessity or simply an unwanted byproduct? In favor of the first scenario, it has been suggested that a low level of p27 induction by MLL-fusion proteins might prevent leukemia-initiating cells from exhaustion (Zhang et al., 2013). In favor of the second scenario, MLL-fusions unavoidably acquire this context-dependent tumor suppressor activity through the common MLL amino terminus. Nevertheless, this capacity appears tightly regulated and can be manipulated by pharmacological means, thereby offering specific therapeutic benefits to patients with pro-B MLL leukemia.

Collectively, these in vitro results suggest that the latent tumor suppression activity of MLL-fusion proteins in pro-B MLL leukemia cells can be activated by proteasome inhibitors. In accordance with our in vitro results, proteasome inhibition rendered therapeutic benefit in an MLL leukemia xenograft mouse model. Proteasome inhibition also rendered complete remission to one patient with pro-B MLL-AF4 leukemia that eventually relapsed. Bortezomib treatment did not appear to benefit the three patients with AML MLL. Notably, in multiple myeloma, a malignancy for which bortezomib is approved, the rate of response to bortezomib was 38%.

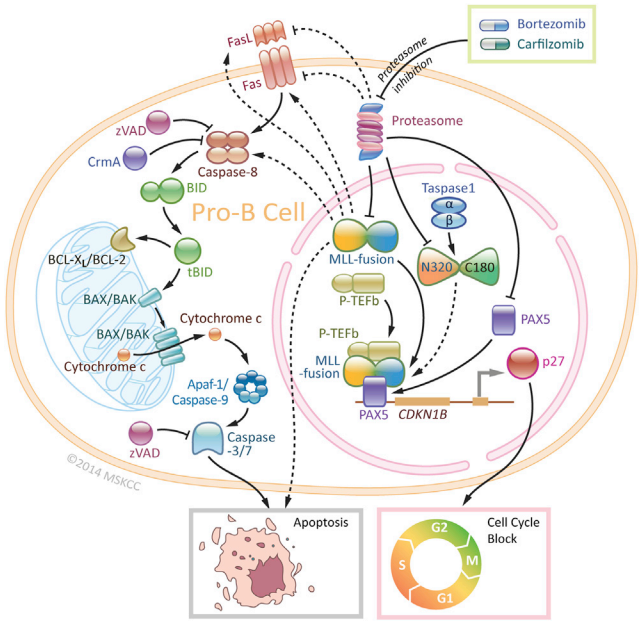

Figure 7. Illustration Depicts How Proteasome Inhibition Induces Specific Cytotoxicity in Pro-B MLL Leukemia Cells

How pro-B MLL leukemia cells display differential sensitivity and acquire resistance to proteasome inhibition warrant future investigation. Because overexpression of BCL-2 or BCL-X_L can abrogate bortezomib-induced apoptosis, apoptosis resistance might represent one refractory mechanism. To overcome resistance, the potential clinical administration of proteasome inhibitors in combination with other anticancer agents, such as cell death-based agents including ABT-263 (Tse et al., 2008), warrant further investigation. ABT-263, a small molecule inhibitor of BCL-2, is in clinical trials and has shown effectiveness and selectivity against certain types of cancers (Davids and Letai, 2012; Walensky, 2012). In conclusion, our findings reveal latent tumor suppression programs that can be aroused through hyperactivating oncogenic fusion proteins. This arousal might be suitably exploited as a cancer-specific therapeutic strategy.

EXPERIMENTAL PROCEDURES

Reagents

Bortezomib (Velcade) was obtained from Millennium Pharmaceutical. Carfizomib was obtained from Proteolix.

Plasmid Constructs

FLAG-tagged fragments consisting of MLL amino acids 1–400, 400–750, 1–750, 750–1,400, 1,400–2,664, and 1–1,400 derived from wild-type MLL were inserted into eukaryotic expression vectors pCI-neo (Promega) for transient transfection assays. FLAG-tagged MLL fusion genes, including MLL-AF4 and MLL-AF9, MLL-ENL and MLL-ELL, in eukaryotic expression vector were described previously (Liu et al., 2007). MLL-AF4 and MLL-AF9 were also inserted into pMSCV-puro vector (Clontech) for retrovirus production. Full-length PAX5 and EBF1 were cloned from JM1 cell cDNA and inserted into the pCMV-HA vector (Clontech). Full-length BCL-2 and BCL-X_L were inserted into the pMSCV-puro (Clontech) or pMIG vector (kindly provided by Dr. William Hahn) for retrovirus production. GFP-tagged CrmA was inserted into pMSCV-puro vector (Clontech) for retrovirus production.

shRNA-Mediated Knockdown

Target sequence (agaaaagcagacctactcc and ctttaagcagacctactcc) against human MLL-AF4 in SEM and RS4;11 cells based on published information (Thomas et al., 2005), target sequence (ttgctccacccatcaaacc) against human MLL N terminus, target sequence (gaatggacatcctgtataa) against human p27, and target sequence (ggatgcttgtctatttcta and ggctccccctactattata) against human PAX5 were inserted into the pSUPER.retro.puro vector, according to the manufacturer's protocol (Oligoengine). Generated retrovirus carrying indicated shRNA was used to infect target cells for 2 days, and the cells were subjected to puromycin selection at 2 μg/ml.

Immunoblots

The anti-N terminus MLL (MO435) antibodies were generated using a synthetic peptide of MLL amino acids 752–949 as immunogen. Details of the commercially available antibodies used for immunoblots are available in the Supplemental Experimental Procedures. Antibodies were detected using the enhanced chemiluminescence method (Western Lightning, PerkinElmer). Immunoblot signals were acquired with the LAS-3000 Imaging system (FujiFilm) and were analyzed with ImageGauge software (FujiFilm) as previously described (Liu et al., 2010).

Chromatin Immunoprecipitation Assays

ChIP assays were performed using the Magna ChIP A Kit (Millipore) according to the manufacturer's protocol. One microgram of pre-immune rabbit IgG, anti-MLL (MO435), anti-cyclin T1 (Santa Cruz Biotechnology), or PAX5 (Santa Cruz Biotechnology) antibody was used for each ChIP reaction. Precipitated DNA was analyzed using a ViiA 7 Real-Time PCR System (Applied Biosystems). Primers used for ChIP-PCR assay were CDKN1B Promoter (−50 base pairs [bp] to +74 bp relative to TSS): forward, ccaatggatctcctcctctg, reverse, aaaa caccccgaaaagacg; CDKN1B coding region (+1,441 bp to +1,597 bp relative to TSS): forward, atttcccctgcgcttagatt, reverse, atcaacccaccgagctgtt.

Mouse Studies and In Vivo Imaging

REH and SEM cells were transduced by lentivirus generated using the FUGW-FL lentiviral vector that simultaneously expresses GFP and luciferase (Smith et al., 2004). GFP-positive cells were sorted using MoFlo (Beckman Coulter). NSG mice were purchased from Jackson Laboratory. One million luciferase-expressing cells were intravenously injected via the tail vein into NSG mice. NSG mice were then administered bortezomib intravenously at 0.5 mg/kg on a twice-weekly schedule beginning 2 days after the xenograft. Total body bioluminescence was quantified as previously described (Luker et al., 2003). All animal work was performed in accordance with a protocol approved by the Animal Studies Committee of Washington University in St. Louis.

Statistics

The Student's t test was used to analyze the differences between the groups. A p value less than 0.05 was considered to be statistically significant.

Patients

Retrospective chart review was performed to identify adult patients with MLL leukemia that was treated with bortezomib at the Barnes Jewish Hospital, Washington University in St. Louis, between 2007 and 2010. Institutional Review Board approval for the retrospective data collection was not required. Patients provided verbal consent for the off-label, off-protocol use of bortezomib for those patients with MLL leukemia that failed standard of care therapies. Medical decisions were made at the discretion of the patients' physicians.

SUPPLEMENTAL INFORMATION

Supplemental Information includes Supplemental Experimental Procedures, five figures, and one table and can be found with this article online at http://dx.doi.org/10.1016/j.ccr.2014.03.008.

AUTHOR CONTRIBUTIONS

H.L., T.W., D.P.-W., L.K., E.H., and J.H. designed the experiments; A.C., R.V., and J.D. were physicians for these patients; and H.L., A.C., D. P.-W., C.P., E.C., and J.H. wrote the paper.

ACKNOWLEDGMENTS

We apologize to all the investigators whose research could not be appropriately cited owing to space limitations. This work is supported by R01CA119008, R01CA138505, and the Scholar award of the American Cancer Society to J.J.H. and by R01CA125562 to E.H.C. H.L. is supported by the Chinese National Key Basic Research Project (973: 2013CB966801), the National Natural Science Foundation of China (81370651), the Thousand Young Talents program of China, the Program for Professor of Special Appointment (Eastern Scholar) at Shanghai Institutions of Higher Learning, and the American Society of Hematology Scholar Award. We also thank Ms. Wenjing Wu at the MSK Department of Public Affairs for her expert illustration.

Received: July 9, 2013
Revised: November 24, 2013
Accepted: March 10, 2014
Published: April 14, 2014

REFERENCES

Adams, J. (2004). The proteasome: a suitable antineoplastic target. Nat. Rev. Cancer *4*, 349–360.

Ayton, P.M., and Cleary, M.L. (2001). Molecular mechanisms of leukemogenesis mediated by MLL fusion proteins. Oncogene *20*, 5695–5707.

Barretina, J., Caponigro, G., Stransky, N., Venkatesan, K., Margolin, A.A., Kim, S., Wilson, C.J., Lehár, J., Kryukov, G.V., Sonkin, D., et al. (2012). The Cancer Cell Line Encyclopedia enables predictive modelling of anticancer drug sensitivity. Nature *483*, 603–607.

Bhojwani, D., Howard, S.C., and Pui, C.H. (2009). High-risk childhood acute lymphoblastic leukemia. Clin. Lymphoma Myeloma *9* (*Suppl 3*), S222–S230.

Busslinger, M. (2004). Transcriptional control of early B cell development. Annu. Rev. Immunol. *22*, 55–79.

Caslini, C., Shilatifard, A., Yang, L., and Hess, J.L. (2000). The amino terminus of the mixed lineage leukemia protein (MLL) promotes cell cycle arrest and monocytic differentiation. Proc. Natl. Acad. Sci. USA *97*, 2797–2802.

Chen, Y.N., Sharma, S.K., Ramsey, T.M., Jiang, L., Martin, M.S., Baker, K., Adams, P.D., Bair, K.W., and Kaelin, W.G., Jr. (1999). Selective killing of transformed cells by cyclin/cyclin-dependent kinase 2 antagonists. Proc. Natl. Acad. Sci. USA *96*, 4325–4329.

Cheng, E.H., Wei, M.C., Weiler, S., Flavell, R.A., Mak, T.W., Lindsten, T., and Korsmeyer, S.J. (2001). BCL-2, BCL-X(L) sequester BH3 domain-only molecules preventing BAX- and BAK-mediated mitochondrial apoptosis. Mol. Cell *8*, 705–711.

Chu, I.M., Hengst, L., and Slingerland, J.M. (2008). The Cdk inhibitor p27 in human cancer: prognostic potential and relevance to anticancer therapy. Nat. Rev. Cancer *8*, 253–267.

Cvek, B., and Dvorak, Z. (2011). The ubiquitin-proteasome system (UPS) and the mechanism of action of bortezomib. Curr. Pharm. Des. *17*, 1483–1499.

Danial, N.N., and Korsmeyer, S.J. (2004). Cell death: critical control points. Cell *116*, 205–219.

Davids, M.S., and Letai, A. (2012). Targeting the B-cell lymphoma/leukemia 2 family in cancer. J. Clin. Oncol. *30*, 3127–3135.

Demo, S.D., Kirk, C.J., Aujay, M.A., Buchholz, T.J., Dajee, M., Ho, M.N., Jiang, J., Laidig, G.J., Lewis, E.R., Parlati, F., et al. (2007). Antitumor activity of PR-171, a novel irreversible inhibitor of the proteasome. Cancer Res. *67*, 6383–6391.

Dou, Y., Milne, T.A., Ruthenburg, A.J., Lee, S., Lee, J.W., Verdine, G.L., Allis, C.D., and Roeder, R.G. (2006). Regulation of MLL1 H3K4 methyltransferase activity by its core components. Nat. Struct. Mol. Biol. *13*, 713–719.

Drexler, H.G., Quentmeier, H., and MacLeod, R.A. (2004). Malignant hematopoietic cell lines: in vitro models for the study of MLL gene alterations. Leukemia *18*, 227–232.

Egle, A., Harris, A.W., Bouillet, P., and Cory, S. (2004). Bim is a suppressor of Myc-induced mouse B cell leukemia. Proc. Natl. Acad. Sci. USA *101*, 6164–6169.

Fennell, D.A., Chacko, A., and Mutti, L. (2008). BCL-2 family regulation by the 20S proteasome inhibitor bortezomib. Oncogene *27*, 1189–1197.

Garcia-Calvo, M., Peterson, E.P., Leiting, B., Ruel, R., Nicholson, D.W., and Thornberry, N.A. (1998). Inhibition of human caspases by peptide-based and macromolecular inhibitors. J. Biol. Chem. *273*, 32608–32613.

Gonzalvez, F., Lawrence, D., Yang, B., Yee, S., Pitti, R., Marsters, S., Pham, V.C., Stephan, J.P., Lill, J., and Ashkenazi, A. (2012). TRAF2 Sets a threshold for extrinsic apoptosis by tagging caspase-8 with a ubiquitin shutoff timer. Mol. Cell *48*, 888–899.

Hanahan, D., and Weinberg, R.A. (2011). Hallmarks of cancer: the next generation. Cell *144*, 646–674.

Hemann, M.T., Zilfou, J.T., Zhao, Z., Burgess, D.J., Hannon, G.J., and Lowe, S.W. (2004). Suppression of tumorigenesis by the p53 target PUMA. Proc. Natl. Acad. Sci. USA *101*, 9333–9338.

Hemann, M.T., Bric, A., Teruya-Feldstein, J., Herbst, A., Nilsson, J.A., Cordon-Cardo, C., Cleveland, J.L., Tansey, W.P., and Lowe, S.W. (2005). Evasion of the p53 tumour surveillance network by tumour-derived MYC mutants. Nature *436*, 807–811.

Hideshima, T., Ikeda, H., Chauhan, D., Okawa, Y., Raje, N., Podar, K., Mitsiades, C., Munshi, N.C., Richardson, P.G., Carrasco, R.D., and Anderson, K.C. (2009). Bortezomib induces canonical nuclear factor-kappaB activation in multiple myeloma cells. Blood *114*, 1046–1052.

Hsieh, J.J., Cheng, E.H., and Korsmeyer, S.J. (2003). Taspase1: a threonine aspartase required for cleavage of MLL and proper HOX gene expression. Cell *115*, 293–303.

Karnik, S.K., Hughes, C.M., Gu, X., Rozenblatt-Rosen, O., McLean, G.W., Xiong, Y., Meyerson, M., and Kim, S.K. (2005). Menin regulates pancreatic islet growth by promoting histone methylation and expression of genes encoding p27Kip1 and p18INK4c. Proc. Natl. Acad. Sci. USA *102*, 14659–14664.

Kim, H., Rafiuddin-Shah, M., Tu, H.C., Jeffers, J.R., Zambetti, G.P., Hsieh, J.J., and Cheng, E.H. (2006). Hierarchical regulation of mitochondrion-dependent apoptosis by BCL-2 subfamilies. Nat. Cell Biol. *8*, 1348–1358.

Kim, H., Tu, H.C., Ren, D., Takeuchi, O., Jeffers, J.R., Zambetti, G.P., Hsieh, J.J., and Cheng, E.H. (2009). Stepwise activation of BAX and BAK by tBID, BIM, and PUMA initiates mitochondrial apoptosis. Mol. Cell *36*, 487–499.

Krivtsov, A.V., and Armstrong, S.A. (2007). MLL translocations, histone modifications and leukaemia stem-cell development. Nat. Rev. Cancer *7*, 823–833.

Liedtke, M., and Cleary, M.L. (2009). Therapeutic targeting of MLL. Blood *113*, 6061–6068.

Liu, H., Cheng, E.H., and Hsieh, J.J. (2007). Bimodal degradation of MLL by SCFSkp2 and APCCdc20 assures cell cycle execution: a critical regulatory circuit lost in leukemogenic MLL fusions. Genes Dev. *21*, 2385–2398.

Liu, H., Cheng, E.H., and Hsieh, J.J. (2009). MLL fusions: pathways to leukemia. Cancer Biol. Ther. *8*, 1204–1211.

Liu, H., Takeda, S., Kumar, R., Westergard, T.D., Brown, E.J., Pandita, T.K., Cheng, E.H., and Hsieh, J.J. (2010). Phosphorylation of MLL by ATR is required for execution of mammalian S-phase checkpoint. Nature *467*, 343–346.

Lowe, S.W., Cepero, E., and Evan, G. (2004). Intrinsic tumour suppression. Nature *432*, 307–315.

Luker, G.D., Pica, C.M., Song, J., Luker, K.E., and Piwnica-Worms, D. (2003). Imaging 26S proteasome activity and inhibition in living mice. Nat. Med. *9*, 969–973.

Luo, J., Solimini, N.L., and Elledge, S.J. (2009). Principles of cancer therapy: oncogene and non-oncogene addiction. Cell *136*, 823–837.

Mendoza, N., Fong, S., Marsters, J., Koeppen, H., Schwall, R., and Wickramasinghe, D. (2003). Selective cyclin-dependent kinase 2/cyclin

A antagonists that differ from ATP site inhibitors block tumor growth. Cancer Res. *63*, 1020–1024.

Milne, T.A., Briggs, S.D., Brock, H.W., Martin, M.E., Gibbs, D., Allis, C.D., and Hess, J.L. (2002). MLL targets SET domain methyltransferase activity to Hox gene promoters. Mol. Cell *10*, 1107–1117.

Milne, T.A., Hughes, C.M., Lloyd, R., Yang, Z., Rozenblatt-Rosen, O., Dou, Y., Schnepp, R.W., Krankel, C., Livolsi, V.A., Gibbs, D., et al. (2005). Menin and MLL cooperatively regulate expression of cyclin-dependent kinase inhibitors. Proc. Natl. Acad. Sci. USA *102*, 749–754.

Mohan, M., Lin, C., Guest, E., and Shilatifard, A. (2010). Licensed to elongate: a molecular mechanism for MLL-based leukaemogenesis. Nat. Rev. Cancer *10*, 721–728.

Muntean, A.G., and Hess, J.L. (2012). The pathogenesis of mixed-lineage leukemia. Annu. Rev. Pathol. *7*, 283–301.

Murphy, D.J., Junttila, M.R., Pouyet, L., Karnezis, A., Shchors, K., Bui, D.A., Brown-Swigart, L., Johnson, L., and Evan, G.I. (2008). Distinct thresholds govern Myc's biological output in vivo. Cancer Cell *14*, 447–457.

Muzio, M., Chinnaiyan, A.M., Kischkel, F.C., O'Rourke, K., Shevchenko, A., Ni, J., Scaffidi, C., Bretz, J.D., Zhang, M., Gentz, R., et al. (1996). FLICE, a novel FADD-homologous ICE/CED-3-like protease, is recruited to the CD95 (Fas/APO-1) death—inducing signaling complex. Cell *85*, 817–827.

Oyama, T., Sasagawa, S., Takeda, S., Hess, R.A., Lieberman, P.M., Cheng, E.H., and Hsieh, J.J. (2013). Cleavage of TFIIA by Taspase1 activates TRF2-specified mammalian male germ cell programs. Dev. Cell *27*, 188–200.

Pelengaris, S., Khan, M., and Evan, G.I. (2002). Suppression of Myc-induced apoptosis in beta cells exposes multiple oncogenic properties of Myc and triggers carcinogenic progression. Cell *109*, 321–334.

Perciavalle, R.M., and Opferman, J.T. (2013). Delving deeper: MCL-1's contributions to normal and cancer biology. Trends Cell Biol. *23*, 22–29.

Ren, D., Tu, H.C., Kim, H., Wang, G.X., Bean, G.R., Takeuchi, O., Jeffers, J.R., Zambetti, G.P., Hsieh, J.J., and Cheng, E.H. (2010). BID, BIM, and PUMA are essential for activation of the BAX- and BAK-dependent cell death program. Science *330*, 1390–1393.

Sarkisian, C.J., Keister, B.A., Stairs, D.B., Boxer, R.B., Moody, S.E., and Chodosh, L.A. (2007). Dose-dependent oncogene-induced senescence in vivo and its evasion during mammary tumorigenesis. Nat. Cell Biol. *9*, 493–505.

Sharma, S.V., and Settleman, J. (2007). Oncogene addiction: setting the stage for molecularly targeted cancer therapy. Genes Dev. *21*, 3214–3231.

Smith, M.C., Luker, K.E., Garbow, J.R., Prior, J.L., Jackson, E., Piwnica-Worms, D., and Luker, G.D. (2004). CXCR4 regulates growth of both primary and metastatic breast cancer. Cancer Res. *64*, 8604–8612.

Takeda, S., Chen, D.Y., Westergard, T.D., Fisher, J.K., Rubens, J.A., Sasagawa, S., Kan, J.T., Korsmeyer, S.J., Cheng, E.H., and Hsieh, J.J. (2006). Proteolysis of MLL family proteins is essential for taspase1-orchestrated cell cycle progression. Genes Dev. *20*, 2397–2409.

Takeda, S., Liu, H., Sasagawa, S., Dong, Y., Trainor, P.A., Cheng, E.H., and Hsieh, J.J. (2013). HGF-MET signals via the MLL-ETS2 complex in hepatocellular carcinoma. J. Clin. Invest. *123*, 3154–3165.

Thiel, A.T., Blessington, P., Zou, T., Feather, D., Wu, X., Yan, J., Zhang, H., Liu, Z., Ernst, P., Koretzky, G.A., and Hua, X. (2010). MLL-AF9-induced leukemogenesis requires coexpression of the wild-type Mll allele. Cancer Cell *17*, 148–159.

Thomas, M., Gessner, A., Vornlocher, H.P., Hadwiger, P., Greil, J., and Heidenreich, O. (2005). Targeting MLL-AF4 with short interfering RNAs inhibits clonogenicity and engraftment of t(4;11)-positive human leukemic cells. Blood *106*, 3559–3566.

Tse, C., Shoemaker, A.R., Adickes, J., Anderson, M.G., Chen, J., Jin, S., Johnson, E.F., Marsh, K.C., Mitten, M.J., Nimmer, P., et al. (2008). ABT-263: a potent and orally bioavailable Bcl-2 family inhibitor. Cancer Res. *68*, 3421–3428.

Walensky, L.D. (2012). From mitochondrial biology to magic bullet: navitoclax disarms BCL-2 in chronic lymphocytic leukemia. J. Clin. Oncol. *30*, 554–557.

Wang, Z., Smith, K.S., Murphy, M., Piloto, O., Somervaille, T.C., and Cleary, M.L. (2008). Glycogen synthase kinase 3 in MLL leukaemia maintenance and targeted therapy. Nature *455*, 1205–1209.

Wang, J., Muntean, A.G., and Hess, J.L. (2012). ECSASB2 mediates MLL degradation during hematopoietic differentiation. Blood *119*, 1151–1161.

Xia, Z.B., Popovic, R., Chen, J., Theisler, C., Stuart, T., Santillan, D.A., Erfurth, F., Diaz, M.O., and Zeleznik-Le, N.J. (2005). The MLL fusion gene, MLL-AF4, regulates cyclin-dependent kinase inhibitor CDKN1B (p27kip1) expression. Proc. Natl. Acad. Sci. USA *102*, 14028–14033.

Yip, B.H., and So, C.W. (2013). Mixed lineage leukemia protein in normal and leukemic stem cells. Exp. Biol. Med. (Maywood) *238*, 315–323.

Yokoyama, A., Somervaille, T.C., Smith, K.S., Rozenblatt-Rosen, O., Meyerson, M., and Cleary, M.L. (2005). The menin tumor suppressor protein is an essential oncogenic cofactor for MLL-associated leukemogenesis. Cell *123*, 207–218.

Yokoyama, A., Lin, M., Naresh, A., Kitabayashi, I., and Cleary, M.L. (2010). A higher-order complex containing AF4 and ENL family proteins with P-TEFb facilitates oncogenic and physiologic MLL-dependent transcription. Cancer Cell *17*, 198–212.

Zhang, J., Seet, C.S., Sun, C., Li, J., You, D., Volk, A., Breslin, P., Li, X., Wei, W., Qian, Z., et al. (2013). p27kip1 maintains a subset of leukemia stem cells in the quiescent state in murine MLL-leukemia. Mol. Oncol. *7*, 1069–1082.

Cancer Cell
Errata

Oncogenic *ERBB3* Mutations in Human Cancers

Bijay S. Jaiswal, Noelyn M. Kljavin, Eric W. Stawiski, Emily Chan, Chaitali Parikh, Steffen Durinck, Subhra Chaudhuri, Kanan Pujara, Joseph Guillory, Kyle A. Edgar, Vasantharajan Janakiraman, Rolf-Peter Scholz, Krista K. Bowman, Maria Lorenzo, Hong Li, Jiansheng Wu, Wenlin Yuan, Brock A. Peters, Zhengyan Kan, Jeremy Stinson, Michelle Mak, Zora Modrusan, Charles Eigenbrot, Ron Firestein, Howard M. Stern, Krishnaraj Rajalingam, Gabriele Schaefer, Mark A. Merchant, Mark X. Sliwkowski, Frederic J. de Sauvage, and Somasekar Seshagiri*
*Correspondence: sekar@gene.com
http://dx.doi.org/10.1016/j.ccr.2014.03.030

(Cancer Cell *23*, 603–617; May 13, 2013)

The authors recently became aware of an error in the top panel of Figure 2D showing the expression of ERBB3. An incorrect panel, meant to show ERBB3 expression, was inadvertently included when the figure was originally assembled. The incorrect panel has been replaced below with the correct western blot showing the expression of ERBB3. The correction does not affect the findings reported in the paper. The authors apologize for any confusion the error may have caused.

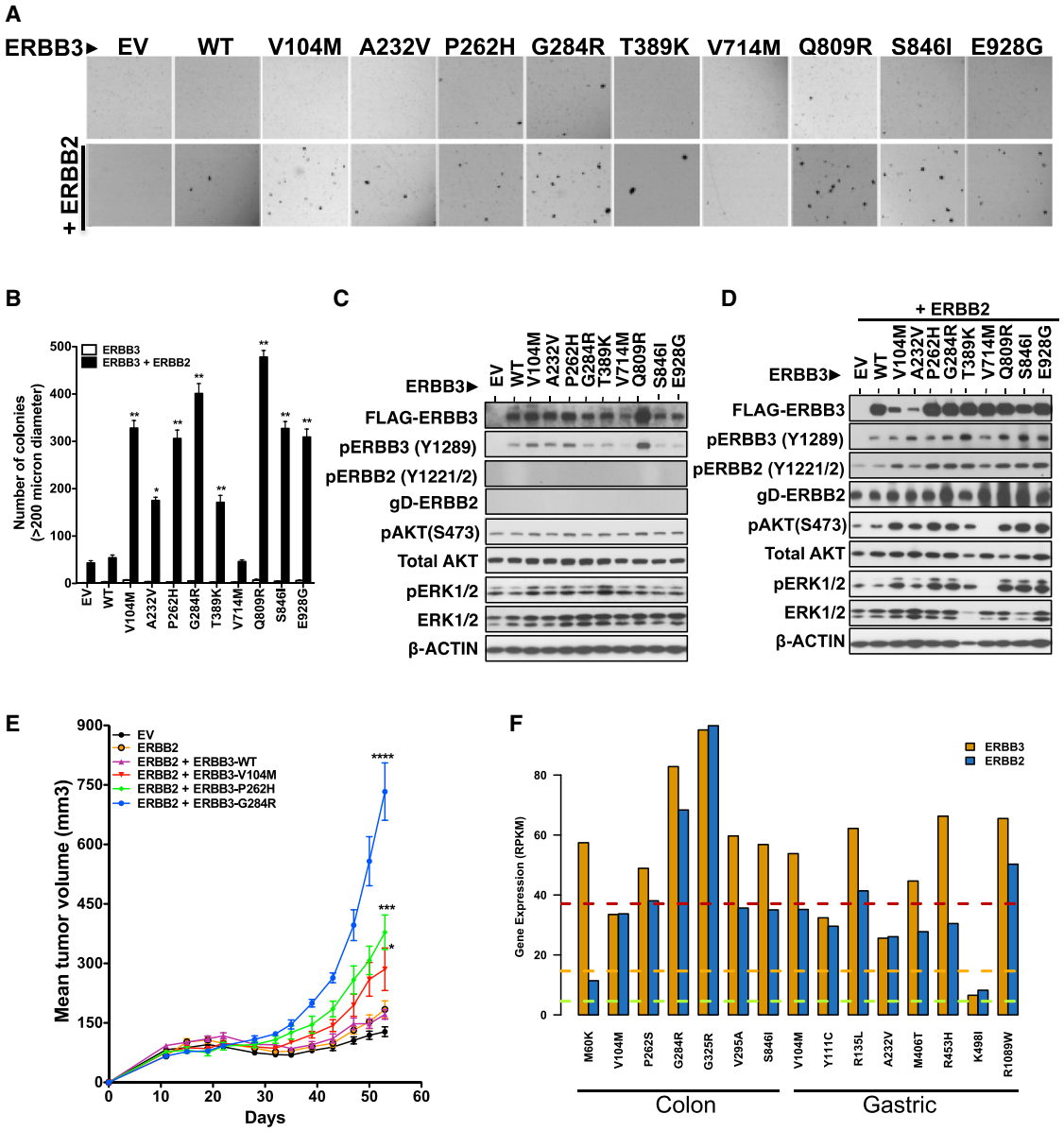

Figure 2. ERBB3 Mutants Support Transformation and In Vivo Tumor Growth of IMCE Colonic Epithelial Cells

Cancer Cell
Errata

Discovery and Characterization of Super-Enhancer-Associated Dependencies in Diffuse Large B Cell Lymphoma

Bjoern Chapuy, Michael R. McKeown, Charles Y. Lin, Stefano Monti, Margaretha G.M. Roemer, Jun Qi, Peter B. Rahl, Heather H. Sun, Kelly T. Yeda, John G. Doench, Elaine Reichert, Andrew L. Kung, Scott J. Rodig, Richard A. Young, Margaret A. Shipp,* and James E. Bradner*
*Correspondence: margaret_shipp@dfci.harvard.edu (M.A.S.), james_bradner@dfci.harvard.edu (J.E.B.)
http://dx.doi.org/10.1016/j.ccr.2014.03.029

(Cancer Cell *24*, 777–790; December 9, 2013)
Following publication of the manuscript, the authors identified an inadvertent error in labeling of the H3K27ac ChIP-Seq tracks at the *PAX5* locus in Figure 7E. The revised Figure 7E, shown below, includes the correctly labeled H3K27ac tracks of the *PAX5* locus in the indicated cell lines and normal tissue control (tonsil) and illustrates the presence of a *PAX5* super-enhancer in each of these cell lines and tonsil. The conclusions remain the same.

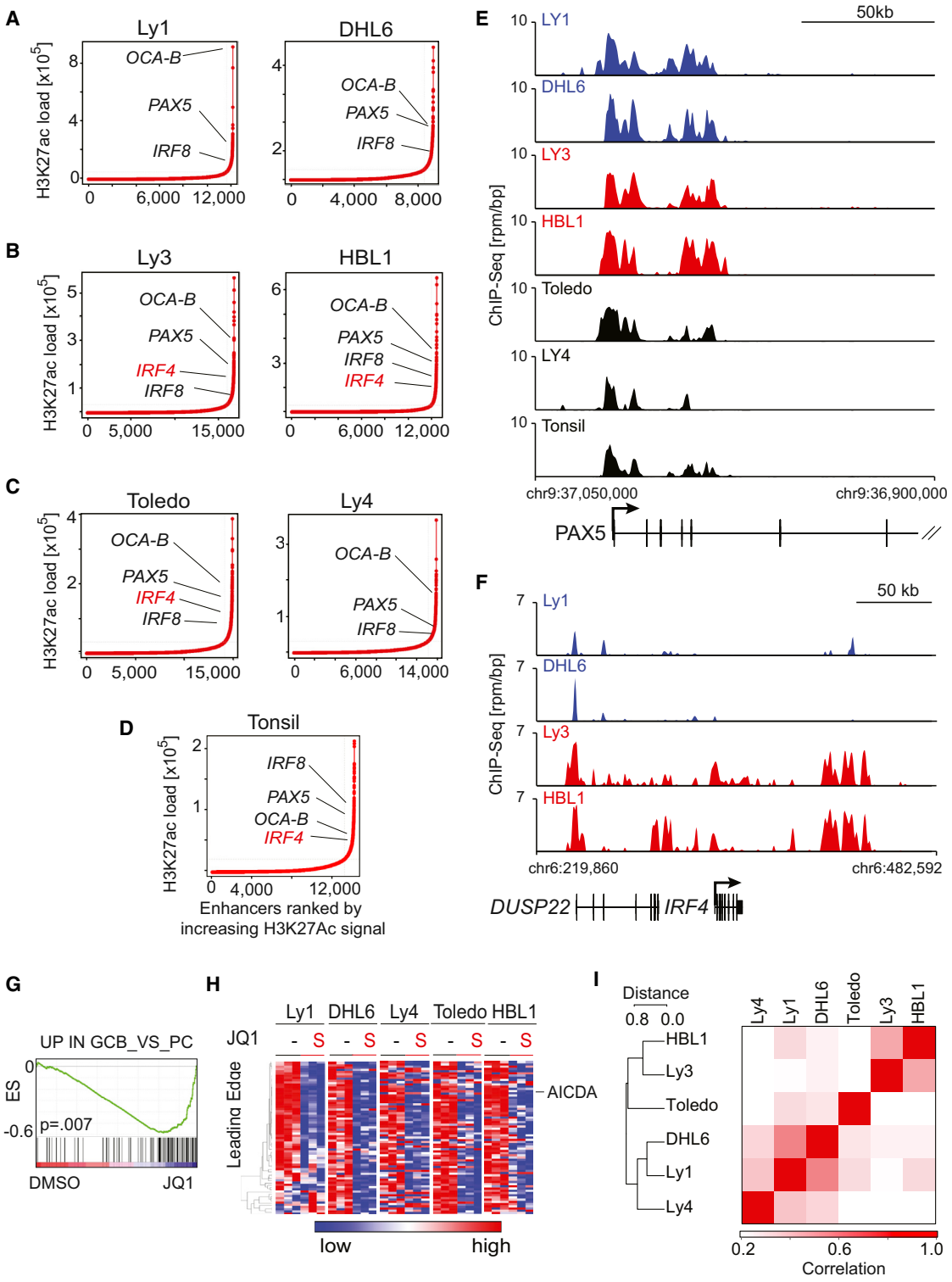

Figure 7. Comparative SE Analysis of DLBCL Cell Lines and Normal Lymphoid Tissue

Cancer Cell
Errata

Cbx4 Governs HIF-1α to Potentiate Angiogenesis of Hepatocellular Carcinoma by Its SUMO E3 Ligase Activity

Jie Li, Ying Xu, Xi-Dai Long, Wei Wang, Hui-Ke Jiao, Zhu Mei, Qian-Qian Yin, Li-Na Ma, Ai-Wu Zhou, Li-Shun Wang, Ming Yao, Qiang Xia, and Guo-Qiang Chen*
*Correspondence: chengq@shsmu.edu.cn
http://dx.doi.org/10.1016/j.ccr.2014.03.013

(Cancer Cell *25*, 118–131; January 13, 2014)

During the course of preparing the HE image of the wild-type (WT) group in Figure 8E, the authors inadvertently duplicated the HE image of the WT from Figure 7F. This was a mistake in constructing these figures. The correction to the HE image of the WT group in Figure 8E does not affect the conclusion of the paper. The authors apologize for any inconvenience that it may have caused. The corrected Figure 8 is printed below.

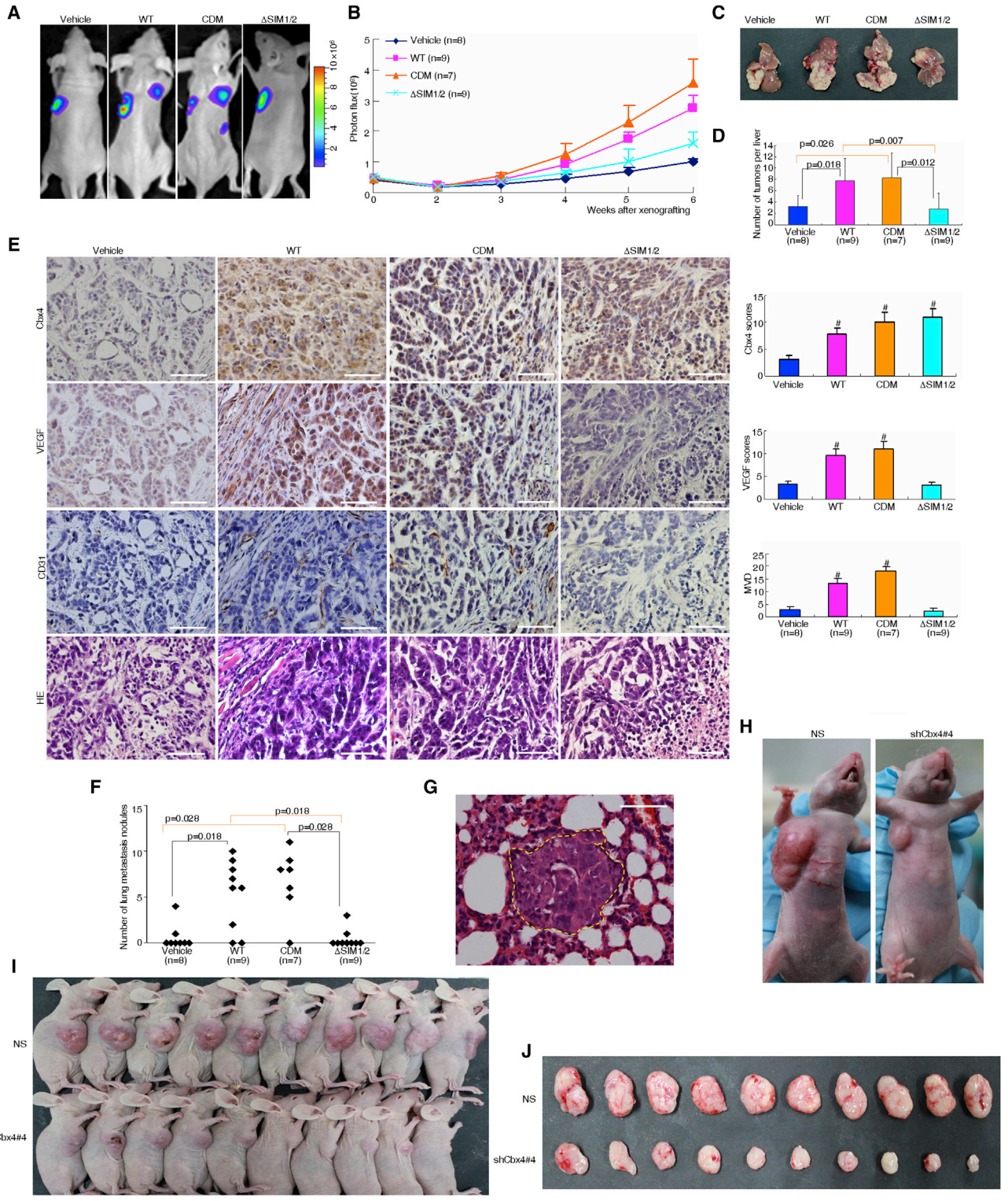

Figure 8. In Vivo Effects of Cbx4 on Tumor Invasion

SnapShot: Hepatocellular Carcinoma

Jens U. Marquardt[1] and Snorri S. Thorgeirsson[2]
[1]Department of Medicine I, Johannes Gutenberg University of Mainz, 55131 Mainz, Germany
[2]Laboratory of Experimental Carcinogenesis, CCR/NCI/NIH, Bethesda, MD 20892, USA

Cancer Cell

CLINICAL PROGRESSION OF LIVER CANCER

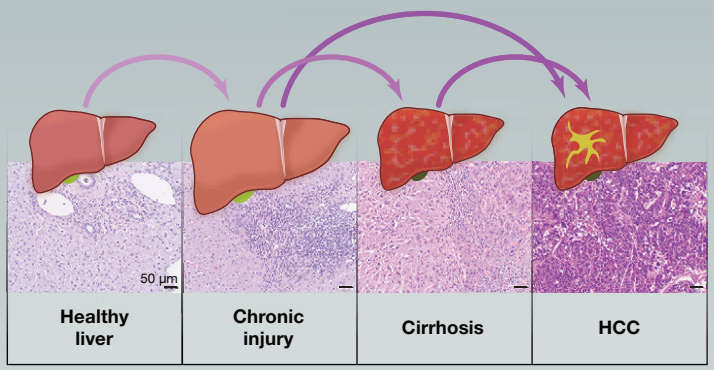

UNIFOCAL HCC

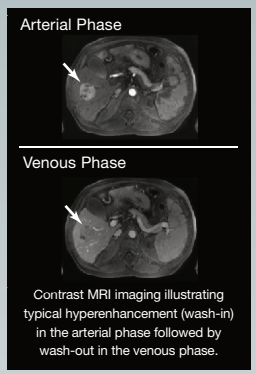

Contrast MRI imaging illustrating typical hyperenhancement (wash-in) in the arterial phase followed by wash-out in the venous phase.

CELL TYPES OF ORIGIN FOR HCC

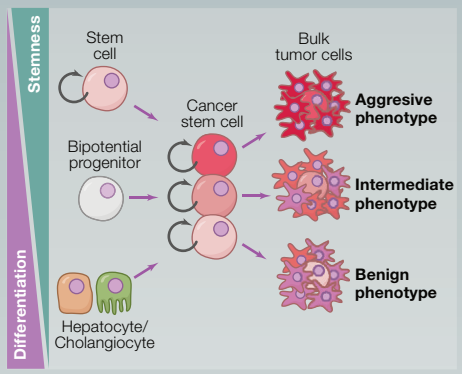

PROGNOSTIC CLASSIFICATION

	Favorable Outcome	Poor Outcome
Clinical/ Morphological features	▪ ECOG 0–1 Well-preserved liver function ▪ High differentiation Hepatocyte morphology ▪ Smaller tumors No vascular invasion	▪ ECOG >2 ▪ Poor liver function Poor differentiation CK19 positive ▪ Larger tumors Vascular invasion Extrahepatic spread
Molecular features	▪ Genomic stability Telomerase repression ▪ *CTNNB1* mutation Polysomy 7 ▪ High miR-122 Low miR-517a ▪ Expression of differentiation factors: HNF4α, CYPs ▪ Low Nault 5-gene score ▪ Beneficial subclass: G4-G5, S3 ▪ Beneficial metabolic profile	▪ Genomic instability Telomerase reactivation ▪ Loss of 8p Global hypomethylation ▪ Low miR-122 High miR-517a ▪ Stemness features: EpCAM, SALL4 ▪ High Nault 5-gene score ▪ Adverse subclass: G1-G3, S1-2, proliferation, HA subtype ▪ Adverse metabolic profile: stearoyl-CoA-desaturase activity, palmitate signaling ▪ Adverse signaling: HGF/MET, TGF-β, CK19, mTOR, IGF, MYC, AKT, WNT, loss of p53

BCLC STAGING & THERAPY

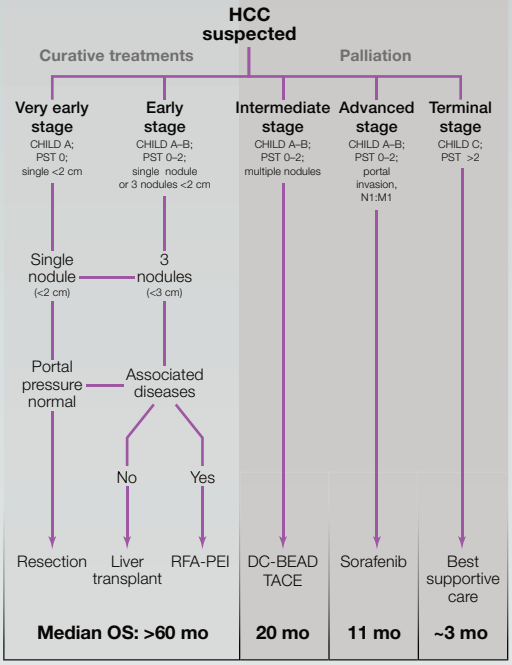

KEY GENETIC ALTERATIONS

Telomere Maintanance
Genes: ***TERT***
Cumulative frequency: **20%-60%**

WNT/β-Catenin
Genes: ***CTNNB1, AXIN1/2, APC***
Cumulative frequency: **2%-33%**

Cell Cycle
Genes: ***TP53, CKN2A/B, CCND/E1, CDKs, RB1***
Cumulative frequency: **4%-35%**

Apoptosis
Genes: ***TNFRSF10A/B, TRADD, CASP3/9, XIAP***
Cumulative frequency: **8%-20%**

Epigenetic Modifiers
Genes: ***ARID1A, ARID2, MLL genes***
Cumulative frequency: **10%-24%**

Proliferation
Genes: ***FGF19, RPS6KA, IRF2, KRAS***
Cumulative frequency: **2%-15%**

Immune Response
Genes: ***IL6R, IL20, IL6, JAK1***
Cumulative frequency: **2%-26%**

Oxidative Stress Regulation
Genes: ***NFEL2, KEAP1***
Cumulative frequency: **6%-8%**

EMERGING MOLECULAR TARGETS

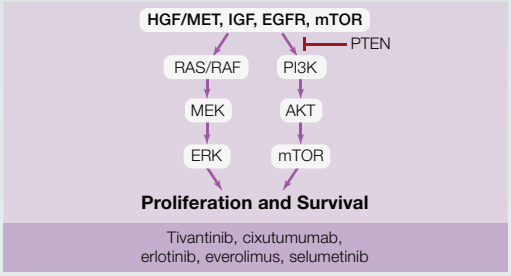

Tivantinib, cixutumumab, erlotinib, everolimus, selumetinib

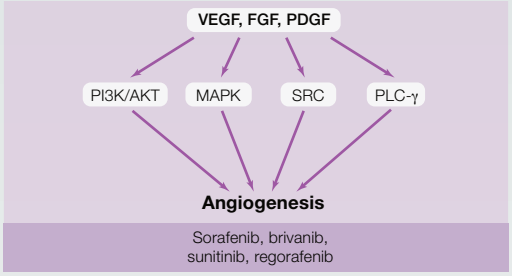

Sorafenib, brivanib, sunitinib, regorafenib

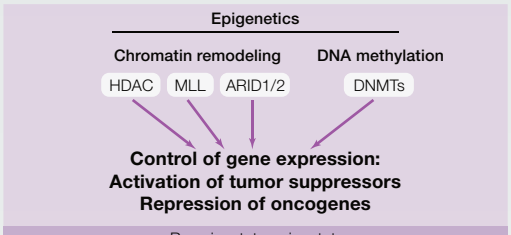

Resminostat, vorinostat, belinostat, zebularine

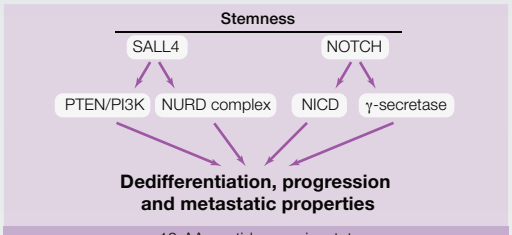

12-AA peptide, resminostat, γ-secretase inhibitors

CHALLENGES & OUTLOOK

- HCC develops on the basis of a predisposing liver disease that causes a chronically altered microenvironment.
- HCC is characterized by phenotypic and molecular heterogeneity reflecting a diverse cellular origin.
- Biopsies are not mandatory to establish the diagnosis. However, biopsies are of utmost importance for molecular classification and individualized therapeutic approaches.
- Our understanding of (epi)genetic pathophysiology is incomplete.
- The most common genetic alterations affect hTERT, β-catenin, and p53. No clear evidence for oncogene addiction has been demonstrated.
- In clinical routine, liver function frequently limits therapeutic options.
- Recurrence rate is high despite curative therapeutic intentions.
- There is an unmet need for new therapies and improved understanding of cancer biology.
- Novel innovative therapeutic strategies involve targeting of stem cell features as well as immune response.

See online version for legend and references.

SnapShot: Hepatocellular Carcinoma

Cancer Cell

Jens U. Marquardt[1] and Snorri S. Thorgeirsson[2]
[1]Department of Medicine I, Johannes Gutenberg University of Mainz, 55131 Mainz, Germany
[2]Laboratory of Experimental Carcinogenesis, CCR/NCI/NIH, Bethesda, MD 20892, USA

Hepatocellular carcinoma (HCC) is the sixth most common cancer globally, with a prevalence of around 600,000 people worldwide. HCC incidence has risen steadily over the last 20 years in western countries such as the United States, Europe, and Japan, predominantly due to increased rates of chronic Hepatitis C virus infections, alcohol abuse, obesity, and type 2 diabetes. As a result, HCC is one of the most rapidly growing cancers in these countries. The number of deaths is proportional to the global incidence, which highlights the aggressive tumor biology and lack of effective therapies. These observations manifest the fact that liver cancer is a major health problem in the United States and Europe and highlight the critical need for improved understanding and better treatment options for this deadly disease.

Sequential Evolution and Cell of Origin

Hepatocarcinogenesis is a complex multistep process driven by chronic hepatitis that alters the hepatic microenvironment. The earliest dysplastic lesions generally develop in cirrhotic livers. Chronic inflammation and liver cirrhosis predispose HCC development by creating an adverse protumorigenic microenvironment that generates pro-oncogenic (epi)genetic changes.

Accumulating evidence indicates that only a subpopulation of cells within liver cancer harbors genuine tumorigenic potential. While the existence of cells with self-renewing capacity in HCC is well supported, the origin of these cells remains uncertain. Experimental evidence suggests that any cell of the hepatic lineage (i.e., hepatocytes/cholangiocytes, progenitor cells, stem cells) can acquire stem cell properties and become a cancer stem cell (CSC) upon acquiring (epi)genetic alterations. However, hepatic CSCs are clearly heterogeneous and may therefore contribute to the observed morphological and biological heterogeneity characteristic of HCC. The CSCs not only initiate HCC, but also drive distant metastasis and relapse after therapy, thereby establishing CSCs as important therapeutic targets.

Genetic Alterations and Key Pathways

The multistep sequence of epigenetic and genetic alterations in liver cancer pathogenesis disrupts core cellular processes such as proliferation, cell death, and genome maintenance. In addition, oncogenic pathways and molecules associated with stemness, angiogenesis, and immune response are changed in HCC due to aberrant signaling downstream of pathways orchestrated by p53, WNT, β-Catenin, MYC, and ErbB family proteins. Therefore, the goal of therapeutic approaches in HCC is the specific targeting of these signaling pathways.

The advent of sophisticated next-generation sequencing technologies has allowed detailed genetic mapping of the liver cancers. Similar to the phenotypic heterogeneity of HCC, the landscape of molecular alterations in HCC is quite extensive. The average mutational burden varies substantially across different tumors and ranges from five to 121 mutations. Unlike other solid tumors (such as in lung, breast, or colon cancers), an important hallmark of HCC is the absence of clear addiction to an oncogene; this impedes the development of targeted therapies. However, highly recurrent somatic mutations are found in genes products in p53 and Wnt/β-Catenin pathways. Other frequently altered genes include those involved in epigenetic modification, proliferation, immune response, and oxidative stress response. Interestingly, among the most prominent and earliest changes present in HCC are genetic changes in the *TERT* promoter, which is observed in up to 60% of advanced HCC cases. Among the future challenges will be the identification of druggable mutations in individual HCCs (such as JAK1 activating mutations observed in up to 10% of HCCs), which might provide an option for novel individualized therapeutic interventions.

Prognostic Classification and Staging

Over the last decade, several phenotypic and molecular HCC hallmarks, which are associated with different prognoses, have been identified. However, the application of these features in clinical settings has so far been limited. A promising prognostic classification includes a newly developed 5-gene score based on combined expression of HN1, RAN, RAMP3, KRT19, and TAF9 that might provide an important step for efficient translational studies. Prospective validation of the score is currently under way.

Patients at risk for HCC development should be screened by abdominal ultrasound every 6 months. The diagnosis HCC can be accurately established by modern imaging techniques such as contrast-enhanced CT or MRI. Once the diagnosis is established, HCCs can be classified according to the Barcelona Clinic Liver Cancer (BCLC) staging classification. The BCLC is widely accepted in clinical practice; it is the first staging that links liver disease stage to a specific treatment strategy and corresponding survival outlook for patients. Liver transplantation and resection are effective therapeutic options at early stages, but more than 70% of HCC patients present with incurable stages.

Emerging Therapies, Challenges, and Outlook

Therapeutic approaches involve the direct targeting of relevant as well as druggable signaling pathways by using a variety of receptor tyrosine kinase inhibitors (RTKi). Several preclinical studies and ongoing clinical trials have shown that targeting of universal oncogenic features such as proliferation and angiogenesis by sequential or concomitant inhibition of overlapping downstream signaling pathways might be an effective treatment strategy for HCC. Other highly innovative approaches involve targeting HCC-specific characteristics related to immune modulation, epigenetic modifications, and stemness.

Liver cancer is the second most lethal cancer worldwide. The phenotypic and molecular heterogeneity of HCC as well as underlying associated chronic inflammatory liver diseases have limited therapeutic options and progress. To date, the RTKi Sorafenib is the only approved treatment for advanced HCCs. Recently, several clinical phase III trials have failed to demonstrate improved overall survival in HCC patients, indicating an unmet need for novel therapeutic strategies. Achieving this goal will require mandatory biopsies and application of next-generation sequencing technologies for molecular analyses. Implementation of recent translational genomic discoveries into routine clinical practice will likely improve the identification of relevant clinical HCC subclasses that might benefit from specific therapies.

ACKNOWLEDGMENTS

J.U.M. is supported by a grant from the German Research Foundation (MA 4443/2-1). We thank Roman Klöckner and Timo Gaiser for help with the radiographic and histological images.

REFERENCES

El-Serag, H.B. (2011). N. Engl. J. Med. *365*, 1118–1127.

European Association For The Study Of The Liver; European Organisation For Research And Treatment Of Cancer (2012). J. Hepatol. *56*, 908–943.

Holczbauer, A., Factor, V.M., Andersen, J.B., Marquardt, J.U., Kleiner, D.E., Raggi, C., Kitade, M., Seo, D., Akita, H., Durkin, M.E., and Thorgeirsson, S.S. (2013). Gastroenterology *145*, 221–231.

Kan, Z., Zheng, H., Liu, X., Li, S., Barber, T.D., Gong, Z., Gao, H., Hao, K., Willard, M.D., Xu, J., et al. (2013). Genome Res. *23*, 1422–1433.

Marquardt, J.U., and Thorgeirsson, S.S. (2013). N. Engl. J. Med. *368*, 2316–2318.

Marquardt, J.U., Galle, P.R., and Teufel, A. (2012). J. Hepatol. *56*, 267–275.

Nault, J.C., De Reyniès, A., Villanueva, A., Calderaro, J., Rebouissou, S., Couchy, G., Decaens, T., Franco, D., Imbeaud, S., Rousseau, F., et al. (2013). Gastroenterology *145*, 176–187.

Thorgeirsson, S.S. (2006). Gastroenterology *131*, 1344–1346.

Villanueva, A., and Llovet, J.M. (2014). Nat. Rev. Clin. Oncol. *11*, 73–74.

Visvader, J.E., and Lindeman, G.J. (2008). Nat. Rev. Cancer *8*, 755–768.

  DOI http://dx.doi.org/10.1016/j.ccr.2014.04.002